# RATIONAL DESIGN AND CHARACTERIZATION OF INNOVATIVE MULTIFUNCTIONAL BIOMIMETIC MATERIALS

EDITED BY: Lia Rimondini, Lorenzo Moroni and Andrea Cochis
PUBLISHED IN: Frontiers in Materials and Frontiers in Bioengineering and Biotechnology

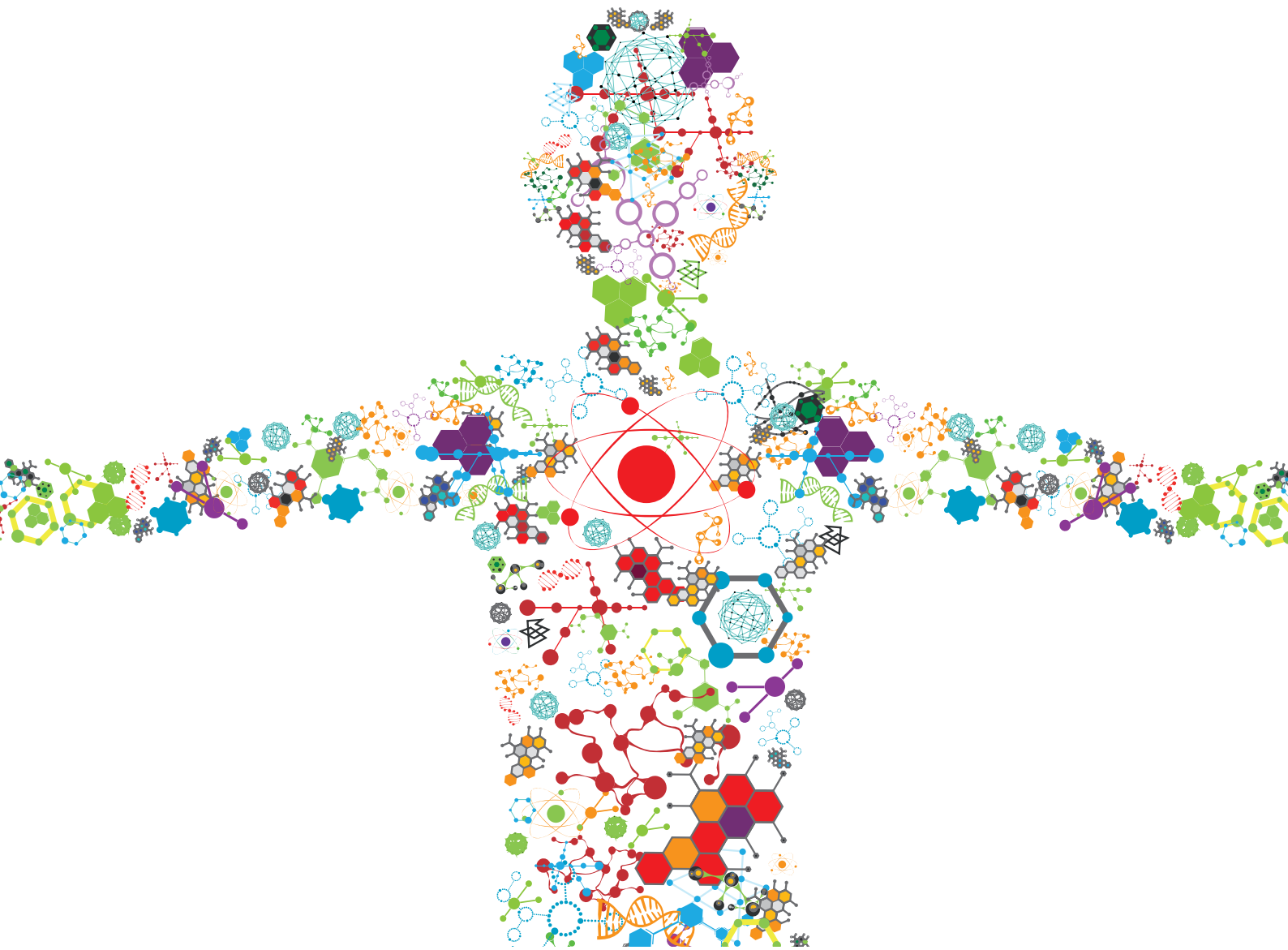

frontiers Research Topics

# frontiers



ISSN 1664-8714
ISBN 978-2-88966-687-4
DOI 10.3389/978-2-88966-687-4

## About Frontiers

Frontiers is more than just an open-access publisher of scholarly articles: it is a pioneering approach to the world of academia, radically improving the way scholarly research is managed. The grand vision of Frontiers is a world where all people have an equal opportunity to seek, share and generate knowledge. Frontiers provides immediate and permanent online open access to all its publications, but this alone is not enough to realize our grand goals.

## Frontiers Journal Series

The Frontiers Journal Series is a multi-tier and interdisciplinary set of open-access, online journals, promising a paradigm shift from the current review, selection and dissemination processes in academic publishing. All Frontiers journals are driven by researchers for researchers; therefore, they constitute a service to the scholarly community. At the same time, the Frontiers Journal Series operates on a revolutionary invention, the tiered publishing system, initially addressing specific communities of scholars, and gradually climbing up to broader public understanding, thus serving the interests of the lay society, too.

## Dedication to Quality

Each Frontiers article is a landmark of the highest quality, thanks to genuinely collaborative interactions between authors and review editors, who include some of the world's best academicians. Research must be certified by peers before entering a stream of knowledge that may eventually reach the public - and shape society; therefore, Frontiers only applies the most rigorous and unbiased reviews.
Frontiers revolutionizes research publishing by freely delivering the most outstanding research, evaluated with no bias from both the academic and social point of view. By applying the most advanced information technologies, Frontiers is catapulting scholarly publishing into a new generation.

## What are Frontiers Research Topics?

Frontiers Research Topics are very popular trademarks of the Frontiers Journals Series: they are collections of at least ten articles, all centered on a particular subject. With their unique mix of varied contributions from Original Research to Review Articles, Frontiers Research Topics unify the most influential researchers, the latest key findings and historical advances in a hot research area! Find out more on how to host your own Frontiers Research Topic or contribute to one as an author by contacting the Frontiers Editorial Office: frontiersin.org/about/contact

# RATIONAL DESIGN AND CHARACTERIZATION OF INNOVATIVE MULTIFUNCTIONAL BIOMIMETIC MATERIALS

Topic Editors:
**Lia Rimondini,** University of Eastern Piedmont, Italy
**Lorenzo Moroni,** Maastricht University, Netherlands
**Andrea Cochis,** University of Eastern Piedmont, Italy

**Citation:** Rimondini, L., Moroni, L., Cochis, A., eds. (2021). Rational Design and Characterization of Innovative Multifunctional Biomimetic Materials. Lausanne: Frontiers Media SA. doi: 10.3389/978-2-88966-687-4

# Table of Contents

frontiers in Materials

EDITORIAL
published: 10 March 2021
doi: 10.3389/fmats.2021.631664

# Editorial: Rational Design and Characterization of Innovative Multifunctional Biomimetic Materials

*Andrea Cochis*[1]*, *Lia Rimondini*[1]* and *Lorenzo Moroni*[2]*

[1]Department of Health Sciences, Center for Translational Research on Autoimmune and Allergic Diseases CAAD, Universitá del Piemonte Orientale UPO, Novara, Italy, [2]Complex Tissue Regeneration Department, MERLN Institute for Technology-Inspired Regenerative Medicine, Maastricht University, Maastricht, Netherlands

**Keywords: biomaterials, biomimetic, multifunctional, tissue engineering, personalized medicine**

## Editorial on the Research Topic

### Rational Design and Characterization of Innovative Multifunctional Biomimetic Materials

Bone tissue engineering has been the most frequent topic as it was addressed by five articles dealing with different aspects with such a challenging aim. In their work entitled "In vivo Regeneration of Mineralized Bone Tissue in Anisotropic Biomimetic Sponges," Serrano-Bello et al. demonstrated the pivotal role of the device architecture for a successful repair; accordingly, alginate 3D scaffolds with anisotropic microporous domains enriched with hydroxyapatite (HA) demonstrated a high osteogenic potency toward dental pulp mesenchymal stem cells. These scaffolds were also successful in the repair of a bone defect *in vivo* realized in a rat calvaria model. Along with scaffold composition improvement, in their article "Enhancement of the Biological and Mechanical Performances of Sintered Hydroxyapatite by Multiple Ions Doping," Sprio et al. demonstrated the importance of ions in ameliorating biological properties. In particular, the addition of $Mg^{2+}$, $Sr^{2+}$, and $Zn^{2+}$ ions to HA composites was crucial in influencing the phase composition and microstructure of HA/βTCP composites formed during the sintering process. Moreover, the ions promoted osteogenesis and inhibited bacterial infection, thus demonstrating strong improvement in comparison with the bulk HA. Similarly, de Melo Pereira et al. demonstrated the role of calcium phosphate mineral in successfully mimicking a bone-like matrix in their article "Proliferation and Osteogenic Differentiation of hMSCs on Biomineralized Collagen." Here, biomineralized collagen with intrafibrillar calcium phosphate mineral was compared to the bulk collagen in terms of proangiogenic potency toward mesenchymal stromal cells; the results demonstrated that biomineralization improved osteogenic gene expression with emphasis toward osteoprotegerin (OPG) due to its involvement in osteoclastogenesis inhibition. Culture conditions and the cell source for bone substitutes were investigated by Salgado et al. in their work "Clarifying the Tooth-Derived Stem Cells Behavior in a 3D Biomimetic Scaffold for Bone Tissue Engineering Applications." Accordingly, mesenchymal stem/stromal cells were isolated from human dental follicles and pulp tissues, showing high propensity to be differentiated into bone-like phenotypes when cultured on a 3D porous scaffold made of collagen-nanohydroxyapatite/phosphoserine cryogel; moreover, dynamic culture was compared to static culture, showing a different outcome in terms of alkaline phosphatase (ALP) and osteopontin (OPN), and also, the use of dental follicle stem cells reported better tissue ingrowth and osteogenic differentiation. Hence, the choice of the cell source and culture condition was crucial in influencing bone maturation. Finally, the possibility to exploit biomaterials as drug delivery systems has been investigated for the treatment of osteosarcoma by Dewhurst et al. in their work "Development of Natural-Based Bone Cement for a Controlled

OPEN ACCESS

***Edited by:***
*Nihal Engin Vrana, Sparta Medical, France*

***Reviewed by:***
*Amir M. Ghaemmaghami, University of Nottingham, United Kingdom*

***Correspondence:**
*Andrea Cochis*
*andrea.cochis@med.uniupo.it*
*Lia Rimondini*
*lia.rimondini@med.uniupo.it*
*Lorenzo Moroni*
*l.moroni@maastrichtuniversity.nl*

***Specialty section:***
*This article was submitted to Biomaterials, a section of the journal Frontiers in Materials*

***Received:*** *20 November 2020*
***Accepted:*** *06 January 2021*
***Published:*** *10 March 2021*

***Citation:***
*Cochis A, Rimondini L and Moroni L (2021) Editorial: Rational Design and Characterization of Innovative Multifunctional Biomimetic Materials. Front. Mater. 8:631664. doi: 10.3389/fmats.2021.631664*

Doxorubicin-Drug Release." PLGA nanoparticles loaded with doxorubicin (DOXO) were mixed with calcium phosphate–based bone cement in order to improve the DOXO release in the tumor site, thus limiting the drug side effect on nontarget sites. This targeting strategy was successful in ameliorating the DOXO release that was observed as particularly effective in reducing the viability of cancer stem cells, cells responsible for metastasis progression and drug resistance headway. Dealing with joint function recovery in patients with end-stage hip and knee arthritis, Couto et al. reported an interesting update about periprosthetic inflammation due to wear debris in the review article "The Mechanisms Underlying the Biological Response to Wear Debris in Periprosthetic Inflammation." The presence of such debris can be the trigger of an acute inflammation, eliciting the activation of osteoclasts and consequent periprosthetic osteolysis (PPOL), ultimately leading to implant aseptic loosening, which is the most common cause of long-term implant failure. Therefore, understanding the cellular and the molecular mechanisms underlying the biological response to implant debris can open to novel therapeutic strategies preventing PPOL.

Hydrogels have also been frequently cited in this special issue due to their tunable properties supporting the healing of different tissues. Neves et al. offered a critical revision of the improvement required by alginate hydrogels in order to ameliorate their mechanical and biological properties in the review article "Modulating Alginate Hydrogels for Improved Biological Performance as Cellular 3D Microenvironments." By fine-tuning different properties, such as the molecular weight, backbone block composition and distribution, polymer concentration, and type/amount of cross-linkers, it is possible to modulate the viscoelastic properties, thus ameliorating the mechanical properties; the use of cell instructive/responsive peptides guiding adhesion (RGD) and degradation can instead influence cell behavior, thus making alginate hydrogels a bioactive 4D dynamic microenvironment. Hydrogels were also shown to be able to mimic a tumor microenvironment to study the metastatic progression, as described by Balion et al. in "Investigation of Cancer Cell Migration and Proliferation on Synthetic Extracellular Matrix Peptide Hydrogels." Here, the relation between the ECM and the tumorigenic cell migration and proliferation was investigated due to the hydrogel composition: so, synthetic hydrogel matrices from multi-arm polyethylene glycol (PEG) functionalized with collagen-like peptide (CLP) CG(PKG)4(POG)4(DOG)4 alone and conjugated with either cell adhesion peptide RGD (mimicking fibronectin) or IKVAV (mimicking laminin) were considered. The results showed that neither RGD nor IKVAV conjugated to PEG–CLP stimulated migratory capacity of melanoma cells, thus giving highlights regarding ECM signaling in cancer progression.

The use of cold atmospheric plasma jet (CAPJ) was treated by Lou et al. in their article "Helium/Argon-Generated Cold Atmospheric Plasma Facilitates Cutaneous Wound Healing" to improve wound healing. Thanks to an accurate regulation of the CAPJ-generated gas helium (He)—or gas mixture of He and argon (He/Ar), it was possible to improve the keratinocyte proliferation and migration through the activation of epithelial-to-mesenchymal transition (EMT) and cell cycle progression, which was evidenced by a decrease in E-cadherin levels. As a consequence, *in vivo* experiments confirmed that the CAPJ treatment facilitated granulation tissue formation and mitigated inflammation in the cutaneous tissue, resulting in accelerated wound closure in a rat model.

Graphene has been renamed as the "miracle material" due to its exceptional mechanical properties. In this special issue, a very interesting article dealing with the use of graphene oxide (GO) to realize superior bioactive materials comes from Majkowska et al. "Interfacial Self-Assembly to Spatially Organize Graphene Oxide Into Hierarchical and Bioactive Structures." The authors described the use of supramolecular co-assembly between an elastin-like recombinamer (ELR5) and a peptide amphiphile (PA) to organize GO flakes into bioactive structures across multiple scales. The process takes advantage of a reaction—diffusion—mechanism to enable the incorporation and spatial organization of GO within multiple ELR5/PA layers. Such technical procedures open the possibility to obtain biocompatible ELR5/PA/GO membranes.

Biomaterials aimed for clinical application are very promising sources to improve the practice. Vascular grafts were realized for dialysis in the article proposed by Wu et al. "Optimization of Anti-kinking Designs for Vascular Grafts Based on Supramolecular Materials," where the authors aimed at developing anti-kinking properties for synthetic vascular grafts to be applied as access grafts for hemodialysis. Supramolecular materials based on hydrogen bonding interactions between bis-urea (BU) or 2-ureido-4[1H]-pyrimidinones (UPy) were combined to produce microporous anti-kinking tubular structures by combining solution electrospinning with 3D printing. Two different tubular grafts were developed: one tubular scaffold composed of BU–polycarbonate electrospun layers with 3D-printed polycaprolactone (PCL) and the other graft fully consisted of supramolecular polymers, using chain-extended UPy–PCL as electrospun layers and a bifunctional UPy–PCL. Both grafts demonstrated a reproducible dimensional stability and anti-kinking behavior under bending stresses.

Finally, the most original article of this special issue comes probably from Contessi Negrini et al. "Plant Tissues as 3D Natural Scaffolds for Adipose, Bone and Tendon Tissue Regeneration," where the authors open the possibility to convert plant tissues (i.e., apple, carrot, and celery) into tissue-decellularized scaffolds coming from vegetables. Thanks to their different mechanical properties and natural fibers orientation, the vegetable scaffolds were able to support cells adhesion, alignment, and osteogenic differentiation. These results suggest that besides the well-known animal source, vegetables represent a new front for decellularized matrices in tissue engineering.

Taken together, these innovative articles fully comply with the broad scope of the special issue to report an overview of novel strategies to improve the field of biomaterials and tissue engineering, thus giving the opportunity to the readers to learn new solutions to keep in mind for their future studies. In our vision, the rationale design of a multifunctional biomaterial should consider and combine the following

properties: 1) *pro-regenerative stimulation,* 2) *tissue-mimicking mechanical resistance and architecture, and* 3) *antibacterial activity.* A common underestimation is probably to consider such properties as single aloof characteristics, whereas it is more and more evident that the implant success depends on each of the abovementioned parameters. So, besides the large literature regarding the exploitability of pro-regenerative biochemical factors, we are now better understanding that other parameters such as the mechanical stimulation and the device tissue-specific architecture were probably underestimated as they represent key factors for the tissue repair as well.

In parallel with the biomaterial design, more efforts should be fueled into improvement of *in vitro* models to study the device performances. Using 3D models, bioreactors, and organ-on-a-chip for mimicking the naive tissue structure and the crosstalk between neighbor tissues are of crucial importance to better simulate a physiological environment, thus better predict biomaterials success.

Finally, we would like to focus on the importance of introducing antibacterial properties as the rapid increase in drug-resistant strains is a primary reason for infections in the implant tissue, leading to implant failure, despite the design and performances of the applied devices. This is still an underestimated problem, so it is of a crucial importance to study and verify the use of innovative antibacterial tools in order to reduce the infection rate of implantable biomaterials.

## AUTHOR CONTRIBUTIONS

All authors listed have made a substantial, direct, and intellectual contribution to the work and approved it for publication.

## ACKNOWLEDGMENTS

The continuous advancement in desgning and using multifunctional biomimetic materials in biomedical engineering applications spurred the interest to initiate this special issue collection. The special issue Rational Design and Characterization of Innovative Multifunctional Biomimetic Materials is now closed, so we would like to take this opportunity to sincerely thanks all the Authors for their exceptional contributions. 12 Manuscripts have been published thanks to the efforts of 89 Authors covering different topics and aspects related to the advances of biomimetic and multifunctional biomaterials.

**Conflict of Interest:** The authors declare that the research was conducted in the absence of any commercial or financial relationships that could be construed as a potential conflict of interest.

frontiers in Materials

ORIGINAL RESEARCH
published: 16 June 2020
doi: 10.3389/fmats.2020.00167

# Interfacial Self-Assembly to Spatially Organize Graphene Oxide Into Hierarchical and Bioactive Structures

*Anna Majkowska[1,2,3], Carlos Redondo-Gómez[2,3], Alistair Rice[4], Mariel Gonzalez[3], Karla E. Inostroza-Brito[3], Estelle C. Collin[3], Jose Carlos Rodriguez-Cabello[5], Armando E. Del Rio Hernandez[4], Egle Solito[1] and Alvaro Mata[2,3,6,7,8]**

[1] Barts and The London School of Medicine and Dentistry, William Harvey Research Institute, Queen Mary University of London, London, United Kingdom, [2] School of Engineering and Materials Science, Institute of Bioengineering, Queen Mary University of London, London, United Kingdom, [3] School of Engineering and Materials Science, Queen Mary University of London, London, United Kingdom, [4] Department of Bioengineering, Imperial College London, London, United Kingdom, [5] BIOFORGE Group, University of Valladolid, CIBER-BBN, Valladolid, Spain, [6] School of Pharmacy, University of Nottingham, Nottingham, United Kingdom, [7] Biodiscovery Institute, University of Nottingham, Nottingham, United Kingdom, [8] Department of Chemical and Environmental Engineering, University of Nottingham, Nottingham, United Kingdom

Multicomponent self-assembly holds great promise for the generation of complex and functional biomaterials with hierarchical microstructure. Here, we describe the use of supramolecular co-assembly between an elastin-like recombinamer (ELR5) and a peptide amphiphile (PA) to organize graphene oxide (GO) flakes into bioactive structures across multiple scales. The process takes advantage of a reaction—diffusion mechanism to enable the incorporation and spatial organization of GO within multiple ELR5/PA layers. Scanning electron microscopy (SEM), transmission electron microscopy (TEM), and ImageJ software were used to demonstrate the hierarchical organization of GO flakes within the ELR5/PA layers and the distribution profiles of GO throughout the ELR5/PA membranes. Furthermore, atomic force microscopy (AFM) revealed improved Young's Moduli of the ELR5/PA/GO membranes compared to the ELR5/PA membranes. Lastly, we investigated biocompatibility of the ELR5/PA/GO membrane via various cell culture methods.

**Keywords: graphene oxide, multicomponent self-assembly, peptide amphiphiles, elastin-like recombinamer, hierarchical biomaterials, composite materials**

OPEN ACCESS

***Edited by:***
*Lorenzo Moroni,*
*Maastricht University, Netherlands*

***Reviewed by:***
*John B. Matson,*
*Virginia Tech, United States*
*Marcel Bouvet,*
*Université de Bourgogne, France*

***Correspondence:**
*Alvaro Mata*
*a.mata@nottingham.ac.uk*

***Specialty section:***
*This article was submitted to Biomaterials, a section of the journal Frontiers in Materials*

***Received:*** *27 March 2020*
***Accepted:*** *06 May 2020*
***Published:*** *16 June 2020*

***Citation:***
*Majkowska A, Redondo-Gómez C, Rice A, Gonzalez M, Inostroza-Brito KE, Collin EC, Rodriguez-Cabello JC, Del Rio Hernandez AE, Solito E and Mata A (2020) Interfacial Self-Assembly to Spatially Organize Graphene Oxide Into Hierarchical and Bioactive Structures. Front. Mater. 7:167. doi: 10.3389/fmats.2020.00167*

## INTRODUCTION

Self-assembly, the process by which multiple smaller components autonomously interact and organize into larger well-defined structures, plays a crucial role in the way nature creates structure and functionality (Whitesides and Grzybowski, 2002). In an attempt to emulate biological systems, molecular self-assembly is being used to design bioinspired materials with a spectrum of exciting properties such as well-defined nanostructure (Zhang, 2003; Gazit, 2007), precise display of bioactive signals (Webber et al., 2010; Azevedo, 2019), temporal control of signaling (Kumar et al., 2018), and tuneable mechanical properties (Pashuck et al., 2010). Further processing has been used to enhance complexity for example via modulation of the assembly process (Zhang et al., 2010), top-down techniques (Mata et al., 2009; Mendes et al., 2013), or incorporation of multiple bioactive epitopes (Stephanopoulos et al., 2013; Gentile et al., 2017). However, the ability to assemble molecules hierarchically into well-defined macroscopic structures with practical use remains limited.

Multicomponent self-assembly offers an attractive route to design and engineer materials with molecular precision while increasing complexity and functionality (Draper et al., 2015). For example, the co-assembly of peptide amphiphiles (PAs) bearing either host or guest moieties has been recently used to develop hydrogels with enhanced mechanical properties (Redondo-Gómez et al., 2019). In a different approach, by co-assembling PAs with a megadalton hyaluronic acid, Capito et al. (2008) created stable sacs and membranes with hierarchical nano-to-micro structure. Inspired by this work, we have used PA molecules as self-assembling chaperones to interact with and guide the assembly of different types of molecules such as 1,3:2,4-dibenzylidene-D-sorbitol (DBS) gelators (Okesola et al., 2019), the protein resilin (Okesola et al., 2020a), or hyaluronan/nanoclay composites (Okesola et al., 2020b), generating hydrogels with tuneable structure and mechanical properties. Furthermore, taking advantage of hydrodynamic forces generated during additive manufacturing, Hedegaard et al. (2018) developed biocompatible hydrogel constructs with well-defined ordered or randomly oriented nanofibers, surface microtopographies, distinct microgeometries, and macroscopic assemblies.

Multicomponent self-assembly offers the possibility to not only take advantage of the properties of the individual components but also emergent assembling phenomena and synergistic properties (Okesola and Mata, 2018). In this context, Inostroza-Brito et al. (2015) demonstrated how PAs can affect the conformation of elastin-like recombinamers (ELRs) to consequently generate a diffusion-reaction assembly process. This mechanism enables the formation of a hierarchical multi-layered ELR5/PA membrane with the capacity to access non-equilibrium and a series of dynamic properties. While the resulting material is fragile (Inostroza-Brito et al., 2017), the study demonstrates the possibility to guide the assembly of complex components, such as proteins, beyond the nanoscale in a controllable and autonomous manner.

Graphene oxide (GO) is a single layer two-dimensional nanomaterial with a wide range of properties such as high surface area, mechanical strength, thermal conductivity, biocompatibility, and ease of functionalization (Zhu et al., 2010; Yang et al., 2013). Graphene-based materials have enormous potential in the biomedical field in applications ranging from biosensors (Justino et al., 2017) and biological imaging (Lin et al., 2016) to drug and gene delivery (Liu et al., 2013) and biomaterials (Shin et al., 2016). A variety of composite biomaterials incorporating a biomacromolecule and GO have been generated in the form of electrospun mats (Azarniya et al., 2016), hydrogels (Kang et al., 2015; Zhou et al., 2017), films (Han et al., 2011), or other 3D structures (Rajan Unnithan et al., 2017). For instance, nanocomposites of GO and chitosan have been prepared resulting in improved mechanical properties (Han et al., 2011; Li et al., 2013), resistance against enzymatic degradation (Shao et al., 2013), enhanced cellular (Depan et al., 2014; Dinescu et al., 2014), and antibacterial (Mazaheri et al., 2014) activity. Other GO-protein composite materials based on GO and gelatin or collagen have led to materials with improved mechanical properties (Wan et al., 2011; Jalaja et al., 2016) and bioactivity (Kang et al., 2015; Lee et al., 2016; Zhou et al., 2017). While these examples elucidate both the interest and progress of incorporating GO within biomaterials, the capacity to organize GO flakes hierarchically remains an unmet challenge.

Here, we report on the use of the ELR5/PA co-assembling system to enable localization and organization of GO flakes into hierarchical and functional structures. We demonstrate how the diffusion-reaction mechanism of formation can be used to guide the assembly of GO flakes between the ELR5/PA layers and generate complex geometries where GO is organized at multiple length scales. Furthermore, we reason that the assembly of GO in this manner will lead to enhanced mechanical properties of the ELR5/PA system. We describe the underlying mechanism of self-assembly, the structure of the composite material, and the biocompatibility of the resulting ELR5/PA/GO biomaterial through extensive *in vitro* cell studies.

# RESULTS AND DISCUSSION

## Rationale

The approach is based on the ELR5/PA co-assembling system (Inostroza-Brito et al., 2015, 2017) and takes advantage of its reaction-diffusion mechanism to recruit, localize, and organize GO flakes at multiple length scales (**Figure 1**). We used 0.04% (v/v) GO (Wick et al., 2014) (pH = 2) with monolayer content >95% and oxygen content >36% given its water dispersability and low cost (**Figure 1E**). We used a cationic PAK3 ($C_{15}H_{31}$CONH-VVVAAAKKK-CONH$_2$) to co-assemble with the oppositely charged ELR5 (MESLLP-[(VPGVG VPGVG VPGEG VPGVG VPGVG)$_{10}$-(VGIPG)$_{60}$]$_2$-[(VPGIG)$_{10}$-AVTGRGDSPASS(VPGIG)$_{10}$]$_2$-V) molecule to evaluate the capacity of the assembling process to recruit and organize GO flakes within the distinctive ELR5/PA multilayers (**Figures 1A–C**). Furthermore, given our previous findings that distinct PA molecules can generate different ELR5/PA membrane structures (Inostroza-Brito et al., 2015), PAs with different charge densities including PAK2 ($C_{15}H_{31}$CONH-VVVAAAKK-CONH$_2$) and PAK4 ($C_{15}H_{31}$CONH-VVVAAAKKKK-CONH$_2$) were also used to co-assemble with ELR5 (**Figure 1D**). In addition, the resulting materials were characterized according to their mechanical properties and used as cell culture substrates to investigate their effect on cell adhesion, proliferation, metabolic activity, and morphology.

## Synthesis of Individual Components

PA molecules were synthesized following standard solid-phase peptide synthesis methods as previously reported (Mata et al., 2012). PA purity and structure were characterized by reverse phase HPLC and electrospray ionization mass spectrometry (**Figure S1**). ELR5 molecules were obtained from Technical Proteins Nanobiotechnology S. L., Spain and GO aqueous dispersions were obtained from Sigma Aldrich, UK.

## Characterization of Interactions Between Components

The ELR5/PA system relies on electrostatic, hydrophobic, and H-bond interactions (Inostroza-Brito et al., 2015). Consequently, we

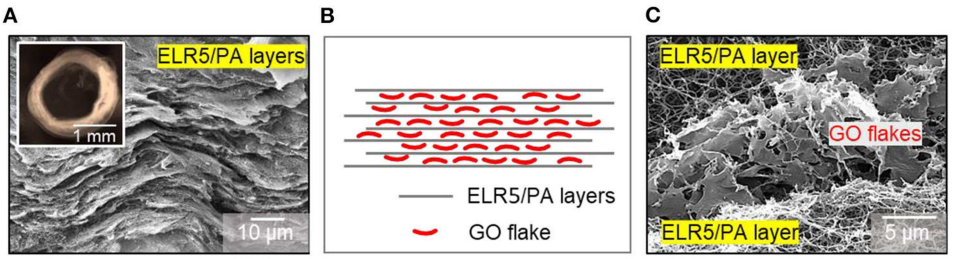


**D**

| MOLECULE | SEQUENCE | $M_w$ (kDa) |
|---|---|---|
| PAK2 | $C_{15}H_{31}$CONH-VVVAAAKK-$CONH_2$ | 1.022 |
| PAK3 | $C_{15}H_{31}$CONH-VVVAAAKKK-$CONH_2$ | 1.150 |
| PAK4 | $C_{15}H_{31}$CONH-VVVAAAKKKK-$CONH_2$ | 1.279 |
| ELR5 | MESLLP-$[(VPGVG\ VPGVG\ VPGEG\ VPGVG\ VPGVG)_{10}$-$(VGIPG)_{60}]_2$-$[(VPGIG)_{10}$-AVTGRGDSPASS$(VPGIG)_{10}]_2$-V | 112.300 |

**E** GRAPHENE OXIDE

pH 2

Lateral size: 7 ± 2 µm

Monolayer content: ≥ 95 %

Zeta potential: -30.58 mV

Oxygen content: ≥ 36%

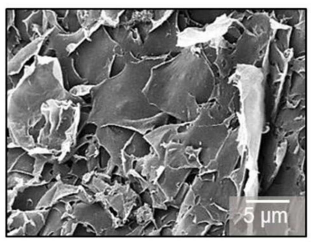


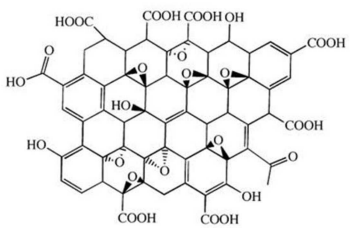


**FIGURE 1 |** Schematic representation and representative images of tubes and tube wall cross-sections of the ELR5/PA/GO system. **(A)** SEM micrograph of an ELR5/PAK3 cross-section with its characteristic multi-layered architecture. Inset: Bright field image of a top view of an ELR5/PA tube. **(B)** Schematic of the ELR5/PA system cross-section with black horizontal lines representing ELR5/PA layers embedded with GO flakes (red). **(C)** SEM micrograph of the cross-section of an ELR5/PA/GO membrane visualizing the localization of GO flakes between ELR5/PA layers. **(D)** Molecular structure and weight of PAs and ELR5 used in this study. **(E)** Molecular information and structure of GO used in this work.

first used circular dichroism (CD) to investigate the secondary structure in aqueous solution of both PAs and ELR5 with and without GO. CD revealed that PAK3 exists in a random coil conformation when dissolved in MilliQ™ water at pH 4.5 and room temperature (RT), and does not undergo conformational change when mixed with GO under the same conditions (**Figure 2A**). However, a slight red-shift at the 195 nm minimum was observed, which might indicate an interaction between PAK3 and GO as previously reported (Pashuck et al., 2010). CD on ELR5 samples dissolved in MilliQ™ water at pH 5 and RT exhibited both random coil and β-sheet conformations (**Figure 2A**) that did not change upon addition of GO. However, lower intensity of the negative 195 nm signal might indicate that GO reduces the content of random coil structures in ELR5 while increasing the content of type I β-turns (Perczel and Fasman, 1992).

We further investigated the ELR5/PA/GO interactions by conducting zeta potential and dynamic light scattering (DLS) measurements. Zeta potential of PAK3 decreased after addition of GO (**Figure 2B**). This is likely a consequence of a drop in the PAK3's surface charge as a result of its electrostatic interactions with carboxyl, hydroxyl, or carbonyl groups present in GO (negatively charged), partially screening the positive charges of PAK3. On the other hand, the zeta potential of ELR5 molecules increased slightly after addition of GO, suggesting absence of electrostatic interactions between these components, which is in agreement with the CD results (**Figure 2A**). DLS measurements revealed a dramatic decrease in GO size after mixing with both PAK3 (**Figure 2C**) and ELR5, which suggests disruption of GO aggregates, known to form in aqueous solutions (Tang et al., 2015), due to electrostatic interactions. It is important to mention that DLS is a well-suited technique for estimating the size of spherical particles. However, this technique has been also used to provide relative changes in size of non-spherical components including GO (Stankovich et al., 2006), PAs (Raymond and Nilsson, 2018), and ELRs (Navon and Bitton, 2016).

Hydrophobic interactions also play a key role in the ELR5/PA system above the ELR5's transition temperature (Tt) (Inostroza-Brito et al., 2015). To investigate whether addition of GO into the ELR5/PA system influences hydrophobic interactions, a turbidity

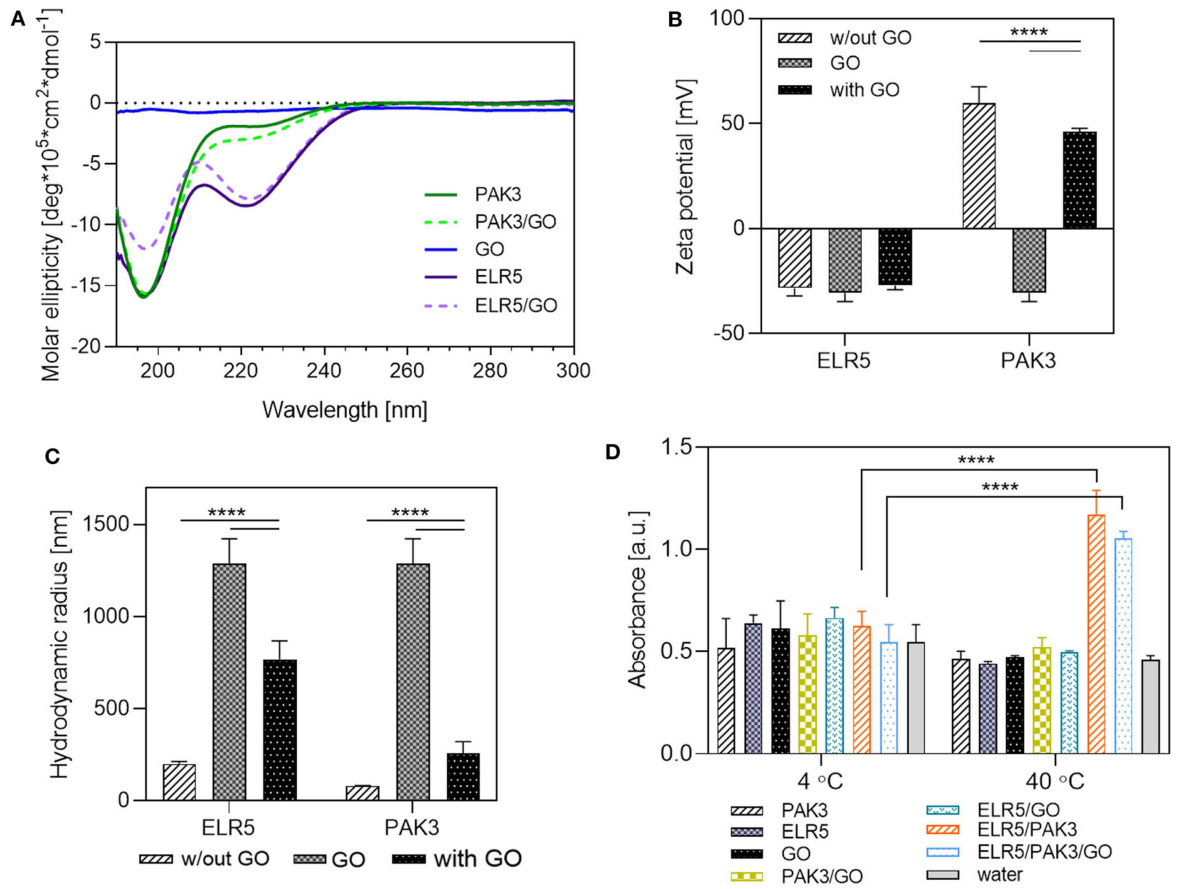


**FIGURE 2 |** Analysis of interactions between PAK3, ELR5, and GO. **(A)** CD spectra of PAK3, ELR5, and their mixtures with GO in aqueous solutions at room temperature. **(B)** Zeta potential measurements of aqueous solutions of PAK3, ELR5, and their mixtures with GO. **(C)** DLS measurements of aqueous solutions of PAK3, ELR5, and their mixtures with GO **(D)** Turbidity of aqueous solutions of PAK3, ELR5, and their mixtures with GO at 4 and 40°C measured at 300 nm. Error bars represent ±SD where ****$p < 0.0001$. The experiments were performed in triplicates.

assay was performed. The results confirmed that significant levels of aggregation between ELR5, PAK3, and GO are only present when the temperature is above the Tt (19C) of ELR5 (**Figure 2D**), which indicates that presence of GO in the solution does not influence the hydrophobic interactions between PAK3 and ELR5, necessary for membrane formation (Inostroza-Brito et al., 2015). Analysis of interactions between ELR5, GO and both PAK2 and PAK2-K4 is presented in **Figures S2** and **S3**.

These results indicate that molecular interaction between GO and both molecular building blocks (PAK3 and ELR5) relies mostly on electrostatic forces. However, both components retain most of their secondary structures in presence of GO and, consequently, hydrophobic interactions from ELR5 seem to also play a key role above the ELR5 transition temperature.

## The ELR5/PA/GO Membrane—Micro and Macroscopic Properties

Upon ELR5/PAK3 co-assembly, a diffusion barrier is formed across which the PAK3 diffuses (**Figure 3A**) (Inostroza-Brito et al., 2015). Electron microscopy was used to investigate the assembly of GO within the ELR5/PAK3 membrane when added into the system. We first mixed GO with the PAK3 solution and subsequently inoculated it into the ELR5 solution. Scanning electron microscopy (SEM) revealed poor incorporation of GO (**Figure 3B**), likely as a result of the inability of the relatively large GO flakes to diffuse through the ELR5/PAK3 diffusion barrier. We then reasoned that combining GO with ELR5 solution might surpass this obstacle. We prepared an ELR5/GO solution followed by inoculation of PAK3 into the mixture. In this case, we observed much higher incorporation of GO in the final membrane (**Figure 3C**). Given these findings, we then mixed GO with both ELR5 and PAK3 solutions, followed by inoculation of PAK3/GO in the ELR5/GO solution. In this setup, membranes qualitatively exhibited the highest incorporation of GO (**Figure 3D**) while maintaining their multi-layered structure and capacity to adhere to interfaces and open controllably, transforming sacs into tubular structures (**Figures 4C–E**). Transmission electron microscopy (TEM) revealed presence of GO flakes (visible as black lines) throughout the thickness of the ELR5/PAK3/GO membrane, positioned within and parallel to the membrane layers (**Figure 4B**). SEM performed on the

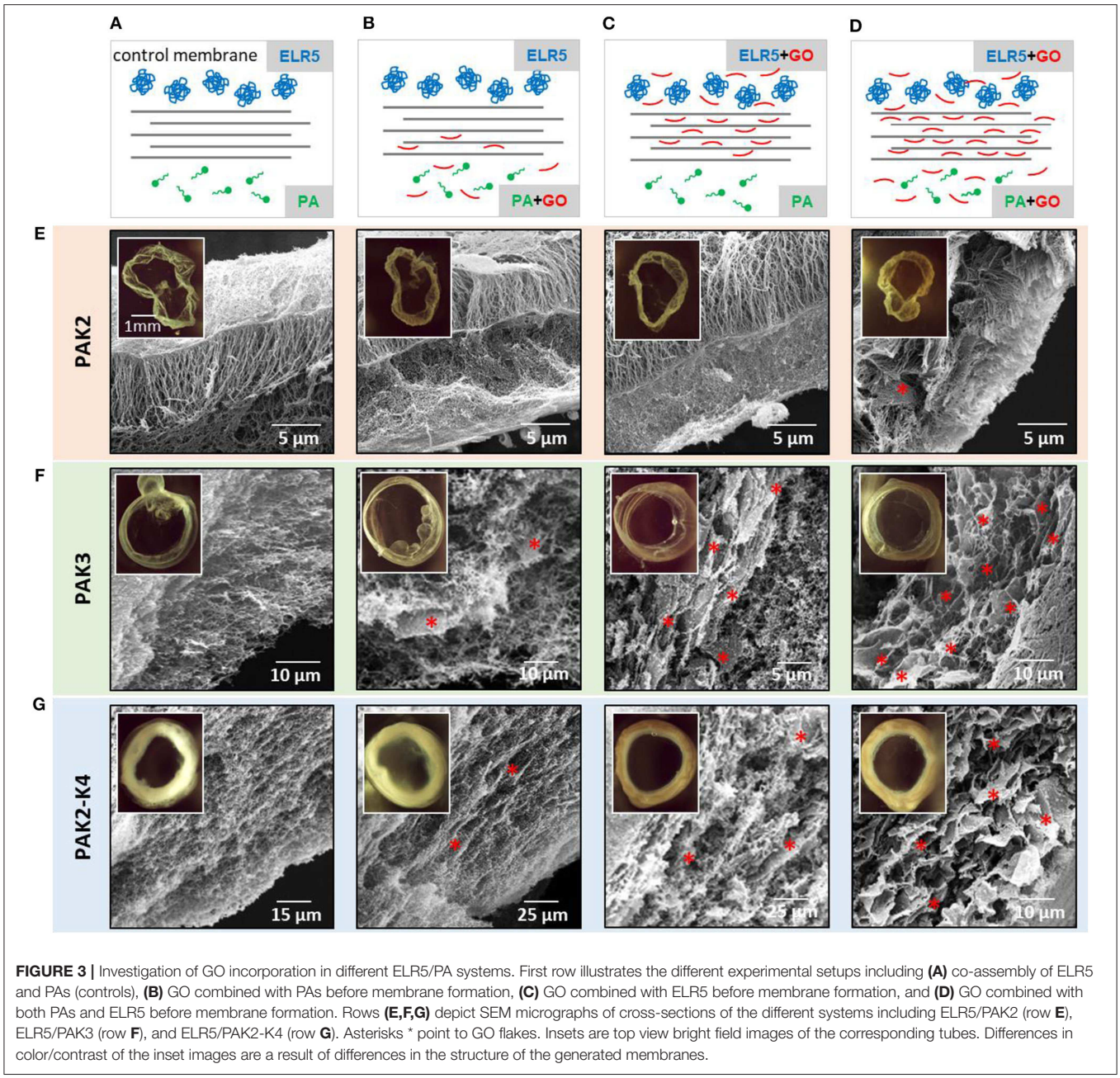


**FIGURE 3 |** Investigation of GO incorporation in different ELR5/PA systems. First row illustrates the different experimental setups including **(A)** co-assembly of ELR5 and PAs (controls), **(B)** GO combined with PAs before membrane formation, **(C)** GO combined with ELR5 before membrane formation, and **(D)** GO combined with both PAs and ELR5 before membrane formation. Rows **(E,F,G)** depict SEM micrographs of cross-sections of the different systems including ELR5/PAK2 (row **E**), ELR5/PAK3 (row **F**), and ELR5/PAK2-K4 (row **G**). Asterisks * point to GO flakes. Insets are top view bright field images of the corresponding tubes. Differences in color/contrast of the inset images are a result of differences in the structure of the generated membranes.

membranes confirmed the multi-layered microarchitecture with embedded GO flakes (**Figure 3F**-row) seen on TEM. These results indicate that GO can be successfully incorporated within the ELR5/PAK3 system by taking advantage of the diffusion-reaction mechanism of assembly to recruit, localize, and organize GO flakes within the multi-layered architecture and as part of a more complex geometrical structure.

## Incorporation Studies

To investigate the possibility to use supramolecular self-assembling processes to guide the organization of GO more broadly, we repeated the experiments using variations of PAK3, PAK2 (C15H31-VVVAAAKK–CONH2) and PAK4 (C15H31-VVVAAAKKKK-CONH2) (**Figure 1D**). We have previously demonstrated that these PA molecules with a different number of lysine residues were also able to form stable ELR5/PA membranes, but exhibiting different cross-sectional architectures (Inostroza-Brito et al., 2015). Membranes formed using PAK4 exhibited a multi-layered architecture with increased thickness and a looser structure compared to ELR5/PAK3 membranes (Inostroza-Brito et al., 2015) while those formed using PAK2 exhibited a different three-level structure with orthogonal fibers (**Figure 3E**-row) (Inostroza-Brito et al., 2015). To study the interaction between GO and the ELR5/PAK2-K4 system, we

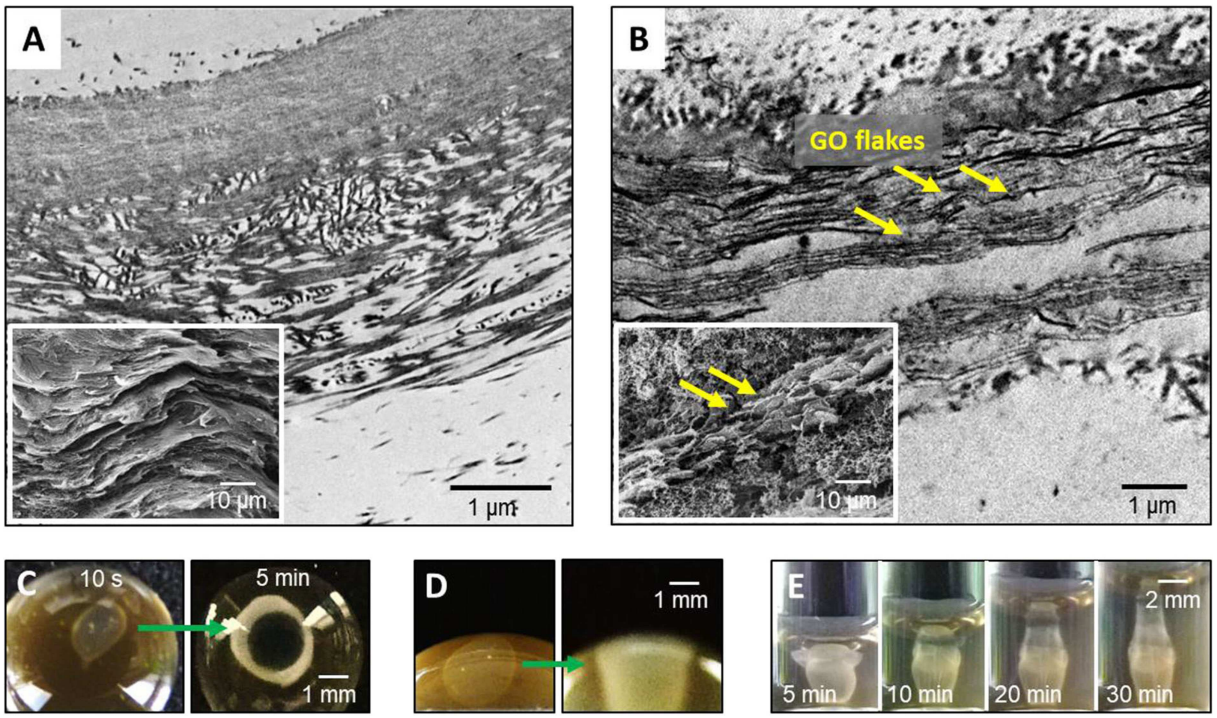


**FIGURE 4 |** Investigation of GO incorporation and ELR5/PAK3/GO membrane properties. **(A)** TEM micrograph of a cross-section of an ELR5/PAK3 membrane (Inset is a representative SEM micrograph). **(B)** TEM micrograph of a cross-section of an ELR5/PAK3/GO membrane with GO flakes (yellow arrows) (Inset is a representative SEM micrograph). **(C–E)** Demonstration of the dynamic properties of the ELR5/PAK3/GO system including spontaneous opening after a drop of PAK3/GO solution is inoculated into an ELR5/GO solution **(C–E)** capacity for longitudinal growth upon increasing the ELR5/GO volume.

also attempted to generate ELR5/PA membranes combining both PAK2 and PAK4 (1:1 mixture). We hypothesized that the different diffusion mechanisms arising from the co-assembly of these different components would guide and organize GO flakes differently. To investigate this hypothesis, experiments were conducted using ELR5/PAK2 and ELR5/PAK2-K4 combinations (**Figures 3E,G**-rows). As before, GO was mixed with (i) PAs alone, (ii) ELR5 alone, and (iii) both components (**Figures 3B–D**, columns). ELR5/PAK2/GO and ELR5/PAK2-K4/GO membranes were stable and robust (**Figures 3E,G** insets) and exhibited darker color suggesting GO incorporation in these conditions, which was assessed by observations under an optical microscope. SEM investigations on membranes revealed GO flakes were incorporated and organized within and throughout the multi-layered architecture of the ELR5/PAK2-K4/GO membranes (**Figure 3G**-row). As with the ELR5/PAK3/GO system, highest incorporation of GO was achieved when the GO was mixed with both PA and ELR5 solutions (**Figures 3D,F**). In contrast, ELR5/PAK2/GO membranes exhibited large quantities of GO on the outer and inner side of the membrane but only marginal incorporation within the membrane.

These results suggest that GO can be incorporated within the ELR5/PA system independently of the PA molecule used. However, the level of incorporation of GO within the membrane depends on the supramolecular mechanism of assembly, with both ELR5/PAK3/GO and ELR5/PAK2-K4/GO presenting more GO in the multilayers than ELR5/PAK2/GO membranes, which present a different mechanism of co-assembly (Inostroza-Brito et al., 2015). Initial formation of a strong diffusion barrier prevents large flakes of GO from diffusing through the barrier, forming membranes with less GO flakes. Addition of GO flakes in the ELR5 solution helps to overcome this obstacle, forming membranes with higher content of GO. Highest incorporation, however, can be achieved only when GO is combined with both PA and ELR5 solutions, particularly in the case of the ELR5/PAK3 and ELR5/PAK2-K4 systems.

## Membrane Thickness

To study the effect of introducing GO into the ELR5/PA system, possible changes in membrane thickness were investigated by SEM (**Figure 5B**). SEM revealed that the thickness of ELR5/PAK3/GO membranes increased when GO was added in either PA or ELR5 solutions prior to assembly, forming the thickest membrane when GO was mixed with both ELR5 and PAK3 (**Figure 5D**). Similar results were observed in ELR5/PAK2-K4/GO membranes (**Figure 5D**). In contrast, the thickness of ELR5/PAK2/GO membranes gradually decreased with addition of GO to either PAK2, ELR5, or both PAK2 and ELR5 solutions. This result suggests that the supramolecular mechanism of assembly of ELR5/PAK2 membranes, which differs from ELR5/PAK3 and ELR5/PAK4 systems (Inostroza-Brito et al., 2015), prevents incorporation of GO. These experiments are in alignment with the SEM observations (**Figure 3**) and confirm that, while supramolecular processes

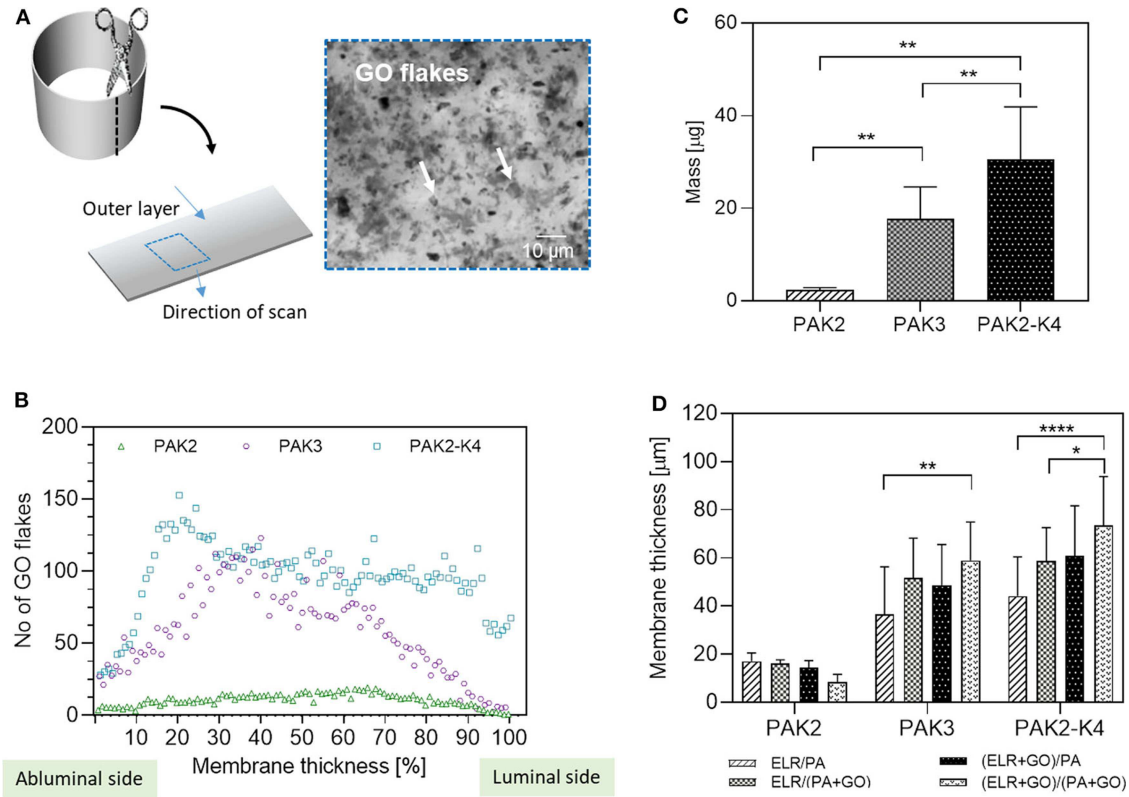


**FIGURE 5 |** GO content and distribution in the membranes. **(A)** Schematic of the experimental setup for measuring GO distribution. **(B)** GO distribution profile throughout the thickness of the ELR5/PAs/GO systems. Number of GO flakes present in each layer of a z-stack image was quantified and presented as number of GO flakes vs. layer number which was normalized as % of the thickness of the membrane. **(C)** GO content per membrane as measured by UV-Vis. **(D)** Thickness of the membranes as measured by SEM. Error bars represent ±SD where ****$p < 0.0001$, **$p < 0.01$, and *$p < 0.5$. The experiments were performed in triplicates.

may be able to organize GO flakes at multiple scales (ELR5/PAK3 and ELR5/PAK2-K4 systems), the size of GO flakes may limit its incorporation in some co-assembling systems (ELR5/PAK2).

## GO Content

To further characterize GO incorporation, the amount of GO within each of the ELR5/PA systems was quantified. After co-assembly, membranes were dissolved in 1,1,1,3,3,3-hexafluoro-2-propanol (HFIP) and GO absorbance was monitored spectrophotometrically in the UV-Vis region. The technique enabled quantification of mass of GO per membrane (**Figure 5C**) and the results revealed the highest incorporation of GO occurred in ELR5/PAK2-K4 membranes, followed by ELR5/PAK3 membranes, and, as expected, ELR5/PAK2 membranes with the lowest incorporation of GO. These results correlate with the previously discussed SEM observations (**Figure 3**) and membrane thickness experiments (**Figure 5B**).

## Distribution of GO

SEM and TEM demonstrated that GO flakes are incorporated and organized within the ELR5/PAK3/GO and ELR5/PAK2-K4/GO membranes. To further characterize the level of incorporation throughout the thickness of the membrane, 3D z-stacked bright field images of the membrane were generated (**Figure 5A**). Using ImageJ software (Schneider et al., 2012), we quantified the number of GO flakes in each layer of the different membranes by generating z-stack images and producing distribution profiles depicting number of GO flakes vs. layer number, which was normalized as % of the thickness of the membrane (**Figure 5B**). These profiles revealed that in ELR5/PAK3/GO membranes, GO is distributed throughout the thickness of the membrane with higher amounts present in the middle. In addition, ELR5/PAK2-K4/GO membranes exhibited similar level of GO incorporation but the flakes were more evenly distributed throughout the membrane (**Figure 5B**). Interestingly, ELR5/PAK2/GO membranes exhibited uniform distribution throughout the membrane but with much lower levels of incorporation (**Figure 5B**). These results confirm that GO flakes were in fact distributed throughout the membranes of all the systems studied but with different levels of incorporation. Highest incorporation and distribution was observed in ELR5/PAK2-K4/GO and ELR5/PAK3/GO membranes, on which we focused to assess applicability.

## Mechanical Properties of the ELR5/PA/GO Systems

Given the unique mechanical properties of GO (Zhu et al., 2010) as well as its incorporation and organization within the ELR5/PA systems, we hypothesized that the mechanical properties of the resulting ELR5/PA/GO membranes would improve compared to the control ELR5/PA membranes. Atomic force microscopy (AFM) measurements were conducted on both luminal (inner) and abluminal (outer) sides of ELR5/PAK3/GO and ELR5/PAK2-K4/GO membranes assembled with GO added to both PA and ELR5 solutions (**Figure 6**). The results revealed significant increase in Young's Moduli of the ELR5/PAK2-K4/GO membrane on both luminal and abluminal sides compared to ELR5/PAK2-K4 membranes (**Figure 6B**). This increase was also evident in ELR5/PAK3/GO membranes compared to ELR5/PAK3 ones (**Figure 6A**). These results suggest that stiffness of the ELR5/PA membrane increases after incorporation of GO on both sides of the membrane, which correlates with the SEM observations (**Figure 3**), membrane thickness measurements (**Figure 5D**), and GO distribution and incorporation (**Figure 5B**) within the membrane's microstructure when GO is added to both ELR5 and PAs solutions.

## Cell Studies

### Cell Adhesion

The potential applicability of the ELR5/PA/GO materials was investigated by assessing the suitability of the membrane to be used in tissue engineering applications. Mouse adipose derived stem cells (mADSCs) were cultured on both sides of the membranes that presented higher incorporation of GO including ELR5/PAK3 (control), ELR5/PAK3/GO, ELR5/PAK2-K4, and ELR5/PAK2-K4/GO. Preliminary biocompatibility was assessed by quantifying cell adhesion, viability, and proliferation.

mADSCs were seeded on both ELR5/PAK3 and ELR5/PAK2-K4 membranes (with and without GO) in serum-free media, incubated for 4 h, rinsed to remove non-adherent cells, cultured for an additional 4 h in full media (DMEM, 20% FBS), and then dyed with the blue dsDNA stain 4'-6-diamino-2-phenylindole (DAPI). Fluorescent microscopy revealed higher numbers of cells growing on ELR5/PAK3 and ELR5/PAK3/GO membranes than on ELR5/PAK2-K4 and ELR5/PAK2-K4/GO membranes (**Figure 7B**). To verify these results, we quantified the amount of double strand DNA (dsDNA) present in the samples by PicoGreen™ assay. This assay allows the quantification of the concentration of dsDNA that can be interpreted as proportional to the number of cells present in the sample. mADSCs from membranes were collected after 7 days of culture and tissue culture plate (TCP) was used as control. The results revealed similar dsDNA concentration of cells growing on ELR5/PAK3 and ELR5/PAK3/GO membranes, suggesting that these membranes facilitate cell adhesion and proliferation (**Figure 7A**). In contrast, dsDNA concentration of cells growing on both ELR5/PAK2-K4 and ELR5/PAK2-K4/GO membranes was significantly lower than TCP. We hypothesize that the decrease in cellular dsDNA may be the result of (i) a greater cytotoxic effect from the positives charges of PAK4 (Newcomb et al., 2014) or (ii) the higher Young's Modulus of both ELR5/PAK2-K4 and ELR5/PAK2-K4/GO (compared to ELR5/PAK3 and ELR5/PAK3/GO; **Figure 6**), which could influence cell adhesion. Previous studies have demonstrated that stiffer surfaces can result on lower mADSCs adhesion (Discher et al., 2005).

In summary, these results reveal that incorporation of GO within both ELR5/PAK3 and ELR5/PAK2-K4 systems does not affect the biocompatibility of the material but differences in the resulting architecture and material properties may lead to differences in the capacity of the material to promote cell adhesion and proliferation.

### Cell Morphology

Cells stained with DAPI (nucleus) and Phalloidin CruzFluor™ 647 (actin) were imaged under an epifluorescent microscope. Analysis of the stained cells revealed that cells grown on ELR5/PAK3 and ELR5/PAK3/GO membranes exhibited a well-spread morphology and formed multiple connections with surrounding cells (**Figure 7E**). In contrast, cells grown on ELR5/PAK2-K4 and ELR5/PAK2-K4/GO membranes displayed a much less spread morphology and formed fewer connections with neighboring cell. These results suggest that ELR5/PAK3 membranes support better cell adhesion compared to ELR5/PAK2-K4 membranes regardless of the GO content.

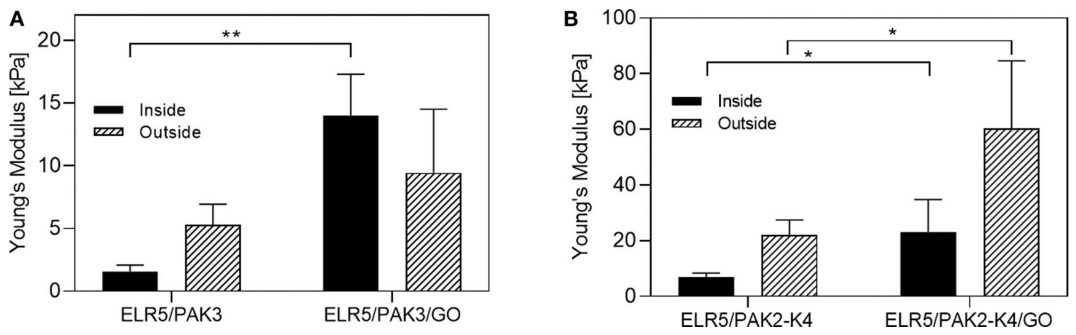


**FIGURE 6 |** Young's Moduli of the membranes. AFM measurements were carried out on the luminal (inner) and abluminal (outer) side of the ELR5/PAK3 ± GO membranes **(A)** and ELR5/PAK2-K4 ± GO membranes **(B)**. Error bars represent ±SEM where $^{**}p < 0.01$, and $^{*}p < 0.5$. The experiments were performed in 5 replicates.

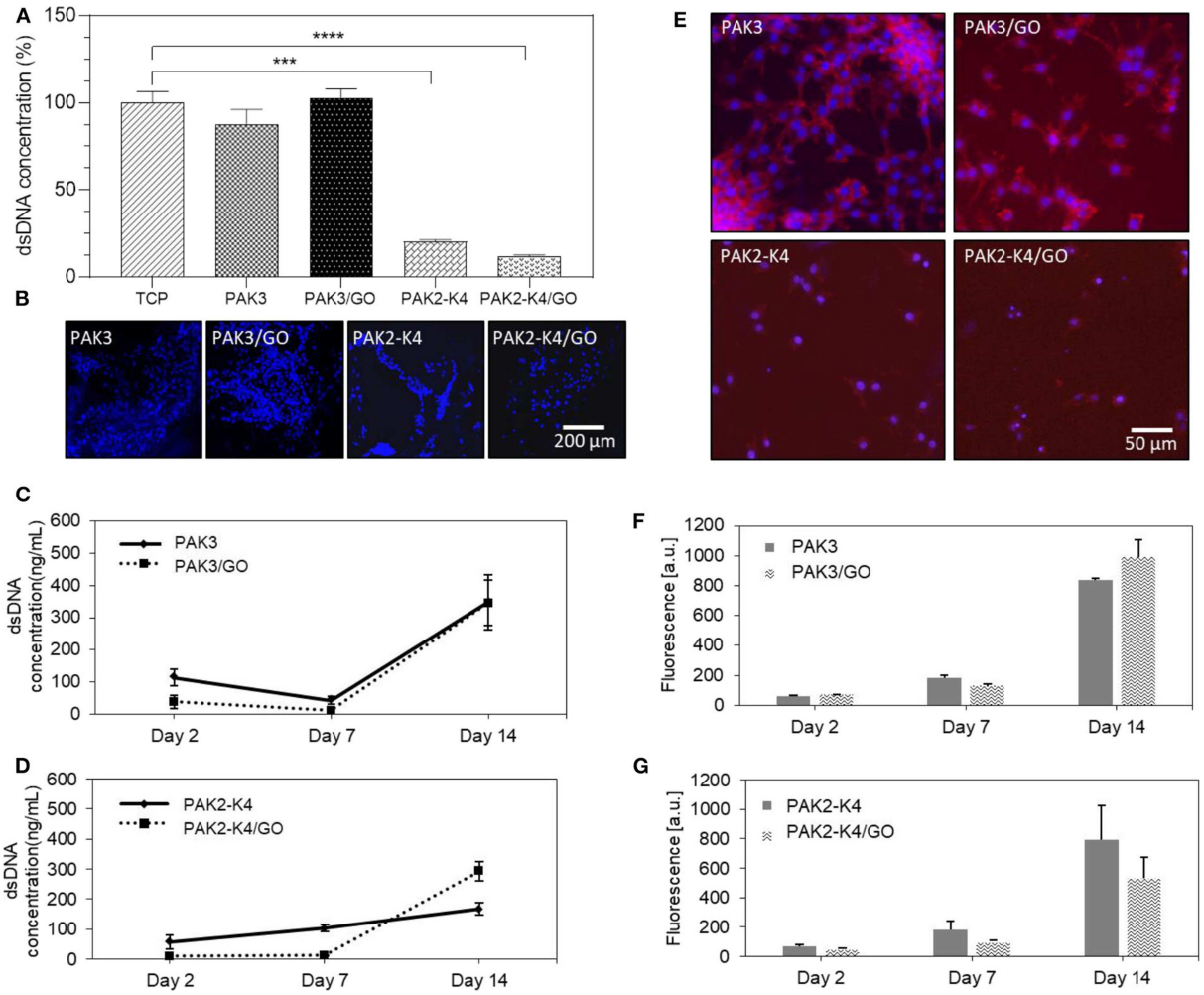


**FIGURE 7 |** Investigation of biocompatibility of ELR5/PAs/GO membranes. Mouse derived adipose stem cells (mADSCs) were grown on the membranes and dsDNA content **(A)** was quantified after 7 days in culture and normalized to TCP (100%) by PicoGreen™ assay. **(B)** Fluorescence microscopy images of mADSCs stained with DAPI (4,6-diamidino-2-phenylindole) after 4 h of cell culture. **(C,D)** Proliferation studies. mADSCs were grown on the ELR5/PAK3 ± GO **(C)** or ELR5/PAK2-K4 ± GO **(D)** membranes. dsDNA content was quantified by PicoGreen™ assay. **(E)** Morphology studies. mADSCs were stained with Phalloidin CruzFluor™ 647 and DAPI. Images indicate a spreading morphology and intercellular connections between mADSCs growing on ELR5/PAK3 and ELR5/PAK3/GO membranes and a barely visible cytoskeleton of mADSCs grown on ELR5/PAK2-K4 and ELR5/PAK2-K4/GO membranes with minimal spreading and connections observed. **(F,G)** Cell metabolic activity studies. mADSCs were grown on the ELR5/PAK3 ± GO **(F)** or ELR5/PAK2-K4 ± GO **(G)** membranes, cell metabolic activity was assessed with Alamar Blue™ assay. The data suggest there is no significant difference in cell metabolic activity between either ELR5/PAK3 and ELR5/PAK3/GO nor ELR5/PAK2-K4 and ELR5/PAK2-K4/GO systems at any of the time points. Error bars represent ±SEM where $^{****}p < 0.0001$ and $^{***}p < 0.001$. The experiments were performed in triplicates.

## Cell Metabolic Activity

To further assess the capacity of the materials to support cell growth, the metabolic activity of mADSCs on the membranes was assessed by Alamar blue™ assay over 2 weeks of cell culture. Same membranes used for cell adhesion studies (**Figure 7E**) revealed no significant difference in metabolic activity for cells growing on the ELR5/PAK3/GO membranes vs. ELR5/PAK3 membranes at any time point (**Figure 7F**). On the other hand, cells grown on ELR5/PAK2-K4/GO membranes exhibited a slight decrease, though not statistically significant, in metabolic activity compared to those grown on ELR5/PAK2-K4 membranes (**Figure 7G**). These results further evidence that addition of GO flakes into the ELR5/PAK3 system does not have a negative impact on the metabolic activity of the cells. However, there is a slight decrease in cell metabolic activity after addition of GO in the ELR5/PAK2-K4 system, suggesting supramolecular organization of GO within the membranes or the possible cytotoxicity of the positively charged PAK4 (Newcomb et al., 2014) might play a role.

## Cell Proliferation

Cell proliferation was then assessed by quantifying dsDNA concentration of mADSCs grown on the different membranes on days 2, 7, and 14 via Quant-iT™ PicoGreen™ assay. The

results revealed that in case of the ELR5/PAK3 system, GO does not have an effect on the proliferation of mADSCs at none of the investigated time points (**Figure 7C**). On the other hand, we observed that GO may be influencing proliferation of mADSCs grown on ELR5/PAK2-K4 membranes, given a decrease in dsDNA concentration at day 7 and an increase at day 14 compared to membranes without GO (**Figure 7D**). These results indicate that both ELR5/PAK3 and ELR5/PAK2-K4 systems support cell proliferation regardless of GO content, although, proliferation rate is slower for cells growing on the ELR5/PAK2-K4 system.

## CONCLUSION

In this study, we report the ability of the ELR5/PA self-assembling system to manipulate, localize, and organize GO flakes into hierarchical structures. By taking advantage of the electrostatic and hydrophobic nature of ELR5 and PAs, the formation of a diffusion barrier upon their co-assembly, and the subsequent diffusion-reaction mechanism of ELR5/PA membrane formation, we demonstrate the potential to use supramolecular mechanisms to guide assembly of GO across scales and into complex architectures. Furthermore, we show that incorporation of GO flakes within the ELR5/PA system improves mechanical properties of the resulting materials and may be beneficial for tissue engineering applications. Also, we demonstrate that incorporation of GO does not affect the capacity of the composite material to support mADSCs adhesion, proliferation, and metabolic activity.

## METHODS

### Membrane Formation

ELR5 and PA molecules were dissolved separately in MilliQ water (10 and 15 mg/mL, respectively). pH was adjusted to pH = 5 (ELR5) and pH = 4.5 (PAs). 190 μl of ELR5 solution was placed in a well in a 48 well plate. 10 μl of PA solution was added by immersing the pipette tip into the ELR5 solution and slowly releasing the liquid. The membrane was left to develop for 48 h at 30°C. For GO membranes: GO 4 mg/mL (pH = 2) was diluted to the required concentration with pH adjusted to pH = 4.5 and mixed with either ELR5 solution or PA solution before membrane formation. Ten microliter of PA-GO solution was added by immersing the pipette tip into the ELR5-GO solution and slowly releasing the liquid. The membrane was left to develop for 48 h at RT.

### Growth Experiment

ELR5 and PA molecules were dissolved separately in MilliQ water (10 and 15, mg/mL respectively). GO 4 mg/mL was diluted to the required concentration and mixed with either ELR5 solution or PA solution before membrane formation. 100 μl of ELR5/GO solution was placed in a glass vial. 5 μl of PA-GO solution was added by immersing the pipette tip into the ELR5 solution and slowly releasing the liquid. Additional 20 μl of ELR5/GO solution was carefully added to the vial every 10 min to observe growth of the membrane.

### Zeta Potential and Dynamic Light Scattering

Zeta potential was measured to investigate the changes in surface charge density of ELR5, PAs and GO molecules when mixed together. ELR5 and PAs were dissolved in MilliQ water [0.1 and 0.15% (w/v), respectively]. GO was diluted to the final concentration of 0.001% (w/v). pH was adjusted to pH = 5 (ELR5), pH = 4.5 (PAs), and pH = 4.5 (GO). All samples were sonicated for 30 min prior taking the measurement. Zeta potential was measured at 25°C on a Zetasizer (Nano-ZS ZEN 3600, Malvern Instruments, UK).

### Circular Dichroism Spectroscopy

ELR5 and PAs were dissolved in MilliQ water [0.025 and 0.01% (w/v), respectively]. In order to carry out the measurement at the same conditions as membrane formation, pH was adjusted to pH = 5 (ELR5) and pH = 4.5 (PAs). GO was diluted to the final concentration of 0.001% (w/v) and pH was adjusted to pH = 4.5. CD spectra were obtained using 1 mm path length and 300 μl volume quartz cuvette (Chirascan, Applied Photophysics, UK) between 195 and 270 nm with a 0.5 nm interval at 25°C. CD measurement was conducted using Chirascan™ CD spectrometer (Chirascan, Applied Photophysics Ltd, UK) equipped with a Peltier temperature controller, under a constant nitrogen purging at a constant pressure of 0.7 MPa. Each represented spectrum is the average of three consecutive spectra.

### Turbidity

ELR5 and PA were dissolved in MilliQ water [0.025 and 0.01% (w/v), respectively]. GO was diluted to the final concentration of 0.001% (w/v). Absorbance of the solutions was measured at 300 nm using a microplate reader (Spetrostarnano, BMG Labtech, UK) at 4 and 40°C.

### Transmission Electron Microscopy

Membranes were formed as described. After washing with MilliQ water membranes were crosslinked with TEM grade glutaraldehyde followed by dehydration with a gradient 30–100% of ethanol. Membranes were then embedded on LRWhite resin and ethanol 50–50% for 1 h and 100% LRW 1 h and again 100% LRW overnight. The following day they were encased in capsules filled with resin and left in the oven at 60°C for 5 h to harden. The block was sectioned with a Reicht microtome to a thickness of 70 nm. The sections were loaded onto a copper grid and stained with 2% uranyl acetate for 4 min and rinsed in MilliQ water. The samples were visualized on a JEOL JEM 1230 electron microscope operating at 80 kV.

### Scanning Electron Microscopy

ELR5/PA/GO membranes were left to develop for 48 h and then washed in MilliQ water and fixed with 2.5% glutaraldehyde in MilliQ water for 2 h at room temperature. Then, the samples were washed in MilliQ water followed by dehydration by immersion in an increasing concentration of ethanol (20, 50, 70, 90, 96, and 100%). The samples were then subjected to a process of critical point drying (K850, Quorum Technologies, UK) followed by

sputter-coating with gold for 90 s. SEM imaging was carried out using an Inspect F50 (FEI Comp, The Netherlands).

### GO Distribution

Membranes were formed as previously described. After washing in MilliQ water membranes were cut open, put flat on a microscope slide and then covered with a slide cover. 3D images were obtained with Zeiss LSM710 confocal microscope.

### GO Mass

Fully formed and washed membranes were dissolved in 1,1,1,3,3,3-hexafluoro-2-propanol (HFIP) followed by sonication for 30 min. GO absorbance was measured spectrophotometrically in the UV-Vis region. Standard curve was prepared using a solution of GO flakes in HFIP at a known concentration.

### Atomic Force Microscopy

Atomic force microscopy was used to measure Young's Modulus of the investigated system. Membranes were attached to a Petri dish using a drop of cyanoacrylate adhesive and left for a minute for the adhesive to dry followed by immersion in ultrapure MilliQ water. Young's Modulus measurements were taken with JPK Nanowizard-1 (JPK Instruments, Germany) in force spectroscopy mode, which was mounted on an inverted optical microscope (IX-81, Olympus, Japan). Indentation was carried out using quadratic pyramidal cantilevers (MLCT, Bruker, MA, USA) with spring constant of 0.07 N/m and half-angle to face of 17.5°. Measurements were taken in multiple areas per sample and multiple times per area.

### Cell Studies

Fully developed membranes were washed with MilliQ water and crosslinked with genipin at a concentration of 25 μl/ml at 37°C overnight. Tubes were then washed in MilliQ water and sterilized under UV light for 20 min. After sterilization, tubes were washed three times in Hank's balanced salt solution. 50,000 mADSCs re-suspended in DMEM (10% FBS, 1% P/S) were seeded on each ELR5/PA/GO tube. Media was changed every 2 to 3 days.

### Cell Attachment

Cells were seeded as previously described in a serum free DMEM media and incubated for 4 h followed by additional 4 h in full media (DMEM with 20% FBS). Cells were fixed with 4% paraform aldehyde for 1 h and stained with blue dye 4'-6-diamino-2-phenylindole (DAPI), followed by imaging under an epifluorescent microscope (Leica DMi8).

*Cell morphology* was assessed by using epifluorescent microscopy (Leica DMi8). After the cell culture membranes were fixed with 4% paraform aldehyde for 1 h and stained with DAPI and Phalloidin CruzFluor™ 647.

*Cell metabolic activity* was assessed on days 2, 7, and 14 with AlamarBlue™ cell metabolic assay. Membranes were incubated for 2 h at 37°C in a 10% (v/v) solution of AlamarBlue™ in DMEM. Fluorescence of the solution was then read at 570 and 595 nm using a microplate reader (Spetrostarnano, BMG Labtech, UK).

*Cell proliferation* was assessed by quantifying the number of adherent cells to membranes with Quant-iT™ PicoGreen™ assay on days 2, 7, and 14. Briefly, cells were lysed and the supernatant solution was diluted in assay buffer followed by addition of Quant-iT™ PicoGreen™ reagent and incubation for 5 min at RT. Fluorescence of the samples was measured at 480 nm (excitation) and 520 nm (emission) using a microplate reader (Spetrostarnano, BMG Labtech, UK). The DNA concentration for each sample was calculated by using a standard curve.

## DATA AVAILABILITY STATEMENT

The raw data supporting the conclusions of this article will be made available by the authors, without undue reservation.

## AUTHOR CONTRIBUTIONS

AMat, ES, AD, and AMaj designed the project and wrote the article. CR-G synthesized Pas. JR-C provided ELR. EC and KI-B helped with data interpretation. AMaj, MG, and AR conducted experiments and analyzed data.

## ACKNOWLEDGMENTS

This work was supported by the ERC Starting Grant (STROFUNSCAFF), the Marie Curie Career Integration Grant (BIOMORPH), the AO Research Fund of the AO Foundation project number AOCMF-17-19M, and the UK Regenerative Medicine Platform (UKRMP2) Acellular Smart Materials. Also, the authors are grateful for funding from the Spanish Government (MAT2016-78903-R), Junta de Castilla y León (VA317P18), Interreg V A España Portugal POCTEP (0624_2IQBIONEURO_6_E), and Centro en Red de Medicina Regenerativa y Terapia Celular de Castilla y León. Furthermore, we would like to acknowledge the Program for Innovation and Human Capital from the Ministry of Science, Technology, and Telecommunications of the Republic of Costa Rica (MICITT-PINN-PED-014-2015-2).

## SUPPLEMENTARY MATERIAL

The Supplementary Material for this article can be found online at: https://www.frontiersin.org/articles/10.3389/fmats.2020.00167/full#supplementary-material

## REFERENCES

Azarniya, A., Eslahi, N., Mahmoudi, N., and Simchi, A. (2016). Effect of graphene oxide nanosheets on the physico-mechanical properties of chitosan/bacterial cellulose nanofibrous composites. *Compos. Part A Appl. Sci. Manuf.* 85, 113–122. doi: 10.1016/j.compositesa.2016.03.011

Azevedo, H. S. (2019). "Biomaterials inspired by biology: from molecules to self-assembly," *Reference Module in Biomedical Sciences* (Elsevier), 109–117.

Capito, R. M., Azevedo, H. S., Velichko, Y. S., Mata, A., and Stupp, S. I. (2008). Self-assembly of large and small molecules into hierarchically ordered sacs and membranes. *Science* 319, 1812–1816. doi: 10.1126/science.1154586

Depan, D., Pesacreta, T. C., and Misra, R. D. K. (2014). The synergistic effect of a hybrid graphene oxide-chitosan system and biomimetic mineralization on osteoblast functions. *Biomater. Sci.* 2, 264–274. doi: 10.1039/C3BM60192G

Dinescu, S., Ionita, M., Pandele, A. M., Galateanu, B., Iovu, H., Ardelean, A., et al. (2014). *In vitro* cytocompatibility evaluation of chitosan/graphene oxide 3D scaffold composites designed for bone tissue engineering. *Biomed. Mater. Eng.* 24, 2249–2256. doi: 10.3233/BME-141037

Discher, D. E., Janmey, P., and Wang, Y. L. (2005). Tissue cells feel and respond to the stiffness of their substrate. *Science* 310, 1139–1143. doi: 10.1126/science.1116995

Draper, E. R., Eden, E. G., McDonald, T. O., and Adams, D. J. (2015). Spatially resolved multicomponent gels. *Nat. Chem.* 7, 848–852. doi: 10.1038/nchem.2347

Gazit, E. (2007). Self-assembled peptide nanostructures: the design of molecular building blocks and their technological utilization. *Chem. Soc. Rev.* 36:1263. doi: 10.1039/b605536m

Gentile, P., Ferreira, A. M., Callaghan, J. T., Miller, C. A., Atkinson, J., Freeman, C., et al. (2017). Multilayer nanoscale encapsulation of biofunctional peptides to enhance bone tissue regeneration *in vivo*. *Adv. Healthc. Mater.* 6:1601182. doi: 10.1002/adhm.201601182

Han, D., Yan, L., Chen, W., and Li, W. (2011). Preparation of chitosan/graphene oxide composite film with enhanced mechanical strength in the wet state. *Carbohydr. Polym.* 83, 653–658. doi: 10.1016/j.carbpol.2010.08.038

Hedegaard, C. L., Collin, E. C., Redondo-Gómez, C., Nguyen, L. T., Ng, K. W., Castrejón-Pita, A. A., et al. (2018). Hydrodynamically guided hierarchical self-assembly of peptide-protein bioinks. *Adv. Funct. Mater.* 28:1703716. doi: 10.1002/adfm.201703716

Inostroza-Brito, K. E., Collin, E., Siton-Mendelson, O., Smith, K. H., Monge-Marcet, A., Ferreira, D. S., et al. (2015). Co-Assembly, spatiotemporal control and morphogenesis of a hybrid protein-peptide system. *Nat. Chem.* 7, 897–904. doi: 10.1038/nchem.2349

Inostroza-Brito, K. E., Collin, E. C., Majkowska, A., Elsharkawy, S., Rice, A., Armando, E., et al. (2017). Cross-linking of a biopolymer-peptide co-assembling system. *Acta Biomater.* 58, 80–89. doi: 10.1016/j.actbio.2017.05.043

Jalaja, K., Sreehari, V. S., Kumar, P. R. A., and Nirmala, R. J. (2016). Graphene oxide decorated electrospun gelatin nanofibers: fabrication, properties and applications. *Mater. Sci. Eng. C* 64, 11–19. doi: 10.1016/j.msec.2016.03.036

Justino, C. I. L., Gomes, A. R., Freitas, A. C., Duarte, A. C., and Rocha-Santos, T. A. P. (2017). Graphene based sensors and biosensors. *TrAC Trends Anal. Chem.* 91, 53–66. doi: 10.1016/j.trac.2017.04.003

Kang, S., Park, J. B., Lee, T. J., Ryu, S., Bhang, S. H., La, W. G., et al. (2015). Covalent conjugation of mechanically stiff graphene oxide flakes to three-dimensional collagen scaffolds for osteogenic differentiation of human mesenchymal stem cells. *Carbon* 83, 162–172. doi: 10.1016/j.carbon.2014.11.029

Kumar, M., Ing, N. L., Narang, V., Wijerathne, N. K., Hochbaum, A. I., and Ulijn, R. V. (2018). Amino-acid-encoded biocatalytic self-assembly enables the formation of transient conducting nanostructures. *Nat. Chem.* 10, 696–703. doi: 10.1038/s41557-018-0047-2

Lee, J. H., Lee, Y., Shin, Y. C., Kim, M. J., Park, J. H., Hong, S. W., et al. (2016). *In situ* forming gelatin/graphene oxide hydrogels for facilitated C2C12 myoblast differentiation. *Appl. Spectrosc. Rev.* 51, 527–539. doi: 10.1080/05704928.2016.1165686

Li, J., Ren, N., Qiu, J., Mou, X., and Liu, H. (2013). Graphene oxide-reinforced biodegradable genipin-cross-linked chitosan fluorescent biocomposite film and its cytocompatibility. *Int. J. Nanomed.* 8, 3415–3426. doi: 10.2147/IJN.S51203

Lin, J., Chen, X., and Huang, P. (2016). Graphene-based nanomaterials for bioimaging. *Adv. Drug Deliv. Rev.* 105, 242–254. doi: 10.1016/j.addr.2016.05.013

Liu, J., Cui, L., and Losic, D. (2013). Graphene and graphene oxide as new nanocarriers for drug delivery applications. *Acta Biomater.* 9, 9243–9257. doi: 10.1016/j.actbio.2013.08.016

Mata, A., Hsu, L., Capito, R., Aparicio, C., Henrikson, K., and Stupp, S. I. (2009). Micropatterning of bioactive self-assembling gels. *Soft Matter* 5, 1228–1236. doi: 10.1039/b819002j

Mata, A., Palmer, L., Tejeda-Montes, E., and Stupp, S. I. (2012). Design of biomolecules for nanoengineered biomaterials for regenerative medicine. *Methods Mol. Biol.* 811, 39–49. doi: 10.1007/978-1-61779-388-2_3

Mazaheri, M., Akhavan, O., and Simchi, A. (2014). Flexible bactericidal graphene oxide-chitosan layers for stem cell proliferation. *Appl. Surf. Sci.* 301, 456–462. doi: 10.1016/j.apsusc.2014.02.099

Mendes, A. C., Baran, E. T., Reis, R. L., and Azevedo, H. S. (2013). Self-assembly in nature: using the principles of nature to create complex nanobiomaterials. *Wiley Interdiscip. Rev. Nanomed. Nanobiotechnol.* 5, 582–612. doi: 10.1002/wnan.1238

Navon, Y., and Bitton, R. (2016). Elastin-like peptides (ELPs) building blocks for stimuli-responsive self-assembled materials. *Isr. J. Chem.* 56, 581–589. doi: 10.1002/ijch.201500016

Newcomb, C. J., Sur, S., Ortony, J. H., Lee, O. S., Matson, J. B., Boekhoven, J., et al. (2014). Cell death versus cell survival instructed by supramolecular cohesion of nanostructures. *Nat. Commun.* 5:3321. doi: 10.1038/ncomms4321

Okesola, B. O., Lau, H. K., Derkus, B., Boccorh, D. K., Wu, Y., Wark, A. W., et al. (2020a). Covalent co-assembly between resilin-like polypeptide and peptide amphiphile into hydrogels with controlled nanostructure and improved mechanical properties. *Biomater. Sci.* 8, 846–857. doi: 10.1039/C9BM01796H

Okesola, B. O., and Mata, A. (2018). Multicomponent self-assembly as a tool to harness new properties from peptides and proteins in material design. *Chem. Soc. Rev.* 47, 3721–3736. doi: 10.1039/C8CS00121A

Okesola, B. O., Ni, S., Derkus, B., Galeano, C. C., Hasan, A., Wu, Y., et al. (2020b). Growth-factor free multicomponent nanocomposite hydrogels that stimulate bone formation. *Adv. Funct. Mater.* 30:1906205. doi: 10.1002/adfm.201906205

Okesola, B. O., Wu, Y., Derkus, B., Gani, S., Wu, D., Knani, D., et al. (2019). Supramolecular self-assembly to control structural and biological properties of multicomponent hydrogels. *Chem. Mater.* 31, 7883–7897. doi: 10.1021/acs.chemmater.9b01882

Pashuck, E. T., Cui, H., and Stupp, S. I. (2010). Tuning supramolecular rigidity of peptide fibers through molecular structure. *J. Am. Chem. Soc.* 132, 6041–6046. doi: 10.1021/ja908560n

Perczel, A., and Fasman, G. D. (1992). Quantitative analysis of cyclic beta-turn models. *Protein Sci.* 26, 1527–1572.

Rajan Unnithan, A., Ramachandra Kurup Sasikala, A., Park, C. H., and Kim, C. S. (2017). A unique scaffold for bone tissue engineering: an osteogenic combination of graphene oxide–hyaluronic acid–chitosan with simvastatin. *J. Ind. Eng. Chem.* 46, 182–191. doi: 10.1016/j.jiec.2016.10.029

Raymond, D. M., and Nilsson, B. L. (2018). Multicomponent peptide assemblies. *Chem. Soc. Rev.* 47, 3659–3720. doi: 10.1039/C8CS00115D

Redondo-Gómez, C., Abdouni, Y., Becer, C. R., and Mata, A. (2019). Self-assembling hydrogels based on a complementary host-guest peptide amphiphile pair. *Biomacromolecules* 20, 2276–2285. doi: 10.1021/acs.biomac.9b00224

Schneider, C. A., Rasband, W. S., and Eliceiri, K. W. (2012). NIH image to imageJ: 25 years of image analysis. *Nat. Methods* 9, 671–675. doi: 10.1038/nmeth.2089

Shao, L., Chang, X., Zhang, Y., Huang, Y., Yao, Y., and Guo, Z. (2013). Graphene oxide cross-linked chitosan nanocomposite membrane. *Appl. Surf. Sci.* 280, 989–992. doi: 10.1016/j.apsusc.2013.04.112

Shin, S. R., Li, Y. C., Jang, H. L., Khoshakhlagh, P., Akbari, M., Nasajpour, A., et al. (2016). Graphene-based materials for tissue engineering. *Adv. Drug Deliv. Rev.* 105, 255–274. doi: 10.1016/j.addr.2016.03.007

Stankovich, S., Piner, R. D., Nguyen, S. B. T., and Ruoff, R. S. (2006). Synthesis and exfoliation of isocyanate-treated graphene oxide nanoplatelets. *Carbon* 44, 3342–3347. doi: 10.1016/j.carbon.2006.06.004

Stephanopoulos, N., Ortony, J. H., and Stupp, S. I. (2013). Self-assembly for the synthesis of functional biomaterials. *Acta Mater.* 61, 912–930. doi: 10.1016/j.actamat.2012.10.046

Tang, H., Liu, D., Zhao, Y., Yang, X., Lu, J., and Cui, F. (2015). Molecular dynamics study of the aggregation process of graphene oxide in water. *J. Phys. Chem. C* 119, 26712–26718. doi: 10.1021/acs.jpcc.5b07345

Wan, C., Frydrych, M., and Chen, B. (2011). Strong and bioactive gelatin-graphene oxide nanocomposites. *Soft Matter* 7, 6159–6166. doi: 10.1039/c1sm05321c

Webber, M. J., Tongers, J., Renault, M. A., Roncalli, J. G., Losordo, D. W., and Stupp, S. I. (2010). Development of bioactive peptide amphiphiles for therapeutic cell delivery. *Acta Biomater.* 6, 3–11. doi: 10.1016/j.actbio.2009.07.031

Whitesides, G. M., and Grzybowski, B. (2002). Self-assembly at all scales. *Science* 295, 2418–2421. doi: 10.1126/science.1070821

Wick, P., Louw-Gaume, A. E., Kucki, M., Krug, H. F., Kostarelos, K., Fadeel, B., et al. (2014). Classification framework for graphene-based materials. *Angew. Chem. Int. Ed.* 53, 7714–7718. doi: 10.1002/anie.201403335

Yang, Y., Asiri, A. M., Tang, Z., Du, D., and Lin, Y. (2013). Graphene based materials for biomedical applications. *Mater. Today* 16, 365–373. doi: 10.1016/j.mattod.2013.09.004

Zhang, S. (2003). Fabrication of novel biomaterials through molecular self-assembly. *Nat. Biotechnol.* 21, 1171–1178. doi: 10.1038/nbt874

Zhang, S., Greenfield, M. A., Mata, A., Palmer, L. C., Bitton, R., Mantei, J. R., et al. (2010). A self-assembly pathway to aligned monodomain gels. *Nat. Mater.* 9, 594–601. doi: 10.1038/nmat2778

Zhou, X., Nowicki, M., Cui, H., Zhu, W., Fang, X., Miao, S., et al. (2017). 3D bioprinted graphene oxide-incorporated matrix for promoting chondrogenic differentiation of human bone marrow mesenchymal stem cells. *Carbon* 116, 615–624. doi: 10.1016/j.carbon.2017.02.049

Zhu, Y., Murali, S., Cai, W., Li, X., Suk, J. W., Potts, J. R., et al. (2010). Graphene and graphene oxide: synthesis, properties, and applications. *Adv. Mater.* 22, 3906–3924. doi: 10.1002/adma.201001068

**Conflict of Interest:** The authors declare that the research was conducted in the absence of any commercial or financial relationships that could be construed as a potential conflict of interest.

frontiers in Bioengineering and Biotechnology

ORIGINAL RESEARCH
published: 26 June 2020
doi: 10.3389/fbioe.2020.00724

# Clarifying the Tooth-Derived Stem Cells Behavior in a 3D Biomimetic Scaffold for Bone Tissue Engineering Applications

*Christiane L. Salgado[1,2]*, Cristina C. Barrias[1,2,3] and Fernando J. M. Monteiro[1,2,4]*

*[1] i3S – Instituto de Investigação e Inovação em Saúde, Universidade do Porto, Porto, Portugal, [2] INEB, Instituto Nacional de Engenharia Biomédica, Universidade do Porto, Porto, Portugal, [3] ICBAS, Instituto de Ciências Biomédicas Abel Salazar, Universidade do Porto, Porto, Portugal, [4] FEUP, Faculdade de Engenharia da Universidade do Porto, Departamento de Engenharia Metalúrgica e Materiais, Porto, Portugal*

Massive amounts of cell are needed for creating tissue engineered 3D constructs, which often requires culture on scaffolds under dynamic conditions to facilitate nutrients and oxygen diffusion. Dynamic cultures are expected to improve cell viability and proliferation rate, when compared to static conditions. However, cells from distinct types and/or tissues sources may respond differently to external stimuli and be incompatible with culture under mechanical shear stress. The first aim of this work was to show that dental stem cells are a valuable source for improving bone regeneration potential of artificial grafts. Mesenchymal stem/stromal cells (MSCs) were isolated from human dental follicle (hDFMSC) and pulp tissues (hDPMSC) and shown to express prototypical stem cell markers. The follicle and pulp dental MSCs capacity to differentiate into osteoblast lineage was evaluated after seeding on 3D porous scaffolds of collagen-nanohydroxyapatite/phosphoserine biocomposite cryogel with osteogenic factors in the culture medium. Both tooth-derived MSCs were able to show high ALP activity, express osteogenic gene markers and secrete osteopontin (OPN). Thereafter, designed multicompartment holder adaptable to spinner flasks was used for dynamic culture (50 rpm) of both dental MSCs types within the porous 3D scaffolds. Standard static culture conditions were used as control. Culture under dynamic conditions promoted follicle MSCs proliferation, while improving their spatial distribution within the scaffold. Under dynamic conditions, the biocomposite scaffold promoted MSCs osteogenic differentiation, as suggested by increased alkaline phosphatase (ALP) activity, higher osteogenic gene expression and OPN deposition. In a similar manner, under dynamic conditions, dental pulp MSCs also showed higher ALP activity and proliferation rate, but lower amounts of osteopontin secretion, when compared to static conditions. After implantation, dental follicle MSCs-loaded 3D scaffolds cultured under dynamic conditions showed higher tissue ingrowth and osteogenic differentiation (higher human OPN secretion) than dental pulp cells. Overall, this study explored the use of tooth-derived stem cells as a clinical alternative source for bone tissue engineering, together

OPEN ACCESS

**Edited by:**
*Lia Rimondini,*
*University of Eastern Piedmont, Italy*

**Reviewed by:**
*Bojana Obradovic,*
*University of Belgrade, Serbia*
*Livia Visai,*
*University of Pavia, Italy*

***Correspondence:**
*Christiane L. Salgado*
*csalgado@ineb.up.pt;*
*christianesalgado@gmail.com*

**Specialty section:**
*This article was submitted to Biomaterials, a section of the journal Frontiers in Bioengineering and Biotechnology*

**Received:** *20 March 2020*
**Accepted:** *09 June 2020*
**Published:** *26 June 2020*

**Citation:**
*Salgado CL, Barrias CC and Monteiro FJM (2020) Clarifying the Tooth-Derived Stem Cells Behavior in a 3D Biomimetic Scaffold for Bone Tissue Engineering Applications. Front. Bioeng. Biotechnol. 8:724. doi: 10.3389/fbioe.2020.00724*

with an innovative device for dynamic culture of cell-laden 3D scaffolds. Results showed that human MSCs response upon culture on 3D scaffolds, depends on the cells source and the culture regimen. This suggests that both the type of cells and their culture conditions should be carefully adjusted according to the final clinical application.

**Keywords: dental pulp and follicle stem cells, 3D multicompartment holder, bone tissue engineering, biomaterials, collagen, nanohydroxyapatite**

## INTRODUCTION

Maxillofacial large bone defects may derive from various causes, such as traffic accidents, falls, inflammatory process, oral tumors, and others, both on their own or in combination with other injuries (Lee, 2012). The surgical treatment relies on amputation of large portions of hard and soft tissue, generating major problems to patients, causing very limitative disabilities and significantly reduced quality of life. Clinical solutions for bone repair include allografts, autografts and commercially available bone grafts eventually associated to titanium internal fixation implants. Therapies employing autografts present the disadvantage of requiring a second surgical site to obtain the donor-bone, consequently increasing the risk of co-morbidity. On the other hand, natural and synthetic bone grafts need only one surgery, but repairing these bone tissues requires the reconstruction of their biological and functional properties, which cannot be accomplished yet through such clinical strategies (Amini et al., 2012).

In a Tissue Engineering strategy, biomimetic 3D scaffolds are a fundamental tool for bone regeneration, but cell adhesion and expansion on the material's surface, fulfilling the overall structure is still a challenge yet to be tackled. Human mesenchymal cell source is a key part to achieve the promise of tissue regeneration. There is the need for high quality adult stem cells from an easily accessible source (Ratajczak et al., 2016). As alternative cell lines, isolated human dental pulp and follicle stem cells were confirmed to show multipotency, and self-renewal capability (Morsczeck et al., 2005), thus being a suitable alternative source of stem cells for the purpose of cell-based therapies for hard-tissue engineering such as for craniofacial defects, as well as in alveolar bone defects. They are also a suitable alternative source of stem cells for the purpose of cell-based therapies in regenerative medicine due to their multilineage differentiation potential as well as their immunomodulatory properties, where they should interplay to suppress excessive inflammation during tissue repair (Sharpe, 2016). The minimally invasive isolation of these stem cells from extracted third molars raised high hopes for potential clinical applications (Sharpe, 2016). Recently, dental pulp stem cells showed bone regeneration efficacy similar to the one of bone marrow MSCs *in vivo* and should be a promising cell source for bone defects repair (Lee et al., 2019). In addition, dental follicle stem cells were found to be the precursor cells of periodontal tissues cells (PTCs) including fibroblasts in the periodontal dental ligament (PDL), alveolar bone cells, and cementoblasts. In addition, studies have shown an abundance of bioactive molecules, factors, and proteins related to dental tissue formation in the mineralized matrix (Yao et al., 2008).

The cell response and stability when cultured inside 3D porous scaffolds in a tissue engineering (TE) assay should require 3D cell culture technologies. Dynamic culture has previously shown to positively affect human MSCs proliferation, differentiation, and ECM production when compared to static 3D cultures (Woloszyk et al., 2014). A dynamic culture system should improve nutrients and oxygen diffusion, avoiding hypoxia-induced central necrosis in cultured tissue constructs (Tsai et al., 2019). However, some bioreactors could promote hydrodynamic stress during cell culture resulting in shear stress, thus causing cell damage (Tanzeglock et al., 2009). Some types of dynamic conditions may also generate air bubbles, and bubble–liquid interphase has shown to cause cells damages (Walls et al., 2017). In this context, dynamic culture systems, such as spinner flasks, are widely used due to their ability to improve mass transfer in cell cultures suspension. However, few studies describe the use of spinner flasks for cell cultures in three-dimensional (3D) scaffolds, because this culture system type is often unsuitable, since several factors, as scaffold geometry, porosity and hydrophilicity should influence the cellular vitality and proliferation rate of cells seeded on/inside porous 3D scaffolds (Gelinsky et al., 2015). To address hypoxia-induced central necrosis in cultured tissue constructs, a multi-compartment holder adaptable to spinner flasks for 3D cell-loaded materials culture was developed in-house (Teixeira et al., 2014). The implementation of adequate dynamic conditions is critical to obtain successful 3D cultures and favor the use of 3D scaffolds as an approach closer to physiological conditions in tissue engineering (Barrias and Goncalves, 2013). This proposed device should protect matrices with low mechanical strength from the shear stress promoted by the stirring process, avoiding inappropriate floating exposure.

Numerous types of biocomposite materials based on collagen and nanohydroxyapatite are widely studied (Teixeira et al., 2010; Rodrigues et al., 2013; Salgado et al., 2016) and are well known to improve bone regeneration and fulfil small craniofacial defects. These composite materials could have surface modifications in order to improve cell behavior, favor mesenchymal stem cells adhesion and control cell differentiation into the desired cell types, allowing the regeneration of the host tissue/organ. Phosphoserine (O-phospho-L-serine) is a phosphorylated amino-acid (OPS) and shall be able to mimic typical osteopontin functionalities, such as the regulation of cell response, such as mitosis (proliferation), signaling, differentiation (D'Ambrosio et al., 2007), and also provide osteoconductive properties (Salgado et al., 2019).

The objectives of this work were to isolate tooth-derived stem cells (follicle and pulp tissues) as potential stem cell

sources and evaluate their capacity to differentiate *in vitro* into bone-like cells in a Collagen-nanohydroxyapatite/OPS (Coll-nanoHA/OPS) biomimetic 3D scaffold. After that, the aim was to evaluate both cell behavior under dynamic and static conditions within the biomaterial and their potential for osteo-differentiation *in vitro* and *in vivo*. To the best of our knowledge, the application of human dental stem cells in 3D biomimetic scaffolds with the purpose of bone tissue engineering has not been totally explored yet.

## MATERIALS AND METHODS

### Establishment of Stem Cell Cultures From the Human Dental Pulp and Follicle (hDPMSC and hDFMSC)

Human dental tissues fragments (pulp and follicle tissue) were collected, digested and MSCs were isolated by adherent culture on plastic tissue culture substrates (**Supplementary Material**). After confluence, cells were detached and characterized by flow cytometry and RT-PCR analysis (**Supplementary Data**). Human follicle and pulp MSCs were cultured in α-MEM (alpha modification of Eagle minimum essential medium, Sigma-Aldrich) with 10% fetal bovine serum (FBS, Gibco), 1% penicillin-streptomycin ($3 \times 10^{-4}$ mol/L and $5 \times 10^{-4}$ mol/L, Gibco) and maintained at 37°C in a 5% carbon dioxide ($CO_2$) atmosphere.

### Preparation of 3D Porous Scaffolds of Collagen, Nanohydroxyapatite and Phosphoserine (Coll-nanoHA/OPS) by a Cryogelation Method

Cryogels were produced as previously described (Rodrigues et al., 2013; Salgado et al., 2016, 2019). Briefly, bovine collagen Type I (Sigma-Aldrich, Germany) was homogenized (Ultra Turrax T25, IKA) at 10000 rpm, in 5 mM HCl (36.5–38% grade, Sigma-Aldrich, Germany) at a concentration of 2% (w/v). Collagen-nanoHA biocomposites were prepared by mixing the collagen solution with 1% nanoHA (particle size 5.0 ± 1.0, nanoXIM.HAp202, FLUIDINOVA, S.A, Portugal), final composition Collagen-nanoHA 50:50 w/w%). O-phospho-L-serine (OPS, ≥98% grade, Sigma-Aldrich, Germany) was added to the nanoHA suspension (0.5% w/w%) with the final mass proportion of 1:1:0.5 for the Coll-nanoHA/OPS scaffold. For the preparation of cryogels, materials were crosslinked with 10 mM of N-hydroxysuccinimide (NHS, 98% grade, Sigma-Aldrich, Germany) and 20 mM of 1-Ethyl-3-(3-dimethylaminopropyl)carbodiimide (EDC, ≥98% grade, Sigma-Aldrich, Germany), at the final mass proportion of 1:0.012:0.031 (collagen/NHS/EDC), and were kept in a freezer at −18°C for 24 h to complete the crosslinking. Afterward, materials were thawed at room temperature and the scaffolds were washed with distilled water and finally dried in a freeze-dryer (Labconco, FreeZone 6) at −80°C for 24 h.

### Cell Culture Into Biomimetic 3D Scaffolds (Coll-nanoHA/OPS)

A biocompatibility study was performed by culturing of human dental follicle and pulp mesenchymal stem cells (hDFMSC and hDPMSC) within osteoconductive scaffolds in basic or osteoinductive medium (0.1 mM dexamethasone, 0.1 mg/mL ascorbic acid and 10 mM b-glycerophosphate) that was added after 3 days of the culture. Scaffolds of collagen with nanohydroxyapatite and phosphoserine (Coll-nanoHA/OPS) were produced as described above and cut into 48 discs for each dental MSCs (5 mm × 4 mm). A total of $3 \times 10^5$ cells were seeded within each scaffold (12 samples with each cell type, hDFMSC or hDPMSC) by drop method. The cells were centrifuged and concentrated in a small volume ($3 \times 10^5$ cells/20 μl) and dropped onto the scaffold surface. Afterward, the scaffolds were placed inside a non-tissue culture 24-wells plate for four hours and put in the standard incubator (37°C, 95% humidified air and 5% v/v $CO_2$) to allow cell adhesion. Afterward, the wells were full filled (1.5 mL) with basic or osteoinductive cell culture medium and incubated for 1, 7, 14 and 21 days. These experiments aimed at evaluating hDFMSC and hDPMSC cells adhesion and viability within the biomaterials, measuring the cells proliferation and osteogenic differentiation potential, as well as determining cell morphology. Three independent experiments were performed to evaluate the cells viability and differentiation behavior.

### Dental MSCs-Loaded Coll-nanoHA/OPS 3D Scaffolds Under Static and Dynamic Conditions in the Multicompartment Holder for Spinner Flasks

Twenty-four scaffolds disks (Coll-nanoHA/OPS – 5 × 4 mm discs) loaded with hDFMSC and hDPMSC cells ($3 \times 10^5$ cells/scaffold) were cultured into 24 well-plate for 24 h. Later, twelve samples were transferred to a six-well culture plates (static culture - control) and the others to the multicompartment holder in a 25 mL spinner flask (dynamic conditions). Each multi-compartment holder had two containers with six independent compartments (6 mm diameter × 6 mm height) to house disk-shaped samples with a maximum size of 5 mm diameter × 5 mm height. Each individual compartment had 6 perforations of 1 mm on the top, bottom, and side, allowing fluid perfusion through 3D cell-material constructs. The container had a perforated lid to avoid free-floating samples. Under dynamic conditions, the spinner flask was kept under continuous agitation (50 rpm) with a total volume of 24 mL and, once a week the basic medium was half-renewed. The entire apparatus, including a magnetic stirring plate, was placed in a standard incubator (37°C, 95% humidified air and 5% v/v $CO_2$). Static cultures in six-well plates were performed, with one scaffold per well in 4 mL of basic medium, to maintain the same volume-to-disk ratio used under dynamic conditions. Medium feeding regimen was also identical to the one used for dynamic conditions. In both cases, cell-loaded materials were maintained during 7, 14 and 21 days. At the determined the time-points, the samples were collected and cell proliferation (DNA quantification by PicoGreen assay,

osteogenic differentiation by ALP activity and qPCR gene expression protocols described at section "Bone Differentiation of Human Dental MSCs in 3D Culture: Proliferation, Morphology and Differentiation."). Cell viability was checked after 7, 14 and 21 days (LIVE/DEAD assay). Three independent experiments were performed to evaluate the scaffold biocompatibility and differentiation behavior of the cells.

## Bone Differentiation of Human Dental MSCs in 3D Culture: Proliferation, Morphology and Differentiation

### DNA Extraction Assay

DNA content was measured using the Quant-iT$^{TM}$ Picogreen® DNA assay (Invitrogen, United Kingdom) according to the manufacturer's instructions. Briefly, after each time point, three scaffolds were washed with PBS, they were placed at 37°C and 5% $CO_2$ for 1 h with 0.5 ml of ultra-pure water. Subsequently, they were placed in a freezer at −80°C for 1 h and then thawed at room temperature to lyse all the cells membranes cultured on the materials. Finally, the fluorescence intensity was measured with a microplate spectrofluorometer (SynergyMx, BioTek) at 530 and 590 nm excitation and emission, respectively. The results are expressed in nanograms of DNA per milliliter.

### Confocal Laser Scanning Microscope

Two samples from each time-point were fixed (4% paraformaldehyde – Sigma) and incubated for 5 min with 0.1% Triton X100 solution (Sigma), washed with 1% bovine serum albumin solution in PBS (BSA, Sigma) and the actin (cytoplasm) were stained with Alexa Fluor-conjugated Phalloidin 594 nm (Invitrogen) at 2.5% for 1 h under darkness. Nuclei were stained with DAPI (4′-6-diamidine-2-phenylindole at 0.2%, Invitrogen). Finally, the scaffolds images were acquired with a Leica SP2 AOBS SE camera, with the excitation laser of 358 and 594 nm.

### Alkaline Phosphatase Activity and Protein Content

The same supernatant with the lysed cells obtained as described above (2.4.1) was used for the enzyme activity and total protein content protocol. ALP activity was assessed by the p-nitrophenol phosphate substrate hydrolysis (Sigma-Aldrich, Germany). After 1 h incubation at 37°C, the reaction was quantified by absorbance measurements at 405 nm, using a plate reader (Synergy$^{TM}$ HTX, BioTek). The ALP activity results were normalized to total protein content and were expressed in nanomoles of p-nitrophenol produced per minute per mg of protein. Total protein content was measured by Lowry's method with bovine serum albumin (Sigma-Aldrich, Germany) used as standard.

### Osteogenic Phenotype Analyses Through mRNA Expression of Runx-2, Osteopontin (OPN), BMP-2 and Osteocalcin (OC)

Total RNA was extracted from 3 dental MSCs-loaded scaffolds at each time point with NucleoSpin kit (NucleoSpin RNA, Macherey-Nagel, Germany), as recommended by the manufacturer. Subsequently, cDNA synthesis was obtained with the iScript$^{TM}$ cDNA Synthesis Kit (BioRad, United States) as recommended by the manufacturer. After cDNA synthesis reaction, quantitative real-Time PCR was carried out in mixture containing 1 μL of cDNA, 10 μM of each forward and reverse primers (**Supplementary Table 2**) and 10 μL of iTaq$^{TM}$ Universal SYBR® Green Supermix (BioRad, United States). qPCR experiments were run using an iQ5 (BioRad, United States) and analyzed with the iCycler IQ software (BioRad, United States). The housekeeping gene glyceraldehyde 3-phosphate dehydrogenase (GAPDH) was used as the endogenous assay control. Relative quantification of gene amplification by qPCR was performed using the cycle threshold (Ct) values and relative expression levels were calculated using the $2^{\wedge}(-\Delta\Delta CT)$ method. For each PCR, samples were analyzed in duplicate and three independent experiments were performed.

## Animal Model of Ectopic Intramembranous Ossification (IMO)

Twelve Coll-nanoHA/OPS scaffolds (5 × 4 mm discs) were seeded with hDFMSC or hDPMSC cells ($3 \times 10^5$ cells/scaffold) and cultured in a 24 well-plate for 24 h [similar as described above – section "Cell Culture Into Biomimetic 3D Scaffolds (Coll-nanoHA/OPS)"]. Afterward, samples were transferred to the multicompartment holder and cultured in the osteoinductive medium (described above) under dynamic conditions (50 rpm) for 7 days. Afterward, one control scaffold without cells, and one scaffold seeded with cells (hDFMSC or hDPMSC per scaffold) were subcutaneously transplanted into the dorso of each nude female mouse (4 animals), 6 week-old (i3S animal house, Portugal). The study was performed and approved by the Animal based studies Ethical Committee and fulfilled all legal requirements (i3S Animal Ethical Committee and DGAV, Portugal). Animals were anesthetized with 3–5% isoflurane for induction and 1–2% for surgical procedures that were performed under standard aseptic conditions. A midline incision through the dorsal skin was performed and three subcutaneous pockets were created, one on the right side (control material – without cells) and two on the left side (scaffolds with cells). The dorsal wound was then closed with surgical staples. After recovery, the mice were caged in pairs and allowed to move in their cages without restriction. They were fed with commercial mice chow and water for 8 weeks' ad lib. After the foreseen period of time, the mice were euthanized with carbon dioxide asphyxiation. A pilot *in vivo* test was performed with two animals to evaluate the *in vitro* cell culture with osteoinductive medium and different implantation time-points (4–8 weeks) to set the final experimentation conditions.

### Histology Analysis

All samples were explanted and fixed in 10% neutralized buffered formalin for three days and then processed for histology. Fixed samples were embedded in paraffin and were sectioned longitudinally with a microtome (5 μm of thickness). The sections were stained with Masson Trichrome and Alizarin red (calcium deposition) staining for light microscopy examination. Image analysis by the ImageJ software (Wayne Rasband) was

used to determine the percentage of total tissue ingrowth area (Masson Trichrome). For the evaluation of such parameter, over 20 images were used.

### Immunohistochemical Analysis

Immunohistochemical analysis were performed to stain the human ECM and cells. The human osteopontin (OPN) and HuNu nucleus were probed after antigen recovery. With this purpose, masked epitopes were exposed by treatment with citrate buffer (pH 9, Sigma-Aldrich, Germany) for 20 min at 97°C. Sections were incubated with mouse anti-human nuclei primary antibody (MAB4383-3 E1.3 Millipore, 1:400, United States) and rabbit anti-human osteopontin (AB 1870, Merck, 1:500, Germany). This procedure was followed by 1 h incubation with Alexa Fluor 594 goat anti-mouse IgG secondary antibody (Invitrogen Molecular Probes, 1:1000, United States) and Alexa Fluor 488 goat anti-rabbit IgG secondary antibody (Invitrogen Molecular Probes, 1:1000, United States). All slides were mounted in Vectashield$^{TM}$ with DAPI (Vector laboratories, United Kingdom). Images were obtained using a fluorescence inverted microscope (Axio Imager Z1, Zeiss, Germany). Image analysis by the ImageJ software (Wayne Rasband) was used to determine the percentage of total human osteopontin presence (Green area). For the evaluation of over 20 images were used.

## Statistical Analysis

Data were presented as mean ± standard deviation ($n = 3$) and they were analyzed using the two way ANOVA test. Differences between groups were considered statistically significant for $p < 0.05$.

# RESULTS

## Dental MSCs Characterization and Osteogenic Differentiation

Dental follicle and dental pulp stem cells markers expressions were investigated by flow cytometry analysis. Briefly, $10^6$ cells per sample were immune-labeled to evaluate positive expressions for CD44, CD90, CD73 and lack of expressions of CD34 and CD45, that indicate a mesenchymal stem cell phenotype. Results may be seen in **Supplementary Figure 1**. Both cells isolated from dental follicle and pulp highly expressed the positive marker CD90. Both cell types did not express the negative marker CD34 and CD45. A very important factor in elucidating the cellular basis of tissue regeneration is determining the multipotential capabilities of stem cells to differentiate into desired target tissue. Odontogenic tissues deriving from neural crest such as hDFMSCs, showed typical features of multipotency and were characterized by a high degree of plasticity. These stemness gene expression factors were evaluated by RT-PRC (**Supplementary Figure 2**). Both dental MSCs showed positive expression for SCF, Thy-1, (CD90), CXCR4, and negative expression for TERT. After osteogenic induction for 21 days in the supplemented culture medium, both hDPMSCs and hDFMSC lost the mesenchymal stem cell gene expression.

In line with other published research data, this work evaluated dental stem cells capacity to induce mineralization *in vitro* and that new bone formation *in vivo* might be possible using these stem cells. Based on existing information, optimal cell culture conditions were studied and it was observed that the biocompatibility of several substrates with dental pulp or follicle stem cells induced the differentiation into osteoblasts. Exposure to osteogenic differentiation environment, such as soluble factors (ascorbic acid, β-glycerol phosphate and dexamethasone) induced osteogenic differentiation of hDPMSC and hDFMSC in this study experiments. Simple osteoinductive medium without growth factors highly increased the gene expression of osteoblast main non-collagenous proteins (osteocalcin) as shown by qPCR. The ALP activity was increased in the osteogenic differentiation medium. Although ALP is a membrane marker of all types of stem cells, it is also a marker of osteogenic differentiation. In early stage differentiation (14 days) an initial peak of ALP was observed, followed by a gradual decrease (**Supplementary Figure 3**).

At that stage, collagen type I was deposited in *de novo* synthesized extracellular matrix. The final stage of osteogenic differentiation (21 days) was characterized by high levels of osteogenic gene expression (osteocalcin and BPM-2), and deposition of calcium phosphate (Alizarin red and Von Kossa staining) (**Supplementary Figures 4, 5**).

## Dental MSCs Proliferation, Morphology and Bone Differentiation Within Biomimetic (Coll-nanoHA/OPS) 3D Scaffolds

Due to their high proliferation rates and capacity to differentiate into osteoblasts, human dental stem cells offer great potential for clinical dentistry (Salasznyk et al., 2007). Recently, research on bioactive materials has been focusing in developing biomaterials with enhanced pro-regenerative potential. In this work, hDFMSC and hDPMSC were seeded within Collagen-nanoHA/OPS biocomposite scaffolds and cell proliferation was estimated by DNA quantification, as shown in **Figure 1**. The total DNA content of hDPMSC in 3D scaffolds for 21 days of culture in basic medium was similar to the one found when using the osteoinductive medium (**Figure 1A**). The same effect was not observed for hDFMSC (**Figure 1B**). It was possible to observe that hDFMSC exhibited higher proliferation rates than hDPMSC. Moreover, total DNA after 21 days were four fold higher in the basic medium when compared to the osteoinductive medium.

Cell distribution within Collagen-nanoHA/OPS biocomposite scaffolds (day 14 and 21) was observed by CLSM. Images (**Figures 1C–J**) show that dental follicle and pulp cells were well spread over all samples, entirely covering the scaffolds surfaces. CLSM images also corroborate that the scaffolds with hDPMSC have fewer cells, when compared to scaffolds with hDFMSC. Furthermore, the distribution of dental MSCs seemed to follow the irregularities of the materials' surfaces, with cells covering the pore walls (**Figures 1C–J**).

The functional activity of hDPMSC and hDFMSC on Collagen-nanoHA/OPS biocomposite scaffolds was assessed by

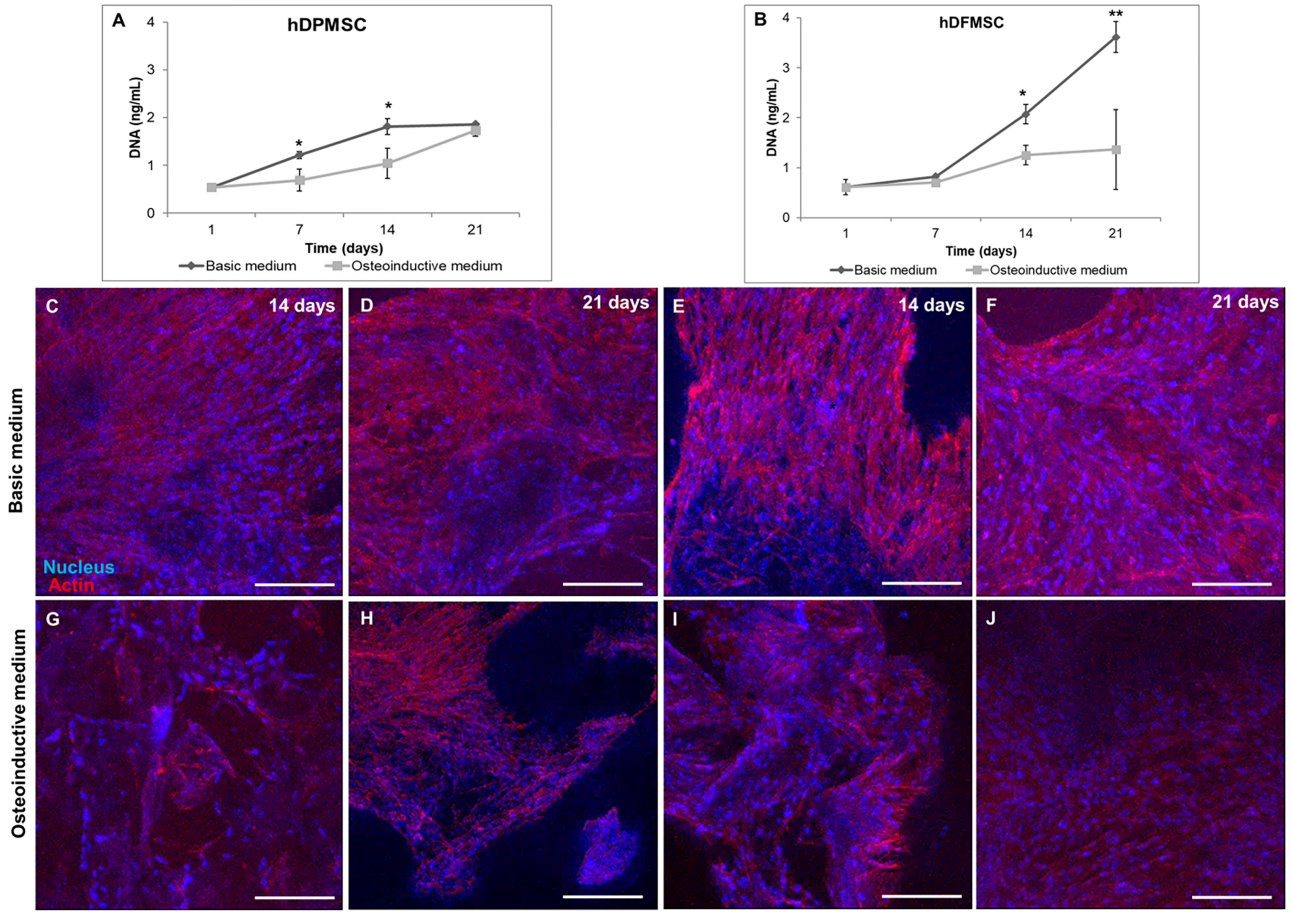


**FIGURE 1 |** DNA concentration of hDPMSC **(A)** and hDFMSC **(B)** cultured within Coll-nanoHA/OPS for 7, 14 and 21 days in the basic vs. osteoinductive medium. Statistical analysis $^{*}p < 0.05$ and $^{**}p < 0.01$. CLSM maximum *Z* projection images (200 μm depth) of hDPMSC **(C,D,G,H)** and hDFMSC **(E,F,I,J)** cultured for 14 and 21 days within collagen-nanoHA/OPS biocomposite scaffolds in the basic or in the osteoinductive medium osteoinductive medium. Scale: 200 μm.

measuring the ALP activity after culture for up to 21 days. ALP produced by the cells was normalized to the total protein content, and results were expressed in nmol/min/ng, as shown in **Figure 2**. hDPMSC cultured on the biomimetic scaffold showed higher ALP activity under osteoinductive than under basic conditions, for all time points, but the difference was only statistically significant at day 14 (**Figure 2A**). However, hDFMSC seeded on Collagen-nanoHA/OPS biocomposite scaffolds exhibited significantly higher ALP levels after 14 and 21 days of culture in osteoinductive medium, and the double of activity when compared to hDPMSCs (**Figure 2**).

In accordance to ALP activity results, the quantitative PCR evaluation after 21 days showed expression of several osteoblast-associated markers by dental MSCs in both osteoinductive and basic culture medium (**Figure 3**). The hDPMSC seeded on scaffolds under basic conditions showed a 2-fold enhancement for Runt related transcription factor 2 (Runx-2) and bone morphogenetic protein type 2 (BMP-2); and 6-fold for osteocalcin (**Figure 3A**). The hDFMSC showed a 30-fold change for Runx-2 and BMP-2 expressions, and 40-fold for OPN (**Figure 3B**). Both dental MSCs lost the expression of the multipotency stem cell gene Oct3/4 (transcription factor for MSC) after osteogenic differentiation (**Figures 3A,B**).

## Cell-Loaded 3D Scaffolds Under Static and Dynamic Conditions in the Multicompartment Holder for Spinner Flasks

Dynamic conditions were established using spinner flasks under 50 rpm agitation speed, equipped with an in-house designed multicompartment holder that protects the scaffolds from damage (Teixeira et al., 2014). Both types of dental MSCs cultured within Coll-nanoHA/OPS 3D scaffolds were able to survive, actively proliferate, and migrate throughout the scaffolds depth, under dynamic conditions. Under dynamic conditions, after 14 days hDPMSC showed higher DNA concentration and an increase in cell numbers, that remained similar after 21 days. Different proliferation rates were observed under static conditions, the hDPMSC number decreased over time (**Figure 4A**). Dental follicle MSCs proliferation was confirmed by the increase in DNA content after 14 days, although

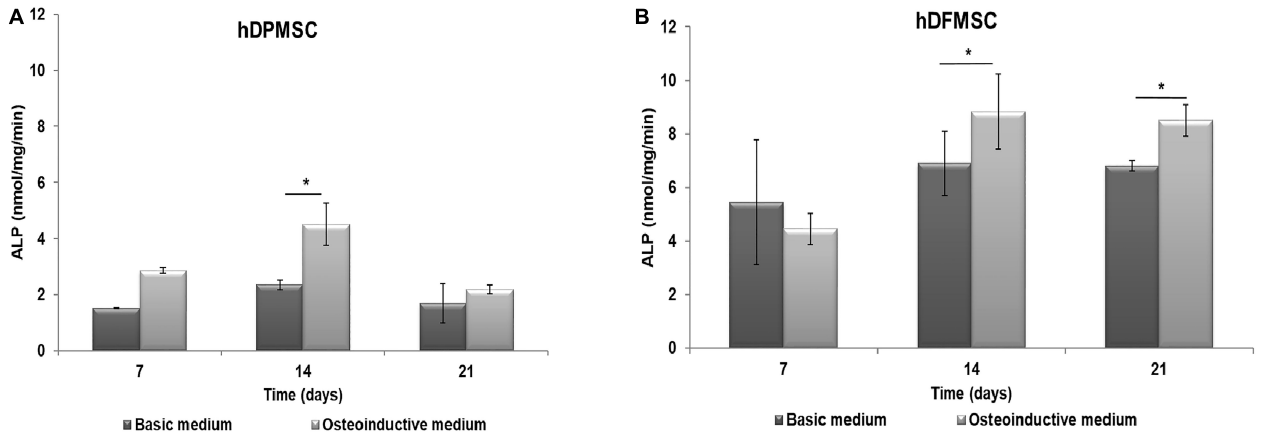


**FIGURE 2 |** ALP activity of **(A)** hDPMSC and **(B)** hDFMSC cells cultured osteoinductive medium within Coll-nanoHA/OPS scaffolds for 7, 14 and 21 days in the basic or osteoinductive medium. Statistical analysis $^{*}p < 0.05$.

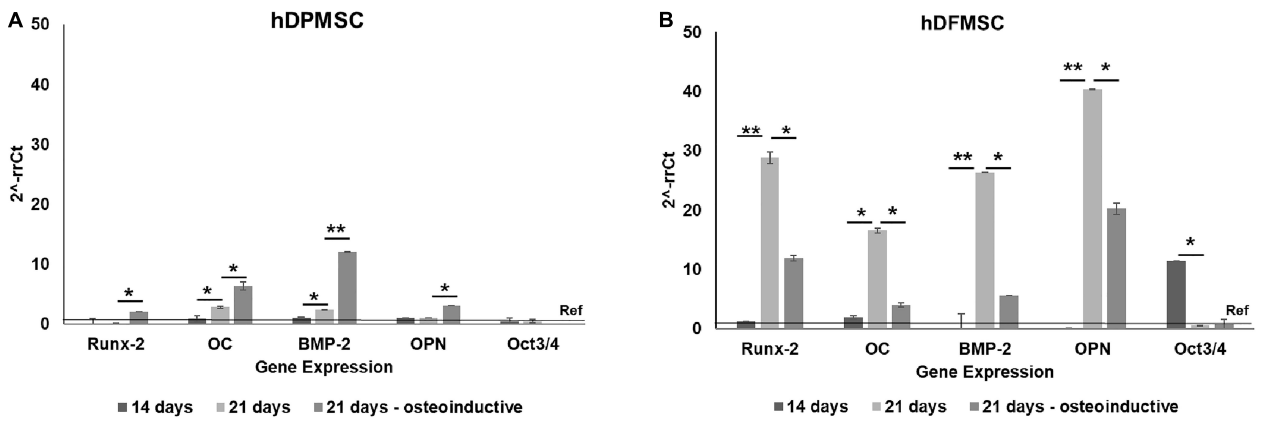


**FIGURE 3 |** Analysis of the expression of osteogenic genes (Runx-2, osteocalcin, BMP-2 and osteopontin) and mesenchymal gene (Oct3/4). Quantitation of data was performed using the $\Delta\Delta$Ct method using GAPDH gene expression as an endogenous reference. Results were normalized to the undifferentiated dental cells (passage 6) average results, and are represented as fold change. **(A)** hDPMSC cells and **(B)** hDFMSC cells cultured for 14 and 21 days (in the basic or in the osteoinductive medium osteogenic induction) within Coll-nanoHA/OPS scaffolds. Statistical analysis $^{*}p < 0.05$ and $^{**}p < 0.01$.

the same proliferation rate was not observed under static conditions, even after 21 days (**Figure 4B**). In both cell culture conditions, DNA concentrations in hDFMSC cultures were 4 times lower than in hDPMSC cultures. Yet, after 21 days under static conditions, hDFMSC showed higher DNA concentration then hDPMSC.

By the CLSM imaging, dental MSCs were observed at the scaffolds' periphery and cross-section, both under dynamic and static conditions. hDPMSC cross-section images showed lower cell numbers under dynamic conditions, when compared to the scaffolds' periphery area (**Figures 4C,D**). In both culture regimens (static and dynamic), cells remained viable on the materials' periphery and throughout the cross-section, but hDFMSC showed better and more homogeneous spatial distribution of viable cells (calcein positive) in the 3D scaffold (surface and center) after 21 days of culture (**Figures 4E,F**). These observations are in agreement with the live/dead assay images that showed high numbers of viable cells with a homogeneous distribution within the 3D structures (**Figures 4G–J**). After 21 days, both types of dental MSCs showed OPN secretion, suggesting osteogenic differentiation, under dynamic culture in basic medium (**Figures 4K,L**). At the same time point, hDPMSC showed lower OPN deposition, when compared to hDFMSC, but both cell types showed protein accumulation at the materials periphery.

Histology sections of these samples showed differences in the cell presence at the surface and at the inner region of the scaffold. Both MSC types cultured under static conditions showed higher presence of cells at the surface and an empty scaffold's inner region after 14 and 21 days (**Figures 5A,B,E,F**). On the contrary, hDPMSC and hDFMSC cultured under dynamic conditions showed better cell distribution within the scaffolds for both time points (**Figures 5C,D,G,H**).

The potential of both dental MSCs to undergo osteogenic differentiation was further explored by analyzing ALP activity

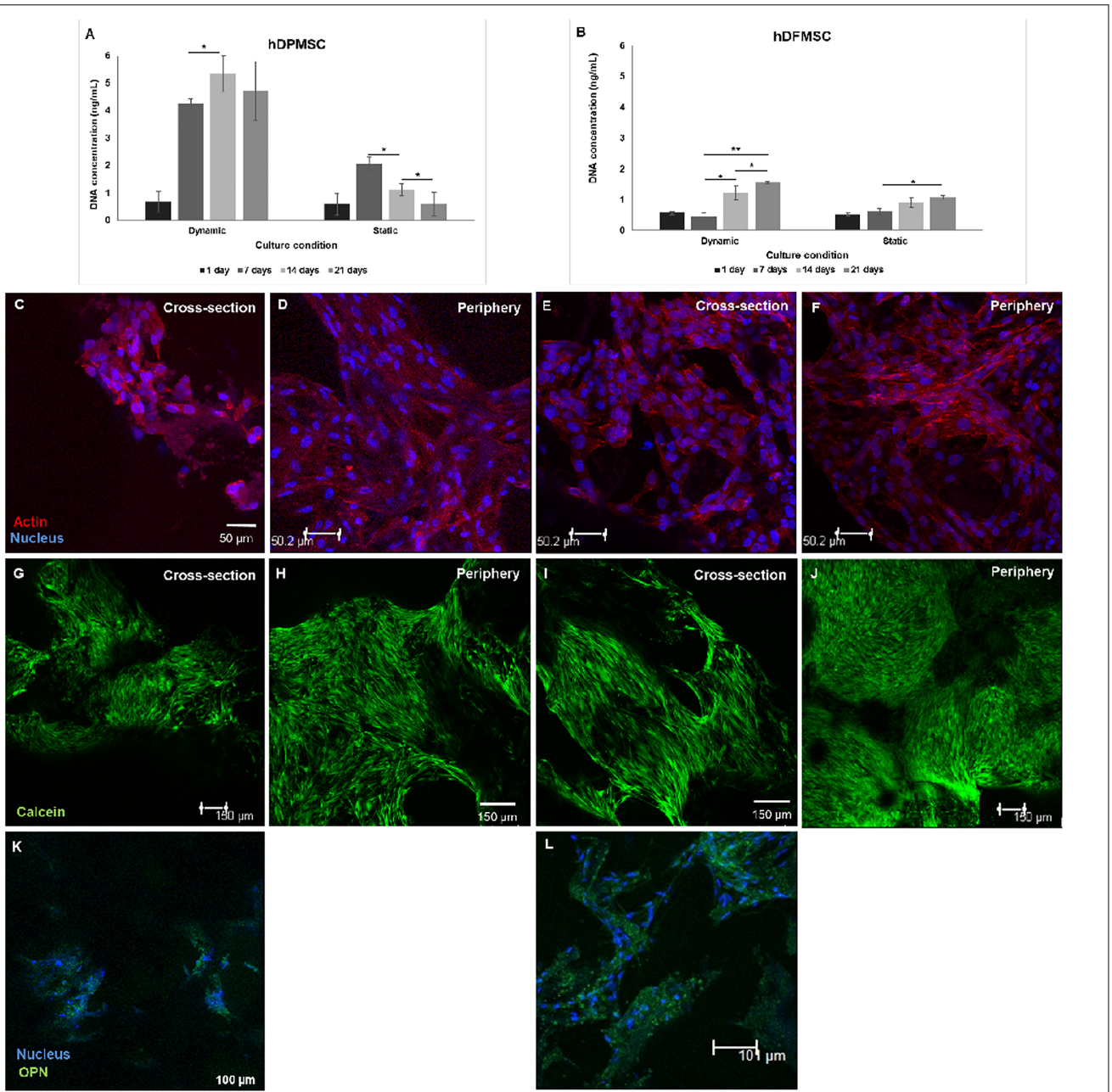


**FIGURE 4 |** Proliferation (DNA concentration) of hDPMSC **(A)** and hDFMSC **(B)** cultured within Coll-nanoHA/OPS for different time points (7–21 days) in static vs. dynamic conditions. Statistical analysis $^{*}p < 0.05$ and $^{**}p < 0.01$. CLSM images of dental MSCs cells (Pulp – **C–D**, Follicle – **E–F**) cultured for 21 days. Cross-section of the material **(C,E,G,I)** and of the periphery **(D,F,H,J)** within collagen-nanoHA/OPS scaffolds under dynamic culture. Scale: **(C–F)** 50 µm and **(G–J)** 150 µm. Human OPN immunostaining (Green: **(K,L)**, scale: 100 µm). Blue – Nucleus, Red – cytoskeleton (actin), Green – calcein and red - propidium iodide.

and osteogenic gene expressions. In **Figure 6**, at comparing the two tooth-delivered cells, hDPMSC showed three-fold higher ALP activity under static conditions after 21 days. Importantly enough, hDFMSC, showed a 2-fold higher ALP activity in dynamic 3D cultures after 14 days, but pulp cells showed reduction in the ALP activity after 21 days. Still, follicle MSCs had the lowest enzyme activity under the same conditions (**Figure 6**).

The results of gene expression related to osteogenic differentiation, showed that hDFMSC presented an early peak of BMP-2 expression after 14 days under dynamic conditions, when compared to the static control. After 21 days, there was an 18-fold increase on osteocalcin expression for hDPMSC, and a 7-fold for hDFMSC (**Figure 7**). A similar enhancement in the BMP-2 expression was also observed for both dental MSCs (8-fold change).

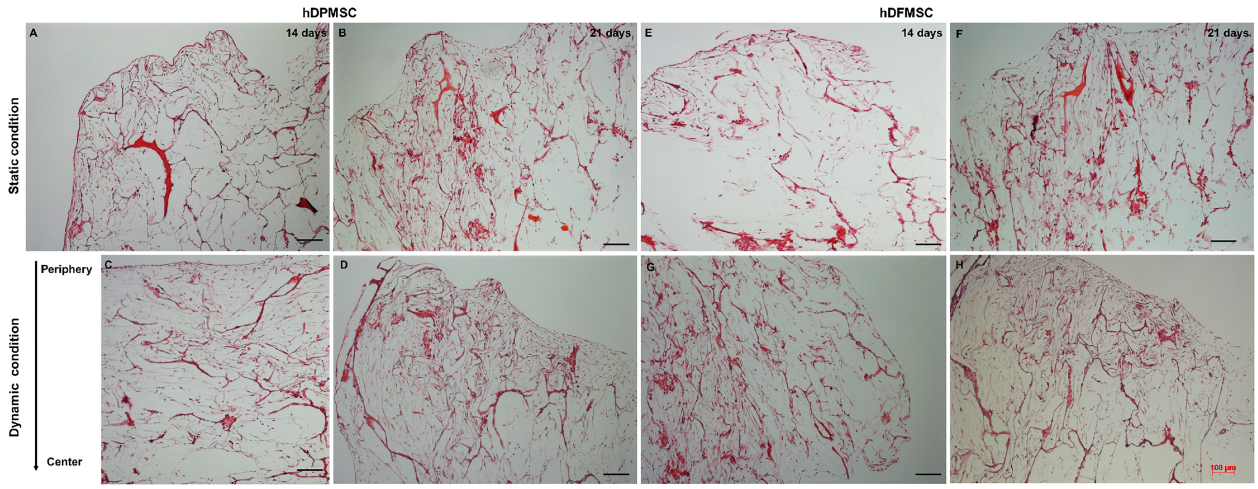


**FIGURE 5 |** Optical microscopy images of dental MSCs (hDPMSC: **A–D** and hDFMSC: **E–H**) within Collagen-nanoHA/OPS scaffolds under static vs. dynamic conditions for 14 and 21 days. Slides were stained using H&E. Scale: 100 μm.

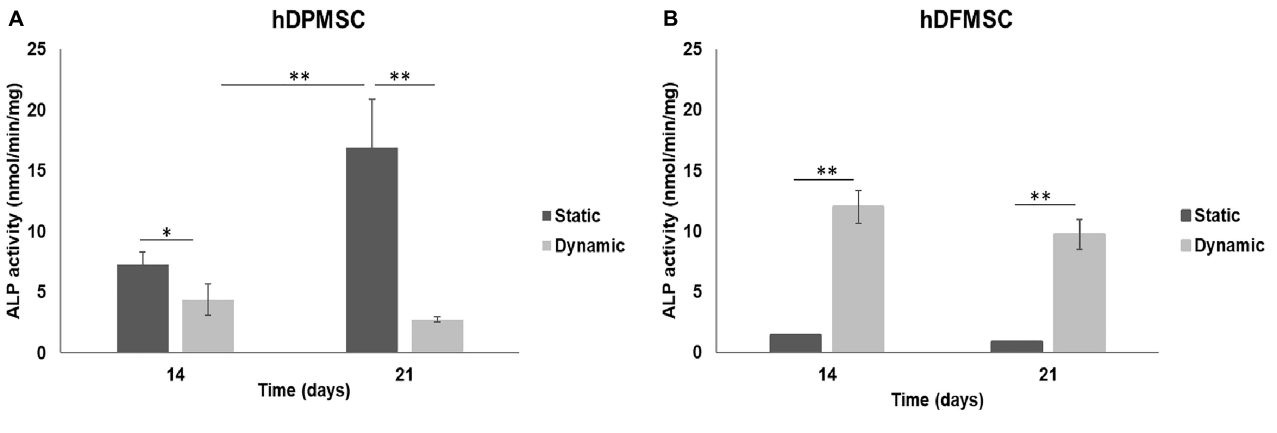


**FIGURE 6 |** ALP activity on human dental follicle and pulp MSCs cultured within Coll-nanoHA/OPS for different time points (14 and 21 days) under static vs. dynamic conditions. Statistical analysis $^{*}p < 0.05$ and $^{**}p < 0.01$.

## Animal Model of Ectopic Intramembranous Ossification (IMO)

3D scaffolds seeded with both dental cell types were cultured under dynamic conditions and osteogenic medium for 7 days, and then implanted subcutaneously in immunocompromised mice. These scaffolds under osteoinduction medium were characterized by DNA concentration, ALP activity and osteogenic gene expression to compare with the results for basic medium, although the results showed no statistically significant difference between the culture mediums (**Supplementary Figure 6**). In a previous work (Salgado et al., 2019) and according to the literature (Scotti et al., 2013; Stüdle et al., 2018), the *in vivo* experiment was performed with 3D cultures in the presence of the osteoinductive medium. Dynamic culture conditions were chosen, as they enhanced the dental follicle MSCs migration into the inner part of the scaffold, favoring mass transfer and oxygenation, avoiding the hypoxia-necrosis effect of *in vitro* engineered tissues. Both cellularized 3D constructs (with hDPMSC and hDFMSC) showed significant tissue ingrowth after 8 weeks (**Figure 8**). Higher number of multinucleated cells (giant-cells) could be observed next to the 3D scaffolds surface (**Figures 8A,G**). The results also showed that the materials seeded with MSCs induced the continuous growth of the surrounding tissue inside the porous scaffold. In the control samples (scaffolds without cells – **Figures 8M–O**) of the *in vivo* subcutaneous model, it was possible to observe the presence of giant cells and inflammatory cells such as macrophages surrounding the apatite particles (**Figure 8N**). Nanohydroxyapatite particles could be observed by Alizarin red staining (red dots – **Figure 8O**), but calcium deposits could not be observed within the scaffold. The total tissue area within the artificial 3D scaffolds were calculated with the Image J software and plotted as a total percentage. It was observed that the presence of both dental MSCs enhanced the percentage of the total tissue ingrowth after 8 weeks, but

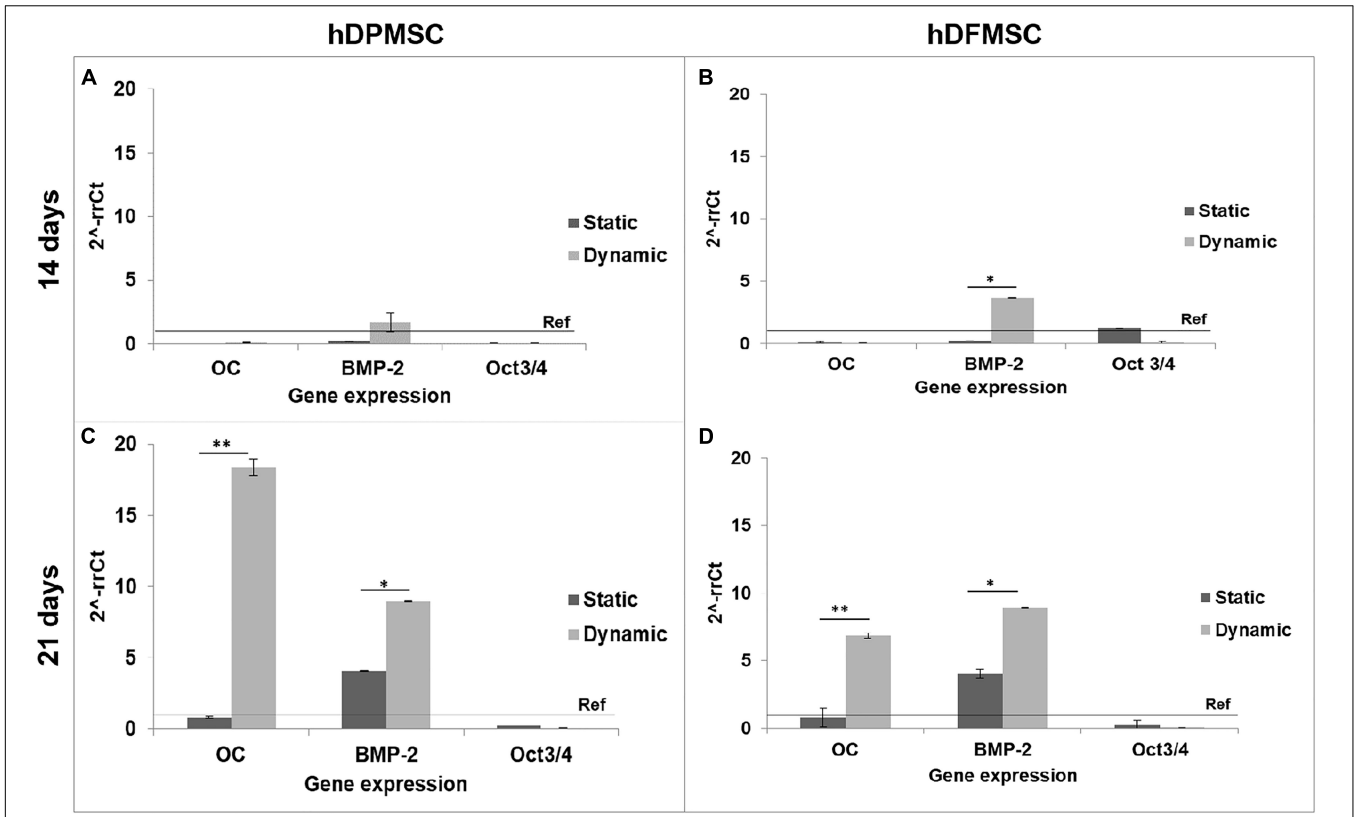


**FIGURE 7 |** Quantitative real-time polymerase chain reaction (qPCR) for osteogenic genes (Osteocalcin and BMP-2) and mesenchymal gene (Oct3/4) for dental pulp and follicle MSCs cultured within the scaffold for 14 and 21 days under static vs. dynamic conditions. Quantitative data were calculated by the $\Delta\Delta$Ct method using GAPDH gene expression as an endogenous reference. Samples results were normalized to the undifferentiated cells (passage 6) average results. These are represented as fold change. Statistical analysis $^{*}p < 0.05$ and $^{**}p < 0.01$.

they were not statistically different from the material without the human cells (**Figure 8P**).

At the periphery of the implant, a bone-like structure surrounding the nanohydroxyapatite particles could be observed (**Figures 8B,H**). Nanohydroxyapatite particles and tissue calcium deposition could be seen with Alizarin red staining. This histochemical analysis showed that these tissue areas were positive for the mineralization staining (Calcium deposits – **Figures 8C,I**). According to the Masson trichrome staining, the bone-like structures (red color – calcium deposits) were more intensely present in the periphery of the scaffold, which could be directly related to the *in vitro* dental MSCs seeding cells in the presence of the osteoinductive medium for 7 days (**Supplementary Figure 8**).

After immunostaining human cells inside the implants, it could be observed that in all the cell-loaded scaffolds implanted for 8 weeks, small amounts of both human dental MSCs were still present inside the materials. The number of dental cells inside the biocomposites after 60 days was considerably lower and the outward migration/invasion of these cells into adjacent mouse tissue was not remarkable (**Figures 8F,L**). The human proteins secreted by the dental MSCs were evaluated by the detection of human OPN inside the scaffold (**Figures 8D,E,J,K**). hDPMSC showed OPN accumulation at the periphery of the scaffold (**Figures 8D**, **9E**). On the contrary, the presence of OPN was more evident in hDFMSC-loaded scaffolds, and the protein was homogeneously distributed throughout the porous structure (**Figures 8J,K**), in accordance with the more significative presence of human cells in that region (**Figure 8L**). Eight weeks after implantation, newly synthesized ECM with human OPN area was quantified by the Image J Software, but, the human protein presence did not show statistical difference between hDPMSC and hDFMSC-loaded scaffold implants (**Figure 8Q**).

## DISCUSSION

Access to tooth-derived stem cells is comparatively easier, if compared to other sources, produces very low patient morbidity and cell extraction is highly efficient. In addition, dental mesenchymal cells have good osteogenic differentiation ability and present high capacity to adhere to biomaterials' surface, thus making them a promising source for bone tissue regeneration (Graziano et al., 2008). The search for alternative sources of MSC(such as the dental follicle and pulp) for bone regeneration is of considerable importance since bone marrow-derived MSCs show significant age-related decrease in frequency and differentiation potential (Brady et al., 2014). Compared to

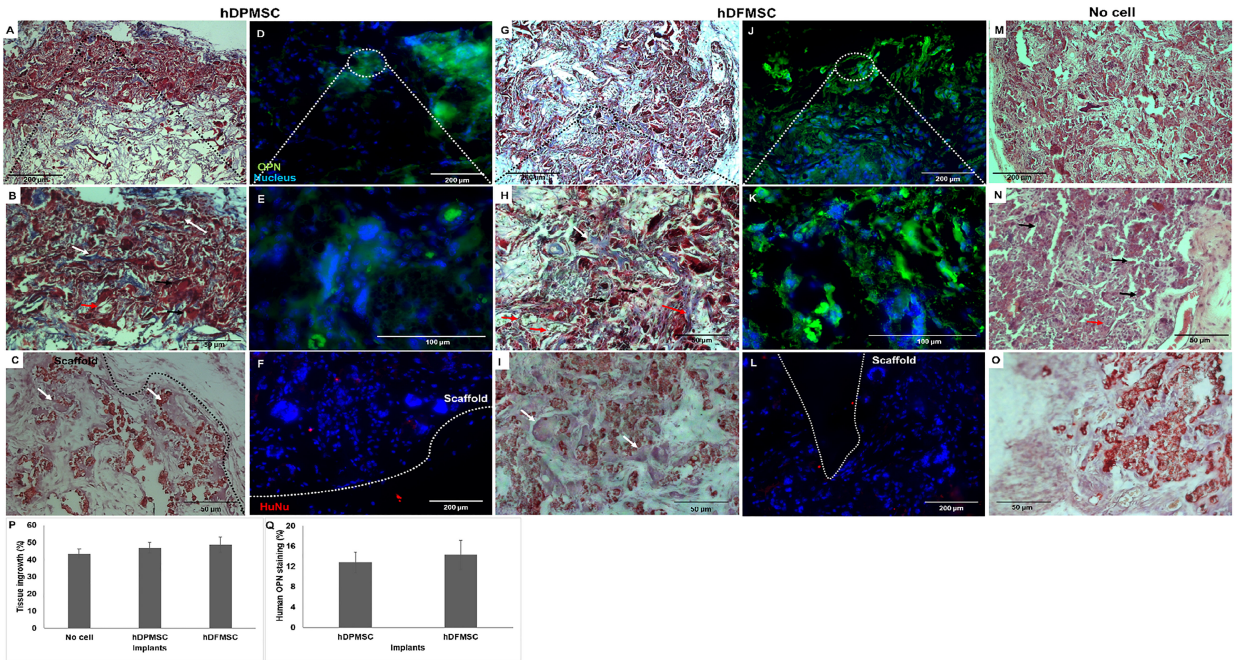


**FIGURE 8 |** Optical microscopy images of dental MSCs (hDPMSC – **A**,**B**,**C** and hDFMSC – **G**,**H**,**I**) within Collagen-nanoHA/OPS scaffolds implanted for 8 weeks. Slides were stained by Masson Trichrome **(A,B,G,H)** and Alizarin red **(C,I)**. **(M,N)** Implants of scaffolds without cells after 8 weeks. **(O)** Implants without cells were stained with Alizarin red. Black dashed line - scaffold surface, white arrows – bone-like tissue, red arrows - new blood vessels and black arrows - giant cells. Scale: **(A,G,M)** 200 μm and **(B,C,H,I,N,O)** 50 μm. Fluorescence microscopy images of dental MSCs (hDPMSC – **D**,**E**,**F**,hDFMSC – **J**,**K**,**L**) within collagen-nanoHA/OPS scaffolds and implanted for 8 weeks. Blue – Nucleus (DAPI), Green – Human Osteopontin, Red – human nucleus (HuNu), White dashed line – scaffold surface. Scale: **(A,F,J,L)** 200 μm and **(E,F)** 100 μm. **(P)** 3D Coll/nanoHA scaffolds with and without human dental MSCs (percentage of the total section area). **(Q)** Human OPN presence within the scaffolds with hDPMSC or hDFMSC.

other stem cell sources from the oral cavity, tooth pulp and follicle are considerably large tissues (Mori et al., 2012), easier to access, and with higher proliferation capacity (Shoi et al., 2014).

A very important factor in elucidating the cellular basis of tissue regeneration is determining the multipotential capabilities of stem cells to differentiate into the desired target tissue (Chambers et al., 2003). Odontogenic cells deriving from neural crest, such as dental follicle stem cells, show typical features of multipotency and are characterized by a high degree of plasticity, with capacity to differentiate into cell lines derived from two germ layers (i.e., osteoblasts and adipocytes, as well as neuronal cells) (Dominici et al., 2006). The objectives of this work was to combine three experimental series to evaluate (i) the follicle and pulp dental MSCs capacity to differentiate into osteogenic lineage under supplementation of osteogenic factors in the culture medium within a biomimetic scaffold based on type 1 collagen, nanohydroxyapatite and phosphoserine; (ii) the hydrodynamic and mass transfer conditions that could influence the tooth-derived MSCs osteogenesis in a 3D scaffold; (iii) to clarify the viability, migration and osteogenesis within a 3D scaffold of the two different dental MSCs with a pre-clinical animal model that is predictive and translational such as an ectopic ossification in rodents.

In this work dental follicle and dental pulp stem cells markers expression were studied by flow cytometry analysis (**Supplementary Material**). Both cells isolated from dental follicle and pulp expressed the positive mesenchymal surface markers CD90, 44 and 73, as well as the absence of expression of the negative markers CD34 and CD45. RT-PCR results after 21 days *in vitro* culture confirmed the dental MSCs commitment to the osteoblastic lineage, with high expression of several osteoblast-associated gene expression markers and decrease of undifferentiated stem cell transcriptional markers (**Supplementary Figure 1**).

At present, there is a particular interest in the role of dental stem cells application to bone regeneration, in particular dental pulp and follicle MSCs (Huang et al., 2009; Mori et al., 2012; Zhang and Cheng, 2013; Bojic et al., 2014; Kim et al., 2019; Lee et al., 2019). In line with other published documents, this work showed that hDPMSC and hDFMSC could be induced to differentiate into osteoblasts *in vitro* (osteogenic induction). Therefore, after 21 days of osteoinduction, the dental pulp and follicle MSCs showed higher ALP activity and enhanced osteogenic gene expression (osteocalcin and BMP-2) when compared to the same cells cultured in basic medium (**Supplementary Figure 3**).

Composite materials reinforced with calcium phosphate ceramics showed a higher mechanical stability and a much slower degradation rate when compared to simple polymeric materials. This type of scaffolds has shown osteoconductive

properties to MSCs which expressed osteoblast-like gene markers (McCafferty et al., 2014). Also, recent studies showed that nanohydroxyapatite integrated in scaffolds was capable to recruit bone marrow MSCs and promote their osteogenic differentiation (Rodrigues et al., 2013; Salgado et al., 2016, 2019). In this work, the results illustrated the ability of dental MSCs cultured in biocomposite cryogels to differentiate into osteoblastic cells, with high ALP enzyme activity and bone phenotype gene expression. The biomimetic scaffold induced the osteogenic differentiation without osteinductive medium and enhanced the differentiation capacity of the dental-derived cells between days 14 and 21 while decreasing their levels of proliferation. These results are in accordance with previous works showing that biomaterials combined with dental MSCs under osteoinductive medium improved osteogenic differentiation (Woloszyk et al., 2014; Vecchiatini et al., 2015). RT- PCR studies indicated that Runx-2 and ALP were up-regulated on both MSCs (from dental follicle and pulp tissue). Runx-2 expression is necessary for multipotent MSCs to differentiate along the osteoblastic lineage and its level of expression is increased during osteoblast differentiation, during the mineralization phase. Thus, Runx-2 overexpression upregulates ALP activity and the expression of osteoblast-specific genes such as osteocalcin (OC) and osteopontin (OPN) (Ducy et al., 1997; zur Nieden et al., 2003; Stein et al., 2004; Mikami et al., 2007; Datta et al., 2008; Shoi et al., 2014). The significantly higher level of OC expression, a late osteogenic marker, was shown by the dental pulp MSCs when compared to the basic culture medium reference. This result indicated that these cells in the 3D construct were in a later phase of osteogenic differentiation, presenting features of mature osteoblasts and matrix mineralization. However, hDFMSC showed overexpression of BMP-2 that is directly involved on the increased gene expression of Runx-2 that strongly promotes MSCs osteogenic differentiation (early pre-osteoblast differentiation) (Carreira et al., 2014).

The method to culture 3D scaffolds in spinner flasks used in this work had the advantage of providing a dynamic environment in 3D, while protecting the structures from mechanical damage, without requiring complex approaches for holding and securing the samples. Acceptable levels of shear stress are a critical parameter in dynamic culture of mammalian cells. Usually, high agitation speeds (80 rpm) of spinner flasks result in decreased cell viability when compared to low agitation speeds (45 rpm), due to shear stress cell damage resulting in cell death (Chen et al., 2013), particularly for MSCs culture in polymeric scaffolds (Kim et al., 2007; Cetin et al., 2012). The results obtained for pulp MSCs showed lower proliferation rate after 7 days (**Figures 4A,B**). The shear stress seemed to affect the hDPMSC proliferation rate, but the cells remained viable after 21 days (**Figures 4**, **5**). On the contrary, hDFMSC proliferation rate confirmed the good performance of the dynamic conditions with the multicompartment holder, since an increase in DNA content was observed after 14 days, which was not observed under static conditions even after 21 days. However, under static condition (6 well-plate), the cells showed a lower proliferation rate (lower DNA concentration – **Figures 4A,B**), when compared to the results from static culture (24 well-plate) in **Figures 1A,B**. The lower basic media volume in the first experiment (1.5 mL) resulted in the media being exchanged twice a week, instead of once a week on the 6-well plate experiment. The higher basic medium refresh revealed a positive effect on the hDFMSC proliferation rate.

One outstanding feature of this dynamic system for cell-loaded materials culture is its clear effect on spatial cell distribution and higher viability inside 3D structures (**Figure 5**). The dynamic conditions used in this study may offer a more favorable hydrodynamic environment, providing the necessary physical stimuli and nutrient transport to support tissue development (Bilgen et al., 2005; Bilgen and Barabino, 2007). However, it was clear by the results obtained that human dental MSCs from different tissue sources showed different spatial distribution. The hDPMSC showed intense cellular presence at the periphery of the scaffold, but with the scaffold cross-section remaining almost empty (**Figures 4C,D**, **5A–D**). Previous studies indicated that the application of mechanical loading (turbulent flow) accelerates the process of hDPMSCs differentiation and mineral deposition while reducing their proliferation activity (Woloszyk et al., 2014; Marrelli et al., 2018). But, it was observed that only the hDFMSCs under dynamic culture within the 3D scaffolds were well-distributed through the materials porous structure (**Figures 4E,F**, **5E,F**), showing higher osteogenic differentiation capacity (higher ALP activity and enhanced expression of osteogenic markers).

The mice model of subcutaneous implants for ectopic bone formation should allow for the evaluation of transplanted human cells in terms of viability, proliferation, migration and osteogenic differentiation capacity. For this work, 8-week duration period was the time selected to assess the new bone formation ability of human cells in a scaffold, and evaluate the long-term inflammatory response. Histology analysis revealed that some of the nanohydroxyapatite particles remained in the tissue, but the bovine collagen was no longer detectable at that time point. The maintenance of the nanohydroxyapatite must be related to its low biodegradation rate, since these were sintered particles composed by aggregates of nanocrystals strongly bond to each other. Besides, the histological findings support that the cell-loaded scaffold enhanced animal tissue ingrowth and angiogenesis. Importantly enough, newly formed extra cellular matrix stained for human OPN and a bone tissue-like structure with calcium deposition was also observed (**Figures 8C,I**). This bone-like tissue formation was progressively decreasing as it went from the periphery toward the center of the scaffolds. This may be related to the dynamic flow from inside the spinner flask and the fact that higher numbers of dental MSCs were adhered on the materials' surface after 7 days of *in vitro* culture (**Supplementary Figure 7**). Even in intra-bone critical defects, implants did not show the formation of mature and organized trabecular bone structure after the 8 weeks of implantation. Usually, in ectopic bone formation models, the bone tissue growth should be observed after 12 weeks (Scotti et al., 2013), but in a previous work, evidence of mineralized tissue was observed in a study after only 4 weeks post-implantation, suggesting

that the employed scaffold had an osteoinductive effect and promoted bone tissue ingrowth (Salgado et al., 2019). To track the transplanted cells, immunostaining for human nucleus was performed, allowing to observe a few human dental MSCs at the periphery of the scaffold, which showed some migration capacity toward the animal surrounding tissue (**Figures 8F,L**). These cells were apparently viable and secreted human osteopontin. The presence of human OPN was only observed inside the cell-loaded implants (dental pulp or follicle MCSs) and not in the empty implanted 3D scaffolds.

## CONCLUSION

In this work, it was shown that isolated dental follicle and pulp stem cells meet the necessary criteria to be named as MSC and present remarkable osteogenic potential. This work proved that both dental MSCs exhibited a progressively *in vitro* proliferation, high cellular viability and osteogenic differentiation within the 3D biomimetic scaffolds during the period of observation. When combined, the biomimetic scaffold and the dental follicle MSCs promoted high cellular proliferation rate, while cells remained viable and well-distributed within the 3D biocomposite structure and osteoblast-like cell phenotype gene expression and high ALP activity were found. But, only hDFMSC behavior was more improved under dynamic conditions. *In vivo* studies showed a disorganized subcutaneous tissue ingrowth with the observation of a bone-like structure on the materials periphery, showing a desirable hDFMSC and hDPMSC differentiation into bone tissue. In addition, these dental follicle tissues proved to be an excellent source of stem cells with a controlled and reproducible differentiation behavior to be applied in bone tissue engineering. In the future, these MSCs shall be tested in pre-clinical animal models with critical bone defects to observe their potential to promote bone tissue regeneration.

## DATA AVAILABILITY STATEMENT

All datasets presented in this study are included in the article/**Supplementary Material**.

## ETHICS STATEMENT

The animal study was reviewed and approved by Ethical Animal Commission of Instituto de Investigação e Inovação em Saúde (i3S), Universidade do Porto (UPorto), Portugal.

## AUTHOR CONTRIBUTIONS

CS substantially contributed to the conception and design of the biocomposite, biological and animal experiments, performed all acquisition, and analysis and interpretation of data. CS agreed to be accountable for all aspects of the work in ensuring that questions related to the accuracy or integrity of any part of the work are appropriately investigated and resolved. CS prepared and revised the draft critically for important intellectual content. CB contributed to the analysis and interpretation of data and critically revised the draft for important intellectual content and gave CS final approval on the version to be published. FM revised the draft critically for important intellectual content and gave his final approval of the version to be published. All authors contributed to the article and approved the submitted version.

## FUNDING

This article is a result of the project NORTE-01-0145-FEDER-000012, supported by North Portugal Regional Operational Programme (NORTE 2020), under the PORTUGAL 2020 Partnership Agreement, through the European Regional Development Fund (ERDF). In addition, it was supported by Portuguese funds through FCT/MCTES in the framework of the project UID/BIM/04293/2019 and CS contract (DL 57/2016/CP1360/CT0001).

## ACKNOWLEDGMENTS

We thank Dr. Bruno Leitão from Instituto de Ciências da Saúde (UCP) for the samples of human dental tissue. Microscopy imaging was performed at the Bioimaging Center for Biomaterials and Regenerative Therapies (b.IMAGE) and Advanced Light Microscopy (ALM) at i3S (PPBI-POCI-01-0145-FEDER-022122). The authors also thank Paula Magalhães (CCGEN), Cláudia Machado (i3S), and Rui Rocha (CEMUP). We also thank FLUIDINOVA, S.A. for the provision of nanohydroxyapatite (nanoXIM.HAp202) and Artur Salgado Lda.

## SUPPLEMENTARY MATERIAL

The Supplementary Material for this article can be found online at: https://www.frontiersin.org/articles/10.3389/fbioe.2020.00724/full#supplementary-material

## REFERENCES

Amini, A. R., Laurencin, C. T., and Nukavarapu, S. P. (2012). Bone tissue engineering: recent advances and challenges. *Crit. Rev. Biomed. Eng.* 40, 363–408. doi: 10.1615/critrevbiomedeng.v40.i5.10

Barrias, C., and Goncalves, R. M. (2013). Container for dynamic 3D cell culture: useful in spinner flask assembly and kit for culturing cell samples in three-dimensional matrix, comprises chambers for containing cell samples, where one of the walls of chambers are perforated to allow culture media and a lid. Portugal Patent No. WO 2013/043072 Al. Lisbon: Portuguese Institute of Industrial Property.

Bilgen, B., and Barabino, G. A. (2007). Location of scaffolds in bioreactors modulates the hydrodynamic environment experienced by engineered tissues. *Biotechnol. Bioeng.* 98, 282–294. doi: 10.1002/bit.21385

Bilgen, B., Chang-Mateu, I. M., and Barabino, G. A. (2005). Characterization of mixing in a novel wavy-walled bioreactor for tissue engineering. *Biotechnol. Bioeng.* 92, 907–919. doi: 10.1002/bit.20667

Bojic, S., Volarevic, V., Ljujic, B., and Stojkovic, M. (2014). Dental stem cells–characteristics and potential. *Histol. Histopathol.* 29, 699–706.

Brady, K., Dickinson, S. C., Guillot, P. V., Polak, J., Blom, A. W., Kafienah, W., et al. (2014). Human fetal and adult bone marrow-derived mesenchymal stem cells use different signaling pathways for the initiation of chondrogenesis. *Stem Cells Dev.* 23, 541–554. doi: 10.1089/scd.2013.0301

Carreira, A. C., Alves, G. G., Zambuzzi, W. F., Sogayar, M. C., and Granjeiro, J. M. (2014). Bone morphogenetic proteins: structure, biological function and therapeutic applications. *Arch. Biochem. Biophys.* 561, 64–73. doi: 10.1016/j.abb.2014.07.011

Cetin, D., Kahraman, A. S., and Gumusderelioglu, M. (2012). Novel pHEMA-gelatin SPHs as bone scaffolds in dynamic cultures. *J. Mater. Sci. Mater. Med.* 23, 2803–2812. doi: 10.1007/s10856-012-4726-z

Chambers, I., Colby, D., Robertson, M., Nichols, J., Lee, S., Tweedie, S., et al. (2003). Functional expression cloning of Nanog, a pluripotency sustaining factor in embryonic stem cells. *Cell* 113, 643–655. doi: 10.1016/s0092-8674(03)00392-1

Chen, A. K., Reuveny, S., and Oh, S. K. (2013). Application of human mesenchymal and pluripotent stem cell microcarrier cultures in cellular therapy: achievements and future direction. *Biotechnol. Adv.* 31, 1032–1046. doi: 10.1016/j.biotechadv.2013.03.006

D'Ambrosio, C., Salzano, A. M., Arena, S., Renzone, G., and Scaloni, A. (2007). Analytical methodologies for the detection and structural characterization of phosphorylated proteins. *J. Chromatogr. B Analyt. Technol. Biomed. Life Sci.* 849, 163–180. doi: 10.1016/j.jchromb.2006.06.033

Datta, H. K., Ng, W. F., Walker, J. A., Tuck, S. P., and Varanasi, S. S. (2008). The cell biology of bone metabolism. *J. Clin. Pathol.* 61, 577–587.

Dominici, M., Le Blanc, K., Mueller, I., Slaper-Cortenbach, I., Marini, F., Krause, D., et al. (2006). Minimal criteria for defining multipotent mesenchymal stromal cells. The international society for cellular therapy position statement. *Cytotherapy* 8, 315–317. doi: 10.1080/14653240600855905

Ducy, P., Zhang, R., Geoffroy, V., Ridall, A. L., and Karsenty, G. (1997). Osf2/Cbfa1: a transcriptional activator of osteoblast differentiation. *Cell* 89, 747–754. doi: 10.1016/s0092-8674(00)80257-3

Gelinsky, M., Bernhardt, A., and Milan, F. (2015). Bioreactors in tissue engineering: advances in stem cell culture and three-dimensional tissue constructs. *Eng. Life Sci.* 15, 670–677. doi: 10.1002/elsc.201400216

Graziano, A., D'aquino, R., Laino, G., and Papaccio, G. (2008). Dental pulp stem cells: a promising tool for bone regeneration. *Stem Cell Rev.* 4, 21–26. doi: 10.1007/s12015-008-9013-5

Huang, G. T., Gronthos, S., and Shi, S. (2009). Mesenchymal stem cells derived from dental tissues vs. those from other sources: their biology and role in regenerative medicine. *J. Dent. Res.* 88, 792–806. doi: 10.1177/0022034509340867

Kim, H. J., Kim, U. J., Leisk, G. G., Bayan, C., Georgakoudi, I., and Kaplan, D. L. (2007). Bone regeneration on macroporous aqueous-derived silk 3-D scaffolds. *Macromol. Biosci.* 7, 643–655. doi: 10.1002/mabi.200700030

Kim, H. J., Sung, I. Y., Cho, Y. C., Kang, M. S., Rho, G. J., Byun, J. H., et al. (2019). Three-dimensional spheroid formation of cryopreserved human dental follicle-derived stem cells enhances pluripotency and osteogenic induction properties. *Tissue Eng. Regen. Med.* 16, 513–523. doi: 10.1007/s13770-019-00203-0

Lee, K. (2012). Global trends in maxillofacial fractures. *Craniomaxillof. Traum. Reconstruct.* 5, 213–222. doi: 10.1055/s-0032-1322535

Lee, Y. C., Chan, Y. H., Hsieh, S. C., Lew, W. Z., and Feng, S. W. (2019). Comparing the osteogenic potentials and bone regeneration capacities of bone marrow and dental pulp mesenchymal stem cells in a rabbit calvarial bone defect model. *Int. J. Mol. Sci.* 20:5015. doi: 10.3390/ijms20205015

Marrelli, M., Codispoti, B., Shelton, R. M., Scheven, B. A., Cooper, P. R., Tatullo, M., et al. (2018). Dental pulp stem cell mechanoresponsiveness: effects of mechanical stimuli on dental pulp stem cell behavior. *Front. Physiol.* 9:1685. doi: 10.3389/fphys.2018.01685

McCafferty, M. M., Burke, G. A., and Meenan, B. J. (2014). Calcium phosphate thin films enhance the response of human mesenchymal stem cells to nanostructured titanium surfaces. *J. Tissue Eng.* 5:2041731414537513.

Mikami, Y., Omoteyama, K., Kato, S., and Takagi, M. (2007). Inductive effects of dexamethasone on the mineralization and the osteoblastic gene expressions in mature osteoblast-like ROS17/2.8 cells. *Biochem. Biophys. Res. Commun.* 362, 368–373. doi: 10.1016/j.bbrc.2007.07.192

Mori, G., Ballini, A., Carbone, C., Oranger, A., Brunetti, G., Di Benedetto, A., et al. (2012). Osteogenic differentiation of dental follicle stem cells. *Intern. J. Med. Sci.* 9, 480–487.

Morsczeck, C., Gotz, W., Schierholz, J., Zeilhofer, F., Kuhn, U., Mohl, C., et al. (2005). Isolation of precursor cells (PCs) from human dental follicle of wisdom teeth. *Matrix Biol.* 24, 155–165. doi: 10.1016/j.matbio.2004.12.004

Ratajczak, J., Bronckaers, A., Dillen, Y., Gervois, P., Vangansewinkel, T., Driesen, R. B., et al. (2016). The neurovascular properties of dental stem cells and their importance in dental tissue engineering. *Stem Cells Int.* 2016, 9762871.

Rodrigues, S. C., Salgado, C. L., Sahu, A., Garcia, M. P., Fernandes, M. H., and Monteiro, F. J. (2013). Preparation and characterization of collagen-nanohydroxyapatite biocomposite scaffolds by cryogelation method for bone tissue engineering applications. *J. Biomed. Mater. Res. A* 101, 1080–1094. doi: 10.1002/jbm.a.34394

Salasznyk, R. M., Klees, R. F., Williams, W. A., Boskey, A., and Plopper, G. E. (2007). Focal adhesion kinase signaling pathways regulate the osteogenic differentiation of human mesenchymal stem cells. *Exp. Cell Res.* 313, 22–37. doi: 10.1016/j.yexcr.2006.09.013

Salgado, C. L., Grenho, L., Fernandes, M. H., Colaco, B. J., and Monteiro, F. J. (2016). Biodegradation, biocompatibility, and osteoconduction evaluation of collagen-nanohydroxyapatite cryogels for bone tissue regeneration. *J. Biomed. Mater. Res. A* 104, 57–70. doi: 10.1002/jbm.a.35540

Salgado, C. L., Teixeira, B. I. B., and Monteiro, F. J. M. (2019). Biomimetic composite scaffold with phosphoserine signaling for bone tissue engineering application. *Front. Bioeng. Biotechnol.* 7:206. doi: 10.3389/fbioe.2019.00206

Scotti, C., Piccinini, E., Takizawa, H., Todorov, A., Bourgine, P., Papadimitropoulos, A., et al. (2013). Engineering of a functional bone organ through endochondral ossification. *Proc. Natl. Acad. Sci. U.S.A.* 110:3997. doi: 10.1073/pnas.1220108110

Sharpe, P. T. (2016). Dental mesenchymal stem cells. *Development* 143, 2273–2280. doi: 10.1242/dev.134189

Shoi, K., Aoki, K., Ohya, K., Takagi, Y., and Shimokawa, H. (2014). Characterization of pulp and follicle stem cells from impacted supernumerary maxillary incisors. *Pediatr. Dent.* 36, 79–84.

Stein, G. S., Lian, J. B., Van Wijnen, A. J., Stein, J. L., Montecino, M., Javed, A., et al. (2004). Runx2 control of organization, assembly and activity of the regulatory machinery for skeletal gene expression. *Oncogene* 23, 4315–4329. doi: 10.1038/sj.onc.1207676

Stüdle, C., Vallmajó-Martín, Q., Haumer, A., Guerrero, J., Centola, M., Mehrkens, A., et al. (2018). Spatially confined induction of endochondral ossification by functionalized hydrogels for ectopic engineering of osteochondral tissues. *Biomaterials* 171, 219–229. doi: 10.1016/j.biomaterials.2018.04.025

Tanzeglock, T., Soos, M., Stephanopoulos, G., and Morbidelli, M. (2009). Induction of mammalian cell death by simple shear and extensional flows. *Biotechnol. Bioeng.* 104, 360–370. doi: 10.1002/bit.22405

Teixeira, G. Q., Barrias, C. C., Lourenco, A. H., and Goncalves, R. M. (2014). A multicompartment holder for spinner flasks improves expansion and osteogenic differentiation of mesenchymal stem cells in three-dimensional scaffolds. *Tissue Eng. Part C Methods* 20, 984–993. doi: 10.1089/ten.tec.2014.0067

Teixeira, S., Fernandes, M. H., Ferraz, M. P., and Monteiro, F. J. (2010). Proliferation and mineralization of bone marrow cells cultured on macroporous hydroxyapatite scaffolds functionalized with collagen type I for bone tissue regeneration. *J. Biomed. Mater. Res. A* 95, 1–8. doi: 10.1002/jbm.a.32600

Tsai, H. H., Yang, K. C., Wu, M. H., Chen, J. C., and Tseng, C. L. (2019). The effects of different dynamic culture systems on cell proliferation and osteogenic differentiation in human mesenchymal stem cells. *Int. J. Mol. Sci.* 20:4024. doi: 10.3390/ijms20164024

Vecchiatini, R., Penolazzi, L., Lambertini, E., Angelozzi, M., Morganti, C., Mazzitelli, S., et al. (2015). Effect of dynamic three-dimensional culture on osteogenic potential of human periodontal ligament-derived mesenchymal stem cells entrapped in alginate microbeads. *J. Periodont. Res.* 50, 544–553. doi: 10.1111/jre.12225

Walls, P. L. L., Mcrae, O., Natarajan, V., Johnson, C., Antoniou, C., and Bird, J. C. (2017). Quantifying the potential for bursting bubbles to damage suspended cells. *Sci. Rep.* 7:15102.

Woloszyk, A., Holsten Dircksen, S., Bostanci, N., Muller, R., Hofmann, S., and Mitsiadis, T. A. (2014). Influence of the mechanical environment on the

engineering of mineralised tissues using human dental pulp stem cells and silk fibroin scaffolds. *PLoS One* 9:e111010. doi: 10.1371/journal.pone.0111010

Yao, S., Pan, F., Prpic, V., and Wise, G. E. (2008). Differentiation of stem cells in the dental follicle. *J. Dent. Res.* 87, 767–771. doi: 10.1177/154405910808700801

Zhang, C., and Cheng, X. R. (2013). Isolation and characterization of dental follicle cells from adult human dental follicle tissues. *Zhonghua Kou Qiang Yi Xue Za Zhi* 48, 96–101.

zur Nieden, N. I., Kempka, G., and Ahr, H. J. (2003). In vitro differentiation of embryonic stem cells into mineralized osteoblasts. *Differentiation* 71, 18–27. doi: 10.1046/j.1432-0436.2003.700602.x

**Conflict of Interest:** The authors declare that the research was conducted in the absence of any commercial or financial relationships that could be construed as a potential conflict of interest.

frontiers in Bioengineering and Biotechnology

ORIGINAL RESEARCH
published: 30 June 2020
doi: 10.3389/fbioe.2020.00723

# Plant Tissues as 3D Natural Scaffolds for Adipose, Bone and Tendon Tissue Regeneration

*Nicola Contessi Negrini*[1,2*†], *Nadia Toffoletto*[1,2†], *Silvia Farè*[1,2] *and Lina Altomare*[1,2]

[1] *Department of Chemistry, Materials and Chemical Engineering "G. Natta", Politecnico di Milano, Milan, Italy,* [2] *National Interuniversity Consortium of Materials Science and Technology, Local Unit Politecnico di Milano, Milan, Italy*

Decellularized tissues are a valid alternative as tissue engineering scaffolds, thanks to the three-dimensional structure that mimics native tissues to be regenerated and the biomimetic microenvironment for cells and tissues growth. Despite decellularized animal tissues have long been used, plant tissue decellularized scaffolds might overcome availability issues, high costs and ethical concerns related to the use of animal sources. The wide range of features covered by different plants offers a unique opportunity for the development of tissue-specific scaffolds, depending on the morphological, physical and mechanical peculiarities of each plant. Herein, three different plant tissues (i.e., apple, carrot, and celery) were decellularized and, according to their peculiar properties (i.e., porosity, mechanical properties), addressed to regeneration of adipose tissue, bone tissue and tendons, respectively. Decellularized apple, carrot and celery maintained their porous structure, with pores ranging from 70 to 420 μm, depending on the plant source, and were stable in PBS at 37°C up to 7 weeks. Different mechanical properties (i.e., $E_{apple}$ = 4 kPa, $E_{carrot}$ = 43 kPa, $E_{celery}$ = 590 kPa) were measured and no indirect cytotoxic effects were demonstrated *in vitro* after plants decellularization. After coating with poly-L-lysine, apples supported 3T3-L1 preadipocytes adhesion, proliferation and adipogenic differentiation; carrots supported MC3T3-E1 pre-osteoblasts adhesion, proliferation and osteogenic differentiation; celery supported L929 cells adhesion, proliferation and guided anisotropic cells orientation. The versatile features of decellularized plant tissues and their potential for the regeneration of different tissues are proved in this work.

**Keywords: plant tissues, decellularization, adipose tissue engineering, bone tissue engineering, tendon tissue engineering**

OPEN ACCESS

***Edited by:***
*Lia Rimondini,*
*University of Eastern Piedmont, Italy*

***Reviewed by:***
*Francesca Gervaso,*
*Institute of Nanotechnology (CNR), Italy*
*Helen E. Berry,*
*University of Leeds, United Kingdom*

****Correspondence:***
*Nicola Contessi Negrini*
*nicola.contessi@polimi.it*

*† These authors have contributed equally to this work*

***Specialty section:***
*This article was submitted to Biomaterials, a section of the journal Frontiers in Bioengineering and Biotechnology*

***Received:*** *08 April 2020*
***Accepted:*** *09 June 2020*
***Published:*** *30 June 2020*

***Citation:***
*Contessi Negrini N, Toffoletto N, Farè S and Altomare L (2020) Plant Tissues as 3D Natural Scaffolds for Adipose, Bone and Tendon Tissue Regeneration. Front. Bioeng. Biotechnol. 8:723. doi: 10.3389/fbioe.2020.00723*

## INTRODUCTION

Tissue engineering requires an accurate design of engineered biomaterials able to sustain the regeneration of pathological/missing tissues. Both synthetic and natural-derived biomaterials have been proposed and are still under investigation to achieve the appropriate morphological, physical, mechanical and biological properties to suit the specific requirements for the regeneration of different target human tissues. Synthetic polymer-based scaffolds are reproducible, possess a defined chemical composition and tuneable properties according to the application requirements. Natural-derived polymer-scaffolds, despite the limited reproducibility, are characterized by a

superior biological response compared to synthetic scaffolds, a good biocompatibility and ecological safety (Alaribe et al., 2016). However, in both cases, the polymeric materials must be processed to fabricate scaffolds with the appropriate properties and, despite advanced fabrication technologies have been developed to process polymers, reproducing the correct microarchitecture of the tissues to be regenerated is still challenging (Jammalamadaka and Tappa, 2018).

Decellularization of tissues offers a valid alternative to avoid materials' processing since the biomimetic native structure can be preserved while removing the cellular components to obtain three-dimensional acellular scaffolds for tissue engineering applications (Urciuolo et al., 2018). Decellularized matrices are a suitable morphological and biochemical microenvironment for cell adhesion, proliferation and differentiation (Wu et al., 2015). Moreover, compared to allogeneic and xenogeneic transplant, decellularized structures have lower immunogenic response in the host after implantation, as immunogenicity is associated to intracellular components that are removed by the decellularization process.

Different animal-derived tissues were decellularized to obtain extracellular matrix (ECM) scaffolds with a preserved vascular structure for the transfer of oxygen and nutrients, including skin, (Farrokhi et al., 2018) bone (Smith et al., 2017) and vascular grafts (Lin et al., 2018). Some of these acellular patches are now commercially available, such as Alloderm,® ReadiGRAFT,® OrACELL,® and ArthroFLEX®. In the last decade, decellularization of whole organs also gained an increasing interest [e.g., acellular heart, (Kitahara et al., 2016) lungs, (Crabbé et al., 2015) kidney, (Xue et al., 2018) liver, (Bühler et al., 2015), and pancreas (Guruswamy Damodaran and Vermette, 2018) from animal or human donors] and a partial organ functionality was successfully restored after cell recolonization (Petersen et al., 2010). Despite these promising results, animal and human sources are controversial and affected by limited availability, high production costs and ethical concerns (Porzionato et al., 2018). Moreover, the variability among different donors (e.g., age, pathology, explant site) (Song and Ott, 2011) is a critical aspect in clinical applications and the use of animal sources may lead to a host reaction to xenoantigens (Scarrit, 2015) or the transmission of infectious agents (Gilbert et al., 2006).

Very recently, plant-derived tissues gained tremendous interest (Gershlak et al., 2017; Phan et al., 2020) as an alternative to animal sources to obtain decellularized scaffolds for tissue engineering applications. Since a wide variety of plant architectures exists in the plant kingdom, decellularized plant-derived scaffolds could be selected depending on their native structure and properties to mimic a multiplicity of mammalian tissues (Gershlak et al., 2017). In fact, in addition to their readily availability, low cost, ease of use, and absence of ethical issues, plant tissues exhibit good cytocompatibility (Modulevsky et al., 2014) and biocompatibility (Modulevsky et al., 2016). For instance, 2D scaffolds were obtained after decellularization of leaves [e.g., Artemisia annua, (Gershlak et al., 2017) Anthurium, (Fontana et al., 2017) Ficus hispida, (Adamski et al., 2018) spinach leaves] (Gershlak et al., 2017; Dikici et al., 2019) by preserving their branched vessels, resembling mammalian vasculature. On decellularized spinach leaves, (Gershlak et al., 2017) a contractile function and calcium handling capabilities were observed after 21 days of cardiomyocytes culture, confirming the suitability of the scaffold for *in vitro* cardiac tissue regeneration. Tubular scaffolds resulting from parsley, bamboo and vanilla stems (Fontana et al., 2017) were successfully decellularized and an efficient cell proliferation was observed after recellularization. Three-dimensional plant structures were also obtained by decellularization procedures from green onion bulb (Cheng et al., 2020) and apple hypanthium (Modulevsky et al., 2014, 2016; Hickey et al., 2018; Lee et al., 2019). A similar strategy was adopted for fungi tissues to obtain decellularized mushroom caps (Balasundari et al., 2012). Decellularized apple scaffolds, characterized by an open porosity, provided media transfer and supported mammalian cell growth up to 12 weeks of *in vitro* culture (Modulevsky et al., 2014). The *in vivo* implantation of apple-derived scaffolds resulted in the growth of functional blood vessels in the material after 8 weeks (Modulevsky et al., 2016; Lee et al., 2019). Thus, the pro-angiogenic features of scaffolds obtained from vegetables and their interconnected porous structures make them potential candidates for the proliferation and survival of cells and tissues growth.

Despite the advantages offered by decellularized plant-derived scaffolds and the promising results obtained so far, the versatility of these structures in terms of tissues to be potentially regenerated has not been fully investigated yet. The wide range of features covered by different plants (i.e., morphology, structure, cell-instructive properties) constitutes a unique alternative for the development of tissue-engineered scaffolds, and the peculiarities of selected plants potentially matching the requirements for the regeneration of specific human body tissues has still to be fully explored. In this context, we identified three different plant tissues (i.e., apple, carrot, and celery) that are characterized by diverse internal architectures. Then, according to the obtained morphological, physical and mechanical characterization, we selected specific applications for each plant and investigated the *in vitro* potential as scaffolds for the regeneration of different tissues (i.e., adipose tissue, bone tissue and tendons, respectively).

## MATERIALS AND METHODS

All reagents were purchased from Sigma Aldrich, unless differently specified. Fresh plants were acquired from the same chain store and stored at 4°C, for a maximum of 2 days, prior to use.

### Plant Tissues Preparation and Decellularization

Three different plant tissues (**Figure 1A**) were selected and tested as potential scaffolds for human tissues regeneration: Golden Delicious apple (*Malus domestica),* carrot (*Daucus carota*), and celery (*Apium graveolens*). Slices (thickness $t$ = 2 mm) were cut with a mandolin slicer. Cylindrical samples (diameter Ø = 10 mm) were then carved by biopsy punch

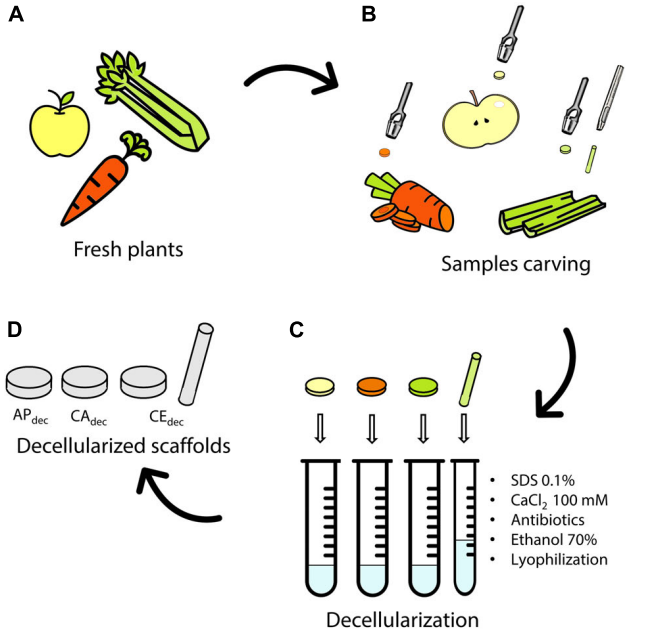


**FIGURE 1 |** Decellularization of plant tissues. **(A)** Selected fresh plants are **(B)** carved by a biopsy punch. **(C)** Samples are decellularized by subsequent immersion in decellularization/washing solution to obtain **(D)** apple ($AP_{dec}$), carrot ($CA_{dec}$) and celery ($CE_{dec}$) scaffolds. Icons The Noun Project.

(**Figure 1B**). Apple specimens ($AP_{dec}$) were carved from the outer hypanthium tissue. Carrot specimens ($CA_{dec}$) were obtained by punching the xylem from the transversal section. Celery samples ($CE_{dec}$) were sliced in longitudinal direction and punched selecting the stem pith. CE samples (Ø = 4 mm, length $L$ = 25 mm) were also carved in longitudinal direction to be used for mechanical testing.

Decellularization (**Figure 1C**) was performed according to a previously established protocol for plant tissues (Hickey et al., 2018). Briefly, each sample was immersed 5 ml of 0.1% w/v sodium dodecyl sulfate (SDS) solution for 48 h at room temperature under continuous shaking at 180 rpm. After 24 h, samples were sonicated for 5 min at 40°C and the SDS solution was renewed. Samples were then washed three times in distilled water and washed in 100 mM $CaCl_2$ for 24 h. Control samples ($AP_{ctr}$, $CA_{ctr}$, and $CE_{ctr}$) were freshly cut from the plants following the previously described procedure and were not treated by the described decellularization process. Both decellularized and control samples were washed three times in distilled water and subsequently incubated with 1% w/v penicillin/streptomycin and 1% w/v amphotericin B for 3 h under shaking at 140 rpm. Finally, samples were disinfected in 70% v/v ethanol solution for 1 h, washed three times in sterile distilled water and frozen at −20°C overnight. The obtained structures were then lyophilized (Freeze drier Lio 5Pascal; −40°C, 24 h, $P < 0.5$ mbar) and sterilized by UV irradiation for 15 min on each side.

## Characterization of Decellularized Plant Tissues

### Morphological Characterization

The morphology of decellularized plant tissues was investigated by stereomicroscopy (Wild M8 stereomicroscope and Leica LAS core software, 6× magnification) and compared with fresh-cut samples. Scanning Electron Microscopy (SEM, Cambridge StereoScan 360) analysis was conducted on gold-sputter coated samples to observe pore morphology and size in both decellularized and control samples. The analysis was performed in secondary electron mode (10 kV), at 15 and 100× magnification. Celery samples were observed in both longitudinal and transversal direction to investigate the anisotropic structure. From the obtained images, the average pore size was calculated according to ASTM D3576 – 15 standard; results are expressed as mean ± inter-image variability ($n$ = 3).

### Physical Characterization

The dimension of the scaffolds (thickness and diameter) was measured by a caliper on fresh-cut samples ($n$ = 4). Then, samples were measured, after decellularization, in the hydrated state and results were compared to the dimension of fresh-cut samples to investigate possible volumetric changes (i.e., percentage shrinkage) due to the decellularization treatment.

Water absorption and retention over time were evaluated by soaking decellularized and control dehydrated samples ($n$ = 4) in phosphate buffered saline (PBS) with 0.02% sodium azide (used as bacteriostatic) at 37°C, up to 7 weeks. The mass of anhydrous samples was measured ($w_0$) and samples were weighted ($w_t$) at established time points ($t$ = 1, 2, 3, 4, 5, 6, 24, 48, 72 h, and weekly for 7 weeks), after gentle swabbing to remove excess water from the surface. The water uptake Δw[%] at the different time points was then calculated using Eq. 1:

$$\Delta w\,[\%] = \frac{w_t - w_0}{w_t} \times 100 \qquad (1)$$

### *In vitro* Indirect Cytotoxicity Test

Indirect cytotoxicity test was performed *in vitro* according to the standard practice EN ISO 10993-5, to evaluate the effect of possible release of cytotoxic products resulting from the decellularization procedure or from the scaffolds' composition. L929 murine fibroblast cells (ECACC No 85011425) were seeded in 96-well tissue culture polystyrene (TCPS) plates ($1 \times 10^4$ cells per well) and cultured (i.e., culture medium $M_{fibr}$: Dulbecco's Modified Eagle's Medium, DMEM, added with 10% fetal bovine serum, 1 mM sodium pyruvate, 1% penicillin-streptomycin, 10 mM 4(2-hydroxyethyl)-1-piperazine ethanesulfonic acid and 4 mM L-glutamine) at 37°C in 5% $CO_2$ humidified atmosphere, until 70% confluence was reached. Eluates were obtained by incubating decellularized samples ($n$ = 3 per type, per time point) in the culture medium for 1, 4, and 7 days. The volume of incubation medium was adapted from EN ISO 10993-12. At each time point, culture medium was also incubated without samples, as control. Cells were then cultured for 24 h with culture medium eluates or culture medium controls. Cell viability was assessed by alamarBlue assay; culture medium was replaced

by 10% v/v alamarBlue solution in fresh culture medium and cells were incubated for 3 h. Then, 100 μl of surnatants were transferred from each well to a new 96-well TCPS, in triplicate, and fluorescence was read by a spectrophotometer (GENios Plus Reader, TECAN; $\lambda_{exc}$ = 540 nm, $\lambda_{em}$ = 595 nm). The percentage cell viability was calculated as ratio between the fluorescence values measured for cells cultured with eluates ($f_{eluates}$) to the fluorescence values obtained from cells cultured in culture medium controls ($f_{control}$), after subtracting the background of the alamarBlue solution ($f_{AlamarBlue}$), as for Eq. 2:

$$Cell\ viability\ [\%] = \frac{f_{eluates} - f_{AlamarBlue}}{f_{control} - f_{AlamarBlue}} \times 100 \qquad (2)$$

## Apple-Derived Scaffolds for Adipose Tissue Engineering

### Mechanical Properties

The compression properties of apple-derived scaffolds were tested by Dynamic Mechanical Analyzer (DMA Q800, TA instruments). Control and decellularized apple samples ($n$ = 4, Ø = 10 mm, $t$ = 2 mm) were soaked in PBS at 37°C for 1 week (i.e., Δw plateau) and then tested in the swollen state by applying one hysteresis compression cycle. Each test consisted in a load phase at a rate of 2.5% $min^{-1}$ down to −30% strain, as previously reported for adipose tissue engineering, (Chang et al., 2013; Contessi Negrini et al., 2020) and subsequent unload phase at a rate of 5% $min^{-1}$. From the stress-strain curves, the elastic modulus E (calculated as the slope in the 0–5% strain range), stiffness k (slope in the 15–20% strain range), maximum stress $\sigma_{max}$, residual strain $\varepsilon_{res}$ and hysteresis area H (calculated as the area between the load and unload curves) were calculated.

### *In vitro* Direct Cytocompatibility Test

Decellularized apple scaffolds ($n$ = 4) were lodged into 24-well TCPS plates and coated to promote cell adhesion by incubation in 0.01% w/v poly-L-lysine (PLL) overnight, with gentle agitation (50 rpm) at 37°C, then washed 3 times with PBS to remove the excess of PLL and transferred to new plates. 3T3-L1 murine cell line (ECACC No 86052701) was selected as *in vitro* model for adipose tissue engineering. Cells were seeded on decellularized apple samples ($2 \times 10^5$ cells per sample) and on 24-well TCPS plates, as control, and incubated (37°C, 5% $CO_2$) for 20 min to promote cell adhesion. Then, 1.2 ml of preadipocyte growth medium ($M_{preadipo}$: DMEM with 10% v/v fetal calf serum, 10 mM HEPES, 4 mM L-glutamine, 1 mM sodium pyruvate and 1% penicillin – streptomycin) was added to culture cells by renewing the medium every 2 days. After 7 days of culture, adipogenic differentiation was induced by culture in differentiation culture medium for 48 h ($M_{diff}$: DMEM with 10% v/v fetal bovine serum, 10 mM HEPES, 4 mM L-glutamine, 1 mM sodium pyruvate, 1% penicillin-streptomycin, 1 μg $ml^{-1}$ insulin, 0.5 mM 3-isobutyl-1-methylxanthine (IBMX), 1 μM dexamethasone (DEX) and 1 μM rosiglitazone) (Zebisch et al., 2012). Then, differentiation-induced samples ($AP_{adipo}$) and wells ($TCPS_{adipo}$) were kept in maintenance medium up to 14 days of culture, renewed each 2 days ($M_{maint}$: composed by $M_{diff}$ without IBMX, DEX and rosiglitazone). As control (i.e., no adipogenesis induced), seeded samples ($AP_{preadipo}$) and wells ($TCPS_{preadipo}$) were kept in preadipocyte growth medium for the whole duration of the test, by renewing culture medium every 2 days.

Metabolic activity of cells cultured on apple-derived scaffolds and TCPS wells ($n$ = 4) was investigated by alamarBlue assay after 1, 3, 7, 10, and 14 days of culture. At each time point, scaffolds were transferred to new plates to discharge cells on the well bottom. Samples were incubated in 1.2 ml of 10% v/v alamarBlue solution in culture medium for 4 h; then 100 μl of eluates were transferred in triplicate in a 96-well plate and fluorescence was read as previously described. Samples were rinsed twice with PBS and incubated with culture medium ($M_{preadipo}$, $M_{diff}$ or $M_{maint}$) until the subsequent time point. After 7 days of culture, a LIVE/DEAD staining was performed on scaffolds ($n$ = 3) to qualitatively investigate the distribution of viable and dead cell. Samples were incubated in the staining solution (10 μM propidium iodide and 2 μM calcein-AM in PBS) for 40 min, washed three times with PBS and immersed in culture medium without FBS. Images ($n$ = 7) were acquired by fluorescence microscope (Olympus BX51W1) and analyzed by ImageJ Fiji software (NIH, United States). The percentage of viable cells was quantitatively measured as ratio of the number of viable cells (detected in green) to the total number of cells (viable cells and dead cells, detected in red).

### Adipogenic Differentiation

The adipogenic differentiation of 3T3-L1 pre-adipocytes was qualitatively investigated by Oil Red O staining of accumulated lipid droplets after 14 days of culture. The staining solution was prepared by dissolving 300 mg of Oil Red O powder in 100 ml isopropanol, subsequently diluted 2:3 in distilled water and sterile filtered. After 14 days of culture, samples ($n$ = 4) were washed twice in TRIS-buffered saline (TBS)/$CaCl_2$ 1×, fixed by submersion in 4% w/v paraformaldehyde for 30 min and washed again with TBS/$CaCl_2$. After that, samples were incubated in Oil Red O staining solution for 30 min and washed twice with TBS/$CaCl_2$ prior to observation by optical microscopy (Leica DFC290) at 5 and 20× magnification.

## Carrot-Derived Scaffolds for Bone Tissue Engineering

### Mechanical Properties

The compression properties of control and decellularized carrot-derived scaffolds ($n$ = 4, Ø = 10 mm, $t$ = 4 mm) were tested by DMA, after immersion in PBS for 1 week (i.e., Δw plateau). A compression load was applied at a rate of 5% $min^{-1}$ up to 60% strain, as previously reported for bone tissue engineering (Du et al., 2018). The elastic modulus was calculated as the slope in the 0–20% strain range from the obtained σ–ε curves. The stress at maximum strain and the area A under the σ–ε curves are also considered.

### *In vitro* Direct Cytocompatibility Test

*In vitro* direct cytocompatibility test was performed using MC3T3-E1 cell line (ECACC No 99072810) as *in vitro* model for bone tissue engineering. Prior to seeding, scaffolds ($n$ = 4) were coated with PLL and then transferred to new 24-well

TCPS plates. Cells were seeded on scaffolds and 24-well TCPS plates ($2 \times 10^5$ cells per samples) following the above-stated procedure. Then, osteogenic differentiation was induced on samples ($CA_{osteo}$) and wells ($TCPS_{osteo}$) by culturing cells in osteogenic medium ($M_{osteo}$: α MEM (M8042), 10% v/v FBS, 1% penicillin-streptomycin, 2 mM L-glutamine, 50 μg $ml^{-1}$ ascorbic acid and 10 mM β-glycerophosphate) up to 14 days of culture; controls ($CA_{preosteo}$, $TCPS_{preosteo}$) were obtained by culturing cells in pre-osteoblast medium up to 14 days ($M_{preosteo}$: αMEM (M8042), 10% FBS, 1% penicillin-streptomycin and 2 mM L-glutamine). Culture medium was renewed 24 h after seeding and, subsequently, every 2 days.

Metabolic activity of cells cultured on scaffolds and TCPS wells was assessed by alamarBlue assay at established time points (i.e., $t$ = 1, 3, 7, 10, and 14 days), as previously described. Viable cells distribution was qualitatively and quantitatively investigated by LIVE/DEAD assay ($n$ = 3) after 7 days of culture, as previously described.

### Osteogenic Differentiation

Osteogenic differentiation of MC3T3-L1 cells seeded on decellularized carrot scaffolds ($n$ = 4) was assessed by Alkaline Phosphatase (ALP) Assay (BioVision) after 14 days of culture. Briefly, samples were soaked in lysis buffer (1% w/v Triton X-100 and 50 mM HEPES) overnight. Lysates were transferred from each well to a new 96-well TCPS plate in triplicate; then, p-nitrophenyl phosphate (pNPP) solution was added to each well. The plate was incubated for 60 min to allow ALP enzyme to catalyze pNPP hydrolysis and the absorbance was measured by a spectrophotometer (λ = 405 nm). ALP activity was quantified by an ALP enzyme standard curve and normalized over DNA content. The amount of DNA was determined using SYBR Green I stain, with a calibration curve built by salmon sperm standards. Morphology of differentiation-induced and non-induced cells was observed by SEM analysis after 7 and 14 days of culture. Samples were fixed in 4% paraformaldehyde solution, washed three times with PBS and dehydrated by submersion in increasing ethanol concentrations (10% v/v: 10: 100% v/v, 10 min each step), lyophilized for 4 h and observed by SEM.

## Celery-Derived Scaffolds for Tissue Engineering of Tendons

### Mechanical Properties

The tensile mechanical properties of control and decellularized celery-derived scaffolds ($n$ = 4, Ø = 4 mm, $L$ = 25 mm) were tested by DMA, after soaking samples in PBS for 1 week (i.e., Δw plateau). A tensile load was applied at a rate of 30% $min^{-1}$ up to failure (Zitnay et al., 2018). The elastic modulus was calculated as the slope in the 0–5% strain range from the obtained σ–ε curves. Stress-strain curves were reported up to 20% strain (strain value reached by all the tested samples before failure); the stress at 20% strain and the area A under the stress-strain curve are also considered.

### *In vitro* Direct Cytocompatibility Tests

*In vitro* direct cytocompatibility tests were performed on decellularized celery-derived scaffolds (Ø = 10 mm, $h$ = 2 mm, $n$ = 4). Mouse L929 fibroblastic cell line (ECACC No 85011425) was selected to investigate cell viability and contact guidance on celery structures. Cells were seeded on PLL-coated scaffolds and TCPS wells ($2 \times 10^5$ cells per well) following the above-stated procedure and cultured in $M_{fibr}$ by renewing culture medium 24 h after seeding and, subsequently, every 2 days up to 14 days of culture.

Metabolic activity of cells cultured on scaffolds and TCPS wells was assessed by alamarBlue assay at established time points (i.e., $t$ = 1, 3, 7, 10, and 14 days), while distribution of viable cells was qualitatively and quantitatively investigated by LIVE/DEAD assay after 7 days ($n$ = 3), as described before.

Immunofluorescence microscopy was conducted on celery-derived scaffolds ($n$ = 4) after 7 days of cell culture to assess actin microfilaments and nuclei alignment. Samples were washed in 1× TBS/$CaCl_2$, fixed in 4% w/v paraformaldehyde for 30 min and washed again. Cells were permeabilized by submersion in 0.1% v/v Triton-X-100 for 15 min, soaked in 1% w/v bovine serum albumin (BSA) for 15 min, and washed three times in TBS/$CaCl_2$. Actin staining was performed by incubating samples in phalloidin – FITC P5282 (1:1000 in 1% BSA, 45 min), while nuclei staining was performed with Hoechst 33258 (1 μg $ml^{-1}$ in 1% BSA, 15 min). Samples were washed twice again and observed by fluorescence microscope (phalloidin: $\lambda_{em}$ = 570 nm, Hoechst: $\lambda_{em}$ = 460 nm). Results were analyzed by ImageJ Fiji software (NIH, United States): the preferential directionality was defined as the angle between the long axis of each cell and the preferential orientation (0°) of the observed cells. The percentage of aligned cells (0° ± 20°) over the total number of stained cells was then calculated.

## Statistical Analysis

Data are presented as mean ± standard deviation. Statistical analysis was performed by $t$-test to compare two data sets or by one-way ANOVA test, with Tukey's multiple comparison test, to compare more data sets. GraphPad Prism 7 software was used; significance level was set at $p < 0.05$.

# RESULTS

## Morphological and Physical Characterization

The morphology of plant tissues was investigated prior to and after decellularization to observe possible effects of the adopted protocol. All the considered plant tissues underwent a loss of pigmentation after the decellularization treatment (**Figure 2Ai** vs. **Figure 2Aii**), particularly noticeable in carrot samples due to the orange-colored appearance of the native tissue. The translucent, milky white appearance of the obtained treated samples is typical of decellularized structures, as widely described for both animal (Bühler et al., 2015; Fu et al., 2016) and plant-derived (Fontana et al., 2017; Gershlak et al., 2017) tissues.

Detected dimensional variations (**Figure 2B**) were assessed to be lower than 6% (i.e., maximum shrinkage registered for carrot-derived scaffolds), thus proving the absence of considerable volumetric changes and structural damage at the macroscale. This

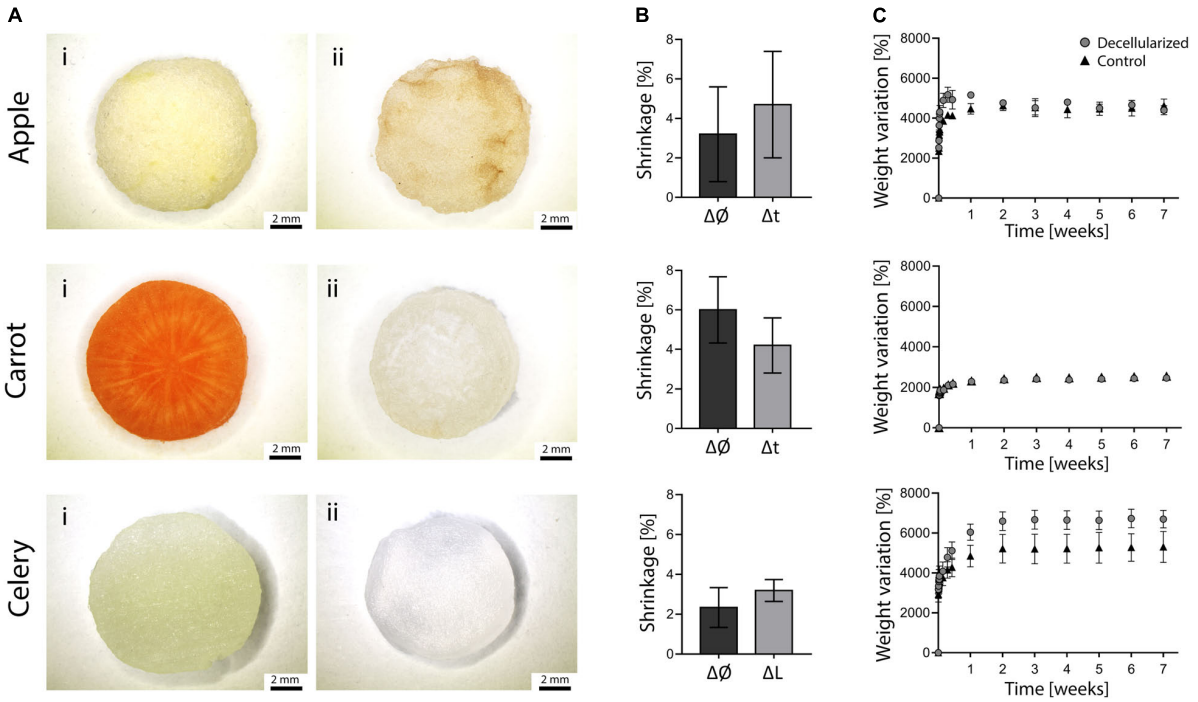


**FIGURE 2 | (A)** Stereomicroscopy images of apple, carrot and celery – derived samples **(Ai)** prior to and **(Aii)** after decellularization (scale bar lower panel: 2 mm). **(B)** Dimensional variation of the diameter (Ø) and thickness (t) or length (L) of apple, carrot and celery samples after decellularization ($n$ = 4). **(C)** Percentage weight variation of decellularized and control samples immersed in PBS at 37°C for 7 weeks ($n$ = 4).

aspect is fundamental since possible changes in the dimension must be considered to design patient-specific and site-specific implantable scaffolds.

The weight variation of decellularized and control samples immersed in PBS at 37°C is shown in **Figure 2C**. Each sample absorbed water (i.e., 24 to 66 times their initial anhydrous weight) and reached a plateau value during the first week of immersion, after which the stable weights recorded up to 7 weeks proved the ability of the samples in retaining the absorbed fluid. In particular, stable weights were reached by apples after 24 h and by carrot and celery samples after 7 days of incubation. The weight variation at plateau for apple-derived and carrot-derived samples was 4500 and 2450%, respectively, with no difference comparing decellularized and native tissues ($p > 0.05$). The weight variation at plateau of celery-derived scaffolds was 6660%, with a significant increase in water absorption for decellularized samples compared to native tissue ($p < 0.05$). These data prove that the peculiar presence of high amount of water in plant tissues is preserved after decellularization and that the obtained structure is thus capable of fluids absorption, fundamental for the survival of cells in the tissue volume. In fact, water retention is a crucial aspect for the development of successful scaffolds able to substitute natural body tissues.

Scanning electron microscopy analysis was then performed on decellularized and control samples to investigate their structures at the microscale. A three-dimensional, highly porous structure is observed for all the considered plant tissues (**Figure 3**). No pore walls disruption or changes in the morphological structures were observed after the decellularization treatment (**Supplementary Data 1**), thus confirming that the used decellularization procedure (Hickey et al., 2018) allows for the preservation of the native morphology of the plant tissues. Apple-derived scaffolds (**Figure 3Ai**) show a homogeneous porosity, with roundish pores characterized by an average diameter of 420 ± 33 μm (**Figure 3Aii**). Differently, carrot-derived scaffolds were characterized by a heterogeneous structure. Thin channels, surrounded by radially oriented pores (70 ± 12 μm average size), run transversal to the sample section and constitute the central area of the xylem (**Figure 3Bii**). In the peripheral region, pores assume a round shape and a larger size (130 ± 26 μm average diameter), with no preferred orientation (**Figure 3Biii**). Finally, celery-derived samples were analyzed in both longitudinal (**Figures 3Ci,ii**) and transversal (**Figures 3Ciii,iv**) directions: the tissues appear to be constituted by packed pores (125 ± 11 μm average size), forming longitudinally oriented parallel channels. As typically detected in natural structures, both from mammalian and plant origin, intra-species small defects are often observed, such as irregularities in the surface morphology along the celery channels, such as changes in the channel diameter and path (i.e., bifurcations and convergences).

## *In vitro* Cytotoxicity

The percentage cell viability, expressed as the ratio of metabolic activity of cells cultured with eluates obtained from samples to the metabolic activity of cells cultured in control medium, is shown in **Figure 4**. The percentage cell viability is higher than 95%

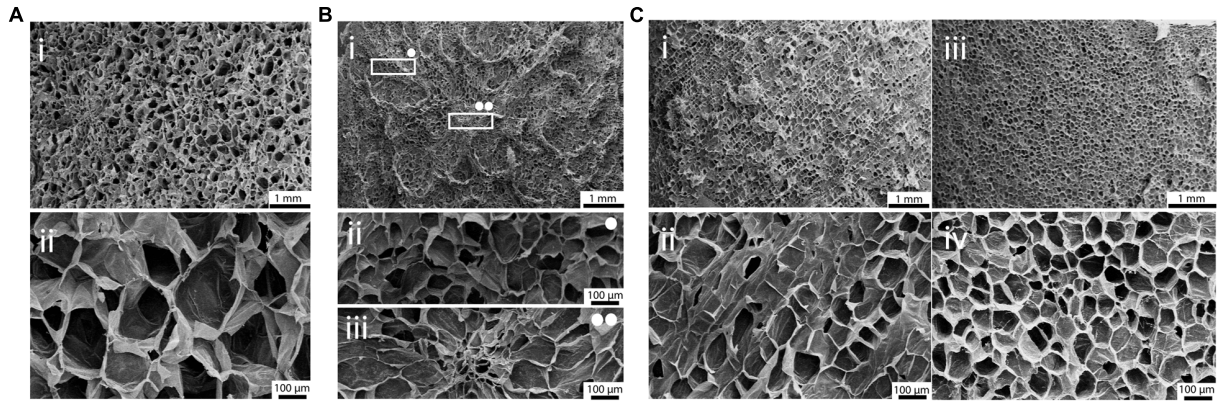


**FIGURE 3 |** SEM micrographs of **(A)** apple, **(B)** carrot and **(C)** celery-derived scaffolds. **(A)** Decellularized apples, observed at (i) 15× and (ii) 100× magnification, show a homogeneous pores size and distribution. **(B)** Decellularized carrots present a non-homogeneous pores distribution **(Bi)**: round porosity and smaller pores are observed in the peripheral region (**Bii**, 100× magnification), oriented pores are observed in the central region (**Biii**, 100× magnification). **(C)** Decellularized celery were observed in both longitudinal (**Ci,Cii**) and transversal **(Ciii,Civ)** directions, to investigate their anisotropic structure. Scale bar upper panel: 1 mm; scale bar lower panel: 100 µm.

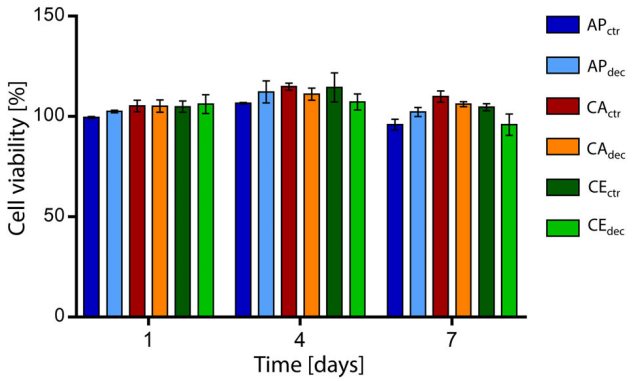


**FIGURE 4 |** Percentage viability of L929 cells cultured with culture medium eluates obtained in contact with decellularized plant tissues (i.e., $AP_{dec}$, $CA_{dec}$, and $CE_{dec}$) and control tissues (i.e., $AP_{ctr}$, $CA_{ctr}$, and $CE_{ctr}$) for 1, 4, and 7 days ($n$ = 3 per time point).

for each sample at each considered time point, confirming the absence of cytotoxic residues of the decellularization procedure in the vegetal structures and no cytotoxic effects caused by the chemical of the selected plants. Moreover, no statistical difference ($p > 0.05$) was detected comparing the viability of cells cultured in eluates obtained in contact with decellularized and control samples.

Since no cytotoxic effects were detected by *in vitro* indirect cytotoxicity tests, the suitability of the decellularized plant tissues for the regeneration of specific target human tissues was investigated by mechanical and *in vitro* direct cytocompatibility tests. In particular, according to their morphology and porosity, apple-derived scaffolds were investigated for applications in adipose tissue engineering for the isotropic structure, carrot-derived scaffolds for bone tissue engineering for the presence two different ranges of porosity in the same structure, and celery-derived scaffolds for the regeneration of tendons due to the possibility of vertically align cells in a tubular, anisotropic structure. Mechanical test procedures and consistent cell line models were selected according to the target tissue of each decellularized plant scaffold.

## Apple-Derived Scaffolds

Apple-derived scaffolds showed a relatively large and homogeneous porosity, suitable for adipose tissue regeneration. In fact, a pore size greater than 100 µm is adequate for an efficient provision of oxygen and nutrients in adipose tissue (AT) regeneration (Van Nieuwenhove et al., 2017) and it is widely described for other scaffolds developed for AT engineering [e.g., collagen-hyaluronic acid: (Van Nieuwenhove et al., 2017) 100–220 µm, polyurethane-based foams: (Gerges et al., 2018) 300–500 µm].

To deeper investigate the suitability of this plant tissue for AT engineering, compression mechanical properties were tested. A representative hysteresis cycle of hydrated decellularized and control samples is shown in **Figure 5A** and calculated mechanical parameters are summarized in **Table 1**. Samples were tested up to 30% strain to replicate AT physiological conditions (Frydrych et al., 2015) and were able to sustain this deformation without failure. Hydrated decellularized apple-derived samples were characterized by a compression modulus of 4.17 ± 0.17 kPa; this is comparable to that of native human adipose tissue [e.g., E breast tissue (Van Nieuwenhove et al., 2017) = 2 kPa, E abdomen tissue (Omidi et al., 2014) = 3.3 kPa] and to those of recently proposed scaffolds for AT regeneration, including polyamidoamine foams (Rossi et al., 2016) ($E$ = 3.4–4.4 kPa), decellularized AT (Yu et al., 2013) ($E$ = 2.4–4 kPa) and collagen-hyaluronic acid scaffolds (Davidenko et al., 2010) ($E$ = 5.39–6.73 kPa). No statistical difference was observed between the elastic moduli of decellularized and control samples (**Table 1**). An energy loss was observed during the unloading phase (**Table 1**), typical of the viscoelastic response that also characterizes native

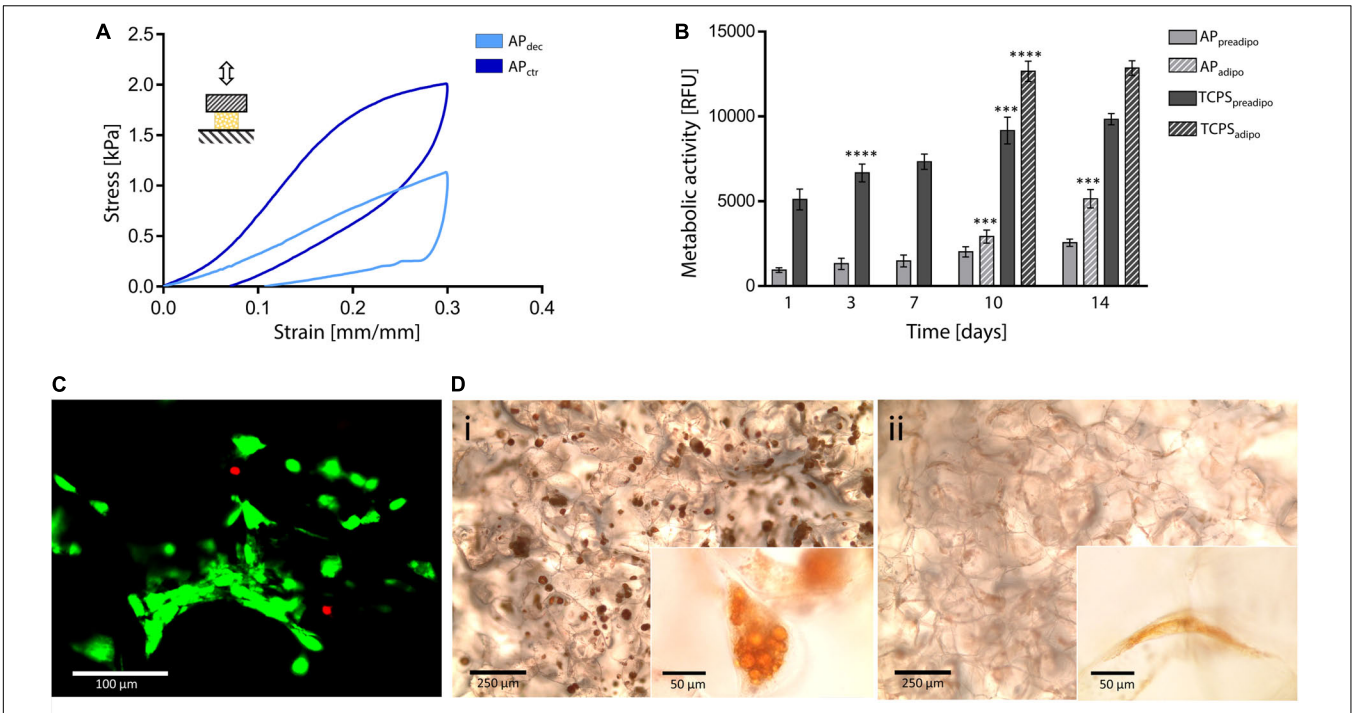


**FIGURE 5 |** Decellularized apple for adipose tissue engineering. **(A)** Representative compression hysteresis cycle of apple-derived scaffolds and control samples. **(B)** Metabolic activity of 3T3-L1 preadipocytes cultured up to 14 days on apple scaffolds and TCPS plates. After 7 days of culture, cells were either induced toward adipogenic differentiation (i.e., $AP_{adipo}$ and $TCPS_{adipo}$) or cultured in pre-adipocyte medium (i.e., $AP_{preadipo}$ and $TCPS_{preadipo}$). $n = 4$ per time point, one-way ANOVA: $^{***}p < 0.001$, $^{****}p < 0.0001$ comparing the metabolic activity of the same sample at one time point to the previous time point. **(C)** Representative LIVE/DEAD staining of 3T3-L1 cells cultured on apple-derived scaffolds (scale bar: 100 µm). **(D)** Oil Red O staining of intracellular lipid droplets in **(Di)** differentiated and **(Dii)** non-differentiated 3T3-L1 cells cultured on apple-derived scaffolds. Differentiated cells are characterized by a round morphology and red-stained accumulated lipid droplets (scale bar: 250 µm; scale bar inset image: 50 µm).

**TABLE 1 |** Mechanical properties of decellularized (dec) apple (AP), carrot (CA), and celery (CE) tissues and non-decellularized tissues, as controls (ctr).

| | Apple$^{\chi}$ | | Carrot$^{\chi}$ | | Celery$^{\tau}$ | |
|---|---|---|---|---|---|---|
| | $AP_{dec}$ | $AP_{ctr}$ | $CA_{dec}$ | $CA_{ctr}$ | $CE_{dec}$ | $CE_{ctr}$ |
| Elastic modulus E [kPa] | 4.17 ± 0.17 | 4.36 ± 0.02 | 43.43 ± 5.22* | 83.48 ± 22.14* | 594.78 ± 94.24 | 552.49 ± 12.44 |
| Stiffness K [kPa] | 4.33 ± 1.98* | 9.47 ± 1.85* | – | – | – | – |
| Residual strain ε [%] | 6.42 ± 0.08 | 6.48 ± 0.01 | – | – | – | – |
| Maximum stress [kPa] | 1.17 ± 0.28* | 2.07 ± 0.05* | 44.31 ± 8.59 | 51.49 ± 7.17 | 175.93 ± 40.96 | 174.60 ± 29.28 |
| Hysteresis area H [J $dm^{-3}$] | 0.112 ± 0.023 | 0.153 ± 0.003 | – | – | – | – |
| Area under the curve A [J $dm^{-3}$] | – | – | 11.1 ± 1.72 | 14.56 ± 2.30 | 15.37 ± 3.24 | 14.85 ± 1.75 |

*Apple and carrot samples were tested by compression tests; celery samples were tested by tensile tests. n = 4, t-test: *p < 0.05. $^{\chi}$Compression test; $^{\tau}$tensile test.*

AT (Riaz et al., 2016). Moreover, the obtained H areas from apple-derived scaffolds are comparable to those of previously designed scaffolds (Chang et al., 2013; Contessi Negrini et al., 2019) for AT regeneration. A residual strain was observed in both control and decellularized samples at the end of the unloading phase (**Table 1**), as often observed in scaffolds for soft tissue engineering (Gao et al., 2014). Decellularized apple-derived scaffolds exhibit a decrease ($p < 0.05$) in stiffness k (i.e., calculated in the 15–20% strain) and maximum stress at 30% strain compared to untreated apple samples (**Table 1**), as experienced in previously developed plant-derived and organ-derived decellularized tissues [e.g., spinach-derived scaffold (Gershlak et al., 2017)]. Despite the lowered mechanical properties of apple-derived scaffolds, compared to the native tissues, the obtained mechanical properties correctly fit the range of those of native human AT, thus validating the adopted treatment for the production of tissue-mimicking scaffolds, in term of mechanical properties.

*In vitro* direct cytocompatibility tests were performed using a pre-adipogenic cell line (3T3-L1). The metabolic activity of cells cultured on the apple-derived scaffolds increased throughout the 14 days of culture (**Figure 5B**), proving the ability of the apple scaffolds in sustaining pre-adipocyte cells growth and

proliferation. The presence of viable cells adhered to the apple scaffold was also qualitatively proved by the LIVE/DEAD staining images (viability = 92.3 ± 4.9%, **Figure 5C**), where cells are shown to be distributed following the porous structure of the scaffold after 7 days of culture.

Adipogenic differentiation, induced after 7 days of culture, led to a rapid increase of metabolic activity for differentiated cells, compared to non-differentiated cells (**Figure 5B**, $p < 0.05$ differentiated vs. non-differentiated cells at the same time points) for both scaffolds and TCPS. Higher metabolic activity values were detected on TCPS wells compared to the scaffolds, which might be given by a higher cell seeding efficiency on the TCPS. In fact, apple-derived scaffolds were moved to new plates at each time point, to discharge cells adhered to the TCPS and not consider their contribution in the fluorescence signal. However, the percentage increase in metabolic activity (i.e., fluorescence value at 14 days vs. 1 day) was higher for cells cultured on the scaffolds than for those on TCPS (5.55-fold vs. 2.51-fold increase for differentiation-induced scaffolds and TCPS, respectively, and 2.70-fold vs. 1.92-fold increase for undifferentiated scaffolds and TCPS, respectively), evidencing a more efficient cell proliferation in the three-dimensional culture environment, compared to the traditional 2D plastic. After 14 days of culture, red droplets were observed by Oil Red O staining in differentiated cells cultured on apple-derived scaffolds (**Figure 5Di**), evidencing the intracellular lipid accumulation typical of adipocytes and an effective possible adipogenic differentiation of preadipocytes cultured on the apple scaffolds. Moreover, an increased size and roundness were observed in differentiated adipocytes compared to cells cultured in the pre-adipogenic medium (**Figure 5Dii**), typical morphology of adipocytes (Zoico et al., 2016).

## Carrot-Derived Scaffolds

The heterogeneous structure of carrot-derived scaffolds is characterized by radially oriented pores (70 ± 12 μm average size) in the central region and round larger pores (130 ± 26 μm average size) in the peripheral region, whose dimensions are comparable to the porosity of scaffolds designed for bone tissue regeneration (e.g., collagen/hydroxyapatite scaffold:(He et al., 2018) 50–100 μm, Na-alginate/hydroxyethylcellulose scaffold:(Tohamy et al., 2018) 89–217 μm, gelatin/alginate-coated β-TCP scaffold:(Pacelli et al., 2018) 141 ± 43 μ m).

Compression tests were performed on both hydrated control and decellularized samples up to 60%. A representative stress-strain curve is shown in **Figure 6A** and calculated mechanical parameters are summarized in **Table 1**. No failure evidence was found in samples during the tests, evidencing that decellularized carrots can bear strains up to 60%. The obtained compression modulus of carrot-derived scaffolds is 43.43 ± 5.22 kPa, considerably lower than natural bone tissue (Bayraktar et al., 2004) ($E$ = 3.5–18 GPa). However, mechanical properties comparable to those of carrot-derived samples have been widely proposed for non-load bearing bone scaffolds (e.g., calcium-silicate/chitosan scaffold $E$ = 150–190 kPa; (Peng et al., 2019) PEG-dimethacrylate scaffold $E$ = 225–300 kPa) (Chatterjee et al., 2010). Hence, a possible application for decellularized carrot-derived scaffolds could be bone fillers in non-load bearing conditions. Furthermore, an inorganic ECM deposition *in vitro* or *in vivo* by cells could improve the mechanical properties of the obtained scaffold over time, (Goyal et al., 2017) thus decreasing the mechanical gap between the native tissue and the scaffold.

*In vitro* direct cytocompatibility tests were conducted using a pre-osteoblast cell line (MC3T3-E1), by inducing osteogenic differentiation after cell seeding (Zamani et al., 2019). Metabolic activity resulted stable up to 7 days after seeding (**Figure 6B**). No statistical difference was observed ($p > 0.05$) between the metabolic activity of differentiation-induced and non-induced samples during the entire testing time, for both carrot-derived scaffolds and TCPS wells. An increase in the fluorescence values ($p < 0.05$) was then detected at day 10 in both differentiation-induced (i.e., $CA_{osteo}$) and non-induced (i.e., $CA_{preosteo}$) samples, then values remained stable up to 14 days of culture, with a 3.41-fold increase in cell metabolic activity from day 1 to day 14. The ability of the carrot scaffolds in sustaining pre-osteoblast cells growth and proliferation is therefore demonstrated. A plateau value in metabolic activity was reached after 7 days of culture on TCPS wells (i.e., $TCPS_{preosteo}$ and $TCPS_{osteo}$), with a slower cell growth rate when compared to carrot scaffolds (1.44-fold increase in metabolic activity from day 1 to day 14). Viable cells adhered to the decellularized carrot tissue were also qualitatively observed by LIVE/DEAD staining after 7 days of culture, with a percentage cell viability of 85.0 ± 7.2% (**Figure 6C**). ALP activity was investigated after 14 days of culture on carrot-derived scaffolds and TCPS plates (**Figure 6D**). Osteogenic differentiation was proved by an increased ALP activity ($p < 0.05$) for cells cultured in osteogenic medium (i.e., $CA_{osteo}$ and $TCPS_{osteo}$) compared to not induced cells (i.e., $CA_{preosteo}$ and $TCPS_{preosteo}$). After 14 days of culture, a uniform colonization was observed by SEM on both differentiation-induced (**Figure 6E**) and non-induced scaffolds (**Supplementary Data 2**). Cells uniformly colonized the pore walls of the carrot scaffolds, assuming an elongated morphology, typical of adhered cells (**Figure 6E**, arrow 1); nano-fiber three-dimensional nets were also observed (**Figure 6E**, arrow 2), which might be attributable to extracellular matrix deposition (López-Álvarez et al., 2011). Extracellular secretions were found on the surface of differentiation-induced cells (**Figure 6E**, arrow 3), evidencing an on-going mineralization as evidence in Thu et al. (2017). In fact, the nano-sized particles detected for carrots structures could be possibly attributed to apatite crystals or bone sialoprotein, a osteogenic marker associated to mineralization, as experienced in previous studies where MC3T3-E1 cells were seeded on collagen scaffolds (Cao et al., 2015).

## Celery-Derived Scaffolds

Celery-derived scaffolds are characterized by a longitudinally oriented structure, constituted by 125 ± 11 μm size pores aligned to form parallel channels. Scaffolds with an oriented morphology are particularly suitable for cell alignment and to mimic the structure of native anisotropic connective tissue of tendons (Gurkan et al., 2010). Due to their oriented structure, celery-derived scaffolds were therefore subjected to mechanical and *in vitro* biological tests to assess their potential adequacy as scaffolds for tendon regeneration.

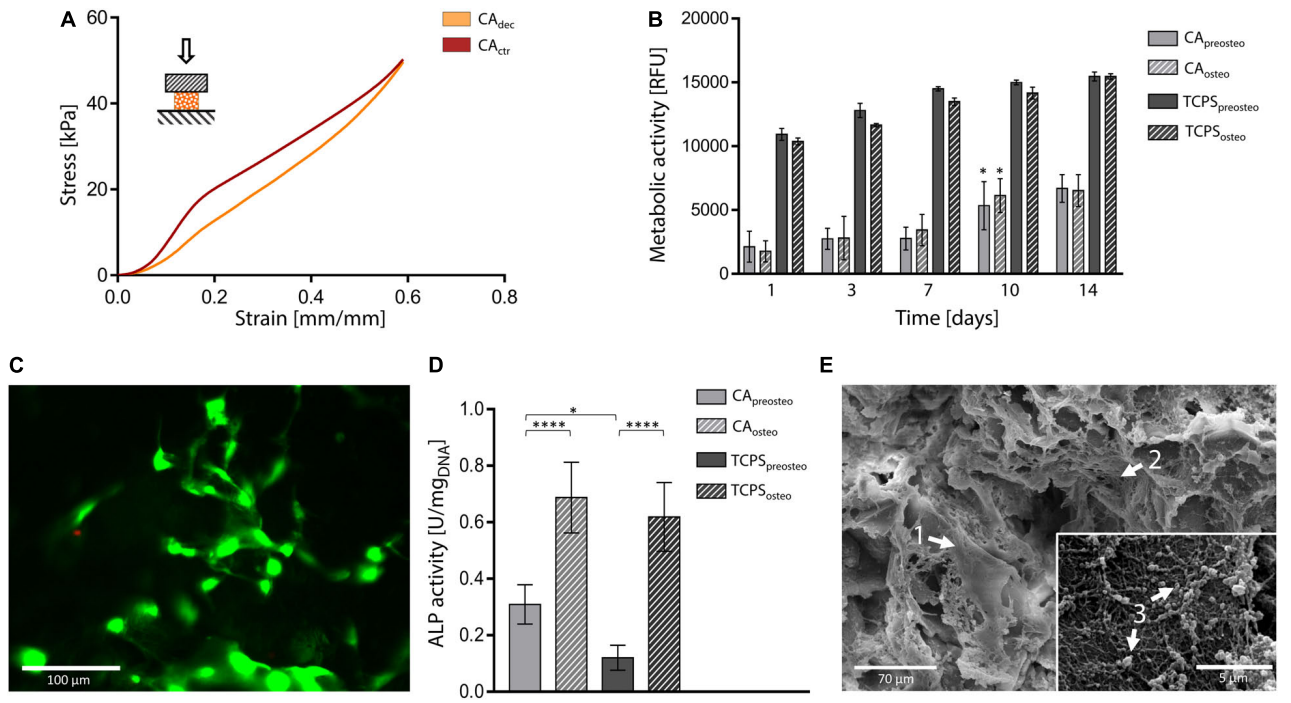


**FIGURE 6 |** Decellularized carrot for bone tissue engineering. **(A)** Representative compression mechanical curve of carrot-derived scaffolds and control samples up to 60% strain. **(B)** Metabolic activity of MC3T3-E1 pre-osteoblast cultured up to 14 days on carrot scaffolds and TCPS plates. Cells were either induced toward osteogenic differentiation (i.e., $CA_{osteo}$ and $TCPS_{osteo}$) or cultured in pre-osteogenic medium (i.e., $CA_{preosteo}$ and $TCPS_{preosteo}$). $n = 4$ per time point, one-way ANOVA: $^{*}p < 0.05$ comparing the metabolic activity of the same sample at one time point to the previous time point. **(C)** Representative LIVE/DEAD staining of MC3T3-E1 cells cultured on carrot-derived scaffolds (scale bar: 100 µm). **(D)** ALP activity of MC3T3-E1 cells culture on decellularized carrots and TCPS for 14 days (values are normalized over DNA content); $n = 4$ per time point, one-way ANOVA: $^{*}p < 0.05$, $^{****}p < 0.0001$. **(E)** SEM micrographs of osteogenic-differentiated MC3T3-E1 cells (arrow 1) cultured for 14 days on carrot-derived scaffolds. Nano-fiber nets (arrow 2), attributable to ECM deposition, and inorganic extracellular secretion (arrow 3) can be observed and attributed to an on-going mineralization process (scale bar: 70 µm; scale bar inset image: 5 µm).

Tensile tests were performed to investigate the mechanical properties of control and decellularized samples. Representative σ–ε curves are shown in **Figure 7A** and in **Supplementary Data 3**, while calculated mechanical parameters are summarized in **Table 1**. The samples were able to withstand 20% strain without failure, corresponding to the maximum value of deformation to which natural tendons are subjected *in vivo* (Mathew et al., 2012). The elastic modulus E of the decellularized celery scaffolds is equal to 0.59 ± 0.09 MPa, with no statistical difference ($p < 0.05$) compared to control. Despite the higher stiffness registered in native tendons ($E$ = 500–1200 MPa), (Islam et al., 2017) scaffolds with relatively low elastic modulus have also been designed (e.g., Agar-PVA hydrogel $E$ = 0.12–2.3 MPa;(Sabzi et al., 2017) silk fibroin scaffolds $E$ = 1.2–1.4 MPa;(Font Tellado et al., 2017) GelMA-alginate hydrogel $E$ = 5–9 kPa), (Rinoldi et al., 2019) proving the potential of celery-derived scaffolds for the regeneration of low-loaded anatomical regions, such as in hand tendons [physiological loads of 3–24 N were registered in human hand flexor tendons, (Edsfeldt et al., 2015) while 920–1510 N loads were detected in Achilles tendons] (Taylor and Arnold, 2016). The tensile strain at break was 23.9 ± 2.5 and 27.8 ± 3.5% and the tensile stress at break was 200.5 ± 49.9 and 246.1 ± 15.4 kPa for $CE_{dec}$ and $CE_{ctr}$, respectively. However, samples rupture occurred in correspondence of the clamps, which might result in an underestimation of the obtained values at break.

*In vitro* direct cytocompatibility was investigated using L929 fibroblast cell line. The metabolic activity (**Figure 7B**) increased until a plateau value was reached ($t$ = 7 days of culture on celery-derived scaffolds, $t$ = 3 days of culture on TCPS wells). Then, the detected fluorescence values were stable for the entire testing time ($t$ = 14 days), suggesting cell confluence. Despite the higher metabolic activity on TCPS wells, the percentage increase of metabolic activity at $t$ = 14 days compared to $t$ = 1 day was significantly higher on celery-derived scaffolds, evidencing an efficient cell growth on the scaffolds (4.03-fold increase in celery-derived scaffolds vs. 1.86-fold increase on TCPS wells). The LIVE/DEAD staining confirmed the presence of viable L929 cells adhered to the decellularized celery scaffolds (**Figure 7C**, percentage cell viability equal to 84.5 ± 7.2%).

Cell alignment was also observed in several regions of the celery surface by LIVE/DEAD staining and was further investigated by immunofluorescence assay. Nuclei were stained with Hoechst 33258, while actin microfilaments were stained with phalloidin – FITC. In several regions of the scaffold surface, corresponding to the previously observed well-defined areas in the scaffold morphology (**Figure 3Cii**), a preferential cell orientation was evidenced and more than 60% of the cells were

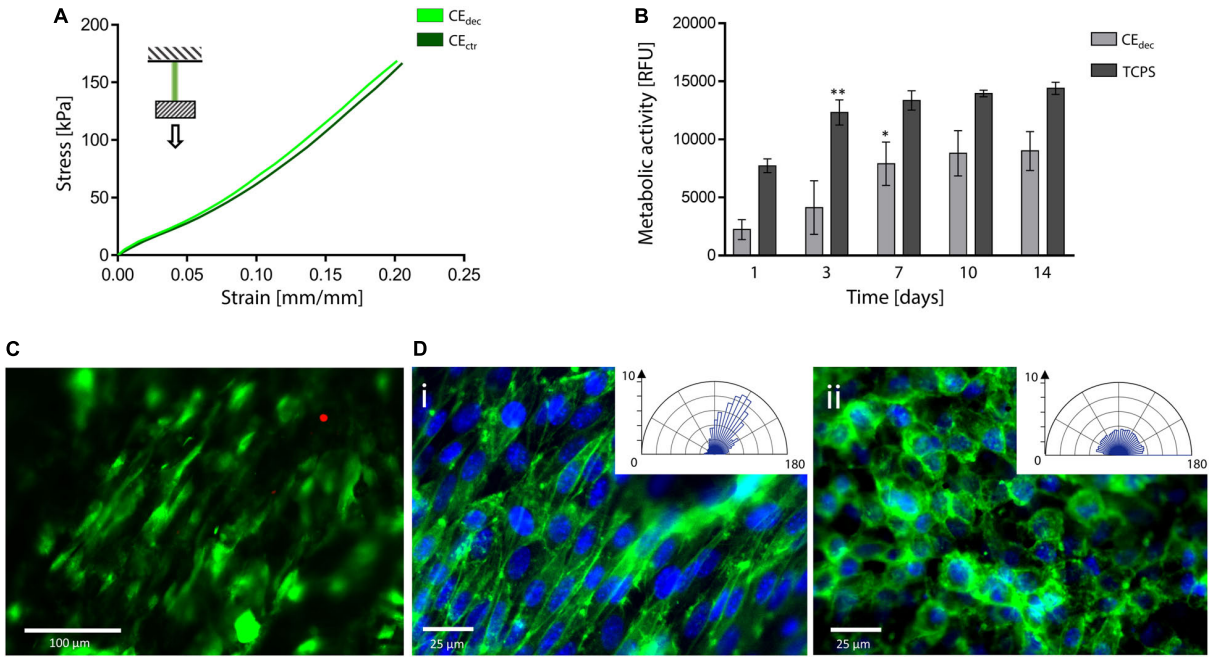


**FIGURE 7 |** Decellularized celery for tendon/ligament engineering. **(A)** Representative tensile mechanical curve of decellularized and control celery samples. **(B)** Metabolic activity of L929 cells seeded on celery-derived scaffolds and TCPS wells up to 14 days of culture. $n = 4$ per time point, one-way ANOVA: $^{*}p < 0.05$, $^{**}p < 0.01$ comparing the metabolic activity of the same sample at one time point to the previous time point. **(C)** Representative LIVE/DEAD staining of L929 cells cultured on celery-derived scaffolds (scale bar: 100 µm). **(D)** Representative immunofluorescence microscopy images of aligned **(Di)** and randomly organized **(Dii)** cells after 7 days of culture on celery scaffolds. Nuclei are stained in blue (Hoechst 33258), while actin microfilaments are stained (phalloidin – FITC) in green (scale bar: 25 µm). Polar histograms of the cell directionality are depicted in the inset boxes.

assessed to have a <20° alignment angle (**Figure 7Di**). This result is comparable to the aligned cells percentage observed on previously developed oriented scaffolds (Schoenenberger et al., 2018; Wang et al., 2018) addressed to tendon tissue engineering. Randomly organized regions were also detected, where cells are characterized by a round morphology with no preferential orientation (**Figure 7Dii**). The presence of both aligned and random cells is consistent with the structure of native tendons, characterized by bundles of aligned collagen fibers surrounded by soft interfascicular matrix, with a less defined and oriented structure (Thorpe et al., 2016).

## DISCUSSION

The use of decellularized plant tissues represents a valid alternative in the development of three-dimensional scaffolds for tissue engineering applications. However, their application for tissue engineering purposes [i.e., cardiac tissue regeneration, (Gershlak et al., 2017) muscle regeneration] (Modulevsky et al., 2014) is still poorly investigated, (Modulevsky et al., 2014) focused on few 3D tissues, such as apple, (Modulevsky et al., 2016) or limited to 2D plant tissues, such as leaves (Gershlak et al., 2017). Moreover, most pioneer works published so far on the use of decellularized plant tissues aim at demonstrating the suitability of plant tissues as potential scaffolds, (Modulevsky et al., 2016; Fontana et al., 2017; Adamski et al., 2018; Dikici et al., 2019) with only few examples targeting at the regeneration of specific tissues (Gershlak et al., 2017; Lee et al., 2019; Cheng et al., 2020). The decellularized plants microarchitectures can mimic the complexity of native human tissues, with no need of multi-step material processing associated to the majority of natural and synthetic polymer derived scaffolds (Jammalamadaka and Tappa, 2018; Zhang et al., 2019). Plants can be considered an alternative source of scaffolds for their low cost, high and easy availability and the absence of ethical issues compared to animal and human-harvested decellularized tissues. Moreover, as animal and human sources are often associated to an important interpatient variability and to the possible transmission of pathogenic agents, (Gilbert et al., 2006; Song and Ott, 2011) the adoption of plant sources may constitute a more reliable path for the obtainment of commercially suitable scaffolds. However, compared to mammalian-derived decellularized tissues, plant tissues are composed by relevant percentages of cellulose, which is not degradable or very slowly degradable in humans, so that cellulose modifications are under investigation to promote cellulose-based bioresorbable scaffolds degradation (Novotna et al., 2013). Thus, considering the plant-derived scaffolds here proposed, their use has potentially to be referred to as biostable scaffolds that, after implantation, integrate with the surrounding tissues and promote cells and tissues colonization (Hickey and Pelling, 2019). In fact, our data show stability in PBS at 37°C up to 7 weeks (i.e., duration of the test), which are in line with previously published data demonstrating absence of apple

scaffolds degradation subcutaneously implanted *in vivo* that, however, showed a successful integration with the surrounding tissues (Modulevsky et al., 2016).

Previous studies (Modulevsky et al., 2014, 2016; Fontana et al., 2017; Gershlak et al., 2017; Hickey et al., 2018) on plant-derived scaffolds (e.g., spinach leaves, parsley, apple hypanthium) assessed the cytocompatibility, biocompatibility and pro-angiogenic properties of the decellularized plant structures even in the absence of a pre-existing vascular network, opening up a broad range of possibilities for these emerging biomaterials. However, the potential in tissue engineering associated to the plant kingdom is still to be deeply and fully investigated: the wide variety of sizes, textures, structures and compositions offered by nature may allow for the targeting of specific human tissues to be regenerated, depending on the peculiar mechanical, physical and morphological features requested for the specific application. Three different plant tissues (i.e., apple hypanthium, carrot xylem, and celery stem) were here selected for the production of decellularized scaffolds to address site-specific human tissues regeneration. The large-size and round porosity adequate for adipocyte colonization and the isotropic structure of apple hypanthium present interesting similarities with human AT, and mechanical investigation confirmed its suitability in mimicking the mechanical features of the native AT ($E_{apple}$ = 4 kPa vs. $E_{adiposetissue}$ = 2–20 kPa) (Omidi et al., 2014; Van Nieuwenhove et al., 2017). The decellularized scaffolds also show mechanical features comparable to those of other AT scaffolds proposed in literature (Davidenko et al., 2010; Yu et al., 2013; Rossi et al., 2016). Carrot-derived scaffolds are characterized by a smaller and heterogeneous porosity, related to higher mechanical properties and lower water adsorption, compared to the apple structures. In particular, the average pore size found in carrot samples is comparable to previously developed scaffolds (He et al., 2018; Pacelli et al., 2018; Tohamy et al., 2018) for bone tissue engineering. Thus, decellularized carrot tissue was addressed to bone tissue engineering and, according to the obtained mechanical properties ($E_{carrot}$ = 43.43 ± 5.22 kPa), non-load bearing applications were selected, such as maxillo-facial and cranial bone regeneration. In fact, despite the superior mechanical features of natural bone (e.g., $E$ = 25–240 MPa for mandibular trabecular bone), (Lakatos et al., 2014) the obtained carrot-derived scaffolds have mechanical properties comparable to other proposed scaffolds for the regeneration of non-load bearing bone tissue ($E$ = 150–300 kPa) (Chatterjee et al., 2010; Peng et al., 2019). Finally, celery stems are characterized by an anisotropic structure, constituted by packed pores organized in parallel longitudinal channels. This peculiar architecture, functional in nature for water transport along the stem to the leaves and maintained after the decellularization treatment, is fundamental for the development of successful scaffolds, since it would allow to nutrients and fluids transport. Due to its oriented structure, celery was selected for the regeneration of naturally anisotropic tissues (i.e., tendons); in particular, morphology and size of samples (Ø = 4 mm, $L$ = 25 mm) are comparable to the natural size of hand tendons (e.g., *palmaris longus*, Ø = 4–4.5 mm) (Ito et al., 2001). Mechanical tests demonstrated the capability of celery samples to withstand the physiological deformation to which tendons are subjected *in vivo*, (Mathew et al., 2012) thus proving their mechanical adequacy. The elastic modulus ($E_{celery}$ = 0.59 ± 0.09 MPa) is comparable to other proposed scaffolds for similar applications ($E$ = 0.12 – 2.3 MPa), (Font Tellado et al., 2017; Sabzi et al., 2017) despite being lower than those of natural tendon tissue ($E_{tendon}$ = 500–1200 MPa) (Islam et al., 2017).

The produced decellularized plant tissues were able not only to support cells adhesion and proliferation, but also to sustain a correct functionality of cells for the specific tissue to be regenerated, as proved by the conducted *in vitro* tests, fundamental for the regeneration of functional tissues. For instance, lipid droplets accumulation was demonstrated on apple scaffolds for adipose tissue engineering, increased ALP activity and inorganic matrix deposition was assessed on carrot scaffolds for bone tissue engineering, and preferred orientation of cells was observed for celery samples for anisotropic tissue regeneration (e.g., tendon). Finally, we adopted a previously published protocol for plants decellularization, (Hickey et al., 2018) and we qualitatively checked the decellularization as a change in color of the decellularized scaffolds (Gershlak et al., 2017). However, more detailed tests will be required to quantitatively assess the effective decellularization of the proposed plants that, given the different structures, might respond differently to the adopted decellularization procedure and the protocol could be adapted for a more efficient decellularization, as recently demonstrated by the use of DNAse (Phan et al., 2020). Despite these tests and further studies on the *in vivo* biocompatibility, degradation or integration with the surrounding tissues of the here proposed scaffolds are required, the obtained results suggest the potential versatile use of plant-derived scaffolds for different tissue engineering purposes.

## CONCLUSION

The potential of decellularized apple, carrot and celery-derived tissues as scaffolds for the regeneration of adipose tissue, bone tissue and tendons, respectively, is here demonstrated. Adequate morphological, physical and mechanical features were obtained for the decellularized scaffolds toward the specific tissues to be regenerated. Furthermore, *in vitro* tests proved the ability of the decellularized plant tissues in supporting cells adhesion, proliferation and functionality, fundamental for the regeneration of the selected functional human tissues. Despite further studies are required to verify the feasibility of *in vivo* implant of decellularized plants and their integration with the host organism, the results here presented suggest a possible use of different plant tissues for versatile tissue engineering applications.

## DATA AVAILABILITY STATEMENT

All datasets presented in this study are included in the article/**Supplementary Material**.

## AUTHOR CONTRIBUTIONS

The manuscript was written through contributions of all authors. All authors have given approval to the final version of the manuscript.

## SUPPLEMENTARY MATERIAL

The Supplementary Material for this article can be found online at: https://www.frontiersin.org/articles/10.3389/fbioe.2020.00723/full#supplementary-material

## REFERENCES


Adamski, M., Fontana, G., Gershlak, J. R., Gaudette, G. R., Le, H. D., and Murphy, W. L. (2018). Two methods for decellularization of plant tissues for tissue engineering applications. *J. Vis. Exp.* 31:57586. doi: 10.3791/57586

Alaribe, F. N., Manoto, S. L., and Motaung, S. C. K. M. (2016). Scaffolds from biomaterials: advantages and limitations in bone and tissue engineering. *Biologia* 71, 353–366. doi: 10.1515/biolog-2016-0056

Balasundari, R., Bishi, D. K., Mathapati, S., Naser, S. B., Cherian, K. M., and Guhathakurta, S. (2012). Nanocoated botanical scaffold in salvage for human tissue regeneration. *J. Biomater. Tissue. Eng.* 2, 330–335. doi: 10.1166/jbt.2012.1058

Bayraktar, H. H., Morgan, E. F., Niebur, G. L., Morris, G. E., Wong, E. K., and Keaveny, T. M. (2004). Comparison of the elastic and yield properties of human femoral trabecular and cortical bone tissue. *J. Biomech.* 37, 27–35. doi: 10.1016/S0021-9290(03)00257-4

Bühler, N. E. M., Schulze-Osthoff, K., Königsrainer, A., and Schenk, M. (2015). Controlled processing of a full-sized porcine liver to a decellularized matrix in24h. *J. Biosci. Bioeng.* 119, 609–613. doi: 10.1016/j.jbiosc.2014.10.019

Cao, S., Li, H., Li, K., Lu, J., and Zhang, L. (2015). In vitro mineralization of MC3T3-E1 osteoblast-like cells on collagen / nano-hydroxyapatite scaffolds coated carbon / carbon composites. *J. Biomed. Mater. Res. A.* 104, 533–543. doi: 10.1002/jbm.a.35593

Chang, K. H., Liao, H. T., and Chen, J. P. (2013). Preparation and characterization of gelatin/hyaluronic acid cryogels for adipose tissue engineering: in vitro and in vivo studies. *Acta Biomater.* 9, 9012–9026. doi: 10.1016/j.actbio.2013.06.046

Chatterjee, K., Lin-Gibson, S., Wallace, W. E., Parekh, S. H., Lee, Y. J., Cicerone, M. T., et al. (2010). The effect of 3D hydrogel scaffold modulus on osteoblast differentiation and mineralization revealed by combinatorial screening. *Biomaterials* 31, 5051–5062. doi: 10.1016/j.biomaterials.2010.03.024

Cheng, Y.-W., Shiwarski, D. J., Ball, R. L., Whitehead, K. A., and Feinberg, A. W. W. (2020). Engineering aligned skeletal muscle tissue using decellularized plant-derived scaffolds. *ACS Biomater. Sci. Eng.* 6, 3046–3054. doi: 10.1021/acsbiomaterials.0c00058

Contessi Negrini, N., Celikkin, N., Tarsini, P., Farè, S., and Święszkowski, W. (2020). Three-dimensional printing of chemically crosslinked gelatin hydrogels for adipose tissue engineering. *Biofabrication* 12:025001. doi: 10.1088/1758-5090/ab56f9

Contessi Negrini, N., Tarsini, P., Tanzi, M. C., and Farè, S. (2019). Chemically crosslinked gelatin hydrogels as scaffolding materials for adipose tissue engineering. *J. Appl. Polym. Sci.* 136:47104. doi: 10.1002/app.47104

Crabbé, A., Liu, Y., Sarker, S. F., Bonenfant, N. R., Barrila, J., Borg, Z. D., et al. (2015). Recellularization of decellularized lung scaffolds is enhanced by dynamic suspension culture. *PLoS One* 10:e0126846. doi: 10.1371/journal.pone.0126846

Davidenko, N., Campbell, J. J., Thian, E. S., Watson, C. J., and Cameron, R. E. (2010). Collagen-hyaluronic acid scaffolds for adipose tissue engineering. *Acta Biomater.* 6, 3957–3968. doi: 10.1016/j.actbio.2010.05.005

Dikici, S., Claeyssens, F., and MacNeil, S. (2019). Decellularised baby spinach leaves and their potential use in tissue engineering applications: studying and promoting neovascularisation. *J. Biomater. Appl.* 34, 546–559. doi: 10.1177/0885328219863115

Du, J., Zuo, Y., Lin, L., Huang, D., Niu, L., Wei, Y., et al. (2018). Effect of hydroxyapatite fillers on the mechanical properties and osteogenesis capacity of bio-based polyurethane composite scaffolds. *J. Mech. Behav. Biomed. Mater.* 88, 150–159. doi: 10.1016/j.jmbbm.2018.08.028

Edsfeldt, S., Rempel, D., Kursa, K., Diao, E., and Lattanza, L. (2015). In vivo flexor tendon forces generated during different rehabilitation exercises. *J. Hand. Surf. Eur. Vol.* 40, 705–710. doi: 10.1177/1753193415591491

Farrokhi, A., Pakyari, M., Nabai, L., Pourghadiri, A., Hartwell, R., Jalili, R., et al. (2018). Evaluation of detergent-free and detergent-based methods for decellularization of murine skin. *Tissue. Eng. Part A.* 24, 955–967. doi: 10.1089/ten.tea.2017.0273

Font Tellado, S., Bonani, W., Balmayor, E. R., Foehr, P., Motta, A., Migliaresi, C., et al. (2017). Fabrication and characterization of biphasic silk fibroin scaffolds for tendon/ligament-to-bone tissue engineering. *Tissue. Eng. Part A.* 23, 859–872. doi: 10.1089/ten.tea.2016.0460

Fontana, G., Gershlak, J., Adamski, M., Lee, J. S., Matsumoto, S., Le, H. D., et al. (2017). Biofunctionalized plants as diverse biomaterials for human cell culture. *Adv. Healthc. Mater.* 6:10.1002/adhm.201601225. doi: 10.1002/adhm.201601225

Frydrych, M., Román, S., Macneil, S., and Chen, B. (2015). Biomimetic poly(glycerol sebacate)/poly(l-lactic acid) blend scaffolds for adipose tissue engineering. *Acta Biomater.* 18, 40–49. doi: 10.1016/j.actbio.2015.03.004

Fu, Y., Fan, X., Tian, C., Luo, J., Zhang, Y., Deng, L., et al. (2016). Decellularization of porcine skeletal muscle extracellular matrix for the formulation of a matrix hydrogel: a preliminary study. *J. Cell. Mol. Med.* 20, 740–749. doi: 10.1111/jcmm.12776

Gao, S., Zhao, P., Lin, C., Sun, Y., Wang, Y., Zhou, Z., et al. (2014). Differentiation of human adipose-derived stem cells into neuron-like cells which are compatible with photocurable three-dimensional scaffolds. *Tissue. Eng. Part A.* 20, 1271–1284. doi: 10.1089/ten.tea.2012.0773

Gerges, I., Tamplenizza, M., Martello, F., Recordati, C., Martelli, C., Ottobrini, L., et al. (2018). Exploring the potential of polyurethane-based soft foam as cell-free scaffold for soft tissue regeneration. *Acta Biomater.* 73, 141–153. doi: 10.1016/j.actbio.2018.04.011

Gershlak, J. R., Hernandez, S., Fontana, G., Perreault, L. R., Hansen, K. J., Larson, S. A., et al. (2017). Crossing kingdoms: using decellularized plants as perfusable tissue engineering scaffolds. *Biomaterials* 125, 13–22. doi: 10.1016/j.biomaterials.2017.02.011

Gilbert, T. W., Sellaro, T. L., and Badylak, S. F. (2006). Decellularization of tissues and organs. *Biomaterials* 27, 3675–3683.

Goyal, R., Guvendiren, M., Freeman, O., Mao, Y., and Kohn, J. (2017). Optimization of polymer-ecm composite scaffolds for tissue engineering: effect of cells and culture conditions on polymeric nanofiber mats. *J. Funct. Biomater.* 8:1. doi: 10.3390/jfb8010001

Gurkan, U. A., Cheng, X., Kishore, V., Uquillas, J. A., and Akkus, O. (2010). Comparison of morphology, orientation, and migration of tendon derived fibroblasts and bone marrow stromal cells on electrochemically aligned collagen constructs. *J. Biomed. Mater. Res. Part A* 94, 1070–1079. doi: 10.1002/jbm.a.32783

Guruswamy Damodaran, R., and Vermette, P. (2018). Decellularized pancreas as a native extracellular matrix scaffold for pancreatic islet seeding and culture. *J. Tissue. Eng. Regen. Med.* 12, 1230–1237. doi: 10.1002/term.2655

He, X., Fan, X., Feng, W., Chen, Y., Guo, T., Wang, F., et al. (2018). Incorporation of microfibrillated cellulose into collagen-hydroxyapatite scaffold for bone tissue engineering. *Int. J. Biol. Macromol.* 115, 385–392. doi: 10.1016/j.ijbiomac.2018.04.085

Hickey, R. J., and Pelling, A. E. (2019). Cellulose biomaterials for tissue engineering. *Front. Bioeng. Biotechnol.* 7:45. doi: 10.3389/fbioe.2019.00045

Hickey, R. J., Modulevsky, D. J., Cuerrier, C. M., and Pelling, A. E. (2018). Customizing the shape and microenvironment biochemistry of biocompatible macroscopic plant-derived cellulose scaffolds. *ACS Biomater. Sci. Eng.* 4, 3726–3736. doi: 10.1021/acsbiomaterials.8b00178

Islam, A., Mbimba, T., Younesi, M., and Akkus, O. (2017). Effects of substrate stiffness on the tenoinduction of human mesenchymal stem cells. *Acta Biomater.* 58, 244–253. doi: 10.1016/j.actbio.2017.05.058

Ito, M. M., Aoki, M., Kida, M. Y., Seiichi, I., Kumaki, K., and Shigenori, T. (2001). Length and width of the tendinous portion of the palmaris longus: a cadaver study of adult Japanese. *J. Hand. Surg. Am.* 26, 706–710. doi: 10.1053/jhsu.2001.26026

Jammalamadaka, U., and Tappa, K. (2018). Recent advances in biomaterials for 3D printing and tissue engineering. *J. Funct. Biomater.* 9:22. doi: 10.3390/jfb9010022

Kitahara, H., Yagi, H., Tajima, K., Okamoto, K., Yoshitake, A., Aeba, R., et al. (2016). Heterotopic transplantation of a decellularized and recellularized whole porcine heart. *Interact. Cardiovasc. Thorac. Surg.* 22, 571–579. doi: 10.1093/icvts/ivw022

Lakatos, É, Magyar, L., and Bojtár, I. (2014). Material properties of the mandibular trabecular bone. *J. Med. Eng.* 2014:470539. doi: 10.1155/2014/470539

Lee, J., Jung, H., Park, N., Park, S. H., and Ju, J. H. (2019). Induced osteogenesis in plants decellularized scaffolds. *Sci. Rep.* 9, 1–10. doi: 10.1038/s41598-019-56651-0

Lin, C.-H., Hsia, K., Ma, H., Lee, H., and Lu, J.-H. (2018). In vivo performance of decellularized vascular grafts: a review article. *Int. J. Mol. Sci.* 19:2101. doi: 10.3390/ijms19072101

López-Álvarez, M., Pereiro, I., Serra, J., De Carlos, A., and González, P. (2011). Osteoblast-like cell response to macro- and micro-patterned carbon scaffolds obtained from the sea rush *Juncus maritimus*. *Biomed. Mater.* 6:045012. doi: 10.1088/1748-6041/6/4/045012

Mathew, A. P., Oksman, K., Pierron, D., and Harmand, M. F. (2012). Fibrous cellulose nanocomposite scaffolds prepared by partial dissolution for potential use as ligament or tendon substitutes. *Carbohydr. Polym.* 87, 2291–2298. doi: 10.1016/j.carbpol.2011.10.063

Modulevsky, D. J., Cuerrier, C. M., and Pelling, A. E. (2016). Biocompatibility of subcutaneously implanted plant-derived cellulose biomaterials. *PLoS One* 11:e0157894. doi: 10.1371/journal.pone.0157894

Modulevsky, D. J., Lefebvre, C., Haase, K., Al-Rekabi, Z., and Pelling, A. E. (2014). Apple derived cellulose scaffolds for 3D mammalian cell culture. *PLoS One* 9:e97835. doi: 10.1371/journal.pone.0097835

Novotna, K., Havelka, P., Sopuch, T., Kolarova, K., Vosmanska, V., Lisa, L., et al. (2013). Cellulose-based materials as scaffolds for tissue engineering. *Cellulose* 20, 2263–2278. doi: 10.1007/s10570-013-0006-4

Omidi, E., Fuetterer, L., Reza Mousavi, S., Armstrong, R. C., Flynn, L. E., and Samani, A. (2014). Characterization and assessment of hyperelastic and elastic properties of decellularized human adipose tissues. *J. Biomech.* 47, 3657–3663. doi: 10.1016/j.jbiomech.2014.09.035

Pacelli, S., Basu, S., Berkland, C., Wang, J., and Paul, A. (2018). Design of a cytocompatible hydrogel coating to modulate properties of ceramic-based scaffolds for bone repair. *Cell Mol. Bioeng.* 11, 211–217. doi: 10.1007/s12195-018-0521-3

Peng, X. Y., Hu, M., Liao, F., Yang, F., Ke, Q. F., Guo, Y. P., et al. (2019). La-Doped mesoporous calcium silicate/chitosan scaffolds for bone tissue engineering. *Biomater. Sci.* 7, 1565–1573. doi: 10.1039/c8bm01498a

Petersen, T. H., Calle, E. A., Zhao, L., Lee, E. J., Gui, L., Raredon, M. B., et al. (2010). Tissue-engineered lungs for in vivo implantation. *Science* 329, 538–541. doi: 10.1126/science.1189345

Phan, N. V., Wright, T., Rahman, M. M., Xu, J., and Coburn, J. M. (2020). In vitro biocompatibility of decellularized cultured plant cell-derived matrices. *ACS Biomater. Sci. Eng.* 6, 822–832. doi: 10.1021/acsbiomaterials.9b00870

Porzionato, A., Stocco, E., Barbon, S., Grandi, F., Macchi, V., and De Caro, R. (2018). Tissue-engineered grafts from human decellularized extracellular matrices: a systematic review and future perspectives. *Int. J. Mol. Sci.* 19:4117. doi: 10.3390/ijms19124117

Riaz, N., Wolden, S. L., Gelblum, D. Y., and Eric, J. A. (2016). rate insensitive linear viscoelastic model for soft tissues. *Biomaterials* 118, 6072–6078. doi: 10.1002/cncr.27633.Percutaneous

Rinoldi, C., Costantini, M., Kijeńska-Gawrońska, E., Testa, S., Fornetti, E., Heljak, M., et al. (2019). Tendon tissue engineering: effects of mechanical and biochemical stimulation on stem cell alignment on cell-laden hydrogel yarns. *Adv. Healthc. Mater.* 8:e1801218. doi: 10.1002/adhm.201801218

Rossi, E., Gerges, I., Tocchio, A., Tamplenizza, M., Aprile, P., Recordati, C., et al. (2016). Biologically and mechanically driven design of an RGD-mimetic macroporous foam for adipose tissue engineering applications. *Biomaterials* 104, 65–77. doi: 10.1016/j.biomaterials.2016.07.004

Sabzi, M., Samadi, N., Abbasi, F., Mahdavinia, G. R., and Babaahmadi, M. (2017). Bioinspired fully physically cross-linked double network hydrogels with a robust, tough and self-healing structure. *Mater. Sci. Eng. C* 74, 374–381. doi: 10.1016/j.msec.2016.12.026

Scarrit, M. E. (2015). A review of cellularization strategies for tissue engineering of whole organs. *Front. Bioeng. Biotechnol.* 3:43. doi: 10.3389/fbioe.2015.00043

Schoenenberger, A. D., Foolen, J., Moor, P., Silvan, U., and Snedeker, J. G. (2018). Substrate fiber alignment mediates tendon cell response to inflammatory signaling. *Acta Biomater.* 71, 306–317. doi: 10.1016/j.actbio.2018.03.004

Smith, C. A., Board, T. N., Rooney, P., Eagle, M. J., Richardson, S. M., and Hoyland, J. A. (2017). Human decellularized bone scaffolds from aged donors show improved osteoinductive capacity compared to young donor bone. *PLoS One* 12:e0177416. doi: 10.1371/journal.pone.0177416

Song, J. J., and Ott, H. C. (2011). Organ engineering based on decellularized matrix scaffolds. *Trends Mol. Med.* 17, 424–432. doi: 10.1016/j.molmed.2011.03.005

Taylor, D. J., and Arnold, A. S. (2016). Quantifying achilles tendon force in vivo from ultrasound images. *J. Biomech.* 49, 3200–3207. doi: 10.1016/j.jbiomech.2016.07.036

Thorpe, C. T., Peffers, M. J., Simpson, D., Halliwell, E., Screen, H. R. C., and Clegg, P. D. (2016). Anatomical heterogeneity of tendon: fascicular and interfascicular tendon compartments have distinct proteomic composition. *Sci. Rep.* 6:20455. doi: 10.1038/srep20455

Thu, H. E., Mohamed, I. N., Hussain, Z., and Shuid, A. N. (2017). Eurycoma longifolia as a potential alternative to testosterone for the treatment of osteoporosis: exploring time-mannered proliferative, differentiative and morphogenic modulation in osteoblasts. *J. Ethnopharmacol.* 195, 143–158. doi: 10.1016/j.jep.2016.10.085

Tohamy, K. M., Soliman, I. E., Mabrouk, M., ElShebiney, S., Beherei, H. H., Aboelnasr, M. A., et al. (2018). Novel polysaccharide hybrid scaffold loaded with hydroxyapatite: fabrication, bioactivity, and in vivo study. *Mater. Sci. Eng. C Mater. Biol. Appl.* 93, 1–11 doi: 10.1016/j.msec.2018.07.054

Urciuolo, A., Urbani, L., Perin, S., Maghsoudlou, P., Scottoni, F., Gjinovci, A., et al. (2018). Decellularised skeletal muscles allow functional muscle regeneration by promoting host cell migration. *Sci. Rep.* 8:8398. doi: 10.1038/s41598-018-26371-y

Van Nieuwenhove, I., Tytgat, L., Ryx, M., Blondeel, P., Stillaert, F., Thienpont, H., et al. (2017). Soft tissue fillers for adipose tissue regeneration: from hydrogel development toward clinical applications. *Acta Biomater.* 63, 37–49. doi: 10.1016/j.actbio.2017.09.026

Wang, Z., Lee, W. J., Koh, B. T. H., Hong, M., Wang, W., and Lim, P. N. (2018). Functional regeneration of tendons using scaffolds with physical anisotropy engineered via microarchitectural manipulation. *Sci. Adv.* 4:eaat4537. doi: 10.1126/sciadv.aat4537

Wu, Q., Bao, J., Zhou, Y., Wang, Y. J., Du, Z. G., Shi, Y. J., et al. (2015). Optimizing perfusion-decellularization methods of porcine livers for clinical-scale whole-organ bioengineering. *Biomed. Res. Int.* 2015, 1–9. doi: 10.1155/2015/785474

Xue, A., Niu, G., Chen, Y., Li, K., Xiao, Z., Luan, Y., et al. (2018). Recellularization of well-preserved decellularized kidney scaffold using adipose tissue-derived stem cells. *J. Biomed. Mater. Res. Part A.* 106, 805–814. doi: 10.1002/jbm.a.36279

Yu, C., Bianco, J., Brown, C., Fuetterer, L., Watkins, J. F., Samani, A., et al. (2013). Porous decellularized adipose tissue foams for soft tissue regeneration. *Biomaterials* 34, 3290–3302. doi: 10.1016/j.biomaterials.2013.01.056

Zamani, Y., Mohammadi, J., Amoabediny, G., Visscher, D. O., Helder, M. N., Zandieh-Doulabi, B., et al. (2019). Enhanced osteogenic activity by MC3T3-E1 pre-osteoblasts on chemically surface-modified poly($\epsilon$-caprolactone) 3D-printed scaffolds compared to RGD immobilized scaffolds. *Biomed Mater.* 14:015008. doi: 10.1088/1748-605X/aaeb82

Zebisch, K., Voigt, V., Wabitsch, M., and Brandsch, M. (2012). Protocol for effective differentiation of 3T3-L1 cells to adipocytes. *Anal. Biochem.* 425, 88–90. doi: 10.1016/j.ab.2012.03.005

Zhang, L., Yang, G., Johnson, B. N., and Jia, X. (2019). Three-dimensional (3D) printed scaffold and material selection for bone repair. *Acta Biomater.* 84, 16–33. doi: 10.1016/j.actbio.2018.11.039

Zitnay, J. L., Reese, S. P., Tran, G., Farhang, N., Bowles, R. D., and Weiss, J. A. (2018). Fabrication of dense anisotropic collagen scaffolds using biaxial compression. *Acta Biomater.* 65, 76–87. doi: 10.1016/j.actbio.2017.11.017

Zoico, E., Darra, E., Rizzatti, V., Budui, S., Franceschetti, G., Mazzali, G., et al. (2016). Adipocytes WNT5a mediated dedifferentiation: a possible target in pancreatic cancer microenvironment. *Oncotarget* 7, 20223–20235. doi: 10.18632/oncotarget.7936

**Conflict of Interest:** The authors declare that the research was conducted in the absence of any commercial or financial relationships that could be construed as a potential conflict of interest.

The handling editor LR declared a past co-authorship with several of the authors SF and NC.

frontiers in Bioengineering and Biotechnology

ORIGINAL RESEARCH
published: 30 June 2020
doi: 10.3389/fbioe.2020.00683

# Helium/Argon-Generated Cold Atmospheric Plasma Facilitates Cutaneous Wound Healing

*Bih-Show Lou[1,2], Jang-Hsing Hsieh[3,4], Chun-Ming Chen[3], Chun-Wei Hou[1], Hui-Yu Wu[5], Pang-Yun Chou[6], Chih-Ho Lai[5,7,8,9]* and Jyh-Wei Lee[3,4,6,10]**

[1] Chemistry Division, Center for General Education, Chang Gung University, Taoyuan, Taiwan, [2] Department of Nuclear Medicine and Molecular Imaging Center, Chang Gung Memorial Hospital, Taoyuan, Taiwan, [3] Center for Plasma and Thin Film Technologies, Ming Chi University of Technology, New Taipei, Taiwan, [4] Department of Materials Engineering, Ming Chi University of Technology, New Taipei, Taiwan, [5] Department of Microbiology and Immunology, College of Medicine, Graduate Institute of Biomedical Sciences, Chang Gung University, Taoyuan, Taiwan, [6] Plastic and Reconstructive Surgery and Craniofacial Research Center, Chang Gung Memorial Hospital, Taoyuan, Taiwan, [7] Department of Pediatrics, Molecular Infectious Disease Research Center, Chang Gung Memorial Hospital, Linkou, Taiwan, [8] Department of Medical Research, School of Medicine, China Medical University and Hospital, Taichung, Taiwan, [9] Department of Nursing, Asia University, Taichung, Taiwan, [10] Department of Mechanical Engineering, Chang Gung University, Taoyuan, Taiwan

OPEN ACCESS

**Edited by:**
*Andrea Cochis, University of Eastern Piedmont, Italy*

**Reviewed by:**
*Subhamoy Das, Stanford University, United States*
*Vignesh Muthuvijayan, Indian Institute of Technology Madras, India*

***Correspondence:**
*Chih-Ho Lai*
*chlai@mail.cgu.edu.tw*
*Jyh-Wei Lee*
*jefflee@mail.mcut.edu.tw*

**Specialty section:**
*This article was submitted to Biomaterials, a section of the journal Frontiers in Bioengineering and Biotechnology*

**Received:** *20 February 2020*
**Accepted:** *02 June 2020*
**Published:** *30 June 2020*

**Citation:**
*Lou B-S, Hsieh J-H, Chen C-M, Hou C-W, Wu H-Y, Chou P-Y, Lai C-H and Lee J-W (2020) Helium/Argon-Generated Cold Atmospheric Plasma Facilitates Cutaneous Wound Healing. Front. Bioeng. Biotechnol. 8:683. doi: 10.3389/fbioe.2020.00683*

Cold atmospheric plasma jet (CAPJ) or non-thermal plasma jet has been employed in various biomedical applications based on their functions in bactericidal activity and wound healing. However, the effect of CAPJ generated by a particular composition of gases on wound closure and the underlying mechanisms that regulate wound healing signals remain elusive. In the present study, we investigated the impact of helium (He)- or a gas mixture of He and argon (He/Ar)-generated CAPJ on cell proliferation, which is a pivotal step during the wound healing process. With careful treatment duration control, He/Ar-CAPJ effectively induced keratinocyte proliferation and migration mediated through the activation of epithelial-to-mesenchymal transition (EMT) and cell cycle progression, which was evidenced by a decrease in E-cadherin levels and increases in N-cadherin, cyclin D1, Ki-67, Cdk2, and p-ERK levels. Rat wound healing studies showed that He/Ar-CAPJ treatment facilitated granulation tissue formation and mitigated inflammation in cutaneous tissue, resulting in accelerated wound closure. These findings highlight the possibility that He/Ar-CAPJ can be developed as a therapeutic agent for enhancing wound healing.

**Keywords: cold atmospheric plasma jet, wound healing, keratinocyte, cell proliferation, cell cycle**

## INTRODUCTION

Cold atmospheric plasma jet (CAPJ), also known as non-thermal plasma jet, is mainly operated at near human body temperature (<40°C) and provides several reactive species, including electrons, ions, neutral particles, UV radiation, heat, and reactive oxygen and nitrogen species (RONS) (Isbary et al., 2013; von Woedtke et al., 2013; Weltmann and von Woedtke, 2017). CAPJ with unique constituents and characteristics has become widely used in clinical applications, such as cancer remission, control of drug resistant bacteria, root canal treatment, and promotion of wound healing (Ehlbeck et al., 2008; Daeschlein et al., 2015).

The RONS produced by CAPJ play a key role in anti-bacterial activity, which can treat infectious diseases and promote the healing effects of skin lesions (Dunnill et al., 2017). Since CAPJ possesses

bactericidal activity, recent studies have used it to treat pathogenic infections in cutaneous and soft tissues, including dermatitis and chronic ulcerative wounds (Mai-Prochnow et al., 2014; Brehmer et al., 2015). Our recent study demonstrated that CAPJ with appropriate parameters has potent anti-microbial activity that is mediated through cell wall destruction and DNA breaks of the bacteria (Lou et al., 2019). Furthermore, the application of CAPJ to wounds created on rats showed a marked reduction in bacterial load compared to that of wounds not treated with CAPJ, indicating that CAPJ is effective when applied *in vivo*.

In addition to bactericidal effects, plasma-generated RONS possess wound healing activity, which may stimulate signaling pathways to regulate tissue repair in the skin (Isbary et al., 2010; Kubinova et al., 2017). Notably, RONS play a pivotal role in tissue repair, including cell migration and proliferation, as well as the formation of blood vessels at wound sites (Dunnill et al., 2017). Furthermore, RONS-induced endothelial cell proliferation after plasma treatment is related to the release of fibroblast growth factors (Ngo et al., 2014). Despite *in vitro* studies that have revealed valuable information on the role of plasma at the cellular level, few investigations have explored the detailed mechanistic and biological effects of plasma on skin wounds using live animal models.

Given the close association of plasma with antiseptic functioning, it has been found to be crucial for wound healing, although the specific molecules that contribute to this interaction still require further investigations. In the present study, we explored the effect of CAPJ into the plasma-activated medium (PAM) with different treatment durations under a pure He gas and particular composition of He and Ar mixed gases on human keratinocytes. We further identified its mechanism of action in several signaling pathways. Moreover, we assessed the healing activity of CAPJ when treating skin injuries using rat models. The results of the combined cell-based and animal studies demonstrate that the He and Ar mixed gases generated CAPJ can be developed as an effective treatment for cutaneous wounds.

# MATERIALS AND METHODS

## Antibodies and Reagents

Antibodies specific against E-cadherin, N-cadherin, ERK, and phosphorylated ERK were purchased from Cell Signaling (Danvers, MA, United States). Antibodies specific to cyclin $D_1$ and Cdk2 were purchased from Proteintech (Chicago, IL, United States). Antibodies against β-actin and Ki-67, rabbit or mouse horseradish peroxidase (HRP)-conjugated antibodies were purchased from Santa Cruz Biotechnology (Santa Cruz, CA, United States). All other reagents were purchased from Sigma-Aldrich (St. Louis, MO, United States).

## Cell Culture

Human keratinocytes (HaCaT cells, ATCC 12191) were cultured in Dulbecco's modified Eagle's medium (DMEM, Hyclone, Logan, UT, United States) containing 100 U/mL penicillin, and 100 μg/mL streptomycin. De-complement fetal bovine serum (10%; HyClone) was added to the culture medium. The cells were maintained at 37°C in a humidified atmosphere containing 5% $CO_2$.

## Generation of CAPJ

All experiments with the plasma treatment were operated by the CAPJ as described in our previous study (Lou et al., 2019). An indirect treatment method was applied for the cell culture experiments, which the DMEM was activated by CAPJ before usage. Parameters of the CAPJ included a working voltage of 6.5 kV and a distance of 15 mm between CAPJ and DMEM surface. Five different treatment periods: 15, 30, 45, 60, and 90 s, were applied into DMEM under two different gas flowing conditions, one is the pure He gas under a flow rate of 5 slm (standard liter per min) (defined as He-CAPJ hereafter), and the other is the gas mixture of He and Ar with the flow rates of 5 and 0.5 slm (defined as He/Ar-CAPJ hereafter), respectively. The flow rate ratio of He and Ar gas mixture was 10:1 due to its ability for producing higher amounts of OH and NO radicals (Lou et al., 2019). The DMEM surface temperature was maintained at 34.5°C during CAPJ treatment as described in our previous reports (Lou et al., 2019).

## Cell Proliferation Assay

The MTT [3-(4,5-dimethylthiazol-2-yl)-2,5-diphenyltetrazolium bromide] assay (Sigma-Aldrich) was used to determine the effects of plasma gas on cell viability. Complete cell culture medium was pretreated with He-CAPJ and He/Ar-CAPJ for 15, 30, 45, 60, and 90 s, respectively, referring as PAM, followed by the incubation with HaCaT cells for an additional 24 h. MTT reagent was added to the cells and incubated for 4 h at 37°C. DMSO (Dimethyl sulfoxide) was added to each well to effectively dissolve the formazan crystals. Cell proliferation was measured by analyzing the ability of viable cells to reduce MTT reagent to formazan at the wavelength of 570 nm (Chen et al., 2017). The results were expressed as the means of three independent experiments performed in duplicate.

## Cell Migration Assay

HaCaT cells were culture in 12-well plates at a density of approximately $1 \times 10^5$ and were grown to reach 100% confluence for 24 h. Two perpendicular scratches were performed by using a sterile p200 pipette tip. The culture media were replaced with PAM and cultured for an additional 24 h. Microscopic images of the wounded area were taken immediately after wounding at 24 h. The images were measured for the fields of each well by using ImageJ (National Institute of Health, Bethesda, MD, United States) (Chen et al., 2018). The average of three widths taken from upper, middle, and bottom of each wound area was analyzed for the closure scratch width (%) calculation using $\frac{W_i - W_f}{W_i} \times 100$, where $W_i$ and $W_f$ are initial and final wound widths, respectively (Romaldini et al., 2018). Each analysis was executed in duplicates and was repeated three times.

## Western Blot Assay

HaCaT cells ($3 \times 10^5$) were plated in 6-cm dishes and incubated with complete cell culture media which were pretreated with

various conditions of He/Ar-CAPJ for 24 h. The treated cells were lysed with 100 μL RIPA reagent containing with protease and phosphatase inhibitors (Roch, Indianapolis, IN, United States). The cell lysates resolved by 10% SDS-PAGE and then performed the Western blot assay. The samples were transferred onto a polyvinylidene difluoride (PVDF) membrane (Millipore, Billerica, MA, United States) and immersed with 5% dehydrated skim milk to block non-specific protein binding. The membranes were incubated with primary antibodies as indicated in each experiment. The blots were then probed with the HRP-conjugated secondary antibody. The proteins of interest were detected using ECL Western blotting detection reagents (GE Healthcare, Piscataway, NJ, United States) and visualized by using Azure c400 system and AzureSpot Analysis Software (Azure Biosystems, Dublin, CA, United States). The signal intensity of each protein was quantified with UN-SCAN-IT software (Silk Scientific Corporation, Orem, UT, United States) as described previously (Lin et al., 2019). These data were expressed as the mean ± standard deviation determined from three independent experiments.

## Animal Study

The evaluation of CAPJ treatment was performed on cutaneous wounded male Sprague-Dawley (SD) rats. A total of twenty seven male SD rats (8 weeks old, BW 250 ± 30 g) were obtained from the National Laboratory Animal Center of Taiwan. The rates were treated in accordance with the Animal Care and Use Guidelines for Chang Gung University under a protocol approved by the Institutional Animal Care Use Committee (Approval No. CGU105-032). The experimental protocol was performed from July 1, 2018 to June 31, 2019, in accordance with the guidelines. Twenty one rats were separated into He-CAPJ ($n$ = 6) and He/Ar-CAPJ ($n$ = 15, amongst, 9 for histological analysis) groups. The working voltage, sample distance, and treatment period for the He-CAPJ and He/Ar-CAPJ treatments were 7.5 kV, 20 mm, and 60 s, respectively. Two full-thickness wounds with 17 mm in diameter were produced on both sides of a rat's shoulders under anesthesia and muscle relaxant with zoletil (25 mg/kg) and rompun (10 mg/kg), respectively. The right-side wounds were treated with CAPJ once, and the left side wounds were kept untreated as controls for comparison. The CAPJ treatment on each wound was divided into 9 points starting from upper left corner to bottom right corner as shown in **Figure 1** for evenly treated wound areas. Rats ($n$ = 3) were euthanized by $CO_2$ on days 3, 7, and 14 after He/Ar-CAPJ treatment. The tissue samples were collected from the both sides of cutaneous wounded rats for the followed histological analysis. The wounds and adjacent skin were removed by operating scissors with a diameter of 15 mm. The removed tissues were placed on tissue embedding cassettes and soaked in 10% neutral buffered formalin for tissue fixation and hematoxylin-eosin (H&E) staining, which were performed by a manufacturer (Helix Technology Co., Ltd., Taiwan). The evaluation of wound closure and tissue inflammation was executed based on histopathological examination and verified by a dermatological physician. Six rats were further used to evaluate the effect of CAPJ treatment period, which were treated for 3 min (right side) and 5 min (left side) under He/Ar-CAPJ with constant working voltage of 7.5 kV and sample distance of 20 mm. The photos of the wound areas were taken every other day until fully recovery and analyzed using ImageJ (National Institute of Health, Bethesda, MD, United States).

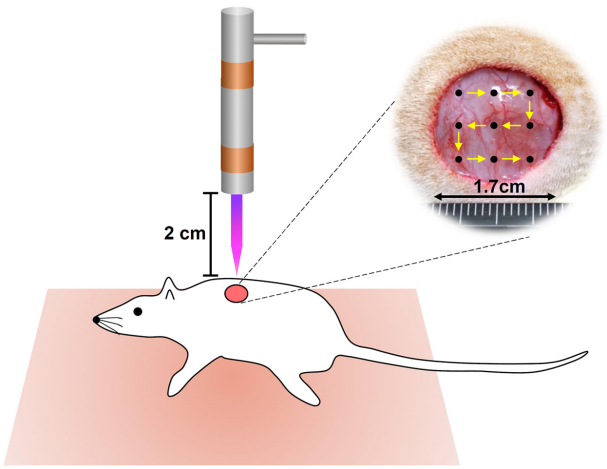


**FIGURE 1 |** Schematic representation of CAPJ treated wounds in rats. Two full-thickness wounds, 17 mm in diameter, were created on both sides of a rat's shoulder. Right: treated with He-CAPJ and He/Ar-CAPJ, left: untreated control (not shown).

## Statistical Analysis

The relation of between-group comparisons was performed using the chi-square with Fisher exact test. Statistics analysis comparisons of more than two groups were evaluated using two-way analysis of variance (ANOVA). The statistical analysis was performed by using the SPSS program (version 18.0 for windows, SPSS Inc., Chicago, IL, United States). A $P$-value less than 0.05 was considered statistically significant.

# RESULTS

## Establishment and Characterization of CAPJ

The PAM was produced by the activation of the cell culture medium using CAPJ as shown in **Figure 2A**. The distance from the quartz tube nozzle to the liquid surface was fixed at 1.5 cm, and the working voltage was maintained at 6.5 kV. Various RONS generated in PAM by non-thermal plasma sources have been well reviewed in literature (Kaushik et al., 2018). Based on the optical emission spectroscopy (OES) spectra of He-based CAPJ, as observed in our previous study (Lou et al., 2019), the compositions and abundances of RONS generated by CAPJ are most likely dependent on the composition of the working gas. The intensity of the hydroxyl (OH) radical at a wavelength of 309 nm increased with increasing Ar gas flow rate but was unaffected at various application voltages (Lou et al., 2019). In addition, the intensity of nitrogen monoxide (NO) emission at a wavelength of 283 nm can be observed under the mixture

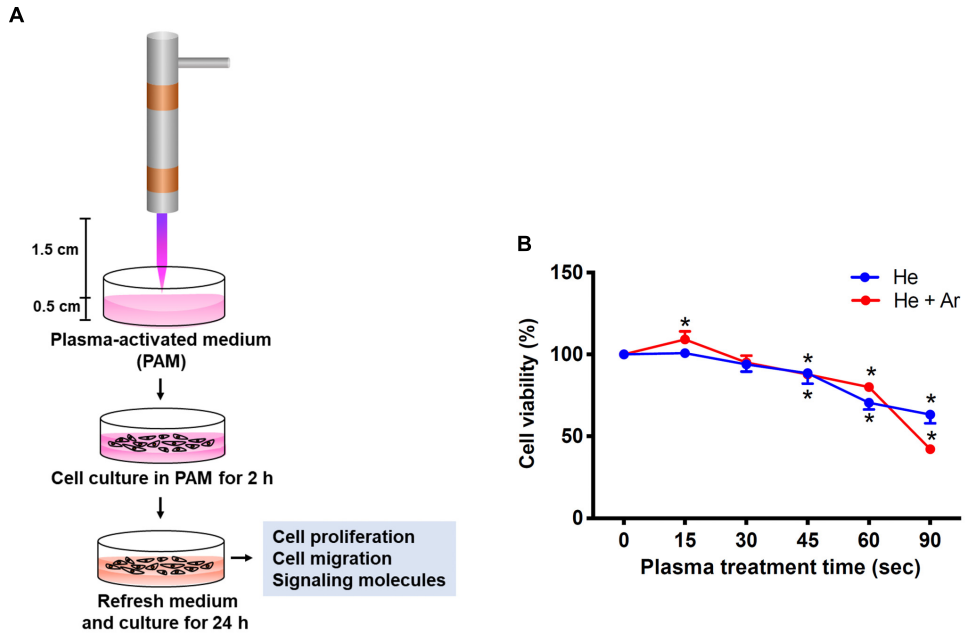


**FIGURE 2 |** Experimental establishment of CAPJ system for the treatment of human keratinocytes. **(A)** The schematic configuration of the CAPJ device. CAPJ was operated with a working voltage of 6.5 kV. The gas flow rates of He and Ar were 5 and 0.5 slm, respectively. The distance between the CAPJ and DMEM surfaces was 15 mm. **(B)** HaCaT cells were exposed to plasma-activated medium (PAM) that was pretreated with either He-CAPJ or He/Ar-CAPJ for the indicated times. After culturing for 24 h, cell proliferation was analyzed using the MTT assay. These results were presented as the mean ± standard deviation from three independent experiments. Statistical significance was determined using the Student's *t*-test (*$P < 0.05$).

of various Ar gas flow rates with fixed He gas, but not with pure He gas (Lou et al., 2019). These OH and NO radicals are the primary reactive species and relatively short-lived. These species are then converted to secondary and long-lived species (Kaushik et al., 2018). In this study, PAM was first pretreated with CAPJ under various conditions, such as different treatment durations and mixtures of the working gases (He or He/Ar). The major reactive species of $NO_2$- concentrations in each PAM were carefully estimated using Griess reagents (Sigma-Aldrich, St. Louis, MO, United States). The concentrations of $NO_2$ were gradually increased when the treatment time of PAM by He-CAPJ and He/Ar-CAPJ was increased (**Supplementary Figure S1**). The quantities of $NO_2$- obtained in this study are consistent with that reported in literature (Kurake et al., 2016; Uchida et al., 2018). Human keratinocyte-derived cells, i.e., HaCaT cells, were then cultured with PAM for evaluation of cell proliferation, migration, and protein expression to extensively investigate the CAPJ interacting with cells (**Figure 2A**).

## He/Ar-CAPJ Enhances Keratinocyte Proliferation

HaCaT cells were exposed to PAM pretreated with He-CAPJ and He/Ar-CAPJ for different durations (15–90 s). After incubation for an additional 24 h, cell proliferation was analyzed using the MTT assay. As shown in **Figure 2B**, the keratinocyte proliferation is markedly increased when PAM was pretreated by He/Ar-CAPJ for 15 s. However, this trend was not observed in cells cultured with He-CAPJ treated PAM. In contrast, incubation of cells with He-CAPJ or He/Ar-CAPJ treated PAM for 45–90 s resulted in markedly inhibited cell proliferation in a time-dependent manner.

## He/Ar-CAPJ Promotes Keratinocyte Migration

To further explore the impact of CAPJ on keratinocyte migration activity, a wound-healing assay was conducted. As shown in the cell images in **Figure 3A** and the relative wound closure results in **Figure 3B**, the migration activities of HaCaT cells were significantly elevated in PAM pretreated with He-CAPJ for 15 and 30 s but degraded for longer times from 45-90 s as compared to those of the untreated control groups ($P < 0.05$ for 15 s). Noticeably, the He/Ar-CAPJ pretreated group effectively promoted the cell migration as compared to the groups with untreated controls or He-CAPJ pretreatment. These results indicate that He/Ar-CAPJ treatment for shorter period possesses potent activity for promoting keratinocyte migration. According to the above cell proliferation and migration results, PAM pretreated with He/Ar-CAPJ for 15 s at a distance of 15 mm using a gas mixture of He and Ar with gas flow of 5.0 and 0.5 slm, respectively, was selected to perform the subsequent studies.

## He/Ar-CAPJ Activates Cell Proliferation Regulatory Molecules

Since EMT and cell cycle progression were involved in wound healing (Das and Baker, 2016; Haensel and Dai, 2018), we therefore analyzed the effects of CAPJ on the regulators of

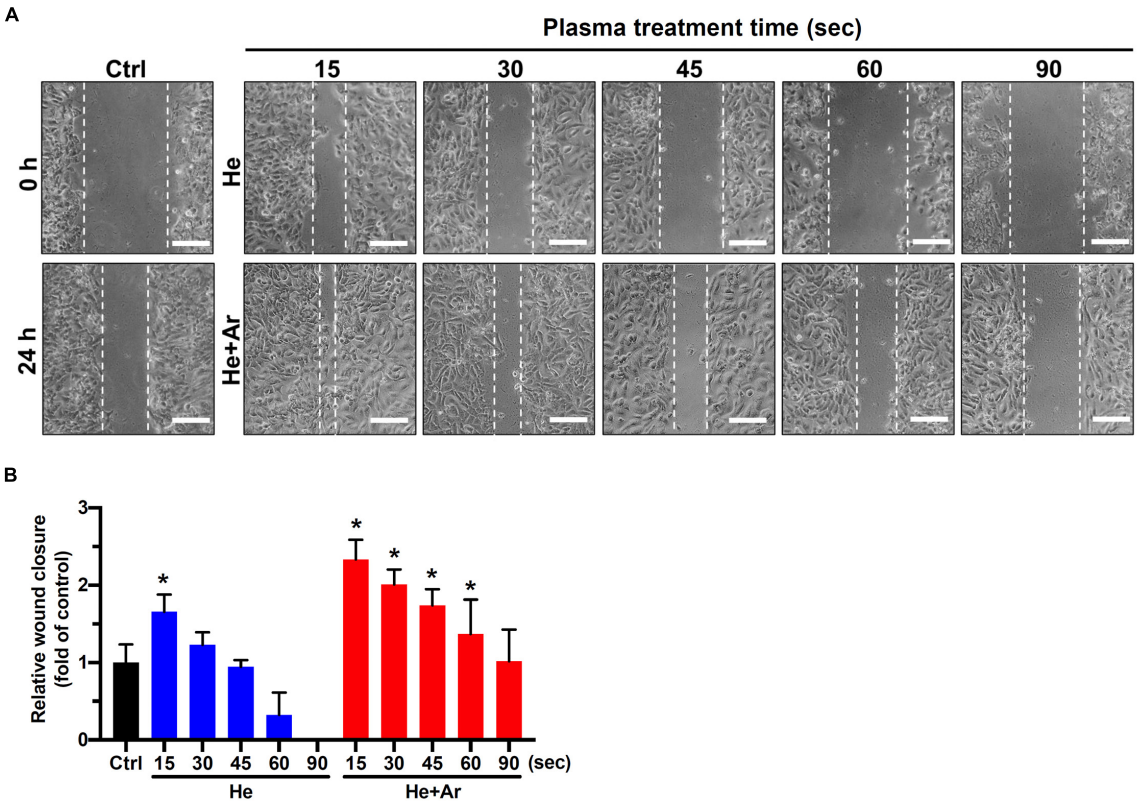


**FIGURE 3 |** CAPJ facilitates human keratinocyte migration. HaCaT cells were treated with PAM that was pretreated with He-CAPJ or He/Ar-CAPJ for the indicated times. The cells were then subjected to a wound healing assay and cultured for 24 h to analyze cell migration activity. **(A)** The images were acquired after scratching for 0 or 24 h. Scale bars, 300 μm. **(B)** Cell migration activity was assessed by determining the relative wound closure, as described in section "Materials and Methods." The data were presented as the mean ± standard deviation of three independent experiments. Statistical significance was determined using the Student's *t*-test. $^*P < 0.05$ when compared to the control group.

EMT and cell cycle. HaCaT cells were exposed to He/Ar-CAPJ treated PAM followed by replacement of complete media and cultured for an additional 24 h, and the expression levels of E-cadherin, N-cadherin, cyclin D1, and Cdk2 were assessed using western blotting. As shown in **Figure 4**, markedly decreased E-cadherin (**Figure 4B**) and increased N-cadherin (**Figure 4C**) were observed in cells incubated with He/Ar-CAPJ treated PAM. Moreover, He/Ar-CAPJ effectively elevated the expression of p-ERK, a cell proliferation molecule (**Figures 4D,G**). The expression level of Ki-67 was increased upon cultured with PAM exposed to He/Ar-CAPJ (**Supplementary Figure S2**). We then determined the key effectors that contributed toward regulating the cell cycle. Our results showed that He/Ar-CAPJ significantly increased the expression levels of cyclin D1 and Cdk2 (**Figures 4E,F**). These results represent that He/Ar-CAPJ promotes keratinocyte proliferation and migration, which were evidenced by a decrease in E-cadherin with concomitant increases in N-cadherin, p-ERK, cyclin D1, and Cdk2.

## He/Ar-CAPJ Facilitates Wound Closure

To further assess the effects of non-thermal plasma on wound closure, we established rat cutaneous wound models. The wound closure for each wound was measured on days 0, 2, 4, 6, 8, 10, and 14 after He-CAPJ and He/Ar-CAPJ treatment for 60 s. Our results showed that the wound area was significantly reduced by the plasma treatment as compared to that of the untreated control group shown in the photographs of the full thickness skin wounds and subsequent wound contraction (**Figure 5A**). Noticeably, a pronounced cutaneous wound contraction was occurred after treated with He/Ar-CAPJ for 8–14 days. Moreover, the effect of He/Ar-CAPJ on wound closure was better than He-CAPJ after treated for 2–8 days as depicted by the quantification of the wound area in **Figure 5B**. For the evaluation of plasma treatment period effect, wound closure was further determined by assessing the wound area treated with He/Ar-CAPJ for 1, 3, and 5 min on the indicated days. As shown in **Figure 6**, rat cutaneous wounds treated with He/Ar-CAPJ for 1 min featured a wound area that was substantially diminished as compared to those of control groups and other treatment periods (3 and 5 min). Skin tissue sections were further prepared for histological analysis. As shown in **Figure 7**, there was a decrease in inflammatory cell infiltration around the wounds that were treated with He/Ar-CAPJ as compared to those untreated control groups. In addition, the presence of granulation and re-epithelialization tissue were markedly increased in wounds treated with He/Ar-CAPJ after day 7 (framed region with

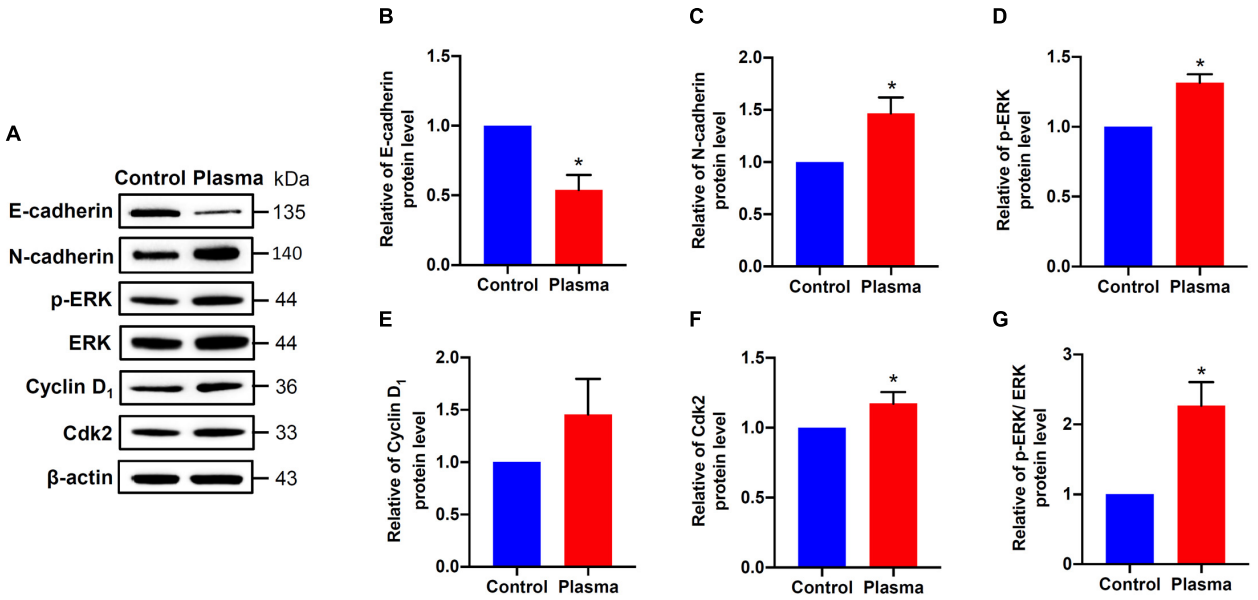


**FIGURE 4 |** CAPJ regulates cell proliferation-related molecules in human keratinocytes. HaCaT cells were treated with PAM that was pretreated with He/Ar-CAPJ for 15 s, followed by incubation for 24 h. **(A)** Cell lysates were prepared to determine protein expression using western blot assay. The expression levels of **(B)** E-cadherin, **(C)** N-cadherin, **(D)** p-ERK, **(E)** cyclin D1, **(F)** Cdk2, and **(G)** ratio of p-ERK to ERK were determined by densitometric analysis and normalized to β-actin. Results are expressed as the mean ± standard deviation derived from three independent experiments. The cells untreated with PAM was set as 1.0. Fold change of each protein expressed in He/Ar-CAPJ treated cells was compared to PAM untreated control group. Statistical significance was determined using the Student's *t*-test. $^*P < 0.05$.

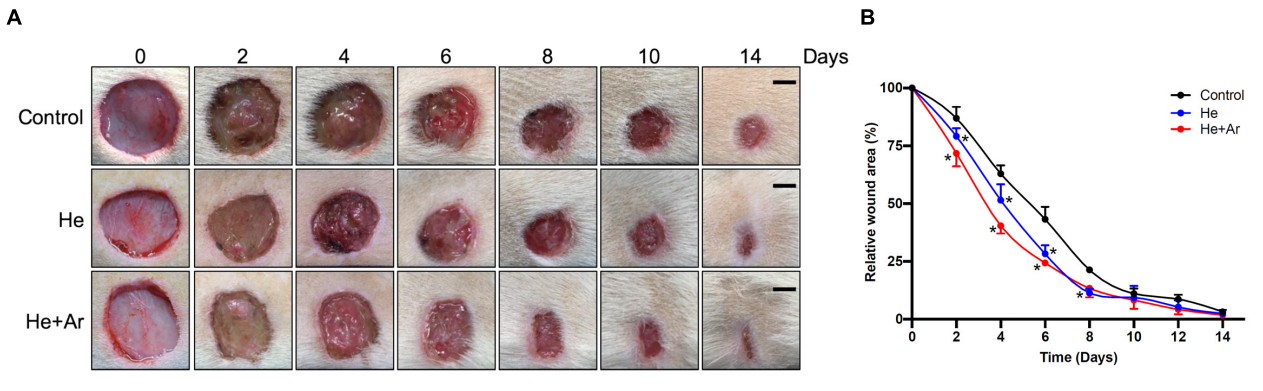


**FIGURE 5 |** Images for skin wounds treated with CAPJ and enhanced cutaneous wound closure rate. Eighteen rats were separated into control ($n = 6$), treatment with He-CAPJ ($n = 6$) or He/Ar-CAPJ ($n = 6$) groups. **(A)** Photographs of cutaneous wound closures, which were untreated (control), treated with He-CAPJ and He/Ar-CAPJ on days 0, 2, 4, 6, 8, 10, and 14 are presented. Scale bars, 5 mm. **(B)** Wound closure rates were quantified on the indicated days. Statistical significance was determined using the Student's *t*-test. $^*P < 0.05$ when compared to control treatment.

magnified image in **Figure 7**). Together, these results illustrate that tissue contraction and re-epithelialization can promote wound closure after He/Ar-CAPJ treatment.

## DISCUSSION

CAPJ, a cold or non-thermal plasma, has been reported to possess various biomedical applications *in vitro* and *in vivo* (Zimmermann et al., 2011; Arndt et al., 2013; Chatraie et al., 2018; Cheng et al., 2018; Gilmore et al., 2018; Guo et al., 2018). The CAPJ has been applied in the plasma medicine by direct and indirect approaches (von Woedtke et al., 2013). The indirect use of CAPJ for generating the PAM has been extensively studied for its potential in real application. Meanwhile, the direct use of CAPJ in the human or animal body has been adopted for evaluating the effects of wound healing and cancer treatment by plasma treatment. We conducted the indirect and direct CAPJ treatments and achieved remarkable results on the *in vitro* and *in vivo* studies, respectively.

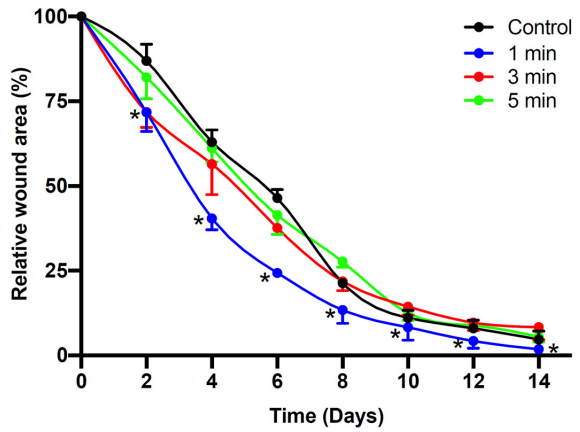


**FIGURE 6 |** Time dependent CAPJ treatment on cutaneous wound closure rate. Cutaneous wounds were untreated (control) or treated with He/Ar-CAPJ for 1, 3, 5 min ($n$ = 6 for each group). Wound closure rates on days 0, 2, 4, 6, 8, 10, 12, and 14 were quantified. Statistical significance was determined using the Student's $t$-test. *$P < 0.05$ when compared to control treatment.

In this study, we demonstrated that the He/Ar-CAPJ effectively enhanced keratinocyte proliferation and promoted wound closure with carefully controlled treatment duration. The most significant induction in cell proliferation was noted by He/Ar-CAPJ under a voltage of 6.5 kV and exposure for 15 s. Following the He/Ar-CAPJ treatment, we demonstrated signaling pathways that led to elevated levels of cell proliferation and cell cycle progression. The animal studies further showed that the He/Ar-CAPJ therapy to be responsible for accelerating cutaneous tissue repair in rat cutaneous wounds. In our current study, using cell-based and animal studies, we revealed the mechanism activated by the He/Ar-CAPJ treatment, namely, cell proliferation-regulating molecules, which in turn facilitated cell growth and wound healing.

The treatment effects of CAPJ for biomedical applications depend on key species formation and the abundance of RONS, which have rendered CAPJ treatment relevant to a broad range of research outcomes from cancer cell eradication to wound-healing promotion. In this study, based on the direct and indirect applications of CAPJ to SD rats and HaCaT cells, respectively, RONS and appropriate doses of CAPJ treatment can be adjusted by changing the CAPJ working gas composition and treatment durations (Lou et al., 2019).

NO, which was awarded as the Molecule of the Year in 1992 by the American Association for the Advancement of Science, is a specific molecule that acts as a biological messenger in the body, relaying information from the nerves to cells (Culotta and Koshland, 1992). Endogenous NO in terms of health acts as a functional cell regulator and messenger, and this activity is well-known. Notably, the amount of NO at low concentrations is beneficial, however, high levels of NO cause harmful effects on human health (Pacher et al., 2007). In addition, the production of NO and ROS functions as a potent defense against bacterial pathogens by decomposing macromolecules, including DNA and proteins (Hosseinzadeh Colagar et al., 2013). We previously reported that mixed He/Ar-generated CAPJ produces nitrogen and oxygen species, which leads to the destruction of the bacterial cell wall and damages double-stranded DNA to gain bactericidal activity (Lou et al., 2019). Decreasing bacterial loads of skin lesions attenuates inflammatory response and promotes tissue repair, thereby enhancing wound closure (Yu et al., 2011). Our present study showed that He/Ar-CAPJ with a proper cell treatment duration effectively activated cell proliferation, which in turn induced wound healing. These results combined with previous findings have elucidated the mechanism of the He/Ar-CAPJ is not only acting through antiseptic activity but also promoting tissue repair and in turn improving wound healing.

Our recent study has revealed that the He/Ar-CAPJ plasma can generate higher intensities of reactive oxygen species (ROS), including OH and NO radicals, nitrogen, and oxygen species (Lou et al., 2019). It has been reported that treatment of cells with low-temperature plasma can increase the production of ROS, activation of NF-κB, and protein expression cyclin D1, which promoted the cell cycle progression in responses to cell proliferation in wound healing (Liu et al., 2017; Shi et al., 2018). In addition, activation of ERK and p38 MAPK,

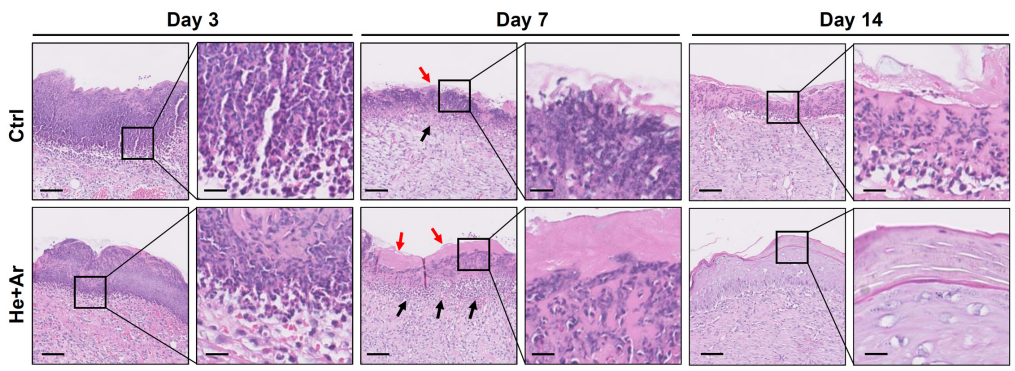


**FIGURE 7 |** Histological analysis of wound healing with 60 s He/Ar-CAPJ treatment. Wound tissue sections were prepared on days 3, 7, and 14, and subjected to hematoxylin-eosin (HandE) staining. Black arrows indicate the formation of granulation tissues and red arrows show the epidermis. The magnified images are shown in the right panel of each cropped area. Scale bars in original and magnified images are 80 and 400 μm, respectively.

which are responsible for the distinct activation of transcription factors NF-κB, can further enhance the skin wound closure in mice (Yun et al., 2014). In this study, we investigated the molecular mechanism through which the He/Ar-CAPJ induces keratinocyte migration, which is a key step in cutaneous wound healing (Usui et al., 2008). Our data showed that He/Ar-CAPJ with a proper time duration treatment elicits both the proliferation and migration of keratinocytes. These findings are supported by evidence that a reduction in the epithelial marker molecule, E-cadherin, leads to EMT activation (Gonzalez and Medici, 2014). Downregulation of E-cadherin enhances wound re-epithelialization (Terao et al., 2011), which is crucial for promoting epidermal cell migration and tissue repair (Haensel and Dai, 2018). The expression levels of cyclin D1 and Cdk2 are increased and drive the G1/S phase transition of the cell cycle, thereby enforcing cell proliferation (Lee et al., 2014). In addition, the activation of the ERK family, which is involved in the MAPK pathways, plays a pivotal role in the regulation of cell proliferation (Escuin-Ordinas et al., 2016). In consistent with our previous findings, our current results indicate that the He/Ar-CAPJ generates high intensities of reactive nitrogen and oxygen species for reducing E-cadherin and triggering p-ERK, cyclin D1, and Cdk2 expression, which are crucial factors for EMT and cell proliferation, resulting in the acceleration of cutaneous wound healing (**Figure 8**).

Since our animal model did not add the ring fixtures to restrict the surrounding of wound edge during the healing process (**Figure 5**), muscular contraction was occurred to enhance wound healing *in vivo*. In the treatment of CAPJ focusing in the central zone of the wound, the residual plasma gas may diffuse and influence on the margin of the wound edge, thereby inducing keratinocyte migration as well. In addition, the histological examination showed that keratinocyte migration could be activated to improve the wound healing by diminishing the wound size (**Figure 7**, day 14, He + Ar treatment group), which was consistently with previous studies (Lee et al., 2018; Zhang et al., 2019). Taken together, the *in vitro* study showing the keratinocyte activation can be histologically observed in the *in vivo* study and accompanying with muscular contraction that provide evidence for the underlying mechanisms of CAPJ to promote wound healing.

Full-thickness wounds destroy the dermis, which were healed by re-epithelialization and the formation of granulation tissue for filling the void of the wound before epithelial covering (Rittie, 2016). The re-epithelialization reaction then reaches its full significance, as a larger surface needs to be covered with new keratinocytes. In the present study, we used HaCaT cells as an *in vitro* assay platform, which is a long-lived, spontaneously immortalized human keratinocyte line (Carretero et al., 2008). Notably, HaCaT line exhibits basal cell properties and serves as a suitable model to follow the cell migration and release of inflammatory cytokines (Colombo et al., 2017). Our results found that plasma induction in HaCaT keratinocytes contributed to the signaling events and led to the activation of cell migration and proliferation. In addition to the *in vitro* data, we provided *in vivo* evidence, through plasma administration to excisional wounds in rates, showing improved wound healing by increasing the re-epithelialization and granulation tissue formation. Owing to the importance of keratinocyte migration substrates in re-epithelialization and muscular contraction, these findings combined the *in vitro* and *in vivo* studies provided more explicit mechanisms for the plasma that promoted the wound healing.

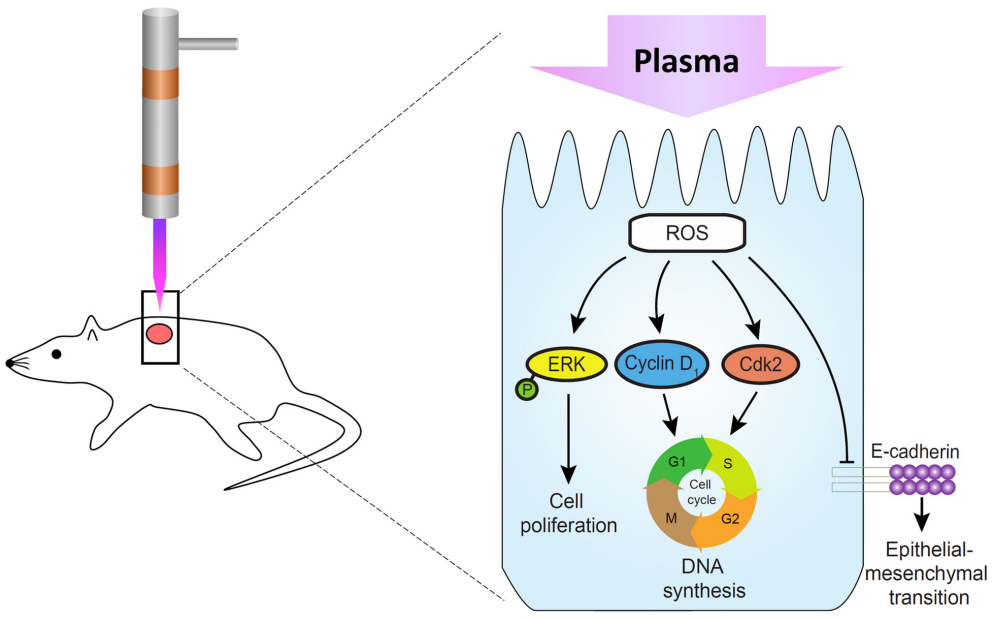


**FIGURE 8 |** Molecular mechanism underlying the promotion of skin wound healing by CAPJ. He/Ar-CAPJ inhibits E-cadherin and activates cyclin D1, Cdk2, and p-ERK, which induce EMT and cell cycle progression, leading to cell proliferation and enhanced wound closure.

Our animal studies revealed that He/Ar-CAPJ treatment induces wound contraction on day 2, which is an initial step in the early phase of the cutaneous healing process (Reinke and Sorg, 2012). Further, there was a significant reduction in the wound area and obvious skin contraction in rats treated with He/Ar-CAPJ for 1 min as compared to that of the untreated control group on days 2–8. Histological analysis showed increased granulation tissue formation and re-epithelization, and mitigated inflammation after He/Ar-CAPJ treatment. These results are consistent with recent studies performed using plasma generated from Ar, He, and other gases (Shao et al., 2016; Kubinova et al., 2017; Schmidt et al., 2017).

## CONCLUSION

Our results demonstrate that the He/Ar-CAPJ with appropriate treatment duration enhanced skin tissue repair most likely by accelerating the cell cycle and activating cell proliferation pathways. The present study is the first to provide evidence that He/Ar-CAPJ generated reactive species possess bactericidal activity, increase granulation tissue formation, and alleviate inflammatory response, leading to enhanced cutaneous wound closure. Our observations revealed that the level of the ROS is very critical for wound healing, which is beneficial at low ROS concentrations yet harmful at high levels. This study provides insights into the mechanisms through which He/Ar-CAPJ enhances cell proliferation to repair skin lesions, suggesting the possibility of He/Ar-CAPJ therapy as a potent treatment for promoting wound healing.

## DATA AVAILABILITY STATEMENT

The datasets generated for this study are available on request to the corresponding author.

## ETHICS STATEMENT

The animal study was reviewed and approved by the Institutional Animal Care Use Committee (Approval No. CGU105-032), Chang Gung University, Taiwan.

## AUTHOR CONTRIBUTIONS

B-SL, J-HH, C-HL, and J-WL: conception or design of this work. C-MC, C-WH, H-YW, and P-YC: experimental study and data analysis and interpretation. B-SL, J-HH, C-HL, and J-WL: writing the manuscript. All authors contributed to the article and approved the submitted version.

## FUNDING

This work was supported by the Ministry of Science and Technology (105-2313-B-182-001, 106-2218-E-131-003, 106-2320-B-182-012-MY3, 107-2218-E-131-001, and 108-2221-E-182-030), the Chang Gung Memorial Hospital (CMRPD5H0032, CMRPD1I0061-3, CMRPD1J0021-3, BMRP280, and BMRPE90), and the Tomorrow Medical Foundation.

## ACKNOWLEDGMENTS

We would like to thank the editor and reviewers for the editorial assistance and their valuable comments. We sincerely appreciate the assistance for analyzing microscopy (Microscopy Center, Chang Gung University).

## SUPPLEMENTARY MATERIAL

The Supplementary Material for this article can be found online at: https://www.frontiersin.org/articles/10.3389/fbioe.2020.00683/full#supplementary-material

**FIGURE S1 |** Concentrations of $NO_2^-$ in the PAM versus the treatment time of He-CAPJ and He/Ar-CAPJ. These data were measured using Criess reagents and expressed as the mean ± standard deviation determined from three independent experiments.

**FIGURE S2 |** He/Ar-CAPJ increases Ki-67 expression in human keratinocytes. HaCaT cells were cultured with PAM treated with He/Ar-CAPJ for 15 s, followed by incubation for 24 h. Cell lysates were prepared to determine the protein expression levels of Ki-67 and caspase 3 by using western blot assay. β-actin expression was used as the loading control.

**FIGURE S3 |** Original western blots for **Figure 4A**. Representative western blot results from three independent experiments are shown.

## REFERENCES

Arndt, S., Unger, P., Wacker, E., Shimizu, T., Heinlin, J., Li, Y. F., et al. (2013). Cold atmospheric plasma (CAP) changes gene expression of key molecules of the wound healing machinery and improves wound healing *in vitro* and *in vivo*. *PLoS One* 8:e79325. doi: 10.1371/journal.pone.0079325

Brehmer, F., Haenssle, H. A., Daeschlein, G., Ahmed, R., Pfeiffer, S., Gorlitz, A., et al. (2015). Alleviation of chronic venous leg ulcers with a hand-held dielectric barrier discharge plasma generator (PlasmaDerm((R)) VU-2010): results of a monocentric, two-armed, open, prospective, randomized and controlled trial (NCT01415622). *J. Eur. Acad. Dermatol. Venereol.* 29, 148–155. doi: 10.1111/jdv.12490

Carretero, M., Escamez, M. J., Garcia, M., Duarte, B., Holguin, A., Retamosa, L., et al. (2008). *In vitro* and *in vivo* wound healing-promoting activities of human cathelicidin LL-37. *J. Invest. Dermatol.* 128, 223–236. doi: 10.1038/sj.jid.5701043

Chatraie, M., Torkaman, G., Khani, M., Salehi, H., and Shokri, B. (2018). *In vivo* study of non-invasive effects of non-thermal plasma in pressure ulcer treatment. *Sci Rep.* 8:5621. doi: 10.1038/s41598-018-24049-z

Chen, Y. A., Lien, H. M., Kao, M. C., Lo, U. G., Lin, L. C., Lin, C. J., et al. (2017). Sensitization of radioresistant prostate cancer cells by resveratrol isolated from *Arachis hypogaea* stems. *PLoS One* 12:e0169204. doi: 10.1371/journal.pone.0169204

Chen, Y. A., Tzeng, D. T. W., Huang, Y. P., Lin, C. J., Lo, U. G., Wu, C. L., et al. (2018). Antrocin sensitizes prostate cancer cells to radiotherapy through inhibiting PI3K/AKT and MAPK signaling pathways. *Cancers* 11:34. doi: 10.3390/cancers11010034

Cheng, K. Y., Lin, Z. H., Cheng, Y. P., Chiu, H. Y., Yeh, N. L., Wu, T. K., et al. (2018). Wound healing in streptozotocin-induced diabetic rats using atmospheric-pressure argon plasma jet. *Sci. Rep*. 8:12214. doi: 10.1038/s41598-018-30597-1

Colombo, I., Sangiovanni, E., Maggio, R., Mattozzi, C., Zava, S., Corbett, Y., et al. (2017). HaCaT cells as a reliable in vitro differentiation model to dissect the inflammatory/repair response of human keratinocytes. *Med. Inflamm.* 2017:7435621. doi: 10.1155/2017/7435621

Culotta, E., and Koshland, D. E. Jr. (1992). NO news is good news. *Science* 258, 1862–1865. doi: 10.1126/science.1361684

Daeschlein, G., Napp, M., Lutze, S., Arnold, A., von Podewils, S., Guembel, D., et al. (2015). Skin and wound decontamination of multidrug-resistant bacteria by cold atmospheric plasma coagulation. *J. Dtsch. Dermatol. Ges.* 13, 143–150. doi: 10.1111/ddg.12559

Das, S., and Baker, A. B. (2016). Biomaterials and nanotherapeutics for enhancing skin wound healing. *Front. Bioeng. Biotechnol.* 4:82. doi: 10.3389/fbioe.2016.00082

Dunnill, C., Patton, T., Brennan, J., Barrett, J., Dryden, M., Cooke, J., et al. (2017). Reactive oxygen species (ROS) and wound healing: the functional role of ROS and emerging ROS-modulating technologies for augmentation of the healing process. *Int. Wound J.* 14, 89–96. doi: 10.1111/iwj.12557

Ehlbeck, J., Brandenburg, R., von Woedtke, T., Krohmann, U., Stieber, M., and Weltmann, K. D. (2008). PLASMOSE - antimicrobial effects of modular atmospheric plasma sources. *GMS Krankenhhyg Interdiszip.* 3:Doc14.

Escuin-Ordinas, H., Li, S., Xie, M. W., Sun, L., Hugo, W., Huang, R. R., et al. (2016). Cutaneous wound healing through paradoxical MAPK activation by BRAF inhibitors. *Nat. Commun.* 7:12348. doi: 10.1038/ncomms12348

Gilmore, B. F., Flynn, P. B., O'Brien, S., Hickok, N., Freeman, T., and Bourke, P. (2018). Cold Plasmas for biofilm control: opportunities and challenges. *Trends Biotechnol.* 36, 627–638. doi: 10.1016/j.tibtech.2018.03.007

Gonzalez, D. M., and Medici, D. (2014). Signaling mechanisms of the epithelial-mesenchymal transition. *Sci. Signal.* 7:re8. doi: 10.1126/scisignal.2005189

Guo, L., Xu, R., Gou, L., Liu, Z., Zhao, Y., Liu, D., et al. (2018). Mechanism of virus inactivation by cold atmospheric-pressure plasma and plasma-activated water. *Appl. Environ. Microbiol.* 84:e00726-18. doi: 10.1128/AEM.00726-18

Haensel, D., and Dai, X. (2018). Epithelial-to-mesenchymal transition in cutaneous wound healing: where we are and where we are heading. *Dev. Dyn.* 247, 473–480. doi: 10.1002/dvdy.24561

Hosseinzadeh Colagar, A., Memariani, H., Sohbatzadeh, F., and Valinataj Omran, A. (2013). Nonthermal atmospheric argon plasma jet effects on *Escherichia coli* biomacromolecules. *Appl. Biochem. Biotechnol.* 171, 1617–1629. doi: 10.1007/s12010-013-0430-9

Isbary, G., Morfill, G., Schmidt, H. U., Georgi, M., Ramrath, K., Heinlin, J., et al. (2010). A first prospective randomized controlled trial to decrease bacterial load using cold atmospheric argon plasma on chronic wounds in patients. *Br. J. Dermatol.* 163, 78–82. doi: 10.1111/j.1365-2133.2010.09744.x

Isbary, G., Shimizu, T., Li, Y. F., Stolz, W., Thomas, H. M., Morfill, G. E., et al. (2013). Cold atmospheric plasma devices for medical issues. *Expert. Rev. Med. Devices* 10, 367–377. doi: 10.1586/erd.13.4

Kaushik, N. K., Ghimire, B., Li, Y., Adhikari, M., Veerana, M., Kaushik, N., et al. (2018). Biological and medical applications of plasma-activated media, water and solutions. *Biol Chem*. 400, 39–62. doi: 10.1515/hsz-2018-0226

Kubinova, S., Zaviskova, K., Uherkova, L., Zablotskii, V., Churpita, O., Lunov, O., et al. (2017). Non-thermal air plasma promotes the healing of acute skin wounds in rats. *Sci. Rep.* 7:45183. doi: 10.1038/srep45183

Kurake, N., Tanaka, H., Ishikawa, K., Kondo, T., Sekine, M., Nakamura, K., et al. (2016). Cell survival of glioblastoma grown in medium containing hydrogen peroxide and/or nitrite, or in plasma-activated medium. *Arch. Biochem. Biophys*. 605, 102–108. doi: 10.1016/j.abb.2016.01.011

Lee, D. H., Choi, K. H., Cho, J. W., Kim, S. Y., Kwon, T. R., Choi, S. Y., et al. (2014). Recombinant growth factor mixtures induce cell cycle progression and the upregulation of type I collagen in human skin fibroblasts, resulting in the acceleration of wound healing processes. *Int. J. Mol. Med.* 33, 1147–1152. doi: 10.3892/ijmm.2014.1698

Lee, S., Kim, M. S., Jung, S. J., Kim, D., Park, H. J., and Cho, D. (2018). ERK activating peptide, AES16-2M promotes wound healing through accelerating migration of keratinocytes. *Sci. Rep*. 8:14398. doi: 10.1038/s41598-018-32851-y

Lin, H. J., Jiang, Z. P., Lo, H. R., Feng, C. L., Chen, C. J., Yang, C. Y., et al. (2019). Coalescence of RAGE in lipid rafts in response to cytolethal distending toxin-induced inflammation. *Front. Immunol.* 10:109. doi: 10.3389/fimmu.2019.00109

Liu, J. R., Xu, G. M., Shi, X. M., and Zhang, G. J. (2017). Low temperature plasma promoting fibroblast proliferation by activating the NF-κB pathway and increasing cyclinD1 expression. *Sci. Rep*. 7:11698. doi: 10.1038/s41598-017-12043-w

Lou, B. S., Lai, C. H., Chu, T. P., Hsieh, J. H., Chen, C. M., Su, Y. M., et al. (2019). Parameters affecting the antimicrobial properties of cold atmospheric plasma jet. *J. Clin. Med.* 8:930. doi: 10.3390/jcm8111930

Mai-Prochnow, A., Murphy, A. B., McLean, K. M., Kong, M. G., and Ostrikov, K. K. (2014). Atmospheric pressure plasmas: infection control and bacterial responses. *Int. J. Antimicrob. Agents* 43, 508–517. doi: 10.1016/j.ijantimicag.2014.01.025

Ngo, M. H. T., Liao, J. D., Shao, P. L., Weng, C. C., and Chang, C. Y. (2014). Increased fibroblast cell proliferation and migration using atmospheric N-2/Ar micro-plasma for the stimulated release of fibroblast growth factor-7. *Plasma Proc. Poly.* 11, 80–88. doi: 10.1002/ppap.201300098

Pacher, P., Beckman, J. S., and Liaudet, L. (2007). Nitric oxide and peroxynitrite in health and disease. *Physiol. Rev.* 87, 315–424. doi: 10.1152/physrev.00029.2006

Reinke, J. M., and Sorg, H. (2012). Wound repair and regeneration. *Eur. Surg. Res.* 49, 35–43. doi: 10.1159/000339613

Rittie, L. (2016). Cellular mechanisms of skin repair in humans and other mammals. *J. Cell Commun. Signal.* 10, 103–120. doi: 10.1007/s12079-016-0330-1

Romaldini, A., Mastrogiacomo, M., Cancedda, R., and Descalzi, F. (2018). Platelet lysate activates human subcutaneous adipose tissue cells by promoting cell proliferation and their paracrine activity toward epidermal keratinocytes. *Front. Bioeng. Biotechnol.* 6:203. doi: 10.3389/fbioe.2018.00203

Schmidt, A., Bekeschus, S., Wende, K., Vollmar, B., and von Woedtke, T. (2017). A cold plasma jet accelerates wound healing in a murine model of full-thickness skin wounds. *Exp. Dermatol.* 26, 156–162. doi: 10.1111/exd.13156

Shao, P. L., Liao, J. D., Wong, T. W., Wang, Y. C., Leu, S., and Yip, H. K. (2016). Enhancement of wound healing by non-thermal N2/Ar micro-plasma exposure in mice with fractional-co2-laser-induced wounds. *PLoS One* 11:e0156699. doi: 10.1371/journal.pone.0156699

Shi, X. M., Xu, G. M., Zhang, G. J., Liu, J. R., Wu, Y. M., Gao, L. G., et al. (2018). Low-temperature plasma promotes fibroblast proliferation in wound healing by ROS-activated NF-κB signaling pathway. *Curr. Med. Sci*. 38, 107–114. doi: 10.1007/s11596-018-1853-x

Terao, M., Ishikawa, A., Nakahara, S., Kimura, A., Kato, A., Moriwaki, K., et al. (2011). Enhanced epithelial-mesenchymal transition-like phenotype in N-acetylglucosaminyltransferase V transgenic mouse skin promotes wound healing. *J. Biol. Chem.* 286, 28303–28311. doi: 10.1074/jbc.M111.220376

Uchida, G., Ito, T., Ikeda, J. I., Suzuki, T., Takenaka, K., and Setsuhara, Y. (2018). Effect of a plasma-activated medium produced by direct irradiation on cancer cell killing. *Jpn. J. App. Phys*. 57:096201. doi: 10.7567/JJAP.57.096201

Usui, M. L., Mansbridge, J. N., Carter, W. G., Fujita, M., and Olerud, J. E. (2008). Keratinocyte migration, proliferation, and differentiation in chronic ulcers from patients with diabetes and normal wounds. *J. Histochem. Cytochem.* 56, 687–696. doi: 10.1369/jhc.2008.951194

von Woedtke, T., Reuter, S., Masur, K., and Weltmann, K. D. (2013). Plasmas for medicine. *Phys. Rep. Rev. Sect. Phys. Lett.* 530, 291–320.

Weltmann, K. D., and von Woedtke, T. (2017). Plasma medicine-current state of research and medical application. *Plasma Phys. Control. Fusion* 59:14031. doi: 10.1088/0741-3335/59/1/014031

Yu, Y., Tan, M., Chen, H., Wu, Z., Xu, L., Li, J., et al. (2011). Non-thermal plasma suppresses bacterial colonization on skin wound and promotes wound healing in mice. *J. Huazhong. Univ. Sci. Technol. Med. Sci.* 31, 390–394. doi: 10.1007/s11596-011-0387-2

Yun, S. P., Lee, S. J., Oh, S. Y., Jung, Y. H., Ryu, J. M., Suh, H. N., et al. (2014). Reactive oxygen species induce MMP 12-dependent degradation of collagen 5 and fibronectin to promote the motility of human umbilical cord-derived mesenchymal stem cells. *Br. J. Pharmacol.* 171, 3283–3297. doi: 10.1111/bph.12681

Zhang, J. P., Guo, L., Chen, Q. L., Zhang, K. Y., Wang, T., An, G. Z., et al. (2019). Effects and mechanisms of cold atmospheric plasma on skin wound healing of rats. *Contrib. Plasma Phys.* 59, 92–101. doi: 10.1002/ctpp.201800025

Zimmermann, J. L., Dumler, K., Shimizu, T., Morfill, G. E., Wolf, A., Boxhammer, V., et al. (2011). Effects of cold atmospheric plasmas on adenoviruses in solution. *J. Phys. D Appl. Phys.* 44:5201. doi: 10.1088/0022-3727/44/50/505201

**Conflict of Interest:** The authors declare that the research was conducted in the absence of any commercial or financial relationships that could be construed as a potential conflict of interest.

frontiers in Bioengineering and Biotechnology

REVIEW
published: 30 June 2020
doi: 10.3389/fbioe.2020.00665

# Modulating Alginate Hydrogels for Improved Biological Performance as Cellular 3D Microenvironments

*Mariana Isabel Neves*[1,2,3], *Lorenzo Moroni*[4,5] *and Cristina Carvalho Barrias*[1,2,6*]

[1] i3S - Instituto de Investigação e Inovação em Saúde, Universidade do Porto, Porto, Portugal, [2] INEB – Instituto de Engenharia Biomédica, Universidade do Porto, Porto, Portugal, [3] FEUP - Faculdade de Engenharia da Universidade do Porto, Porto, Portugal, [4] MERLN Institute for Technology-Inspired Regenerative Medicine, Maastricht University, Maastricht, Netherlands, [5] CNR NANOTEC - Institute of Nanotechnology, Università del Salento, Lecce, Italy, [6] ICBAS - Instituto de Ciências Biomédicas Abel Salazar, Universidade do Porto, Porto, Portugal

The rational choice and design of biomaterials for biomedical applications is crucial for successful *in vitro* and *in vivo* strategies, ultimately dictating their performance and potential clinical applications. Alginate, a marine-derived polysaccharide obtained from seaweeds, is one of the most widely used polymers in the biomedical field, particularly to build three dimensional (3D) systems for *in vitro* culture and *in vivo* delivery of cells. Despite their biocompatibility, alginate hydrogels often require modifications to improve their biological activity, namely via inclusion of mammalian cell-interactive domains and fine-tuning of mechanical properties. These modifications enable the addition of new features for greater versatility and control over alginate-based systems, extending the plethora of applications and procedures where they can be used. Additionally, hybrid systems based on alginate combination with other components can also be explored to improve the mimicry of extracellular microenvironments and their dynamics. This review provides an overview on alginate properties and current clinical applications, along with different strategies that have been reported to improve alginate hydrogels performance as 3D matrices and 4D dynamic systems.

**Keywords: alginate, biomaterial, biofunctionalization, 3D cell culture, 4D systems**

OPEN ACCESS

***Edited by:***
*Hae-Won Kim,*
*Institute of Tissue Regeneration Engineering (ITREN), South Korea*

***Reviewed by:***
*Feng-Huei Lin,*
*National Taiwan University, Taiwan*
*Jung-Hwan Lee,*
*Institute of Tissue Regeneration Engineering (ITREN), South Korea*

***Correspondence:**
*Cristina Carvalho Barrias*
*ccbarrias@ineb.up.pt*

***Specialty section:***
*This article was submitted to Biomaterials, a section of the journal Frontiers in Bioengineering and Biotechnology*

***Received:*** *22 February 2020*
***Accepted:*** *28 May 2020*
***Published:*** *30 June 2020*

***Citation:***
*Neves MI, Moroni L and Barrias CC (2020) Modulating Alginate Hydrogels for Improved Biological Performance as Cellular 3D Microenvironments. Front. Bioeng. Biotechnol. 8:665. doi: 10.3389/fbioe.2020.00665*

## INTRODUCTION

Alginate is a natural, marine-derived polysaccharide widely used in the food industry and, more recently, in the biomedical field. In food industry, alginate is used as thickener, texturizer, and stabilizer. More recently, alginate has also been explored for the development of "functional" food (Qin et al., 2018; Bambace et al., 2019), to improve delivery of bioactive compounds (Lupo et al., 2015), as additive of foods and beverages to increase satiety, modulating appetite, glycemia or insulinemia (El Khoury et al., 2014), and in the development of edible food coatings and films (Bambace et al., 2019; Reyes-Avalos et al., 2019) for food packaging applications (Senturk Parreidt et al., 2018).

In biomedical applications, alginate and their hydrogels have been explored, either alone or in combination with other materials, mainly in drug delivery (Nair et al., 2014; Garcia-Astrain and Averous, 2018; Rossi et al., 2018; Shtenberg et al., 2018), tissue regeneration and wound healing (Bidarra et al., 2014; Liu Q. et al., 2017; Luo Z. et al., 2018; Zeyang et al., 2018; Campiglio et al., 2020), three dimensional (3D)-printing (Liu H. et al., 2017; Luo Y. et al., 2018; Wang et al., 2018)

and *in vitro* modeling (Cavo et al., 2018; Chu et al., 2018). For tissue engineering, in particular, alginate-based biomaterials have been applied in the repair of both soft and hard tissues, including skin (Han et al., 2017), heart (Sapir et al., 2011; Hayoun-Neeman et al., 2019), bone (Maia et al., 2014a,c), cartilage (Lee H. P. et al., 2017; Liao et al., 2017; Jin and Kim, 2018) and vascular tissue (Bidarra et al., 2011; Torres et al., 2018, 2020), among others. In these fields, chemical modification of polymer-based biomaterials is a frequently used strategy to improve not only their structural and mechanical properties but also their biological activity. Despite being biocompatible, alginate promotes very low protein adsorption due to its high hydrophilicity, being therefore considered a non-fouling material (Morra and Cassineli, 1999). This high hydrophilicity, along with the absence of cell-interactive domains, make alginate hydrogels a non-adhesive biomaterial, as cells cannot establish specific attachment points with the polymer itself. Still, instead of disadvantageous, this characteristic can be useful in biomaterials design, as non-modified alginate can play the role of a blank slate, and be chemically modified to promote specific biological responses in a highly controlled way (Lee and Mooney, 2012).

This review focuses on the use of alginate to develop biomaterials, with emphasis in its application and design to create cellular 3D microenvironments with improved biological performance. First, a brief description on alginate structure and properties will be given followed by examples of alginate-based applications in clinics. Then, alginate modifications for developing hydrogel-based 3D matrices with modulated biochemical and mechanical properties will be explored, including strategies for creating stimuli responsive dynamic systems, also referred to as 4D systems.

## OVERVIEW OF ALGINATE AS BIOMATERIAL

### Composition, Structural Properties, and Gel-Forming Ability

Alginate is an anionic polysaccharide present in the cell wall of different species of brown algae. Its linear chains contain repeating monomeric units of α-L-guluronic acid (G) blocks and 1,4-linked β-D-mannuronic acid (M) epimers, bearing free functional hydroxyl (OH) and carboxyl (COOH) groups (**Figure 1**). The relative amount of these monomers (M/G ratio) and their arrangement, either as homopolymeric (GG or MM) or heteropolymeric (GM) blocks, as well as the molecular weight of polymer chains, are highly dependent on the alginate source, regional and seasonal conditions and extraction processes (Haug and Larsen, 1966; Borazjani et al., 2017; Rhein-Knudsen et al., 2017).

Regarding biomedical applications, one attractive characteristic of alginate is its ability to interact with divalent cations (e.g., $Ca^{2+}$), producing hydrogels (polymeric 3D meshes capable of retaining large levels of water) under mild, biocompatible conditions. In this process, alginate undergoes ionic gelation as a result of interactions between divalent cations and alginate free carboxylate ($COO^-$) groups, particularly, but not exclusively, those present in G blocks. This ionic gelation process has been previously described by the "egg-box" model (Grant et al., 1973; Braccini et al., 1999; Braccini and Perez, 2001).

Besides $Ca^{2+}$, other divalent cations such as $Ba^{2+}$, $Mn^{2+}$, $Sr^{2+}$, $Zn^{2+}$, and $Mg^{2+}$ may also trigger alginate crosslinking, but with differing affinities (Topuz et al., 2012; Harper et al., 2014). Particularly, $Ba^{2+}$ and $Sr^{2+}$ present higher affinity toward alginate than $Ca^{2+}$ (Kohn, 1975; Siew et al., 2005; Harper et al., 2014). Additionally, trivalent cations of iron ($Fe^{3+}$) are also described to be able to ionically interact with alginate (Sreeram et al., 2004), presenting more affinity than their divalent counterparts ($Fe^{2+}$).

Alginate intrinsic features differently affect the ionic crosslinking process. For instance, ionic interactions with cations is greatly dependent on alginate block composition. Morch et al. (2006) reported distinct cation G/M-dependent binding affinity using alginate microbeads. The authors employed polyuronates to mimic the G, M, and GM blocks of alginate, and studied gelation upon exposure to $Ca^{2+}$, $Ba^{2+}$, or $Sr^{2+}$ (Morch et al., 2006). Whereas $Ca^{2+}$ was able to coordinate with GG and MG sequences, the same was not observed for MM sequences (Morch et al., 2006). On the other hand, $Ba^{2+}$ was able to interact mainly with GG or MM sequences but not with MG sequences (Morch et al., 2006). Finally, $Sr^{2+}$ was able to mainly interact with GG sequences, minimally with MG sequences and not with MM sequences (Morch et al., 2006).

Also, while alginate molecular weight can affect the viscosity and gelation kinetics of alginate solutions, the type, amount and length of G/M block affects the gelation process itself (Braccini et al., 1999; Braccini and Perez, 2001; Fernández Farrés and Norton, 2014; Jensen et al., 2015). In fact, a minimum number of consecutive G blocks is proposed to be required for a junction of the "egg-box" to form (Stokke et al., 1991). The fraction of heteropolymeric (GM) or homopolymeric (GG or MM) regions in alginate also affects gel strength. Alginates with high fraction of heteropolymeric regions produce gels with lower mechanical strength than alginates with high fraction of homopolymeric regions (Draget et al., 1994), which stabilize intermolecular bonds. This can be partially perceived by the structural implications of G and M stereoisomers block content in alginate chains, as schematically represented in **Figure 1**, where heteropolymeric regions are shown to sterically hinder the packing of adjacent chains and, thus, the formation of junction zones.

These processes can also be affected by external factors. For example, the presence of $Na^+$ can affect the viscosity and gelation of alginate solutions and the mechanical properties of ionic hydrogels. Harper et al. (2014) observed that NaCl increases the viscosity of alginate solutions most likely due to increased interpolymer interactions via charge shielding. Additionally, the authors observed a significant decrease in the tensile strength, force to puncture and work to puncture of alginate hydrogel films formed with $Ca^{2+}$, $Ba^{2+}$, $Sr^{2+}$, $Zn^{2+}$ in the presence of NaCl, as compared to films in the absence of NaCl (Harper et al., 2014). These may result from $Na^+$ competition with the divalent cations, disrupting some junction zones and producing weaker

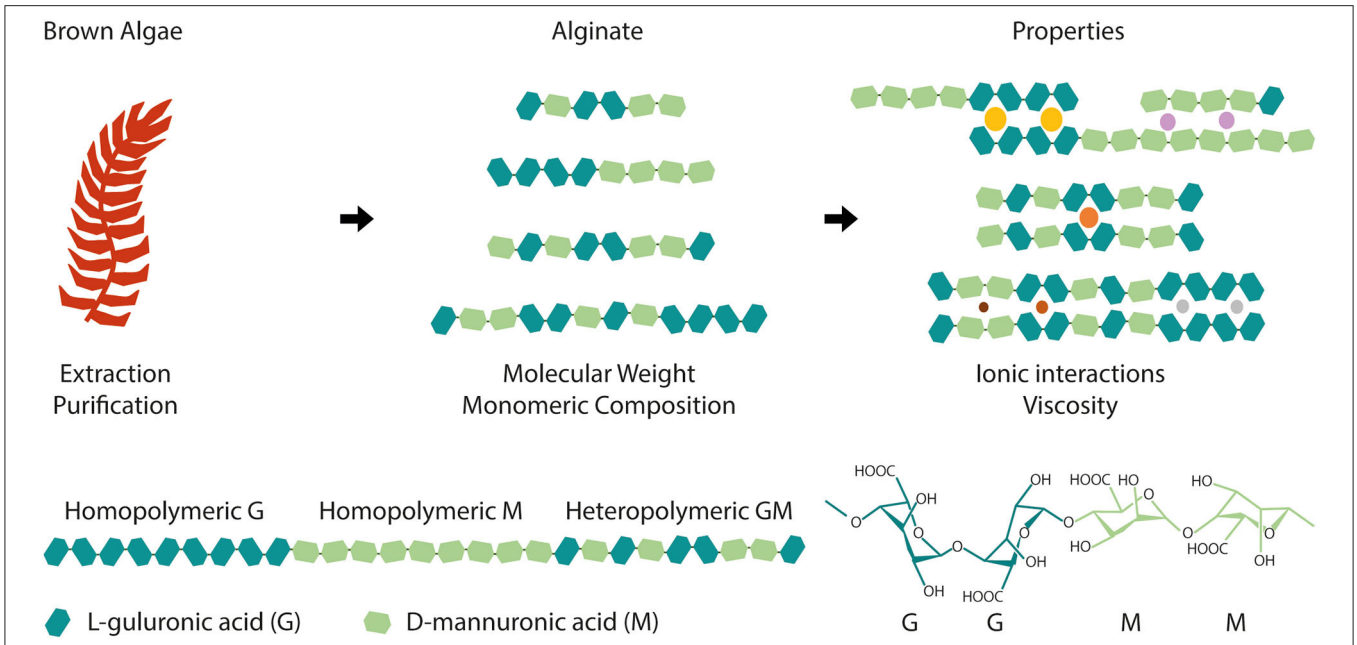


**FIGURE 1 |** Alginate is extracted and purified from a wide variety of brown algae and it is composed of α-L-guluronic acid (G) and β-D-mannuronic acid (M) blocks. Depending on the species, extraction and purification, alginate can have distinct molecular weight and monomeric composition, namely different G and M blocks content and arrangement (homopolymeric or heteropolymeric regions). These structural differences translate into different material properties, such as alginate affinity toward ions (colored circles exemplify cations with varying radius) and viscosity that will ultimately condition biomaterial development and dictate its final properties and applications.

gels. Temperature also has an impact in the gelation rate and final elastic modulus of ionically crosslinked alginate hydrogels (Moe et al., 1992), with increasing temperatures leading to faster gelation (Kuo and Ma, 2001). The pH interferes with gelation by altering the protonation state of carboxyl groups in alginate chains. These become charged, and thus repulsive at higher pH, destabilizing the hydrogel network, while at acidic pH intermolecular hydrogen bonds stabilize the network as carboxylate groups become protonated. In fact, besides ionic crosslinking, alginate hydrogels can be produced in acidic environments via hydrogen bonding. Such alginic acid hydrogels can be obtained either by acidifying an alginate solution or by exchanging ions with protons in a pre-formed ionically crosslinked alginate gel (Draget et al., 1994).

## Alginate Purification

In order to be used in biomedical applications, careful extraction and purification processes are required to ensure safety of alginate products. Common alginate contaminants include proteins, polyphenolic compounds, lipopolysaccharides (endotoxins) and genetic material (DNA and RNA), some of which may trigger undesirable host responses. Several works have compared the performance of purified vs. unpurified alginates regarding biological properties, particularly the possibility of eliciting undesirable immunological response (Dusseault et al., 2006; Tam et al., 2006; Sondermeijer et al., 2016; Torres et al., 2019). Despite the much lower levels of contaminants in purified alginates comparing to unpurified ones (Sondermeijer et al., 2016), purification is still one of the roadblocks for translational application of alginate-based products to the clinics (Krishnan et al., 2017). Fortunately, alginates of ultrapure grade are already commercially available, with well-defined compositions (i.e., G/M ratio, molecular weight/viscosity), and can be even acquired as sterilized products, if desired (Bidarra et al., 2014).

## Alginate in the Clinics

Alginate biocompatibility, along with its unique physicochemical properties, have led to its wide utilization in clinical applications. Currently, around 120 clinical trials are a match for the term "alginate" in the U. S. National Library of Medicine (ClinicalTrials.gov, 2019), with more than half of these studies being considered "completed." While many of these studies (**Figure 2**) relate to the use of alginate as dietary supplement, it has also been largely used in drug development. Alginate-based drugs are being studied for the treatment of different types of diseases, such as cystic fibrosis (OligoG by AlgiPharma AS) (AlgiPharma, 2019) or osteosarcomas (Chen et al., 2017). In biomedical applications, most of the matching results correspond to clinical trials of devices, and injectable or implantable products (**Figure 2**). Such is the case of alginate wound dressings [such as Restore Calcium Alginate Dressing —Silver (Hollister©), AqualCel Ag Dressing (Convatec), Algidex Ag® (DeRoyal)], frequently used in clinical trials and probably the most typical commercially available alginate-based biomedical device. Alginate has also been applied in contact lenses (Chong et al., 2016), or as material for dental impression (Ismail et al., 2010).

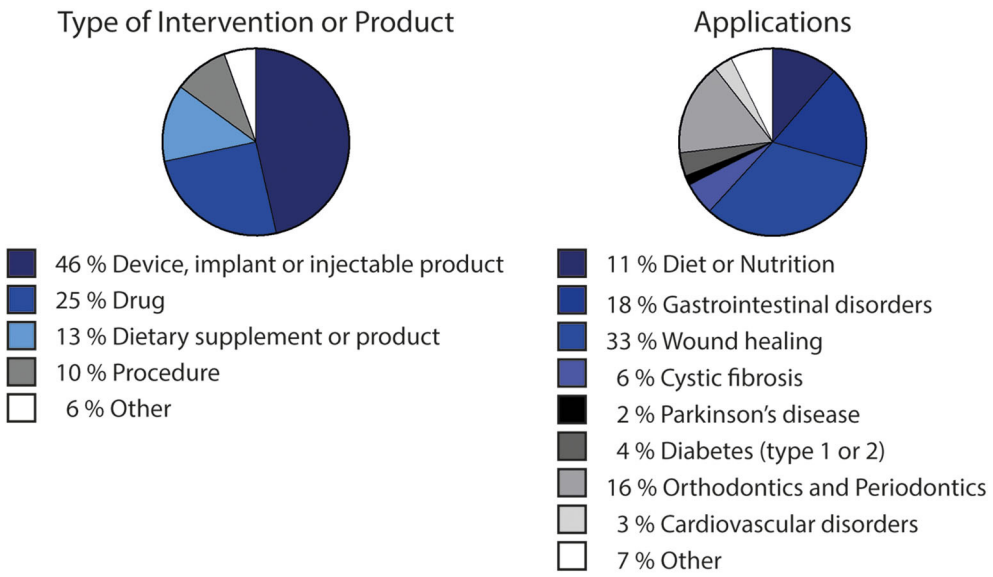


**FIGURE 2 |** Clinical trials involving alginate-based products or procedures, divided by type of intervention or product and by application. Data adapted from search results matching "alginate" term at ClinicalTrials.gov (2019), i.e., including clinical trials that use alginate-based products/procedures/devices for sake of comparison as standard procedures. Chart showing type of intervention or product considers "Other" matches defined also as "other," "biological" or "behavioral" by the platform. Applications chart considers applications occurring more than once.

Injectable alginate-based materials are also being developed, such as Algisyl-LVR™ (LoneStar Heart, Inc.), developed for left ventricular augmentation and restoration for patients with dilated cardiomyopathy (Lee et al., 2015; Sack et al., 2018).

Some clinical applications regarding the specific use of alginate-based products as 3D cellular microenvironments present promising results. In xenotransplantation settings, implantation of cells from a different species in humans presents high risk of immunological rejection (Smith et al., 2018). Also, cell therapies involving free cell delivery often result in low cell survival and retention in diseased tissues, which compromises efficacy (Tong and Yang, 2018). In this context, cell encapsulation provides a suitable strategy for functional cellular xenografts without requiring immunosuppression (Smith et al., 2018). Alginate hydrogels can work as carriers for cell transplantation, protecting cells from the adverse host environment and improving their longevity at target sites. Alginate-based capsules for xenogeneic cell therapy have been explored in pre-clinical and clinical trials for applications such as type 1 diabetes, pain, Parkinson's disease and liver failure (Smith et al., 2018). For example, NTCELL® (Living Cell Technologies, 2019) was developed for xenotransplantation of porcine choroid plexus cells for neural applications. LCT recently completed phase 1 and 2 clinical trials on the safety and efficacy of NTCELL® in patients with Parkinson disease (NCT02683629) and announced a successful result comparing to placebo group, prospecting a possible phase 3 study in the near future (Matsumoto et al., 2016). DIABECELL® (Diatranz Otsuka Ltd) is an alginate-based system for immunoprotection of encapsulated porcine islets for patients with type 1 diabetes mellitus, which underwent several clinical trials (NCT00940173, NCT01736228, NCT01739829). Promising results indicated safety in the use of alginate-encapsulated neonatal porcine islet and improvement in diabetic patients (Matsumoto et al., 2016).

Despite positive outcomes in clinical trials, the strict implementation of regulatory guidelines for the development and application of novel therapies is paramount for greater safety and benefit of patients. The use of "combination products", where biomaterials are used together with bioactive compounds and/or cells has been increasing overtime. This demands stricter and well-defined guidelines and regulation regarding device classification. For instance, in 2013, EMA released a scientific recommendation regarding the classification of advanced therapy medicinal products (EMA/277458/2013), specifically describing the case of alginate encapsulated porcine pancreatic islet cells for type 1 diabetes mellitus. The multiplicity of available approaches and applications of biomedical products prospects that this will be more frequently required for each particular device.

## BIOFUNCTIONALIZATION OF ALGINATE HYDROGELS WITH CELL INSTRUCTIVE/RESPONSIVE PEPTIDES

Different types of chemical modifications have been performed to increase the versatility of alginate as biomaterials, taking advantage of its native OH or COOH functional groups, using alternative reaction routes, like oxidations (Liu et al., 2018), thiolations (Maleki et al., 2015), reductive-aminations (Rinaudo, 2011; Akhter et al., 2018), sulfations (Kerschenmeyer et al., 2017; Yu et al., 2017), esterifications (Ye et al., 2017),

and amidations (Heo et al., 2017; Kondaveeti et al., 2018). Such approaches have been used either as intermediate steps to introduce specific reactive groups for further chemical modifications (Maleki et al., 2015; Liu et al., 2018; Pei et al., 2018), or to directly incorporate new moieties on alginate molecules. This allows to tune different features of alginate polymers and create derivatives with improved properties, such as bioactivity (Kerschenmeyer et al., 2017), mechanical properties (Liu et al., 2018), degradation rate (Fonseca et al., 2014a), fluorescence (Akhter et al., 2018; Araujo et al., 2020), drug loading capacity or release profile (Ye et al., 2017), and antimicrobial activity (Kondaveeti et al., 2018), amongst others. For the design of artificial 3D microenvironments, the incorporation of moieties that specifically modulate cell-material interactions is pivotal. In fact, unlike mammalian polysaccharides such as hyaluronan, a glycosaminoglycan present in the extracellular matrix (ECM) that intrinsically contains functional domains (e.g., cell receptors such as CD44) (Misra et al., 2015), alginate lacks the ability to specifically interact with mammalian cells. To address this, chemical modifications to incorporate cell instructive/responsive moieties in otherwise "bioinert" polymers have been widely performed both in alginate and in several other natural or artificial polymers (Bidarra et al., 2010; Neves et al., 2015; Heo et al., 2017; Zhao et al., 2017; Kudva et al., 2018; Pereira et al., 2018a,b). These "biofunctionalizations" can thus be designed to confer key biological features, like cell adhesiveness (Neves et al., 2015; Zhao et al., 2017; Kudva et al., 2018) or sensitivity to proteolytic degradation (Fonseca et al., 2011; Pereira et al., 2018b), in polymers that despite being biocompatible are inert, non-fouling or non-adhesive materials (**Figure 3**). Frequently, these bioactive moieties comprise peptide sequences known to specifically interact with cells or cell-derived components. In **Table 1** a summary of some peptide sequences that have already been grafted to alginate is presented, and some selected examples will be discussed in detail in the following subsections, which are typical and illustrative rather than all-inclusive.

## Modification With Cell-Adhesive Peptides

A typical functionalization approach to promote integrin-mediated cell adhesion to alginate hydrogels is the incorporation of RGD (arginine-guanidine-aspartate), a tripeptide sequence naturally present in adhesive ECM proteins (e.g., fibronectin, Pierschbacher and Ruoslahti, 1984; laminin, Sasaki et al., 1988, etc.) (Pierschbacher and Ruoslahti, 1984; Farrell and Al-Mondhiry, 1997). Cells can recognize and bind RGD sequences via cell-surface integrin receptors forming adhesion complexes, namely focal adhesions. These complexes connect the cell cytoskeleton with the ECM, promoting cell-matrix crosstalk and triggering important intracellular signaling cascades, involved in key processes such as adhesion, spreading, proliferation, migration, differentiation and mechanotransduction (Wang et al., 1993; Choquet et al., 1997; Schwartz and Assoian, 2001; Nieberler et al., 2017). Rowley et al. (1999) first reported the modification of alginate with RGD via a carbodiimide chemical reaction. In their work, RGD-coupled alginate improved the adhesion, spreading and differentiation of myoblast cells in hydrogels (Rowley et al., 1999). Since then, not only alginate (Rowley et al., 1999; Rowley and Mooney, 2002; Bidarra et al., 2010, 2011; Maia et al., 2014b; Desai et al., 2015) but also other carbohydrate polymers like dextran (Riahi et al., 2017), pectin (Munarin et al., 2011, 2012; Neves et al., 2015; Pereira et al., 2018b) or gellan gum (Ferris et al., 2015) have been successfully grafted with RGD peptide sequences.

Cellular response is known to vary according to the density and patterning of RGD peptides present in the modified polymer, and the characteristics of the polymer itself (Rowley and Mooney, 2002; Riahi et al., 2017; Pereira et al., 2018b). For instance, Rowley *and coworkers* (Rowley and Mooney, 2002) studied the effect of alginate monomeric ratio and RGD density on the cellular behavior of myoblasts, by comparing high G-content and high M-content alginates (Rowley and Mooney, 2002). For the same RGD density, cells seeded onto alginate hydrogels with increasing amounts of G blocks had increased proliferation rates, as well as extensive myoblast fusion and increased levels of muscle creatine kinase activity, indicating that cells were also differentiating (Rowley and Mooney, 2002). On the other hand, the authors observed that cell adhesion, spreading, proliferation, and differentiation were reduced in low RGD densities (1 fmol/cm$^2$) and increased significantly at intermediate values (10 fmol/cm$^2$) (Rowley and Mooney, 2002). Interesting, the length of linkers interspacing the grafted peptide sequences from the polymer backbone has also been reported to affect cellular response (Lee et al., 2010, 2016), most likely by affecting the orientation/presentation of the peptide sequence, and, thus, its availability to engage in integrin binding events.

Alginate matrices modified with RGD peptide have been used to develop 3D microenvironments for multiple cell types and reported to improve different aspects of the behavior of MSC (Maia et al., 2014b), endothelial cells (EC) (Bidarra et al., 2011), among others, when compared to the correspondent non-modified polymer. For instance, Bidarra et al. (2011) showed that human umbilical vein endothelial cells preserved their viability, along with the ability to proliferate and migrate when entrapped in RGD-alginate hydrogels, whereas in non-modified alginate cells remained round and unable to spread or migrate. Maia et al. (2014b) observed that MSC embedded in soft RGD-alginate hydrogels were able to exert traction forces and pull the modified alginate network, but not its unmodified counterpart, in order to aggregate into a tissue-like structure and produce endogenous ECM. Desai et al. (2015) reported NIH 3T3 fibroblasts adhesion, spreading and formation of cellular branched interconnected networks in alginate hydrogels, which were RGD-dependent, further illustrating the importance of RGD binding in promoting cell-matrix interactions. Significantly, the modification of bioinert hydrogels such as alginate with RGD peptides is often mandatory and it is typically used in combination with other bioactive peptides.

While the RGD sequence is recognized by specific integrins present in the membrane of most cell types, for some applications, it may be desirable to have some level of control over the type of cell adhering to the biomaterial. Therefore, in those cases, peptide sequences with higher affinity toward particular cell types may be used. For instance, specific peptides

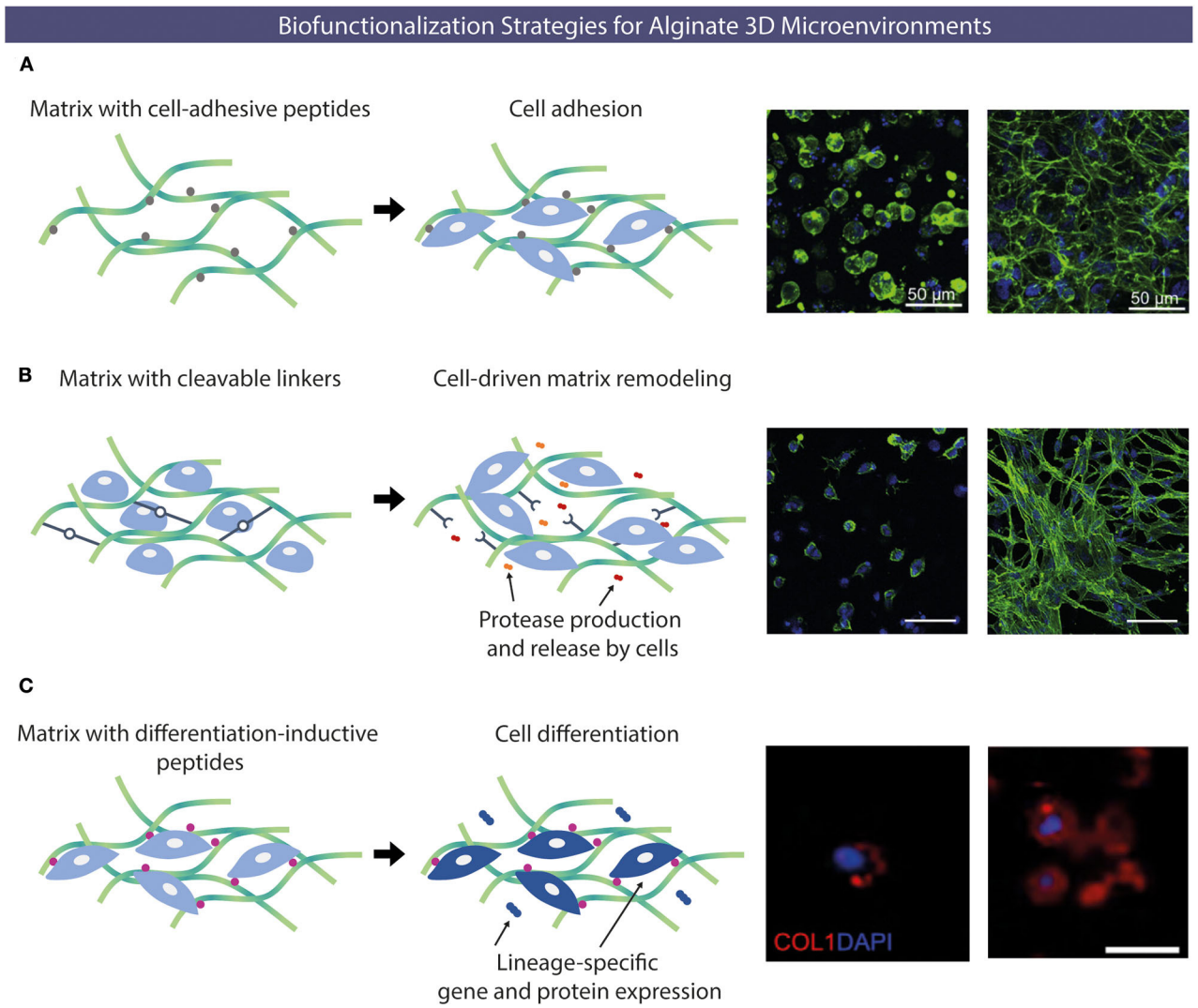


**FIGURE 3 |** Examples of alginate chemical functionalization with bioactive peptides. **(A)** Cell-adhesion peptides able to interact with different types of cells (e.g., RGD) can be incorporated to promote cell-hydrogel adhesion. Confocal microscopy images of human umbilical vein endothelial cells (HUVECs) cultured under 3D conditions within alginate hydrogels without (left) or with (right) RGD peptides after 48 h (actin in green and nuclei in blue). **(B)** Protease-sensitive sequences peptides can be incorporated, to be degraded upon exposure to proteases (e.g., MMP) produced by cells allowing cell-driven matrix remodeling. Morphology of embryonic mouse fibroblasts entrapped within non-degradable (left) or enzymatically-degradable (right) peptide-crosslinked alginate hydrogels after 14 days (actin in green and nuclei in blue). **(C)** Alginate matrices can also be modified with peptides capable of inducing specific cell differentiation. Collagen type I deposition by MSC transplanted within RGD-alginate (left) and OGP/RGD-alginate (right), showing higher staining intensity for the condition where osteogenic-inductive OGP peptides were incorporated. Different biofunctionalizations strategies can be combined to yield multifunctional hydrogels (collagen type I in red and nuclei in blue). Reproduced/adapted from **(A)** (Bidarra et al., 2011), **(B)** (Fonseca et al., 2011), and **(C)** (Maia et al., 2014a).

can be used to selectively promote adhesion of EC, which play a pivotal role in the formation of new blood vessels, i.e., neovascularization, as reported by Wang et al. (2017). The authors modified alginate and gold nanoparticles with an arginine-glutamate-aspartate-valine (REDV) peptide sequence that is recognized by α4β1 integrin, predominantly expressed by EC (Wang et al., 2017). When modified with REDV, both alginate and gold nanoparticles promoted substantial adhesion of EC, but significantly lower rates of fibroblast adhesion (Wang et al., 2017).

## Modification With Proteolytically-Degradable Peptides

*In vivo*, the ability of cells to remodel the ECM surrounding them is crucial to several cellular activities, such as cell proliferation and migration, being central to (patho)physiological events such as wound healing (Xue and Jackson, 2015), neovascularization (Neve et al., 2014; Bishop, 2015), and tumor formation/progression (Mohan et al., 2020), among others. Likewise, when 3D cultured cells are surrounded by dense polymer meshes, their ability to degrade/remodel the polymer

**TABLE 1 |** Peptide sequences covalently linked to alginate.

| Parental molecule(s) | Peptide (sequence) | References |
|---|---|---|
| **Fibronectin and Vitronectin** | | |
| RGD-containing | GRGDSP | Formo et al., 2015; Dalheim et al., 2016 |
| | CGGGRGDS | Ooi et al., 2018 |
| | GGGGRGDSP | Bidarra et al., 2010, 2011; Nakaoka et al., 2013; Fonseca et al., 2014a; Maia et al., 2014a,b; Desai et al., 2015; Lee and Lee, 2017 |
| | GRGDY | Rowley et al., 1999 |
| | GRGDYP | Dalheim et al., 2016 |
| | GGGGRGDY | Rowley and Mooney, 2002; Hayoun-Neeman et al., 2019 |
| | AAAAAAKRGDY, VVVVVVKRGDY, GGGGGGKRGDY | Ochbaum and Bitton, 2017 |
| | RGDfK (cyclic) | Sondermeijer et al., 2018 |
| Heparin binding-peptide | GGGGSPPRRARVTY | Sapir et al., 2011; Hayoun-Neeman et al., 2019 |
| PHSRN-containing | GGGGPHSRN | Nakaoka et al., 2013 |
| REDV-containing (from Fn CS5 domain) | CGGREDV, GREDV | Wang et al., 2017 |
| **Osteonectin** | | |
| GHK-containing | GGGGHKSP | Jose et al., 2014; Klontzas et al., 2019 |
| **Laminin** | | |
| IKVAV-containing | GIKVAV | Formo et al., 2015 |
| YIGSR-containing | GYIGSR | Formo et al., 2015 |
| | GGGGYIGSR | Lee and Lee, 2017 |
| **Collagens** | | |
| Collagen type I (α1 chain) | GFOGER | Stephan et al., 2015 |
| **Immunoglobulin superfamily** | | |
| NCAM | KHIFSDDSSE | Dalheim et al., 2016 |
| **Cadherin superfamily** | | |
| N-cadherin (LRP5 peptide) | DSCPPSPATERSYFHLFPPPPSPCTDSS | Lee J. W. et al., 2017 |
| **Growth factors** | | |
| BMP-2 | GGGGDWIVA, CGKIPKASSVPTELSAISTLYL | Madl et al., 2014 |
| | NSVNSKIPKACCVPTELSAI | Suzuki et al., 2000 |
| BMP-7 (BFP-1 peptide) | GQGFSYPYKAVFSTQ | Luo et al., 2016; Yang et al., 2018 |
| OGP | GGGYGFGG, GGGIVGPLGYGFGG | Maia et al., 2014a |
| **Matrix metalloproteinases (MMP) sensitive** | | |
| PVGLIG-containing | GGYGPVG↓LIGGK | Fonseca et al., 2011, 2014a |
| | GGPVG↓LIGGYGFGG | Maia et al., 2014a |
| PMSMR-containing | GCRDVPMS↓MRGGDRCG | Lueckgen et al., 2019 |
| Type I collagen-derived | GCRDGPQG↓IWGQDRCG | Lueckgen et al., 2019 |

*BFP-1 (bone forming peptide-1), BMP (bone morphogenic protein), NCAM (neural cell adhesion molecule), OGP (osteogenic growth peptide). Amino acid nomenclature: alanine (A), cysteine (C), aspartic acid (D), glutamic acid (E), phenylalanine (F), glycine (G), isoleucine (I), histidine (H), lysine (K), leucine (L), asparagine (N), proline (P), glutamine (Q), arginine (R), serine (S), threonine (T), valine (V), tyrosine (Y). ↓ denotes cleavable site.*

matrix dictates their ability to spread, migrate, proliferate and undergo morphogenesis (Fonseca et al., 2014b). The rate at which degradation/remodeling occurs is also important and should ideally be synchronized with the deposition of new cell-derived ECM.

Following this rationale, biomaterials can be chemically modified to include degradation sites for cell-derived enzymes (Fonseca et al., 2013, 2014a,b). Fonseca et al. (2011) modified alginate with RGD and the proline-valine-glycine-leucine-isoleucine-glycine (PVG↓LIG) peptide sequence that is recognized and cleaved by matrix metalloproteinases (MMP) secreted by cells. The authors cultured MSC under 3D conditions in modified alginate hydrogels and the incorporation of PVG↓LIG along with RGD showed to promote cell spreading and formation of multicellular networks, which was not observed in hydrogels containing only RGD-alginate, where cells remained essentially round and dispersed (Fonseca et al., 2011). This suggests that enzymatic-degradation of PVGLIG motifs allowed cells to create paths within the matrix, at the pericellular space, and partially overcome the biophysical resistance offered by the 3D network (Fonseca et al., 2011, 2013). Upon subcutaneous implantation in immunodeficient mice, MSC-laden RGD/PVGLIG alginate hydrogels were invaded by new collagenous tissue and blood vessels and degraded

faster than RGD-alginate hydrogels (Fonseca et al., 2014a). The incorporation of PVGLIG domains also promoted the outward migration of transplanted MSC into host tissue, suggesting that MMP-sensitive alginate hydrogels are adequate vehicles for cell delivery (Fonseca et al., 2014a).

Lueckgen et al. (2019) developed a photocrosslinkable alginate-based system using VPMS↓MRGG or GPQG↓IWGQ containing sequences as degradable crosslinkers. These sequences are MMP-cleavable and had been previously studied for the development of proteolytic degradable PEG hydrogels (Patterson and Hubbell, 2010). In the study of Lueckgen et al. (2019), both sequences were flanked by a linker sequence (GCRD-XXX-DRCG) to react with a norbornene-modified alginate through cysteine thiol groups (Lueckgen et al., 2019). Hydrogels produced with both peptide sequences had similar mechanical and rheological properties, such as elastic modulus and swelling ratio, but degradation kinetics was slower for hydrogels with VPMS↓MRGG in comparison to GPQG↓IWGQ crosslinker when exposed to collagenase (Lueckgen et al., 2019). On the other hand, non-degradable hydrogels produced using non-enzymatically cleavable variants of these sequences and presenting similar mechanical properties showed no susceptibility toward this collagenase, validating the bioactivity of the protease-sensitive sequences (Lueckgen et al., 2019). Ultimately, the incorporation of degradable crosslinkers promoted spreading of embedded fibroblasts within these hydrogels whereas in non-degradable counterparts cells remained essentially round even after 14 days (Lueckgen et al., 2019). *In vivo* results showed higher tissue and cell infiltration into degradable hydrogels in comparison to non-degradable hydrogels (Lueckgen et al., 2019), highlighting the importance of including matrix remodeling cues in the biological performance of biomaterial systems.

## Modification With Differentiation-Inductive Peptides

Specific cell-instructive cues can be incorporated into alginate hydrogels to direct specific lineage commitment of entrapped stem cells. For example, an alginate hydrogel functionalized with an osteoinductive peptide has been developed as vehicle for MSC delivery (Maia et al., 2014a). The bioactive region (the amino acid sequence YGFGG) of the osteogenic growth peptide (OGP) was incorporated into the design of two peptides, where it was flanked by a protease-sensitive linker (PVGLIG) or its scrambled sequence, to provide different OGP release rates (Maia et al., 2014a). OGP peptides were grafted to alginate hydrogels by carbodiimide chemistry, and MSC-laden OGP/RGD–alginate hydrogels were subcutaneously implanted in immunocompromised mice (Maia et al., 2014a). Four weeks after implantation, OGP–alginate hydrogels were more degraded and colonized by vascularized connective tissue as compared to the OGP-free control (RGD-alginate) (Maia et al., 2014a). *In vivo*, hydrogel-entrapped MSC were able to proliferate, migrate from the hydrogels, produce endogenous ECM and induce/trigger mineralization. Significantly, hydrogels with OGP were more effective in promoting osteogenic differentiation of transplanted MSC, than the control (Maia et al., 2014a). Overall, the ability of OGP/RGD-alginate hydrogels to direct the fate of transplanted MSC *in situ* was demonstrated, emerging as a potentially useful system to promote bone regeneration (Maia et al., 2014a).

Guidance of MSC fate commitment into the osteogenic lineage has also been explored in alginate hydrogels integrating peptide sequences derived from bone morphogenic proteins (BMP). For example, BMP-2 derived peptides containing DWIVA and KIPKASSVPTELSAISTLYL (BMP-2 knuckle epitope, BMP-2 KE), have been conjugated to alginate (Madl et al., 2014; Oki et al., 2019). Madl et al. (2014) modified alginate with peptides containing RGD and these two sequences, observing a significant increase in alkaline phosphatase (ALP) activity of osteoblasts entrapped within RGD/BMP-2 KE alginate hydrogels, but not significant differences in osteoblasts entrapped in RGD hydrogels or RGD/DWIVA hydrogels (Madl et al., 2014). Similarly, RGD/BMP-2 KE alginate hydrogels were able to promote osteogenesis in MSC, as observed by the upregulation of Smad signaling pathway, osteopontin overexpression and increased mineral deposition, whereas the same response was not observed for RGD/DWIVA hydrogels (Madl et al., 2014). Likewise, Yang et al. (2018) covalently incorporated BMP-7 derived peptide BFP-1 by carbodiimide chemistry into alginate to develop a lyophilized, porous scaffold capable of inducing MSC osteo-differentiation. The authors observed a significant increase in ALP activity and expression of bone-related genes [osteocalcin, collagen 1, runt-related transcription factor 2 (Runx2) and ALP] and proteins (osteocalcin and collagen 1) in MSC seeded onto BFP-1 modified alginate as opposed to pristine alginate scaffolds (Yang et al., 2018).

# TUNING ALGINATE HYDROGELS MECHANICAL PROPERTIES

The modulation of hydrogels mechanical properties is highly relevant, not only to improve their structural and mechanical stability, but also to guide cellular response via mechanotransduction. As referred above, alginate ability to undergo gelation upon exposure to divalent cations makes alginate quite convenient for biomedical applications. However, such physically crosslinked systems may not present the most adequate rheological and mechanical properties regarding the production steps of biomaterial design or even their final application. On the other hand, it is well-established that cells can mechanically sense and process signals provided by their extracellular environment, to make fate decisions (Lee et al., 2013; Chaudhuri et al., 2016; Lou et al., 2018; Stowers et al., 2019), being thus pertinent to modulate the mechanical features of biomaterials accordingly.

## Covalent Crosslinking for Improved Structural/Mechanical Properties

Alginate can be chemically modified for allowing covalent crosslinking to improve structural stability and modulate rheological and/or mechanical properties. For instance,

degradation rates can be reduced when compared to ionic hydrogels, where diffusion and loss of crosslinking ions, presence of chelators (e.g., phosphates) and competition with monovalent cations (e.g., $Na^+$) typically present in physiological scenarios interferes with hydrogel integrity over time. Moreover, dual crosslinking strategies can still be explored in alginate covalent hydrogels that still enable non-covalent crosslinking.

One of the most frequent chemical modification performed is the incorporation of photosensitive groups, which allow *in situ* covalent crosslinking under light exposure, in the presence of a photoinitiator (Chou and Nicoll, 2009; Jeon et al., 2014; Pereira et al., 2018b). Photocrosslinking strategies are advantageous by providing spatio-temporal control over the crosslinking process, through the tuning of intensity and duration of light exposure, the concentration and type of photoinitiator and the extent/pattern of exposed vs. non-exposed regions. Samorezov et al. (2015) incorporated methacrylate groups in alginate and explored different modification degrees to produce hydrogels that could be either ionically crosslinked, photocrosslinked or both (dual crosslinking) (Samorezov et al., 2015). The authors showed that shear moduli (storage and loss) were significantly increased in dual crosslinked alginates, while the swelling ratio was significantly decreased (Samorezov et al., 2015). By further modifying methacrylate alginate with RGD sequences, the authors showed that pre-osteoblastic cells were able to adhere and spread on-top of both ionically and dual crosslinked hydrogels, while presenting higher proliferation rates in dual crosslinked hydrogels (Samorezov et al., 2015). By controlling the regions exposed to UV light, the authors were also able to create patterned structures with regions of dual crosslinked (exposed regions) or ionically crosslinked regions (non-exposed regions) presenting differences in mechanical properties and cell response (i.e., adhesion and spreading) (Samorezov et al., 2015). Desai et al. (2015) developed covalently-crosslinked alginate by introducing norbornene and tetrazine groups in the polymer backbone by carbodiimide chemistry, which react with each other promoting crosslinking, and posteriorly modified it with a mono-thiol RGD sequence by a thiol-ene photoreaction. Ooi et al. (2018) used thiol-ene click chemistry for reacting norbornene-alginate with thiol-containing polymers (e.g., PEG dithiol or 4-arm PEG thiol) crosslinkers, which enabled better spatio-temporal control of alginate rheological and mechanical properties during bioprinting. The authors were able to tune hydrogel properties by varying the concentration, molecular weight and number of arms (2 or 4) of PEG crosslinker used (Ooi et al., 2018). For instance, hydrogels produced with higher crosslinker concentration, lower molecular weight PEG or 4-arm PEG presented lower swelling ratios, as they form more compact networks (Ooi et al., 2018). On the other hand, the storage moduli increased with increasing crosslinker concentration and number of arms, but hydrogels produced with longer PEG crosslinkers (5000 Da) were slightly stiffer than the ones produced with smaller PEG (1500 Da) (Ooi et al., 2018). By further ionically crosslinking these hydrogels, the authors were able to significantly increase storage and loss modulus (Ooi et al., 2018). Indeed, the possibility of producing alginate derivatives for covalent crosslinking while retaining, even if partially, its ability to undergo ionic crosslinking, is one of the key features increasing the versatility of alginate regarding the tuning of mechanical properties.

Temperature can also be used to catalyze the crosslinking of alginate hydrogels. For instance, Wang et al. (2015) developed a thermal polymerizable modified alginate incorporating glycidyl methacrylate groups. In the presence of a thermal initiator, the modified alginate could be rapidly (5 to 20 min) crosslinked at 37°C (Wang et al., 2015). This type of modification can be of great interest when developing biomaterials for implantation, as these can be crosslinked *in situ*, triggered by normal body temperature, in a rather short period of time.

Covalent alginate hydrogels can also be enzymatically crosslinked. Hou et al. (2015) conjugated alginate with dopamine and tyramine by carbodiimide chemistry, which react in the presence of hydrogen peroxide ($H_2O_2$) and horseradish peroxidase (HRP), promoting crosslinking (Veitch, 2004). In this system, HRP reacts with $H_2O_2$, eventually leading to the formation of catechol or phenol radicals in the dopamine or tyramine molecules, respectively, that then bind to form covalent links. In this case, the mechanical properties and gelation times can be tuned by altering the amount of $H_2O_2$ in the system (Hou et al., 2015). Ganesh et al. (2013) developed a similar system based in tyramine substituted alginate for cell encapsulation and delivery.

## Mechanical Modulation for Specific Cell Guidance

In the development of 3D hydrogel systems, stiffness is probably one of the most routinely characterized mechanical parameters. Indeed, stiffness is known to impact cell adhesion, spreading, proliferation and even differentiation, at different levels, for different cell types (Yeung et al., 2005; Park et al., 2011; Mao et al., 2016). Studies on RGD clustering and traction forces exerted by cells in 2D alginate substrates showed that spreading of preosteoblastic cells was independent on matrix stiffness, but the formation of focal adhesion and cell proliferation was significantly enhanced with increasing substrate rigidity (Kong et al., 2005). The authors proposed that a particular resistance to ligand displacement may be required for cells to initiate the necessary apparatus to generate traction forces, while softer gels may fail to provide sustainable anchor sites, impairing the formation of focal adhesions (Kong et al., 2005). Within 3D alginate hydrogels with varying stiffness, entrapped MSCs were reported to present stiffness-dependent proliferation and differentiation (Huebsch et al., 2010; Maia et al., 2014b). In their work, Maia et al. (2014b) modulated stiffness by varying alginate dry mass content, with the storage modulus of 2 wt% hydrogels being 40-fold higher than 1 wt% hydrogels, and with this latter possessing higher viscous-to-elastic ratio (Maia et al., 2014b). Even though MSCs viability was independent of matrix composition, in softer hydrogels cells were able to proliferate and contract the polymeric network, forming dense multicellular aggregates with extensive cell spreading and cell-cell contact, whereas in stiffer hydrogels MSCs remained round and disperse (Maia et al., 2014b). ECM production was also affected by stiffness, with softer alginate matrices leading

to higher fibronectin production than stiffer matrices, where fibronectin remained confined to the intracellular space (Maia et al., 2014b). Also, Maia et al. (2014b) observed that cells were only able to substantially contract the artificial matrix in the presence of RGD (Maia et al., 2014b). Similarly, Huebsch et al. (2010) observed that encapsulated MSC preferably undergo osteogenic differentiation within 11–30 kPa hydrogels, whereas in 2.5–5 kPa hydrogels they tended to undergo adipogenesis (Huebsch et al., 2010). However, when blocking RGD binding to α5 integrins, osteogenesis was significantly impaired and adipogenesis enhanced, showing a partial modulation of cell fate by integrin/adhesion-ligand bond formation (Huebsch et al., 2010). In fact, α5-RGD bonds presented a biphasic dependence on matrix stiffness that peaked at 22 kPa, the optimal value for osteogenic differentiation, whereas on softer and stiffer matrices this cell-RGD bond formation would decrease (Huebsch et al., 2010). Also, it was in 22 kPa matrices that the authors observed the highest traction-mediated matrix reorganization (Huebsch et al., 2010). This suggests that there is a minimum of matrix stiffness required for the formation of sustainable anchor sites, allowing cells to exert traction forces, while in excessively stiff hydrogels the tension exerted by cells may not be sufficient for matrix deformation (Kong et al., 2005; Huebsch et al., 2010).

More recently, it has been acknowledged that stress relaxation, i.e., the time-dependent decrease in stress under a constant strain, also impacts cell behavior both in 2D and 3D systems, including on alginate hydrogels (Chaudhuri et al., 2015, 2016; Bauer et al., 2017; Lee H. P. et al., 2017). Stress relaxing alginate hydrogels are often produced by ionic crosslinking, as physical alginate hydrogels more closely resemble the viscoelastic properties of the native ECM, as opposed to covalent hydrogels which are mainly elastic and present significantly less stress relaxation (Chaudhuri et al., 2016). Stress relaxation observed in physical alginate hydrogels is thought to occur due to the unbinding and rebinding of ionic crosslinkers (Zhao et al., 2010) and can be modulated by varying alginate molecular weight or by covalent incorporation of spacers into the polymer backbone (Chaudhuri et al., 2016; Nam et al., 2019). Decreasing alginate molecular weight leads to enhanced stress relaxation, most likely due to altered connectivity and chain mobility (Chaudhuri et al., 2016). Incorporating spacers onto alginate backbone can enhance stress relaxation, in comparison to unmodified alginate, by sterically impairing ionic crosslinking, as observed by Chaudhuri et al. (2016) who coupled 5 kDa PEG spacers to low molecular weight alginate (35 kDa) (Chaudhuri et al., 2016). Similarly, the length and density of PEG spacers coupled to alginate can be used to modulate stress relaxation independently of elastic modulus, with higher PEG density and length leading to faster stress relaxation rates (Nam et al., 2019).

Interestingly, modulating stress relaxation can be used to guide cell behavior and matrix remodeling, in a stiffness-independent manner. For instance, even though cells spread more when seeded onto stiffer substrates, faster stress relaxation leads to higher cell spreading and stress fiber formation in softer substrates (Chaudhuri et al., 2015). Such effects of stress relaxation are dependent on cell-adhesive peptide density, being enhanced in the presence of high RGD densities and promoting the formation of focal adhesions (Chaudhuri et al., 2015). Cell proliferation and lineage commitment can also be modulated by stress relaxation (Chaudhuri et al., 2015, 2016). Chaudhuri et al. (2016) observed that MSCs differentiation into adipogenic and osteogenic lineages was differently affected by stiffness and stress relaxation (Chaudhuri et al., 2016). MSCs entrapped within 9 kPa hydrogels committed to the adipogenic lineage but presented lower differentiation levels with faster stress relaxation (Chaudhuri et al., 2016). On the other hand, cells within 17 kDa hydrogels which committed to the osteogenic lineage had enhanced differentiation levels within hydrogels with faster stress relaxation (Chaudhuri et al., 2016). Such interference of stress relaxation in cell behavior and fate seems to correlate with local RGD clustering, myosin contractility and localization of the transcriptional factor YAP, known to regulate cellular response to mechanical and geometrical cues, particularly during osteogenesis (Chaudhuri et al., 2016).

Matrix formation by encapsulated chondrocytes is also reported to be affected by stress relaxation in alginate hydrogels with non-relaxing hydrogels leading to matrix deposition adjacent to cells, whereas fast relaxing hydrogels allow higher collagen and aggrecan deposition in an interconnected manner (Lee H. P. et al., 2017). Additionally, the upregulation of anabolic genes (collagen II and aggrecan) within faster relaxing hydrogels is reported, as opposed to slow relaxing hydrogels that promote the upregulation of catabolic genes (ADAMTS4 and MMP13) (Lee H. P. et al., 2017).

Altogether, these studies show the impact of mechanical properties in cell-matrix interactions and, consequently, in the ability of cells to sense, respond and transform the surrounding 3D network. In particular, these findings strength the versatility of alginate hydrogels as 3D microenvironments with tunable mechanical properties, allowing the independent modulation of different parameters such as stiffness and stress relaxation. The intrinsic bioinertness of alginate is a clear advantage in these scenarios, since the presence and density of cell adhesive moieties can be finely controlled, which may elucidate their role in cell-ECM interactions, particularly regarding the mechanical environment. Overall, these examples illustrate the possibility of designing systems for cell guidance via adequate tuning of mechanical cues, alone or in combination with biological cues as the ones presented in the previous section, with improved mimicry of the native ECM.

## ALGINATE 4D SYSTEMS AS DYNAMIC MICROENVIRONMENTS

In native tissues, the ECM is a highly dynamic environment, being constantly altered both under physiological and pathophysiological contexts, not only regarding its biochemical composition but also in terms of mechanical properties. As explored on the previous sections, exposing cells to biological moieties and/or particular mechanical conditions can elicit specific cellular outcomes. However, in most of the reported studies these stimuli were present from the beginning, with cell-material and cell-cell interactions being conditioned right

upon culture within these 3D microenvironments. Nevertheless, temporal changes may be relevant for biomaterials performance, and understanding how cells react to certain cues in a specific time point or at a specific biological phase can be of profound interest in the study of cell-microenvironment interplay. Inspired on that, biomaterials design has been evolving into the creation of four-dimensional (4D) systems that are able to dynamically change in response to an applied stimulus, a long time, in a predictable or on-demand manner.

Controlled presentation of biological moieties, as the ones explored in section Biofunctionalization of Alginate Hydrogels with Cell Instructive/Responsive Peptides, in alginate hydrogels has already been reported. One example is the covalent coupling of peptides, *in situ*, after cell encapsulation. Oki et al. (2019) produced an alginate derivative containing maleimide groups, which were able to react under physiological conditions with thiol-containing peptides (Oki et al., 2019). The authors explored this platform to switch cell proliferation and differentiation by encapsulating cells within maleimide-alginate microcapsules and then exposing them to the cell adhesive RGD peptide and the BMP-2 mimetic DWIVA and BMP-2 KE peptides 1 day after encapsulation (Oki et al., 2019). Efficient peptide coupling occurred, without affecting mechanical properties (Oki et al., 2019). On days following RGD coupling, fibroblasts proliferation significantly increased when compared to cells encapsulated within microcapsules where RGD was non-covalently bound or not present (Oki et al., 2019). Similarly, only when BMP-2 mimetic peptides were covalently bound to the alginate, preosteoblastic cells were able to differentiate into osteoblasts (Oki et al., 2019). Even though no other timepoints for peptide coupling were explored in this study, this strategy can be envisioned for dynamic systems were peptide moieties can be coupled in a sequential and timely fashion for guided cell behavior.

Structural/mechanical alterations of alginate hydrogels can also be promoted in a dynamic and controlled fashion for cell guidance. Gillette et al. (2010) developed a hybrid hydrogel combining alginate and collagen I, where the dynamic switch of alginate gelation was used to modulate the structural features of the microenvironment (Gillette et al., 2010). In this case, the structural switch was achieved by exposing hybrid hydrogels to either crosslinking $Ca^{2+}$ ions to reinforce gelation, producing a tighter biomaterial network, or to sodium citrate ($Ca^{2+}$ chelator), producing a more permissive microenvironment with a more open network (Gillette et al., 2010). The authors observed that cell spreading and migration were impaired in matrices where alginate was more heavily crosslinked, but when crosslinking was reverted, cells were able to spread and, interestingly, cell spreading was retained even after alginate recrosslinked (Gillette et al., 2010). Noteworthy, this type of switch affects not only the structural features (i.e., the mesh size), but also the mechanical properties of hydrogels. On one hand, diffusion of biological compound and cell motility may be affected by alteration in the network mesh size. On the other hand, cells may also respond to concomitant changes in matrix stiffness. Thus, dissociating the effect of each individual factor may be challenging.

Temporal control over hydrogel matrix stiffness can also be achieved by $Ca^{2+}$ release from temperature sensitive liposomal vesicles incorporated within alginate hydrogels. In this case, the release of divalent cations from liposomes can be achieved simply by heating (Westhaus and Messersmith, 2001), or in alternative, exposure to near infrared (NIR) light if temperature-sensitive nanoparticles, as gold nanorods, are included within the lipidic vesicles (Stowers et al., 2015, 2017; Joyce et al., 2018). In this latter example, upon NIR light exposure, gold nanorods undergo surface plasmon resonance, increasing local temperature and disrupting the liposomal lipid bilayer, ultimately leading to $Ca^{2+}$ release and matrix stiffening (Stowers et al., 2015). Notably, the same strategy can be used to encapsulate $Ca^{2+}$ chelators within liposomes, which will revert hydrogel crosslinking upon release, promoting matrix softening instead (Stowers et al., 2015). Besides preserving cell viability (Stowers et al., 2015), the use of NIR light can be advantageous for biomedical applications due to its high penetration through biological tissues, when compared to UV light. Indeed, in their work, Stowers et al. (2015) were able to induce matrix stiffness *in vivo* upon transdermal NIR exposure (Stowers et al., 2015). Alginate-liposome hydrogels with dynamic mechanical features have also been used to study the impact of stiffening in the formation of acinar structures by mammary epithelial cells (MEC) (Stowers et al., 2017). Non-malignant MEC were cultured within alginate-matrigel hydrogels and cultured for 14 days to allow for acinar development, being afterwards exposed to NIR light to achieve stiffening until tumor-like moduli ($\sim$ 0.5 up to 1 kPa) (Stowers et al., 2017). Interestingly, the authors observed that cells embedded within stiffened gels presented an invasive phenotype with multicellular protrusions and collective cell migration, as well as significantly increased proliferation and acini size, as opposed to cells within non-stiffened matrices, which preserved their original phenotype (Stowers et al., 2017). Studies with dynamic systems such as the ones described herein clearly illustrate that cells effectively respond to dynamic microenvironmental changes. These artificial microenvironments provide better representations of native processes and may improve current knowledge on fundamental biological events. They can also be helpful tools for the development of therapeutic strategies, which can take into consideration alterations in drug resistance by cells, as a result of all phenotypical alterations triggered by the structural changes of the extracellular microenvironment, for example (Joyce et al., 2018). Dynamic photo-induced mechanical modulation can be also used to create mechanical gradients and patterns to assess cell-material and cell-cell interactions under identical culture conditions but structurally distinct local microenvironments (Stowers et al., 2015).

## CONCLUSIONS

After its extensive use in food and pharmaceutical industries, alginate clearly settled its potential for biomedical applications. Despite the lack of inherent mammalian cell-interactive domains, the composition and structure of this natural polysaccharide along with its biocompatibility enable the development of biomaterials for a wide range of applications. By fine-tuning different properties, such as the molecular weight, backbone block composition and distribution, polymer concentration, and type/amount of crosslinkers it is possible to modulate the

viscoelastic properties of alginate solutions and their hydrogels. The ability of alginates to form hydrogels under mild and biocompatible conditions, is indeed one of its most appealing characteristics, when developing biomaterials for *in vitro* and *in vivo* applications.

Alginate relevance in the biomedical field is certainly potentiated by the possibility of creating different types of derivatives through chemical modifications, to render alginate cell-interactive and and/or modulate its crosslinking mechanisms, as discussed in this review. Such (bio)functionalizations greatly increase the versatility of alginate as a biomaterial, and ultimately reflect on its biological performance. While the field of biomaterials science is continuously evolving through the design of increasingly complex and "smarter" systems, of which dynamic 4D systems are probably the best example, alginate remains one of the most frequently used natural-based polymers.

Collectively, alginate attractive characteristics and safety have surely contributed to the existence of multiple alginate-based products in the biomedical field, and further prospects its potential for more complex and combinatorial therapeutic approaches, as indicated by the ongoing clinical trials.

## AUTHOR CONTRIBUTIONS

MN conceptualized and wrote the main manuscript and prepared the figures. LM edited and reviewed the manuscript. CB conceptualized, edited, and reviewed the manuscript. All authors approved the submitted version of the manuscript.

## FUNDING

Project ANGIONICHE (POCI-01-0145-FEDER-028744 and PTDC/BTMMAT/28744/2017), doctoral grant SFRH/BD/129855/2017 (MN), and research position IF/00296/2015 (CB).

## ACKNOWLEDGMENTS

LM is grateful to the European Research Council starting grant Cell Hybridge (Grant #637308), the Dutch Province of Limburg, Progetto FISR - C.N.R. Tecnopolo di nanotecnologia e fotonica per la medicina di precisione (CUP B83B17000010001), and Tecnopolo per la medicina di Precisione - Regione Puglia (CUP: B84I18000540002). The authors would like to acknowledge FEDER - Fundo Europeu de Desenvolvimento Regional funds through the COMPETE 2020 - Operational Programme for Competitiveness and Internationalization (POCI), Portugal 2020, and Portuguese funds through FCT - Fundação para a Ciência e a Tecnologia/ Ministério da Ciência, Tecnologia e Ensino Superior in the framework of Project ANGIONICHE (POCI-01-0145-FEDER-028744 and PTDC/BTMMAT/28744/2017). The authors thank to FCT the doctoral grant SFRH/BD/129855/2017 to MN and the research position IF/00296/2015 to CB.

## REFERENCES

Akhter, K. F., Mumin, M. A., Lui, E. M. K., and Charpentier, P. A. (2018). Fabrication of fluorescent labeled ginseng polysaccharide nanoparticles for bioimaging and their immunomodulatory activity on macrophage cell lines. *Int. J. Biol. Macromol.* 109, 254–262. doi: 10.1016/j.ijbiomac.2017.12.050

AlgiPharma. (2019). Available online at: https://algipharma.com/ (accessed July 29, 2019)

Araujo, M., Bidarra, S. J., Alves, P. M., Valcarcel, J., Vazquez, J. A., and Barrias, C. C. (2020). Coumarin-grafted blue-emitting fluorescent alginate as a potentially valuable tool for biomedical applications. *J. Mater. Chem. B* 8, 813–825. doi: 10.1039/C9TB01402K

Bambace, M. F., Alvarez, M. V., and Moreira, M. D. R. (2019). Novel functional blueberries: fructo-oligosaccharides and probiotic lactobacilli incorporated into alginate edible coatings. *Food Res. Int.* 122, 653–660. doi: 10.1016/j.foodres.2019.01.040

Bauer, A., Gu, L., Kwee, B., Li, W. A., Dellacherie, M., Celiz, A. D., et al. (2017). Hydrogel substrate stress-relaxation regulates the spreading and proliferation of mouse myoblasts. *Acta Biomater.* 62, 82–90. doi: 10.1016/j.actbio.2017.08.041

Bidarra, S. J., Barrias, C. C., Barbosa, M. A., Soares, R., and Granja, P. L. (2010). Immobilization of human mesenchymal stem cells within RGD-grafted alginate microspheres and assessment of their angiogenic potential. *Biomacromolecules* 11, 1956–1964. doi: 10.1021/bm100264a

Bidarra, S. J., Barrias, C. C., Fonseca, K. B., Barbosa, M. A., Soares, R. A., and Granja, P. L. (2011). Injectable *in situ* crosslinkable RGD-modified alginate matrix for endothelial cells delivery. *Biomaterials* 32, 7897–7904. doi: 10.1016/j.biomaterials.2011.07.013

Bidarra, S. J., Barrias, C. C., and Granja, P. L. (2014). Injectable alginate hydrogels for cell delivery in tissue engineering. *Acta Biomater.* 10, 1646–1662. doi: 10.1016/j.actbio.2013.12.006

Bishop, P. N. (2015). The role of extracellular matrix in retinal vascular development and preretinal neovascularization. *Exp. Eye Res.* 133, 30–36. doi: 10.1016/j.exer.2014.10.021

Borazjani, N. J., Tabarsa, M., You, S., and Rezaei, M. (2017). Effects of extraction methods on molecular characteristics, antioxidant properties and immunomodulation of alginates from Sargassum angustifolium. *Int. J. Biol. Macromol.* 101, 703–711. doi: 10.1016/j.ijbiomac.2017.03.128

Braccini, I., Grasso, R. P., and Pérez, S. (1999). Conformational and configurational features of acidic polysaccharides and their interactions with calcium ions: a molecular modeling investigation. *Carbohydr. Res.* 317, 119–130. doi: 10.1016/S0008-6215(99)00062-2

Braccini, I., and Perez, S. (2001). Molecular basis of $Ca^{2+}$-induced gelation in alginates and pectins: the egg-box model revisited. *Biomacromolecules* 2, 1089–1096. doi: 10.1021/bm010008g

Campiglio, C. E., Bidarra, S. J., Draghi, L., and Barrias, C. C. (2020). Bottom-up engineering of cell-laden hydrogel microfibrous patch for guided tissue regeneration. *Mater. Sci. Eng. C Mater. Biol. Appl.* 108:110488. doi: 10.1016/j.msec.2019.110488

Cavo, M., Caria, M., Pulsoni, I., Beltrame, F., Fato, M., and Scaglione, S. (2018). A new cell-laden 3D Alginate-Matrigel hydrogel resembles human breast cancer cell malignant morphology, spread and invasion capability observed *in vivo*. *Sci. Rep.* 8:5333. doi: 10.1038/s41598-018-23250-4

Chaudhuri, O., Gu, L., Darnell, M., Klumpers, D., Bencherif, S. A., Weaver, J. C., et al. (2015). Substrate stress relaxation regulates cell spreading. *Nat. Commun.* 6:6364. doi: 10.1038/ncomms7365

Chaudhuri, O., Gu, L., Klumpers, D., Darnell, M., Bencherif, S. A., Weaver, J. C., et al. (2016). Hydrogels with tunable stress relaxation regulate stem cell fate and activity. *Nat. Mater.* 15, 326–334. doi: 10.1038/nmat4489

Chen, J., Hu, Y., Zhang, L., Wang, Y., Wang, S., Zhang, Y., et al. (2017). Alginate oligosaccharide dp5 exhibits antitumor effects in osteosarcoma patients following surgery. *Front. Pharmacol.* 8:623. doi: 10.3389/fphar.2017.00623

Chong, P. Q. Y., Yeo, S., Too, C. L., Boo, C., and Tong, L. (2016). Effects of wearing a daily disposable lens on tear film: a randomised controlled trial. *Clin. Exp. Optom.* 99, 241–247. doi: 10.1111/cxo.12357

Choquet, D., Felsenfeld, D. P., and Sheetz, M. P. (1997). Extracellular matrix rigidity causes strengthening of integrin–cytoskeleton linkages. *Cell* 88, 39–48. doi: 10.1016/S0092-8674(00)81856-5

Chou, A. I., and Nicoll, S. B. (2009). Characterization of photocrosslinked alginate hydrogels for nucleus pulposus cell encapsulation. *J. Biomed. Mater. Res. A* 91, 187–194. doi: 10.1002/jbm.a.32191

Chu, Y. P., Li, H. C., Ma, L., and Xia, Y. (2018). Establishment of a tumor neovascularization animal model with biomaterials in rabbit corneal pouch. *Life Sci.* 202, 98–102. doi: 10.1016/j.lfs.2018.03.043

ClinicalTrials.gov. (2019). Available online at: https://clinicaltrials.gov/ (accessed July 27, 2019).

Dalheim, M. Ø., Vanacker, J., Najmi, M. A., Aachmann, F. L., Strand, B. L., and Christensen, B. E. (2016). Efficient functionalization of alginate biomaterials. *Biomaterials* 80, 146–156. doi: 10.1016/j.biomaterials.2015.11.043

Desai, R. M., Koshy, S. T., Hilderbrand, S. A., Mooney, D. J., and Joshi, N. S. (2015). Versatile click alginate hydrogels crosslinked via tetrazine-norbornene chemistry. *Biomaterials* 50, 30–37. doi: 10.1016/j.biomaterials.2015.01.048

Draget, K. I., Skjåk Bræk, G., and Smidsrød, O. (1994). Alginic acid gels: the effect of alginate chemical composition and molecular weight. *Carbohyd. Polym.* 25, 31–38. doi: 10.1016/0144-8617(94)90159-7

Dusseault, J., Tam, S. K., Menard, M., Polizu, S., Jourdan, G., Yahia, L., et al. (2006). Evaluation of alginate purification methods: effect on polyphenol, endotoxin, and protein contamination. *J. Biomed. Mater. Res. A* 76, 243–251. doi: 10.1002/jbm.a.30541

El Khoury, D., Goff, H. D., Berengut, S., Kubant, R., and Anderson, G. H. (2014). Effect of sodium alginate addition to chocolate milk on glycemia, insulin, appetite and food intake in healthy adult men. *Eur. J. Clin. Nutr.* 68, 613–618. doi: 10.1038/ejcn.2014.53

Farrell, D. H., and Al-Mondhiry, H. A. (1997). Human fibroblast adhesion to fibrinogen. *Biochemistry* 36, 1123–1128. doi: 10.1021/bi962446r

Fernández Farrés, I., and Norton, I. T. (2014). Formation kinetics and rheology of alginate fluid gels produced by *in-situ* calcium release. *Food Hydrocoll.* 40, 76–84. doi: 10.1016/j.foodhyd.2014.02.005

Ferris, C. J., Stevens, L. R., Gilmore, K. J., Mume, E., Greguric, I., Kirchmajer, D. M., et al. (2015). Peptide modification of purified gellan gum. *J. Mater. Chem. B* 3, 1106–1115. doi: 10.1039/C4TB01727G

Fonseca, K. B., Bidarra, S. J., Oliveira, M. J., Granja, P. L., and Barrias, C. C. (2011). Molecularly designed alginate hydrogels susceptible to local proteolysis as three-dimensional cellular microenvironments. *Acta Biomater.* 7, 1674–1682. doi: 10.1016/j.actbio.2010.12.029

Fonseca, K. B., Gomes, D. B., Lee, K., Santos, S. G., Sousa, A., Silva, E. A., et al. (2014a). Injectable MMP-Sensitive alginate hydrogels as hMSC delivery systems. *Biomacromolecules* 15, 380–390. doi: 10.1021/bm4016495

Fonseca, K. B., Granja, P. L., and Barrias, C. C. (2014b). Engineering proteolytically-degradable artificial extracellular matrices. *Progr. Polym. Sci.* 39, 2010–2029. doi: 10.1016/j.progpolymsci.2014.07.003

Fonseca, K. B., Maia, F. R., Cruz, F. A., Andrade, D., Juliano, M. A., Granja, P. L., et al. (2013). Enzymatic, physicochemical and biological properties of MMP-sensitive alginate hydrogels. *Soft Matter.* 9:3283. doi: 10.1039/c3sm27560d

Formo, K., Cho, C. H., Vallier, L., and Strand, B. L. (2015). Culture of hESC-derived pancreatic progenitors in alginate-based scaffolds. *J. Biomed. Mater. Res. A* 103, 3717–3726. doi: 10.1002/jbm.a.35507

Ganesh, N., Hanna, C., Nair, S. V., and Nair, L. S. (2013). Enzymatically cross-linked alginic-hyaluronic acid composite hydrogels as cell delivery vehicles. *Int. J. Biol. Macromol.* 55, 289–294. doi: 10.1016/j.ijbiomac.2012.12.045

Garcia-Astrain, C., and Averous, L. (2018). Synthesis and evaluation of functional alginate hydrogels based on click chemistry for drug delivery applications. *Carbohydr. Polym.* 190, 271–280. doi: 10.1016/j.carbpol.2018.02.086

Gillette, B. M., Jensen, J. A., Wang, M., Tchao, J., and Sia, S. K. (2010). Dynamic hydrogels: switching of 3D microenvironments using two-component naturally derived extracellular matrices. *Adv. Mater.* 22, 686–691. doi: 10.1002/adma.200902265

Grant, G. T., Morris, E. R., Rees, D. A., Smith, P. J. C., and Thom, D. (1973). Biological interactions between polysaccharides and divalent cations: the egg-box model. *FEBS Lett.* 32, 195–198. doi: 10.1016/0014-5793(73)80770-7

Han, Y., Li, Y., Zeng, Q., Li, H., Peng, J., Xu, Y., et al. (2017). Injectable bioactive akermanite/alginate composite hydrogels for *in situ* skin tissue engineering. *J. Mater. Chem. B* 5, 3315–3326. doi: 10.1039/C7TB00571G

Harper, B. A., Barbut, S., Lim, L. T., and Marcone, M. F. (2014). Effect of various gelling cations on the physical properties of "wet" alginate films. *J. Food Sci.* 79, E562–567. doi: 10.1111/1750-3841.12376

Haug, A., and Larsen, B. (1966). "A study on the constitution of alginic acid by partial hydrolysis," in *Proceedings of the Fifth International Seaweed Symposium, Halifax,* eds E. G. Young and J. L. Mclachlan (Pergamon), 271–277. doi: 10.1016/B978-0-08-011841-3.50043-4

Hayoun-Neeman, D., Korover, N., Etzion, S., Ofir, R., Lichtenstein, R. G., and Cohen, S. (2019). Exploring peptide-functionalized alginate scaffolds for engineering cardiac tissue from human embryonic stem cell-derived cardiomyocytes in serum-free medium. *Polym. Adv. Technol.* 30, 2493–2505. doi: 10.1002/pat.4602

Heo, E. Y., Ko, N. R., Bae, M. S., Lee, S. J., Choi, B.-J., Kim, J. H., et al. (2017). Novel 3D printed alginate–BFP1 hybrid scaffolds for enhanced bone regeneration. *J. Ind. Eng. Chem.* 45, 61–67. doi: 10.1016/j.jiec.2016.09.003

Hou, J., Li, C., Guan, Y., Zhang, Y., and Zhu, X. X. (2015). Enzymatically crosslinked alginate hydrogels with improved adhesion properties. *Polym. Chem.* 6, 2204–2213. doi: 10.1039/C4PY01757A

Huebsch, N., Arany, P. R., Mao, A. S., Shvartsman, D., Ali, O. A., Bencherif, S. A., et al. (2010). Harnessing traction-mediated manipulation of the cell/matrix interface to control stem-cell fate. *Nat. Mater.* 9, 518–526. doi: 10.1038/nmat2732

Ismail, H. A., Mahross, H. Z., and Shikho, S. (2017). Evaluation of dimensional accuracy for different complete edentulous impressions immersed in different disinfectant solutions. *Eur. J. Dent.* 11, 242–249. doi: 10.4103/ejd.ejd_268_16

Jensen, H. M., Larsen, F. H., and Engelsen, S. B. (2015). Characterization of alginates by nuclear magnetic resonance (NMR) and vibrational spectroscopy (IR, NIR, Raman) in combination with chemometrics. *Methods Mol. Biol.* 1308, 347–363. doi: 10.1007/978-1-4939-2684-8_22

Jeon, O., Samorezov, J. E., and Alsberg, E. (2014). Single and dual crosslinked oxidized methacrylated alginate/PEG hydrogels for bioadhesive applications. *Acta Biomater.* 10, 47–55. doi: 10.1016/j.actbio.2013.09.004

Jin, G. Z., and Kim, H. W. (2018). Efficacy of collagen and alginate hydrogels for the prevention of rat chondrocyte dedifferentiation. *J. Tissue Eng.* 9:2041731418802438. doi: 10.1177/2041731418802438

Jose, S., Hughbanks, M. L., Binder, B. Y., Ingavle, G. C., and Leach, J. K. (2014). Enhanced trophic factor secretion by mesenchymal stem/stromal cells with glycine-histidine-lysine (GHK)-modified alginate hydrogels. *Acta Biomater.* 10, 1955–1964. doi: 10.1016/j.actbio.2014.01.020

Joyce, M. H., Lu, C., James, E. R., Hegab, R., Allen, S. C., Suggs, L. J., et al. (2018). Phenotypic basis for matrix stiffness-dependent chemoresistance of breast cancer cells to doxorubicin. *Front. Oncol.* 8:337. doi: 10.3389/fonc.2018.00337

Kerschenmeyer, A., Arlov, O., Malheiro, V., Steinwachs, M., Rottmar, M., Maniura-Weber, K., et al. (2017). Anti-oxidant and immune-modulatory properties of sulfated alginate derivatives on human chondrocytes and macrophages. *Biomater. Sci.* 5, 1756–1765. doi: 10.1039/C7BM00341B

Klontzas, M. E., Reakasame, S., Silva, R., Morais, J. C. F., Vernardis, S., Macfarlane, R. J., et al. (2019). Oxidized alginate hydrogels with the GHK peptide enhance cord blood mesenchymal stem cell osteogenesis: a paradigm for metabolomics-based evaluation of biomaterial design. *Acta Biomater.* 88, 224–240. doi: 10.1016/j.actbio.2019.02.017

Kohn, R. (1975). Ion binding on polyuronates - alginate and pectin. *Pure Appl. Chem.* 42:371. doi: 10.1351/pac197542030371

Kondaveeti, S., Bueno, P. V. A., Carmona-Ribeiro, A. M., Esposito, F., Lincopan, N., Sierakowski, M. R., et al. (2018). Microbicidal gentamicin-alginate hydrogels. *Carbohydr. Polym.* 186, 159–167. doi: 10.1016/j.carbpol.2018.01.044

Kong, H. J., Polte, T. R., Alsberg, E., and Mooney, D. J. (2005). FRET measurements of cell-traction forces and nano-scale clustering of adhesion ligands varied by substrate stiffness. *Proc. Natl. Acad. Sci. U.S.A.* 102, 4300–4305. doi: 10.1073/pnas.0405873102

Krishnan, R., Ko, D., Foster, C. E. 3rd, Liu, W., Smink, A. M., De Haan, B., De Vos, P., et al. (2017). Immunological challenges facing translation of alginate encapsulated porcine islet xenotransplantation to human clinical trials. *Methods Mol. Biol.* 1479, 305–333. doi: 10.1007/978-1-4939-6364-5_24

Kudva, A. K., Luyten, F. P., and Patterson, J. (2018). RGD-functionalized polyethylene glycol hydrogels support proliferation and *in vitro* chondrogenesis of human periosteum-derived cells. *J. Biomed. Mater. Res. A* 106, 33–42. doi: 10.1002/jbm.a.36208

Kuo, C. K., and Ma, P. X. (2001). Ionically crosslinked alginate hydrogels as scaffolds for tissue engineering: Part 1. Structure, gelation rate and mechanical properties. *Biomaterials* 22, 511–521. doi: 10.1016/S0142-9612(00)00201-5

Lee, H. P., Gu, L., Mooney, D. J., Levenston, M. E., and Chaudhuri, O. (2017). Mechanical confinement regulates cartilage matrix formation by chondrocytes. *Nat. Mater.* 16, 1243–1251. doi: 10.1038/nmat4993

Lee, J., Abdeen, A. A., Zhang, D., and Kilian, K. A. (2013). Directing stem cell fate on hydrogel substrates by controlling cell geometry, matrix mechanics and adhesion ligand composition. *Biomaterials* 34, 8140–8148. doi: 10.1016/j.biomaterials.2013.07.074

Lee, J. W., An, H., and Lee, K. Y. (2017). Introduction of N-cadherin-binding motif to alginate hydrogels for controlled stem cell differentiation. *Colloids Surf B Biointerfaces* 155, 229–237. doi: 10.1016/j.colsurfb.2017.04.014

Lee, J. W., Kim, H., and Lee, K. Y. (2016). Effect of spacer arm length between adhesion ligand and alginate hydrogel on stem cell differentiation. *Carbohydr. Polym.* 139, 82–89. doi: 10.1016/j.carbpol.2015.12.024

Lee, J. W., and Lee, K. Y. (2017). Dual peptide-presenting hydrogels for controlling the phenotype of PC12 cells. *Colloids Surf B Biointerfaces* 152, 36–41. doi: 10.1016/j.colsurfb.2017.01.001

Lee, J. W., Park, Y. J., Lee, S. J., Lee, S. K., and Lee, K. Y. (2010). The effect of spacer arm length of an adhesion ligand coupled to an alginate gel on the control of fibroblast phenotype. *Biomaterials* 31, 5545–5551. doi: 10.1016/j.biomaterials.2010.03.063

Lee, K. Y., and Mooney, D. J. (2012). Alginate: properties and biomedical applications. *Prog. Polym. Sci.* 37, 106–126. doi: 10.1016/j.progpolymsci.2011.06.003

Lee, R. J., Hinson, A., Bauernschmitt, R., Matschke, K., Fang, Q., Mann, D. L., et al. (2015). The feasibility and safety of Algisyl-LVR$^{TM}$ as a method of left ventricular augmentation in patients with dilated cardiomyopathy: initial first in man clinical results. *Int. J. Cardiol.* 199, 18–24. doi: 10.1016/j.ijcard.2015.06.111

Liao, J., Wang, B., Huang, Y., Qu, Y., Peng, J., and Qian, Z. (2017). Injectable alginate hydrogel cross-linked by calcium gluconate-loaded porous microspheres for cartilage tissue engineering. *ACS Omega* 2, 443–454. doi: 10.1021/acsomega.6b00495

Liu, H., Zhou, H., Lan, H., Liu, T., Liu, X., and Yu, H. (2017). 3D Printing of artificial blood vessel: study on multi-parameter optimization design for vascular molding effect in alginate and gelatin. *Micromachines* 8:237. doi: 10.3390/mi8080237

Liu, Q., Huang, Y., Lan, Y., Zuo, Q., Li, C., Zhang, Y., et al. (2017). Acceleration of skin regeneration in full-thickness burns by incorporation of bFGF-loaded alginate microspheres into a CMCS-PVA hydrogel. *J. Tissue Eng. Regen. Med.* 11, 1562–1573. doi: 10.1002/term.2057

Liu, S., Kang, M., Li, K., Yao, F., Oderinde, O., Fu, G., et al. (2018). Polysaccharide-templated preparation of mechanically-tough, conductive and self-healing hydrogels. *Chem. Eng. J.* 334, 2222–2230. doi: 10.1016/j.cej.2017.11.103

Living Cell Technologies (2019). Available online at: http://www.lctglobal.com (accessed July 20, 2019).

Lou, J., Stowers, R., Nam, S., Xia, Y., and Chaudhuri, O. (2018). Stress relaxing hyaluronic acid-collagen hydrogels promote cell spreading, fiber remodeling, and focal adhesion formation in 3D cell culture. *Biomaterials* 154, 213–222. doi: 10.1016/j.biomaterials.2017.11.004

Lueckgen, A., Garske, D. S., Ellinghaus, A., Mooney, D. J., Duda, G. N., and Cipitria, A. (2019). Enzymatically-degradable alginate hydrogels promote cell spreading and *in vivo* tissue infiltration. *Biomaterials* 217:119294. doi: 10.1016/j.biomaterials.2019.119294

Luo, Y., Li, Y., Qin, X., and Wa, Q. (2018). 3D printing of concentrated alginate/gelatin scaffolds with homogeneous nano apatite coating for bone tissue engineering. *Mater. Des.* 146, 12–19. doi: 10.1016/j.matdes.2018.03.002

Luo, Z., Yang, Y., Deng, Y., Sun, Y., Yang, H., and Wei, S. (2016). Peptide-incorporated 3D porous alginate scaffolds with enhanced osteogenesis for bone tissue engineering. *Colloids Surf B Biointerfaces* 143, 243–251. doi: 10.1016/j.colsurfb.2016.03.047

Luo, Z., Zhang, S., Pan, J., Shi, R., Liu, H., Lyu, Y., et al. (2018). Time-responsive osteogenic niche of stem cells: a sequentially triggered, dual-peptide loaded, alginate hybrid system for promoting cell activity and osteo-differentiation. *Biomaterials* 163, 25–42. doi: 10.1016/j.biomaterials.2018.02.025

Lupo, B., Maestro, A., Gutiérrez, J. M., and González, C. (2015). Characterization of alginate beads with encapsulated cocoa extract to prepare functional food: comparison of two gelation mechanisms. *Food Hydrocoll.* 49, 25–34. doi: 10.1016/j.foodhyd.2015.02.023

Madl, C. M., Mehta, M., Duda, G. N., Heilshorn, S. C., and Mooney, D. J. (2014). Presentation of BMP-2 mimicking peptides in 3D hydrogels directs cell fate commitment in osteoblasts and mesenchymal stem cells. *Biomacromolecules* 15, 445–455. doi: 10.1021/bm401726u

Maia, F. R., Barbosa, M., Gomes, D. B., Vale, N., Gomes, P., Granja, P. L., et al. (2014a). Hydrogel depots for local co-delivery of osteoinductive peptides and mesenchymal stem cells. *J. Control Release* 189, 158–168. doi: 10.1016/j.jconrel.2014.06.030

Maia, F. R., Fonseca, K. B., Rodrigues, G., Granja, P. L., and Barrias, C. C. (2014b). Matrix-driven formation of mesenchymal stem cell-extracellular matrix microtissues on soft alginate hydrogels. *Acta Biomater.* 10, 3197–3208. doi: 10.1016/j.actbio.2014.02.049

Maia, F. R., Lourenco, A. H., Granja, P. L., Goncalves, R. M., and Barrias, C. C. (2014c). Effect of cell density on mesenchymal stem cells aggregation in RGD-alginate 3D matrices under osteoinductive conditions. *Macromol. Biosci.* 14, 759–771. doi: 10.1002/mabi.201300567

Maleki, L., Edlund, U., and Albertsson, A. C. (2015). Thiolated hemicellulose as a versatile platform for one-pot click-type hydrogel synthesis. *Biomacromolecules* 16, 667–674. doi: 10.1021/bm5018468

Mao, A. S., Shin, J. W., and Mooney, D. J. (2016). Effects of substrate stiffness and cell-cell contact on mesenchymal stem cell differentiation. *Biomaterials* 98, 184–191. doi: 10.1016/j.biomaterials.2016.05.004

Matsumoto, S., Abalovich, A., Wechsler, C., Wynyard, S., and Elliott, R. B. (2016). Clinical benefit of islet xenotransplantation for the treatment of type 1 diabetes. *EBioMedicine* 12, 255–262. doi: 10.1016/j.ebiom.2016.08.034

Misra, S., Hascall, V. C., Markwald, R. R., and Ghatak, S. (2015). Interactions between hyaluronan and its receptors (CD44, RHAMM) regulate the activities of inflammation and cancer. *Front. Immunol.* 6:201. doi: 10.3389/fimmu.2015.00201

Moe, S. T., Draget, K. I., Skjåk-Bræk, G., and Simdsrød, O. (1992). Temperature dependence of the elastic modulus of alginate gels. *Carbohydr. Polym.* 19, 279–284. doi: 10.1016/0144-8617(92)90081-Z

Mohan, V., Das, A., and Sagi, I. (2020). Emerging roles of ECM remodeling processes in cancer. *Semin. Cancer Biol.* 62, 192–200. doi: 10.1016/j.semcancer.2019.09.004

Morch, Y. A., Donati, I., Strand, B. L., and Skjak-Braek, G. (2006). Effect of Ca2+, Ba2+, and Sr2+ on alginate microbeads. *Biomacromolecules* 7, 1471–1480. doi: 10.1021/bm060010d

Morra, M., and Cassineli, C. (1999). Non-fouling properties of polysaccharide-coated surfaces. *J. Biomater. Sci. Polym. Ed.* 10, 1107–1124. doi: 10.1163/156856299X00711

Munarin, F., Guerreiro, S. G., Grellier, M. A., Tanzi, M. C., Barbosa, M. A., Petrini, P., et al. (2011). Pectin-based injectable biomaterials for bone tissue engineering. *Biomacromolecules* 12, 568–577. doi: 10.1021/bm101110x

Munarin, F., Petrini, P., Tanzi, M. C., Barbosa, M. A., and Granja, P. L. (2012). Biofunctional chemically modified pectin for cell delivery. *Soft Matter.* 8:4731. doi: 10.1039/c2sm07260b

Nair, D. P., Podgórski, M., Chatani, S., Gong, T., Xi, W., Fenoli, C. R., et al. (2014). The thiol-michael addition click reaction: a powerful and widely used tool in materials chemistry. *Chem. Mater.* 26, 724–744. doi: 10.1021/cm402180t

Nakaoka, R., Hirano, Y., Mooney, D. J., Tsuchiya, T., and Matsuoka, A. (2013). Study on the potential of RGD- and PHSRN-modified alginates as artificial extracellular matrices for engineering bone. *J. Artif. Organs.* 16, 284–293. doi: 10.1007/s10047-013-0703-7

Nam, S., Stowers, R., Lou, J., Xia, Y., and Chaudhuri, O. (2019). Varying PEG density to control stress relaxation in alginate-PEG hydrogels for 3D cell culture studies. *Biomaterials* 200, 15–24. doi: 10.1016/j.biomaterials.2019.02.004

Neve, A., Cantatore, F. P., Maruotti, N., Corrado, A., and Ribatti, D. (2014). Extracellular matrix modulates angiogenesis in physiological and pathological conditions. *BioMed. Res. Int.* 2014, 756078–756078. doi: 10.1155/2014/756078

Neves, S. C., Gomes, D. B., Sousa, A., Bidarra, S. J., Petrini, P., Moroni, L., et al. (2015). Biofunctionalized pectin hydrogels as 3D cellular microenvironments. *J. Mater. Chem. B* 3, 2096–2108. doi: 10.1039/C4TB00885E

Nieberler, M., Reuning, U., Reichart, F., Notni, J., Wester, H. J., Schwaiger, M., et al. (2017). Exploring the role of RGD-recognizing integrins in cancer. *Cancers (Basel).* 9:116. doi: 10.3390/cancers9090116

Ochbaum, G., and Bitton, R. (2017). Effect of peptide self-assembly on the rheological properties of alginate-peptide conjugates solutions. *Polymer* 108, 87–96. doi: 10.1016/j.polymer.2016.11.048

Oki, Y., Kirita, K., Ohta, S., Ohba, S., Horiguchi, I., Sakai, Y., et al. (2019). Switching of cell proliferation/differentiation in thiol-maleimide clickable microcapsules triggered by *in situ* conjugation of biomimetic peptides. *Biomacromolecules* 20, 2350–2359. doi: 10.1021/acs.biomac.9b00333

Ooi, H. W., Mota, C., Ten Cate, A. T., Calore, A., Moroni, L., and Baker, M. B. (2018). Thiol-ene alginate hydrogels as versatile bioinks for bioprinting. *Biomacromolecules* 19, 3390–3400. doi: 10.1021/acs.biomac.8b00696

Park, J. S., Chu, J. S., Tsou, A. D., Diop, R., Tang, Z., Wang, A., et al. (2011). The effect of matrix stiffness on the differentiation of mesenchymal stem cells in response to TGF-β. *Biomaterials* 32, 3921–3930. doi: 10.1016/j.biomaterials.2011.02.019

Patterson, J., and Hubbell, J. A. (2010). Enhanced proteolytic degradation of molecularly engineered PEG hydrogels in response to MMP-1 and MMP-2. *Biomaterials* 31, 7836–7845. doi: 10.1016/j.biomaterials.2010.06.061

Pei, M., Jia, X., Zhao, X., Li, J., and Liu, P. (2018). Alginate-based cancer-associated, stimuli-driven and turn-on theranostic prodrug nanogel for cancer detection and treatment. *Carbohydr. Polym.* 183, 131–139. doi: 10.1016/j.carbpol.2017.12.013

Pereira, R. F., Barrias, C. C., Bartolo, P. J., and Granja, P. L. (2018b). Cell-instructive pectin hydrogels crosslinked via thiol-norbornene photo-click chemistry for skin tissue engineering. *Acta Biomater.* 66, 282–293. doi: 10.1016/j.actbio.2017.11.016

Pereira, R. F., Sousa, A., Barrias, C. C., Bártolo, P. J., and Granja, P. L. (2018). A single-component hydrogel bioink for bioprinting of bioengineered 3D constructs for dermal tissue engineering. *Mater. Horiz.* 5, 1100–1111. doi: 10.1039/C8MH00525G

Pierschbacher, M. D., and Ruoslahti, E. (1984). Cell attachment activity of fibronectin can be duplicated by small synthetic fragments of the molecule. *Nature* 309, 30–33. doi: 10.1038/309030a0

Qin, Y., Jiang, J., Zhao, L., Zhang, J., and Wang, F. (2018). "Chapter 13 - Applications of alginate as a functional food ingredient," in *Biopolymers for Food Design,* eds A. M. Grumezescu and A. M. Holban (London: Academic Press), 409–429. doi: 10.1016/B978-0-12-811449-0.00013-X

Reyes-Avalos, M. C., Minjares-Fuentes, R., Femenia, A., Contreras-Esquivel, J. C., Quintero-Ramos, A., Esparza-Rivera, J. R., et al. (2019). Application of an alginate–chitosan edible film on figs (ficus carica): effect on bioactive compounds and antioxidant capacity. *Food Bioprocess Technol.* 12, 499–511. doi: 10.1007/s11947-018-2226-y

Rhein-Knudsen, N., Ale, M. T., Ajallouеian, F., and Meyer, A. S. (2017). Characterization of alginates from Ghanaian brown seaweeds: *Sargassum* spp. and *Padina* spp. *Food Hydrocoll.* 71, 236–244. doi: 10.1016/j.foodhyd.2017.05.016

Riahi, N., Liberelle, B., Henry, O., and De Crescenzo, G. (2017). Impact of RGD amount in dextran-based hydrogels for cell delivery. *Carbohydr. Polym.* 161, 219–227. doi: 10.1016/j.carbpol.2017.01.002

Rinaudo, M. (2011). New amphiphilic grafted copolymers based on polysaccharides. *Carbohydr. Polym.* 83, 1338–1344. doi: 10.1016/j.carbpol.2010.09.054

Rossi, S., Mori, M., Vigani, B., Bonferoni, M. C., Sandri, G., Riva, F., et al. (2018). A novel dressing for the combined delivery of platelet lysate and vancomycin hydrochloride to chronic skin ulcers: hyaluronic acid particles in alginate matrices. *Eur. J. Pharm. Sci.* 118, 87–95. doi: 10.1016/j.ejps.2018.03.024

Rowley, J. A., Madlambayan, G., and Mooney, D. J. (1999). Alginate hydrogels as synthetic extracellular matrix materials. *Biomaterials* 20, 45–53. doi: 10.1016/S0142-9612(98)00107-0

Rowley, J. A., and Mooney, D. J. (2002). Alginate type and RGD density control myoblast phenotype. *J. Biomed. Mater. Res.* 60, 217–223. doi: 10.1002/jbm.1287

Sack, K. L., Aliotta, E., Choy, J. S., Ennis, D. B., Davies, N. H., Franz, T., et al. (2018). Effect of intra-myocardial Algisyl-LVR$^{TM}$ injectates on fibre structure in porcine heart failure. *J. Mech. Behav. Biomed. Mater.* 87, 172–179. doi: 10.1016/j.jmbbm.2018.07.005

Samorezov, J. E., Morlock, C. M., and Alsberg, E. (2015). Dual ionic and photo-crosslinked alginate hydrogels for micropatterned spatial control of material properties and cell behavior. *Bioconjug. Chem.* 26, 1339–1347. doi: 10.1021/acs.bioconjchem.5b00117

Sapir, Y., Kryukov, O., and Cohen, S. (2011). Integration of multiple cell-matrix interactions into alginate scaffolds for promoting cardiac tissue regeneration. *Biomaterials* 32, 1838–1847. doi: 10.1016/j.biomaterials.2010.11.008

Sasaki, M., Kleinman, H. K., Huber, H., Deutzmann, R., and Yamada, Y. (1988). Laminin, a multidomain protein. The A chain has a unique globular domain and homology with the basement membrane proteoglycan and the laminin B chains. *J. Biol. Chem.* 263, 16536–16544.

Schwartz, M. A., and Assoian, R. K. (2001). Integrins and cell proliferation: regulation of cyclin-dependent kinases via cytoplasmic signaling pathways. *J. Cell. Sci.* 114, 2553–2560.

Senturk Parreidt, T., Muller, K., and Schmid, M. (2018). Alginate-based edible films and coatings for food packaging applications. *Foods* 7:170. doi: 10.3390/foods7100170

Shtenberg, Y., Goldfeder, M., Prinz, H., Shainsky, J., Ghantous, Y., Abu El-Naaj, I., et al. (2018). Mucoadhesive alginate pastes with embedded liposomes for local oral drug delivery. *Int. J. Biol. Macromol.* 111, 62–69. doi: 10.1016/j.ijbiomac.2017.12.137

Siew, C. K., Williams, P. A., and Young, N. W. G. (2005). New insights into the mechanism of gelation of alginate and pectin: charge annihilation and reversal mechanism. *Biomacromolecules* 6, 963–969. doi: 10.1021/bm049341l

Smith, K. E., Johnson, R. C., and Papas, K. K. (2018). Update on cellular encapsulation. *Xenotransplantation* 25: e12399. doi: 10.1111/xen.12399

Sondermeijer, H. P., Witkowski, P., Seki, T., Van Der Laarse, A., Itescu, S., and Hardy, M. A. (2018). RGDfK-peptide modified alginate scaffold for cell transplantation and cardiac neovascularization. *Tissue Eng. A* 24, 740–751. doi: 10.1089/ten.tea.2017.0221

Sondermeijer, H. P., Witkowski, P., Woodland, D., Seki, T., Aangenendt, F. J., Van Der Laarse, A., et al. (2016). Optimization of alginate purification using polyvinylidene difluoride membrane filtration: effects on immunogenicity and biocompatibility of three-dimensional alginate scaffolds. *J. Biomater. Appl.* 31, 510–520. doi: 10.1177/0885328216645952

Sreeram, K. J., Yamini Shrivastava, H., and Nair, B. U. (2004). Studies on the nature of interaction of iron(III) with alginates. *Biochim. Biophys. Acta* 1670, 121–125. doi: 10.1016/j.bbagen.2003.11.001

Stephan, S. B., Taber, A. M., Jileaeva, I., Pegues, E. P., Sentman, C. L., and Stephan, M. T. (2015). Biopolymer implants enhance the efficacy of adoptive T-cell therapy. *Nat. Biotechnol.* 33, 97–101. doi: 10.1038/nbt.3104

Stokke, B. T., Smidsroed, O., Bruheim, P., and Skjaak-Braek, G. (1991). Distribution of uronate residues in alginate chains in relation to alginate gelling properties. *Macromolecules* 24, 4637–4645. doi: 10.1021/ma00016a026

Stowers, R. S., Allen, S. C., Sanchez, K., Davis, C. L., Ebelt, N. D., Van Den Berg, C., et al. (2017). Extracellular matrix stiffening induces a malignant phenotypic transition in breast epithelial cells. *Cell. Mol. Bioeng.* 10, 114–123. doi: 10.1007/s12195-016-0468-1

Stowers, R. S., Allen, S. C., and Suggs, L. J. (2015). Dynamic phototuning of 3D hydrogel stiffness. *Proc. Natl. Acad. Sci. U.S.A.* 112, 1953–1958. doi: 10.1073/pnas.1421897112

Stowers, R. S., Shcherbina, A., Israeli, J., Gruber, J. J., Chang, J., Nam, S., et al. (2019). Matrix stiffness induces a tumorigenic phenotype in mammary epithelium through changes in chromatin accessibility. *Nat. Biomed. Eng.* 3, 1009–1019. doi: 10.1038/s41551-019-0420-5

Suzuki, Y., Tanihara, M., Suzuki, K., Saitou, A., Sufan, W., and Nishimura, Y. (2000). Alginate hydrogel linked with synthetic oligopeptide derived from BMP-2 allows ectopic osteoinduction *in vivo*. *J. Biomed. Mater. Res.* 50,

405–409. doi: 10.1002/(SICI)1097-4636(20000605)50:3<405::AID-JBM15>3.0.CO;2-Z

Tam, S. K., Dusseault, J., Polizu, S., Menard, M., Halle, J. P., and Yahia, L. (2006). Impact of residual contamination on the biofunctional properties of purified alginates used for cell encapsulation. *Biomaterials* 27, 1296–1305. doi: 10.1016/j.biomaterials.2005.08.027

Tong, X., and Yang, F. (2018). Recent progress in developing injectable matrices for enhancing cell delivery and tissue regeneration. *Adv. Healthcare Mater.* 7:e1701065. doi: 10.1002/adhm.201701065

Topuz, F., Henke, A., Richtering, W., and Groll, J. (2012). Magnesium ions and alginate do form hydrogels: a rheological study. *Soft Matter*. 8:4877. doi: 10.1039/c2sm07465f

Torres, A. L., Bidarra, S. J., Pinto, M. T., Aguiar, P. C., Silva, E. A., and Barrias, C. C. (2018). Guiding morphogenesis in cell-instructive microgels for therapeutic angiogenesis. *Biomaterials* 154, 34–47. doi: 10.1016/j.biomaterials.2017.10.051

Torres, A. L., Bidarra, S. J., Vasconcelos, D. P., Barbosa, J. N., Silva, E. A., Nascimento, D. S., et al. (2020). Microvascular engineering: dynamic changes in microgel-entrapped vascular cells correlates with higher vasculogenic/angiogenic potential. *Biomaterials* 228:119554. doi: 10.1016/j.biomaterials.2019.119554

Torres, M. L., Fernandez, J. M., Dellatorre, F. G., Cortizo, A. M., and Oberti, T. G. (2019). Purification of alginate improves its biocompatibility and eliminates cytotoxicity in matrix for bone tissue engineering. *Algal. Res.* 40:101499. doi: 10.1016/j.algal.2019.101499

Veitch, N. C. (2004). Horseradish peroxidase: a modern view of a classic enzyme. *Phytochemistry* 65, 249–259. doi: 10.1016/j.phytochem.2003.10.022

Wang, B., Wang, W., Yu, Y., Zhang, Y., Zhang, J., and Yuan, Z. (2017). The study of angiogenesis stimulated by multivalent peptide ligand-modified alginate. *Colloids Surf B Biointerfaces* 154, 383–390. doi: 10.1016/j.colsurfb.2017.03.049

Wang, L., Xu, M. E., Luo, L., Zhou, Y., and Si, P. (2018). Iterative feedback bio-printing-derived cell-laden hydrogel scaffolds with optimal geometrical fidelity and cellular controllability. *Sci. Rep.* 8:2802. doi: 10.1038/s41598-018-21274-4

Wang, N., Butler, J. P., and Ingber, D. E. (1993). Mechanotransduction across the cell surface and through the cytoskeleton. *Science* 260, 1124–1127. doi: 10.1126/science.7684161

Wang, X., Hao, T., Qu, J., Wang, C., and Chen, H. (2015). Synthesis of thermal polymerizable alginate-GMA hydrogel for cell encapsulation. *J. Nanomater.* 2015, 1–8. doi: 10.1155/2015/412071

Westhaus, E., and Messersmith, P. B. (2001). Triggered release of calcium from lipid vesicles: a bioinspired strategy for rapid gelation of polysaccharide and protein hydrogels. *Biomaterials* 22, 453–462. doi: 10.1016/S0142-9612(00)00200-3

Xue, M., and Jackson, C. J. (2015). Extracellular matrix reorganization during wound healing and its impact on abnormal scarring. *Adv. Wound. Care* 4, 119–136. doi: 10.1089/wound.2013.0485

Yang, Y., Luo, Z., and Zhao, Y. (2018). Osteostimulation scaffolds of stem cells: BMP-7-derived peptide-decorated alginate porous scaffolds promote the aggregation and osteo-differentiation of human mesenchymal stem cells. *Biopolymers* 109:e23223. doi: 10.1002/bip.23223

Ye, F., Astete, C. E., and Sabliov, C. M. (2017). Entrapment and delivery of α-tocopherol by a self-assembled, alginate-conjugated prodrug nanostructure. *Food Hydrocoll.* 72, 62–72. doi: 10.1016/j.foodhyd.2017.05.032

Yeung, T., Georges, P. C., Flanagan, L. A., Marg, B., Ortiz, M., Funaki, M., et al. (2005). Effects of substrate stiffness on cell morphology, cytoskeletal structure, and adhesion. *Cell. Motil. Cytoskeleton.* 60, 24–34. doi: 10.1002/cm.20041

Yu, M., Ji, Y., Qi, Z., Cui, D., Xin, G., Wang, B., et al. (2017). Anti-tumor activity of sulfated polysaccharides from Sargassum fusiforme. *Saudi. Pharm. J.* 25, 464–468. doi: 10.1016/j.jsps.2017.04.007

Zeyang, L., Minmin, L., Masaru, T., Tao, Y., Yasuhisa, H., Qiang, H., et al. (2018). *In vitro* mimicking the morphology of hepatic lobule tissue based on Ca-alginate cell sheets. *Biomed. Mater.* 13:035004. doi: 10.1088/1748-605X/aaa4c4

Zhao, N., Battig, M. R., Xu, M., Wang, X., Xiong, N., and Wang, Y. (2017). Development of a dual-functional hydrogel using RGD and anti-VEGF aptamer. *Macromol. Biosci.* 17:1700201. doi: 10.1002/mabi.201700201

Zhao, X., Huebsch, N., Mooney, D. J., and Suo, Z. (2010). Stress-relaxation behavior in gels with ionic and covalent crosslinks. *J. Appl. Phys.* 107:63509. doi: 10.1063/1.3343265

**Conflict of Interest:** The authors declare that the research was conducted in the absence of any commercial or financial relationships that could be construed as a potential conflict of interest.

frontiers in Bioengineering and Biotechnology

BRIEF RESEARCH REPORT
published: 07 July 2020
doi: 10.3389/fbioe.2020.00587

# *In vivo* Regeneration of Mineralized Bone Tissue in Anisotropic Biomimetic Sponges

*Janeth Serrano-Bello[1], Iriczalli Cruz-Maya[1,2], Fernando Suaste-Olmos[3], Patricia González-Alva[1], Rosaria Altobelli[4], Luigi Ambrosio[2], Luis Alberto Medina[5,6], Vincenzo Guarino[2]* and Marco Antonio Alvarez-Perez[1]**

[1] Tissue Bioengineering Laboratory, Postgraduate Studies and Research Division, Faculty of Dentistry, National Autonomous University of Mexico, Mexico City, Mexico, [2] Institute of Polymers, Composites, and Biomaterials, National Research Council of Italy, Naples, Italy, [3] Instituto de Fisiología Celular, Universidad Nacional Autónoma de México, Mexico City, Mexico, [4] Institute of Composite and Biomedical Materials, National Research Council of Italy, Naples, Italy, [5] Instituto de Física, Universidad Nacional Autónoma de México, Mexico City, Mexico, [6] Unidad de Investigación Biomédica en Cáncer, Instituto Nacional de Cancerología/Universidad Nacional Autónoma de México, Mexico City, Mexico

OPEN ACCESS

**Edited by:**
*Lorenzo Moroni,*
*Maastricht University, Netherlands*

**Reviewed by:**
*Ravi Sinha,*
*Maastricht University, Netherlands*
*Rajendra Kumar Singh,*
*Institute of Tissue Regeneration Engineering (ITREN), South Korea*

***Correspondence:**
*Vincenzo Guarino*
*vguarino@unina.it;*
*vincenzo.guarino@cnr.it*
*Marco Antonio Alvarez-Perez*
*marcoalv@unam.mx*

**Specialty section:**
*This article was submitted to Biomaterials, a section of the journal Frontiers in Bioengineering and Biotechnology*

**Received:** *22 February 2020*
**Accepted:** *14 May 2020*
**Published:** *07 July 2020*

**Citation:**
*Serrano-Bello J, Cruz-Maya I, Suaste-Olmos F, González-Alva P, Altobelli R, Ambrosio L, Medina LA, Guarino V and Alvarez-Perez MA (2020) In vivo Regeneration of Mineralized Bone Tissue in Anisotropic Biomimetic Sponges. Front. Bioeng. Biotechnol. 8:587. doi: 10.3389/fbioe.2020.00587*

In the last two decades, alginate scaffolds have been variously studied as extracellular matrix analogs for tissue engineering. However, relevant evidence is still lacking concerning their ability to mimic the microenvironment of hierarchical tissues such as bone. Hence, an increasing amount of attention has recently been devoted to the fabrication of macro/microporous sponges with pore anisotropy able to more accurately replicate the cell niche structure as a trigger for bioactive functionalities. This paper presents an *in vivo* study of alginate sponges with anisotropic microporous domains (MAS) formed by ionic crosslinking in the presence of different fractions (30 or 50% v) of hydroxyapatite (HA). In comparison with unloaded sponges (MAS0), we demonstrated that HA confers peculiar physical and biological properties to the sponge, depending upon the inorganic fraction used, enabling the sponge to bio-mimetically support the regeneration of newly formed bone. Scanning electron microscopy analysis showed a preferential orientation of pores, ascribable to the physical constraints exerted by HA particles during the pore network formation. Energy dispersive spectroscopy (EDS) and X-Ray diffraction (XRD) confirmed a chemical affinity of HA with the native mineral phase of the bone. *In vitro* studies via WST-1 assay showed good adhesion and proliferation of human Dental Pulp-Mesenchymal Stem Cells (hDP-MSC) that increased in the presence of the bioactive HA signals. Moreover, *in vivo* studies via micro-CT and histological analyses of a bone model (e.g., a rat calvaria defect) confirmed that the maximum osteogenic response after 90 days was achieved with MAS30, which supported good regeneration of the calvaria defect without any evidence of inflammatory reaction. Hence, all of the results suggested that MAS is a promising scaffold for supporting the regeneration of hard tissues in different body compartments.

**Keywords: alginate, hydroxyapatite, anisotropic structure, microporous sponges, hard tissues, *in vivo* models**

## INTRODUCTION

The ability to reproduce the complex hierarchal organization of a tissue architecture still represents one of the greatest challenges for the regeneration and repair of a broad range of damaged anisotropic tissues (Perez et al., 2018). It is well known that the absence of a porous hierarchical structure may represent a strong limitation for cells in terms of directional migration and spatial organization, consequently compromising morpho-functional integration (Zhu et al., 2019). For this reason, the extracellular matrix (ECM) of most human tissues naturally exhibits heterogeneous anisotropic domains that are characterized by the presence of pore gradients with some peculiar differences as a function of the specific bone tissue (Kang et al., 2018).

In the last two decades, the efficient use of anisotropic porous scaffolds has been largely validated in bone surgery, due to the opportunity to impart instructive functions to cells – by optimizing specific features of the materials (i.e., porosity, roughness, stiffness, biodegradation, fluid, and molecular transport) – able to synchronously guide the regeneration process, while the porous scaffold disappears in the local microenvironment (Guarino et al., 2012b). In this view, the gold standard is currently represented by composite scaffolds obtained by the combination of polymer and ceramic biomaterials, sagely processed to provide a well-defined pattern of physical and biochemical signals able to trigger the basic activities of progenitor cells toward a more efficient proliferation and cell differentiation (Funda et al., 2020). In this context, hydroxyapatite (HA), a calcium phosphate compound electively used in the pure formulation for bone repair (Mohd Pu'ad et al., 2019) due to the excellent physicochemical properties it derives from its monoclinic ($P2_1/b$) or hexagonal ($P6_3/m$) crystalline structure, and with a Ca/P molar ratio of 1.67 similar to human bone (Dong-Hyun et al., 2015), has been preferentially used in combination with biodegradable polymers [i.e., polylactic acid (PLA) and polycaprolactone (PCL)] for tissue engineering (Guarino et al., 2012a). Indeed, bioresorbable properties coupled with proved osteoconductive response make HA an ideal candidate for preventing any local or systemic toxicity, inflammation, or foreign response in host tissues (Guarino et al., 2014). Moreover, the use of formulations doped with specific chemical elements (i.e., Zn, and Mg) can promote direct chemical bonds with the adjacent natural bone tissue by assuring higher stability of crystals into the body fluids as the osteointegration mechanism goes on (Veronesi et al., 2015).

Taking into consideration the natural composition of the natural bone matrix – made of biologically recognized ceramics (i.e., hydroxyapatite) and bioactive proteins (i.e., collagen) – current interest is gradually addressing the design of scaffolds from naturally available sources. These scaffolds, based on polysaccharides (Dinoro et al., 2019), proteins (Yadav and Srivastava, 2019), and polyalkenoates (Elmowafy et al., 2019), show several biochemical affinities with biological macromolecules naturally present into the ECM and are, therefore, able to support a more efficient control of molecular transport, with relevant benefits for cell signaling at *in vivo* regeneration (Li et al., 2014; Ki et al., 2019). Among them, alginates represent one of the most interesting choices, being certified by the Food and Drug Administration (FDA) for tissue engineering due to their chemical similarity to ECM components, which ensures their excellent biocompatibility, immunological non-responsiveness (Li et al., 2015), and *in vivo* stability (Guarino et al., 2015). Alginate is an anionic polysaccharide derived from seaweed. It is composed of blocks of 1,4-linked β-D-mannuronate (M residues) and 1,4-linked α-L-guluronate (G residues) that can interact by different chemical/physical crosslinking methods [i.e., ionic interaction, free radical polymerization, or click reaction (Sun and Tan, 2013)] to form stable hydrogels with controlled porosity as a function of the reaction triggers (i.e., $Ca^{2+}$, $Ba^{2+}$, $Mg^{2+}$, $Fe^{2+}$, $Al^{3+}$, $La^{3+}$, $Pr^{3+}$, and $Nd^{3+}$; Zhang et al., 2017).

Accordingly, several works have investigated the biological validation of alginate scaffolds in combination with calcium phosphates in the form of HA (Suárez-González et al., 2010) or bioactive glasses (Haider et al., 2020) to develop bioactive scaffolds suitable for mimicking the mineralized ECM to promote *in vitro* cell differentiation or *in vivo* cell response in an osteogenic way (Jin et al., 2012; Singh et al., 2014). However, no studies have yet investigated the biological response in the presence of bioactive alginate scaffolds with an anisotropic structure.

Herein, we have proposed the fabrication of microporous alginate sponges (MAS) loaded with HA at loadings of 30% (MAS30) and 50% (MAS50) via ionic crosslinking. It was demonstrated that the addition of HA rigid phases influences the mechanism of phase transition during the sponge fabrication, thus inducing the formation of macro-domains with anisotropic properties – i.e., preferential orientation of pores into a single domain. In this study, the effect of this peculiar scaffold architecture on hDP-MSC behavior will be investigated, and long-term *in vivo* application on a bone defect model in calvaria of rats will be validated for mineralized tissue regeneration.

## MATERIALS AND METHODS

### Morphological Characterization

Microporous alginate sponges were prepared as reported elsewhere (Guarino et al., 2008). A brief description of the process is schematized in **Supplementary Figure S1**. Microporous alginate sponges morphology was investigated with scanning electron microscopy (SEM) in secondary electron mode using a field emission microscope (FESEM Quanta 200, FEI, Netherlands). Specimens were fractured in liquid nitrogen by using a razor blade along preferred directions parallel and perpendicular to the surface. The resulting transverse and longitudinal sections were gold-coated under a vacuum using an automatic coating sputter set at 15 mA for about 20 min (Emiscope SC500, Italy). Moreover, X-ray energy dispersive spectroscopy (EDS, Genesis 2000i) was used for qualitative mapping and quantitative analysis of chemical elements composing inorganic phases into the composite sponges.

## *In vitro* Biocompatibility of Microporous Alginate Sponges

To establish the effect of the peculiar MAS scaffold architecture on biocompatibility, human dental pulp stem cells (hDP-MSC) were used. Cells were maintained in α-MEM supplemented with 10% FBS and a solution of antibiotics (penicillin 100 IU/mL and streptomycin 100 μg/mL) at 37°C in a humidified atmosphere with 5% $CO_2$. Cellular biocompatibility was evaluated by analyzing two important processes: (1) cell adhesion and (2) cell viability of hDP-MSC by WST-1 assay. Briefly, cells were seeded at $1 \times 10^4$ cells/mL density in triplicate onto MAS0, MAS30, and MAS50. Cell adhesion was analyzed after 4 and 24 h of cell culture, and cell viability was evaluated after 2, 4, 6, and 8 days of culture. After the prescribed time period, substrates were rinsed three times with PBS to remove non-adherent cells and then incubated with 400 μL fresh culture medium containing 40 μL of the WST-1 solution for 4 h at 37°C. After the incubation time, 200 μL of the supernatant was placed in a 96-well plate, and the optical absorption was quantified by spectrophotometry at 450 nm with a plate reader (ChroMate, Awareness Technology, Palm City, FL, United States). Sponges without any presence of HA were used as control, and during the experimental viability time, the culture medium was changed every two days.

## *In vivo* Studies of the Osteogenic Capacity of Microporous Alginate Sponges

### Animal Model

To evaluate the osteogenic capacity potential of MAS0, MAS30, and MAS50, a calvaria rat model was used for preliminary *in vivo* studies. The animals used for the animal model were male, young-adults *Wistar* rats weighing 250 g. They were kept under laboratory conditions at a temperature of 22°C, with a photoperiod of 12 h and relative humidity at 50%, and with food and water *ad libitum*. All rats were sedated and tranquilized with ketamine (80 mg/kg) and Xylazine (10 mg/kg), intramuscularly, and then the calvaria surgical site was shaved, followed by routine antisepsis. Briefly, a 3-cm linear incision was made through the skin and the shell of the periosteum to expose the cranial vertex. The critical defect was created by using a trephine with a diameter of 9 mm mounted on a surgical engine at 4,000 rpm. A defect of standardized size was created on the middle portion of the frontal bone by using a chisel to cleave the bone fragment while irrigating with sterile phosphate buffer (PBS). This was done carefully to avoid damaging the dura, and the site was rinsed with sterile PBS to remove debris. Subsequently, four groups were randomly formed as follows: (1) MAS0, (2) MAS30, (3) MAS50, and (4) without the presence of any scaffold (NT). After that, Satin S-100 was applied to fix the scaffold to the defect and also to prevent the remaining periosteum from invading the defect area. The surgical site in all animal groups was closed with continuous 4-0 polyglycolic acid suture. Finally, the external surgical wound was cleaned with sterile PBS. All groups were clinically evaluated during the study period, considering the Grimace scale, changes in behavior, fur, and weight. The study was performed following the Mexican Legislation (NOM-062-ZOO-1999) and fulfilled all legal requirements of the Internal Committee for the Care and Use of Laboratory Animals of the Faculty of Medicine, UNAM, with approval number 027-CIC-2019. At the end of the *in vivo* studies, the animals were euthanized with carbon dioxide; the samples were fixed and processed for histological evaluation, obtaining serial sections 5 μm thick and stained with hematoxylin and eosin (H&E).

### Bone Assessment by μCT Images

*In vivo* studies of the rat calvaria were conducted under inhaled anesthesia (2% isoflurane/oxygen) at 8, 30, 60, and 90 days after surgery. Images were obtained with the micro-CT unit of an Albira small animal microPET/SPECT/CT imaging system (Bruker), using settings of a 0.4 mA current, 35 kV voltage, and a total of 1,000 projections over 360°. The field of view was located in the defect zone (calvaria). Image reconstruction was performed using the filtered back-projection algorithm (FBP) with Albira Reconstructor software, resulting in a 558 × 558 × 516 image matrix with voxel size 125 $\mu m^3$, for a total height of 64.5 mm. OsiriX MD software (Pixmeo SARL, 2019) was used for processing and visualization of 2D and 3D images.

The bone mineral density (BMD) was calculated from attenuation values using a linear model (density calibration) obtained from scans of a HA phantom (MicroMouse Phantom 090 CIRS, United States), following a procedure recommended by the manufacturer of the Albira scanner (Sasser et al., 2012). The BMD values were normalized to bone tissue adjacent to the defect and used as an indicator of the quality of regenerated bone in reference to healthy tissue. To evaluate the quantity of bone regeneration, 3D images were registering at different time points to determine the precise locations of bone formation or resorption. Briefly, for each sample, a region of interest (ROI), represented by the area of regenerated bone at the defect site, was manually drawn in each of the 280 cuts obtained from the micro-CT images. Then, to determine its volume, the results were normalized by the total volume of defect size. Only tomographic transverse views were used for this calculation.

### Histological Analysis

The scaffolds and the surrounding tissue were retrieved immediately after euthanasia and prepared for histological evaluation. In brief, tissue samples were thoroughly washed and fixed in 10% formalin for 24 h. Subsequently, the samples were demineralized in Evans and Krajian solution. Finally, samples were dehydrated in a series of alcohol solutions ranging from 50 to 100% and embedded in paraffin blocks. Embedded blocks were cut into serial sections (∼150 μm) and stained with H&E. Histological samples were qualitatively evaluated at various magnifications.

### Statistical Analysis

Cell biocompatibility data are presented as mean ± standard deviation ($n$ = 3). In the animal model, twenty-four male Wistar rats were used and randomly placed in four groups of six rats each. Data regarding the groups are presented as mean ± standard deviation ($n$ = 6). The sample size corresponds to the value of the standard deviation, with $Z\alpha$ ($Z$

of alpha) referring to the type I error (confidence level $\alpha = 0.05$ corresponding to a value of $Z = 1.96$) and $Z\beta$ (beta $Z$) with a power of 80% (value of $Z = 0.84$). Inter-group analysis of variance (ANOVA) was performed using the SPSS statistical analysis package (ver. 20) followed by *post hoc* test (Bonferroni) to make multiple comparisons between groups. A value of $p < 0.05$ was considered to determine statistically significant differences.

## RESULTS AND DISCUSSION

In bone surgery, the regeneration of a large bone defect after tumor isolation, trauma, or infection still represents a tremendously relevant clinical issue. To date, the use of osteoconductive materials such as HA embedded in porous polymer matrices had been identified as the most valid strategy for creating ECM analogs that replicate the morphological and/or chemical signals of the bone microenvironment and trigger *in vitro* functions of cells, i.e., migration, proliferation, and differentiation from progenitor cells (Kazem-Arki et al., 2018). In the last few years, several efforts have been addressed to optimizing easy-to-use processes with the required flexibility/versatility to mix different organic and inorganic biomaterials and generate porous networks with controlled porosity features at the micro-/submicro-scale. In this view, it has been demonstrated that low viscous sodium alginate (SA) can promote the formation of fully interconnected porous sponges with average pore sizes of around 100 μm (**Supplementary Figure S1**) that are suitable for supporting cell adhesion and proliferation (Thein-Han and Misra, 2009), as confirmed by preliminary studies. However, the ability to generate anisotropic pore patterns still remains one of the crucial points to really mimic the complex architecture of bony ECM because it allows morphological signals to be imparted to cells that are able to orchestrate – spatially and temporally – the regeneration and repair of the mineralized tissue (Ueon et al., 2010).

Herein, a consolidated and straightforward methodology was proposed to fabricate porous alginate sponges in agreement with previous studies (Haugh et al., 2010). In particular, the ion gelation mechanism was properly particularized in order to obtain a peculiar anisotropy of the three-dimensional pore network, mainly imparted by the presence of HA particles that stabilize the pore surfaces during the phase separation process. This was highlighted by the qualitative morphological study of alginate sponges with different HA volume fractions, MAS0, MAS30, and MAS50, respectively, which is extremely useful for investigating pore morphological features (**Figure 1**).

Certain HA fractions – 30 or 50%, respectively – were selected in order to partially mimic the natural composition of bone – i.e., the 30% organic matrix represented by type I collagen and 60% mineral phase, mainly HA crystals (Kolb and Bussard, 2019). In **Figure 1A**, SEM images of MAS30 and MAS50 clearly show the formation of macro-domains (see red arrows) in which the pores are organized in canaliform structures characterized by unidirectional orientation. This peculiar morphology of pores is strictly related to the preparation method used, which was based on the use of insulating molds and is able to trigger thermal flow gradients locally that give raise to the formation of oriented pores since the growth of ice crystals is confined into the single domain. Indeed, the growth of the ice crystals during the freeze-drying process follows the direction of thermal flow, and consequently, causes the pores to all be oriented in the same direction. This peculiar effect is strictly related to the presence of HA particles that – in consideration of their physical (e.g., rigidity) properties and geometry – offer a physical constraint to the growth of ice crystals. This effect is coupled with a general reduction in the pore size and the degree of interconnection as the HA content increases.

Accordingly, **Figure 1B** shows the pores at a higher magnification, revealing a homogeneous distribution of HA along the pore surfaces, with a tendency to form clusters at higher HA fractions. In the case of MAS30, this result was corroborated by the mapping of chemical elements via EDS analysis, which confirms the presence of apatites with a Ca/P ratio close to those of the native bone, with relevant benefits in terms of being an osteogenic interface for cells. More interestingly, macroscopically, MAS30 and MAS50 show a peculiar 3D lamellar architecture ascribable to the self-arrangement of pores with preferential orientations in macro-sized domains. This confers a peculiar anisotropic architecture to the sponges that positively influences the *in vivo* growth of the mineralized bone, in agreement with previous studies on similar alginate sponges with a controlled pore architecture (McMahon et al., 2013; Zhang et al., 2017; Kolb and Bussard, 2019).

Sponges were preliminarily investigated *in vitro* to evaluate the contribution of HA particles to adhesion and proliferation of hDP-MSC (**Figure 2**). The hDP-MSC cells adhered onto MAS pore surface scaffolds, independently of the HA content, as confirmed by there being no statistically significant differences after 4 and 24 h (**Figure 2A**). Cell viability was investigated at 2, 4, 6, and 8 days after seeding the hDP-MSC using WST-1 assay (**Figure 2B**). No difference in cell viability was detected in the cases of MAS30 and MAS50 at 2 days of cell culture in comparison with MAS0, which was used as a control. Contrariwise, an evident increase in cell viability was recognized after 4, 6, and 8 days in comparison with the control. Accordingly, viability assay demonstrated that all the sponge scaffolds are non-cytotoxic, also confirming the higher biocompatibility of MAS30 and MAS50 with respect to MAS0.

The capability to stimulate the recapitulation of mineralized ECM *in vivo* by the precipitation of mineral deposit calcification was explored for all of the samples via the rat calvaria defect model (Spicer et al., 2012). The different groups (MAS0, MAS30, MAS50, and the NT control group) were analyzed microtomographically at 8, 30, 60, and 90 days after surgery, and sequences of representative photographs of the groups at different time points were examined (**Figures 3A–D**). The NT group has a minimal region of regeneration in the defect area, i.e., the defect was still visible after 30 days, which increased in density but not in size at 60 and 90 days (**Figure 3A**). In the case of MAS0, 30 days after surgery, small trabeculae with variable density were recognized, mainly at the edges of the defect, and the response increased after 90 days (**Figure 3B**). The MAS30 group exhibited positive behavior since, from 8 days, the adaptation of

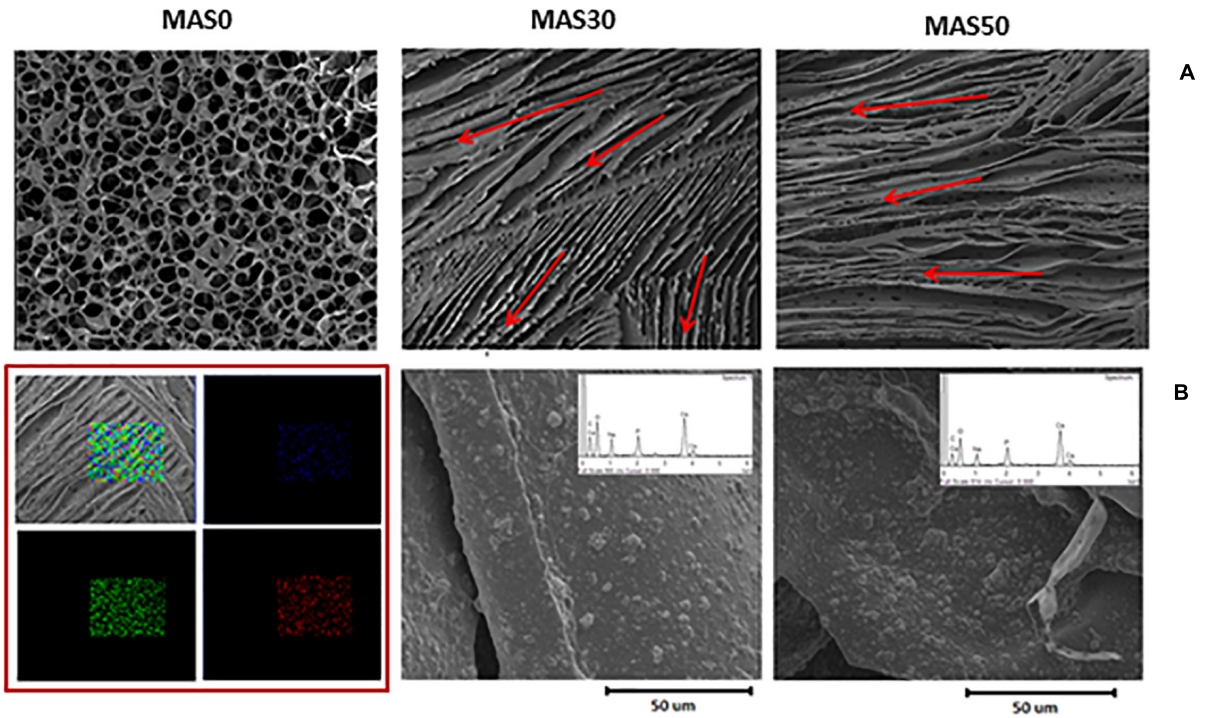


**FIGURE 1 |** Pore morphology of alginate porous sponges as a function of the HA volume fraction. **(A)** SEM images of sponge cross-sections (scale bar: 1 mm). Pores originated by the development of crystal domains with preferential orientation (see red arrows). This was determined by the presence of rigid HA phases that constrain the formation of pores to make them anisotropic. **(B)** SEM images of the pore surface to evaluate HA distribution. In the red square, EDS analysis and mapping for MAS30: the results confirmed the homogeneous elemental distribution along a portion of the surface -carbon (green), calcium (red), and phosphorus (blue).

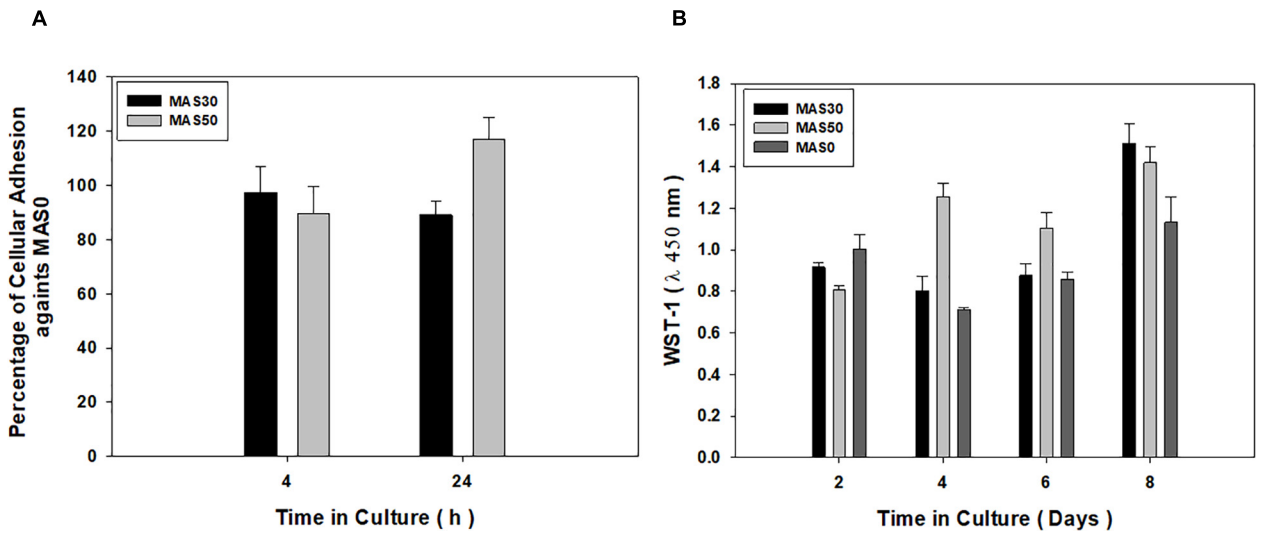


**FIGURE 2 |** *In vitro* biological response of hDP-MSC to MAS0, MAS30, and MAS50. **(A)** Cell adhesion at 4 and 24 h and **(B)** cell viability after 2, 4, 6, and 8 days of cell culture.

the sponge to the defect area can be clearly observed. At 30 days, areas of hyperdense tissue deposited around the defect could be distinguished. The border center had a more significant amount of hyperdense tissue, which decreased in the upper and lower parts of the defect. At 60 and 90 days, similar behavior could be observed on the mineral tissue deposit; however, the density of the area was enhanced (**Figure 3C**). The MAS50 group was observed after 8 days to show correct sealing of the sponge edges

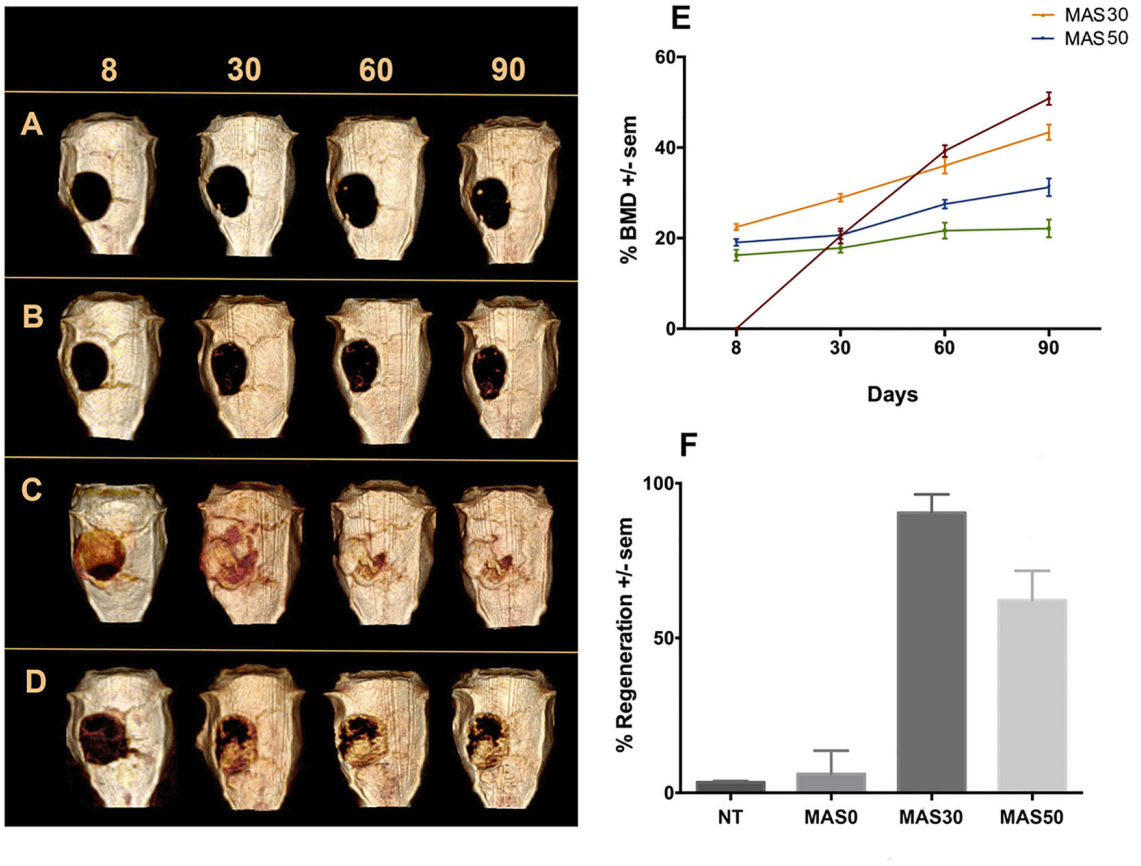


**FIGURE 3 | (A)** Sequence of micro-CT images of sponges after 8, 30, 60, and 90 days in the *in vivo* calvaria defect model. **(A)** No treatment (NT), **(B)** MAS0, **(C)** MAS30, and **(D)** MAS50. **(E)** Measurement of bone mineral density (BMD) after 8, 30, 60, and 90 days in the calvaria defect model. **(F)** Percentage of *in vivo* total bone regeneration after 90 days in the calvaria defect model.

to the defect, coupled with a limited mineral deposit. Moreover, after 30 to 90 days, an increased amount of mineral tissue had been deposited, with areas of variable density (**Figure 3D**).

The degree of mineralization in the defect area was evaluated by the percentage of BMD of the neo-formed tissue around the healthy adjacent bone at different periods of time of 8, 30, 60, and 90 days (**Figure 3E**). In the NT control group, the BMD was only quantified after 30 days, due to the limited size of the regenerated tissue (only at the edges of the defect). After 8 days, the BMD measured in the cases of MAS0 and MAS50 was comparable to the values measured after 30 days. At 30 days, it was equal to 20.47 ± 1.64% for the control, 17.78 ± 0.97% for MAS0, and 20.60 ± 0.88% for MAS50, without statistically significant differences, but, in the case of MAS30, the BMD value increased to 28.91 ± 0.86%, with statistical significance ($p = 0.05$) with respect to the other groups. At 60 days, BMD measured only near the periphery of the defect was 39.25 ± 1.28% for the control group and 36 ± 1.72% for MAS30, with the difference that the mineral tissue was more homogeneously distributed in the defect and onto the scaffold. By comparison, the values of the BDM percentage for MAS0 (21. 66 ± 1.73) and MAS50 (27.50 ± 0.94) were low. At 90 days, the lowest value of BMD was for MAS0, 22.12 ± 1.95, followed for MAS50 with a value of 31.23% ± 1.97. However, for MAS30, the BMD continued to increase homogeneously over the whole defect area with a value of 43.39 ± 1.69, in contrast to the control group, which presented a higher degree of mineralization (50.83% ± 1.37) but only in specific areas of the defect, with a statistically significant difference of $p = 0.0054$.

**Figure 3F** shows the analysis of the total regenerated volume of mineralized tissue deposited in the defect area, as calculated after 90 days. To obtain the value of the total volume, 280 image slices were measured in high-resolution microtomography, calculating the percentage of regeneration to the original size of the defect. For the NT control group, the percentage of regeneration was 3.43 ± 0.35%, which corresponds to the clusters formed near the edges at the periphery of the defect. For MAS0 (6.11 ± 7.54), the percentage of regeneration was statistically similar to that of the NT group. Moreover, for MAS50, the percentage of the total

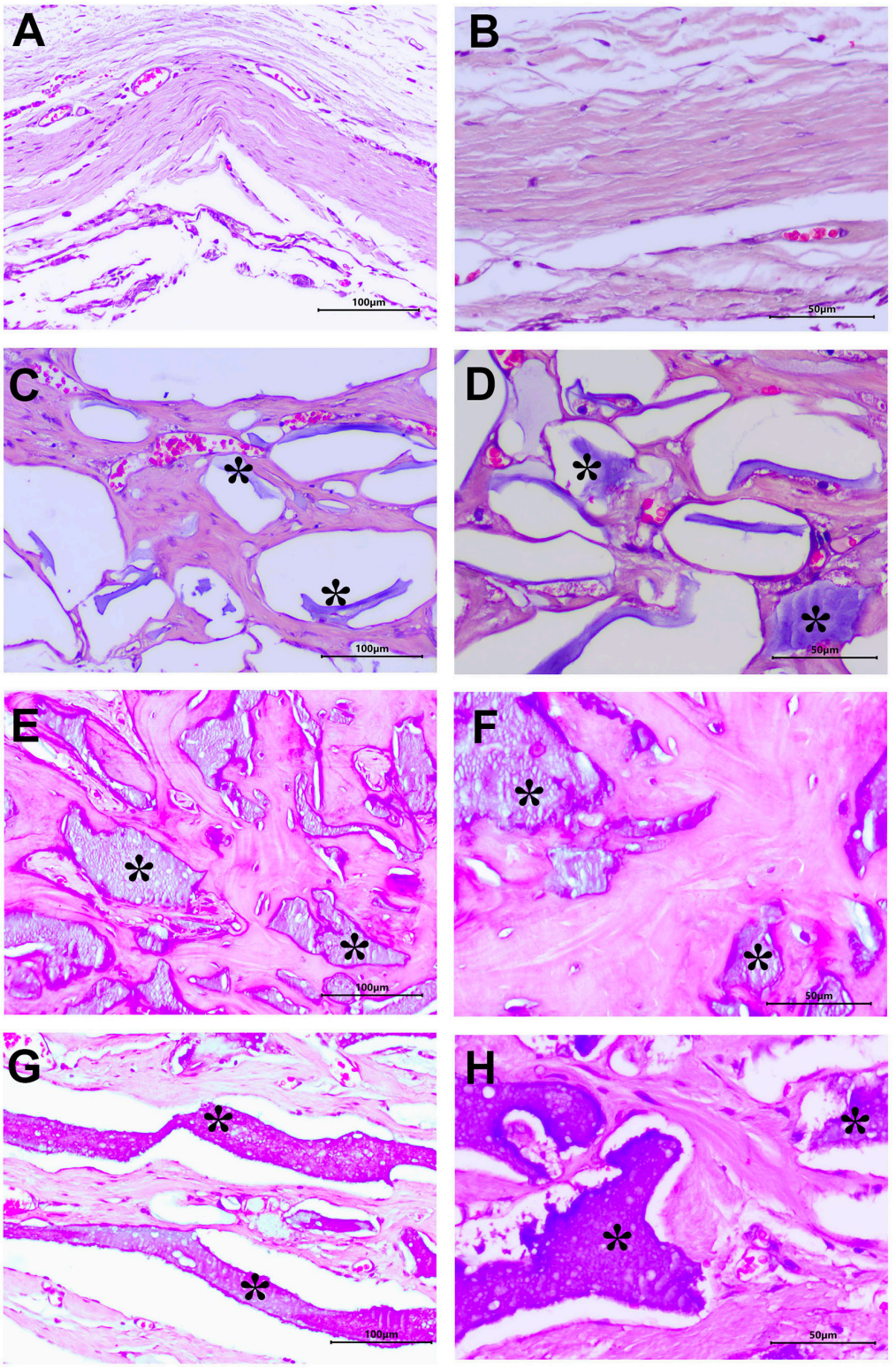


**FIGURE 4 |** Photomicrographs of histological sections stained with H&E. The images are representative of the different groups at 90 days. **(A,B)** No treatment (NT). **(C,D)** MAS0. **(E,F)** MAS30. **(G,H)** MAS50. All images are shown at 20× and 40×, respectively. The asterisks correspond to the MAS scaffolds.

volume of the regenerated mineral was 62.17 ± 9.53% and was statistically different from the NT and MAS0 groups ($p = 0.0033$). Finally, for the group corresponding to MAS30, the total volume of the regenerated area was about 90 ± 5.88%, being statistically significant with regard to the other three groups ($p = 0.020$). This suggests that the MAS scaffold composite material itself could induce the mineralization of the defect area. This biological response is in agreement with the properties of interconnected porosity, which would maximize bone in-growth, leading to osteointegration and strengthening graft fixation due to a larger surface area and more directional in-growth of bone. The osteointegration response of MAS composite scaffold suggests that the material serves as a template for bone-forming cells regulating cell adhesion, migration, growth, and the formation of new mineral tissue related to the presence of HA particles, which serve as nucleation sites and release ions that could serve as stimulatory cues for cell proliferation and cell differentiation, actively induces bone regeneration (Veis and Dorvee, 2013; Gariboldi and Best, 2015; Lotsari et al., 2018).

Upon completing the experimental duration of 90 days, the animals underwent euthanasia so that the quantity and quality of the neo-formed tissue in the area of the defect could be observed by histological analysis. Based on the results, it can be seen that in all of the groups, the defect borders remain well-defined, with a very particular response during the time of the *in vivo* model to the presence or absence of the scaffold in the area of the defect (**Supplementary Figure S3**).

In the NT control group, the presence of well-organized dense fibrous connective tissue with a proliferation of blood vessels along the defect and small areas of mineralized tissue around the edges were observed (**Supplementary Figure S3A** and **Figures 4A,B**). For the MAS0 group, a well-defined border could be observed, with small areas of mineral tissue on the scaffold in the defect zone as well as spaces of different sizes (**Supplementary Figure S3B**). Moreover, it could be observed to be basophilic and in the form of sheets of different densities and sizes surrounded by partitions of vascularized connective tissue with active fibroblasts. It is important to notice that there were no signs of inflammatory or infiltrate response (**Figures 4C,D**). The MAS30 group showed a defined border to the defect area, along with multiple zones of basophilic material and *de novo* bone mineral tissue on the cranial defect (**Supplementary Figure S3C**). At higher magnification, the material could be seen to be a homogenous distribution of bone mineral tissue of irregular shape and density. Around the bone-like tissue, multiple osteocytes in their lacunae, areas of higher osteoid matrix related to the active osteoblast cells, and blood vessel formation could also be seen (**Figures 4E,F**). For the MAS50 group, irregular dense mineral material could be seen to partially fill the calvarial defect (**Supplementary Figure S3D**). At higher magnification, the material is eosinophilic, and around it, fibroconnective tissue including blood vessels and few bone-like mineral tissue deposit could be observed (**Figures 4G,H**). Our results indicate that when the MAS scaffold was loaded with HA, there was earlier osteointegration surrounding the immature new bone trabeculae in the graft area, osteocyte cells became embedded in the lacuna, and there was a decrease in inflammatory cells. This suggests an improvement of the bone-like tissue formation and vascularization processes that are necessary for bone formation by improving the osteoconductivity and osteoinductivity. This can be related to the positive effects of the microporosity of the scaffolds, which allows proper cell migration and proliferation for bone-forming cells as well as tissue vascularization and diffusion of nutrients and oxygen (Gariboldi and Best, 2015; Zhang et al., 2016; Chatzipetros et al., 2018). The improvement of the microporous alginate sponge by loading with HA particles, in conjunction with there being no cytotoxic response or signs of edema and an absence of inflammation, infection, or clinical evidence of gas pocket formation around the scaffolds, means that this could represent an innovative strategy for bone implant materials or as an attractive approach to osteochondral defect regeneration because no significant complications were observed immediately after surgery and throughout the time course of the study.

## CONCLUSION

In this work, the use of SA sponges with an anisotropic architecture was validated *in vivo*. The sponges efficiently supported the *in vitro* response of hDP-MSC, while bioactive HA embedded in the porous matrix promoted the development of a newly formed mineralized matrix at an *in vivo* calvaria defect. *In vivo* studies confirmed that the presence of the HA phase induces the formation of preferentially oriented pore domains that promote a more ordered spatial organization of the bone ECM architecture, thus supporting a more efficient restoration of the bone defect for long-term clinical trials. In particular, MAS30 delivered the best results in terms of bone-like tissue growth, as confirmed by μCT, BMD, and histological studies, probably due to its more homogeneous distribution and limited tendency to form clusters that are less recognized by cells. Hence, all of the *in vivo* results suggested that these are promising devices for supporting the regeneration of hard tissues such as bone and the mineralized compartment of the osteochondral defect.

## DATA AVAILABILITY STATEMENT

All datasets generated for this study are included in the article/**Supplementary Material**.

## ETHICS STATEMENT

The animal study was reviewed and approved by the Internal Committee for the Care and Use of Laboratory Animals of the Faculty of Medicine, UNAM, with approved protocol number 027-CIC-2019.

## AUTHOR CONTRIBUTIONS

IC-M, RA, and VG were involved in the fabrication of sponges and their physicochemical characterization. JS-B, FS-O, MA-P, PG-A, IC-M, and LM contributed substantially to the biological assessment experiments and the animal experiments, and performed most of the acquisition, analysis, and interpretation of *in vitro* and *in vivo* data. MA-P, LA, and VG prepared and revised the draft critically for important intellectual content. All authors contributed to the article and approved the submitted version.

## FUNDING

The authors want to give their thanks for financial support from the DGAPA-UNAM: PAPIIT IA205818 and IT203618 projects and CONACYT through the particular program Fondo Sectorial de Investigación para la Educación A1S-9178. The authors also thank NEWTON (FIRB-RBAP11BYNP) and the INCIPIT project COFUND, European Union Horizon 2020, under Marie Skłodowska-Curie project no. 665403.

## ACKNOWLEDGMENTS

Scanning Electron Microscopy was supported by the Transmission and Scanning Electron Microscopy Labs (LAMEST) of the National Research Council.

## SUPPLEMENTARY MATERIAL

The Supplementary Material for this article can be found online at: https://www.frontiersin.org/articles/10.3389/fbioe.2020.00587/full#supplementary-material

## REFERENCES

Chatzipetros, E., Christopoulos, P., Donta, C., Tosios, K. I., Tsiambas, E., Tsiourvas, D., et al. (2018). Application of nano-hydroxyapatite/chitosan scaffolds on rat calvarial critical-sized defects: a pilot study. *Med. Oral Patol. Oral Cir. Bucal.* 23, e625–e632. doi: 10.4317/medoral.22455

Dinoro, J., Maher, M., Talebian, S., Jafarkhani, M., Mehrali, M., Orive, G., et al. (2019). Sulfated polysaccharide-based scaffolds for orthopaedic tissue engineering. *Biomaterials* 214:119214. doi: 10.1016/j.biomaterials.2019.05.025

Dong-Hyun, K., Kyu-Hong, H., Ju Dong, L., Hong-Chae, P., and Seog-Young, Y. (2015). Long and short range order structural analysis of in-situ formed biphasic calcium phosphates. *Biomater. Res.* 19:14. doi: 10.1186/s40824-015-0036-0

Elmowafy, E., Abdal-Hay, A., Skouras, A., Tiboni, M., Casettari, L., and Guarino, V. (2019). Polyhydroxyalkanoate (PHA): applications in drug delivery and tissue engineering. *Expert. Rev. Med. Devices.* 16, 467–482. doi: 10.1080/17434440.2019.1615439

Funda, G., Taschieri, S., Bruno, G. A., Grecchi, E., Paolo, S., Girolamo, D., et al. (2020). Nanotechnology scaffolds for alveolar bone regeneration. *Materials* 13:E201. doi: 10.3390/ma13010201

Gariboldi, M. I., and Best, S. M. (2015). Effect of ceramic scaffold architectural parameters on biological response. *Front. Bioeng. Biotechnol.* 3:151. doi: 10.3389/fbioe.2015.00151

Guarino, V., Caputo, T., Altobelli, R., and Ambrosio, L. (2015). Degradation properties and metabolic activity of alginate and chitosan polyelectrolytes for drug delivery and tissue engineering applications. *AIMS Mater. Sci.* 2, 497–501. doi: 10.3934/matersci.2015.4.497

Guarino, V., Causa, F., Salerno, A., Ambrosio, L., and Netti, P. A. (2008). Design and manufacture of microporous polymeric materials with hierarchal complex structure for biomedical application. *Mater. Sci. Tech.* 24, 1111–1117. doi: 10.1179/174328408X341799

Guarino, V., Gloria, A., Raucci, M. G., and Ambrosio, L. (2012a). Hydrogel-based platforms for biomedical applications. *Polymers* 4, 1590–1612. doi: 10.3390/polym4031590

Guarino, V., Gloria, A., Raucci, M. G., De Santis, R., and Ambrosio, L. (2012b). Bio-inspired cell instructive composite platforms for bone regeneration. *Int. Mater. Rev.* 57, 256–275. doi: 10.1179/0950660812Z.00000000021

Guarino, V., Scaglione, S., Sandri, M., Alvarez-Perez, M. A., Tampieri, A., Quarto, R., et al. (2014). MgCHA particles dispersion in porous PCL scaffolds: in vitro mineralization and in vivo bone formation. *J. Tissue Eng. Reg. Med.* 8, 291–303. doi: 10.1002/term.1521

Haider, A., Waseem, A., Karpukhina, N., and Mohsin, S. (2020). Strontium- and Zinc-containing bioactive glass and alginates scaffolds. *Bioengineering* 7:E10. doi: 10.3390/bioengineering7010010

Haugh, M. G., Murphy, C. M., and O'Brien, F. J. (2010). Novel freeze-drying methods to produce a range of collagen glycosaminoglycan scaffolds with tailored mean pore sizes. *Tissue Eng. Part C Methods* 16, 887–894. doi: 10.1089/ten.TEC.2009.0422

Jin, H.-H., Kim, D.-H., Kim, T.-W., Shin, K.-K., Jung, J. S., Park, H.-C., et al. (2012). In vivo evaluation of porous hydroxyapatite/chitosan–alginate composite scaffolds for bone tissue engineering. *Int. J. Biol. Macromol.* 51, 1079–1085. doi: 10.1016/j.ijbiomac.2012.08.027

Kang, H., Zeng, Y., and Varghese, S. (2018). Functionally graded multilayer scaffolds for in vivo osteochondral tissue engineering. *Acta Biomater.* 78, 365–377. doi: 10.1016/j.actbio.2018.07.039

Kazem-Arki, M., Kabiri, M., Rad, I., Roodbari, N. H., Hosseinpoor, H., Mirzaei, S., et al. (2018). Enhancement of osteogenic differentiation of adiposederived stem cells by PRP modified nanofibrous scaffold. *Cytotechnology* 70, 1487–1498. doi: 10.1007/s10616-018-0226-4

Ki, H. H., Young-Min, K., and Soo-Chang, S. (2019). Fine-tunable and injectable 3d hydrogel for on-demand stem cell niche. *Adv. Sci.* 6:1900597. doi: 10.1002/advs.201900597

Kolb, A. D., and Bussard, K. M. (2019). The Bone extracellular matrix as an ideal milieu for cancer cell metastases. *Cancers* 11:E1020. doi: 10.3390/cancers11071020

Li, J., Baker, B. A., Mou, X., Ren, N., Qui, J., Boughton, R., et al. (2014). Biopolymer/calcium phosphate scaffolds for bone tissue engineering. *Adv. Healthc. Mater.* 3, 469–484. doi: 10.1002/adhm.201300562

Li, Y., Fang, X., and Jiang, T. (2015). Minimally traumatic alveolar ridge augmentation with a tunnel injectable thermo-sensitive alginate scaffold. *J. Appl. Oral Sci.* 23, 215–223. doi: 10.1590/1678-775720140348

Lotsari, A., Rajasekharan, A. K., Halvarsson, M., and Andersson, M. (2018). Transformation of amorphous calcium phosphate to bone-like apatite. *Nat. Commun.* 9:4170. doi: 10.1038/s41467-018-06570-x

McMahon, R. E., Wang, L., Skoracki, R., and Mathur, A. B. (2013). Development of nanomaterials for bone repair and regeneration. *J. Biomed. Mater. Res. B Appl. Biomater.* 101, 387–397. doi: 10.1002/jbm.b.32823

Mohd Pu'ad, N. A. S., Koshy, P., Abdullah, H. Z., Idris, M. I., and Lee, T. C. (2019). Syntheses of hydroxyapatite from natural sources. *Helyion* 5:e01588. doi: 10.1016/j.heliyon.2019.e01588

Perez, J. R., Kouroupis, D., Li, D. J., Best, T. M., Kaplan, L., and Correa, D. (2018). Tissue engineering and cell-based therapies for fractures and bone defects. *Front. Bioeng. Biotechnol.* 6:105. doi: 10.3389/fbioe.2018.00105

Sasser, T. A., Chapman, S. E., Li, S., Hudson, C., Orton, S. P., Diener, J. M., et al. (2012). Segmentation and measurement of fat volumes in murine obesity models using x-ray computed tomography. *J. Vis. Exp.* 62:e3680. doi: 10.3791/3680

Singh, D., Tripathi, A., Zo, S., Singh, D., and Han, S. S. (2014). Synthesis of composite gelatin-hyaluronic acid-alginate porous scaffold and evaluation for in vitro stem cell growth and in vivo tissue integration. *Colloids Surf. B Biointerfaces* 116, 502–509. doi: 10.1016/j.colsurfb.2014.01.049

Spicer, P. P., Kretlow, J. D., Young, S., Jansen, J. A., Kasper, F. K., and Mikos, A. G. (2012). Evaluation of bone regeneration using the rat critical size calvarial defect. *Nat. Protoc.* 7, 1918–1929. doi: 10.1038/nprot.2012.113

Suárez-González, D., Barnhart, K., Saito, E., Vanderby, R., Hollister, S. J., and Murphy, W. L. (2010). Controlled nucleation of hydroxyapatite on alginate scaffolds for stem cell-based bone tissue engineering. *J. Biomed. Mater. Res. Part. A*. 95A, 222–234. doi: 10.1002/jbm.a.32833

Sun, J., and Tan, H. (2013). Alginate-based biomaterials for regenerative medicine applications. *Materials* 6, 1285–1309. doi: 10.3390/ma6041285

Thein-Han, W. W., and Misra, R. D. (2009). Biomimetic chitosan-nanohydroxyapatite composite scaffolds for bone tissue engineering. *Acta Biomater.* 5, 1182–1197. doi: 10.1016/j.actbio.2008.11.025

Ueon, S. S., Jeong-Hui, P., Seok-Jung, H., Jong-Eun, W., Hye-Sun, Y., and Hae-Won, K. (2010). Porous biomedical composite microspheres developed for cell delivering scaffold in bone regeneration. *Mater. Lett.* 64, 2261–2264. doi: 10.1016/j.matlet.2010.06.069

Veis, A., and Dorvee, J. R. (2013). Biomineralization mechanisms: a new paradigm for crystal nucleation in organic matricies. *Calcif. Tissue Int.* 93, 307–315. doi: 10.1007/s00223-012-9678-2

Veronesi, F., Giavaresi, G., Guarino, V., Raucci, M. G., Sandri, M., Tampieri, A., et al. (2015). Bioactivity and bone healing properties of biomimetic porous composite scaffold: in vitro and in vivo studies. *J. Biomed. Mater. Res. A*. 103, 2932–2241. doi: 10.1002/jbm.a.35433

Yadav, N., and Srivastava, P. (2019). Osteoblast studied on gelatin based biomaterials in rabbit Bone Bioengineering. *Mater. Sci. Eng. C Mater. Biol. Appl.* 104:109892. doi: 10.1016/j.msec.2019.109892

Zhang, H., Mao, X., Du, Z., Jiang, W., Han, X., Zhao, D., et al. (2016). Three dimensional printed macroporous polylactic acid/hydroxyapatite composite scaffolds for promoting bone formation in a critical-size rat calvarial defect model. *Sci. Technol. Adv. Mater.* 17, 136–148. doi: 10.1080/14686996.2016.1145532

Zhang, Y., Wang, C., Jiang, W., Zuo, W., and Han, G. (2017). Influence of stage cooling method on pore architecture of biomimetic alginate scaffolds. *Sci. Rep.* 7:16150. doi: 10.1038/s41598-017-16024-x

Zhu, M., Li, W., Dong, X., Yuan, X., Midgley, A. C., Chang, H., et al. (2019). In vivo engineered extracellular matrix scaffolds with instructive niches for oriented tissue regeneration. *Nat. Commun* 10:4620. doi: 10.1038/s41467-019-12545-3

**Conflict of Interest:** The authors declare that the research was conducted in the absence of any commercial or financial relationships that could be construed as a potential conflict of interest.

frontiers in Bioengineering and Biotechnology

ORIGINAL RESEARCH
published: 09 July 2020
doi: 10.3389/fbioe.2020.00754

# Development of Natural-Based Bone Cement for a Controlled Doxorubicin-Drug Release

*Rebecca Marie Dewhurst[1], Annachiara Scalzone[2], Joseph Buckley[2], Clara Mattu[3], Kenneth S. Rankin[1], Piergiorgio Gentile[2]* and Ana Marina Ferreira[2]**

*[1] Translational and Clinical Research Institute, Newcastle University, Newcastle upon Tyne, United Kingdom, [2] School of Engineering, Newcastle University, Newcastle upon Tyne, United Kingdom, [3] Department of Mechanical and Aerospace, Politecnico di Torino, Turin, Italy*

Osteosarcoma (OS) accounts for 60% of all global bone cancer diagnoses. Intravenous administration of Doxorubicin Hydrochloride (DOXO) is the current form of OS treatment, however, systemic delivery has been linked to the onset of DOXO induced cardiomyopathy. Biomaterials including calcium phosphate cements (CPCs) and nanoparticles (NPs) have been tested as localized drug delivery scaffolds for OS cells. However, the tumor microenvironment is critical in cancer progression, with mesenchymal stem cells (MSCs) thought to promote OS metastasis and drug resistance. The extent of MSC assisted survival of OS cells in response to DOXO delivered by CPCs is unknown. In this study, we aimed at investigating the effect of DOXO release from a new formulation of calcium phosphate-based bone cement on the viability of OS cells cocultured with hMSC in vitro. NPs made of PLGA were loaded with DOXO and incorporated in the formulated bone cement to achieve local drug release. The inclusion of PLGA-DOXO NPs into CPCs was also proven to increase the levels of cytotoxicity of U2OS cells in mono- and coculture after 24 and 72 h. Our results demonstrate that a more effective localized DOXO delivery can be achieved via the use of CPCs loaded with PLGA-DOXO NPs compared to CPCs loaded with DOXO, by an observed reduction in metabolic activity of U2OS cells in indirect coculture with hMSCs. The presence of hMSCs offer a degree of DOXO resistance in U2OS cells cultured on PLGA-DOXO NP bone cements. The consideration of the tumor microenvironment via the indirect inclusion of hMSCs in this study can act as a starting point for future direct coculture and *in vivo* investigations.

**Keywords: bone cement, nanoparticles, osteosarcoma, stem cells, regenerative medicine**

OPEN ACCESS

***Edited by:***
*Lia Rimondini,*
*University of Eastern Piedmont, Italy*

***Reviewed by:***
*Silvia Fare,*
*Politecnico di Milano, Italy*
*Maria Grazia Raucci,*
*National Research Council (CNR), Italy*

****Correspondence:***
*Piergiorgio Gentile*
*Piergiorgio.gentile@newcastle.ac.uk;*
*piergiorgio.gentile@ncl.ac.uk*
*Ana Marina Ferreira*
*ana.ferreira-duarte@newcastle.ac.uk;*
*ana.ferreira-duarte@ncl.ac.uk*

***Specialty section:***
*This article was submitted to Biomaterials, a section of the journal Frontiers in Bioengineering and Biotechnology*

***Received:*** *22 March 2020*
***Accepted:*** *12 June 2020*
***Published:*** *09 July 2020*

***Citation:***
*Dewhurst RM, Scalzone A, Buckley J, Mattu C, Rankin KS, Gentile P and Ferreira AM (2020) Development of Natural-Based Bone Cement for a Controlled Doxorubicin-Drug Release. Front. Bioeng. Biotechnol. 8:754. doi: 10.3389/fbioe.2020.00754*

## INTRODUCTION

Osteosarcoma (OS) is one of the main types of malignant skeletal tumors, accounting for 60% of diagnosed bone cancers globally (Ottaviani and Jaffe, 2009). In England, OS accounted for 34% of all diagnosed malignant bone sarcoma cases between the years 1979 and 2007 (Whelan et al., 2012). Most cases diagnosed were in one of two demographic groups; the first group was predominantly between 10 and 24 years old, while the second was 70 plus (Whelan et al., 2012). The common

OS diagnosis is via plain radiographic imaging of the affected bone (Gorlick and Khanna, 2010) with around 70% of cases treated with chemotherapy and surgery (Collins et al., 2013). Along with advancements in the surgical technique, the addition of chemotherapy has dramatically increased the chances of survival. Current OS treatment involves surgical tumor removal combined with intravenous neo-adjuvant and adjuvant chemotherapy offering event free survival rates of 70% for localized cases and 20% for metastatic patients (Kansara and Thomas, 2007; Harrison et al., 2018). However, the current systemic administration of DOXO has been proven to induce side effects such as cardiomyopathy (Kumar et al., 2012; Abdullah et al., 2019), therefore localized delivery would be beneficial. The source of OS is still unknown, however, literature studies suggest it may stem from increased bone rates of growth during puberty (Rankin et al., 2012; Endicott et al., 2017) or the inhibition of tumor suppressor genes like *p53* (Kansara and Thomas, 2007). Mesenchymal stem cells (MSCs) have been linked to the survival of OS cells during chemotherapy by mediating proliferation, enabling metastasis and promoting drug resistance (Zheng et al., 2018). Two major forms of MSC are present in multiple types of cancer including OS patients, normal healthy MSCs (NMSC) and tumor MSCs (TMSC) (De Wever et al., 2014; Zheng et al., 2018). Broadly, NMSCs follow strictly regulated patterns of proliferation (Sun et al., 2014); however, after recruitment to tumor sites they undergo "educational" processes becoming TMSCs thus promoting cancer cell survival (Sun et al., 2014; Zheng et al., 2018). A major part of this educational process is the acquisition of a tumor-associated fibroblast (TAF) phenotype, allowing for the promotion of tumor cell growth (De Wever et al., 2014). This transformational process poses major implications in successful cancer treatment especially in OS patients due to the close proximity of NMSCs to diseased tissues.

The generation of materials and structures with promotional bone regenerative properties, growth, and controlled localized chemotherapeutic drug release preventing recurrence *in situ* can be beneficial following OS tumor removal. Natural polymers such as collagen and chitosan (CH) have been used to create osteoconductive substrates (Hockin and Simon, 2005; Zhang et al., 2014) when partnered with an apatite matrix, which provides the mechanical properties (Wang and Min-Hsiung, 2003). Moreover, CH has been used in wound healing with antibacterial properties (Islam et al., 2020), drug delivery carrier (Lee et al., 2009; Ashan et al., 2018), and bone regeneration (Saravanan et al., 2016). Ceramics including calcium phosphates, bioactive glasses and SiO2- and TiO2-(Hertz and Bruce, 2007; Mohammadi et al., 2011) have been used in the biomedical industry since the 1920s, due to their biocompatibility and good mechanical properties. They are most commonly used as the bioactive, reinforcing phase in bioactive tissue substitutes (LeGeros and LeGeros, 2003). Hydroxyapatite (HA) is one of the most commonly used calcium phosphates as a replacement bone apatite. Nano-hydroxyapatite (NHA), a synthetic calcium phosphate, offers a similar chemical composition, trace elements and crystal structure as native hydroxyapatite (Akram et al., 2014). As up to 70% of human bone tissue is HA (Dutta et al., 2015), calcium phosphates and synthetic HA are good candidates for bone tissue engineering applications. Calcium phosphate cements (CPC) and calcium sulphate cements (CSC) have both demonstrated to improve biocompatibility, bioactivity and osteoconductivity compared to HA alone under neutral pH conditions (Xu et al., 2017).

In a clinical context, CPCs have been developed and reported in several studies for the treatment of bone defects as injectable alternative fillers, supplementing internal fixation, during surgical treatment of bone metastasis, following tumor removal. CPC presence could help to avoid the spreading of tumor cells, which may result in new lesions developing in surrounding tissues, during an intralesional resection (Tanzawa et al., 2011). CPC has been exploited in several clinical applications, including traumatic and craniofacial surgery, spinal reconstruction and arthroplasty, showing promising results (Matsumanie et al., 2006). Relevant advantages of CPC are: (i) they are easily shaped to meet the bone defect's dimensions; (ii) they have good osteoconductivity and biocompatibility (Frankenburg et al., 1998); (iii) they have chemical stability, enabling its loading with several drugs; (iv) and display a remarkable sustained-release capacity. Broadly, CPCs are replaced with newly formed bone once degraded, showing good levels of biodegradability and bio-reabsorbility (Weitao et al., 2008; He et al., 2018). Furthermore, loading anticancer drugs within the CPCs could offer the potential for reducing the risk of local tumor recurrence. Studies on CPCs used as localized drug delivery systems, loaded with synthetic polymer nanoparticles containing painkillers, antibiotics, and chemotherapeutic drugs (including OS treating drugs) to treat bone cancers demonstrated a reduced risk of local cancer recurrence due to localized and targeted delivery of drugs (Lopez-Heredia et al., 2011; Tanzawa et al., 2011; Farbod et al., 2016; Liang et al., 2020).

Recently, nanoparticles (NPs) have been widely used as drug delivery vehicles for multiple cancers, allowing for improvements in drug potency and targeted delivery (Pathak and Pathak, 2019). Different materials have been used to produce NPs, including metals such as iron (Singh et al., 2018), silver (Chaloupka et al., 2010) or gold (Patra et al., 2010) and biodegradable polymers such as lipid polymer base (Dehaini et al., 2016; Yalcin et al., 2020) and poly(D,L-lactide-co-glycolide) (PLGA) (Sokol et al., 2019); the latter enable a quick release of the drug carrier in cancer treatment. Doxorubicin Hydrochloride (DOXO), an anthracycline antibiotic used as a drug to treat multiple forms of cancers, has proven effective in stimulating apoptosis of lymphoma, leukemia and endothelium cells (Shafei et al., 2017; Mattu et al., 2018). It is also capable of inducing senescence in solid tumor depending upon concentrations administered (Kozhukharova et al., 2018). In OS treatment, DOXO is administered intravenously along with other chemotherapeutic drugs including methotrexate (MAP) and cisplatinum (Yu et al., 2019). *In vitro* studies assessing the effect of DOXO in human OS cell lines showed that cellular metabolic activity and growth of U2OS spheroids decrease after 24 h DOXO drug exposure, following endocytosis (Baek et al., 2016). However, U2OS cells are capable of developing DOXO resistance when overexposed to the drug (Buondonno et al., 2019). The use of NPs has shown promise in attempts to overcome associated limitations of free

intravenous DOXO in cancer treatments such as breast cancer (Prados et al., 2012) and hepatic cancers (Krishnamurthy et al., 2017), indicating DOXO loaded NPs could be a viable method of stimulating residual osteosarcoma cell apoptosis. Attempts incorporating therapeutic NPs loaded with Adriamycin (ADM, the commercial name for DOXO) into porous NHA and collagen scaffolds have shown successful growth inhibition of human osteosarcoma cell line MG63 (Rong et al., 2016). From this work, it was demonstrated that the combination of NHA and collagen scaffolds loaded with DOXO NPs can be beneficial in inhibiting tumor growth while assisting bone regeneration (Rong et al., 2016). This success has also been reflected in *in vivo* studies conducted in rats (Hoving et al., 2005) and murine models of Saos2 and MG63 (Ma et al., 2015), showing the immense benefit of DOXO loaded biomaterials.

In this study, we aimed at investigating the effect of DOXO release from biodegradable/bioactive constructs on the viability of OS cells cocultured with hMSC *in vitro*. For this purpose, a new formulation of biodegradable calcium phosphate-based bone cement with radiopaque properties was developed. NPs made of PLGA were loaded with DOXO and incorporated in the formulated bone cement to achieve local drug release. The impact of DOXO release from bone cement on cell viability and metabolic activity of U2OS osteosarcoma cells either in monoculture and in coculture with hMSCs was assessed in vitro. This pioneering study shows that hMSCs play a modulatory role on U2OS cells survival when exposed to DOXO.

# MATERIALS AND METHODS

## Materials

For bone cement preparation chitosan (CH, 95% deacetylation, molecular weight 500 kDa) was provided by Heppe Medical Chitosan. Gelatin Type A (G, derived from pig skin, CAS No. 9000-70-80), Nano-Hydroxyapatite (NHA, particle size between 49 and 152 nm, molecular weight 502.31, CAS No. 12167-74-7), Bismuth Salicylate (BS, molecular weight of 362.09 g/mol, CAS No. 14882-18-9) Acetic Acid (Glacial, Reagent Plus, ≥99%, molecular weight 60.05, CAS No. 64-19-7), and Sodium Hydroxide (NaOH, Ultra dry crystals, 99.99% trace metals basis, molecular weight 40.00, CAS No. 1310-732), where all purchased from Sigma-Aldrich. Genipin (GP, CAS No. 6902-77-8) was supplied from Challenge Bioproduct Co. For nanoparticle preparations Resomer® RG 858 S (ester terminated Poly(D,L-lactide-co-glycolide (PLGA), lactide:glycolide 85:15, molecular weight 170,000–230,000 Da, CAS No 26780-50-7), Acetone (≥99.9%, molecular weight 58.08, CAS No. 67-64-1), Tween 80 (CAS No. 9005-65-6) and Dimethyl Sulfate (DMSO, molecular weight 78.13, CAS No. 6768-5) were all purchased from Sigma Aldrich. For cell culture tests, Fetal Bovine Serum (FBS, ThermoFisher, Gibco CAS No. 10500056), penicillin/streptomycin (P/S, Sigma-Aldrich, P0781100 mL), Human Fibroblast Growth Factor (hFGF-2, Sigma-Aldrich, 106096-939), L-Glutamine (LG, 5 mM, Sigma-Aldrich, TMS-002), Phosphate Buffered Saline (PBS Sigma-Aldrich, MFCD00131855), Trypsin/EDTA (Sigma-Aldrich, MFCD00130286), Dulbecco's Modified Eagles Medium (DMEM, Sigma-Aldrich, Gibco high glucose 4500 mg/L, 11995-065) were used. Doxorubicin Hydrochloride (DOXO, European Pharmacopoeia Reference Standard, molecular weight 579.98, CAS No. 25316-40-9) was purchased from Sigma-Aldrich.

## Bone Cement Characterizations

### Bone Cement Preparation

Four different bone cement formulas were initially tested (40/60, 50/50, 60/40, and 70/30 of polymer to NHA). Briefly, a 2:1 weight/weight (w/w) solution of CH:G was dissolved into 2% Acetic Acid and left under magnetic stirring at 40°C until dissolved (Mi, 2005; Pullieri et al., 2008). Then, NHA powder was added to polymeric solutions, forming cements with 40/60, 50/50, 60/40, and 70/30 ratios of CH:G to NHA, followed by BS addition (quantities shown in **Table 1**). Once mixed, the pH of the solution was adjusted to 6 by adding drop wise 1M NaOH, then the mixture was stirred for 1 h at 40°C until NHA was homogenously dispersed. The cross-linker GP was added to the mixture and stirred vigorously until homogenous (about 10 min). Cements were then transferred to 24 well plates and incubated for 24 h at 37°C for solidification. Once GP reacted, a dark blue color was observed and cements were stored at 4°C for further analysis.

### Curing Time and Injectability

To investigate both injectability and curing time of four bone cements compositions, 5 ml of each of bone composition cements was loaded in a 5 ml syringe, following mixing step. The injectability was calculated as the percentage of mass that can be extruded from the syringe during about 1 min, as described elsewhere (Xiaopeng et al., 2008). For this, the mass of the syringe loaded and unloaded with the bone cement was recorded. This process was repeated three times per each cement composition.

To investigate cement curing time, 2 mL of bone cements containing GP were transferred in triplicate into clear plastic vials and incubated at 37°C. The setting time was determined by tilting each vial at least 45° angle every 60-s intervals until set. Cements were set once they stopped flowing by tilting the vial, showing firm consistency and color change from white to blue as evidence of GP cross-linking reaction.

### Unconfined Compression Test

The compressive mechanical properties of four bone cements compositions (without DOXO or PLGA-DOXO NPs) specimens

**TABLE 1 |** Percentages in weight (%wt) of the different components for bone cement preparation at 40:60, 50:50, 60:40, and 70:30 CH+G:NHA ratios (contains Nanohydroxyapatite (NHA), Bismuth Salicylate (BS) as radiopaque agent, Genipin (GP) as crosslinker, chitosan (CH) and gelatin (G) as biopolymers).

| Component | Composition of Bone Cement (CH+G to NHA) | | | |
|---|---|---|---|---|
| | 40/60 | 50/50 | 60/40 | 70/30 |
| Chitosan (CH) | 26.7% wt | 33.3% wt | 40% wt | 46.67% wt |
| Gelatin (G) | 13.3% wt | 17.7% wt | 20% wt | 23.33% wt |
| Nanohydroxyapatite (NHA) | 60% wt | 50% wt | 40% wt | 30% wt |
| Bismuth Salicylate (BS) | 15% w/w | 15% w/w | 15% w/w | 15% w/w |
| Genipin (GP) | 7.5% w/w | 7.5% w/w | 7.5% w/w | 7.5% w/w |

was measured by using a Universal testing machine (SHIMADZU ES-SX, Japan) equipped with 50N loading cell at a crosshead speed of 1 mm $min^{-1}$. Test specimens were cylinder-shaped cements with a 1.3 cm diameter and an average height of about 1 cm. A pre-load of 0.15N was applied, and further sample loading was recorded until the specimen was compressed to around 80% of its original height before break. Compression tests of five samples for each composition was evaluated at room temperature in dry state, stress was calculated by dividing the applied force with the initial scaffold surface area, whereas strain was calculated from the displacement of the scaffolds in relation to the original thickness. Young's modulus (E) was also calculated as the slope of the linear elastic regime (0–15%).

### Spectroscopy Fourier Transform Infrared (FTIR) – Attenuated Total Reflectance (ATR)

FTIR spectra were obtained using a Spectrum Two PE instrument equipped with attenuated total reflectance (ATR) crystal (diamond crystal) (Frontier PerkinElmer Inc., United States). Bone cements were frozen at −0°C for 48 h and then freeze dried for 48 h (Alpha 1-2 LD plus, CHRIST, Germany). Samples were placed directly onto the ATR crystal and spectra were collected in transmittance mode. FTIR spectra measurements were an average of 36 scans at 4 $cm^{-1}$ resolution in the wavelength range of 4000 - 550 $cm^{-1}$. Triplicate samples of each bone cement composition (without DOXO or PLGA-DOXO NPs) were analyzed.

### Radiopacity Properties

The four bone cements (40:60, 50:50, 60:40, and 70:30 ratios of CH+G:NHA) were investigated by X-ray to confirm if BS concentration offers viable radiopacity. Triplicate samples of each cement containing 15% w/w BS were imaged via X-ray at 40 kV, with two exposure times of 11 mAs and 5.6 mAs (Royal Victoria Infirmary, Newcastle). Radiopacity was also investigated via phantom imaging (Radiology Department, RVI Hospital Newcastle) used as control, to compare the radiopacity of the samples to the actual radiopacity of bone. Bone cements visibly brighter than phantom were considered to have a viable radiopacity.

### Pore Size and Degradation

Mass loss was investigated for 40/60 bone cement (in absence of DOXO or PLGA-DOXO NPs). The degradation degree of samples ($n$ = 3, with dimensions of 1.3 cm diameter and height 1 cm) was calculated gravimetrically using an analytical balance (Sartorius, Sartorius AG). Briefly, freeze dried samples were initially weighted (day 0) and then immersed into 5 mL of Phosphate Buffered Solution (PBS) (Sigma Aldrich, United Kingdom) at pH 7.0, with the solution refreshed weekly for 14 days. Following 14 days of incubation at 37°C, samples were removed from the buffer solution and freeze dried for re-weighing of sample mass.

The inner morphology of freeze-dried (40/60) bone cement, with and without free DOXO (40 μM) and PLGA-DOXO NPs (100 μM), were analyzed by Scanning Electron Microscopy (SEM, Hitachi TM3030 Tabletop, Germany) at accelerating voltage of 10 kV. The samples were cut into small squares and fixed on the aluminum stub using carbon tape. SEM images were analyzed using an image software (ImageJ) for pores size measurement. Three images per type of sample were analyzed measuring at least 30 pores for each one. The pore size was averaged, assuming all pores were circular.

Changes of pH of bone cements (40/60) in absence (0 μM) presence of PLGA-DOXO NPs (40 μM and 100 μM) at physiological conditions (PBS pH 7.0, 37°C) were monitored over 3 days by using portable FG2-Kit Five Go™ pH meter (Mettler Toledo Ltd., United Kingdom).

### Drug Release

Bone cements (40/60 composition) containing free DOXO (to achieve a final concentration of 40 μM and 100 μM in the tissue culture well) and PLGA-DOXO NPs (to achieve the same final DOXO concentration of 40 μM and 100 μM in tissue culture well) were prepared in triplicate in a 48 well plate, as described previously. DOXO drug release was determined by immersing samples in 5 mL of a PBS solution (pH 7.0) and incubating at 37°C over 7 days' time-period. At pre-determined time intervals (1, 2, 3, 4, and 7 days), samples solutions were removed and replaced with fresh buffer. Samples solutions were transferred to a flat-bottom 96 well plate for further UV–Vis spectroscopy analysis in absorbance at 480 nm, and compared to a standard curve generated using free DOXO in PBS at known concentrations. All tests were performed in triplicate and results were expressed as cumulative released DOXO (% of the drug loaded in the construct), compared to a standard curve generated using free DOXO in PBS at known concentrations.

## PLGA-DOXO NP Characterizations

### PLGA-DOXO NP Preparation

DOXO-loaded nanoparticles were prepared by the nanoprecipitation method, by adapting the original method described elsewhere (Mattu et al., 2012). Briefly, 30 mg of PLGA ester-terminated was dissolved into 3 mL pure acetone, and 100 μL of 10 mM DOXO stock solution (1:1 of DMSO:PBS) was added to the polymer solution (2% w/w with respect to the polymer weight). PLGA-loaded NPs were prepared by adding dropwise this primary solution into 7 ml of 1% w/v deionized water containing Tween 80 (10 mg/mL), followed by gently stirring for 1 h at room temperature. PLGA-DOXO NPS were collected by selective centrifugation steps at 3.000 rpm, followed by centrifugation at 10.000 rpm. The nanoparticles pellet obtained from the two centrifugation steps were collected and washed three times with distilled water. The final particle suspension was frozen at −20°C and subsequently freeze-dried for 48 h (Alpha 1-2 LD plus, CHRIST, Germany).

### Encapsulation Efficiency of Doxorubicin Into PLGA Nanoparticles

Encapsulation efficiency (EE) was determined via UV/VIS spectroscopy. Freeze dried PLGA-DOXO NPs were incubated in PBS (1 mg/ml) for 30 min at 37°C, centrifuged at 1500 rpm for 15 min, and the supernatant was collected. This process was

repeated by suspending remaining particles in PBS (by vigorously shaking for 5 min) and centrifuging at 1500 rpm. Supernatants collected from each step were analyzed at 480 nm to detect DOXO. Each sample was read in triplicate and, referred to a standard curve generated using free DOXO in PBS at known concentrations. The EE of PLGA-DOXO NP was calculated using the following equation;

$$Encapsulation\ Efficiency(\%) = \left( \frac{\left[drug\ released\ in\ PBS\right] + \left[drug\ from\ PBS\ wash\right]}{\left[drug\ added\ during\ NP\ formation\right]} \right) \times 100$$

### Morphology and Size of Polymeric NP

The morphology of freeze-dried PLGA-DOXO NPs was analyzed by Scanning Electron Microscopy (SEM, Hitachi TM3030 Tabletop, Germany) at accelerating voltage of 10 kV. SEM images were obtained at a magnification of X 6K and analyzed using an image software (ImageJ) for size measurement. Moreover, the particle size analysis and size distribution analysis were performed by using a dynamic laser light scattering technology (Malvern Zetasizer, Nano ZS) at room temperature in ultrapure water. PLGA-DOXO NPs were suspended in DI water (0.5 mg/mL) with a material refractive index of 1.49 and absorbance of 0.001 to obtain NP hydrodynamic diameter (nm). Results are an average of triplicate samples.

## Cellular Characterizations

### Cell Culture

Bone marrow derived hMSCs (Sigma-Aldrich, SCC034) at passage 1 were cultured in Dulbecco's Modified Eagles Medium (DMEM) supplemented with 10% Fetal Bovine Serum (FBS), 1% penicillin/streptomycin (P/S) and 8 ng/mL Human Fibroblast Growth Factor (hFGF) at 37°C until 70% confluent. Human U2OS cells (Sigma-Aldrich, 92022711) at passage 21 were cultured in DMEM supplemented with 10% FBS, 1% P/S and 1% L-Glutamine at 37°C until 80% confluent. Cells were washed with PBS before trypsinization with Trypsin/EDTA, centrifugation and resuspension in their respective media. Media was changed every 2–3 days. For spheroids, $2 \times 10^5$ U2OS cells were seeded in a "v" bottom 96 well plate and left for 3–5 at 37°C, 5% $CO_2$, 90% humidity. Media was changed every 2–3 days.

### IC50 Characterization and DOXO Concentration Selection for Cement Loading

For IC50 measurement, U2OS were cultured in a 48 well-plate and in 96 well "V" bottom plate for U2OS spheroids formation at $2 \times 10^5$cells/well, while hMSCs were cultured in a 48 well-plate at $2 \times 10^4$ cells/well with 24 h incubation for cell attachment. Then, media was removed and replaced with media suspension containing DOXO at concentrations ranging from 0 μM (no DOXO) to 200 μM for investigating the effect of different drug doses. Following 24 h incubation, drug media suspension was removed, and cell viability was assessed via the MTT assay in absorbance at λ = 570 nm, as described below in metabolic activity section. Then, IC50, which indicates the half maximal effective drug concentration that induces half cellular response between the baseline and the maximum response at specific exposure time, was calculated by the non-linear regression (sigmoidal dose–response) using GraphPad (GraphPad Prism Software Inc., San Diego, CA, United States). From U2OS IC50 obtained results, DOXO concentrations of 40 μM and 100 μM were selected to be incorporated into bone cements (40/60), either as free DOXO or loaded into NPs. The cellular behavior of U2OS mono- and indirect cocultures (U2OS and hMSCs) in presence of bone cements containing 40 μM and 100 μM free DOXO or/and drug-loaded into NPs was investigated. All tests were performed in triplicate.

### Cellular Seeding Onto Bone Cements

From physical-chemical characterizations, the 40/60 composition was selected for further bone cement cytocompatibility assessment. Bone cements with and without free DOXO and PLGA-DOXO NPs (40 μM and 100 μM DOXO) were prepared and sterilized by UV light (245 nm) prior to cell seeding. Samples were then incubated for 30 min at 37°C in U2OS cell media, while hanging millipore cell inserts (pore size 8.0 μm) were incubated in hMSC media. Following this, U2OS media was read in absorbance at 480 nm (using the FLUOstar OMEGA microplate reader) to determine any potential DOXO drug release during pre-incubation. U2OS cells ($1 \times 10^5$) were seeded directly onto cements placed in well bottom, while hMSCs ($2 \times 10^4$) were seeded onto hanging inserts. Cells were left at 37°C for 15–20 min to allow their adhesion, prior to the well topping up with the media. For immunostaining analysis, sudan black solution was used onto bone cement prior to cell seeding to minimize background fluorescence given by Genipin. All tests were performed in triplicate.

### Metabolic Activity

Metabolic activity was assessed via the MTT assay (Sigma-Aldrich, ≥97.5%, HPLC, molecular weight 414.32, CAS No. 298-93-1). Briefly, $2 \times 10^5$ U2OS cells were seeded directly onto (40/60) bone cements with free DOXO and PLGA-DOXO NPs at concentrations 40 μM and 100 μM, and cements without free DOXO or PLGA-DOXO NPs (0 μM). In co-culture systems, hMSCs were seeded onto Millipore cell inserts (pore size 8.0 μm) at $2 \times 10^4$ cells/insert, jointly with U2OS cultured onto bone cements. The metabolic activity was measured individually for U2OS and hMSCs (if in co-culture) by transferring the inserts with hMSCs into a new 24 multiwell plate. Following cellular incubation 24 and 72 h, the culture media was removed and 200 μL of 1 mg/mL MTT in DMEM (phenol red and serum free) was added to each well. Samples treated with MTT reagent were incubated for 2 h at 37°C, protected from light. Media was then carefully removed and 200 μL of DMSO was added to each well to solubilize the tretrazolium crystals. The multiwell plate was covered with tinfoil and agitated on an orbital shaker for 20 min. Solubilized formazan (100 μL) was transferred to a 96-multiwell plate and read at λ = 570 nm using the FLUOstar OMEGA microplate reader. Standard curves for hMSCs, U2OS, and U2OS spheroids were generated at known cell densities. All tests were performed in triplicate.

### Cytotoxicity by LDH and Live/Dead Assays

Cytotoxicity of U2OS cells in mono- and co-culture (with hMSCs) grown on bone cements with and without PLGA-DOXO NPs was measured using the Lactate Dehydrogenase (LDH) Assay Kit (Fluorometric, ab197000, Abcam, United Kingdom) and Live/Dead assay (LIVE/DEAD® Cell Imaging Kit, Life Technologies, United Kingdom). LDH kit was used according to manufacturer instructions. In this assay, LDH converts lactate into pyruvate and NADH, which reacts with the specific fluorescent probe to generate an intense fluorescent product (Ex/Em = 535/587 nm). Live/Dead Cell Imaging Kit was used according to the manufacturer's instructions. This fluorescence-based kit uses calcein AM and ethidium bromide to identify live cells (green) from the dead cells (red) from cell populations. Samples were washed twice with PBS before incubation with staining. Briefly, 4 μM ethidium homodimer-1 and 10 μM calcein were diluted in DPBS, and samples were incubated with Live/Dead staining for 30 min at 37°C. Images were collected at 1 and 3 days using an EVOS$^{TM}$ M5000 fluorescence microscope equipped.

### Cellular Morphology by Confocal Immunostaining and SEM Analysis

For immunostaining analysis, after 72 h, samples were fixed in pre-warmed 4% w/v paraformaldehyde (PFA) for 30 min at room temperature (RT) prior to cell permeabilization using 0.1% v/v Tween20® in PBS (PBS/Tween20®). For the cement, DAPI solution (Vector Laboratories, United Kingdom) (1:2500 in 0.1% PBS/Tween20®) was added to the samples for 10 min at RT and then washed three times with 0.1% PBS/Tween20®. For the insert, DAPI staining was performed in the same way as for the cement and after that Phalloidin staining was carried out. Rhodamine-phalloidin was prepared using phalloidin-tetramethylrhodamine B isothiocyanate (1:1000 in 0.1% PBS/Tween20®) for 20 min at RT. Then, samples were washed with 0.1% PBS/Tween20® solution. Experiments were light sensitive, and images were collected at 72 h using a Nikon A1R inverted confocal microscope. For the SEM analysis, at 72 h, samples were fixed in pre-warmed 2% Glutaraldehyde overnight, rinsed in PBS twice and dehydrated in ethanol grades: 30 min in each 25, 50, and 75% EtOH and 1 h in 100% EtOH (twice). Samples were stored at 4°C in 100% EtOH until critical point dried using a BAL-TEC 030 Critical Point Dryer (Leica Geosystems Ltd., Milton Keynes, United Kingdom). Finally, cements were mounted on carbon disks (TAAB Laboratory Equipment) and gold-coated using a Polaron E5000 SEM Coating unit (Quorum Technologies Ltd., United Kingdom). Samples were imaged with a Tescan Vega LMU scanning electron microscope. The brightness of images was adjusted to aid visibility of cell nuclei.

## Statistical Analysis

Statistical analysis was performed using GraphPad Prism 8.2.1 with three independent experiments performed. Data was analyzed using two-way ANOVA (Bonferroni, unless differently stated) and paired *t*-test, with the significant difference set at $p < 0.05$. Data is presented as mean ± SD.

# RESULTS

## Bone Cement Physical-Chemical Characterizations

### Curing Time and Injectability

Setting time was investigated in all four compositions of cements, with the 40/60 ratio found to have the quickest mean setting time of 19 min (±0.5 min), with data presented in **Figure 1A**. As NHA content decreased, there was an increase in the setting time of the cement with significant differences when comparing cements with a 50/50 (20.17 ± 1.26 min), 60/40 (23.67 ± 0.76 min) and 70/30 (23.33 ± 0.76 min) ratio after statistical analysis. Injectability ranged between 97.23 and 99.6% in cements with varying concentrations of NHA and is presented in **Figure 1B**. Cements with 70/30 NHA compositions had the best injectability (99.30 ± 3.0%) followed by 40/60 (98.61% ± 0.31%), 50/50 (98.51 ± 0.15%) and 60/40 (97.67 ± 0.44%). Significant differences were found via one-way ANOVA (Bonferroni) with injectability decreasing with decreased levels of NHA, with an exception observed in the 70/30 cements.

### Mechanical Properties: Compression Tests

The cements containing either equal or less NHA to CH and G were found to have no significant difference in Young's compressive modulus (50/50: 48.71 ± 1.85 kPa, 60/40: 46.47 ± 6.45k Pa and 70/30: 45.06 ± 3.89 kPa, respectively), data presented in **Figure 1C**. However, when the ratio of CH and G to NHA was increased to 40/60 considerable increases in young's compressive modulus were observed (97.04 ± 18.04 kPa). A significant difference was found between cements containing 40/60 CH and G to NHA and all other NHA concentrations.

### Chemical Analysis by FTIR-ATR

Fourier Transformed Infrared analysis in Attenuated Total Reflectance spectra were measured for the four compositions of bone cement (40/60, 50/50, 60/40, and 70/30), with results shown in **Figure 1D**. In general, spectra of four bone cements showed Gelatin (G) peaks between 3300 and 3500 $cm^{-1}$ for O-H and N-H bands, primary and secondary amide bands (C = O and N-H) appearing at 1655 $cm^{-1}$ and 1540 $cm^{-1}$, respectively. Similarly, for chitosan (CH), peaks are observed between 3400 and 3500 $cm^{-1}$ due to vibrational stretching of N-H and O-H groups. Due to the content of amide bonds in both, chitosan and gelatin, there is an overlapping in C = O band at 1655 $cm^{-1}$ and N-H peaks at 1540 $cm^{-1}$ in bone cement spectra. Also, peaks at 1062–1150 $cm^{-1}$ associated with C-O-C stretching and at 2970–2880 $cm^{-1}$ stretching vibration of aliphatic groups (-$CH_2$ and -$CH_3$) are observed. On this regard, by increasing the content of the biopolymers (gelatin and chitosan), it was evidenced an increase of the peaks in the range of 3300–3500 $cm^{-1}$ as well as those corresponding to the amide group (C = O bonds at 1655 $cm^{-1}$ and the deformation of N-H groups at 1540 $cm^{-1}$). While, an increasing of the NHA content in bone cements showed an increasing of two peaks intensity at 869 $cm^{-1}$ (aliphatic P-O-C stretching) and 1041 $cm^{-1}$ (characteristic of the $PO_4^{2-}$).

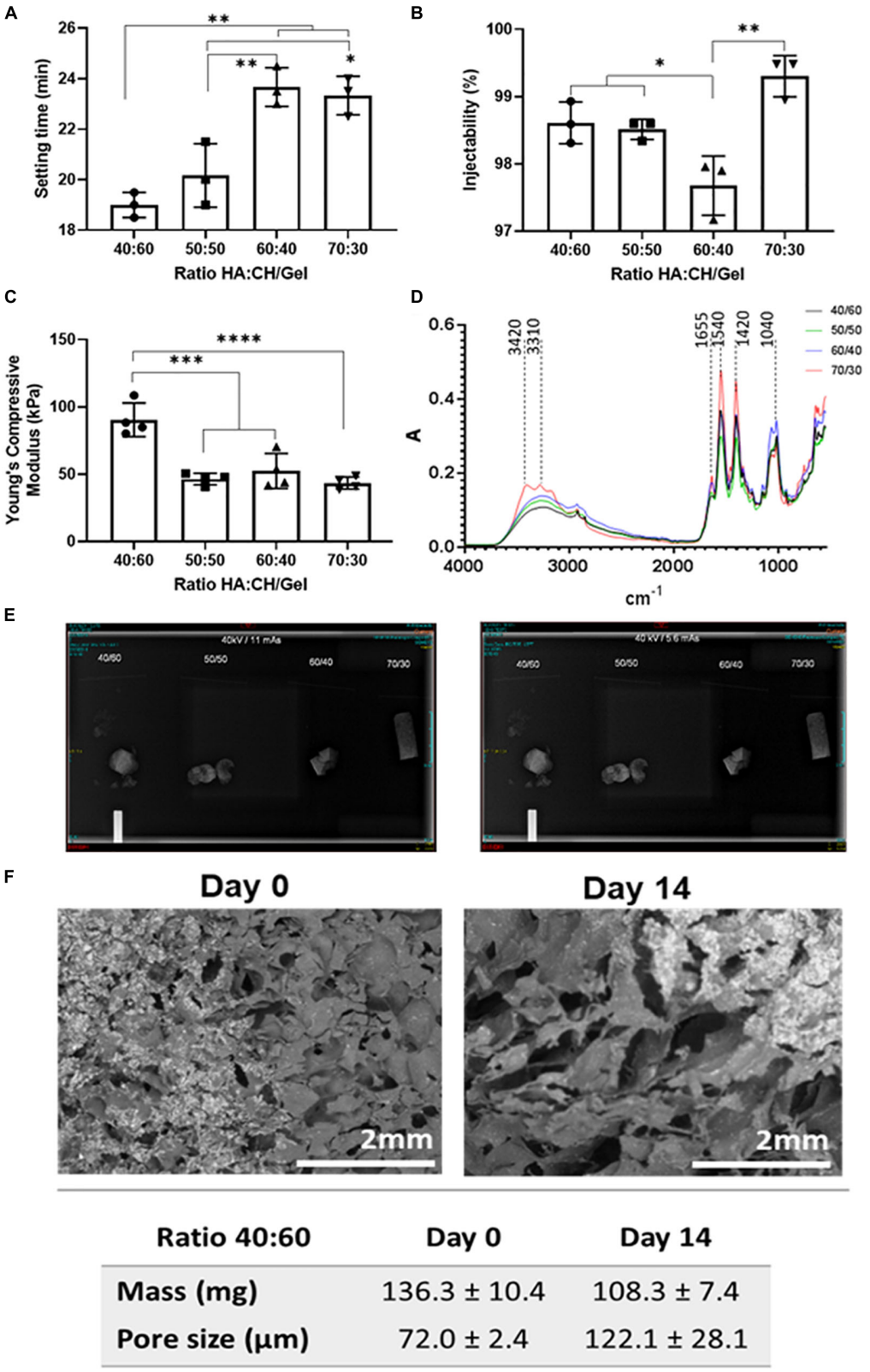


| Ratio 40:60 | Day 0 | Day 14 |
|---|---|---|
| Mass (mg) | 136.3 ± 10.4 | 108.3 ± 7.4 |
| Pore size (μm) | 72.0 ± 2.4 | 122.1 ± 28.1 |

**FIGURE 1 | (A)** Setting time (in minutes), **(B)** Injectability as (%), **(C)** Compressive Young modulus, **(D)** FTIR-ATR spectra, **(E)** 40 kV 11 mAs (left) and 5.6 mAs X-Ray (right) Images visible for bone cements at different ratios of hydroxyapatite and Chitosan/Gelatin 40/60, 50/50, 60/40, and 70/30. **(F)** SEM micrographs of bone cements (40/60) after 14 days incubation in PBS at 37°C. Statistics: $^{*}p < 0.05$, $^{**}p < 0.007$, $^{***}p < 0.0007$, $^{****}p < 0.0001$.

### Radiopacity

Radiopacity properties of the four different compositions of bone cement (40/60, 50/50, 60/40, and 70/30) were assessed via X-ray imaging at 40 kV at 11 mAs and 5.6 mAs. The images obtained (**Figure 1E**) show that all bone cement compositions were visible, exhibiting radio contrast properties and bright white shapes. Furthermore, X-rays demonstrated that the cements containing BS were quite homogenous, except slight speckled effects observed due to potential uneven BS distribution.

### Morphology and Structure by Quantification of Pore Size and Degradation

Initial bone cement formulation (40/60) was studied in terms of degradation and mass changes over 14 days period of incubation at physiological conditions. From **Figure 1F**, it can be observed that bone cement scaffolds have changed their morphology over time by increasing the size of the pores of about 50.1 μm (from day 0 to day 14) and significant mean mass reduction (about 28 mg) following 14 days incubation period, as consequence of materials degradation.

In **Supplementary Figure S3A** are reported the SEM images of bone cements (40/60 ratio), containing either no DOXO (0 μM), free DOXO (40 μM) and PLGA-DOXO NPs (100 μM), which were analyzed using ImageJ software to calculate the mean pore area shown in **Supplementary Figure S3B**. The morphology and pore size were found to drastically change with the addition of DOXO ($p < 0.0001$) for 40 μM and 100 μM compared to the control (0 μM). In particular, a significant reduction of the mean pore size is observed when DOXO is incorporated into bone cements. From SEM micrographs, it is observed macroscopically that the number of pores increase while the pore size is significantly reduced when DOXO (40 μM and 100 μM) is incorporated in the bone cements. Bone cements without DOXO had the largest pore area (0.56 $\mu m^2$) compared to the 40 μM and 100 μM cements (0.0195 $\mu m^2$ and 0.0198 $\mu m^2$, respectively).

### Drug Release of Doxorubicin

In **Figure 2**, a significant difference is observed between DOXO release between cements (40/60) containing PLGA-DOXO NPs and free DOXO at concentrations of 40 μM and 10 μM ($p < 0.0007$ and $p < 0.0146$, respectively). A higher cumulative drug release (%) is detected in cements containing PLGA-DOXO NPs, with around 80% of DOXO released from cements at 40 μM and 100 μM DOXO over 7 days. However, less than 20% of DOXO was released from cements without NPs, reaching a plateau in drug release following 2–3 days of incubation.

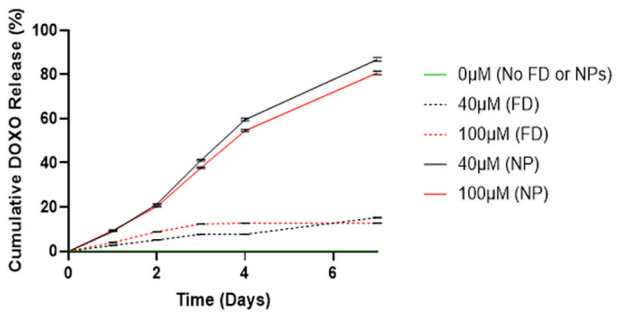


**FIGURE 2 |** Drug release profiles of DOXO from bone cements (40/60) containing no DOXO (0 μM), free DOXO (40 μM and 100 μM) and PLGA-DOXO NPs (40 μM and 100 μM), into PBS after 7 days incubation at 37°C. Data presented as mean ± standard deviation, ($n = 3$ replicates).

## PLGA-DOXO NP Characterizations

### Morphology, Size Measurements and Encapsulation Efficient of PLGA-DOXO Nanoparticles

SEM micrographs of freeze-dried PLGA-DOXO NPs are shown in **Figure 3A** and evidence a spherical morphology, not affected by the freeze-drying process. The EE of DOXO was about 32.8 ± 0.6%. PLGA-DOXO NPs ($n = 3$) were found to be monodisperse in size with a mean hydrodynamic diameter of 152 nm (**Figure 3B**) and a polydispersity index of 0.181. The amount of NPs to be embedded in the cement required to achieve final DOXO concentrations of 40 μM (0.6 mg/ml) and 100 μM (1.5 mg/ml) was calculated based on the EE.

## Cellular Characterizations

### Assessment of IC50 of Doxorubicin

The IC50 for U2OS and hMSCs cells at different DOXO concentrations are shown in **Figures 4A,B** as percentage of cell viability. Obtained IC50 values (min and max range for U2OS) were used identify the two DOXO concentrations to be used (40 μM and 100 μM), either as free DOXO loaded into NPs in bone cements. U2OS cells appear more responsive to DOXO when compared to hMSCs (27.359 μM and 31.147 μM, respectively). Further analysis on IC50 for U2OS spheroids (96.158 μM) was also explored to understand DOXO drug effect in micromass of tumoral cells (**Figure 4C**). In general, by contrasting IC50 (as % cell viability) and cell response to different DOXO concentrations (**Figure 4D**), U2OS cells appear more vulnerable against DOXO drug when compared to hMSCs and U2OS spheroid.

### Osteosarcoma and hMSCs Metabolic Activity

The metabolic activity of U2OS cells cultured either in monoculture or indirect coculture with hMSCs, onto bone cement (40/60) with free DOXO (FD) or PLGA-DOXO NPs (NPs), at 40 μM and 100 μM, or without FD or NPs (0 μM, referred as control) are shown in **Figure 5**. **Figure 5A** shows that there was a significant difference in the metabolic activity of monocultured U2OS cells after 24h between 0 and 100 μM ($p < 0.0107$) and 40 and 100 μM ($p < 0.0001$). This trend was also seen in U2OS cells cocultured with hMSCs (**Figure 5A**) between 0 and 100 μM ($p < 0.0001$) and 40 and 100 μM ($p < 0.0001$). Significant differences were also found in hMSC metabolic activity (**Figure 5A**) between 0 and 40 μM ($p < 0.0001$) and 40 and 100 μM ($p < 0.0001$). In comparison, no significant difference was found in the metabolic activity of U2OS cells in mono- or coculture with hMSCs after 72 h on any cement containing free DOXO (40 or 100 μM) (**Figure 5B**). A similar trend was reflected in hMSCs metabolic activity after 72 h (**Figure 5B**).

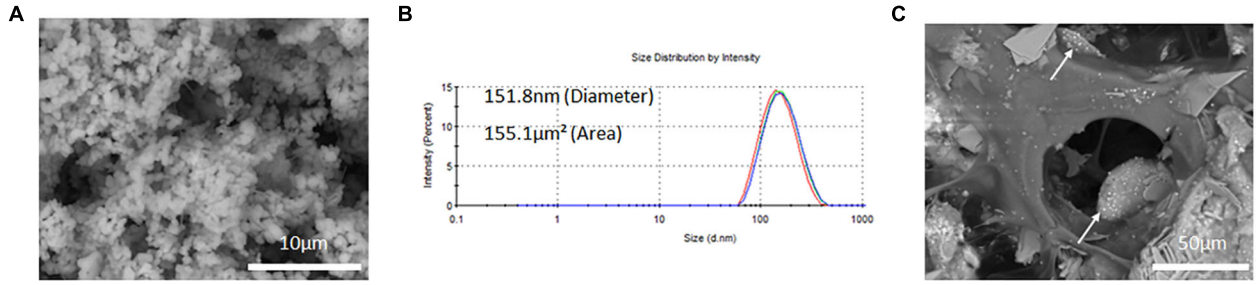


**FIGURE 3 | (A)** SEM image of free PLGA-DOXO NPs. Scale bar represents 10 μm. **(B)** Zetasizer DLS readings of PLGA-DOXO NPs suspended in DI water. **(C)** SEM image of PLGA-DOXO NPs loaded bone cement (40/60 composition) (visible as white spheres). Scale bar represents 50 μm.

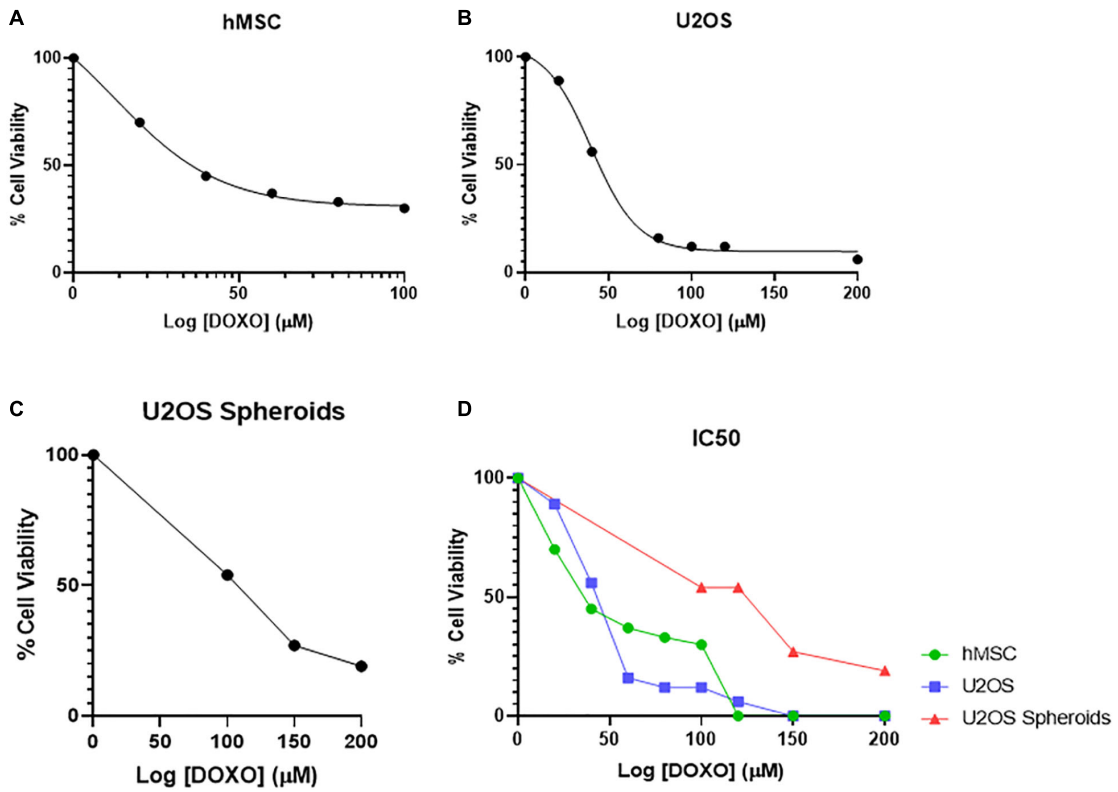


**FIGURE 4 |** Mean percentage cell viability of **(A)** hMSC, **(B)** U2OS cells, and **(C)** U2OS spheroids after 24 h incubation with varying concentrations of free DOXO (0–200 μM) in the respective growth media at 37°C, used to identify the IC50 value of DOXO in these cell types ($n$ = 3 replicas, ±SD) **(D)**.

In regards to cultures grown on bone cement (40/60) loaded with PLGA-DOXO NPs significant differences were found between monocultured U2OS cells at 0 and 40 μM ($p < 0.0064$), and cocultured U2OS at 0 and 40 μM ($p < 0.0243$), 0 and 100 μM ($p < 0.0176$) and 40 and 100 μM ($p < 0.0001$) after 24 h (**Figure 5C**). There was no significant difference in hMSC metabolic activity after 24 h (**Figure 5C**). After 72 h of culture with cements loaded with PLGA-DOXO NPs (**Figure 5D**), a significant difference in metabolic activity was observed in monocultured U2OS between 0 and 100 μM ($p < 0.0.0001$) and 40 and 100 μM ($p < 0.0001$); this was also true for cocultured U2OS cells between 0 and 100 μM ($p < 0.0001$) and 40 μM and 100 μM ($p < 0.0004$). A similar trend was followed by hMSCs cells, with statistical significant differences in their metabolic activity detected after 72 h between 0 and 100 μM ($p < 0.0001$) and 40 and 100 μM ($p < 0.006$) (**Figure 5D**). This apparent improved reduction in U2OS cell metabolic activity with the use of PLGA-DOXO NP loaded bone cements validated the decision to use the PLGA-DOXO NP loaded formulation in the following investigations.

## Osteosarcoma and hMSCs Cytotoxicity

A statistically significant difference was found between mono- and cocultured cells exposed to bone cements (40/60) with and

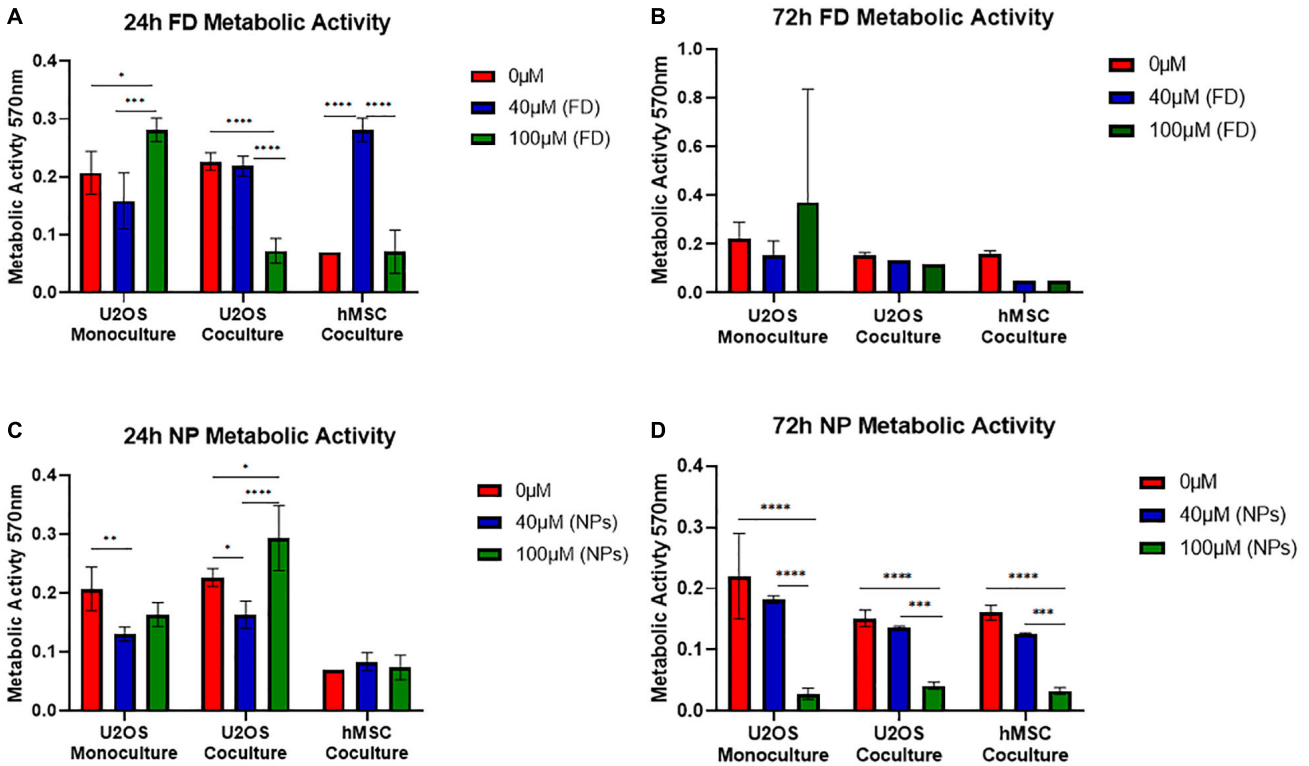


**FIGURE 5 |** Mean metabolic activity of U2OS cells in monoculture, U2OS cells in coculture and hMSCs in coculture grown on bone cements (40/60 composition) without DOXO (0 μM) and with Free DOXO (FD, 40 μM and 100 μM) **(A)** 24 and **(B)** 72 h. Mean metabolic activity of U2OS cells in monoculture, U2OS cells in coculture and hMSCs in coculture grown on bone cements with a 40/60 CH+G to NHA composition on cements without PLGA-DOXO NPs (0 μM) and with PLGA-DOXO NPs (40 μM and 100 μM) after **(C)** 24 and **(D)** 72 h. ($n$ = 3 replicas, *$p < 0.05$, **$p < 0.01$, ***$p > 0.001$, and ****$p > 0.0001$, respectively).

without PLGA-DOXO NPs, at a concentration of 40 μM, after 24 and 72 h, data presented in **Figure 6A**. Data presented in **Figure 6B** shows that there was no significant difference in the metabolic activity of U2OS cells monocultured on bone cements (40/60) without PLGA-DOXO NPs (-NP) and with PLGA-DOXO NPs at 40 μM (+NPs) after 24 and 72 h. There was, however, a statistical difference found between the metabolic activity of cocultured U2OS cells on cements fabricated with PLGA-DOXO NPs at 40 μM (+NPs) and without PLGA-DOXO NPs (-NPs) after 24, and 72 h, shown in **Figure 6B**.

Live and Dead images of U2OS cells in mono- and indirect coculture (with hMSCs) were taken after 24 and 72 h exposure to bone cements (40/60) with PLGA-DOXO NPs (40 μM, +NPs) and without PLGA-DOXO NPs (-NPs), data presented in **Figure 6C**. After 24 h of incubation, no significant difference between the different culture systems, either in presence or absence of NPs, can be appreciated. However, at 72 h incubation, it is possible to observe a greater amount of live cells (green) on bone cements without PLGA-DOXO NPs (-NPs) if compared to the dead cells (red), in both mono- and cocultures. In contrast, bone cements containing PLGA-DOXO NPs (40 μM, +NPs) showed a greater ratio of dead cells (red) when compared to live cells (green), in both mono- and indirect coculture with hMSCs (**Figure 6C**).

## Osteosarcoma Cells Morphology on Bone Cements

For cements (40/60 composition) without PLGA-DOXO NPs (**Figure 7**, -NPs), cell nuclei stained in blue (DAPI immunostaining analysis) shows a slight increase of U2OS cells number in monoculture and coculture (135 and 130 nuclei, respectively). Whilst in cements (40/60) containing PLGA-DOXO NPs, fewer nuclei can be observed in monoculture and coculture (27 and 12 nuclei, respectively) indicating a decrease of viable U2OS cells onto these (**Figure 7**, +NPs). Regarding the hMSCs morphology, nuclei (blue, stained with DAPI) and the cytoskeleton (red, stained with rhodamine-phalloidin), suggests no visible changes in term of morphology independently if seeded in indirect coculture with U2OS cells grown on bone cements with and without PLGA-DOXO NPs (**Figure 7**). Cytoskeleton of hMSCs appeared typically elongated, spread and attached to the insert's surface. However, there is an apparent slight reduction in the number of hMSCs present when indirectly cocultured with U2OS cells seeded onto cements (40/60) containing PLGA-DOXO NPs (40 μM), which may indicate a potential cytotoxic effect from released DOXO. SEM analysis of U2OS onto cements (40/60) without PLGA-DOXO NPs showed round-shaped osteosarcoma cells agglomerated after 72 h (**Figure 7**).

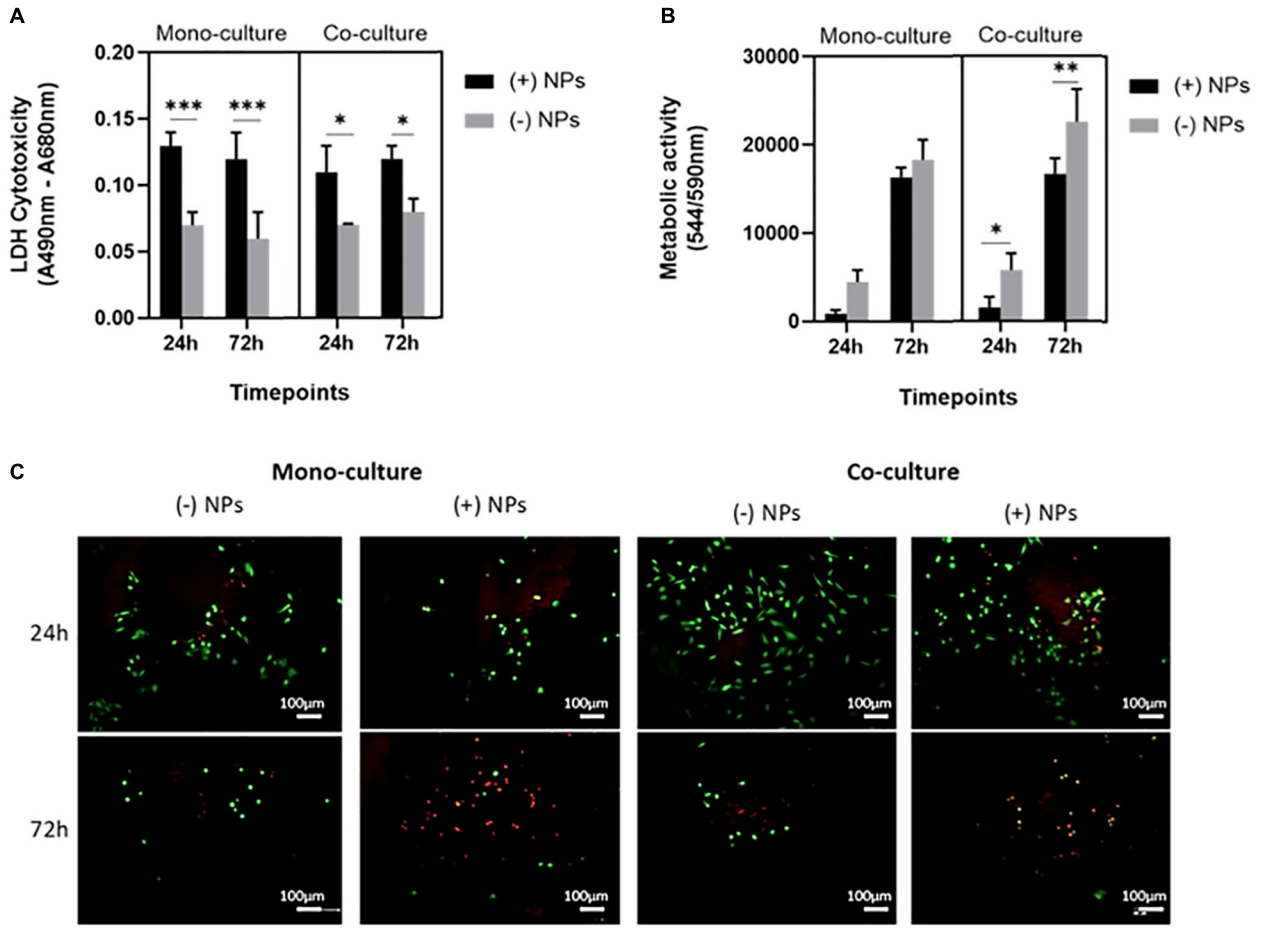


**FIGURE 6 | (A)** Cellular cytotoxicity, **(B)** metabolic activity and **(C)** live dead images (live cells visible in green, dead cells visible in red) of U2OS cells in mono- and co-culture (with hMSCs) grown on bone cements (with 40/60 composition) containing PLGA-DOXO NPs at 40 μM DOXO (+NPs) and without PLGA-DOXO NPs at 0 μM (-NPs, control). Scale bars represent 100 μm. Data presented as mean ± SD ($n$ = 3 replicas, $^{*}p < 0.05$, $^{**}p < 0.01$ and, $^{***}p < 0.001$).

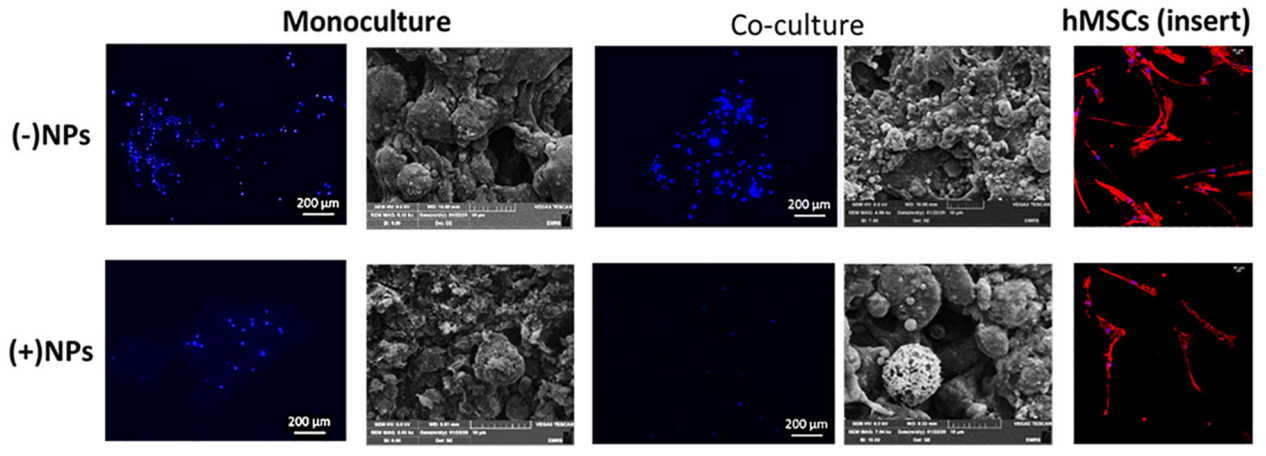


**FIGURE 7 |** Nucleus staining and cellular-bone cement morphology and interaction of U2OS cells in mono- and indirect co-cultures (with hMSCs) grown on bone cements with a 40/60 composition of CH+G to NHA with and without loaded PLGA-DOXO NPs (40 μM) after 72 h of incubation. Scale bars represent 200, 100, and 20 μm, respectively.

## DISCUSSION

As a major inorganic component of bone, calcium phosphate possesses an excellent biocompatibility in both the dissolved and solid form. Consequently, these are attractive biomaterials for potential hard-tissue applications (Tanzawa et al., 2011). Poor injectability and excessively rapid curing times are common limitations preventing the use of calcium phosphate cements-based into widespread clinical settings (Tariq et al., 2019). Therefore, and increased attention is placed on cement manipulation and appropriate setting times to expand its chemotherapeutic and regenerative capacities. The results obtained in this work showed that cement with a 40/60 composition had the quickest mean setting time (19 ± 0.5 min, shown in **Figure 1A**). Even though setting-times were improved by decreasing the concentration of biopolymers (CH:G) in bone cement formulations, these must be further improved if intended for clinical applications. In clinical settings, it is desirable to use cements with fast curing time (around 10–15 min), to prevent crumbling of unset cement mixtures when exposed to bodily fluids (Xu et al., 2007).

From results presented in **Figure 1B**, cements with a 70/30 composition of liquid-to-powder (CH/G:NHA) showed the best injectability properties; however, it performed poorly in mechanical testing after setting (**Figure 1C**). Broadly, it was observed a trend of increased injectability with the increasing of biopolymers content,. The reduction of the powder-to-liquid ratio has been found to improve CPC injectability due to changes in viscosity, however, it prolongs setting time while jeopardizing the cement mechanical properties (Yousefi, 2019). On this regard, the injectability of the 40/60 composition was found to be 98.6 ± 0.3% effective with minimal cement loss during the process with the highest young's compressive modulus (97.04 ± 18.04 kPa), offering a good compromise between mechanical properties and easy handling that makes it a suitable injectable cement (Bohner, 2010). In general, the 40/60 composition was found to perform best under increasing levels of force, while mimicking the percentage of CP found in natural bones. Cements classified as CPCs are described as second-generation biomaterials, with compositions closely resembling natural bone (Yousefi, 2019). CPCs with decreased powder components, like NHA, result in decreased mechanical properties (Barralet et al., 2004), seen in the 50/50, 60/40 and 70/30 cements, presented in **Figure 1C**. NHA is the key inorganic hydration product used in CPCs (Khairoun et al., 1999), in formulated cements (**Figure 1D**) is found to increase with NHA content evidenced by bands within the range between 3300 and 3500 $cm^{-1}$ (associated to O-H). On this regard, it can be anticipated that the incorporation of NHA may influence CPC resorbability properties (Sakai et al., 2016). In summary and based on shown outcomes on setting time, injectability, mechanical properties; the authors have identified the composition 40/60 ratio of biopolymer (Chitosan and Gelatin):NHA as the best composition to carry forward in further *in vitro* analysis since it demonstrated a good compromise of overall properties as injectable biodegradable material.

The relatively low level of radiopacity associated with CPCs are another reason for their limitation in widespread clinical use (Wu et al., 2018). To overcome this, bismuths, a family of radiopacifiers (Antonijevic et al., 2014), are often used to increase the level of CPC radiopacity (Wu et al., 2018). The ability to track cement placement, and identify any leakage, are both vital to minimize the effects of any complications. Moreover, bismuths have large atomic numbers and for this, they are not toxic and therefore, ideal candidates for the use in CPCs. As reported in **Figure 1E**, all the compositions analyzed with X-Rays demonstrated that the BS was homogeneously distributed in the polymer, obtaining optically lucent radiopaque cements. The bone cements (40/60 composition) containing BS concentration of 15% w/w showed cements with radiopacity properties as visibly clear as the bone replica controls (as seen when using the phantom). It is anticipated that the radiopaque contrast properties may be improved by a further increase of BS quantity; and consequently, the physical-chemical properties should be also investigated for new formulations.

A lack of degradation can limit bone regeneration (Lodoso-Torrecilla et al., 2019) due to limited space for the formation of new bone tissue (Habraken et al., 2007). Attempts to overcome this have focused on the addition of porogens to CPC compositions (Liao et al., 2011) with PLGA addition proven to be successful in the generation of cement pores (Lanao et al., 2011). This allows for a quicker rate of degradation and improved bone regeneration (Lodoso-Torrecilla et al., 2019). This is a finding reflected in the data presented in this work, with increased pore sizes and decreased mass of cements containing PLGA NPs visible after 14 days (**Figure 1F**). From this result, it can be anticipated that over a prolonged period, cements of a 40/60 composition containing loaded PLGA-DOXO NPs would degrade further following this time, allowing for bone tissue regeneration. However, increase porosity and mass loss would also point toward a potential decrease in the mechanical properties, which could also impact regeneration rates. Also, the addition of DOXO, whether free or loaded in PLGA-DOXO NPs, affected the porosity of cements, as seen in **Supplementary Figure S3A**. Although, potential reasons can be foreseen, including (1) the presence of $NH_2$ groups in DOXO molecule that could potentially react with unreacted $NH_2$ groups (either from CH or G), if exists an excess of Genipin; or (2) a potential interaction of DOXO and loaded-DOXO NPs with water or other components, leading to an increased hydration capability and consequent changes in bone cements porosity, after freeze-drying. However, any of these theories should be further investigated and proven. As reported elsewhere, the porosity of CPCs can be affected via the use and interaction with different materials, including polymers (Shariff et al., 2016), calcium carbonates (Espanol et al., 2009), foaming agents (Ginebra et al., 2007), etc.

PLGA-DOXO NPs obtained via the nano-precipitation method showed a spherical morphology and a narrow, mono-modal size distribution. Small size nanoparticles, at ∼150 nm (**Figure 3B**), were obtained with a DOXO EE of 32.7 ± 0.6%. Our data for EE is in agreement with previously published work. For instance, Mattu et al. reported an EE of DOXO ranging

from 22 to 45% inside block-copolymer nanoparticles, with EE increasing with increasing amount of hydrophilic blocks in the co-polymer composition (Mattu et al., 2018). Similarly, Dessy and collaborators reported EE of hydrophilic DOXO to be in the range 22–26%(Dessy et al., 2012). Doxorubicin is a water soluble drug, which may easily diffuse toward the water phase during the nanoprecipitation process, explaining the relatively low values of EE. The data presented in **Figure 3C** show that PLGA-DOXO NPs are evenly distributed throughout the bone cement and preserve their spherical morphology, indicating that the cement preparation process did not affect the integrity of the NPs (Ferreira et al., 2014; Gentile et al., 2016).

A minimum of 24 h is required for endocytosis of DOXO before U2OS spheroid undergo cellular arrest (Baek et al., 2016). However, following tumor removal minimal cancerous cells remain, therefore a 2D U2OS model may prove more beneficial in understanding therapeutic bone cement potential. The U2OS cultures in 2D showed a significantly lower IC50 of DOXO, a trend reflected in hMSCs. This implies the concentration of DOXO administered locally via bone cement, would be reduced compared to pre-adjuvant treatments. This suggests chemotherapeutic resistant mechanisms present in spheroids do not occur in 2D cultures. The lack of architectural complexity in 2D cultures allows for easier drug penetration compared to 3D cultures (Imamura et al., 2015). While in the undifferentiated state, hMSCs have increased resistance to DOXO compared to their differentiated counterparts (Kozhukharova et al., 2018). These chemoprotective properties, under the correct conditions could be passed onto OS cells because of MSC education (Sun et al., 2014), thus further investigations into 2D co-cultures containing both U2OS and hMSCs is essential.

Data presented in **Figure 6A** showed a significant difference in cytotoxicity of monocultured U2OS and cocultures U2OS with hMSCs cells grown on cements in presence and absence PLGA-DOXO NPs after 24 and 72 h. More cells survived on cements without NPs, in both cases. Furthermore, immunostaining and SEM analysis, presented in **Figure 7** confirmed this tendency, with less cells found in the NPs loaded samples. Taken together, these results suggested that adequate levels of DOXO have been released from loaded NPs, thus resulting in increased levels of cytotoxicity, inhibiting U2OS growth and inducing their apoptosis. The presence of hMSCs allows for a more accurate representation *in vitro* model mimicking the complexity of the OS tumor microenvironment. Data presented in **Figure 5** shows significant differences between U2OS cells cocultured with hMSCs on varying concentrations of bone cements with PLGA-DOXO NPs, after 24 and 72 h. However, following 72 h culturing with cements containing free DOXO, there was no significant difference between U2OS cells in mono- or coculture with hMSCs on varying concentrations of bone cement. As reported by Sun et al. (2014), when close to the tumor site, hMSCs undergo the "educational" process via the acquisition of TAF phenotype, promoting OS cells proliferation and tumor growth, suppressing the inhibition effect of DOXO on them. These findings demonstrate that the presence of hMSCs is sufficient to suppress even a high (100 μM) dosage of DOXO in free drug cements, explaining why no differences were found between the different drug concentrations in our work. Resistance during the undifferentiated stage is vital in ensuring that the tumor microenvironment is maintained, as U2OS cells produce increased levels of transforming growth factor-β (TGF-β) preventing hMSC differentiation into osteoblasts (Tu et al., 2014). Maintenance of an undifferentiated state in hMSCs is thought to increase the production of pro-tumor cytokines (Tu et al., 2014), explaining why no significant difference was seen between U2OS cells cocultured with hMSCs on increasing concentrations of free DOXO bone cements.

## CONCLUSION

In conclusion, bone cements containing PLGA-DOXO NP have better-controlled DOXO release over 7 days compared to bone cements containing free DOXO, suggesting a better approach for modulating drug delivery at tumor sites. To prolong the release of DOXO from these cements, the combination of free DOXO and PLGA-DOXO NPs should be considered in future works. The presence of hMSCs offer a degree of DOXO resistance in U2OS cells cultured on PLGA-DOXO NP bone cements. This multidirectional attack of OS cells could support apoptosis of residual cancer cells, as well as minimize the effects of hMSCs that display pro-tumor characteristics. Still, the effectiveness of this approach to treat osteosarcoma needs to be studied in animal models. These findings contribute to pre-existing knowledge in the field of bioengineering involving bone reconstruction and NP technology for the localized controlled delivery of drugs. By combining these two disciplines there is an exciting potential to create a positive impact in cancer treatment of osteosarcoma, offering a less demanding form of adjuvant chemotherapy to future patients.

## DATA AVAILABILITY STATEMENT

Data supporting this publication is openly available under an "Open Data Commons Open Database License." Additional metadata are available at: doi: 10.25405/data.ncl.12047292. Please contact Newcastle Research Data Service at rdm@ncl.ac.uk for access instructions.

## AUTHOR CONTRIBUTIONS

RD, AF, PG, CM, and KR contributed to the conception and design of the study. RD, AF, JB, and AS collected the data. RD, AF, and JB performed the statistical analysis. RD, AS, and JB wrote the first draft of the manuscript. All authors contributed to the article and approved the submitted version.

## FUNDING

AS acknowledges support from EPSRC for their Ph.D. studentship (EPSRC Grant EP/R51309X/1).

## SUPPLEMENTARY MATERIAL

The Supplementary Material for this article can be found online at: https://www.frontiersin.org/articles/10.3389/fbioe.2020.00754/full#supplementary-material

**FIGURE S1 | (A)** Mean contrast of bone cements bone cements with CH+G to NHA composition of 40/60, 50/50, 60/40, and 70/30 imaged at 40 kV/11 mAs. **(B)** Mean contrast of bone cements bone cements with CH+G to NHA composition of 40/60, 50/50, 60/40, and 70/30 imaged at 40 kV/5.6 mAs. **(C)** X-ray images of bone cements with 40/60, 50/50, 60/40, and 70/30 compositions taken at t 40 kV/5.6 mAs. **(D)** X-ray images of bone cements with 40/60, 50/50, 60/40, and 70/30 compositions taken at 40 kV/5.6 mAs. ($n$ = 3 replicas $^{*}p < 0.05$, $^{**}p < 0.005$).

**FIGURE S2 |** FTIR-ATR spectra, of bone cements with **(A)** 40/60, **(B)** 50/50, **(C)** 60/40, and **(D)** 70/30 compositions of CH+G to NHA. **(E)** Mean changes in pH of bone cements (40/60) containing no DOXO (0 μM), 40 μM Free DOXO and 100 μM PLGA-DOXO NPs over 3 days incubation in PBS at 37°C ($n$ = 3 replicas).

**FIGURE S3 | (A)** SEM images of 0 μM, 40 μM Free DOXO and 100 μM PLGA-DOXO NP bone cements (40/60 composition). Scale bars represent 1 mm. **(B)** Mean Pore Area of bone cements (40/60) in absence of DOXO (0 μM), Free DOXO (dissolved DOXO at 40 μM) and PLGA-DOXO NPs (at concentration 100 μM). Data presented as mean ± standard deviation, ($n$ = 3 replicates) $^{****}p < 0.001$.

**FIGURE S4 |** Mean cell viability of U2OS cells in monoculture, U2OS cells in coculture and hMSCs in coculture grown on bone cements with a 40/60 CH+G to NHA composition on cements without Free DOXO (0 μM) and with Free DOXO (40 μM and 100 μM) after **(A)** 24 and **(B)** 72 h. Mean cell viability of U2OS cells in monoculture, U2OS cells in coculture and hMSCs in coculture grown on bone cements with a 40/60 CH+G to NHA composition on cements without PLGA-DOXO NPs (0 μM) and with PLGA-DOXO NPs (40 μM and 100 μM) after **(C)** 24 and **(D)** 72 h ($n$ = 3 replicas, $^{*}p < 0.05$, $^{**}p < 0.005$, $^{***}p < 0.001$).

## REFERENCES


Abdullah, C. S., Alam, S., Aishwarya, R., Miriyala, S., Bhuiyan, A. F. N., Panachatcharam, M., et al. (2019). Doxorubicin-induced cardiomyopathy associated with inhibition of autophagic degradation process and defects in mitochondrial respiration. *Sci. Rep.* 9:2002.

Akram, M., Ahmed, R., Shakir, I., Ibrahim, W. A. W., and Hussain, R. (2014). Extracting hydroxyapatite and its precursors from natural resources. *J. Mater. Sci.* 49, 1461–1475. doi: 10.1007/s10853-013-7864-x

Antonijevic, D., Medigovic, I., Zrilic, M., Jokic, B., Vukovic, Z., and Todorovic, L. (2014). The influence of different radiopacifying agents on the radiopacity, compressive strength, setting time, and porosity of Portland cement. *Clin. Oral Investig.* 18, 1597–1604. doi: 10.1007/s00784-013-1130-0

Ashan, S. M., Thomas, M., Reddy, K. K., Sooraparaju, S. G., Asthana, A., and Bhatnager, I. (2018). Chitosan as biomaterial in drug delivery and tissue engineering. *Int. J. Biol. Macromol.* 110, 97–109.

Baek, N., Seo, O. W., Kim, M., and Hulme, J. (2016). An SSA. Monitoring the effects of doxorubicin on 3D-spheroid tumor cells in real-time. *Onco Targets Ther.* 9:7207. doi: 10.2147/ott.s112566

Barralet, J., Grover, L., and Gbureck, U. (2004). Ionic modification of calcium phosphate cement viscosity. Part II: hypodermic injection and strength improvement of brushite cement. *Biomaterials* 25, 2197–2203. doi: 10.1016/j.biomaterials.2003.09.085

Bohner, M. (2010). Resorbable biomaterials as bone graft substitutes. *Mater. Today* 13, 24–30. doi: 10.1016/s1369-7021(10)70014-6

Buondonno, I., Gazzano, E., Tavanti, E., Chegaev, K., Kopecka, J., Fanelli, M., et al. (2019). Endoplasmic reticulum-targeting doxorubicin: a new tool effective against doxorubicin-resistant osteosarcoma. *Cell Mol. Life Sci.* 76, 609–625. doi: 10.1007/s00018-018-2967-9

Chaloupka, K., Malam, Y., and Seifalian, A. M. (2010). Nanosilver as a new generation of nanoproduct in biomedical applications. *Trends Biotechnol.* 28, 580–588. doi: 10.1016/j.tibtech.2010.07.006

Collins, M., Wilhelm, M., Conyers, R., Herschtal, A., Whelan, J., Bielack, S., et al. (2013). Benefits and adverse events in younger versus older patients receiving neoadjuvant chemotherapy for osteosarcoma: findings from a meta-analysis. *J. Clin. Oncol.* 31, 2303–2312. doi: 10.1200/jco.2012.43.8598

De Wever, O., Van Bockstal, M., Mareel, M., Hendrix, A., and Bracke, M. (2014). Carcinoma-associated fibroblasts provide operational flexibility in metastasis. *Semin. Cancer Biol.* 25, 33–46. doi: 10.1016/j.semcancer.2013.12.009

Dehaini, D., Fang, R. H., Luk, B. T., Pang, Z., Hu, C. M., Kroll, A. V., et al. (2016). Ultra-small lipid-polymer hybrid nanoparticles for tumor-penetrating drug delivery. *Nanoscale* 8, 14411–14419. doi: 10.1039/c6nr04091h

Dessy, A. P. A., Alderighi, M., Sandreschi, S., and Chiellini, F. (2012). Doxorubicin loaded polyurethanes nanoparticles. *Nano Biomed. Eng.* 4:6.

Dutta, S. R., Passi, D., Singh, P., and Bhuibhar, A. (2015). Ceramic and non-ceramic hydroxyapatite as a bone graft material: a brief review. *Irish J. Med. Sci.* 184, 101–106. doi: 10.1007/s11845-014-1199-8

Endicott, A. A., Morimoto, L. M., Kline, C. N., Wiemels, J. L., Metayer, C., and Walsh, K. M. (2017). Perinatal factors associated with clinical presentation of osteosarcoma in children and adolescents. *Pediatr. Blood Cancer* 64:e26349. doi: 10.1002/pbc.26349

Espanol, M., Perez, R., Montufar, E., Marichal, C., Sacco, A., and Ginebra, M. (2009). Intrinsic porosity of calcium phosphate cements and its significance for drug delivery and tissue engineering applications. *Acta Biomater.* 5, 2752–2762. doi: 10.1016/j.actbio.2009.03.011

Farbod, K., Sariibrahimoglu, K., Curci, A., Hayrapetyan, A., Hakvoort, J. N., van den Beucken, J. J., et al. (2016). Controlled release of chemotherapeutic platinum-bisphosphonate complexes from injectable calcium phosphate cements. *Tissue Eng. Part A* 22, 788–800. doi: 10.1089/ten.tea.2016.0001

Ferreira, A. M., Mattu, C., Ranzato, E., and Ciardelli, G. (2014). Bioinspired Porous membranes containing polymer nanoparticles for wound healing. *J. Biomed. Mater. Res. Part A* 102, 4394–4405.

Frankenburg, E. P., Goldstein, M. S., Steven, A., Thomas, W., Harris, S. A., and Poser, R. D. (1998). Biomechanical and histological evaluation of a calcium phosphate cement. *J. Bone Joint Surg.* 80, 1112–1124.

Gentile, P., Nandagiri, V. K., Day, J., Chiono, V., Mattu, C., Tonda-Turo, C., et al. (2016). Localised controlled release of simvastatin from porous chitosan-gelatin scaffolds engrafted with simvastatin loaded PLGA-microparticles for bone tissue engineering application. *Mater. Sci. Eng. C Mater. Biomed. Appl.* 59, 249–257. doi: 10.1016/j.msec.2015.10.014

Ginebra, M. P., Delgado, J. A., Harr, I., Almirall, A., Del Valle, S., and Planell, J. A. (2007). Factors affecting the structure and properties of an injectable self setting calcium phosphate foam. *J. Biomed. Mater. Res. Part A* 80, 351–361. doi: 10.1002/jbm.a.30886

Gorlick, R., and Khanna, C. (2010). Osteosarcoma. *J. Bone Miner Res.* 25, 683–691.

Habraken, W., Wolke, J., and Jansen, J. (2007). Ceramic composites as matrices and scaffolds for drug delivery in tissue engineering. *Adv. Drug Delivery Rev.* 59, 234–248. doi: 10.1016/j.addr.2007.03.011

Harrison, D. J., Geller, D. S., Gill, J. D., Lewis, V. O., and Gorlick, R. (2018). Current and future therapeutic approaches for osteosarcoma. *Expert Rev Anticancer Ther.* 18, 39–50.

He, H., Qiao, Z., and Liu, C. (2018). "Accelerating biodegradation of calcium phosphate cement," in *Developments and Applications of Calcium Phosphate Bone Cements*, eds C. Liu and H. He (Singapore: Springer), 227–255. doi: 10.1007/978-981-10-5975-9_5

Hertz, A., and Bruce, I. J. (2007). Inorganic materials for bone repair or replacement applications. *Nanomedicine* 2, 899–918. doi: 10.2217/17435889.2.6.899

Hockin, H. K. X., and Simon, C. G. Jr. (2005). Fast setting calcium phosphate–chitosan scaffold: mechanical properties and biocompatibility. *Biomaterials* 26, 1337–1348. doi: 10.1016/j.biomaterials.2004.04.043

Hoving, S., Seynhaeve, A. L. B., van Tiel, S. T., Eggermont, A. M. M., and ten Hagen, T. L. M. (2005). Addition of low-dose tumor necrosis factor-α to systemic treatment with STEALTH liposomal doxorubicin (Doxil) improved anti-tumor

activity in osteosarcoma-bearing rats. *Anti Cancer Drugs* 16, 667–674. doi: 10.1097/00001813-200507000-00012

Imamura, Y., Mukohara, T., Shimono, Y., Funakoshi, Y., Chayahara, N., Toyoda, M., et al. (2015). Comparison of 2D-and 3D-culture models as drug-testing platforms in breast cancer. *Oncol. Rep.* 33, 1837–1843. doi: 10.3892/or.2015.3767

Islam, M. M., Shahruzzaman, M., Biswas, S., Sakib, M. N., and Rashid, T. U. (2020). Chitosan based bioactive materials in tissue engineering applications-A review. *Bioactive Mater.* 5, 164–183. doi: 10.1016/j.bioactmat.2020.01.012

Kansara, M., and Thomas, D. M. (2007). Molecular pathogenesis of osteosarcoma. *DNA Cell Biol.* 26, 1–18. doi: 10.1089/dna.2006.0505

Khairoun, I., Driessens, F., Boltong, M., Planell, J., and Wenz, R. (1999). Addition of cohesion promotors to calcium phosphate cements. *Biomaterials* 20, 393–398. doi: 10.1016/s0142-9612(98)00202-6

Kozhukharova, I., Zemelko, V., Kovaleva, Z., Alekseenko, L., Lyublinskaya, O., and Nikolsky, N. (2018). Therapeutic doses of doxorubicin induce premature senescence of human mesenchymal stem cells derived from menstrual blood, bone marrow and adipose tissue. *Int. J. Hematol.* 107, 286–296. doi: 10.1007/s12185-017-2346-6

Krishnamurthy, P., Brown, M., Agrawal, S., and Short, R. F. (2017). Acute pancreatitis as a complication of trans-arterial chemoembolization of hepatocellular cancer—case report and review of literature. *J. Gastrointest. Oncol.* 8:E26.

Kumar, S., Marfatia, R., Tannenbaum, S., Yang, C., and Avelar, E. (2012). Doxorubicin-induced cardiomyopathy 17 years after chemotherapy. *Texas Heart Institute J.* 39, 424–427.

Lanao, R. P. F., Leeuwenburgh, S. C., Wolke, J. G., and Jansen, J. A. (2011). Bone response to fast-degrading, injectable calcium phosphate cements containing PLGA microparticles. *Biomaterials* 32, 8839–8847. doi: 10.1016/j.biomaterials.2011.08.005

Lee, M., Li, W., Siu, R. K., Whang, J., Zhang, X., Soo, C., et al. (2009). Biomimetic apatite-coated alginate/chitosan microparticles as osteogenic protein carriers. *Biomaterials* 30, 6094–6101. doi: 10.1016/j.biomaterials.2009.07.046

LeGeros, R. Z., and LeGeros, J. P. (2003). Calcium phosphate bioceramics: past, present and future. *Key Eng. Mater.* 240–242, 3–10. doi: 10.4028/www.scientific.net/kem.240-242.3

Liang, B., Zuo, D., Yu, K., Cai, X., Qiao, B., Deng, R., et al. (2020). Multifunctional bone cement for synergistic magnetic hyperthermia ablation and chemotherapy of osteosarcoma. *Mater. Sci. Eng. C* 108:110460. doi: 10.1016/j.msec.2019.110460

Liao, H., Walboomers, X. F., Habraken, W. J., Zhang, Z., Li, Y., Grijpma, D. W., et al. (2011). Injectable calcium phosphate cement with PLGA, gelatin and PTMC microspheres in a rabbit femoral defect. *Acta Biomater.* 7, 1752–1759. doi: 10.1016/j.actbio.2010.12.020

Lodoso-Torrecilla, I., Grosfeld, E. C., Marra, A., Smith, B. T., Mikos, A. G., Ulrich, D. J., et al. (2019). Multimodal porogen platforms for calcium phosphate cement degradation. *J. Biomed. Mater. Res. Part A* 107, 1713–1722.

Lopez-Heredia, M. A., Kamphuis, G. J., Thune, P. C., Oner, F. C., Jansen, J. A., and Walboomers, X. F. (2011). An injectable calcium phosphate cement for the local delivery of paclitaxel to bone. *Biomaterials* 32, 5411–5416. doi: 10.1016/j.biomaterials.2011.04.010

Ma, H., He, C., Cheng, Y., Yang, Z., Zang, J., Zang, J., et al. (2015). Localized Co-delivery of doxorubicin, cisplatin, and methotrexate by thermosensitive hydrogels for enhanced osteosarcoma treatment. *Appl. Mater. Interf.* 7, 27040–27048. doi: 10.1021/acsami.5b09112

Matsumanie, A., Kuzsuzaki, K., Matsubara, T., Okamura, A., Okuyama, N., Miyazaki, S., et al. (2006). Calcium phosphate cement in musculoskeletal tumor surgery. *J. Surg. Oncol.* 93, 212–220. doi: 10.1002/jso.20355

Mattu, C., Boffito, M., Sartori, S., Ranzato, E., Bernardi, E., Sassi, M. P., et al. (2012). Therapeutic nanoparticles from novel multiblock engineered polyesterurethanes. *J. Nanopart. Res.* 14:1306.

Mattu, C., Brachi, G., Menichetti, L., Flori, A., Armanetti, P., Ranzato, E., et al. (2018). Alternating block copolymer-based nanoparticles as tools to modulate the loading of multiple chemotherapeutics and imaging probes. *Acta Biomater.* 80, 341–351. doi: 10.1016/j.actbio.2018.09.021

Mi, F. (2005). Synthesis and characterization of a novel chitosan-gelatin bioconjugate with fluorescence emission. *Biomacromolecules* 6, 975–987. doi: 10.1021/bm049335p

Mohammadi, M. S., Ahmed, I., Muja, N., Rudd, C. D., Bureau, M. N., and Nazhat, S. N. (2011). Effect of phosphate-based glass fibre surface properties on thermally produced poly(lactic acid) matrix composites. *J. Mater. Sci. Mater. Med.* 22, 2659–2672. doi: 10.1007/s10856-011-4453-x

Ottaviani, G., and Jaffe, N. (2009). The epidemiology of osteosarcoma. *Cancer Treat. Res.* 152, 3–13. doi: 10.1007/978-1-4419-0284-9_1

Pathak, N., and Pathak, P. (2019). Nanoparticles and target drug delivery for cancer treatment: a comprehensive review. *Int. J. Drug Regul. Affairs (IJDRA)* 7, 53–58.

Patra, C. R., Bhattacharya, R., Mukhopadhyay, D., and Mukherjee, P. (2010). Fabrication of gold nanoparticles for targeted therapy in pancreatic cancer. *Adv. Drug Delivery Rev.* 62, 346–361. doi: 10.1016/j.addr.2009.11.007

Prados, J., Melguizo, C., Ortiz, R., Velez, C., Alvarez, P. J., Arias, L. J., et al. (2012). Doxorubicin-loaded nanoparticles: new advances in breast cancer therapy. *Anti Cancer Agents Med. Chem.* 12, 1058–1070. doi: 10.2174/187152012803529646

Pullieri, E., Chiono, V., Ciardelli, G., Vozzi, G., Ahluwalia, A., Domenici, C., et al. (2008). Chitosan/gelatin blends for biomedical applications. *J. Biomed. Mater. Res. Part A* 86, 311–322. doi: 10.1002/jbm.a.31492

Rankin, K. S., Starkey, M., Lunec, J., Gerrand, C. H., Murphy, S., and Biswas, S. (2012). Of dogs and men: comparative biology as a tool for the discovery of novel biomarkers and drug development targets in osteosarcoma. *Pediatr. Blood Cancer* 58, 327–333. doi: 10.1002/pbc.23341

Rong, Z.-J., Yang, L.-J., Cai, B.-T., Zhu, L.-X., Cao, Y.-L., Wu, G.-F., et al. (2016). Porous nano-hydroxyapatite/collagen scaffold containing drug-loaded ADM–PLGA microspheres for bone cancer treatment. *J. Mater. Sci. Mater. Med.* 27:89.

Sakai, S., Anada, T., Tsuchiya, K., Yamazaki, H., Margolis, H. C., and Suzuki, O. (2016). Comparative study on the resorbability and dissolution behavior of octacalcium phosphate, β-tricalcium phosphate, and hydroxyapatite under physiological conditions. *Dent Mater. J.* 35, 216–224. doi: 10.4012/dmj.2015-255

Saravanan, S., Leena, R., and Selvamurugan, N. (2016). Chitosan based biocomposite scaffolds for bone tissue engineering. *Int. J. Biol. Macromol.* 93, 1354–1365. doi: 10.1016/j.ijbiomac.2016.01.112

Shafei, A., El-Bakly, W., Sobhy, A., Wagdy, O., Reda, A., Aboelenin, O., et al. (2017). A review on the efficacy and toxicity of different doxorubicin nanoparticles for targeted therapy in metastatic breast cancer. *Biomed. Pharmacother.* 95, 1209–1218. doi: 10.1016/j.biopha.2017.09.059

Shariff, K. A., Tsuru, K., and Ishikawa, K. (2016). Fabrication of interconnected pore forming α-tricalcium phosphate foam granules cement. *J. Biomater. Appl.* 30, 838–845. doi: 10.1177/0885328215601939

Singh, H., Du, J., Singh, P., Mavlonov, G. T., and Yi, T. H. (2018). Development of superparamagnetic iron oxide nanoparticles via direct conjugation with ginsenosides and its in-vitro study. *J. Photochem. Photobiol. B Biol.* 185, 100–110. doi: 10.1016/j.jphotobiol.2018.05.030

Sokol, M. B., Nikolskaya, E. D., Yabbarov, N. G., Zenin, V. A., Faustova, M. R., Belov, A. V., et al. (2019). Development of novel PLGA nanoparticles with co-encapsulation of docetaxel and abiraterone acetate for a highly efficient delivery into tumor cells. *J. Biomed. Mater. Res. Part B Appl. Biomater.* 107, 1150–1158. doi: 10.1002/jbm.b.34208

Sun, Z., Wang, S., and Zhao, R. C. (2014). The roles of mesenchymal stem cells in tumor inflammatory microenvironment. *J. Hematol. Oncol.* 7:14. doi: 10.1186/1756-8722-7-14

Tanzawa, Y., Tsuchiya, H., Shirai, T., Nishida, H., Hayashi, K., Takeuchi, A., et al. (2011). Potentiation of the antitumor effect of calcium phosphate cement containing anticancer drug and caffeine on rat osteosarcoma. *J. Orthopaedic Sci.* 16, 77–84. doi: 10.1007/s00776-011-0045-3

Tariq, U., Hussain, R., Tufail, K., Haider, Z., Tariq, R., and Ali, J. (2019). Injectable dicalcium phosphate bone cement prepared from biphasic calcium phosphate extracted from lamb bone. *Mater. Sci. Eng. C* 103:109863. doi: 10.1016/j.msec.2019.109863

Tu, B., Peng, Z.-X., Fan, Q.-M., Du, L., Yan, W., and Tang, T.-T. (2014). Osteosarcoma cells promote the production of pro-tumor cytokines in mesenchymal stem cells by inhibiting their osteogenic differentiation through the TGF-β/Smad2/3 pathway. *Exp. Cell Res.* 320, 164–173. doi: 10.1016/j.yexcr.2013.10.013

Wang, J.-W., and Min-Hsiung, H. (2003). Sugar-mediated chitosan/poly(ethylene glycol)-β-dicalcium pyrophosphate composite: Mechanical and microstructural

properties. *J. Biomed. Materials Res. Part A* 64, 262–272. doi: 10.1002/jbm.a.10358

Weitao, Y., Kangmei, K., Xinjia, W., and Weili, Q. (2008). Bone regeneration using an injectable calcium phosphate/autologous iliac crest bone composites for segmental ulnar defects in rabbits. *J. Mater. Sci. Mater. Med.* 19, 2485–2492. doi: 10.1007/s10856-008-3383-8

Whelan, J., McTiernan, A., Cooper, N., Wong, Y. K., Francis, M., Vernon, S., et al. (2012). Incidence and survival of malignant bone sarcomas in England 1979–2007. *Int. J. Cancer* 131, E508–E517.

Wu, T., Yang, S., Shi, H., and Ye, J. (2018). Preparation and cytocompatibility of a novel bismuth aluminate/calcium phosphate cement with high radiopacity. *J. Mater. Sci. Mater. Med.* 29:149.

Xiaopeng, Q., Jiandong, Y., and Yingjun, W. (2008). Improved injectability and in vitro degradation of a calcium phosphate cement containing poly(lactide-co-glycolide) microspheres. *Acta Biomater.* 4, 1837–1845. doi: 10.1016/j.actbio.2008.05.009

Xu, H. H., Wang, P., Wang, L., Bao, C., Chen, Q., Weir, M. D., et al. (2017). Calcium phosphate cements for bone engineering and their biological properties. *Bone Res.* 5:17056.

Xu, H. H. K., Carey, L. E., Simon, C. G. Jr., Takagi, S., and Chow, L. C. (2007). Premixed calcium phosphate cements: synthesis, physical properties, and cell cytotoxicity. *Dent. Mater.* 23, 433–441. doi: 10.1016/j.dental.2006.02.014

Yalcin, T. E., Ilbasmis-Tamer, S., and Takka, S. (2020). Antitumor activity of gemcitabine hydrochloride loaded lipid polymer hybrid nanoparticles (LPHNs): in vitro and in vivo. *Int. J. Pharm.* 580:119246. doi: 10.1016/j.ijpharm.2020.119246

Yousefi, A.-M. (2019). A review of calcium phosphate cements and acrylic bone cements as injectable materials for bone repair and implant fixation. *J. Appl. Biomater. Funct. Mater.* 17:228080001987 2594.

Yu, D., Zhang, S., Feng, A., Xu, D., Zhu, Q., Mao, Y., et al. (2019). Methotrexate, doxorubicin, and cisplatinum regimen is still the preferred option for osteosarcoma chemotherapy: a meta-analysis and clinical observation. *Medicine* 98:e15582. doi: 10.1097/md.0000000000015582

Zhang, J., Liu, W., Schnitzler, V., Tancret, F., and Bouler, J. M. (2014). Calcium phosphate cements for bone substitution: chemistry, handling and mechanical properties. *Acta Biomater.* 10, 1035–1049. doi: 10.1016/j.actbio.2013.11.001

Zheng, Y., Wang, G., Chen, R., Hua, Y., and Cai, Z. (2018). Mesenchymal stem cells in the osteosarcoma microenvironment: their biological properties, influence on tumor growth, and therapeutic implications. *Stem Cell Res. Ther.* 9:22.

**Conflict of Interest:** The authors declare that the research was conducted in the absence of any commercial or financial relationships that could be construed as a potential conflict of interest.

The handling Editor LR declared past co-authorship with several of the authors, PG and AF.

frontiers in Materials

ORIGINAL RESEARCH
published: 10 July 2020
doi: 10.3389/fmats.2020.00220

# Optimization of Anti-kinking Designs for Vascular Grafts Based on Supramolecular Materials

*Dan Jing Wu[1,2,3], Kim van Dongen[1,2,3], Wojciech Szymczyk[1,3], Paul J. Besseling[4], Ruth M. Cardinaels[5], Giulia Marchioli[1,2,3], Marcel H. P. van Genderen[1,2], Carlijn V. C. Bouten[1,3], Anthal I. P. M. Smits[1,3] and Patricia Y. W. Dankers[1,2,3]**

[1] Institute for Complex Molecular Systems, Eindhoven University of Technology, Eindhoven, Netherlands, [2] Laboratory of Chemical Biology, Department of Biomedical Engineering, Eindhoven University of Technology, Eindhoven, Netherlands, [3] Laboratory for Cell and Tissue Engineering, Department of Biomedical Engineering, Eindhoven University of Technology, Eindhoven, Netherlands, [4] Department of Nephrology and Hypertension, University Medical Center Utrecht, Utrecht, Netherlands, [5] Polymer Technology, Department of Mechanical Engineering, Eindhoven University of Technology, Eindhoven, Netherlands

OPEN ACCESS

**Edited by:**
Lorenzo Moroni,
Maastricht University, Netherlands

**Reviewed by:**
Silvia Farè,
Politecnico di Milano, Italy
Fatemeh Kabirian,
Materials and Energy Research Center, Iran

***Correspondence:**
Patricia Y. W. Dankers
P.Y.W.Dankers@tue.nl

**Specialty section:**
This article was submitted to Biomaterials, a section of the journal Frontiers in Materials

**Received:** 21 April 2020
**Accepted:** 15 June 2020
**Published:** 10 July 2020

**Citation:**
Wu DJ, van Dongen K, Szymczyk W, Besseling PJ, Cardinaels RM, Marchioli G, van Genderen MHP, Bouten CVC, Smits AIPM and Dankers PYW (2020) Optimization of Anti-kinking Designs for Vascular Grafts Based on Supramolecular Materials. Front. Mater. 7:220. doi: 10.3389/fmats.2020.00220

Synthetic vascular grafts to be applied as access grafts for hemodialysis often require anti-kinking properties. Previously, electrospun microporous vascular implants based on synthetic supramolecular materials have been shown to perform adequately as resorbable grafts due to the microstructures, thereby enabling attraction of endogenous cells and consecutive matrix production *in situ*. Here, we use supramolecular materials based on hydrogen bonding interactions between bisurea (BU) or 2-ureido-4[1*H*]-pyrimidinones (UPy) to produce microporous anti-kinking tubular structures by combining solution electrospinning with 3D printing. A custom-made rational axis for 3D printing was developed to produce controlled tubular structures with freedom in design in order to print complex tubular architectures without supporting structures. Two different tubular grafts were developed, both composed of a three-layered design with a 3D printed spiral sandwiched in between luminal and adventitial electrospun layers. One tubular scaffold was composed of BU-polycarbonate electrospun layers with 3D printed polycaprolactone (PCL) strands in between for dimensional stability, and the other graft fully consisted of supramolecular polymers, using chain-extended UPy-PCL as electrospun layers and a bifunctional UPy-PCL for 3D printing. Both grafts, with a 3D printed spiral, demonstrated a reproducible dimensional stability and anti-kinking behavior under bending stresses.

**Keywords: anti-kinking, graft, supramolecular material, 3D printing, shear-thinning, electrospinning, tubular designs**

## INTRODUCTION

Kidney patients who depend on hemodialysis require well-functioning vascular access for blood purification. Synthetic vascular grafts are often implanted when patients lack suitable vasculature. However, extensive movement and bending stresses in these grafts can contribute to graft failure (Kannan et al., 2005; De Vries et al., 2016; Pashneh-Tala et al., 2016). For example, the low

stiffness of unstructured vascular grafts causes the lumen to collapse after implantation. When the synthetic grafts are placed a loop configuration, e.g., for vascular access, it is imminent to prevent kinking of the grafts. Nowadays, anti-kinking grafts made from commercial synthetic materials show improved performance using external support from silicone bead structures (Stenoien et al., 1999), plastic rings (Tuchmann and Dinstl, 1989), autologous veins as splints (Agko et al., 2017), or using modified electrospinning collectors to enhance macroscopic anti-kinking structures (Bode et al., 2015). However, these designs may cause complications during vascular surgery procedure, such as clamping and suturing. Moreover, these grafts are often developed from commercial materials such as poly(tetrafluoro ethylene) (PTFE) and poly(ethylene terephthalate) (Dacron). These commercial materials possess major limitations because of a decreased patency rate with increasing implantation time, while the materials should ideally function inside the human body for life (Riepe et al., 1997; Singh et al., 2019). Low patency rates occur owing to multiple factors, such as thrombosis, constrictive remodeling, intimal hyperplasia, infections, and unstable atherosclerotic lesions (Chester, 2002). Therefore, smart graft designs and suitable biomaterials are required in order to adapt to the biological and mechanical conditions of the vascular grafts application, in combination with anti-kinking properties. A relatively new strategy in the vascular replacements is to use bioresorbable scaffolds to fully exploit the regenerative capacity of the body. This approach, also known as the *in situ* tissue engineering approach makes use of cell-free, synthetic, biodegradable scaffolds that provide a temporary instructive environment to support neotissue formation by recruiting the desired cells directly in the functional site of the host (Talacua et al., 2015; Wissing et al., 2017; Smits and Bouten, 2018).

Previously, supramolecular polymers based on bisurea (BU) and 2-ureido-4[1*H*]-pyrimidinone (UPy)-modified supramolecular polymers were used to develop electrospun microporous vascular grafts that finally are proposed to be biocompatible and fully resorbable (**Figure 1A**; Van Almen et al., 2016; Kluin et al., 2017; van Haaften et al., 2017; Ippel et al., 2019; van Haaften et al., 2019). These supramolecular polymers have been identified as promising candidates to synthetically mimic the complexity of extracellular matrix (Goor et al., 2017; Diba et al., 2018). Due to their reversible and adaptable nature, the supramolecular materials possess extraordinary mechanical, tunable, responsive and processable properties which cannot be achieved with conventional macromolecules (Aida et al., 2012).

The unique and adaptable mechanical properties of BU-modified polymer arise from the molecular composition, where BU hard-blocks with ability of crystallization through hydrogen-bonding are alternated with a rubbery PC soft-block which ensures biocompatibility and slow degradation (**Figure 1B**; Appel et al., 2011; van Haaften et al., 2019). The well-defined BU hard-blocks within thermoplastic elastomers enhance the mechanical properties, which is evident from the high tensile strengths (Versteegen et al., 2006). Importantly, we have previously shown that polycarbonate bisurea (PC-BU) enables restoration of endogenous tissue and supports the infiltration of cells and production of extracellular matrix in *in situ* tissue engineered heart valves and vascular grafts (Brugmans et al., 2015; Kluin et al., 2017). Furthermore, self-complementary UPy-modified thermoplastic elastomers, which can dimerize strongly via quadruple hydrogen bonds, are designed to have load-bearing properties (Sijbesma et al., 1997; Beijer et al., 1998; Dankers et al., 2006; Söntjens et al., 2008). The UPy-modified polymers have previously been developed as bifunctional UPy-polymers in which the UPy-moieties were telechelically coupled to the respective prepolymer (Dankers et al., 2005; Mollet et al., 2014), or as chain-extended UPy-polymers in which the UPy-units are part of the hard block in the main chain of segmented co-polymers (Wisse et al., 2011; Van Almen et al., 2016; Putti et al., 2020). In previous work, biocompatible scaffolds based on different CE-UPy polymers have been applied in *in vivo* vascular graft applications (Muylaert et al., 2016; Van Almen et al., 2016; Bockeria et al., 2017) and have been shown to be mechanical stable, processible and to enhance tissue remodeling, thus support the first steps toward *in situ* tissue engineering (Serruys et al., 2017).

The electrospun microporous supramolecular vascular grafts that we developed previously were implanted in a straight configuration. However, when placement in a loop is needed, e.g., for vascular access, it is imminent to prevent kinking of the grafts. Therefore, here we introduce 3D printing of anti-kinking structures between two electrospun layers (**Figure 1C**). 3D printing techniques enable vast freedom in development of complex architectures with precise control over specific design properties (Jungst et al., 2015; Wu et al., 2017). In order to produce complex tubular geometries, a custom-built rotary apparatus was developed to enable 3D printing in the rotational axis which enables the production of tubular architectures of any design without printing support structures.

In this study, we use PCL for 3D printing, which is widely used as biomaterial for many 3D printing applications in the field of biomedical engineering (Hutmacher et al., 2001; Brown et al., 2012, 2015). Alternatively, a supramolecular polymer based on oligocaprolactone end-functionalized with UPy-moieties (PCLdiUPy) was used in order to produce a fully supramolecular anti-kinking graft. The luminal (i.e., the inner) layer and the adventitial (i.e., the outer) layer were produced by solution electrospinning, and form a heavily interweaved microfibrous tubular scaffold (r**Supplementary Figure 1**). In this way two anti-kinking grafts were designed; one being PC-BU electrospun layers with 3D printed PCL anti-kinking strands, the other being fully supramolecular in nature consisting of CE-UPy-PCL electrospun layers with 3D printed PCLdiUPy anti-kinking strands (**Figure 1**). First, we investigated the printability of PCL and PCLdiUPy by determining the thermal properties and the rheological properties for extrusion-based 3D printing. Then, the optimization was performed on the 3D printing parameters for the rotational collector in order to control the shape and morphology of anti-kinking designs to enhance reinforcement in synthetic vascular grafts. Finally, the bendability of the grafts was studied using a standardized test method according to the ISO-norms and previous research (Bensch et al., 2016; Brandt-Wunderlich et al., 2016).

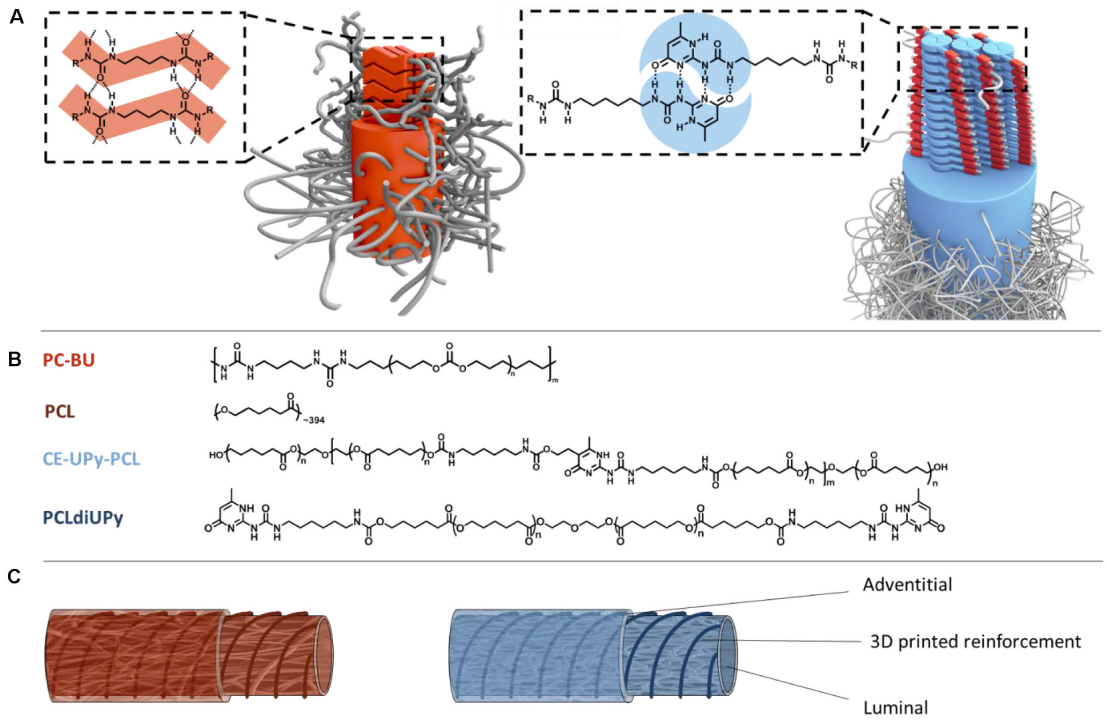


**FIGURE 1 |** Schematic representation of anti-kinking graft design from supramolecular systems. **(A)** Bisurea-bisurea interactions through hydrogen bonds (in red) and UPy-UPy dimerization through quadruple hydrogen bonding. **(B)** Bisurea functionalized polycarbonate (PC-BU) ($M_n$ = 21 kg/mol). Polycaprolactone (PCL) ($M_n$ = 45 kg/mol). Chain-extended UPy-modified polycaprolactone (CE-UPy-PCL) ($M_n$ = 15 kg/mol). End-modified bifunctionalized UPy-polycaprolactone with urethane bonds (PCLdiUPy) ($M_n$ = 3 kg/mol). **(C)** Schematic illustration of the anti-kinking vascular graft design consisting on two electrospun layers with a 3D printed strand between the layers for dimensional stability. One graft consists of PC-BU and PCL and the other a fully supramolecular graft consist of CE-UPy-PCL and PCLdiUPy.

# EXPERIMENTAL SECTION

## Materials

PC-BU ($M_n$ = 21 kg/mol) and PCLdiUPy ($M_n$ = 3 kg/mol) were synthesized by SyMO-Chem BV (Eindhoven, Netherlands). CE-UPy-PCL ($M_n$ = 15 kg/mol) was synthesized by SupraPolix (Eindhoven, Netherlands). PCL ($M_n$ = 45 kg/mol) were purchased from Sigma Aldrich (Zwijndrecht, Netherlands).

## Differential Scanning Calorimetry

Differential scanning calorimetry (DSC) measurements were performed on a DSC Q2000 (TA instruments, United States). The polymers were weighed, and subsequently hermetically sealed in Tzero aluminum pans. Melting ($T_m$) and glass ($T_g$) transition temperatures were measured from the melt, i.e., after the sample had first been brought to the isotropic state, in the second or ensuing heating runs. The samples were subjected to three heating/cooling cycles from −80 to 150°C with a heating/cooling rate of 10 and 40°C/min. The data was analyzed and quantified using Universal Analysis software (V4.5A, TA Instruments).

## Rheology

Films were prepared by compression molding. Discs of 8 mm diameter were prepared by punching. Rotational viscosity experiments were performed on an Anton Paar Physica MCR-501 rheometer (Anton Paar GmbH, Germany). Parallel plates with a plat-plate geometry of 50 mm and gap distance of 1 mm were used. All measurements were performed under a nitrogen atmosphere to prevent thermo-oxidative degradation at 150°C with a shear rate between 0.01 and 100 $s^{-1}$. To estimate the true shear rate first the shear thinning behavior was described by using the power law model (Dantzig and Tucker, 2001):

$$\eta = m\dot{\gamma}^{n-1}$$

## Thermogravimetric Analysis

Measurements were performed on a Perkin-Elmer TGA 7using the high-resolution dynamic mode, from room temperature to 400°C at a heating rate of 10°C/min. Samples were placed in platinum pans, and experiments were performed under an atmosphere of air (flow rate 20 mL/min).

## Electrospinning Equipment

Electrospinning solutions were prepared by dissolving the polymer in organic solvent at room temperature and stirring overnight. Electrospinning was performed on equipment of IME 14 Technologies EC-CLI (IME Technologies, Waalre, Netherlands). A 6 mm collector drum was used, pre-coated with a 2% solution of alginic acid sodium salt from brown algae

in ultra-pure water. Mandrels were coated and left in a 37°C incubator for 5 min. This is repeated once and followed by an incubation step of 30 min.

## Electrospinning Parameters

*Bisurea-based grafts:* an electrospinning solution was prepared consisting of 22 wt% of PC-BU in chloroform ($CHCl_3$)/hexafluoro-2-propanol (HFIP) 85:15. A voltage of 17 kV was applied on the electrospinning nozzle and negatively charge (−1 kV) on the rotating collector (ø 6 mm) and −3 kV for the second layer. Flow rate was set on 70 μL per minute and chloroform vapor in the gas shield module set at 35 mL/min to stabilize the electrospinning jet. Temperature was set on 23°C and relative humidity on 50%. The base layer of each sample was electrospun for 27 min and top layer for 7 min, with a fiber uptake speed of 0.09 m/s. Nozzle speed was 10 mm/s, tip-collector distance 15.5 cm and polymer solution was fed through a needle with an inner diameter of 0.8 mm. A turn delay was used for 1,000 ms on both ends.

*UPy-based grafts:* an electrospinning solution was prepared of 22 wt% of CE-UPy-PCL in HFIP. Applied voltage was 15 kV on the electrospinning nozzle and a negatively charge (−1 kV) on the rotating collector (ø 6 mm) and −3 kV for the second layer. Flow rate was set on 40 μL per minute and nozzle speed was set on 7 mm/s. The polymer solution was fed through a needle with an inner diameter of 0.8 mm. Temperature was 23°C and relative humidity 30%. The first electrospun layer had a spinning time of 65 min and the second layer of 12 min, with a fiber uptake speed of 0.13 m/s. Tip-collector distance was set at 19 cm for the base layer and 17 cm for the second layer. Turn delay was set on 1,500 ms on both ends.

## 3D Printing Reinforced Architectures

Fused deposition modeling (FDM) 3D printing (Biobot 1, Philadelphia, PA, United States) was used to produce the reinforced architectures. A Standard Triangle Language (STL-) file was created using a CAD software (SketchUp, Denver, CO, United States) and with RepetierHost converted into a g-code. *X*-axis speed was a variable in the transcript and extrusion rate was set to 0.54 mm/s. A custom made rotatory collector has been for printing of tubular architectures (**Supplementary Figure 2**). The collector distance between the printing nozzle (25 G: $d_I$ = 260 μm) was calibrated to 5 mm. PCLdiUPy or PCL was loaded and molten at 120°C into a metal syringe and stabilized for 15 min before printing. The printing of the material was performed using pressure of 80 PSI.

Next, the flow rate Q was obtained using the flow of a power law fluid in a tube (represents the printing nozzle) (Dantzig and Tucker, 2001):

$$Q = \int_0^{2\pi} \int_o^R \upsilon_\zeta(r)\, r dr d\theta = \frac{\pi}{s+3}\left(\frac{\Delta p}{2mL}\right)^s R^{s+3}$$

With $v_\zeta(r)$ the velocity, $L$ the length of the nozzle, $R$ its diameter and $\Delta p$ the pressure drop, $s$ equals $1/n$.

The true shear rate at the wall within the printer nozzle was obtained from Morrison (2001):

$$\dot{\gamma}_R = -\left.\frac{d\upsilon_\zeta}{dr}\right|_{r=R} = \left(\frac{4Q}{\pi R^3}\right)\left(\frac{\frac{1}{n}+3}{4}\right)$$

The calculated value is the maximum value due to the consideration of a shear rate distribution from zero in the center of the tube to maximum at the wall. Furthermore, this calculation takes the pressure drop in the printing nozzle into account (this effect in the printing nozzle is dominant), it neglects pressure drop in the printing reservoir and the converging flow from the reservoir toward the printing nozzle. The polymer melt was printed on a 6 mm diameter rotational mandrel with various nozzle speeds (between 0.1 and 11 mm/s). Quantification of fiber diameter, spacing and angles were done with a Keyence VHX-500FE digital microscope prior to electrospinning the second layer and scaffold removal from the mandrel.

## Removal of Anti-kinking Vascular Graft From Mandrel

Electrospun grafts were placed in the vacuum oven overnight at 37°C. Subsequently, they were placed in a bottle with demineralized water and stored in −30°C overnight. The grafts were then subjected to thawing at room temperature and the electrospinning mandrel was gently removed after 40 min. After complete removal of ice, scaffolds were dried at room temperature for at least 24 h and placed in the vacuum oven for at least 2 h.

## Microstructure Characterization

The scaffold microstructures were characterized with scanning electron microscopy (SEM; Quanta 600F, Fei, Hillsboro, OR, United States). Samples were cut in liquid nitrogen prior to imaging and PC-BU scaffolds were treated with gold sputter-coating. Images were taken in high vacuum atmosphere at 2 kV and spot size 3 nm. The fiber diameter and pore size were quantified using software of ImageJ (U.S. National Institutes of Health, Bethesda, MD, United States). Fiber diameter was quantified by measuring at 24 different positions. Pore size was quantified by manual thresholding of the images, followed by skeletonizing.

## Bending Test

Bending tests were performed on an in-house-created set-up, which is developed according to ISO 7198:8:9. The bending radius was measured with a digital caliper for each vascular graft with 6 mm in diameter and a total length of 10 cm. The lumen loss of the examined graft while bent around the respective radius was calculated according to: $\Delta D = 100\% \times (D_0 - D_i)/(D_0)$, with $D_0$ as the diameter of the graft in original configuration and $D_i$ as diameter at the respective bending radius. The testing was performed under atmospheric condition and room temperature.

# RESULTS

## Material Printability

In general, polymers for 3D printing must fulfill a number of key requirements for processing with an extrusion-based 3D printer, such as appropriate melting temperature, degradation temperature, and viscosity of the material. To address the printability, these properties of two selected polymers, PCL and PCLdiUPy, were characterized to gain information that is relevant for the 3D printing process. First, differential scanning calorimetry (DSC) measurements were performed to study the thermal behavior of the polymers and to determine the polymer melting temperature (**Table 1** and **Figure 2A**). For PCL, the DSC thermograph shows a glass transition ($T_g$) at −61°C with a single melting peak ($T_m$) at 55°C (**Figure 2A**). Moreover, an expected phase-separated morphology was observed for PCLdiUPy with two melting transitions. The first melting transition ($T_{m1}$) of 38°C is from the semi-crystalline PCL soft block and a second melting transition ($T_{m2}$) of 81°C is related to the UPy-urethane-moieties forming the hard block.

Thermogravimetric analysis (TGA) was performed to confirm the decay temperature of the polymers to ensure a sufficient thermal stability during 3D printing since it requires melting of the polymer for extrusion and material deposition. The decay temperatures ($T_{decay}$) at 5% weight loss are determined by TGA for PCL at 331.9°C and PCLdiUPy at 275.1°C (**Table 1** and **Figure 2B**). This observation demonstrates no weight loss in all the materials below the decay temperature. Hence, the biomaterials are thermally stable during the 3D printing process with the determined melting temperatures using DSC (**Table 1**).

The viscosity of PCL and PCLdiUPy was analyzed in the range of shear rates that is representative for the extrusion process during 3D printing (**Figure 2C**). The low viscosity of PCL is independent of the shear rate, therefore a Newtonian rheological behavior is observed. This means that the material will flow whereby the flow rate will increase proportionally with the applied pressure. In contrast, the viscosity of PCLdiUPy demonstrates a non-Newtonian rheological behavior, which is shear rate dependent. The decrease of the viscosity with increasing shear rates indicates that the material is shear-thinning. This can be explained by the hydrogen-bonds of the UPy-modified polymers, which can break at high temperatures ($T > T_m$) and shear rates, resulting in flexible polymer chains (Xu et al., 2011). This phenomenon can be beneficial for 3D printing in general; as pressure is applied for polymer extrusion, shear stresses will be generated in the nozzle for polymer extrusion. Moreover, a maximum shear rate of $1.4 \times 10^7$ $s^{-1}$ was calculated using rheological models described in the experimental section for PCLdiUPy, which is based on the flow of a fluid in a tube. This apparent high shear rate confirms that the shear thinning of PCLdiUPy is relevant for the extrusion-based 3D printing technique. Therefore, supramolecular polymers with shear-thinning behavior are promising candidates for 3D printing, as their resistance to flow will decrease with increasing pressure drops. In conclusion, based on these results, PCL and PCLdiUPy are thermally stable at the melting temperature and both materials are able to flow during printing extrusion.

## Designing 3D Printed Tubular Architectures

The dimensional stability of the tubular graft can be manipulated by introducing 3D printed architectures between the luminal and adventitial electrospun layers to reinforce the lumen. With the variation of the architectural design, tubular grafts can resist deformation during bending stresses (Connolly et al., 2015), including axial extension, radial expansion and twisting. For 3D printing, a custom-made rotating cylindrical collector was developed to replace the traditional static printing collector in order to print complex tubular architectures in an rotational axis without supporting structures, which enables additional degree of freedom in 3D printing (**Supplementary Figure 2**). Optimization is required in order to develop a dimensionally stable and reinforced design to enhance anti-kinking of the vascular graft. To determine the kink resistance for vascular grafts in a standardized manner, a custom made bending apparatus with a 4–30 mm bending radius (**Supplementary Figure 3**) was developed in order to determine the kinking at bending stresses.

### Tubular Cross-Pattern, Ring and Spiral Designs

The grafts with various 3D printed tubular patterns have been designed and studied with a custom-made bending apparatus (**Figure 3**). Firstly, pristine electrospun microporous PC-BU and CE-UPy-PCL tubular scaffolds were fabricated and both grafts displayed kinking already at all bending radii (4–30 mm) with more than 50% diameter reduction (**Figures 3A,H,K**).

Subsequently, three types of 3D printed tubular designs were tested, namely a cross-pattern, a ring and a spiral design. A cross-pattern design was introduced with a printed spacing of 7,100 ± 61 μm, fiber thickness of 150 ± 11 μm and angle of 74° (**Figure 3B**). Unfortunately, this graft displayed kinking of the lumen at the intersection of the printed crossing strands. The cross pattern has large open space between the repeating pattern (next to the crossing position) which results in a weak point within the grafts and therefore kinking of the graft was observed (**Figure 3B**). Hence, the cross-pattern design was not further optimized or used for further studies. Ring

**TABLE 1** | Thermal properties of PCL and PCLdiUPy.

| | $M_n$ (kg/mol) | $T_g$ (°C) | $T_{m,1}$ (°C) | Δ $H_{m,1}$ (J/g) | $T_{m,2}$ (°C) | Δ $H_{m,2}$ (J/g) | $T_{decay}$* (°C) |
|---|---|---|---|---|---|---|---|
| PCL | 4.5 | −61 | 55 | 69.8 | – | – | 331.9 |
| PCLdiUPy | 3.0 | −55 | 38 | 70.7 | 81 | 71.6 | 275.1 |

*Values of the second heating runs (10°C/min) are shown. The following variables are shown: the average molecular weight ($M_n$), the glass transition temperature ($T_g$), the melting peaks ($T_{m,1}$ and $T_{m,2}$) the heat fusion ($\Delta H_{m,1}$ and $\Delta H_{m,2}$), the degradation temperature ($T_{decay}$). * Determined at 5% weight loss.*

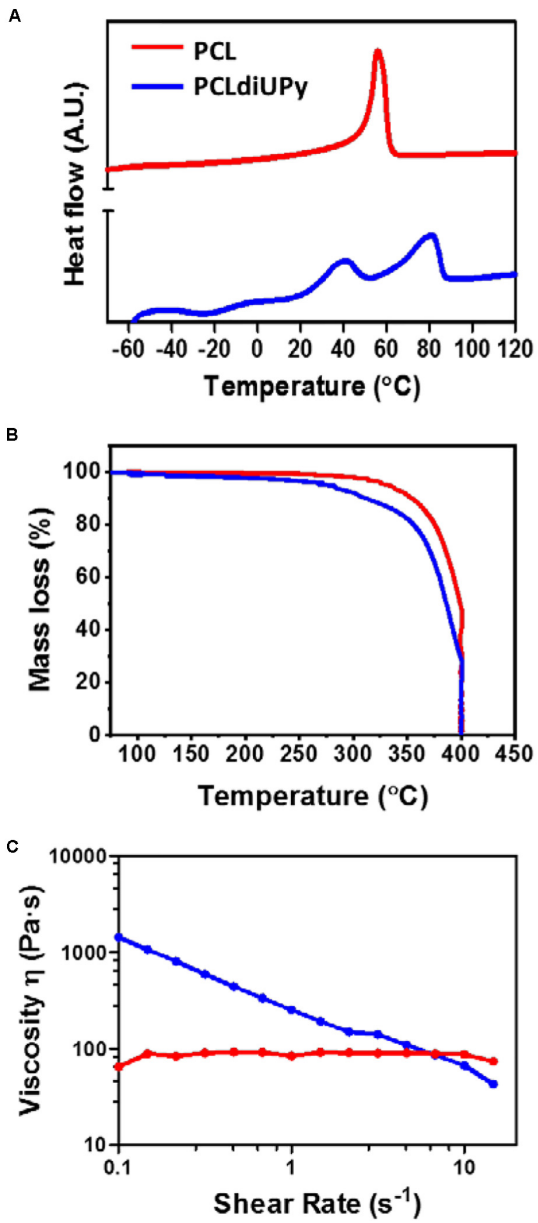


**FIGURE 2 |** Thermal properties and viscosity analysis. **(A)** Thermograms of the second heating runs (10°C/min) are shown. Glass transition temperature ($T_g$) and the onset of melting points ($T_m$) were determined from thermograms with TA universal analysis. Endothermic processes appear as upward peaks. **(B)** TGA was measured to determine the decay temperature of all the polymers. **(C)** Shear-viscosity determined using a rotational rheometer ($n$ = 3) at 150°C. PCLdiUPy polymer exhibit shear thinning property, displayed by a decrease in viscosity upon an increase in shear rate.

design (90°) was developed for both materials: PC-BU graft with PCL rings thickness of 645 ± 25 μm and 2,344 ± 515 μm spacing (**Figure 3C**) and CE-UPy-PCL graft with PCLdiUPy rings thickness of 860 ± 60 μm and 2,093 ± 84 μm spacing (**Figure 3I**). The ring design prevents gross luminal collapse of the graft with less than 50% diameter reduction of the lumen during bending (**Figure 3K**). However, minimal local kinking in between the rings was visually observed. The ring design is intrinsically a dimensionally less stable entity due to the lack of interconnected architecture between the printed structures. Finally, a spiral design was produced with a PCL strand thickness of 709 ± 9.0 μm, 2,434 ± 75 μm spacing and angle of 84° (**Figure 3D**). For PCLdiUPy strand, a spiral thickness of 1,030 ± 18 μm, 1,898 ± 33 μm spacing and an 83° angle was produced (**Figure 3J**). The spiral design displayed local kinking resistance and dimensional stability in the lumen no occurrence of folds was observed. The spiral design showed promising results with good anti-kinking properties for the BU- and UPy-based grafts.

### Optimization of Spiral Architectures

Having established the superior anti-kinking properties of the spiral design, we proceeded to optimize the parameters of the printed spiral graft design. In order to study the influence of the second electrospun layer on anti-kinking properties, a spiral-reinforced graft without the adventitial layer produced and tested (**Figure 3E**). Apparent kinking of the lumen was observed when decreasing in bending radius, which indicates dimensional instability without the adventitial electrospun layer of the vascular graft. Next, a graft with an adjusted thickness of the 3D printed strand was developed. The reinforcement in this graft had approximately half of the fiber thickness, with a thickness of 358 ± 30 μm, spacing 2,679 ± 50 μm and angle of 83° (**Figure 3F**). A decreased fiber diameter was achieved by significantly decreasing the printing pressure, due to less material deposition on the rotational mandrel. Using semi-quantitative analysis, dimensional stability in the lumen of the graft was observed, even up to the minimum bending radius of 4 mm (**Figure 3F**). Additionally, 3D printed spirals were developed with larger spacing to explore the limits of dimensional stability (**Figure 3G**). Grafts with an increased spiral spacing of 2,729 ± 120 μm was developed. Interestingly, a diameter reduction in the lumen was observed for this graft up to a bending radius of 4 mm (**Figure 3H**). These results provide an indication for the range of parameters (strand spacing and thickness) in order to develop an optimal design for anti-kinking grafts (**Figure 3K**).

## Systematic Optimization of 3D Printed Spiral Design

The spiral design is interconnected between the luminal and adventitial layers, which provides dimensional stability during bending. However, the spiral architectures can be influenced by many factors such as mandrel rotation and nozzle deposition speed. These are critical factors that can influence the diameter, the spacing and the angle of the printed strands with respect to the vascular graft (Sodupe-Ortega et al., 2018). Therefore, a systematic study was set up to explore the variety of the parameters. The change in the nozzle speed and rotational mandrel velocity resulted in the development of a highly controlled continuous strand with a variety of reproducible spacing, fiber thickness and fiber angle (**Figure 4**). The nozzle speed in the $X$-axis, from 0.1 to 1 mm/s,

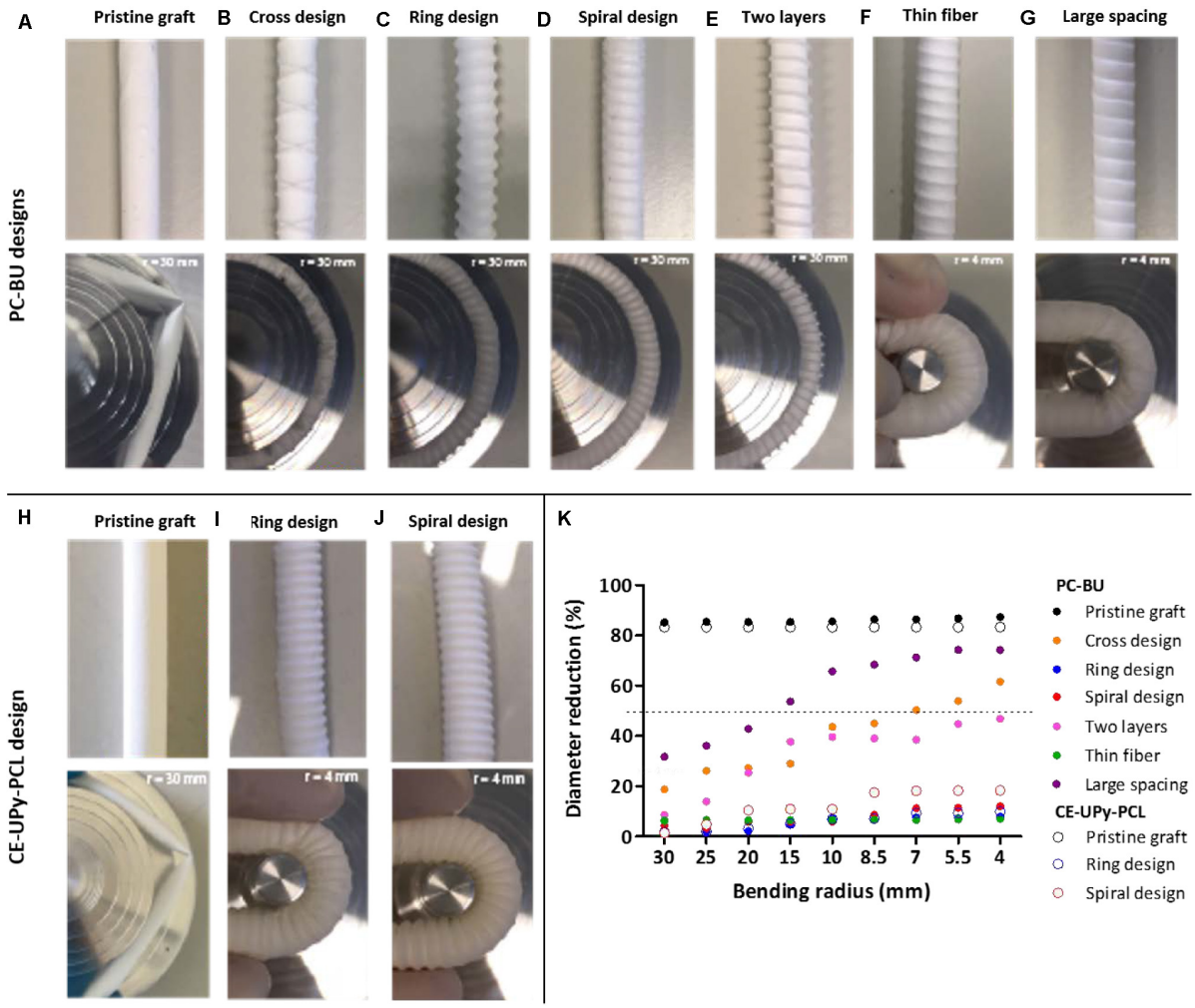


**FIGURE 3 |** Bending test on PC-BU and CE-UPy-PCL. **(A–J)** Vascular grafts with different anti-kinking architectures were designed and studied with a custom-made bending apparatus with a radius of 4–30 mm. **(K)** The percentual diameter reduction of the outer diameter is measured and plotted against the bending radius. Indication for anti-kinking behavior is defined at a diameter reduction less than 50% (marked with the dotted line).

was tested in combination with rotational speed from 0.083 to 2.1 rad/s. In addition, increased nozzle speed (1–9 mm/s) were studied in combination with increased rotational speed (**Supplementary Figure 4**). However, these results did not demonstrate reproducible thickness of the printed strand ranging from 15 to 175 μm due to the increased speed. The increase of the printing velocity in the nozzle and rotational speed resulted in less controlled and poorly reproducible architectures. Therefore, the low nozzle speed (0.1–1 mm/s) and low rotational speed (0.083–2.1 rad/s) were used to produce 3D printed reinforced architectures with reproducible results.

As the pressure during printing might influence the result, the printing pressure was kept constant at 80 PSI in order to extrude the polymer melt. In general, the increase of the nozzle speed resulted in a slight decrease of the fiber diameter for most rotational velocities (Žarko et al., 2017). Interestingly, a decrease in angle degree and increase of spacing size was observed upon increasing of the nozzle speed (**Figure 4**). An increased nozzle speed in the *X*-axis results in faster material deposition. Furthermore, the change in speed of the rotational movement showed to influence the architecture design as well. Specifically, an increase in rotational velocity progressively led to a decrease in fiber diameter and fiber spacing, as well as an increase in fiber angle. These effects were most pronounced at higher nozzle speeds.

## Morphology Analysis of the Anti-kinking Graft

The luminal electrospun layer with an internal diameter of 6 mm was produced from either PC-BU or CE-UPy-PCL polymers. Importantly, SEM micrographs showed non-fused interconnected microfibers in the luminal and adventitial electrospun layers, demonstrating a dense porous network with an average fiber diameter of 3.6 ± 0.35 μm for the PC-BU grafts and 3.0 ± 0.66 μm in the CE-UPy-PCL grafts (**Figure 5A**).

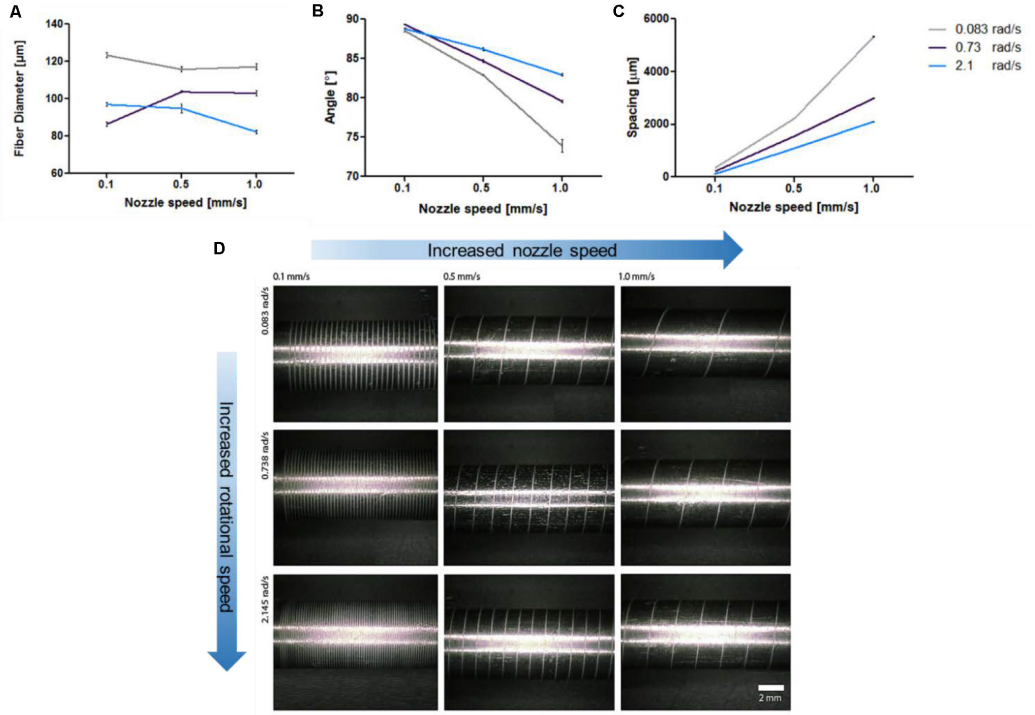


**FIGURE 4 |** Optimization of 3D printed reinforced designs. **(A)** Decrease of fiber diameter with increased speed. **(B)** Decreased fiber angle with respect to the mandrel with increased speed. **(C)** Increased spacing between the 3D printed strands with increased speed. **(D)** Micrographs of 3D printed reinforced architectures on a stainless steel mandrel at different nozzle movement speed and mandrel rotational speed. The optimization was performed using PCL polymer.

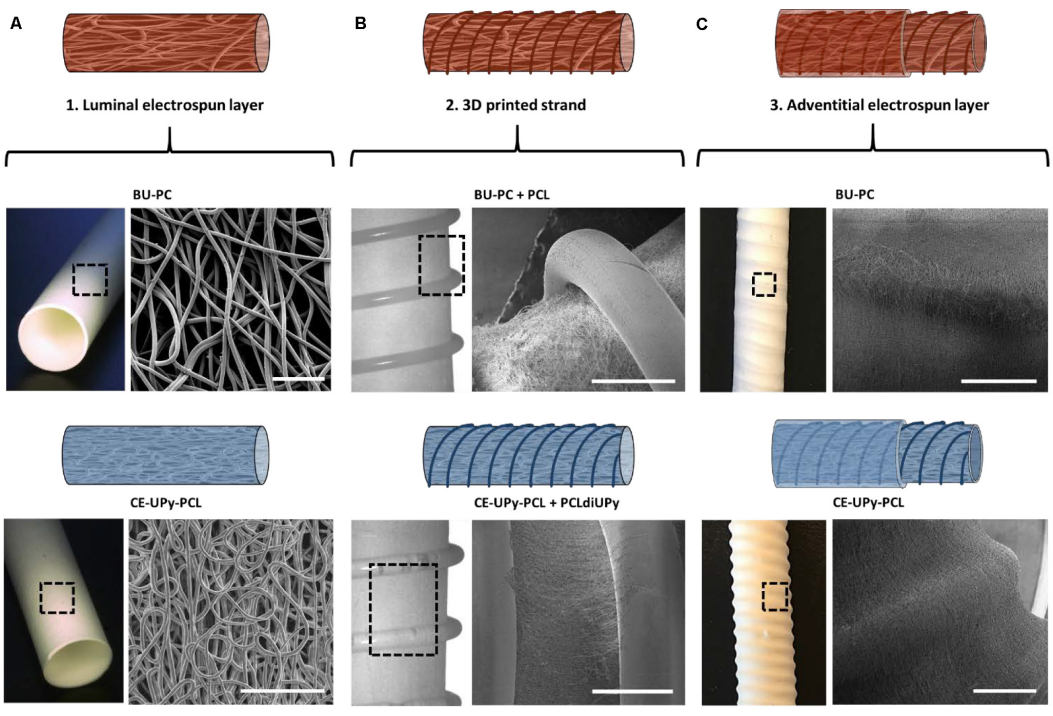


**FIGURE 5 |** Microstructural properties of the three-layered design. **(A)** Microscopic image of the first (luminal) electrospun tubular graft (6 mm diameter) consisting of interconnected microfibers. Scale bars represent 100 µm. **(B)** Second layer composed of 3D printed polymer architecture. A well-attached printed PCL strand on top the PC-BU luminal layer was observed using scanning electron microscopy (SEM). The PCLdiUPy was printed on top of the luminal electrospun CE-UPy-PCL layer **(C)** Adventitial electrospun layer was electrospun on top of the 3D printed layer. Scale bars in panels **(B,C)** represent 1 mm.

The PC-BU graft consist of a luminal electrospun layer of 511 ± 74 μm and an adventitial layer of 261 ± 33 μm. The CE-UPy-PCL graft consists of a luminal wall of 504 ± 36 μm and an adventitial layer of 260 ± 17 μm. The 3D printed reinforced structure was sandwiched between the luminal and adventitial electrospun layer (**Figure 5B**). No morphological changes have been observed after 3D printing on top of the electrospun layer. Moreover, good attachment of the electrospun layers was observed via electron micrograph of the cross section of the grafts (**Supplementary Figure 5**). Finally, the adventitial layer either from PC-BU or CE-UPy-PCL was electrospun on top of the 3D printed strand to support the dimensional change and provide minimal change in the wall of the grafts (**Figure 5C**).

## DISCUSSION AND CONCLUSION

Previous *in situ* tissue engineering studies have shown that synthetic grafts based on supramolecular materials are able to perform as regenerative resorbable grafts, which enable attraction of endogenous cells and consecutive matrix production *in situ* (Talacua et al., 2015; Muylaert et al., 2016; Van Almen et al., 2016; van Haaften et al., 2019). However, kinking in the flexible lumen, as well as changes in the wall are complications that cause low patency of the vascular grafts. In this study, we optimized the anti-kinking properties of supramolecular tubular grafts using 3D printing of a continuous strand to reinforce the lumen. In previous work, promising BU-PC and CE-UPy-PCL polymers have been used to develop flexible vascular grafts and heart valves for *in vivo* applications (Brugmans et al., 2015; Muylaert et al., 2016; Van Almen et al., 2016; Bockeria et al., 2017; Kluin et al., 2017). However, kinking in the flexible lumen (of approximately 700 μm thickness) has been observed when the grafts were placed in a loop configuration (**Figures 3A,H**). In general, the lumen of commercial grafts (Dacron) and many other vascular grafts are consisting of a thickness range between 400 and 700 μm (Stanley et al., 1982; Rothuizen et al., 2016). Therefore, Lee et al. studied mechanical enhancement in tubular structures using an efficient dual 3D processing technique by developing two-layered vascular grafts based on electrospinning of a natural polymer, chitosan with poor mechanical properties, fully coated with polycaprolactone (PCL) for reinforcement (Lee et al., 2015). Albeit resulting in enhanced mechanical properties, this design may restrict graft bending due to the complete coverage with PCL, which might limit the surgical approach during implantation. Therefore, the structural design of the tubular architecture is important in order to provide dimensional stability without restriction in bending flexibility of the vascular grafts. Here, we showed the efficiency to provide dimensional stability by developing an interconnected architecture sandwiched between the luminal and adventitial electrospun layers to prevent kinking of the lumen but remain flexibility. Various designs of stable 3D printed architectures were explored by varying printing velocity, i.e., nozzle speed, in combination with a rotating collector. This study showed enhanced dimensional stability of supramolecular vascular grafts under bending stress by improving the design with a three-layered approach. Despite the different material properties, this design has shown to be effective for anti-kinking behavior in both supramolecular BU- and UPy-systems. PC-BU grafts contains a PCL reinforced strand, which could lead to different degradation rates since PCL crystallization is not based on hydrogen bonding. In contrast, a fully UPy-based vascular graft consists of two polymers with comparable components in molecular design and based on hydrogen bonding.

In conclusion, using a 3D printed spiral as reinforcement between the lumen of two electrospun layers showed to be the optimal anti-kinking design for both bisurea and UPy-polymer grafts. Pristine electrospun grafts displayed kinking with more than 50% diameter reduction. Subsequently, three types of 3D printed anti-kinking designs were tested, namely a cross-pattern, a ring and a spiral design. The spiral design demonstrates effective anti-kinking behavior when the graft was placed in a loop configuration. Importantly, a fully supramolecular graft with anti-kinking properties was made from UPy-modified polymers used in the electrospun layers and for the 3D printing of the spiral, which demonstrates the broad possibilities of using UPy-polymers for different purposes and processing methods (i.e., electrospinning and 3D printing).

## DATA AVAILABILITY STATEMENT

The raw data supporting the conclusions of this article will be made available by the authors, without undue reservation.

## AUTHOR CONTRIBUTIONS

DW, KD, GM, and PD conceived and designed the experiments. DW, KD, and WS performed the analysis. PB, RC, CB, AS, PD, and MG analyzed data. All authors contributed to manuscript revision, read and approved the submitted version.

## FUNDING

This work was funded by the Ministry of Education, Culture and Science (Gravity Program 024.001.03) and ZonMW as part of the LSH 2Treat program (Project No. 436001003).

## ACKNOWLEDGMENTS

The authors thank R. Anastasio for the useful discussions on the results, A.M.A.O Pollet for the technical support during some of the 3D printing experiments, and A.W. Bosman (SupraPolix) for providing the CE-UPy-PCL polymer.

## SUPPLEMENTARY MATERIAL

The Supplementary Material for this article can be found online at: https://www.frontiersin.org/articles/10.3389/fmats.2020.00220/full#supplementary-material

## REFERENCES


Agko, M., Liu, E., Huang, T. C. T., Lo Torto, F., Ciudad, P., Manrique, O. J., et al. (2017). The split vein graft "splint" to avoid kinking and compression of the vascular pedicle. *Microsurgery* 37, 739–740. doi: 10.1002/micr.30179

Aida, T., Meijer, E. W., and Stupp, S. I. (2012). Functional supramolecular polymers. *Science* 335, 813–817. doi: 10.1126/science.1205962

Appel, W. P. J., Portale, G., Wisse, E., Dankers, P. Y. W., and Meijer, E. W. (2011). Aggregation of ureido-pyrimidinone supramolecular thermoplastic elastomers into nanofibers: a kinetic analysis. *Macromolecules* 44, 6776–6784. doi: 10.1021/ma201303s

Beijer, F. H., Sijbesma, R. P., Kooijman, H., Spek, A. L., and Meijer, E. W. (1998). Strong dimerization of ureidopyrimidones via quadruple hydrogen bonding. *J. Am. Chem. Soc.* 120, 6761–6769. doi: 10.1021/ja974112a

Bensch, M., Müller, M., Bode, M., and Glasmacher, B. (2016). Automation of a test bench for accessing the bendability of electrospun vascular grafts. *Curr. Dir. Biomed. Eng.* 2, 307–310. doi: 10.1515/cdbme-2016-0068

Bockeria, L. A., Svanidze, O., Kim, A., Shatalov, K., Makarenko, V., Cox, M., et al. (2017). Total cavopulmonary connection with a new bioabsorbable vascular graft: first clinical experience. *J. Thorac. Cardiovasc. Surg.* 153, 1542–1550. doi: 10.1016/j.jtcvs.2016.11.071

Bode, M., Mueller, M., Zernetsch, H., and Glasmacher, B. (2015). Electrospun vascular grafts with anti-kinking properties. *Curr. Dir. Biomed. Eng.* 1:125. doi: 10.1515/cdbme-2015-0125

Brandt-Wunderlich, C., Schwerdt, C., Behrens, P., Grabow, N., Schmitz, K.-P., and Schmidt, W. (2016). A method to determine the kink resistance of stents and stent delivery systems according to international standards. *Curr. Dir. Biomed. Eng.* 2, 289–292. doi: 10.1515/cdbme-2016-0064

Brown, T. D., Edin, F., Detta, N., Skelton, A. D., Hutmacher, D. W., and Dalton, P. D. (2015). Melt electrospinning of poly(ε-caprolactone) scaffolds: phenomenological observations associated with collection and direct writing. *Mater. Sci. Eng. C* 45, 698–708. doi: 10.1016/j.msec.2014.07.034

Brown, T. D., Slotosch, A., Thibaudeau, L., Taubenberger, A., Loessner, D., Vaquette, C., et al. (2012). Design and fabrication of tubular scaffolds via direct writing in a melt electrospinning mode. *Biointerphases* 7, 1–16. doi: 10.1007/s13758-011-0013-7

Brugmans, M. C. P., Söntjens, S. H. M., Cox, M. A. J., Nandakumar, A., Bosman, A. W., Mes, T., et al. (2015). Hydrolytic and oxidative degradation of electrospun supramolecular biomaterials: in vitro degradation pathways. *Acta Biomater.* 27, 21–31. doi: 10.1016/j.actbio.2015.08.034

Chester, J. F. (2002). The causes of synthetic vascular graft failure. *Ann. Coll. Surg. Hong Kong* 6, 97–101. doi: 10.1046/j.1442-2034.2002.00149.x

Connolly, F., Polygerinos, P., Walsh, C. J., and Bertoldi, K. (2015). Mechanical programming of soft actuators by varying fiber angle. *Soft Robot.* 2, 26–32. doi: 10.1089/soro.2015.0001

Dankers, P. Y. W., Harmsen, M. C., Brouwer, L. A., Van Luyn, M. J. A., and Meijer, E. W. (2005). A modular and supramolecular approach to bioactive scaffolds for tissue engineering. *Nat. Mater.* 4, 568–574. doi: 10.1038/nmat1418

Dankers, P. Y. W., van Leeuwen, E. N. M., van Gemert, G. M. L., Spiering, A. J. H., Harmsen, M. C., Brouwer, L. A., et al. (2006). Chemical and biological properties of supramolecular polymer systems based on oligocaprolactones. *Biomaterials* 27, 5490–5501. doi: 10.1016/j.biomaterials.2006.07.011

Dantzig, J. A., and Tucker, C. L. (2001). *Modeling in Materials Processing*. Cambridge: Cambridge university press.

De Vries, M. R., Simons, K. H., Jukema, J. W., Braun, J., and Quax, P. H. A. (2016). Vein graft failure: from pathophysiology to clinical outcomes. *Nat. Rev. Cardiol.* 13, 451–470. doi: 10.1038/nrcardio.2016.76

Diba, M., Spaans, S., Ning, K., Ippel, B. D., Yang, F., Loomans, B., et al. (2018). Self-healing biomaterials: from molecular concepts to clinical applications. *Adv. Mater. Interfaces* 5, 1–21. doi: 10.1002/admi.201800118

Goor, O. J. G. M., Keizer, H. M., Bruinen, A. L., Schmitz, M. G. J., Versteegen, R. M., Janssen, H. M., et al. (2017). Efficient functionalization of additives at supramolecular material surfaces. *Adv. Mater.* 29:1604652. doi: 10.1002/adma.201604652

Hutmacher, D. W., Schantz, T., Zein, I., Ng, K. W., Teoh, S. H., and Tan, K. C. (2001). Mechanical properties and cell cultural response of polycaprolactone scaffolds designed and fabricated via fused deposition modeling. *J. Biomed. Mater. Res.* 55, 203–216. doi: 10.1002/1097-4636(200105)55:2<203::AID-JBM1007<3.0.CO;2-7

Ippel, B. D., Keizer, H. M., and Dankers, P. Y. W. (2019). Supramolecular antifouling additives for robust and efficient functionalization of elastomeric materials. *Mol. Design Matter.* 29:1805375. doi: 10.1002/adfm.201805375

Jungst, T., Muerza-Cascante, M. L., Brown, T. D., Standfest, M., Hutmacher, D. W., Groll, J., et al. (2015). Melt electrospinning onto cylinders: effects of rotational velocity and collector diameter on morphology of tubular structures. *Polym. Int.* 64, 1086–1095. doi: 10.1002/pi.4948

Kannan, R. Y., Salacinski, H. J., Butler, P. E., Hamilton, G., and Seifalian, A. M. (2005). Current status of prosthetic bypass grafts: a review. *J. Biomed. Mater. Res. Part B Appl. Biomater.* 74, 570–581. doi: 10.1002/jbm.b.30247

Kluin, J., Talacua, H., Smits, A. I. P. M., Emmert, M. Y., Brugmans, M. C. P., Fioretta, E. S., et al. (2017). In situ heart valve tissue engineering using a bioresorbable elastomeric implant – from material design to 12 months follow-up in sheep. *Biomaterials* 125, 101–117. doi: 10.1016/j.biomaterials.2017.02.007

Lee, S. J., Heo, D. N., Park, J. S., Kwon, S. K., Lee, J. H., Lee, J. H., et al. (2015). Characterization and preparation of bio-tubular scaffolds for fabricating artificial vascular grafts by combining electrospinning and a 3D printing system. *Phys. Chem. Chem. Phys.* 17, 2996–2999. doi: 10.1039/C4CP04801F

Mollet, B. B., Comellas-Aragonès, M., Spiering, A. J. H., Söntjens, S. H. M., Meijer, E. W., and Dankers, P. Y. W. (2014). A modular approach to easily processable supramolecular bilayered scaffolds with tailorable properties. *J. Mater. Chem. B* 2, 2483–2493. doi: 10.1039/c3tb21516d

Morrison, F. A. (2001). *Understanding Rheology*. Oxford: Oxford University Press.

Muylaert, D. E. P., van Almen, G. C., Talacua, H., Fledderus, J. O., Kluin, J., Hendrikse, S. I. S., et al. (2016). Early in-situ cellularization of a supramolecular vascular graft is modified by synthetic stromal cell-derived factor-1α derived peptides. *Biomaterials* 76, 187–195. doi: 10.1016/j.biomaterials.2015.10.052

Pashneh-Tala, S., MacNeil, S., and Claeyssens, F. (2016). The tissue-engineered vascular graft - Past, present, and future. *Tissue Eng. Part B Rev.* 22, 68–100. doi: 10.1089/ten.teb.2015.0100

Putti, M., Mes, T., Huang, J., Bosman, A. W., and Dankers, P. Y. W. (2020). Multi-component supramolecular fibers with elastomeric properties and controlled drug release. *Biomater. Sci.* 8, 163–173. doi: 10.1039/c9bm01241a

Riepe, G., Loos, J., Imig, H., Schroder, A., Schneider, E., Petermann, J., et al. (1997). Long-term in vivo alterations of polyester vascular grafts in humans. *Eur. J. Vasc. Endovasc. Surg.* 13, 540–548. doi: 10.1016/S1078-5884(97)80062-7

Rothuizen, T. C., Damanik, F. F. R., Lavrijsen, T., Visser, M. J. T., Hamming, J. F., Lalai, R. A., et al. (2016). Development and evaluation of in vivo tissue engineered blood vessels in a porcine model. *Biomaterials* 75, 82–90. doi: 10.1016/j.biomaterials.2015.10.023

Serruys, P. W., Miyazaki, Y., Katsikis, A., Abdelghani, M., Leon, M. B., Virmani, R., et al. (2017). Restorative valve therapy by endogenous tissue restoration: tomorrow's world? Reflection on the EuroPCR 2017 session on endogenous tissue restoration. *EuroIntervention* 13, AA68–AA77. doi: 10.4244/EIJ-D-17-00509

Sijbesma, R. P., Beijer, F. H., Brunsveld, L., Folmer, B. J. B., Hirschberg, J. H. K. K., Lange, R. F. M., et al. (1997). Reversible polymers formed from self-complementary monomers using quadruple hydrogen bonding. *Science* 278, 1601–1604. doi: 10.1126/science.278.5343.1601

Singh, G., Cordero, J., Wiles, B., Tembelis, M. N., Liang, K.-L., Rafailovich, M., et al. (2019). Development of in vitro bioengineered vascular grafts for microsurgery and vascular surgery applications. *Plast. Reconstr. Surg. Glob. Open* 7:e2264. doi: 10.1097/gox.0000000000002264

Smits, A. I. P. M., and Bouten, C. V. C. (2018). Tissue engineering meets immunoengineering: prospective on personalized in situ tissue engineering strategies. *Curr. Opin. Biomed. Eng.* 6, 17–26. doi: 10.1016/j.cobme.2018.02.006

Sodupe-Ortega, E., Sanz-Garcia, A., Pernia-Espinoza, A., and Escobedo-Lucea, C. (2018). Accurate calibration in multi-material 3D bioprinting for tissue engineering. *Materials (Basel)* 11:1402. doi: 10.3390/ma11081402

Söntjens, S. H. M., Renken, R. A. E., Van Gemert, G. M. L., Engels, T. A. P., Bosman, A. W., Janssen, H. M., et al. (2008). Thermoplastic elastomers based on strong and well-defined hydrogen-bonding interactions. *Macromolecules* 41, 5703–5708. doi: 10.1021/ma800744c

Stanley, J. C., Burkel, W. E., Ford, J. W., Vinter, D. W., Kahn, R. H., Whitehouse, W. M., et al. (1982). Enhanced patency of small-diameter, externally supported

Dacron iliofemoral grafts seeded with endothelial cells. *Surgery* 92, 994–1005. doi: 10.5555/uri:pii:0039606082901611

Stenoien, M. D., Drasler, W. J., Scott, R. J., and Jenson, M. L. (1999). *Silicone Composite Vascular Graft. Google Patents*. Washington, DC: U.S. Patent and Trademark Office.

Talacua, H., Smits, A. I. P. M., Muylaert, D. E. P., Van Rijswijk, J. W., Vink, A., Verhaar, M. C., et al. (2015). In situ tissue engineering of functional small-diameter blood vessels by host circulating cells only. *Tissue Eng. Part A* 21, 2583–2594. doi: 10.1089/ten.tea.2015.0066

Tuchmann, A., and Dinstl, K. (1989). Below-knee femoropopliteal bypass using externally supported polytetrafluoroethylene (PTFE) grafts. *Ann. Vasc. Surg.* 3, 177–180. doi: 10.1016/S0890-5096(06)62013-X

Van Almen, G. C., Talacua, H., Ippel, B. D., Mollet, B. B., Ramaekers, M., Simonet, M., et al. (2016). Development of non-cell adhesive vascular grafts using supramolecular building blocks. *Macromol. Biosci.* 16, 350–362. doi: 10.1002/mabi.201500278

van Haaften, E., Bouten, C., and Kurniawan, N. (2017). Vascular mechanobiology: towards control of in situ regeneration. *Cells* 6:19. doi: 10.3390/cells6030019

van Haaften, E. E., Duijvelshoff, R., Ippel, B. D., Söntjens, S. H. M., van Houtem, M. H. C. J., Janssen, H. M., et al. (2019). The degradation and performance of electrospun supramolecular vascular scaffolds examined upon in vitro enzymatic exposure. *Acta Biomater.* 92, 48–59. doi: 10.1016/j.actbio.2019.05.037

Versteegen, R. M., Kleppinger, R., Sijbesma, R. P., and Meijer, E. W. (2006). Properties and morphology of segmented copoly(ether urea)s with uniform hard segments. *Macromolecules* 39, 772–783. doi: 10.1021/ma051874e

Wisse, E., Spiering, A. J. H., Dankers, P. Y. W., Mezari, B., Magusin, P. C. M. M., and Meijer, E. W. (2011). Multicomponent supramolecular thermoplastic elastomer with peptide-modified nanofibers. *J. Polym. Sci. Part A Polym. Chem.* 49, 1764–1771. doi: 10.1002/pola.24598

Wissing, T. B., Bonito, V., Bouten, C. V. C., and Smits, A. I. P. M. (2017). Biomaterial-driven in situ cardiovascular tissue engineering—a multi-disciplinary perspective. *NPJ Regen. Med.* 2, 1–19. doi: 10.1038/s41536-017-0023-2

Wu, D. J., Bouten, C. V. C., and Dankers, P. Y. W. (2017). From molecular design to 3D printed life-like materials with unprecedented properties. *Curr. Opin. Biomed. Eng.* 2, 43–48. doi: 10.1016/j.cobme.2017.06.001

Xu, D., Liu, C.-Y., and Craig, S. L. (2011). Divergent shear thinning and shear thickening behavior of supramolecular polymer networks in semidilute entangled polymer solutions. *Macromolecules* 44, 2343–2353. doi: 10.1021/acs.chemrev.5b00303

Žarko, J., Vladiæ, G., Pál, M., and Dedijer, S. (2017). Influence of printing speed on production of embossing tools using FDM 3d printing technology. *J. Graph. Eng. Des.* 8, 19–27. doi: 10.24867/jged-2017-1-019

**Conflict of Interest:** The authors declare that the research was conducted in the absence of any commercial or financial relationships that could be construed as a potential conflict of interest.

frontiers in Materials

ORIGINAL RESEARCH
published: 28 July 2020
doi: 10.3389/fmats.2020.00224

# Enhancement of the Biological and Mechanical Performances of Sintered Hydroxyapatite by Multiple Ions Doping

*Simone Sprio[1]*, Massimiliano Dapporto[1], Lorenzo Preti[1], Elisa Mazzoni[2], Maria Rosa Iaquinta[2], Fernanda Martini[2], Mauro Tognon[2], Nicola M. Pugno[3,4], Elisa Restivo[5,6], Livia Visai[1,5,6] and Anna Tampieri[1]*

[1] Institute of Science and Technology for Ceramics-National Research Council (ISTEC-CNR), Faenza, Italy, [2] Department of Medical Sciences, University of Ferrara, Ferrara, Italy, [3] Laboratory of Bio-Inspired, Bionic, Nano, Meta Materials & Mechanics, Department of Civil, Environmental and Mechanical Engineering, University of Trento, Trento, Italy, [4] School of Engineering and Materials Science, Queen Mary University of London, London, United Kingdom, [5] Biochemistry Unit, Department of Molecular Medicine, Center for Health Technologies (CHT), UdR INSTM, University of Pavia, Pavia, Italy, [6] Department of Occupational Medicine, Toxicology and Environmental Risks, Istituti Clinici Scientifici (ICS) Maugeri S.p.A, IRCCS, Pavia, Italy

In the present work, hydroxyapatite (HA) nanoparticles doped with $Mg^{2+}$, $Sr^{2+}$, and $Zn^{2+}$ ions are developed by wet neutralization method and then sintered at 1,250°C to obtain bulk consolidated materials. Physicochemical and microstructural analyses show that the presence of doping ions in the HA structure induced the formation of βTCP as secondary phase, during the sintering process, and we found that this effect is depending on the stability of the various doping ions in the hydroxyapatite lattice itself. We also found that the formation of βTCP as secondary phase, in turn, confines the grain growth of HA induced by the high-temperature sintering process, thus leading to a strong increase of the flexural strength of the bulk materials, according to Hall-Petch-like law. Furthermore, we found that the doping ions enter also in the structure of the βTCP phase; besides the grain growth confinement, also the solubility and ion release ability of the final materials were enhanced. In addition to ameliorate the mechanical performance, the described phenomena also activate multiple biofunctionalities: (i) ability to upregulate various genes involved in the osteogenesis, as obtained by human adipose stem cells culture and evaluated by array technology; (ii) enhanced resistance to the adhesion and proliferation of Gram+ and Gram– bacterial strains. Hence, our results open a perspective for the use of sintered multiple ion-doped HA to develop ceramic biodevices, such as plates, screws, or other osteosynthesis media, with enhanced strength, osteointegrability, and the ability to prevent post-surgical infections.

**Keywords: calcium phosphates, ion doping, osteogenic properties, antibacterial properties, mechanical properties, magnesium, strontium, zinc**

OPEN ACCESS

***Edited by:***
*Lia Rimondini,*
*University of Eastern Piedmont, Italy*

***Reviewed by:***
*Cinzia Giannini,*
*Italian National Research Council, Italy*
*Marta Miola,*
*Politecnico di Torino, Italy*

****Correspondence:***
*Simone Sprio*
*simone.sprio@istec.cnr.it*

***Specialty section:***
*This article was submitted to Biomaterials, a section of the journal Frontiers in Materials*

***Received:*** *24 March 2020*
***Accepted:*** *22 June 2020*
***Published:*** *28 July 2020*

***Citation:***
*Sprio S, Dapporto M, Preti L, Mazzoni E, Iaquinta MR, Martini F, Tognon M, Pugno NM, Restivo E, Visai L and Tampieri A (2020) Enhancement of the Biological and Mechanical Performances of Sintered Hydroxyapatite by Multiple Ions Doping. Front. Mater. 7:224. doi: 10.3389/fmats.2020.00224*

## INTRODUCTION

Since decades, extensive research is being engaged for the development of synthetic biodevices with improved biological and mechanical functionality, suitable for application in bone surgery (Munch et al., 2008; Dutta et al., 2015). Particularly, the development of fixation devices as osteosynthesis media capable of enhanced osteointegrability and mechanical properties is highly desired, to

support the stabilization of complex fractures or the fixation of bone implants (Suryavanshi et al., 2016). In spite of their wide use in orthopedics as fixation media (Goodrich et al., 2012), metallic implants can undergo failure due to infections, corrosion, fatigue, and poor osteointegrability, all factors jeopardizing the healing process (Pohler, 2002; Ribeiro et al., 2012). Particularly, mechanical mismatch between the implant and surrounding bone can result in the implant loosening and bone resorption (Alexander and Theodos, 1993; Sheikh et al., 2015). On the other hand, the occurrence of post-surgical infections is a major concern, also due to the antibiotic resistance of various bacterial strains, a phenomenon that is constantly growing and that will become, more and more, a primary cause of failure of surgical interventions, particularly in orthopedics (Li and Webster, 2018; Hofer, 2019). To overcome these drawbacks, a growing literature is investigating the possibility of developing biomaterials capable to establish tight bone-implant interfaces thanks to improved mechanical properties and to superior osteointegrative and anti-infective ability. Previous studies investigated the possibility of achieving materials with inherent antibacterial properties as induced by the surface composition and/or micro-texture (Albers et al., 2013; Slavin et al., 2017). In this respect, hydroxyapatite [HA: $Ca_5(PO_4)_3(OH)$] is since decades considered as elective material for application in bone surgery, thanks to its compositional similarity with the mineral component of bone, even though the relatively poor mechanical properties pose concerns on its use (Polo-Corrales et al., 2014; Eliaz and Metoki, 2017). It is also known that controlled ion substitutions in the structure of HA, attempting to more closely mimic the mineral composition of natural bone, increase its bioactivity and bone-forming ability (Cazalbou et al., 2005; Ballardini et al., 2018; Sprio et al., 2019). Particularly, $Mg^{2+}$ is recognized to promote the formation of new bone mineral nuclei, particularly active in the newly formed bone tissue (Bigi et al., 1992). $Mg^{2+}$ ions, as well as $Sr^{2+}$ and also $Zn^{2+}$, are known as active regulators of osteoblasts and osteoclast cells, thus able to modulate the bone turnover, potentially effective also in the case of osteoporotic bones (Boanini et al., 2010). Recent studies report that the multiple doping of HA with these ions can also promote inherent anti-infective properties (Ballardini et al., 2018; Sprio et al., 2019), thus being promising for the development of new medical devices with enhanced bioactivity and osteointegrability while preventing adverse infective complications, at the same time. These studies were carried out on as-synthesized HA powders. However, the development of 3D ceramic devices with relevant mechanical properties requires the use of sintering process for their consolidation. While several investigations of the effects of doping ions have been carried out on nanocrystalline and nanostructured HAs obtained by low temperature wet synthesis, there are very few studies investigating the biological effect of these ions in sintered ceramics, but they are limited to calcium silicate phases (Wu et al., 2007; Zreiqat et al., 2010; Liu et al., 2019). In particular, in spite of the urging need of implantable biodevices capable of counteracting the formation of biofilms, studies on the antibacterial ability of ion-doped sintered CaPs have not yet been reported.

In this work, various multi-substituted HAs were synthesized by a wet neutralization process and sintered at high temperature to obtain consolidated ceramic materials. The study highlights the effect of the various substituting ions, such as $Mg^{2+}$, $Sr^{2+}$, and $Zn^{2+}$, on the physico-chemical, morphological, and mechanical properties as well as on the biological abilities of the resulting sintered ceramics, as obtained by cellular epigenetic tests and microbiological analyses conducted on *Escherichia coli* and *Staphylococcus aureus*, which are among the most common infective strains responsible of post-operative complications in orthopedics.

# MATERIALS AND METHODS

## Synthesis of the Ion-Doped Apatites

A neutralization reaction was established between an aqueous suspension of calcium hydroxide [$Ca(OH)_2$, Sigma Aldrich, 95% purity], and a solution of phosphoric acid ($H_3PO_4$, Fluka, 85% purity). To introduce foreign ions in the final product, $Mg^{2+}$, $Sr^{2+}$, $Zn^{2+}$ cations were added in the aqueous calcium suspension, as magnesium chloride ($MgCl_2$, Sigma Aldrich), strontium chloride ($SrCl_2$, Sigma Aldrich), and zinc chloride ($ZnCl_2$, Sigma Aldrich). The initial Ca/P ratio was set to 1.67, that is, equal to that of stoichiometric HA.

The reaction is conducted in a round-bottomed flask, filled with an aqueous suspension of calcium hydroxide, containing the salts of the doping cations and kept at 37°C, under mechanical stirring. The neutralization process was conducted by slowly adding $H_3PO_4$ solution to the alkaline suspension (dripping rate = 1 drop/s). At the end of the process, the suspension is left in agitation at 37°C for 2 h, then left to mature overnight at room temperature. Then, the suspension is washed with bi-distilled water for three times, in order to eliminate ions simply adsorbed on the HA surface and then dried at 40°C in oven. Finally, the obtained powder is sieved at 150 μm.

In the present work, four different sets of ion-doped HA powders were synthesized, the first set includes non-doped HA, as reference material (coded as HA), HA doped with magnesium (MgHA), HA doped with magnesium and strontium (MgSrHA), and HA doped with magnesium and zinc (MgZnHA). The symbols $X_{Mg}$, $X_{Sr}$, and $X_{Zn}$ indicates the initial molar fraction, respectively, of $Mg^{2+}$, $Sr^{2+}$, and $Zn^{2+}$, calculated as $\frac{\text{mole of } XX}{\text{mole of Ca}} \cdot 100$, where *XX* indicates Mg, Sr or Zn.

## Development of Sintered Calcium Phosphate Materials

Consolidated ceramics were obtained by thermal sintering of the as-synthesized powders at 1,250°C for 1 h in a muffle furnace. The sintering was carried out on pellets obtained by uniaxial pressing 1.5 g of apatite powders in a steel mold (20 mm in diameter) at 700 bar. The resulting pellets were then further treated by cold isostatic pressing at 2,500 bar, to obtain green ceramic bodies with maximal relative density, suitable to obtain the highest degree of densification in the final sintered bodies. The sintered bodies

are henceforth coded as follows: S-HA, S-MgHA, S-MgSrHA, S-MgZnHA.

## Physico-Chemical Characterization

The crystalline phase composition of the as-obtained and sintered materials was obtained by X-ray diffraction (XRD) with a D8 ADVANCE (Bruker, Karlsruhe, Germany) diffractometer using Cu Kα radiation (λ = 1.54178 Å) generated at 40 kV and 40 mA, a counting time of 0.5 s, and a step size of 0.02° 2θ. Semiquantitative analysis and the evaluation of the cell parameters and domain size of the crystalline structures were performed by full profile analysis of the XRD spectra, using the software TOPAS 5 (Bruker, Karlsruhe, Germany). The experimental XRD spectra were analyzed in reference to previously published crystal structure models. In all the experiments the background was modeled with an 11th-order Chebyshev polynomial. The calculation was carried out, up to convergence, by refining the scale factor, the domain size and the cell parameters at the same time. The domain size was evaluated keeping into account the contribution of the instrumental resolution function, obtained by fitting the diffraction pattern of a $LaB_6$ NIST standard (Giannini et al., 2016).

The chemical analysis of the as-obtained apatite powders was performed on dried samples (20 mg) using ICP-OES spectrometer (Agilent 5100, United States) and primary standards (1,000 ppm, Fluka). The samples were dissolved into 2 ml of nitric acid then diluted in 100 ml of milliQ water.

## Characterization of the Sintered Bodies

Field emission gun scanning electron microscopy (FEG-SEM) (Sigma NTS GmbH, Carl Zeiss, Oberkochen, Germany) was used to evaluate the morphology of the final material at the multi-scale. The samples were placed on an aluminum stub and covered with a thin layer of gold to improve conductivity. The analysis of the microstructure was carried out by mirror-polishing and a subsequent acid attack with HCl 1M for 5 s to put in evidence the grain boundaries. The equipment used is Sigma NTS GmbH (Carl Zeiss, Oberkochen, Germany).

## Mechanical Characterization

The compression and flexural strength of sintered bodies was evaluated with a universal testing machine (MTS Insight 5, Eden Prairie, MN, United States), crosshead speed 2 mm/min, on five sintered samples for each investigated material. For compression tests, the samples were obtained in form of cylinders with a diameter of 10 mm and height of 15 mm. Flexural tests were carried out by 4-point bending on parallelepipeds, with 25.0 mm × 2.5 mm × 2.0 mm in size. Nanoindentation tests were carried out on mirror-polished sintered samples (iNano, Nanomechanics, Inc., United States). A Berkovich indenter was used to perform indentations up to a maximum load of 45 mN, so that hardness and Young's moduli could be obtained.

## Ion Release Tests

The evaluation of the ion release with time was made by immersing tablets (1 g of powder each) into 5 ml of pH = 7.4 buffer solution (Ca- and Mg-free Hank's Balanced Salt solution) and maintained at 37°C under gentle shaking. At scheduled times (i.e., after 1, 2, 3, 7, 11, and 15 days) the solution was removed and 5 ml of fresh solution was added to the tablets. The liquids containing the ions released after the prefixed times were analyzed by ICP-OES for the quantitative determination of Ca, Mg, and Zn. The results were presented as cumulative data. All the experiments were made in triplicate.

## Cells and Cell Culture

Human adipose-derived mesenchymal stem cells (hASC) were purchased from Lonza Milan, Italy (Catalog n. PT-5006) as cryopreserved frozen cells at the first passage. These cells are positive for surface markers CD13, CD29, CD44, CD73, CD90, CD105, CD166, while are negative for other markers, such as CD14, CD31, CD45 (Mazzoni et al., 2020). Cells were expanded in Dulbecco's Modified Eagle Medium F-12 (DMEM/F12; Lonza, Milan, Italy), supplemented with 10% fetal bovine serum (FBS) and 10% antibiotics (Pen/Strep 10.000 U/ml) at a density of 5,000 cells/$cm^2$, in a T75 flask (Falcon BD, Franklin Lakes, NJ, United States) at 37°C with 5% $CO_2$ in a humidified atmosphere (Manfrini et al., 2013; Mazzoni et al., 2017, 2020). At the second passage, hASCs were randomly assigned to five treatment groups: hASCs grown in monolayer in 24-well tissue culture polystyrene plates (TCP) and hASCs grown on biomaterials, such as (i) S-HA, (ii) S-MgHA, (iii) S-MgSrHA, (iv) S-MgZnHA. In biomaterial groups, the samples were placed separately in 24-well plates (Ø = 10 mm) to cover the surface area. hASC cultures were then filled with 200 µl cell suspension containing $10^4$ cells for each sample and incubated for 2 h (Mazzoni et al., 2017). The cell suspension was subjected to gentle shaking every 15 min in order to maximize cell-material interaction. Plates were incubated at 37°C. in humidified air (5% $CO_2$) until the time of the assay. RT$^2$ Profiler$^{TM}$ PCR Array was performed at day 14 (Mazzoni et al., 2020).

## RNA Isolation and RT$^2$ Profiler$^{TM}$ PCR Array Analyses of Extracellular Matrix and Adhesion Molecule Genes

To profile the expression of 84 Osteogenesis-related genes simultaneously we used the Human Osteogenesis RT$^2$ Profiler PCR Array Catalog number PAHS-026Z and product n. 330231 (Qiagen Milan, Italy)[1]. The Human Osteogenesis RT$^2$ Profiler PCR was performed according to the manufacturer's instructions. The list of genes was reported in the product and the primers set used is covered by the patent of this product.

To identify of the extracellular matrix (ECM) and adhesion molecule expression genes activated by the studied materials, RT$^2$ Profiler PCR Array profiles was performed in hASCs grown on selected biomaterials, reported above. Human ASCs were grown on biomaterials and plastic plates employed as the control (TCPS) until day 14. After this period, total RNA was extracted through RNeasy Plus Micro Kit (Qiagen, Milan, Italy) according to the manufacturer's instructions

[1]https://geneglobe.b2b-qiagen.com/product-groups/rt2-profiler-pcr-arrays

(Mazzoni et al., 2020). RNA quality and quantity were assessed using a Nanodrop spectrophotometer (ND-1000, NanoDrop Technologies, Wilmington, DE, United States) and stored at –80°C until the time of the analysis (Mazzoni et al., 2012). Purified RNA from hASCs grown on selected biomaterials and TCPS was reverse transcribed to cDNA using the $RT^2$ First Strand cDNA Kit (Qiagen, Milan, Italy). $RT^2$ Profiler PCR Array (Qiagen, Milan, Italy Catalog n. PAHS-013Z) was used to analyze the expression of 84 genes for human ECM, cell adhesion molecules, and five housekeeping genes, at day 14 (Mazzoni et al., 2017). Specific primers sets employed in real-time PCRs were used to analyze the expression of 84 genes codified for proteins involved in cell-to-cell adhesion, cells to the ECM adhesion, and ECM proteins, such as collagens and ECM protease. $RT^2$ Profiler $PCR^{TM}$ Array $PCR^{TM}$ was performed using SYBR Green method on a CFX96 Touch PCR detection system (Bio-Rad, Milan, Italy) (Mazzoni et al., 2017). In terms of data analysis, fold-changes of each gene expression were calculated using the $2^{-\Delta\ \Delta\ CT}$ method, whereas the housekeeping genes employed as controls were used to normalize the results (Mazzoni et al., 2017, 2020). Two independent experiments were performed simultaneously. Positive values indicated individual upregulated genes, while negative values indicated the downregulated genes, compared to controls. Only twice fold up- or downregulated expression ($Log_2$fold change $< 1$ or $> 1$) was considered significant, whereas a onefold change meant that the same amount of analyzed gene was expressed in cells adherent to the biomaterials when compared to those grown on the polystyrene vessel, the control.

## Bacterial Strains and Culture Conditions

The microorganisms used in this study were *Escherichia coli* ATCC 25922 (*E. coli*), and *Staphylococcus aureus* ATCC 25923 (*S. aureus*), kindly supplied by R. Migliavacca (Department of Clinical Surgical, Diagnostic and Pediatric Sciences, University of Pavia, Italy). Both the bacteria strains were routinely grown in their culture medium overnight under aerobic conditions at 37°C using a shaker incubator (Asal Srl, Italy): *E. coli* in Luria Bertani Broth (LB) (Difco, Detroit, MI, United States) and *S. aureus* in Brain Heart Infusion (BHI) (Difco). Both these cultures were statically incubated at 37°C under aerobic conditions and reduced to a final density of $1 \times 10^{10}$ cells/mL as determined by comparing the optical density ($OD_{600}$) of the sample with a standard curve relating $OD_{600}$ to cell number (Bari et al., 2017).

## Bacterial Viability

All types of ions-doped HA samples were washed in sterile phosphate buffer saline (PBS 1×) and directly incubated with 200 μL ($1 \times 10^5$) *E. coli* or *S. aureus* cell suspensions for 24 h at 37°C, respectively. At the end of the incubation time, an MTT [3-(4,5-dimethylthiazol-2-yl)-2,5-diphenyltetrazolium bromide; Sigma-Aldrich®, United States] test was performed on the following samples: (1) the planktonic bacterial cultures after their removal from the ions-doped HA materials; and (2) directly on the ions-doped HA materials used for the bacterial incubation. The same aliquot of bacteria was also cultured in a Tissue Culture Plate (TCP) used as a positive control. After 3 h of incubation at 37°C, the MTT reaction was stopped by adding 100 μL of solution C (2-propanol, HCl 0.04 N) and further incubated for 15 min at 37°C. The colorimetric reaction was read at CLARIOstar (BMG Labtech, Germany) at 570 nm wavelength with 630 nm as the reference wavelength. Results were firstly normalized to TCP and then to S-HA (undoped HA) set as 100%. The experiments were performed in duplicate and repeated three times.

## Confocal Laser Scanning Microscopy (CLSM) Studies

As previously reported (Pallavicini et al., 2017) for confocal studies, 0.2 mL ($1 \times 10^5$) of both *E. coli* and *S. aureus* suspensions were dispensed into 48-well microplates (Costar) containing on the bottom sterile ions-doped HA materials and incubated for 24 h at 37°C. After 24 h, the bacteria cultures were gently removed and the viability of adherent bacteria was estimated with the BacLight Live/Dead viability kit (Molecular Probes, Eugene, OR, United States). The kit includes two fluorescent nucleic acid stains: SYTO9 and propidium iodide. SYTO9 penetrates both viable and non-viable bacteria, while propidium iodide penetrates bacteria with damaged membranes and quenches SYTO9 fluorescence. Dead bacteria, which take up propidium iodide, fluoresce red, and bacteria fluorescing green, are deemed viable. For assessing viability, 1 μL of the stock solution of each stain was added to 3 mL of PBS 1× and, after being mixed, 200 μL of the solution was dispensed into 48-well microplates containing the apatite samples and incubated at 22°C for 15 min in the dark. Stained bacteria were examined under a Leica CLSM (model TCS SP8 DLS; Leica, Wetzlar, Germany) using a 40× and 63× oil immersion objective. The excitation and emission wavelengths used for detecting SYTO9 were 488 and 525 nm, respectively. Propidium iodide was excited at 520 nm, and its emission was monitored at 620 nm. The optical sections of 0.9 μm were collected over the complete thickness of the sample, and for each sample, images from three randomly selected positions were acquired. The 3D projections were obtained using software LAS X.

## Statistical Analysis

All the statistical calculations related to antibacterial tests were carried out using GraphPad Prism 5.0 (GraphPad Inc., San Diego, CA, United States). Statistical analysis was performed using Student's unpaired, two-sided *t*-test and through one-way variance analysis (ANOVA), followed by Bonferroni *post hoc*, for multiple comparisons (significance level of $p \leq 0.05$).

# RESULTS

## Physicochemical and Morphological Characterization of the As-Synthesized Apatites

The as-obtained powders are all composed of HA as a single crystalline phase (**Figure 1**). The broad profile of the obtained diffraction patterns can be ascribed to low crystallinity, as induced by the powder synthesis carried out at body temperature

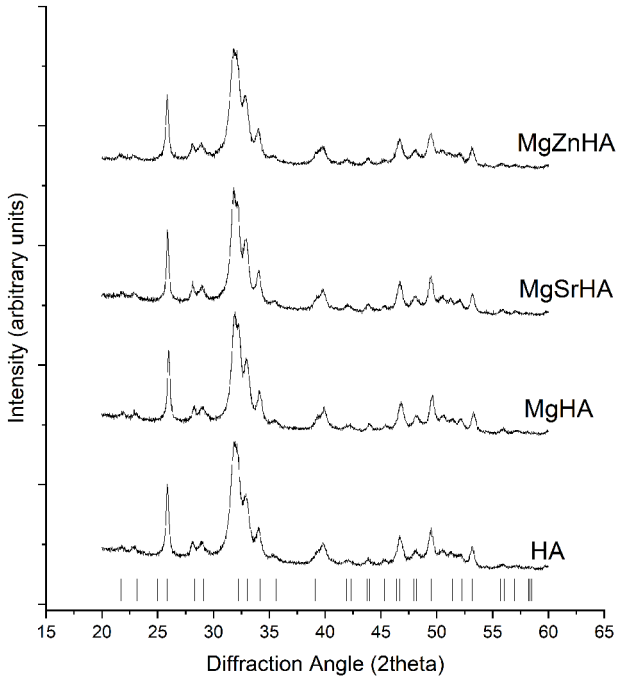


**FIGURE 1 |** XRD spectra of the as-synthesized powders. The markers point to XRD reflections of the HA structure.

and by the incorporation of doping ions in the apatitic structure (Sprio et al., 2008). The chemical analysis by ICP (**Table 1**) reports that only a fraction of the foreign ions initially present in the reaction vessel was actually incorporated into the HA structure, whereas the remaining was eliminated during the powder washing.

The cell parameters and volume, and the average size of crystalline domains in the as-obtained HA powders are reported in **Table 2**. All the as-synthesized apatites show very small domain size ($D_{av}$), ascribed to the low synthesis temperature that limited the crystal growth. Changes in cell parameters and volume of the HA crystal can be related to different ionic radii of doping cations (here $Mg^{2+} \approx 66$ pm, $Sr^{2+} \approx 112$ pm or $Zn^{2+} \approx 74$ pm) substituting $Ca^{2+}$ ($\approx 99$ pm), which influence the interatomic distances (Procopio et al., 2019). It was reported that $Mg^{2+}$ has limited ability to substitute $Ca^{2+}$ in large extent, ascribed to its much smaller ionic radius (Boanini et al., 2010). However, in the single-doped MgHA, we can observe a very little decrease of the *c* axis and of the overall cell volume, in comparison with the undoped HA, in agreement with a previous study (Tampieri et al., 2004), thus suggesting that in the MgHA sample at least a fraction of the introduced $Mg^{2+}$ could substitute $Ca^{2+}$ in the HA lattice. Concerning the multi-doped apatites, during the formation of the HA crystal a competition is established between $Mg^{2+}$-$Sr^{2+}$ (in MgSrHA) or $Mg^{2+}$-$Zn^{2+}$ ions (in MgZnHA) attempting to enter the $Ca^{2+}$ crystal sites, thus making difficult to correlate crystal data with the extent of specific ion occupancy in the apatite crystal sites. As an overall effect, the analysis of the crystal data reports a small increase of the cell volume in MgSrHA, ascribed to partial substitution of $Ca^{2+}$ with the larger $Sr^{2+}$ ions, and a small reduction in MgZnHA, due to the smallest size of both $Mg^{2+}$and $Zn^{2+}$ ions.

Microscopic observation by SEM (**Figure 2**) shows that the as-obtained HA powders are made of primary rounded particles with size of few tens of nanometers, agglomerated in micron-size clusters, due to their high specific surface that enhance electrostatic interactions.

## Physicochemical Characterization of the Sintered Apatites

The sintering of the HA powders was carried out on uniaxially pressed pellets at 1,250°C for 1 h. The XRD analysis of the sintered materials shows that S-HA, prepared using the undoped HA as a raw material, is composed of HA as single phase and traces of calcium oxide (CaO) (**Figure 3**). Conversely, in the samples prepared with ion-doped apatites, different amounts of βTCP phase are found. Besides, magnesium oxide (MgO) is also found in trace amounts. No other oxides or secondary phases involving $Sr^{2+}$ or $Zn^{2+}$ ions are found. **Table 3** also shows that the composition of the HA phase in the S-HA sample is nearly stoichiometric (Ca/P ratio ∼1.67), accounting for the trace amount of CaO found as a secondary phase. The doped materials show reduced Ca/P ratio as an effect of the calcium deficiency related to the incorporation of doping divalent cations in calcium crystal sites.

**Table 3** shows that the concentration of $Sr^{2+}$ and $Zn^{2+}$ in the sintered materials is very close to the values found in the as-synthesized apatite powders (see also **Table 1**). Conversely, a quite reduced amount of $Mg^{2+}$ is found, particularly in S-MgZnHA sample, suggesting that it could be partially evaporated during the high-temperature sintering process. This is reasonable considering that the boiling point of magnesium is ∼1,090°C, that is, lower than the sintering temperature adopted in our work.

The full profile analysis of the XRD spectra was carried out by using TOPAS 5 software and previously published crystal models of HA, βTCP, MgO, and CaO phases (Sasaki et al., 1979; Rodríguez-Lorenzo et al., 2003; Yashima et al., 2003). In every calculation run we refined simultaneously the scale factor, cell parameters and domain size of all the phases present in the sample, until convergence, thus finally obtaining also a semiquantitative estimation of the crystalline structures content. We observe slight variations in cell parameters of the HA phase present in the doped sintered bodies, but a marked decrease of the domain size ($D_{av}$), in respect to the undoped S-HA (**Table 4**). Ion-doped apatite phases are well-known for their reduced thermodynamic stability, compared to the stoichiometric phase. Thus, the thermal treatment yielded the segregation of foreign ions outside the HA lattice and induced the decomposition of the initial apatite phase followed by the formation of βTCP phase at the grain boundaries that could have interfered with the growth of the HA crystals and limit the final size. Whereas $Mg^{2+}$ can be assumed to be completely expelled from the HA lattice during sintering, it is possible that some substitution of $Ca^{2+}$ with $Sr^{2+}$ or $Zn^{2+}$ ions is retained. Indeed, $Sr^{2+}$ ions were previously reported as able to create HAs with general

**TABLE 1 |** ICP analysis showing the effective incorporation of doping ions in the as-synthesized apatite powders.

| Sample | Initial $X_{Mg}$ (mol%) | Actual $X_{Mg}$ (mol%) | Initial $X_{Sr}$ (mol%) | Actual $X_{Sr}$ (mol%) | Initial $X_{Zn}$ (mol%) | Actual $X_{Zn}$ (mol%) |
|---|---|---|---|---|---|---|
| HA | – | – | – | – | – | – |
| MgHA | 15.0 | 6.1 | – | – | – | – |
| MgSrHA | 15.0 | 6.2 | 1.5 | 1.47 | – | – |
| MgZnHA | 15.0 | 5.8 | – | – | 5.0 | 4.9 |

**TABLE 2 |** Crystal data of the as-obtained hydroxyapatite powders.

| Sample | a (Å) | c (Å) | Cell vol. (Å$^3$) | $D_{av}$ (nm) |
|---|---|---|---|---|
| HA | 9.432 | 6.893 | 531.15 | 16.7 |
| MgHA | 9.438 | 6.888 | 531.45 | 19.7 |
| MgSrHA | 9.441 | 6.893 | 532.03 | 19.2 |
| MgZnHA | 9.434 | 6.886 | 530.74 | 15.9 |

composition Ca, $Sr(PO_4)_6(OH)_2$ without any solubility limit, but they are also known for ability to be incorporated in the βTCP phase (Bigi et al., 1997; Kannan et al., 2006), and this explains the much higher extent of secondary phase found in S-MgSrHA sample (**Table 4**). Conversely, the formation of secondary phases occurs in much lower extent in the S-MgZnHA sample. This suggests that $Zn^{2+}$ ions are largely retained in the structure of the HA phase, that is, as Zn-doped HA, even after high-temperature sintering.

In the as-obtained HA/βTCP composites, the βTCP phase can host $Mg^{2+}$, $Sr^{2+}$, and $Zn^{2+}$ ions in partial substitution of $Ca^{2+}$. This is confirmed also by the crystal analysis of the βTCP phase, reporting that the cell parameters, particularly the cell volume, depart from typical values reported in literature toward the values of the whitlockite phase (a Mg-doped βTCP phase) (Schroeder et al., 1977). In the sintered materials, the βTCP phase shows reduced crystal growth, particularly in the multi-doped S-MgSrHA and S-MgZnHA (see $D_{av}$ of βTCP in **Table 4**); here the partial substitution of $Ca^{2+}$ with $Mg^{2+}$ and $Sr^{2+}/Zn^{2+}$ ions in the βTCP lattice could have hampered the crystal growth.

## Morphological and Mechanical Characterization

Gentle chemical etching of polished surfaces of the sintered bodies put in evidence the microstructure and grain morphology (**Figure 4**). Microscopic observation by SEM reveals that the same etching process carried out on the different materials resulted in a more pronounced corrosion effect in the multi-doped ceramics, thus suggesting that the ion doping yielded a reduced chemical stability, thus enhanced biodegradability, in the sintered composites. The analysis of the SEM images reveals that S-HA sample shows some inhomogeneities in the microstructure, reported by large (i.e., >2 μm) grains intercalated with much smaller ones. The average grain size for the four materials is: S-HA = 1.33 ± 0.08 μm; S-MgHA = 0.99 ± 0.05 μm; S-MgSrHA = 0.88 ± 0.04 μm; S-MgZnHA = 0.95 ± 0.06 μm. We thus found a much smaller (about 30%) average grain size in the doped materials -particularly for S-MgSrHA- compared with the undoped S-HA.

We can observe that the smaller grain size detected in the multi-doped sintered materials is consistent with the reduced crystal size of their constituting HA and βTCP phases (**Table 4**). This finding suggests that the microstructure of sintered HA/βTCP composites can be somewhat tailored by specific ions doping in the HA powders used as raw materials.

All the studied materials exhibit compression and flexural strengths in the range of the cortical bone (Keaveny and Hayes, 1993). The multi-doped samples (i.e., S-MgSrHA, S-MgZnHA) result in less resistance to compression in respect to the undoped S-HA and the single doped S-MgHA (**Figure 5A**). Conversely, doped and multi-doped materials show higher flexural strength than the undoped S-HA; particularly, S-MgSrHA exhibits the highest flexural strength (**Figure 5B**). The much lower flexural strength of S-HA can be related to microstructural inhomogeneities that act as critical defects under loading. On the other hand, the much smaller grain size, particularly of S-MgSrHA, can have promoted enhanced fracture strength under flexure. Conversely, multi-doped materials show the lowest compressive strength, in comparison with the undoped S-HA and the single-doped S-MgHA.

Nanoindentation tests reveal no significant differences between the hardness values of the tested sintered bodies (**Figure 6A**). However, doped and multi-doped materials show a slight increase in the hardness mean value. As well, the values of Young's modulus in the multi-doped materials (with a slight prevalence for S-MgSrHA) are about 8% greater compared with S-HA and S-MgHA (**Figure 6B**). Noticeably, the data dispersion is much lower in the multi-doped materials that confirm the structural inhomogeneity detected in S-HA by microscopic observations (**Figure 4**).

The greater flexural strength and higher value of hardness and Young's modulus found in ion-doped sintered materials can be ascribed to the reduced grain size according to a Hall-Petch-like law—which could also be interpreted as a reduced size of critical flaws responsible of the ceramic fracturing—by virtue of the Griffith law ($\sigma\ K_C/c^{1/2}$), where σ is the strength, $K_c$ is the fracture toughness, and $c$ is the size of the critical defect (Griffith, 1921) (in Hall-Petch law $c$ is the grain size thus assumed in Griffith law as proportional to the flaw size). However, note that the exponents observed in our experiments are different from the 0.5 theoretical value and for flexural strength, hardness, and Young's modulus are, respectively, 1.7, thus showing a very efficient strengthening mechanisms, 0.2, and again 0.2.

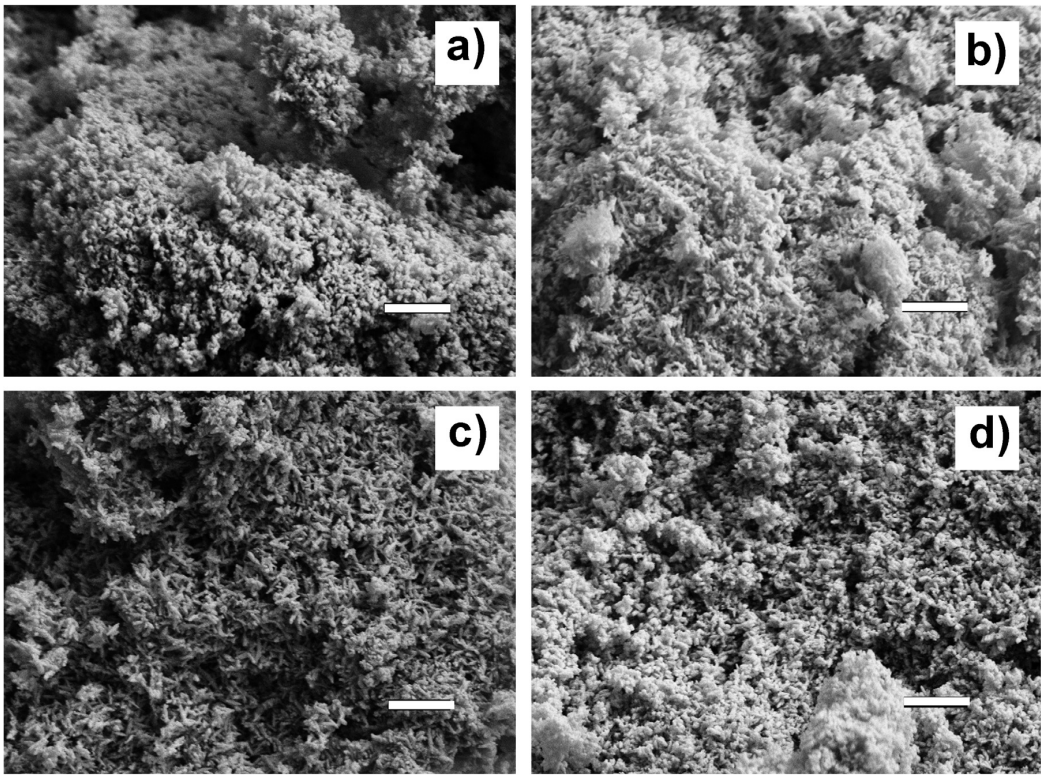


**FIGURE 2 |** SEM micrographs of the as-synthesized apatite powders. **(a)** HA; **(b)** MgHA; **(c)** MgSrHA; and **(d)** MgZnHA. Scale bar: 500 nm.

Accordingly, we can hypothesize that the degradation of the HA phase into βTCP occurring in our doped materials upon sintering resulted in the formation of new crystals at the grain boundaries of HA phase, thus creating a condition of pre-stress further—in addition to grain size reduction—preventing crack propagation and enhancing the flexural strength (as well as hardness and Young's modulus).

## Analysis of the Ions Release Profile

The release of ions from the sintered bodies is investigated to obtain the solubility profile in physiological environment (Hanks' Balanced Salt solution). We show the release profile of $Ca^{2+}$, $Mg^{2+}$, and $Zn^{2+}$ ions, expressed in absolute values (**Figure 7**) and as a percentage of the initial ion content in the material (**Figure 8**). The undoped S-HA shows the lowest extent of $Ca^{2+}$ and $Mg^{2+}$ ion release, whereas S-MgZnHA shows the highest one. No detectable release of $Sr^{2+}$ ions is observed along the whole experiment; conversely, $Mg^{2+}$ ions are released in large extent over time, whereas $Zn^{2+}$ release is detected in much lesser extent than $Mg^{2+}$ and $Ca^{2+}$ (see particularly **Figure 8**). The ions release profile can be described by two distinct mechanisms. In fact, the first 3 days are characterized by fast ion release, while in the subsequent stage the release kinetic was slower. This suggests that, within the first stage, the release process involves ions characterized by relatively weaker bonds; we hypothesize that such ions are located in surface regions characterized by reduced binding energy in respect to the bulk. In the subsequent stage (i.e., days 3–14), the release of $Ca^{2+}$, $Mg^{2+}$, and $Zn^{2+}$ ions is slackened, particularly $Zn^{2+}$ release stops at the day 3. Considering that the HA phase is characterized by low solubility at physiological pH, in respect to βTCP, we can hypothesize that the released ions are prevalently dissolution products of βTCP phase. Taking into account that no $Sr^{2+}$ ions release is detected, we can speculate that $Sr^{2+}$ ions are entirely located in energetically stable substitutional lattice positions of HA and/or βTCP phase. Similarly, the halt of the $Zn^{2+}$ ion release after 7 days suggests that only a small fraction of these ions is located into crystal sites characterized by low binding energy. Indeed, the high electronegativity of zinc, in comparison with calcium and strontium (i.e., Zn = 1.6; Sr = Ca = 1.0), supports the hypothesis that $Zn^{2+}$ ions are stably incorporated into the HA lattice as a Zn-doped HA, thus limiting its segregation into the secondary βTCP phase. Hence, the very low extent of Zn release can be ascribed to the small fraction of $Zn^{2+}$ ions incorporated, together with $Mg^{2+}$, in the βTCP structure, which is characterized by higher solubility at physiological pH.

## Gene Expression of Human Extracellular Matrix and Adhesion Molecules

Gene expression profiles of human ECM and adhesion molecules were evaluated by array technology. To this purpose, hASCs were grown on the sintered apatites and on TCPS, as control, until day 14.

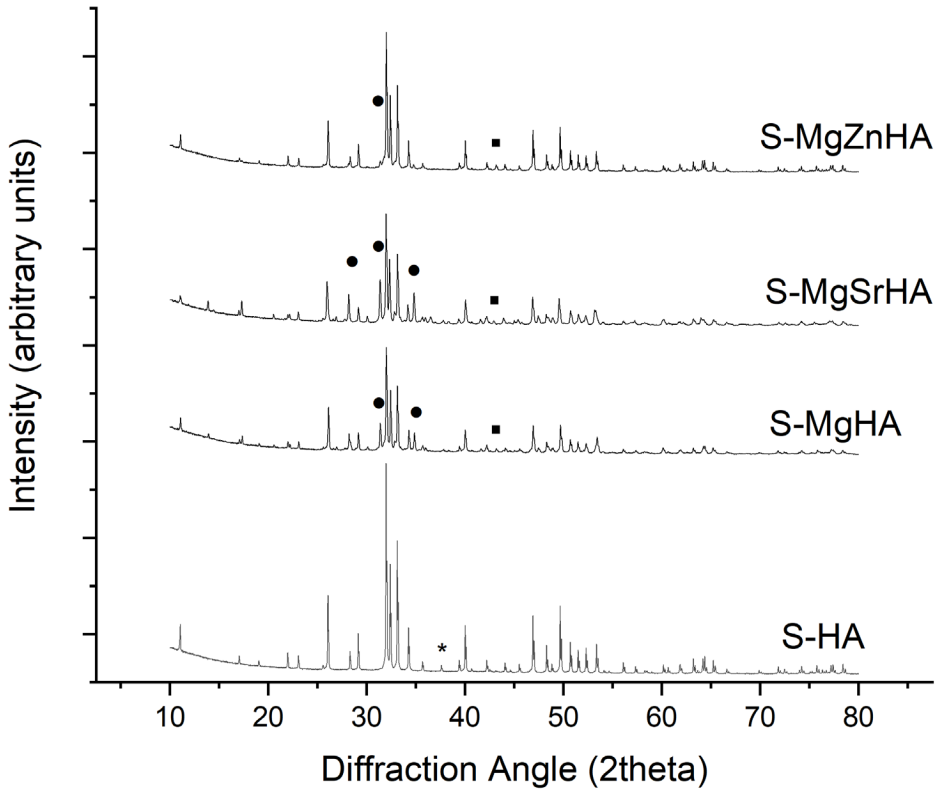


**FIGURE 3 |** XRD spectra of the sintered apatites. The symbols highlight relevant peaks of the secondary phases. * = CaO; ▪ = MgO; • = βTCP. All the remaining reflections belong to hydroxyapatite phase. Miller indices related to the most intense XRD reflections of the various crystalline phases are reported.

**TABLE 3 |** Ca/P molar ratio and doping ions content in the sintered materials, as obtained by ICP analysis.

| Sample | Molar Ca/P | $X_{Mg}$ (mol%) | $X_{Sr}$ (mol%) | $X_{Zn}$ (mol%) |
|---|---|---|---|---|
| S-HA | 1.70 | – | – | – |
| S-MgHA | 1.57 | 5.2 | – | – |
| S-MgSrHA | 1.56 | 5.5 | 1.3 | – |
| S-MgZnHA | 1.53 | 4.1 | – | 5.0 |

A total of 33 differentially expressed genes (DEG) including 31 upregulated genes (red) and 2 downregulated genes (green) are identified in the hASC grown on S-HA material (**Figure 9A**). Specifically, the DEG positively modulated from S-HA material encoding for integrin proteins, such as Integrin alpha-2,3,5,6 (*ITGA-2,3,5,6*) and Integrin beta 5 (*ITGB5*). ECM proteins, such as nine collagen proteins called Collagen, type I, alpha 1; Collagen, type IV, alpha 2; Collagen, type V, alpha 1; Collagen, type VI, alpha 1,2; Collagen, type VII alpha 1; Collagen, type XII, alpha 1; Collagen, type XIV, alpha 1; Collagen, type XVI, alpha 1 (*COL1A1, COL4A2, COL5A1, A2, COL6A1, COL7A1, COL12A1, COL14A, COL16A1*), are detected as upregulated on hASCs grown on S-HA material. Five matrix metalloproteinases (MMPs) are upregulated by S-HA material (*MMP1,2,3,14,16)*. PCR data demonstrated that S-HA material induces in hASCs upregulation of a specific gene involved in bone mineralization and ossification, such as secreted phosphoprotein 1 (*SPP1*). Versican (VCAN) and Integrin beta 1 (*ITGB1*) expression genes are downregulated in hASC grown on S-HA.

A total of 40 DEGs, including 38 upregulated genes and 2 downregulated genes, are identified in hASC cultures grown on S-MgHA material (**Figure 9B**). Specifically, the DEG modulated from S-MgHA genes encoding for four integrin proteins, named integrin alpha-5, 6 (*ITGA- 5,6*), and Integrin beta 3, beta 5 (*ITGB 3, 5*). ECM proteins, such as nine collagen proteins, as a *COL1A1, COL4A2, COL5A1 COL6A1-A2 COL11A1, COL12A1, COL14A1, COL16A1*, are upregulated on hASCs grown on S-MgHA material. The expression of five MMPs genes are upregulated by S-MgHA material, as a *MMP1, 2, 3, 14, 16*. Data obtained by array technology demonstrate that S-MgHA biomaterial induces in hASCs an upregulation of osteoblast-related gene such as secreted protein acidic and rich in cysteine (SPARC). SPARC codified for osteonectin protein that is one of the most abundant non-collagenous protein expressed in mineralized tissues. Versican (VCAN) gene was downregulated in hASCs grown on S-MgHA.

A total of 17 DEGs, including 11 upregulated genes and 6 downregulated genes, are identified in the hASCs at day 14 grown on S-MgSrHA material (**Figure 9C**). The DEG modulated from S-MgSrHA genes encode four integrins, such as *ITGA-2,3,5,6*, compared to the control (TCPS). The S-MgSrHA material behaves in a manner similar to S-HA, that is, positively modulates

**TABLE 4 |** Crystal data on the HA and TCP phases composing the sintered ceramics.

| Sample | a (Å) (HA) | c (Å) (HA) | Cell vol. (Å$^3$) (HA) | $D_{av}$ (nm) (HA) | %β TCP phase | a (Å) (β TCP) | c (Å) (β TCP) | Cell vol. (Å$^3$) (β TCP) | $D_{av}$ (nm) (β TCP) |
|---|---|---|---|---|---|---|---|---|---|
| S-HA | 9.420 | 6.886 | 529.79 | 444 ± 6 | – | – | – | – | – |
| S-MgHA | 9.428 | 6.883 | 529.84 | 163 ± 2 | 20 | 10.363 | 37.355 | 3474.0 | 149 ± 6 |
| S-MgSrHA | 9.413 | 6.910 | 530.23 | 139 ± 2 | 36 | 10.363 | 37.316 | 3470.3 | 126 ± 3 |
| S-MgZnHA | 9.425 | 6.894 | 530.39 | 225 ± 3 | 9 | 10.385 | 37.315 | 3485.3 | 130 ± 5 |

**TABLE 5 |** pH values of all samples incubated for 24 h at 37°C either in physiologic solution or in Luria Bertani culture medium.

| | pH | |
|---|---|---|
| | **Physiologic solution** | **Luria Bertani broth** |
| S-HA | 7 | 7 |
| S-MgHA | 7 | 7 |
| S-MgSrHA | 9 | 9 |
| S-MgZnHA | 7 | 7 |

the expression of the osteogenic gene SPP1. Downregulated genes in hASCs grown on S-MgSrHA were CD44 molecule (*CD44*), ADAM metallopeptidase with thrombospondin type 1 motif, 1 (*ADAMTS1*), Transforming growth factor, beta-induced (*TGFBI*), contactin-1 (*CNTN1*), *COL16A1*, and *ITGB5*.

A total of 30 DEG, including 27 upregulated genes and 3 downregulated genes, are identified in the hASCs grown on S-MgZnHA material (**Figure 9D**). Specifically, the DEG modulated from S-MgZnHA genes encoding for four integrins, specifically *ITGA- 1,5,6* and Integrin beta 3 (*ITGB 3*), are positively modulated by S-MgZnHA compared to the control TCPS. ECM proteins, such as the five collagen proteins *COL6A1, COL11A1, COL14A1, COL16A1, COL4A2*, are detected upregulated on hASCs grown on S-MgZnHA material. The expression of 5 MMPs genes (*MMP 1,2,3, 14, 16)* are upregulated. Downregulated genes in hASCs grown on S-MgZnHA are the Versican (*VCAN*) Integrin beta 1 (*ITGB1*) and CD44 molecule (*CD44*). All materials upregulate the Fibronectin 1(*FN1*) gene expression and Thrombospondin 3 (*THBS3*).

## Microbiological Analyses

The antimicrobial tests on the sintered materials were performed through the MTT colorimetric assay. The viability of both bacterial strains was investigated on (1) both the planktonic bacterial cultures after their removal from the sintered materials (**Figure 10**); and (2) directly onto the sintered materials after 24 h bacterial incubation (**Figure 11**).

In **Figure 10** viability data of both *E. coli* and *S. aureus* planktonic bacterial cultures after being in direct contact for 24 h and then removed from the sintered materials are reported. The comparison of cell viability between *E. coli* (Aa) and *S. aureus* (Ab) related to TCPs set as 100% showed some differences: S-MgZnHA (25%) results as the most active material in reducing *E. coli* cell viability followed by S-MgSrHA (50%), whereas S-MgHA is less effective (76%) (**Figure 10Aa**). For *S. aureus*, the percentage of cell viability is different: S-MgSrHA (76%) and S-MgHA (78%) show similar values whereas S-MgZnHA (95%) does not show any evident decrease (**Figure 10Ab**). The trend is quite similar if the viability data detected for both bacterial strains and all samples are reported to S-HA samples set as 100% (**Figures 10Bc,d**).

In **Figure 11** is shown the percentage of viability of both bacterial strains adherent to the S-HA and to the ion-doped sintered samples. The adhesion of both bacterial strains, considering TCP set as 100% (**Figure 11A**), is quite reduced on S-MgSrHA samples, in particular showing the best performance with *S. aureus* (10%) (**Figure 11Ab**) in comparison to *E. coli* (∼20%) (**Figure 11Aa**). The results on S-MgSrHA samples for both bacterial strains are better in respect to S-HA; the other two materials (S-MgHA and S-MgZnHA) show a reduced cell adhesion even if it was higher in comparison to S-MgSrHA, although more effective in *S. aureus*. The trend is similar if the percentage of adhesion detected for both bacterial strains and all samples are reported to S-HA set as 100% (**Figures 11Bc,d**).

The adhesion data are further supported by CLSM images shown in **Figure 12**. Both bacterial strains were seeded and then incubated for 24 h on S-HA and the ion-doped sintered samples. After washing and staining, dead cells fluoresce red, while cells fluorescing green are deemed viable (see full method description in the Materials and Methods section). **Figure 12** shows green-fluorescing viable cells in the control (S-HA) for both bacterial strains (**Figures 12Aa,b,Bi,l**). While with both bacterial cells cultured on S-MgSrHA almost widespread cellular death is observed (**Figures 12Ae,f,Bo,p**), a partial reduction of viable cells is detected for both strains when incubated onto S-MgZnHA (**Figures 12Ag,h,Bq,r**). The effect is less evident on S-MgHA (**Figures 12Ac,d,Bm,n**). In addition, on S-MgSrHA samples the dead cells are localized close to the surfaces. Interestingly, the pH value of S-MgSrHA samples (**Table 5**) incubated for 24 h at 37°C either in physiologic solution or in Luria Bertani culture medium was around 9, quite higher if compared to the others samples.

# DISCUSSION

The results obtained in the present work show that when HA powders obtained by wet synthesis process are sintered, the doping of the apatitic crystals with multiple ions is able to induce the formation of HA/βTCP composites with enhanced mechanical and biologic ability. In particular, we found that, besides the formation of βTCP as a secondary phase during the sintering process, the ion doping confines the crystal growth

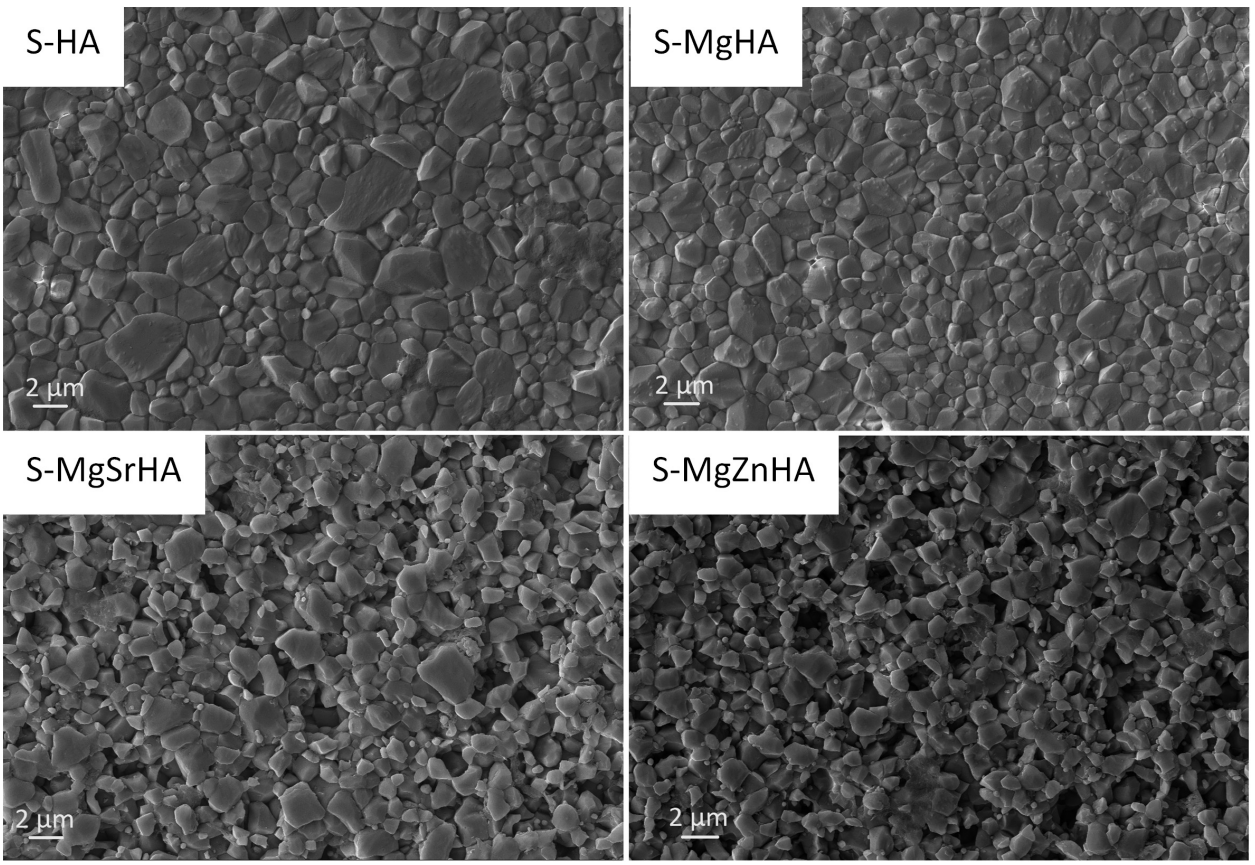


**FIGURE 4 |** SEM images of the sintered bodies subjected to chemical etching.

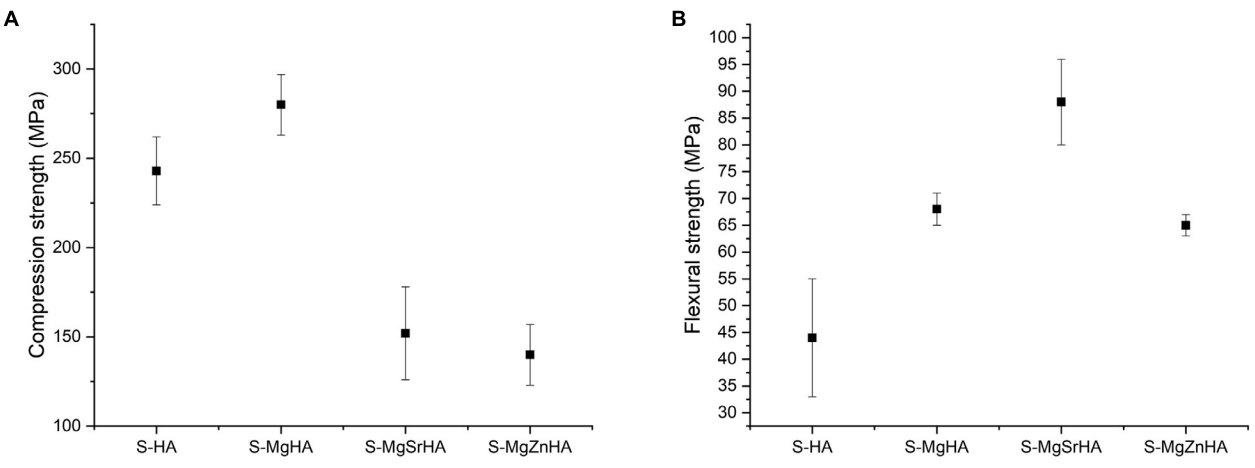


**FIGURE 5 |** Mechanical properties of sintered bodies. **(A)** Compressive strength and **(B)** flexural strength.

and induces microstructural changes in the final ceramics, particularly when the doping is realized with more than one type of ions. Generally, such modifications are found to be effective in enhancing the mechanical properties in the sintered materials, particularly the flexural strength, in comparison with S-HA.

Considering the Mg-doped HA phase, $Mg^{2+}$ ions are unstable in substitutional lattice sites, likely due to its smaller size in comparison with $Ca^{2+}$ ion; therefore, besides a partial substitution in the $Ca^{2+}$ sites, they are supposed to occupy also the disordered hydrated surface layer typical of nanocrystalline

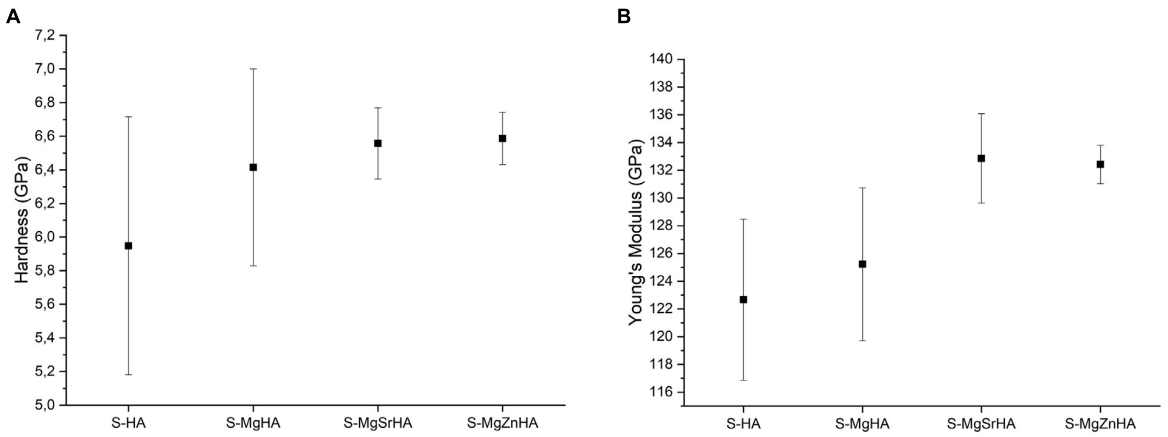


**FIGURE 6 |** Mechanical properties obtained by nanoindentation of sintered bodies. **(A)** Hardness and **(B)** Young's modulus.

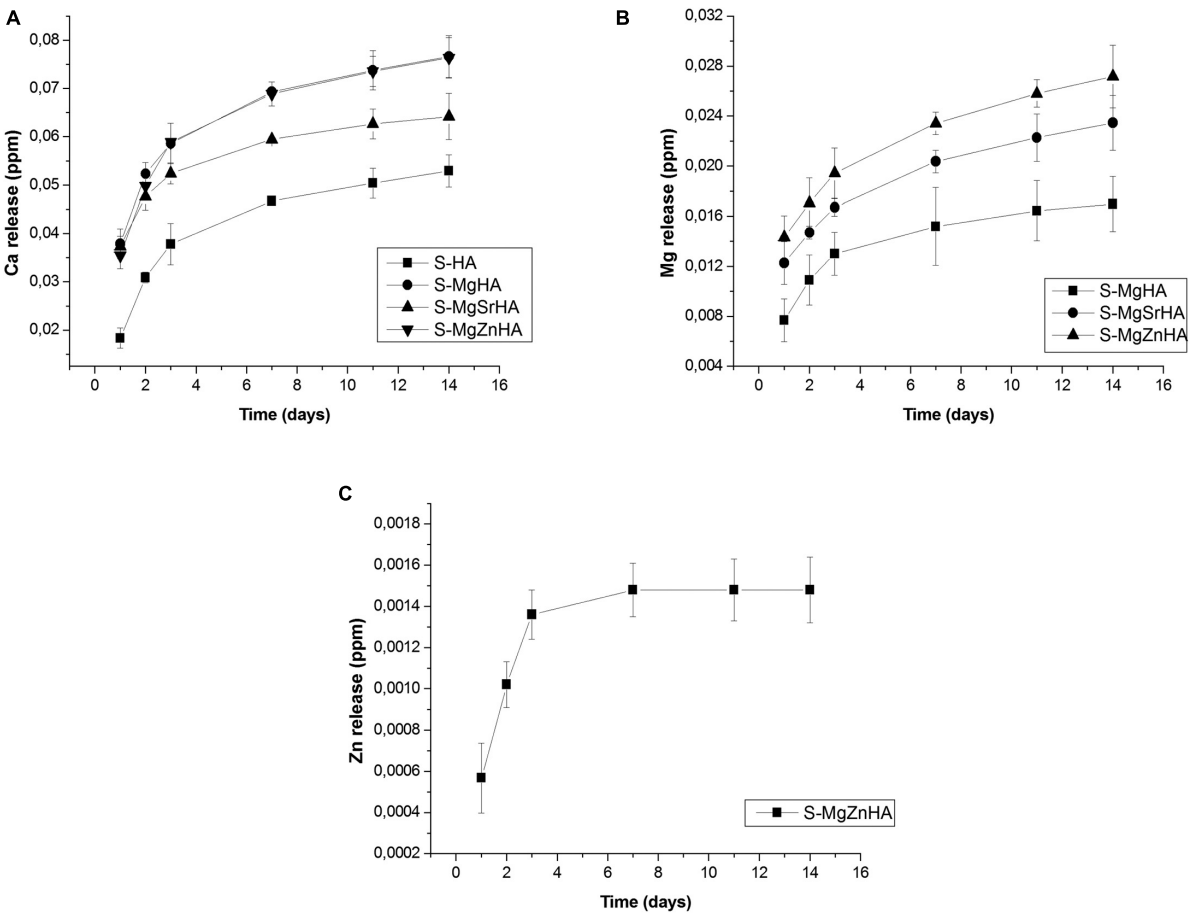


**FIGURE 7 |** Ion release in physiological fluid: absolute values of released ions: **(A)** Ca release; **(B)** Mg release; and **(C)** Zn release.

apatites synthesized at near body temperature (Bertinetti et al., 2009). Thus, during sintering the HA phase tends to crystallize in stable lattice structures, whereas $Mg^{2+}$ ions are segregated at the grain boundaries, inducing the formation of Mg-βTCP phase (whitlockite) (Zima et al., 2011). This phenomenon is associated with a decrease of the grain size, in turn yielding a strong increase of the flexural strength in the S-MgHA material. In the case of multiple ions doping the scenario is more

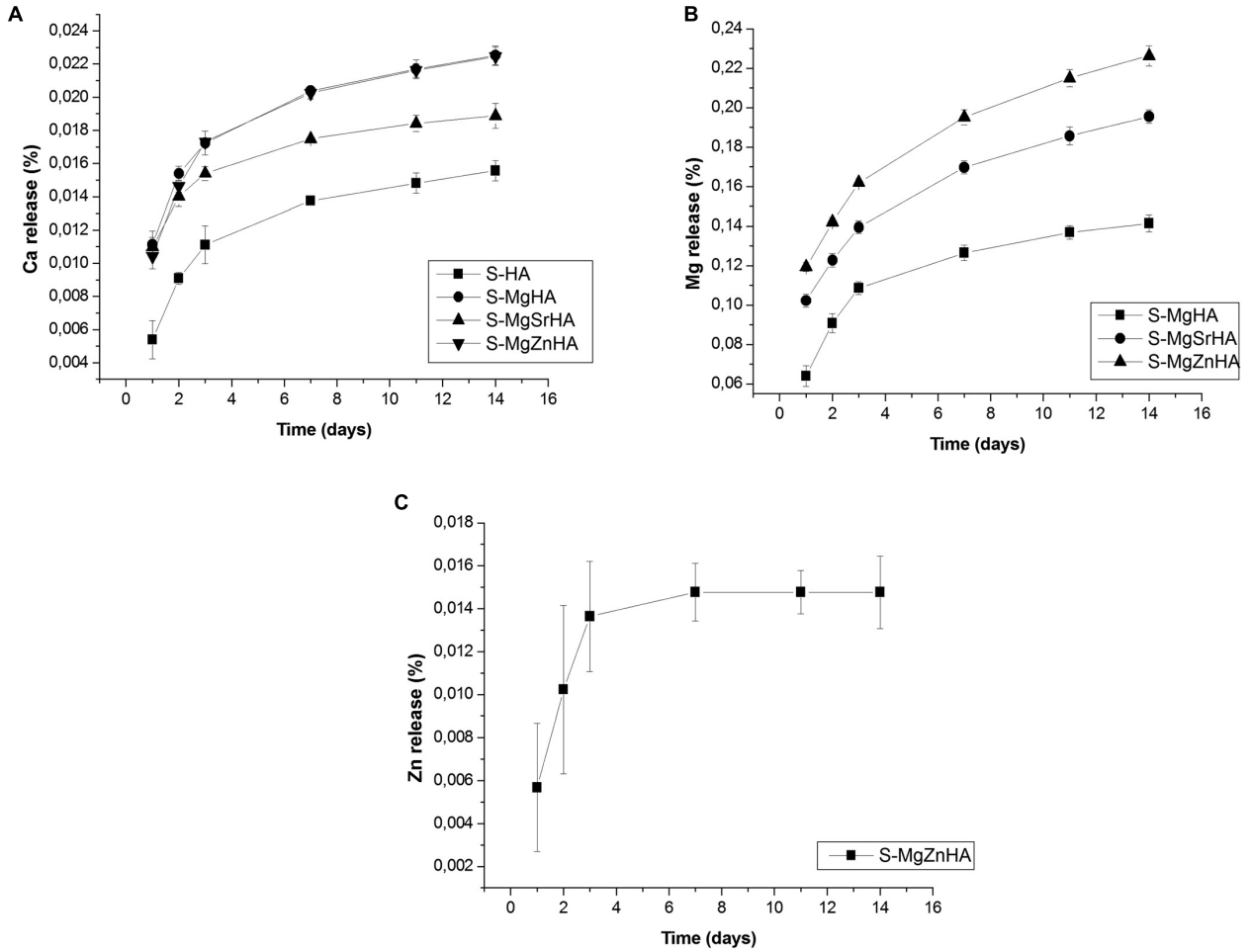


**FIGURE 8 |** Ion release in physiological fluid: percentage values of released ions in respect to those present in the starting material: **(A)** Ca release; **(B)** Mg release; and **(C)** Zn release.

complicated, due to the occurrence of multiple interactions. Contrary to $Mg^{2+}$, both $Sr^{2+}$ and $Zn^{2+}$ have previously shown good ability to substitute $Ca^{2+}$ inside the HA lattice. Particularly, $Sr^{2+}$ can be extensively retained even after sintering, but it is also a promoter of βTCP phase formation (Boanini et al., 2019), as confirmed by our data reporting the formation of 36 wt% of βTCP in the S-MgSrHA material. On the other hand, the co-doping with $Mg^{2+}$ and $Sr^{2+}$ ions results as the most effective to achieve grain size reduction, thus resulting in the highest flexural strength among the studied materials, doubling the values recorded with S-HA. Differently, in the case of S-MgZnHA the co-doping with $Mg^{2+}$ and $Zn^{2+}$ yields limited formation of βTCP phase (9 wt%). βTCP can be partially substituted with $Zn^{2+}$, in agreement with Boanini et al. (2019) reporting a certain solubility of $Zn^{2+}$ in the βTCP phase (max 10%at). As for $Sr^{2+}$, also the doping with $Zn^{2+}$ ions is effective in reducing the grain size of the sintered S-MgZnHA material, and thus greatly increasing the flexural strength, in respect to S-HA. All these results indicate that ion doping can be designed to induce structural disorder in sintered CaPs, that we found to be greatly beneficial for the mechanical performance.

In a different perspective, the changes in the phase composition of the sintered materials, as induced by ion doping, are correlated to enhanced ion exchange ability along 14 days of soaking into a physiological-like medium at body temperature. Particularly, S-MgZnHA shows the highest release of $Ca^{2+}$ and $Mg^{2+}$ ions, but a very low release of $Zn^{2+}$. This confirms recent results obtained with as-synthesized multi-doped (Mg, Zn)-HA powders (Boanini et al., 2019), reporting no Zn release, thus suggesting a high stability of $Zn^{2+}$ ions in the HA lattice. Due to the low extent of Zn release, our results suggest that $Zn^{2+}$ ions retain good stability in the HA lattice even after sintering.

The enhanced physicochemical properties found in ion-doped sintered CaPs can be directly related to the good osteogenic-related gene expression and enhanced resistance to biofilm formation, as shown by the cell tests carried out with hASC and with two different Gram+ and Gram- bacterial strains, frequent in post-surgical infections: *S. aureus* and *E. coli*. In the present study, we found that all the sintered materials

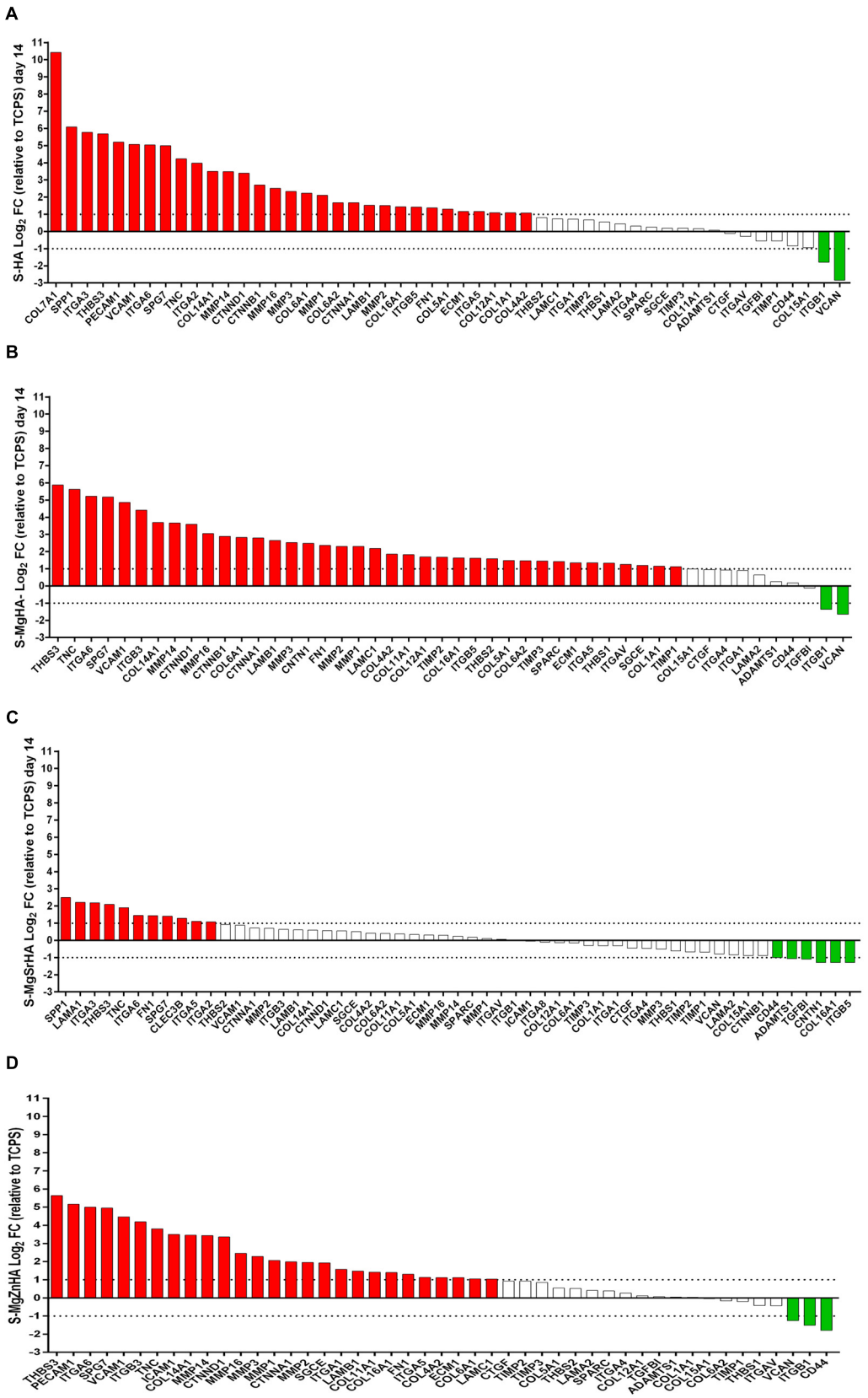


**FIGURE 9 |** Differentially Expressed Genes (DEG) from the sintered apatites. **(A)** S-HA; **(B)** S-MgHA; **(C)** S-MgSrHA; and **(D)** S-MgZnHA.

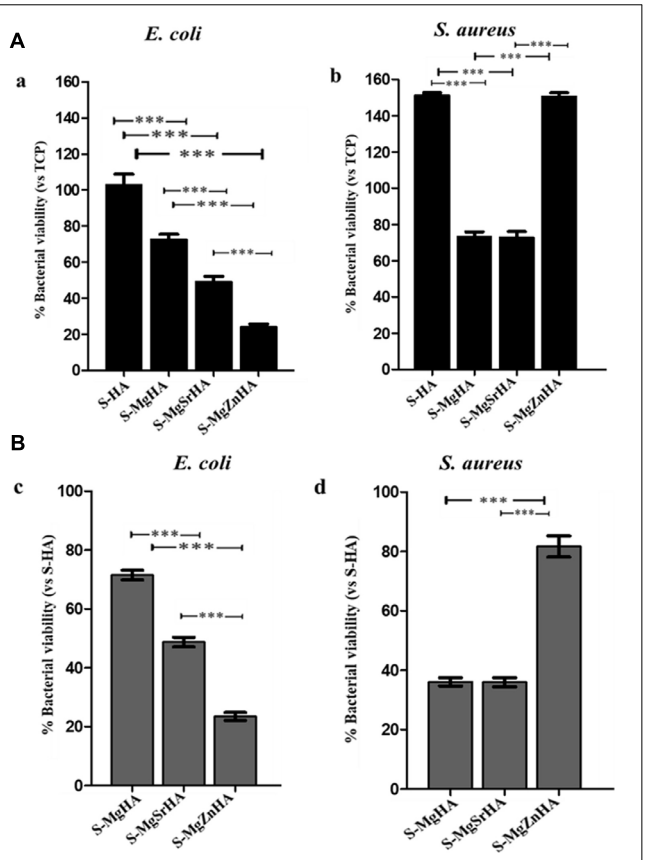


**FIGURE 10 |** Cell viability on planktonic bacterial cultures after their removal from the ions-doped HA samples. After 24 h incubation with S-HA and ion-doped HA samples, both bacterial cultures were removed and cell viability evaluated by MTT test. Panel **(A)** shows the percentage of viability of all samples related to TCP set as 100%. Panel **(B)** reports the viability data of all samples to S-HA (undoped HA) set as 100%. Bars indicate mean values ± SD of the mean of results from three experiments. Statistical significance values were $p < 0.05$ for all samples related to TCP and S-HA, except for *E. coli* on S-HA **(A,a)** (data not shown); the statistical significance between each sample is also indicated as: ***$p < 0.001$.

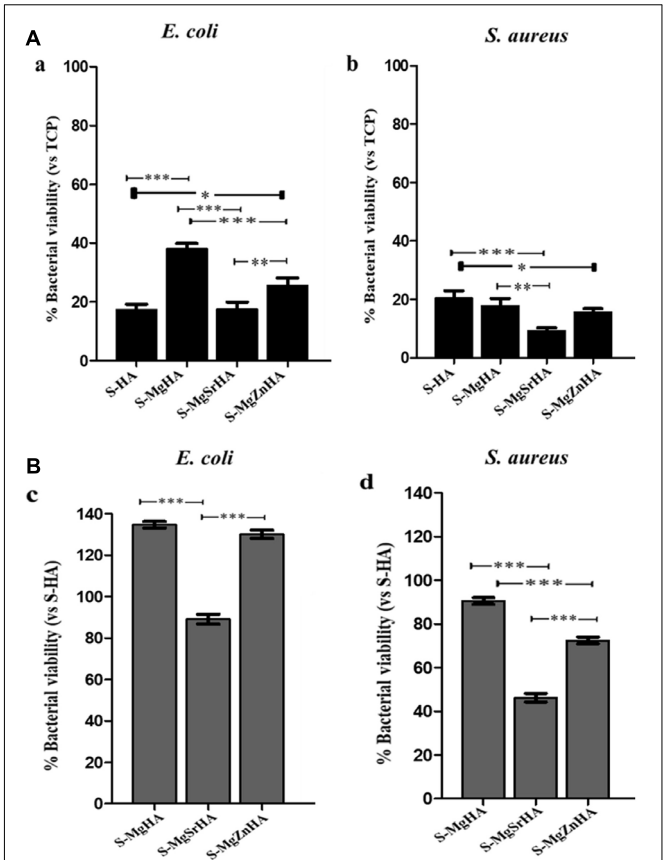


**FIGURE 11 |** Percentage of bacterial adhesion onto S-HA and ions-doped HA. After 24-h incubation and removal of the planktonic cultures, the viability of both bacterial strains adherent to the apatite samples were evaluated by the MTT test. Panel **(A)** shows the percentage of viability of all samples related to TCP set as 100%; Panel **(B)** reports the viability data of all samples to S-HA (undoped HA) set as 100%. Bars indicate mean values ± SD of the mean of results from three experiments. Statistical significance values were $p < 0.05$ for all samples related to TCP and S-HA (data not shown); the statistical significance between each sample is also indicated as: *$p < 0.05$, **$p < 0.01$ and ***$p < 0.001$.

here studied show upmodulation of genes encoding ECM, various adhesion molecules (integrins) and, also, of the gene *Thbs3*, this latter codifying the Thrombospondin 3 protein, a polypeptide structurally similar to the cartilage oligomeric matrix protein (COMP/TSP5), that mediate cell-to-cell and cell-to-matrix interactions. This finding reports good ability of the sintered CaPs to promote cell adhesion and proliferation, as well as favoring new bone tissue formation and osteointegration (Dalby et al., 2014; Docheva et al., 2014). The genes encoding for collagen proteins and MMP, relevant for the regulation of bone tissue maturation and sensitive to nanoscale surface features (Hankenson et al., 2005; von der Mark et al., 2010; Paiva and Granjeiro, 2017), are as well upregulated by all the studied material, with the exception of S-MgSrHA samples. Previous works reported that Sr-doped HA nanoparticles, microcapsules, bioglasses, and bone cements were effective in enhancing collagen type I expression and formation (Capuccini et al., 2009; Huang et al., 2016; Khan et al., 2016; Henriques Lourenço et al., 2017; Montesi et al., 2017), whereas no studies reported on the effect of strontium on MMP expression. However, these previous results were obtained with nanostructured and nanocrystalline materials, synthesized at near body temperature and characterized by high surface activity and greater ability of releasing $Ca^{2+}$, $PO_4{}^{3-}$, and $Sr^{2+}$ ions, in comparison with sintered ceramics. In our case, S-MgSrHA did not release any $Sr^{2+}$ ions along 14 days, thus suggesting high stabilization of this ion in the structure of both HA and βTCP phases that could have affected the expression of collagen-related genes at day 14. To be noted that this study does not consider gene expression in shorter (or longer) follow-up times; therefore, we are unable to say whether collagen-related genes may be upregulated by S-MgSrHA at different times. However, S-MgSrHA shows overexpression of osteogenic genes such

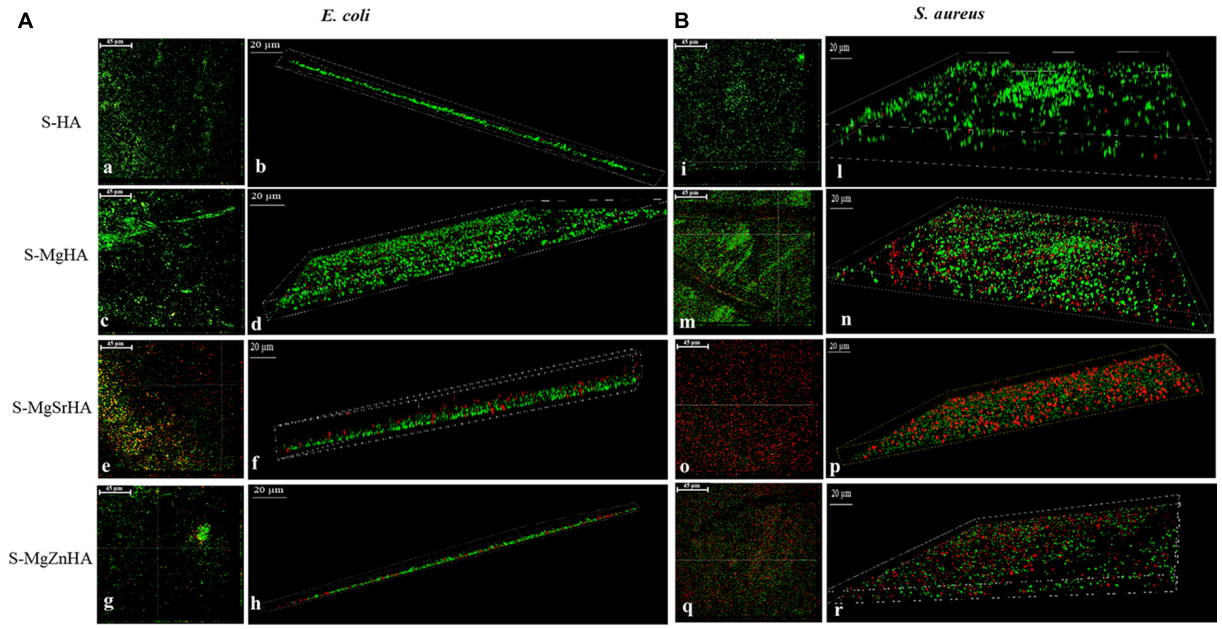


**FIGURE 12 |** CLSM images of *E. coli* **(A,a–h)** and *S. aureus* **(B,i–r)** adhesion onto apatite samples. The bacterial adhesions of both strains were performed and stained as reported in the materials and methods section. Panels **(A,a,b)**, and **(B,i,l)** represent the adhesion to S-HA samples for *E. coli* and *S. aureus,* respectively. Panels **(A,c–h)** and **(B,m–r)** refer to the adhesion to ion-doped HA samples for *E. coli* and *S. aureus,* respectively. Orthogonal projections at 40× magnification for *E. coli* **(A,a,c,e,g)** and for *S. aureus* **(B,i,m,o,q)**: scale bar = 45 µm; 3D projections at 63× magnification for *E. coli* **(A,b,d,f,h)** and for *S. aureus* **(B,l,n,p,r)**: scale bar = 20 µm.

as osteopontin (SPP1) and osteonectin (SPARC). These non-collagenous macromolecules are able to stimulate the hASCs to differentiate into the osteoblast cell lineage and are the structural basis for the formation of the bone-implant interface *in vivo*, which is a key aspect to achieve substantial osteointegration (Shah et al., 2019).

Concerning the antimicrobial ability, our results clearly show that the sintered materials presenting higher solubility, that is, S-MgSrHA and S-MgZnHA, are also the most effective in contrasting the viability of microbial strains. In this respect, an important parameter to consider regarding bacterial proliferation (Andrés et al., 2018) and adhesion (Sheng et al., 2008) is the pH. Our findings regarding the alkaline pH of S-MgSrHA and the neutral one of the other samples, are in accordance to literature because previous studies reported the increase of pH of bacterial culture medium as induced by materials containing $Sr^{2+}$, which contribute to antibacterial effect (Douglas et al., 2018). A recent study reported that $Sr^{2+}$ is released from surfaces when in contact with fluids. Once released it is an activator of the osteoblasts because it activates calcium receptors: it can positively contribute to reduce the risk of bacterial colonization by promoting an early adhesion of the osteoblasts and can also counteract the cytotoxic effect of other ions such as Ag (Cochis et al., 2020) or Mg (Gao et al., 2019), whether the Sr is a co-dopant element. For this excellent property of promoting bone growth, thus inhibiting osteoclasts activity, it can be involved in the treatment of osteoporosis (Frasnelli et al., 2017).

Previous studies pointed out that specific ion doping in the structure of nanocrystalline HA enhances the anti-infective character, thanks to the activation of mechanisms increasing the surface charge and ion mobility (Sprio et al., 2019). It was also observed that low crystallinity is particularly desired to obtain effective anti-proliferative ability, particularly against Gram + bacteria (Wu et al., 2018). The present work shows that these physicochemical effects and related biofunctionalities are found also in our sintered CaPs, in spite the high-temperature treatment caused the loss of nanocrystallinity with grain growth from the nano- to the micron size. Indeed, the presence of doping ions in HA powders yielded, after sintering, the formation of a secondary, bioresorbable, βTCP phase with increased solubility that can be tailored by the type and extent of initial ion doping. Since no release of $Sr^{2+}$ was observed, we can conclude that in our tests $Sr^{2+}$ ions did not come in direct contact with bacteria, so they are supposed to elicit no direct effects on the biologic properties of S-MgSrHA, but rather they were relevant to induce finer microstructure and more intense $Ca^{2+}$ and $Mg^{2+}$ ions release, a phenomenon recently found as a trigger of antibacterial ability (Sprio et al., 2019). Regarding S-MgZnHA, also in this material the co-doping with $Mg^{2+}$ and $Zn^{2+}$ caused a strong grain size reduction that favored the most intense release of $Ca^{2+}$ and $Mg^{2+}$ ions. Since the detected Zn release is very little and limited in time, we can suppose that, even in very small amounts, the release of $Zn^{2+}$, previously reputed as a specific antibacterial agent (Thian et al., 2013), played a role in reducing bacterial viability, particularly effective with *E. coli*. The different effect

in *S. aureus* and *E. coli* is due to the nature of the cell wall of Gram positive and negative bacteria, and these results are in accordance with literature. Gram positive have a thick cell wall, because of the presence of 20–25 layers of peptidoglycan, whereas Gram negative have up to three layers, which are between two membranes (the outer and the inner) (Elander, 2003). Hence, *S. aureus* has a negatively charged cell wall, due to lipoteichoic and teichuronic acids (Bari et al., 2017), which attract positively charges present in HA. By contrast, *E. coli* expose a highly organized compact structure, which is permeable to charged, uncharged, and small molecules. The consequence of these interactions is cell apoptosis *via* protein denaturation and cell membrane disruption (Bari et al., 2017). Indeed, our antibacterial data showed how these scaffolds are more effective against *E. coli* than *S. aureus* because Gram negative are more penetrable for their thin peptidoglycan. In this respect, it is worthy to note that, in comparison with the single-doped S-MgHA, the multi-doped S-MgSrHA and S-MgZnHA materials were found to greatly reduce the viability of Gram negative bacterium.

Resuming, our results report that physicochemical aspects such as ion release ability and microstructure of sintered calcium phosphates are biologically relevant factors and can be tailored by specific ion doping. In particular, we found that, in comparison with the single-doped S-MgHA, the bioactive effects are strengthened by synergistic contribution given by the co-doping with $Sr^{2+}$ and $Zn^{2+}$ ions. Since HA and β-tricalcium phosphate phases can host a very high number of ionic species into their lattice, with consequent alteration of physicochemical properties, the present work suggests that the exploration of different doping agents for CaP phases can yield new sintered materials with optimized biologic performance.

The integrability of osteosynthesis media with the surrounding bone is a primary target in order to ensure stabilization of fractures or of bone implants. Contrary to bioinert ceramic materials unable to establish tight bonding with bone, the good osteogenic and antibacterial ability shown by the sintered CaPs can help to provide strong and more stable biointerfaces, thus lowering the risk of failure. On the other hand, the alteration of the microstructure induced by multiple ion substitutions can help to improve the mechanical properties, thanks to residual stresses induced by ion doping that can reinforce the flexural strength of ceramics—while retaining compressive strength in the range of cortical bone—and be also beneficial for improving the fatigue life (Hearn, 2013; Bao et al., 2019).

## CONCLUSION

HA powders doped with $Mg^{2+}$, $Sr^{2+}$, and $Zn^{2+}$ ions were synthesized and sintered to obtain consolidated bulk materials. We found that ion doping in the HA structure can specifically affect the phase composition and microstructure of HA/βTCP composites, formed during the sintering process. This phenomenon enhances flexural strength and resistance to biofilm formation, in respect to the undoped sintered HA, while retaining upmodulation of various genes involving in osteogenesis. Thanks to the good solubility of many different ionic species in the crystal of bioactive calcium phosphates, the present results suggest that ion doping in sintered calcium phosphates can be designed to obtain tailored composition, microstructure, optimized mechanical properties, and ion release profile, capable to express good osteogenic ability and to achieve optimized eukaryotic vs. prokaryotic cell selectivity. These are biofunctionalities that, co-existing in the same device, are key aspects in favoring osteointegration and enhanced resistance against infections, and they are among the most critical threads in bone surgery. Hence, the obtained results open to the possibility of developing new biodevices, such as plates or screws and other osteosynthesis media with enhanced performance, are suitable for more effective and safer therapies in support of bone surgery procedures.

## DATA AVAILABILITY STATEMENT

The raw data supporting the conclusions of this article will be made available by the authors, without undue reservation.

## AUTHOR CONTRIBUTIONS

MD, LP, EM, and ER were responsible for the conduction of experiments and data acquisition. SS, FM, and MI were responsible for data interpretation. SS, MT, NP, LV, and AT were responsible for conceptualization, design, and supervision of the study. SS, MD, EM, and LV were responsible for manuscript writing and editing. NP, LV, and AT were responsible for funding acquisition. All authors have read and approved the final manuscript.

## FUNDING

The experiments carried out at the University of Ferrara were supported by grants from FESR POR Regione Emilia Romagna Niprogen project, local unit MT and MIUR PRIN 2017 C8RYSS project, national unit FM, respectively. The study was supported by a grant of the Italian Ministry of Education, University and Research (MIUR) to the Department of Molecular Medicine of the University of Pavia under the initiative "Dipartimenti di Eccellenza (2018–2022)." NP is supported by the European Commission under the FET Proactive ("Neurofibres") grant No. 732344, as well as by the Italian Ministry of Education, University and Research (MIUR) under the ARS01-01384-PROSCAN and the PRIN-20177TTP3S grants.

## ACKNOWLEDGMENTS

The authors are grateful to Prof. R. Migliavacca (Department of Clinical-Surgical Diagnostic and Pediatric Sciences, Unit of Microbiology and Clinical Microbiology, University of Pavia, Italy), for providing *E. coli* and *S. aureus* bacteria.

## REFERENCES


Albers, C. E., Hofstetter, W., Siebenrock, K. A., Landmann, R., and Klenke, F. M. (2013). In vitro cytotoxicity of silver nanoparticles on osteoblasts and osteoclasts at antibacterial concentrations. *Nanotoxicology* 7, 30–36. doi: 10.3109/17435390.2011.626538

Alexander, R., and Theodos, L. (1993). Fracture of the bone-grafted mandible secondary to stress shielding: report of a case and review of the literature. *J. Oral Maxillofac. Surg.* 51, 695–697. doi: 10.1016/s0278-2391(10)80273-3

Andrés, N. C., Sieben, J. M., Baldini, M., Rodríguez, C. H., Famiglietti, A., and Messina, P. V. (2018). Electroactive Mg(2+)-hydroxyapatite nanostructured networks against drug-resistant bone infection strains. *ACS Appl. Mater Interf.* 10, 19534–19544. doi: 10.1021/acsami.8b06055

Ballardini, A., Montesi, M., Panseri, S., Vandini, A., Balboni, P. G., Tampieri, A., et al. (2018). New hydroxyapatite nanophases with enhanced osteogenic and anti-bacterial activity. *J. Biomed. Mater. Res. A* 106, 521–530. doi: 10.1002/jbm.a.36249

Bao, Y., Kuang, F., Sun, Y., Li, Y., Wan, D., Shen, Z., et al. (2019). A simple way to make pre-stressed ceramics with high strength. *J. Mater.* 5, 657–662. doi: 10.1016/j.jmat.2019.06.001

Bari, A., Bloise, N., Fiorilli, S., Novajra, G., Vallet-Regi, M., Bruni, G., et al. (2017). Copper-containing mesoporous bioactive glass nanoparticles as multifunctional agent for bone regeneration. *Acta Biomater.* 55, 493–504. doi: 10.1016/j.actbio.2017.04.012

Bertinetti, L., Drouet, C., Combes, C., Rey, C., Tampieri, A., Coluccia, S., et al. (2009). Surface Characteristics of *Nanocrystalline apatites*: effect of Mg surface enrichment on morphology, surface hydration species, and cationic environments. *Langmuir* 25, 5647–5654. doi: 10.1021/la804230j

Bigi, A., Foresti, E., Gandolfi, M., Gazzano, M., and Roveri, N. (1997). Isomorphous substitutions in β-tricalcium phosphate: the different effects of zinc and strontium. *J. Inorgan. Biochem.* 66, 259–265. doi: 10.1016/s0162-0134(96)00219-x

Bigi, A., Foresti, E., Gregorini, R., Ripamonti, A., Roveri, N., and Shah, J. S. (1992). The role of magnesium on the structure of biological apatites. *Calcif. Tissue Intern.* 50, 439–444. doi: 10.1007/bf00296775

Boanini, E., Gazzano, M., and Bigi, A. (2010). Ionic substitutions in calcium phosphates synthesized at low temperature. *Acta Biomater.* 6, 1882–1894. doi: 10.1016/j.actbio.2009.12.041

Boanini, E., Gazzano, M., Nervi, C., Chierotti, M. R., Rubini, K., Gobetto, R., et al. (2019). Strontium and zinc substitution in beta-tricalcium phosphate: an X-ray diffraction, solid state NMR and ATR-FTIR study. *J. Funct. Biomater.* 10:20. doi: 10.3390/jfb10020020

Capuccini, C., Torricelli, P., Boanini, E., Gazzano, M., Giardino, R., and Bigi, A. (2009). Interaction of Sr-doped hydroxyapatite nanocrystals with osteoclast and osteoblast-like cells. *J. Biomed. Mater. Res. A* 89, 594–600. doi: 10.1002/jbm.a.31975

Cazalbou, S., Eichert, D., Ranz, X., Drouet, C., Combes, C., Harmand, M. F., et al. (2005). Ion exchanges in apatites for biomedical application. *J. Mater. Sci. Mater. Med.* 16, 405–409. doi: 10.1007/s10856-005-6979-2

Cochis, A., Barberi, J., Ferraris, S., Miola, M., Rimondini, L., Vernè, E., et al. (2020). Competitive surface colonization of antibacterial and bioactive materials doped with strontium and/or silver ions. *Nanomaterials* 10:120. doi: 10.3390/nano10010120

Dalby, M. J., Gadegaard, N., and Oreffo, R. O. (2014). Harnessing nanotopography and integrin-matrix interactions to influence stem cell fate. *Nat. Mater.* 13, 558–569. doi: 10.1038/nmat3980

Docheva, D., Popov, C., Alberton, P., and Aszodi, A. (2014). Integrin signaling in skeletal development and function. *Birth Def. Res. C Embryo Today* 102, 13–36. doi: 10.1002/bdrc.21059

Douglas, T. E. L., Dziadek, M., Gorodzha, S., Lišková, J., Brackman, G., Vanhoorne, V., et al. (2018). Novel injectable gellan gum hydrogel composites incorporating Zn- and Sr-enriched bioactive glass microparticles: high-resolution X-ray microcomputed tomography, antibacterial and in vitro testing. *J. Tissue Eng. Regen. Med.* 12, 1313–1326. doi: 10.1002/term.2654

Dutta, S. R., Passi, D., Singh, P., and Bhuibhar, A. (2015). Ceramic and non-ceramic hydroxyapatite as a bone graft material: a brief review. *Iran. J. Med. Sci.* 184, 101–106. doi: 10.1007/s11845-014-1199-8

Elander, R. P. (2003). "Industrial microbiology: an introduction," in *The Quarterly Review of Biology*, eds M. J. Waites, N. L. Morgan, J. S. Rockey, and G. Higton (Chicago, IL: University of Chicago Press), 96.

Eliaz, N., and Metoki, N. (2017). Calcium phosphate bioceramics: a review of their history, structure, properties, coating technologies and biomedical applications. *Materials* 10:334. doi: 10.3390/ma10040334

Frasnelli, M., Cristofaro, F., Sglavo, V. M., Dirè, S., Callone, E., Ceccato, R., et al. (2017). Synthesis and characterization of strontium-substituted hydroxyapatite nanoparticles for bone regeneration. *Mater. Sci. Eng. C* 71, 653–662. doi: 10.1016/j.msec.2016.10.047

Gao, Z., Song, M., Liu, R.-L., Shen, Y., Ward, L., Cole, I., et al. (2019). Improving in vitro and in vivo antibacterial functionality of Mg alloys through micro-alloying with Sr and Ga. *Mater. Sci. Eng. C* 104:109926. doi: 10.1016/j.msec.2019.109926

Giannini, C., Ladisa, M., Altamura, D., Siliqi, D., Sibillano, T., and De Caro, L. (2016). X-ray diffraction: a powerful technique for the multiple-length-scale structural analysis of nanomaterials. *Crystals* 6:87. doi: 10.3390/cryst6080087

Goodrich, J., Sandler, A., and Tepper, O. (2012). A review of reconstructive materials for use in craniofacial surgery bone fixation materials, bone substitutes, and distractors. *Child's Nerv. Syst.* 28, 1577–1588. doi: 10.1007/s00381-012-1776-y

Griffith, A. A. (1921). VI. The phenomena of rupture and flow in solids. *Philos. Trans. R. Soc. Lond. A* 221, 163–198. doi: 10.1098/rsta.1921.0006

Hankenson, K. D., Hormuzdi, S. G., Meganck, J. A., and Bornstein, P. (2005). Mice with a disruption of the thrombospondin 3 gene differ in geometric and biomechanical properties of bone and have accelerated development of the femoral head. *Mol. Cell Biol.* 25, 5599–5606. doi: 10.1128/mcb.25.13.5599-5606.2005

Hearn, E. J. (2013). *Mechanics of Materials: An Introduction to the Mechanics of Elastic and Plastic Deformation of Solids and Structural Components*. Amsterdam: Elsevier.

Henriques Lourenço, A., Neves, N., Ribeiro-Machado, C., Sousa, S. R., Lamghari, M., Barrias, C. C., et al. (2017). Injectable hybrid system for strontium local delivery promotes bone regeneration in a rat critical-sized defect model. *Sci. Rep.* 7:5098.

Hofer, U. (2019). The cost of antimicrobial resistance. *Nat. Rev. Microbiol.* 17:3.

Huang, M., Li, T., Pan, T., Zhao, N., Yao, Y., Zhai, Z., et al. (2016). Controlling the strontium-doping in calcium phosphate microcapsules through yeast-regulated biomimetic mineralization. *Regen. Biomater.* 3, 269–276. doi: 10.1093/rb/rbw025

Kannan, S., Pina, S., and Ferreira, J. M. F. (2006). Formation of strontium-stabilized β-tricalcium phosphate from calcium-deficient apatite. *Science* 89, 3277–3280. doi: 10.1111/j.1551-2916.2006.01203.x

Keaveny, T. M., and Hayes, W. C. (1993). "Mechanical properties of cortical and trabecular bone," in *Bone*, ed. B. K. Hall (Boca Raton, FL: CRC Press), 285–344.

Khan, P. K., Mahato, A., Kundu, B., Nandi, S. K., Mukherjee, P., Datta, S., et al. (2016). Influence of single and binary doping of strontium and lithium on in vivo biological properties of bioactive glass scaffolds. *Sci. Rep.* 6:32964.

Li, B., and Webster, T. J. (2018). Bacteria antibiotic resistance: new challenges and opportunities for implant-associated orthopedic infections. *J. Orthop. Res.* 36, 22–32.

Liu, W., Huan, Z., Xing, M., Tian, T., Xia, W., Wu, C., et al. (2019). Strontium-substituted dicalcium silicate bone cements with enhanced osteogenesis potential for orthopaedic applications. *Materials* 12:2276. doi: 10.3390/ma12142276

Manfrini, M., Di Bona, C., Canella, A., Lucarelli, E., Pellati, A., D'agostino, A., et al. (2013). Mesenchymal stem cells from patients to assay bone graft substitutes. *J. Cell Physiol.* 228, 1229–1237. doi: 10.1002/jcp.24276

Mazzoni, E., D'agostino, A., Iaquinta, M. R., Bononi, I., Trevisiol, L., Rotondo, J. C., et al. (2020). Hydroxylapatite-collagen hybrid scaffold induces human adipose-derived mesenchymal stem cells to osteogenic differentiation in vitro and bone regrowth in patients. *Stem Cells Transl. Med.* 9, 377–388. doi: 10.1002/sctm.19-0170

Mazzoni, E., D'agostino, A., Manfrini, M., Maniero, S., Puozzo, A., Bassi, E., et al. (2017). Human adipose stem cells induced to osteogenic differentiation by an innovative collagen/hydroxylapatite hybrid scaffold. *FASEB J.* 31, 4555–4565. doi: 10.1096/fj.201601384r

Mazzoni, E., Rigolin, G. M., Alaribe, F. N., Pancaldi, C., Maniero, S., Comar, M., et al. (2012). Simian virus 40 efficiently infects human T lymphocytes and extends their lifespan. *Exp. Hematol.* 40, 466–476. doi: 10.1016/j.exphem.2012.02.008

Montesi, M., Panseri, S., Dapporto, M., Tampieri, A., and Sprio, S. (2017). Sr-substituted bone cements direct mesenchymal stem cells, osteoblasts and osteoclasts fate. *PLoS One* 12:e0172100. doi: 10.1371/journal.pone.0172100

Munch, E., Franco, J., Deville, S., Hunger, P., Saiz, E., and Tomsia, A. P. (2008). Porous ceramic scaffolds with complex architectures. *JOM* 60, 54–58. doi: 10.1007/s11837-008-0072-5

Paiva, K. B. S., and Granjeiro, J. M. (2017). Matrix metalloproteinases in bone resorption. *Remodel. Repair. Prog. Mol. Biol. Transl. Sci.* 148, 203–303. doi: 10.1016/bs.pmbts.2017.05.001

Pallavicini, P., Arciola, C. R., Bertoglio, F., Curtosi, S., Dacarro, G., D'agostino, A., et al. (2017). Silver nanoparticles synthesized and coated with pectin: an ideal compromise for anti-bacterial and anti-biofilm action combined with wound-healing properties. *J. Coll. Interf. Sci.* 498, 271–281. doi: 10.1016/j.jcis.2017.03.062

Pohler, O. E. M. (2002). "Failures of metallic orthopedic implants[1]," in *Failure Analysis and Prevention*, eds W. T. Becker and R. J. Shipley (Cleveland, OH: ASM International).

Polo-Corrales, L., Latorre-Esteves, M., and Ramirez-Vick, J. E. (2014). Scaffold design for bone regeneration. *J. Nanosci. Nanotechnol.* 14, 15–56.

Procopio, A., Malucelli, E., Pacureanu, A., Cappadone, C., Farruggia, G., Sargenti, A., et al. (2019). Chemical fingerprint of Zn-hydroxyapatite in the early stages of osteogenic differentiation. *ACS Cent. Sci.* 5, 1449–1460. doi: 10.1021/acscentsci.9b00509

Ribeiro, M., Monteiro, F. J., and Ferraz, M. P. (2012). Infection of orthopedic implants with emphasis on bacterial adhesion process and techniques used in studying bacterial-material interactions. *Biomatter* 2, 176–194. doi: 10.4161/biom.22905

Rodríguez-Lorenzo, L. M., Hart, J. N., and Gross, K. A. (2003). Structural and Chemical Analysis of Well-Crystallized Hydroxyfluorapatites. *J. Phys. Chem. B* 107, 8316–8320. doi: 10.1021/jp027556o

Sasaki, S., Fujino, K., Tak, E., and Uchi, Y. (1979). X-Ray determination of electron-density distributions in oxides, MgO, MnO, CoO, and NiO, and atomic scattering factors of their constituent atoms. *Proc. Jpn. Acad. Ser. B* 55, 43–48. doi: 10.2183/pjab.55.43

Schroeder, L. W., Dickens, B., and Brown, W. E. (1977). Crystallographic studies of the role of Mg as a stabilizing impurity in β-Ca3(PO4)2. II. refinement of Mg-containing β-Ca3(PO4)2. *J. Solid State Chem.* 22, 253–262. doi: 10.1016/0022-4596(77)90002-0

Shah, F. A., Thomsen, P., and Palmquist, A. (2019). Osseointegration and current interpretations of the bone-implant interface. *Acta Biomater.* 84, 1–15. doi: 10.1016/j.actbio.2018.11.018

Sheikh, Z., Najeeb, S., Khurshid, Z., Verma, V., Rashid, H., and Glogauer, M. (2015). Biodegradable materials for bone repair and tissue engineering applications. *Materials* 8, 5744–5794. doi: 10.3390/ma8095273

Sheng, X., Ting, Y. P., and Pehkonen, S. O. (2008). The influence of ionic strength, nutrients and pH on bacterial adhesion to metals. *J. Colloid Interf. Sci.* 321, 256–264. doi: 10.1016/j.jcis.2008.02.038

Slavin, Y. N., Asnis, J., Hafeli, U. O., and Bach, H. (2017). Metal nanoparticles: understanding the mechanisms behind antibacterial activity. *J. Nanobiotechnol.* 15:65.

Sprio, S., Preti, L., Montesi, M., Panseri, S., Adamiano, A., Vandini, A., et al. (2019). Surface phenomena enhancing the antibacterial and osteogenic ability of nanocrystalline hydroxyapatite, activated by multiple-ion doping. *ACS Biomater. Sci. Eng.* 5, 5947–5959. doi: 10.1021/acsbiomaterials.9b00893

Sprio, S., Tampieri, A., Landi, E., Sandri, M., Martorana, S., Celotti, G., et al. (2008). Physico-chemical properties and solubility behaviour of multi-substituted hydroxyapatite powders containing silicon. *Mater. Sci. Eng. C* 28, 179–187. doi: 10.1016/j.msec.2006.11.009

Suryavanshi, A., Borse, V., Pawar, V., Kotagudda Ranganath, S., and Srivastava, R. (2016). Material advancements in bone-soft tissue fixation devices. *Sci. Adv. Today* 2, 25236.

Tampieri, A., Celotti, G. C., Landi, E., and Sandri, M. (2004). Magnesium doped hydroxyapatite: synthesis and characterization. *Key Eng. Mater.* 264–268, 2051–2054. doi: 10.4028/www.scientific.net/kem.264-268.2051

Thian, E. S., Konishi, T., Kawanobe, Y., Lim, P. N., Choong, C., Ho, B., et al. (2013). Zinc-substituted hydroxyapatite: a biomaterial with enhanced bioactivity and antibacterial properties. *J. Mater. Sci. Mater. Med.* 24, 437–445. doi: 10.1007/s10856-012-4817-x

von der Mark, K., Park, J., Bauer, S., and Schmuki, P. (2010). Nanoscale engineering of biomimetic surfaces: cues from the extracellular matrix. *Cell Tissue Res.* 339, 131–153. doi: 10.1007/s00441-009-0896-5

Wu, C., Ramaswamy, Y., Kwik, D., and Zreiqat, H. (2007). The effect of strontium incorporation into CaSiO3 ceramics on their physical and biological properties. *Biomaterials* 28, 3171–3181. doi: 10.1016/j.biomaterials.2007.04.002

Wu, V. M., Tang, S., and Uskokovic, V. (2018). Calcium phosphate nanoparticles as intrinsic inorganic antimicrobials: the antibacterial effect. *ACS Appl. Mater. Interf.* 10, 34013–34028. doi: 10.1021/acsami.8b12784

Yashima, M., Sakai, A., Kamiyama, T., and Hoshikawa, A. (2003). Crystal structure analysis of β-tricalcium phosphate Ca3(PO4)2 by neutron powder diffraction. *J. Solid State Chem.* 175, 272–277. doi: 10.1016/s0022-4596(03)00279-2

Zima, A., Ślósarczyk, A., Paszkiewicz, Z., Staszewska, M., Mróz, W., and Chróścicka, A. (2011). Effects of Mg additives on properties of Mg-doped hydroxyapatite ceramics. *Adv. Sci. Technol.* 76, 60–65. doi: 10.4028/www.scientific.net/ast.76.60

Zreiqat, H., Ramaswamy, Y., Wu, C., Paschalidis, A., Lu, Z., James, B., et al. (2010). The incorporation of strontium and zinc into a calcium-silicon ceramic for bone tissue engineering. *Biomaterials* 31, 3175–3184. doi: 10.1016/j.biomaterials.2010.01.024

**Conflict of Interest:** The authors declare that the research was conducted in the absence of any commercial or financial relationships that could be construed as a potential conflict of interest.

frontiers in Materials

REVIEW
published: 28 August 2020
doi: 10.3389/fmats.2020.00274

# The Mechanisms Underlying the Biological Response to Wear Debris in Periprosthetic Inflammation

*Marina Couto[1,2†], Daniela P. Vasconcelos[1,2†], Daniela M. Sousa[1,2], Beatriz Sousa[1,2,3], Francisco Conceição[1,2,4], Estrela Neto[1,2], Meriem Lamghari[1,2,4] and Cecília J. Alves[1,2*]*

[1] Instituto de Investigação e Inovação em Saúde da Universidade do Porto- Associação, Porto, Portugal, [2] Instituto de Engenharia Biomédica, Universidade do Porto, Porto, Portugal, [3] Faculdade de Engenharia, Universidade do Porto, Porto, Portugal, [4] Instituto Ciências Biomédicas Abel Salazar, Universidade do Porto, Porto, Portugal

Joint replacement surgery is the gold-standard therapeutic approach to treat patients with end-stage hip and knee arthritis, providing pain relief and joint function recovery. Despite the improvements in implant design and surgical techniques, revisions after total joint replacement are expected to grow. The periprosthetic inflammation, featured by the sustained inflammatory response to the implant debris, elicits the activation of osteoclasts and consequent periprosthetic osteolysis (PPOL), ultimately leading to implant aseptic loosening, which is the most common cause of long-term implant failure. There are currently no effective strategies to control periprosthetic inflammation, and long-term implant survival remains a major challenge in orthopedics. A broad knowledge of the mechanisms underlying the biological response to implant debris would support the development of novel and effective pharmacological strategies to manage PPOL and promote implant lifespan. In this review, a detailed description of the cellular and the molecular mechanisms underlying the biological response to implant debris is provided, highlighting the most recent findings. Furthermore, we reviewed novel therapeutic strategies that are being investigated to prevent inflammatory periprosthetic osteolysis.

**Keywords: orthopedic implants, implant wear particles, periprosthetic inflammation, osteolysis, aseptic loosening**

OPEN ACCESS

***Edited by:***
*Andrea Cochis,*
*University of Eastern Piedmont, Italy*

***Reviewed by:***
*Jiří Gallo,*
*Palacký University, Olomouc, Czechia*
*Giuseppe Cappellano,*
*University of Eastern Piedmont, Italy*
*Elena Maria Varoni,*
*University of Milan, Italy*

***Correspondence:**
*Cecília J. Alves*
*cjmalves@ineb.up.pt*

*† These authors have contributed equally to this work*

***Specialty section:***
*This article was submitted to Biomaterials, a section of the journal Frontiers in Materials*

***Received:*** *11 April 2020*
***Accepted:*** *23 July 2020*
***Published:*** *28 August 2020*

***Citation:***
*Couto M, Vasconcelos DP, Sousa DM, Sousa B, Conceição F, Neto E, Lamghari M and Alves CJ (2020) The Mechanisms Underlying the Biological Response to Wear Debris in Periprosthetic Inflammation. Front. Mater. 7:274. doi: 10.3389/fmats.2020.00274*

## INTRODUCTION

Joint replacement surgery, one of the most successful procedures in orthopedics, remains the ultimate option to relieve uncontrolled pain and re-establish joint function in end-stage hip and knee arthritis (Learmonth et al., 2007). A regression analysis with age, gender, race and/or ethnicity, census region, and year as covariates, performed using data from the US National Center for Health Statistics, indicate that the number of hip and knee arthroplasties is estimated to grow 174% to 572,000 procedures and 673% to 3.48 million, respectively, by 2030 (Kurtz et al., 2007). The same study projects that about 7 and 15% of knee and hip arthroplasties, respectively, are still expected to fail, causing the need for a revision surgery (Kurtz et al., 2007). The revision surgeries, in addition to the significant healthcare costs, are associated with a high risk of infection and poor clinical outcomes (Vanhegan et al., 2012; Weber et al., 2018).

The slow progressive inflammatory response to the implant-derived wear particles is the hallmark of periprosthetic osteolysis (PPOL) and subsequent implant aseptic loosening (AL)

(Cobelli et al., 2011; Parvizi, 2015; Sukur et al., 2016), a major cause for long-term implant failure (Sharkey et al., 2014; Thiele et al., 2015).

Periprosthetic inflammation is characterized by an innate immune response that occurs due to macrophage reactivity to implant byproducts, resulting in the release of pro-inflammatory factors, activation of osteoclasts, and consequent osteolysis, thus leading to AL (Goodman et al., 2014; Athanasou, 2016; Gallo, 2019).

In the current scenario of increasing life expectancy and growing rate of joint replacement in the younger and more active population (Kurtz et al., 2009; Skytta et al., 2011; Katz, 2012), the long-term survival of joint replacement is a major challenge in orthopedics.

Biomaterials, such as metals, polymers, and ceramics, are currently used to fabricate joint replacement implants, and several bearing surfaces can be obtained by the combination of different materials. Despite the biocompatibility of the materials used and the improvement in the (i) implant designs, (ii) materials themselves, and (iii) surgical techniques, the repeated movement of the bearing surfaces under loading generates wear debris (e.g., wear particles and metal ions) that trigger an exacerbated biologic response (Gibon et al., 2017a,b). Particularly, polymeric and metal debris represent the major concerns.

There are currently no effective strategies for treating periprosthetic inflammation. A clear understanding of the biological mechanisms underlying the response to implant debris would support the development of non-surgical biological approaches to manage inflammatory periprosthetic bone loss and promote implant survival.

Here we presented a detailed review of the pathways involved in the biological response to implant debris, emphasizing the recent findings. In addition, we also reviewed potential therapeutic strategies, which are under investigation, to control inflammation-induced PPOL.

## BIOMATERIALS USED IN JOINT REPLACEMENT IMPLANTS

The selection of a biomaterial for an implant relies on critical aspects, in which the biological requirements are added to the chemical, mechanical, and physical requests. Concepts such as biocompatibility, bioactivity, and osteoinduction are considered as major players in the process of development and selection of a biomaterial for orthopedic implants (Navarro et al., 2008). Metals, polymers, and ceramics are the three categories of materials currently used to design joint replacement implants.

Titanium and its alloys and cobalt–chrome (Co–Cr) alloys are the metals used for their excellent mechanical and corrosion properties (Prasad et al., 2017). Nevertheless, the release of ions and wear particles from the metallic materials is a matter of concern (Hamidi et al., 2017). Despite their excellent biocompatible properties, the ions and the wear particles released from metal alloys may activate an immune response that, as will be discussed in section "Biological Mechanisms Underlying the Response to Implant Wear Debris," can promote osteolysis and, eventually, implant AL.

The ultrahigh molecular weight polyethylene (UHMWPE) is the most commonly used polymer in the design of orthopedic implants (Alothman et al., 2014). It has been considered an exceptional material to be employed in coupling bearing surfaces with metals or ceramics and is highly biocompatible and very resistant to corrosion (Bracco et al., 2017). The release of wear particles is the major source of concern associated with UHMWPE. Despite the reduction in mechanical properties, cross-linking the material has allowed to partially overcome this issue. Highly cross-linked UHMWPE was introduced in the 1990s, and long-term clinical studies showed significant less wear when compared with conventional polyethylene (PE) (Shi et al., 2019).

The biocompatibility features of bioceramics make them very important candidates to be used in orthopedic implants (Campbell et al., 2004). Bioceramics can behave as inert or bioactive materials in an osseous environment, presenting osteoconductive properties and promoting the fixation of joint prostheses (Navarro et al., 2008). Alumina and zirconia have been used to replace metallic materials. Alumina offers lower friction and constant wear, and zirconia presents minor wear, in addition to its strength (Gamble et al., 2017). To overcome inherent disadvantages, such as high brittleness and high elastic modulus, these materials have been combined in order to develop zirconia-toughened alumina. The base of alumina provides high hardness to the material and zirconia promotes resistance to crack propagation (De Aza et al., 2002; Tuan et al., 2002).

Presently, several options of bearing surfaces for joint replacement implants are available. For total hip replacement, surgeons choose between ceramic-on-ceramic (CoC), ceramic-on-polyethylene (CoPE), and metal-on-polyethylene (MoPE), each presenting specific advantages and disadvantages (Gallazzi, 2018). Metal-on-metal bearing surfaces are no longer considered as an option due to the high rate of failure and the serious adverse biological response to the metallic wear debris released (Campbell, 2010; Gill et al., 2012; Gallazzi, 2018). Acetabular liners are commonly made of PE, either UHMWPE or XLPE or ceramics (Gallazzi, 2018). Ceramics and metal alloys are used to manufacture the heads. The bearing surfaces containing acetabular liners made of conventional PE (both MoPE and CoPE) are associated with wear particle release and osteolysis (Gallazzi, 2018). This drawback is less important for XLPE (Sakellariou et al., 2013). CoC bearing surfaces are between the best-performing bearing surfaces, with very low wear rates and high biocompatibility (Petsatodis et al., 2010; Kang et al., 2015). However, the brittleness of the material that increases the risk of breakage (Howard et al., 2017) and the noise from the implant such as squeaking (Swanson et al., 2010) are still important disadvantages of the CoC bearing surfaces. Regarding bearing surfaces in knee replacement implants, UHMWPE of the tibial insert can articulate against metal or ceramic femoral components (Oonishi et al., 2009; Inacio et al., 2013), although ceramic femoral components are yet rarely used in clinical practice (Solarino et al., 2017).

Overall, the choice of the best coupling bearing surfaces requires a deep understanding of the features of each bearing surface and a profound knowledge of the patients' specific characteristics and needs.

## COMMON CAUSES OF JOINT REPLACEMENT IMPLANT FAILURE

The expansion of novel implant devices has been promoting the longevity of orthopedic implants. However, patients submitted to arthroplasties are still facing the multiple risk factors of implant failure. The patients' comorbidities (such as obesity, rheumatoid arthritis, and diabetes mellitus) and the inadequate surgical techniques may cause post-operative complications (e.g., bleeding, wound dehiscence, and infection) (Haleem, 2018; Ravi et al., 2019). When not suitable for pharmacological treatment, these complications compromise, at the early stages, the success of arthroplasty, and a revision surgery may be required (Delaunay et al., 2013).

Periprosthetic infection is the most common and serious complication that can occur at the early stages after a joint replacement (Sharkey et al., 2014; Thiele et al., 2015; Lum et al., 2018), often demanding multiple additional surgeries to replace the infected implant. Although the risk of infection is higher during the first weeks after surgery [mostly associated with the patients' risk factors and inadequate surgery techniques (Haleem, 2018)], periprosthetic infection can occur at later stages. Infection in adjacent tissues can promote the entrance of bacteria in the bloodstream, increasing the risk of implant colonization and infection at any time post-surgery (Feng et al., 2016). The administration of antibiotics often fails to eliminate the infection, making the need for complex subsequent surgical procedures inevitable (Li et al., 2019).

Concerning the long-term implant failures, AL becomes the most common cause of orthopedic implant revision surgeries (Sharkey et al., 2014; Thiele et al., 2015). The causes for AL change overtime after arthroplasty; at the early stages, it is mostly associated with implant fixation failure, while at the later stages, it is related with wear particle-associated osteolysis. The regular use of joint replacement prostheses causes the release of small debris that stimulate an inflammatory response and subsequent periprosthetic bone osteolysis (Gallo, 2019). Currently, revision surgery is the only procedure available to manage AL. Nevertheless, revision surgeries have been associated to high clinical and surgical risks and are not as effective as the primary surgeries, comprising lower outcomes and higher infection rates (Weber et al., 2018).

## BIOLOGICAL MECHANISMS UNDERLYING THE RESPONSE TO IMPLANT WEAR DEBRIS

Biomaterial implantation gives rise to a host response to the foreign material that will determine the integration and the biological performance of the implant. The molecular patterns and the degradation products released by implanted devices can stimulate the immune system (Kubes, 2020). Upon biomaterial implantation, a sequence of events is initiated, beginning with an injury, followed by blood – material interactions, provisional matrix formation, acute inflammatory response that may lead to chronic inflammation, granulation tissue development, foreign body reaction, and fibrosis/fibrous capsule development, impairing the implant function (Anderson et al., 2008).

During the last years, we have witnessed a change in the concept of what is an ideal biomaterial/implant. Instead of being a material design to diminish host responses, biomaterials are now developed to trigger desired immunological responses, improving implant performance, its integration, and subsequent tissue repair (Ning et al., 2016). With the improvement of biomaterials, the half-life of total hip and knee arthroplasty has considerably increased. Recent systematic reviews and meta-analysis, with more than 15 years of follow-up, concluded that total hip and knee replacement can be expected to last 25 years in 58 and 82% of patients, respectively (Evans et al., 2019a,b). However, the slow and progressive inflammatory response at the bone/implant interface to the implant debris released from the bearing surfaces causes PPOL, a major threat to long-term implant survival.

Although implant debris can initiate an innate inflammatory response acting on numerous cells including monocytes, fibroblasts, osteoblasts, osteoclasts, and mesenchymal stem cells (MSCs), resident macrophages are the key population to eliminate wear particles (Nich et al., 2013). In some circumstances, the adaptive immune system can also be activated, primarily in response to metal ions associated with a hypersensitivity reaction to metals (Goodman, 2007; Pajarinen et al., 2014; Schalock, 2017). The activation of macrophages is still the dominant mechanism in periprosthetic inflammation (Athanasou, 2016).

Macrophage reactivity, upon activation by wear particles (**Figure 1**), is driven by the chemical and the physical features of the particles and is determined by pattern recognition receptors (PRRs), which results in the release of pro-inflammatory cytokines [e.g., tumor necrosis factor (TNF)-α, IL-1β, IL-6, prostaglandin E (PGE)-2), growth factors (macrophage colony stimulating factor 1—M-CSF), pro-osteoclastic factors (receptor activator of nuclear factor kappa B ligand—RANKL), and chemokines (e.g., IL-8, macrophage inflammatory protein—MIP-1α, monocyte chemoattractant protein—MCP-1)], leading to the systemic recruitment of more macrophages and osteoclast precursors, promoting inflammation and osteolysis (Landgraeber et al., 2014).

It is well accepted that the inflammatory response to the implant particles leads to osteoclast formation through progenitor recruitment and up-regulation of RANKL (Fisher, 2005; Holding et al., 2006; Abu-Amer et al., 2007; Landgraeber et al., 2014). The release of TNF-α and IL-1β by macrophages in response to wear particles promotes the expression of RANKL and suppresses the expression of osteoprotegerin (OPG) by the osteoblasts and fibroblasts (Lin et al., 2014; Kandahari et al., 2016). RANKL binds to the RANK expressed on osteoclast precursors, activating signaling pathways such as nuclear factor

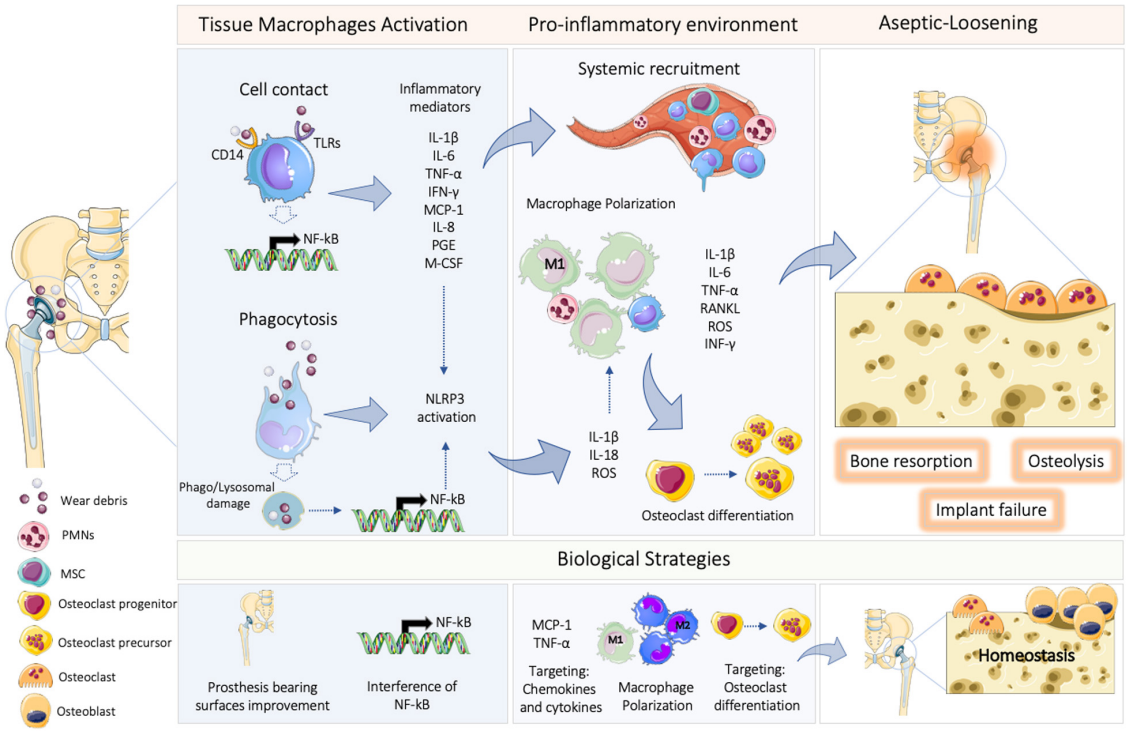


**FIGURE 1 |** Macrophages response to implant wear particles and biological strategies to prevent aseptic loosening. The macrophages' reactivity upon activation by wear particles is driven by cell membrane contact through surface receptors, such as CD14 and TLRs, or through the phagocytosis of wear debris. The activation of NF-κB induces the release of pro-inflammatory cytokines (e.g., TNF-α, IL-1, IL-6, and PGE-2), growth factors (M-CSF), pro-osteoclastic factors (RANKL), and chemokines (e.g., IL-8, MIP-1α, and MCP-1), leading to the systemic recruitment of more macrophages and osteoclast precursors, thus promoting inflammation and osteolysis. This figure also summarizes some proposed biological strategies to prevent and treat aseptic loosening. TLR, Toll-like receptor; PMNs, polymorphonuclear cells; IL, interleukin; NF-κB, nuclear factor kappa B; NLRP3, NOD-, LRR-, and pyrin domain-containing protein 3; TNF, tumor necrosis factor; RANKL, receptor activator of nuclear factor kappa B ligand; ROS, reactive oxygen species; MSC, mesenchymal stem cell; MCP-1, monocyte chemoattractant protein-1; CD, cluster of differentiation; M-CSF, macrophage colony stimulating factor 1; PGE, prostaglandin E; IFN, interferon.

kappa-light-chain-enhancer of activated B cells (NF-κB) and mitogen-activated protein kinase (MAPK), therefore stimulating osteoclastogenesis and excessive bone resorption activity and ultimately leading to implant loosening (Purdue et al., 2007).

Macrophages are remarkable plastic cells with different functions and functional states, which are specified by the complex interplay between microenvironmental signals and a differentiation program that determines the macrophage identity. Two well-established polarized phenotypes are often referred to as classically activated macrophages (M1) and alternatively activated macrophages (M2). The M1 macrophages are characterized by the production of pro-inflammatory cytokines, namely, TNF-α, IL-1, and IL-6, express inducible nitric oxide synthase, and are linked to T helper 1 (Th1) type of immune response (Murray, 2017). M2 macrophages have associated anti-inflammatory cytokines, such as IL-4, IL-10, and IL13, express mammalian chitinase Ym1 and arginase 1, and are related to T helper 2 (Th2) type of immune response (Murray, 2017).

M1 macrophages have been found in high concentrations in periprosthetic tissues from AL patients (Rao et al., 2012). Indeed PMMA (resulting from the bone cement) and UHMWPE particles were shown to polarize macrophages toward an M1 phenotype *in vitro* (Rao et al., 2012; Antonios et al., 2013; Jiang et al., 2016). Mahon et al. (2018) reported that the preferential polarization toward M1 phenotype induced by PMMA particles is dependent on the activation of membrane proximal kinase, spleen tyrosine kinase (Syk), and members of MAPK family. Moreover, they show that pre-treatment with Syk or MAPK inhibitors prevented M1 polarization and reduced the production of pro-inflammatory mediators implicated in PPOL and osteoclast differentiation (Mahon et al., 2018).

The precise mechanisms by which wear particles are recognized and induce macrophage activation have not been fully elucidated. Recent studies have shown that wear debris act as danger signals or alarmins and are recognized by cell membrane contact through surface receptors or after phagocytosis by several PRRs (Goodman, 2014). PRRs can identify a myriad of stimuli, including pathogen-associated molecular patterns (PAMPs) and damage-associated molecular patterns (DAMPs). PAMPs are exogenous molecules derived from bacteria, virus, and fungi (Medzhitov and Janeway, 1997). DAMPs are produced during tissue damage or homeostasis disturbances and include endogenous intracellular molecules [heat-shock protein and high

mobility group protein (HMGB1)], components of extracellular matrix or released by necrotic cells and activated leukocytes (Matzinger, 1994; Venereau et al., 2015).

Based on location, PRRs can be subdivided into two major classes: (i) Toll-like receptors (TLRs) and C-type leptin receptors, which are transmembrane proteins, and (ii) the retinoic acid-inducible protein 1 (RIG)-1-like receptors and the NOD-like receptors (NLRs), which are located intracellularly (Kumar et al., 2011). Evidence supports the DAMPs and the activation of TLRs as dominant mechanisms in macrophage reactivity to implant particles; other mechanisms such as apoptosis, bone catabolism, and hypoxia responses are also involved (Catelas et al., 1999a; Samelko et al., 2013).

The signaling pathways activated by TLRs are divided into myeloid differentiation factor 88 (MyD88)-dependent and MyD88-independent pathways. The MyD88-dependent pathways are the main downstream signaling shared by almost all TLRs, except TLR-3. MyD88 signaling leads to the activation of NF-κB and activating protein-1, responsible for the production of pro-inflammatory cytokines (e.g., TNF-α, IL-1, and IL-12) (O'Neill et al., 2013). The involvement of TLRs in the reactivity to implant particles has been demonstrated both in patient tissues and in animal models. TLRs are highly expressed by the infiltrated macrophages in the periprosthetic tissues of AL patients (Takagi et al., 2007; Lahdeoja et al., 2010; Pajarinen et al., 2010). In *in vitro* cultures of macrophages, the inhibition of MyD88 signaling resulted in the decrease of the inflammatory response to PMMA particles (Pearl et al., 2011). In the same line, MyD88 knockout mice display a reduced inflammatory response to PMMA particles (Pearl et al., 2011).

The NOD-, LRR- and pyrin domain-containing protein 3 (NLRP3/NALP3) inflammasome has also been implicated in the biological response to implant debris (Takagi et al., 2007; Caicedo et al., 2009). The NLRP3 inflammasome is an intracellular multi-protein complex activated upon cellular infection (PAMPs) or stress (DAMPs), triggering the maturation of the highly pro-inflammatory cytokines IL-1β and IL-18 (Martinon et al., 2002; Tschopp, 2010). NLRP3 activation requires a two-step signal. The first one, "priming signal," leads to the activation of NF-κB; the second step of the signal is responsible for the oligomerization of NLRP3 through the recruitment of pro-caspase-1 *via* the adaptor molecule apoptosis-associated speck-like protein containing a CARD (ASC) and the cleavage of cytokine precursors, leading to the maturation and the release of IL-1β and IL-18 (Tschopp, 2010).

The phagocytosis of wear debris by macrophages has been shown to activate the NLRP3 inflammasome pathway, leading to caspase-1 activation, pro-IL-1β cleavage, and mature IL-1β release, a critical cytokine for osteolysis induction (Shiratori et al., 2018). Metal ions and particles were shown to stimulate IL-1β secretion from human macrophages *via* inflammasome activation [i.e., nicotinamide adenine dinucleotide phosphate (NADPH)-, caspase- 1-, Nalp3-, and ASC-dependent] (Caicedo et al., 2009). Regarding this, CoCrMO-alloy particles were reported to stimulate inflammasome through lysosomal destabilization mechanisms in macrophages (Caicedo et al., 2013). Mice lacking caspase-1, the sole effector of the NALP3 inflammasome, also showed reduced PMMA particle-induced osteolysis (Burton et al., 2013). The presence of NLPR3 and their related molecules (caspase-1 and ASC) was detected in periprosthetic tissues (Takagi et al., 2007; Naganuma et al., 2016), ultimately supporting the involvement of NLRP3 inflammasome activation on the host response to implant debris. The continued investigation into how wear debris activate the inflammasome is therefore of great interest.

Differences in PPOL have been observed among individuals, and it is predicted to be associated with genetic variations (Gordon et al., 2010; Del Buono et al., 2012; MacInnes et al., 2015). As recently reviewed by Jagga et al. (2019), candidate gene studies show single nucleotide polymorphisms (SNPs) in several genes involved in both inflammatory signaling and bone turnover pathways in the context of PPOL (Jagga et al., 2019). SNPs have been observed in genes such as TNF-α, IL-1, MMPs, OPG, RANK, and RANKL (Jagga et al., 2019). Nevertheless, the functional effects of SNPs need to be investigated.

It is also known that different implant wear particles and their physical and chemical properties induce specific macrophage responses. In the following sections, we describe the inflammatory mechanisms triggered by wear debris released by the different materials used in the design of joint replacement implants: (i) polymers, (ii) metals, and (iii) ceramics.

## Polymer Wear Particles

The macrophage reactivity to implant particles of polymers such as UHMWPE was shown to involve the activation of TLR signaling (Maitra et al., 2009; Paulus et al., 2014; Valladares et al., 2014). The specific involvement of TLR2 and TLR4 has been suggested in UHMWPE particle-induced osteolysis. UHMWPE induced the up-regulation of TLR2 and TLR4 in a calvarial mouse model (Valladares et al., 2014) and the up-regulation of TLR2 in a mouse model of intraarticular injection (Paulus et al., 2014). Moreover, in addition to the activation of TLR1/2 signaling pathways, UHMWPE particles also trigger the NLRP3 inflammasome through lysosomal damage (Maitra et al., 2009).

A transcriptional profiling analysis of human macrophages stimulated by UHMWPE particles revealed an up-regulation of pro-inflammatory mediators, in agreement with the previous studies, including CCL2, CCL3, CCL4, IL-8, CCL20, TNF-α, IL-1β, and IL-6, and genes involved in osteoclastogenesis and bone resorption, such as CCL3, CCL4, IL-8, CCL20, M-CSF, and MMPs (Terkawi et al., 2018). Overall, in this study, it was shown that macrophages elicited both inflammatory and osteoclastogenesis-related genes in response to UHMWPE particles, and importantly, TLR signaling was identified as being involved in the inflammatory and osteolytic response (Terkawi et al., 2018).

The PMMA particles have also been shown to be involved in the stimulation of osteoclastogenesis and osteolysis (Quinn et al., 1992; Sabokbar et al., 1998). These particles promoted

the release of IL-1β and TNF-α from mouse macrophages (Antonios et al., 2013) and stimulated the production of MCP-1 and, by this way, the recruitment of more macrophages and MSCs (Huang et al., 2010). As previously mentioned, TLR signaling was demonstrated to be involved in macrophage reactivity to PMMA particles (Pearl et al., 2011). The inhibition of MyD88 decreases PMMA particle-induced production of TNF-α in mouse macrophages, and mice lacking the expression of MyD88 developed less PMMA-induced osteolysis (Pearl et al., 2011). The NALP3 inflammasome was also shown to have a critical contribution to PMMA particle-induced osteolysis. Burton et al. (2013) reported that PMMA particles induce caspase-1-dependent release of IL-1β from human monocytes and mouse macrophages and that this is reversed by the inhibition of the NALP3 inflammasome. They also reported that mice lacking caspase-1, the effector of the NALP3 inflammasome, present reduced PMMA-induced calvarial osteolysis (Burton et al., 2013). Recently, Abu-Amer et al. (2019) reported that PMMA particles increase vascular endothelial growth factor (VEGF) expression and vascularization in a mouse calvarial model, and the inhibition of VEGF reduces TNF expression and osteoclastogenesis, highlighting the role of angiogenesis in PMMA particle-induced inflammatory osteolysis.

## Metal Wear Debris

Generation of metallic debris is still a matter of great concern regarding PPOL. In *in vitro* and *in vivo* studies, cobalt alloy debris was shown to elicit inflammasome danger signaling, from initial lysosomal destabilization and NADPH oxidase induction of reactive oxygen species (ROS) to NLRP3-ASC oligomerization and caspase-1 conversion of pro-IL-1β and pro-IL-18 into mature IL-1β and IL-18 (Caicedo et al., 2013; Samelko et al., 2016). On the other hand, the involvement of TLR signaling in macrophage reactivity to cobalt particles has remained controversial. Cobalt and nickel metal ions were shown to facilitate TLR4 activation (Raghavan et al., 2012; Oblak et al., 2015). However, Samelko et al. (2016) reported that cobalt alloy particles do not preferentially activate TLR4-induced inflammation compared with NLRP3 inflammasome danger signaling (IL-1β) in *in vitro* cultures of mouse and human macrophages. Moreover, the authors demonstrated that the inhibition of TLR4 did not decrease the inflammatory response (Samelko et al., 2016). In the same line, a TLR4-independent cobalt alloy-induced extreme inflammatory bone loss was observed in a mouse calvarial model; however, the blockage of the inflammasome pathway completely suppressed the innate inflammatory response to cobalt alloy particles (Samelko et al., 2016). The involvement of other specific toxicity responses, such as hypoxia, has been reported. Hypoxia-like responses were evaluated in human macrophages after challenge with cobalt-alloy particles, and the levels of HIF-1α, VEGF, TNF-α, and ROS were found to be up-regulated (Samelko et al., 2013). The up-regulation of HIF-1α was also observed in periprosthetic tissues after the failure of MoM hip arthroplasties (Samelko et al., 2013).

Titanium implant particles are highly recognized to induce a pronounced macrophage inflammatory response, with up-regulation of pro-inflammatory cytokines, mainly IL-1β, IL-6, and TNF-α (Eger et al., 2017, 2018), and activation of NLRP3 inflammasome through the release of active adenosine triphosphate (Baron et al., 2015). Moreover, it was shown that the IL-1β up-regulation induced by titanium and chromium particles in human macrophages is dependent on NLRP3 inflammasome activation that, in turn, is dependent of TNF-α priming signal (Jamsen et al., 2020).

Adding to the innate inflammatory response, it has been speculated that a delayed type of hypersensitivity-like reaction *via* T lymphocyte activation, though infrequent, could play a role in AL (Goodman, 2007; Pajarinen et al., 2014; Schalock, 2017). This hypothesis is based on the presence of T lymphocytes in periprosthetic tissues and on the ability of metal ions to activate type-IV hypersensitivity by acting as haptens (Granchi et al., 2018). Recently, it was shown that the number of T lymphocytes increases in periprosthetic tissues with increasing time from surgery and the growing concentration of metals (Hobza et al., 2020).

The activation of macrophage by cobalt-alloy particles resulted in a T helper 17 (Th17) cell inflammatory response, which is directly associated with the risk of osteolysis development (Chen et al., 2017). However, in a study using a mouse model, the intraarticular injection of CoCrMo particles induced a significantly enhanced pro-inflammatory cytokine expression (TNF-α, IL-6, and IL-1β) when compared to the intraarticular injection of CoCrMo ions (Cheng et al., 2020). On the other hand, the expression of CD3-positive cells in the synovial membrane of mouse knee did not increase in any of the groups (Cheng et al., 2020). In the same line, data from an epidemiologic study showed that patients with MoM or MoP implants displayed a decrease in blood T lymphocytes despite an increase in the serum level of chromium and cobalt (Granchi et al., 2003). Overall, whether adaptive immune response contributes to the AL induced by metal particles and metal ions is still a matter of intense debate, and more studies are needed to clarify this subject.

## Ceramic Wear Particles

CoC implants display minimal wear debris generation, with a limited incidence of osteolysis, and long-term implant survival rates, being proposed as the best option for young and active patients (Hamadouche et al., 2002; Hannouche et al., 2005). Nevertheless, studies on the toxicity of ceramic particles have been developed. Alumina and zirconia, the common ceramics used in joint implants, have been shown to have low immunotoxicity. In studies evaluating the *in vitro* effect of size and concentration of ceramic particles ($Al_2O_3$ and $ZrO_2$) in macrophages, it was shown that macrophage death increased with particle size and concentration; cell death was still considered to be very low (Catelas et al., 1999b, 1998). Moreover, the release of TNF-α increased with particle concentrations but was lower when compared with the levels induced by polymeric particles (Catelas et al., 1999b, 1998). In other studies, alumina particles were shown to have only limited capacity to stimulate human macrophage release of IL-1β and MCP-1

(Kaufman et al., 2008), and even high concentrations of ceramic particles only induced a mild up-regulation of mRNA expression of RANKL, OPG, and TNF-α (Bylski et al., 2009). Zirconia particles were shown to induce the up-regulation of TLR3, TLR7, and TLR10; however, these had only a slight influence on the production of TNF-α and IL-1β (Lucarelli et al., 2004). Overall, ceramic particles have been reported to induce limited macrophage reactivity.

Despite the efforts made to decrease the generation of wear particles and the impact of AL, through the improvement of the materials, the implant design, the surgical techniques, and the peri-operative rehabilitation, long-term implant survival continues to be a major challenge. Further research is still needed to allow a comprehensive understanding of the mechanisms underlying the biological response to implant wear particles, which will support the development of non-surgical therapeutic modalities to control periprosthetic inflammation and the consequent osteolysis.

# POTENTIAL BIOLOGICAL STRATEGIES TO PREVENT ASEPTIC LOOSENING

Multiple pharmacological strategies have been investigated as putative approaches to mitigate or reverse the implant particle-induced osteolysis. These strategies include the modulation of the inflammatory response (e.g., the blockage of pro-inflammatory cytokines and the modulation of macrophage polarization and NF-κB pathway) and the modulation of the activity of osteoclasts (**Figure 1**).

## Bisphosphonates as a Strategy to Modulate Osteoclast Activity

To avoid bone resorption, the osteoclast activity can be modulated using bisphosphonates. These drugs inhibit osteoclasts activity, suppress the differentiation of osteoclast precursors, and can also induce macrophage apoptosis (Moreau et al., 2007).

Pamidronate, a member of the bisphosphonate family, was shown to inhibit UHMWPE-induced TNF-α release from mouse macrophages and to induce macrophage apoptosis (Huk et al., 2003). Moreover, pamidronate suppressed the PMMA-induced bone resorption in a co-culture model of rat calvaria and macrophages (Horowitz et al., 1996). In the same line, bisphosphonate disodium ethane-1,1-diphosphonate was shown to abolish the differentiation of osteoclast precursors and bone resorption in a co-culture system of mouse monocytes and foreign body macrophages (derived from granulomas formed by a subcutaneous implantation of particles of PMMA, UHMWPE, or titanium) with osteoclasts seeded on bone slices (Pandey et al., 1996).

A meta-analysis of clinical trials of the post-operative administration of bisphosphonates supports short- and mid-term anti-osteolytic effects on periprosthetic bone following arthroplasty (Prieto-Alhambra et al., 2014; Shi et al., 2018a; Su et al., 2018), indicating the beneficial effects of bisphosphonates in reducing mechanically induced bone resorption due to prosthesis insertion. Importantly, bisphosphonates were shown to reduce periprosthetic osteolysis also at later periods after total joint arthroplasty (5 to 10 years), and this is putatively related with effects on periprosthetic inflammation-induced osteolysis (Shi et al., 2018b).

By delaying or preventing bone resorption, bisphosphonates may be a beneficial strategy for preventing AL due to PPOL. However, adverse effects such as pathologic osteonecrosis of the jaw, femoral fracture, and impairment of fracture healing may hamper bisphosphonates' clinical application in AL context (Maalouf, 2012).

## The Targeting of the NF-κB Pathway

The RANKL is a receptor-ligand released from activated cells during the inflammatory process and induces osteoclastogenesis and bone resorption (Wada et al., 2006).

The NF-κB pathway is activated in macrophages and osteoclasts when exposed to implant wear particles (Rao et al., 2012), supporting that the modulation of NF-κB signaling can be a strong strategy to mitigate osteolysis.

Ulrich-Vinther et al. (2002) reported in a titanium-implanted mouse model that the soluble OPG protein, which acts as a decoy receptor by binding to RANK, reducing its bioavailability, decreased the number of osteoclasts and the bone resorption. In the same line, the target of the NF-κB pathway with the NF-κB decoy oligodeoxynucleotide (ODN), which inhibits this transcription factor from binding to the promoter regions of targeted genes, was also shown to mitigate wear particle-induced osteolysis. In a mouse model of continuous femoral particle infusion, the local delivery of NF-κB decoy ODN reversed the bone loss induced by UHMWPE particles and inhibited macrophage infiltration and osteoclast number (Lin et al., 2016). The local injections of ODN in a mouse calvarial model also reduced the UHMWPE-induced expression of TNF-α and RANKL and increased the expression of anti-inflammatory and anti-resorptive cytokines (Sato et al., 2015).

The modulation of the $I_KB$ kinase (IKK) has been highlighted as another potential strategy to inhibit the NF-κB pathway. The reduction of the IKK complex assembly, through a short peptide named NEMO-binding domain (NBD), led to the inhibition of NF-κB activation, preventing RANKL-induced osteoclastogenesis (Karin et al., 2004). Specifically, NBD peptide was reported to inhibit PMMA-induced NF-κB activation *in vitro* and inhibited the PMMA-stimulated osteoclastogenesis and decreased PMMA-induced inflammatory response and osteolysis in a mouse calvarial model (Clohisy et al., 2006). Also in a mouse calvarial model, the intraperitoneal injections of RANK:FC fusion protein, a recombinant RANKL antagonist, inhibit the osteoclastogenesis and the bone resorption induced by titanium particles (Childs et al., 2002). More recently, it was shown that Tussilagone, a natural compound, impairs osteolysis by the inhibition of RANKL-mediated NF-κB and p38-mediated MAPK signaling pathways in a titanium particle-induced murine calvarial model (Hu et al., 2020).

Altogether these studies support the targeting of the NF-κB signaling pathway as a promising strategy to mitigate implant particle-induced inflammatory osteolysis, and further studies are needed to establish the efficacy and the safety of this strategy.

## Modulation of Macrophage Polarization

Despite the complexity of the mechanisms governing macrophage polarization, manipulation toward a more anti-inflammatory phenotype emerges as a potential strategy to diminish implant particle-associated inflammation (Ribeiro-da-Silva et al., 2018; Goodman et al., 2020).

Several *in vitro* and *in vivo* studies showed that macrophage stimulation with IL-4 increases the expression of M2 markers. In PMMA-activated mouse bone marrow-derived macrophages, treatment with IL-4 reduced the TNF-α production (Antonios et al., 2013). This effect was more notorious when IL-4 was added before PMMA particles but was also observed when IL-4 was administrated concurrently or after the challenge with the PMMA particles (Rao et al., 2012; Antonios et al., 2013). Moreover, IL-4 treatment also decreased the production of TNF-α, IL-1β, and GM-CSF in PMMA-stimulated human macrophages (Trindade et al., 1999). A reduction in TNF-α and IL-6 production was also observed in human macrophages exposed to titanium-alloy ($Ti_6Al_4V$) particles and treated with IL-4 (Han, 2001). In the same study, treatment with IL-10 also reduced the production of these pro-inflammatory cytokines (Han, 2001).

In UHMWPE particle-induced osteolysis in the mouse calvarial model, daily treatment with IL-4 significantly decreased bone loss and M1/M2, RANKL/OPG, and TNF-α/IL-1ra ratios (Rao et al., 2013). The coating of implants with IL-4 resulted in a preferential macrophage polarization toward an M2 phenotype, in both *in vivo* and *in vitro* studies (Hachim et al., 2017; Yang et al., 2018), and in an enhanced expression of M2 markers such as IL-10, ARG-1, and platelet-derived growth factor-BB (Yang et al., 2018).

Lately, metformin, an anti-diabetic drug, was shown to promote the release of IL-10 from mouse bone marrow-derived macrophages exposed to UHMWPE particles (Yan et al., 2018). Metformin treatment also reduced the production of pro-inflammatory cytokines, osteoclastogenesis, and osteolysis and promoted IL-10 production and the polarization of macrophages toward a M2 phenotype in the UHMWPE particle-induced osteolysis mouse calvarial model (Yan et al., 2018).

In general, *in vitro* and *in vivo* studies support the modulation of macrophage polarization as a putative effective approach to mitigate implant wear particle-induced inflammation and subsequent osteolysis.

## Pharmacological Blockage of Pro-inflammatory Mediators

As already described, the reactivity of macrophages to implant particles leads to the release of pro-inflammatory factors (cytokines, chemokines, prostaglandins, nitric oxide, and peroxide metabolic intermediates) that will elicit osteolysis and AL. The local inhibition of these pro-inflammatory mediators may reduce inflammation in the periprosthetic tissue. Between the pro-inflammatory mediators, TNF-α is critically involved in wear particle-induced osteolysis, and its inhibition has been investigated as a potential therapeutic strategy.

The antagonism of TNF-α with progranulin [a small anti-inflammatory peptide that inhibits the binding of TNFα to TNFR1/2 (Tian et al., 2014)] effectively inhibited titanium particle-induced inflammation in an air pouch model and osteoclastogenesis and osteolysis *in vitro*, *ex vivo*, and *in vivo* (Zhao et al., 2016). Moreover, it was shown that these effects were achieved primarily *via* inhibition of the TNFα/NF-κB signaling pathway (Zhao et al., 2016). Etanercept, a soluble TNF-α antagonist, was shown also to prevent titanium wear debris-induced osteolysis *in vitro* and osteoclastogenesis and osteolysis *in vivo* (Childs et al., 2001).

Eger et al. (2018) showed, using the mouse calvarial model of titanium particle-induced osteolysis, that blocking TNF-α, IL-1β, and IL-6 with anti-TNFα (adalimunab), anti-IL-1β (anakinra), and anti-IL6 (tocilizumab) antibodies *in vivo* completely abolished titanium-induced osteolysis. Resveratrol, a natural compound with antioxidant, anti-inflammatory, and antitumor effects (Frojdo, 2008), reduced the titanium wear particle-induced oxidative stress in mouse macrophages, and this was accompanied by the reduction of TNF-α release and NF-κB phosphorylation (Luo et al., 2016). Overall, these studies support the inhibition of TNF-α as a putative therapeutic approach to control PPOL.

Further investigation is still deeply needed (i) to establish the effectiveness, safety, and translatability to clinics of the promising pharmacological strategies in ongoing research and (ii) to identify novel therapeutic targets. Importantly, while extensive literature on preclinical data is already available, only moderate clinical research has been performed (Schwarz, 2014). Moreover, studies in humans have mostly focused on the AL conditions, although a different inflammatory profile was observed between AL and non-AL stages of arthroplasty (Dyskova et al., 2019). Information on the time axis of the processes occurring in the periprosthetic tissues, from arthroplasty until the implant AL, will strengthen our understanding of the mechanisms driving inflammation-induced PPOL and further support the development of effective therapeutic approaches.

# CONCLUSION

In the last decades, the biological response to implant wear debris has been investigated and macrophages were identified as the key cells. However, the precise mechanisms by which wear debris are recognized and induce macrophage activation have not been fully elucidated. The information gathered so far demonstrate that wear debris are recognized by several PRRs (e.g., TLRs and NLRs). Among the PRRs, the activation of TLRs has been identified as a dominant mechanism in macrophage reactivity to implant particles. The activation of the NLRP3 inflammasome has also been clearly implicated in this process. The trigger of these mechanisms generates an inflammatory environment that promotes periprosthetic osteolysis and AL.

There are currently no effective pharmacological strategies to manage periprosthetic inflammation. However, several therapeutic approaches are in ongoing research, namely, the (i) blockage of the NF-κB pathway, (ii) modulation of macrophage

polarization toward an anti-inflammatory profile, and (iii) neutralization of TNF-α and other pro-inflammatory cytokines. Further research is still needed to confirm their efficacy, safety, and therapeutic potential in order to be translated to the clinics. Furthermore, a comprehensive understanding of the mechanisms underlying the biological response to implant wear particles will support the identification of novel targets for putative effective therapeutic methods to control periprosthetic inflammation-induced osteolysis.

## AUTHOR CONTRIBUTIONS

MC, DV, and CA conceptualized this work and wrote the manuscript. DS, BS, FC, EN, and ML contributed to the original draft preparation. All authors participated in the revision of the manuscript and read and approved the submitted version.

## FUNDING

This work was financed by the project NORTE-01-0145-FEDER-000012, supported by the Norte Portugal Regional Operational Program (NORTE 2020), under the PORTUGAL 2020 Partnership Agreement, through the European Regional Development Fund (ERDF). DS was a recipient of Fundação para a Ciência e a Tecnologia (FCT) post-doctoral fellowship (SFRH/BPD/115341/2016). FC was a recipient of FCT Ph.D. fellowship (SFRH/BD/128771/2017).

## REFERENCES

Abu-Amer, W., Arra, M., Clohisy, J. C. F., Abu-Amer, Y., and Swarnkar, G. (2019). Targeting vascular endothelial growth factor ameliorates pmma-particles induced inflammatory osteolysis in murine calvaria. *Bone* 123, 86–91. doi: 10.1016/j.bone.2019.03.025

Abu-Amer, Y., Darwech, I., and Clohisy, J. C. (2007). Aseptic loosening of total joint replacements: mechanisms underlying osteolysis and potential therapies. *Arthritis Res. Ther.* 9(Suppl. 1):S6. doi: 10.1186/ar2170

Alothman, O. Y., Fouad, H., Al-Zahrani, S. M., Eshra, A., Al Rez, M. F., and Ansari, S. G. (2014). Thermal, creep-recovery and viscoelastic behavior of high density polyethylene/hydroxyapatite nano particles for bone substitutes: effects of gamma radiation. *Biomed. Eng. Online* 13:125. doi: 10.1186/1475-925X-13-125

Anderson, J. M., Rodriguez, A., and Chang, D. T. (2008). Foreign body reaction to biomaterials. *Semin. Immunol.* 20, 86–100. doi: 10.1016/j.smim.2007.11.004

Antonios, J. K., Yao, Z., Li, C., Rao, A. J., and Goodman, S. B. (2013). Macrophage polarization in response to wear particles in vitro. *Cell Mol. Immunol.* 10, 471–482. doi: 10.1038/cmi.2013.39

Athanasou, N. A. (2016). The pathobiology and pathology of aseptic implant failure. *Bone Joint Res.* 5, 162–168. doi: 10.1302/2046-3758.55.BJR-2016-0086

Baron, L., Gombault, A., Fanny, M., Villeret, B., Savigny, F., Guillou, N., et al. (2015). The nlrp3 inflammasome is activated by nanoparticles through atp, adp and adenosine. *Cell Death Dis.* 6:e1629. doi: 10.1038/cddis.2014.576

Bracco, P., Bellare, A., Bistolfi, A., and Affatato, S. (2017). Ultra-high molecular weight polyethylene: influence of the chemical, physical and mechanical properties on the wear behavior. a review. *Materials* 10:791. doi: 10.3390/ma10070791

Burton, L., Paget, D., Binder, N. B., Bohnert, K., Nestor, B. J., Sculco, T. P., et al. (2013). Orthopedic wear debris mediated inflammatory osteolysis is mediated in part by nalp3 inflammasome activation. *J. Orthop. Res.* 31, 73–80. doi: 10.1002/jor.22190

Bylski, D., Wedemeyer, C., Xu, J., Sterner, T., Loer, F., and von Knoch, M. (2009). Alumina ceramic particles, in comparison with titanium particles, hardly affect the expression of rank-, tnf- alpha-, and opg-mrna in the thp-1 human monocytic cell line. *J. Biomed. Mater. Res. A* 89, 707–716. doi: 10.1002/jbm.a.31956

Caicedo, M. S., Desai, R., McAllister, K., Reddy, A., Jacobs, J. J., and Hallab, N. J. (2009). Soluble and particulate co-cr-mo alloy implant metals activate the inflammasome danger signaling pathway in human macrophages: a novel mechanism for implant debris reactivity. *J. Orthop. Res.* 27, 847–854. doi: 10.1002/jor.20826

Caicedo, M. S., Samelko, L., McAllister, K., Jacobs, J. J., and Hallab, N. J. (2013). Increasing both cocrmo-alloy particle size and surface irregularity induces increased macrophage inflammasome activation in vitro potentially through lysosomal destabilization mechanisms. *J. Orthop. Res.* 31, 1633–1642. doi: 10.1002/jor.22411

Campbell, P. (2010). Nanotoxicology of metal wear particles in total joint arthroplasty: a review of current concepts. *J. Appl. Biomater. Biomech.* 8, 1–6.

Campbell, P., Shen, F. W., and McKellop, H. (2004). Biologic and tribologic considerations of alternative bearing surfaces. *Clin. Orthop. Relat. Res.* 418, 98–111. doi: 10.1097/00003086-200401000-00017

Catelas, I., Huk, O. L., Petit, A., Zukor, D. J., Marchand, R., and Yahia, L. (1998). Flow cytometric analysis of macrophage response to ceramic and polyethylene particles: effects of size, concentration, and composition. *J. Biomed. Mater. Res.* 41, 600–607. doi: 10.1002/(sici)1097-4636(19980915)41:4<600::aid-jbm12<3.0.co;2-i

Catelas, I., Petit, A., Marchand, R., Zukor, D. J., Yahia, L., and Huk, O. L. (1999a). Cytotoxicity and macrophage cytokine release induced by ceramic and polyethylene particles in vitro. *J. Bone Joint Surg. Br.* 81, 516–521. doi: 10.1302/0301-620x.81b3.8737

Catelas, I., Petit, A., Zukor, D. J., Marchand, R., Yahia, L., and Huk, O. L. (1999b). Induction of macrophage apoptosis by ceramic and polyethylene particles in vitro. *Biomaterials* 20, 625–630. doi: 10.1016/s0142-9612(98)00214-2

Chen, F., Chen, R., Liu, H., Sun, R., Huang, J., Huang, Z., et al. (2017). Bmp-7 ameliorates cobalt alloy particle-induced inflammation by suppressing th17 responses. *APMIS* 125, 880–887. doi: 10.1111/apm.12730

Cheng, X., Dirmeier, S. C., Hasselt, S., Baur-Melnyk, A., Kretzer, J. P., Bader, R., et al. (2020). Biological reactions to metal particles and ions in the synovial layer of mice. *Materials* 13:1044. doi: 10.3390/ma13051044

Childs, L. M., Goater, J. J., O'Keefe, R. J., and Schwarz, E. M. (2001). Efficacy of etanercept for wear debris-induced osteolysis. *J. Bone Miner. Res.* 16, 338–347. doi: 10.1359/jbmr.2001.16.2.338

Childs, L. M., Paschalis, E. P., Xing, L., Dougall, W. C., Anderson, D., Boskey, A. L., et al. (2002). In vivo rank signaling blockade using the receptor activator of nf-kappab:Fc effectively prevents and ameliorates wear debris-induced osteolysis via osteoclast depletion without inhibiting osteogenesis. *J. Bone Miner. Res.* 17, 192–199. doi: 10.1359/jbmr.2002.17.2.192

Clohisy, J. C., Yamanaka, Y., Faccio, R., and Abu-Amer, Y. (2006). Inhibition of ikk activation, through sequestering nemo, blocks pmma-induced osteoclastogenesis and calvarial inflammatory osteolysis. *J. Orthop. Res.* 24, 1358–1365. doi: 10.1002/jor.20184

Cobelli, N., Scharf, B., Crisi, G. M., Hardin, J., and Santambrogio, L. (2011). Mediators of the inflammatory response to joint replacement devices. *Nat. Rev. Rheumatol.* 7, 600–608. doi: 10.1038/nrrheum.2011.128

De Aza, A. H., Chevalier, J., Fantozzi, G., Schehl, M., and Torrecillas, R. (2002). Crack growth resistance of alumina, zirconia and zirconia toughened alumina ceramics for joint prostheses. *Biomaterials* 23, 937–945. doi: 10.1016/s0142-9612(01)00206-x

Del Buono, A., Denaro, V., and Maffulli, N. (2012). Genetic susceptibility to aseptic loosening following total hip arthroplasty: a systematic review. *Br. Med. Bull.* 101, 39–55. doi: 10.1093/bmb/ldr011

Delaunay, C., Hamadouche, M., Girard, J., Duhamel, A., and So, F. G. (2013). What are the causes for failures of primary hip arthroplasties in france? *Clin. Orthop Relat. Res.* 471, 3863–3869. doi: 10.1007/s11999-013-2935-5

Dyskova, T., Kriegova, E., Slobodova, Z., Zehnalova, S., Kudelka, M., Schneiderova, P., et al. (2019). Inflammation time-axis in aseptic loosening of total knee arthroplasty: a preliminary study. *PLoS One* 14:e0221056. doi: 10.1371/journal.pone.0221056

Eger, M., Hiram-Bab, S., Liron, T., Sterer, N., Carmi, Y., Kohavi, D., et al. (2018). Mechanism and prevention of titanium particle-induced inflammation and osteolysis. *Front. Immunol.* 9:2963. doi: 10.3389/fimmu.2018.02963

Eger, M., Sterer, N., Liron, T., Kohavi, D., and Gabet, Y. (2017). Scaling of titanium implants entrains inflammation-induced osteolysis. *Sci. Rep.* 7:39612. doi: 10.1038/srep39612

Evans, J. T., Evans, J. P., Walker, R. W., Blom, A. W., Whitehouse, M. R., and Sayers, A. (2019a). How long does a hip replacement last? A systematic review and meta-analysis of case series and national registry reports with more than 15 years of follow-up. *Lancet* 393, 647–654. doi: 10.1016/S0140-6736(18)31665-9

Evans, J. T., Walker, R. W., Evans, J. P., Blom, A. W., Sayers, A., and Whitehouse, M. R. (2019b). How long does a knee replacement last? A systematic review and meta-analysis of case series and national registry reports with more than 15 years of follow-up. *Lancet* 393, 655–663. doi: 10.1016/S0140-6736(18)32531-5

Feng, W., Geng, Z., Li, Z., Cui, Z., Zhu, S., Liang, Y., et al. (2016). Controlled release behaviour and antibacterial effects of antibiotic-loaded titania nanotubes. *Mater. Sci. Eng. C Mater. Biol. Appl.* 62, 105–112. doi: 10.1016/j.msec.2016.01.046

Fisher, J. (2005). The role of macrophages in osteolysis of total joint replacement. *Biomaterials* 26, 1271–1286. doi: 10.1016/j.biomaterials.2004.04.035

Frojdo, S. (2008). Resveratrol: one molecule, many targets. *IUBMB Life* 60, 323–332. doi: 10.1002/iub.47

Gallazzi, E. (2018). Bearing surfaces in primary total hip arthroplasty. *EFORT Open Rev.* 3, 217–224. doi: 10.1302/2058-5241.3.180300

Gallo, J. (2019). Periprosthetic osteolysis: mechanisms, prevention and treatment. *J. Clin. Med.* 8:2091. doi: 10.3390/jcm8122091

Gamble, D., Jaiswal, P. K., Lutz, I., and Johnston, K. D. (2017). The use of ceramics in total hip arthroplasty. *Ortho. Theum.* 4:555636.

Gibon, E., Amanatullah, D. F., Loi, F., Pajarinen, J., Nabeshima, A., Yao, Z., et al. (2017a). The biological response to orthopaedic implants for joint replacement: part I: metals. *J. Biomed. Mater. Res. B Appl. Biomater.* 105, 2162–2173. doi: 10.1002/jbm.b.33734

Gibon, E., Cordova, L. A., Lu, L., Lin, T. H., Yao, Z., Hamadouche, M., et al. (2017b). The biological response to orthopedic implants for joint replacement. Ii: polyethylene, ceramics, pmma, and the foreign body reaction. *J. Biomed. Mater. Res. B Appl. Biomater.* 105, 1685–1691. doi: 10.1002/jbm.b.33676

Gill, H. S., Grammatopoulos, G., Adshead, S., Tsialogiannis, E., and Tsiridis, E. (2012). Molecular and immune toxicity of cocr nanoparticles in mom hip arthroplasty. *Trends Mol. Med.* 18, 145–155. doi: 10.1016/j.molmed.2011.12.002

Goodman, S. B. (2007). Wear particles, periprosthetic osteolysis and the immune system. *Biomaterials* 28, 5044–5048. doi: 10.1016/j.biomaterials.2007.06.035

Goodman, S. B. (2014). Role of macrophages in the biological reaction to wear debris from joint replacements. *J. Long Term. Eff. Med. Implants* 24, 259–265. doi: 10.1615/jlongtermeffmedimplants.2014010562

Goodman, S. B., Gallo, J., Gibon, E., and Takagi, M. (2020). Diagnosis and management of implant debris-associated inflammation. *Expert. Rev. Med. Devices* 17, 41–56. doi: 10.1080/17434440.2020.1702024

Goodman, S. B., Gibon, E., Pajarinen, J., Lin, T. H., Keeney, M., Ren, P. G., et al. (2014). Novel biological strategies for treatment of wear particle-induced periprosthetic osteolysis of orthopaedic implants for joint replacement. *J. R. Soc. Interface* 11:20130962. doi: 10.1098/rsif.2013.0962

Gordon, A., Greenfield, E. M., Eastell, R., Kiss-Toth, E., and Wilkinson, J. M. (2010). Individual susceptibility to periprosthetic osteolysis is associated with altered patterns of innate immune gene expression in response to pro-inflammatory stimuli. *J. Orthop. Res.* 28, 1127–1135. doi: 10.1002/jor.21135

Granchi, D., Savarino, L. M., Ciapetti, G., and Baldini, N. (2018). Biological effects of metal degradation in hip arthroplasties. *Crit. Rev. Toxicol.* 48, 170–193. doi: 10.1080/10408444.2017.1392927

Granchi, D., Savarino, L., Ciapetti, G., Cenni, E., Rotini, R., Mieti, M., et al. (2003). Immunological changes in patients with primary osteoarthritis of the hip after total joint replacement. *J. Bone Joint Surg. Br.* 85, 758–764. doi: 10.1302/0301-620x.85b5.13729

Hachim, D., LoPresti, S. T., Yates, C. C., and Brown, B. N. (2017). Shifts in macrophage phenotype at the biomaterial interface via il-4 eluting coatings are associated with improved implant integration. *Biomaterials* 112, 95–107. doi: 10.1016/j.biomaterials.2016.10.019

Haleem, A. (2018). Prosthetic joint infections: an update. *Curr. Infect Dis. Rep.* 20:15. doi: 10.1007/s11908-018-0622-0

Hamadouche, M., Boutin, P., Daussange, J., Bolander, M. E., and Sedel, L. (2002). Alumina-on-alumina total hip arthroplasty: a minimum 18.5-year follow-up study. *J. Bone Joint Surg. Am.* 84, 69–77. doi: 10.2106/00004623-200201000-00011

Hamidi, M., Harun, W. S. W., Samykano, M., Ghani, S. A. C., Ghazalli, Z., Ahmad, F., et al. (2017). A review of biocompatible metal injection moulding process parameters for biomedical applications. *Mater. Sci. Eng. C Mater. Biol. Appl.* 78, 1263–1276. doi: 10.1016/j.msec.2017.05.016

Han, J. D. (2001). Suppressive effects of interleukin-4 and interleukin-10 on the production of proinflammatory cytokines induced by titanium-alloy particles. *J. Biomed. Mater. Res.* 58, 531–536. doi: 10.1002/jbm.1051

Hannouche, D., Hamadouche, M., Nizard, R., Bizot, P., Meunier, A., and Sedel, L. (2005). Ceramics in total hip replacement. *Clin. Orthop. Relat. Res.* 430, 62–71. doi: 10.1097/01.blo.0000149996.919740.83

Hobza, M., Milde, D., Slobodova, Z., and Gallo, J. (2020). The number of lymphocytes increases in the periprosthetic tissues with increasing time of implant service in non-metal-on-metal total joint arthroplasties: a role of metallic byproducts?. *Biomed. Pap. Med. Fac. Univ. Palacky Olomouc Czech. Repub.* 164. doi: 10.5507/bp.2020.019

Holding, C. A., Findlay, D. M., Stamenkov, R., Neale, S. D., Lucas, H., Dharmapatni, A. S., et al. (2006). The correlation of rank, rankl and tnfalpha expression with bone loss volume and polyethylene wear debris around hip implants. *Biomaterials* 27, 5212–5219. doi: 10.1016/j.biomaterials.2006.05.054

Horowitz, S. M., Algan, S. A., and Purdon, M. A. (1996). Pharmacologic inhibition of particulate-induced bone resorption. *J. Biomed. Mater. Res.* 31, 91–96. doi: 10.1002/(SICI)1097-4636(199605)31:1<91::AID-JBM11<3.0.CO;2-P

Howard, D. P., Wall, P. D. H., Fernandez, M. A., Parsons, H., and Howard, P. W. (2017). Ceramic-on-ceramic bearing fractures in total hip arthroplasty: an analysis of data from the national joint registry. *Bone Joint J.* 99-B, 1012–1019. doi: 10.1302/0301-620X.99B8.BJJ-2017-0019.R1

Hu, X., Yin, Z., Chen, X., Jiang, G., Yang, D., Cao, Z., et al. (2020). Tussilagone inhibits osteoclastogenesis and periprosthetic osteolysis by suppressing the nf-kappab and p38 mapk signaling pathways. *Front. Pharmacol.* 11:385. doi: 10.3389/fphar.2020.00385

Huang, Z., Ma, T., Ren, P. G., Smith, R. L., and Goodman, S. B. (2010). Effects of orthopedic polymer particles on chemotaxis of macrophages and mesenchymal stem cells. *J. Biomed. Mater. Res. A* 94, 1264–1269. doi: 10.1002/jbm.a.32803

Huk, O. L., Zukor, D. J., Antoniou, J., and Petit, A. (2003). Effect of pamidronate on the stimulation of macrophage tnf-alpha release by ultra-high-molecular-weight polyethylene particles: a role for apoptosis. *J. Orthop. Res.* 21, 81–87. doi: 10.1016/S0736-0266(02)00099-2

Inacio, M. C. S., Cafri, G., Paxton, E. W., Kurtz, S. M., and Namba, R. S. (2013). Alternative bearings in total knee arthroplasty: risk of early revision compared to traditional bearings an analysis of 62,177 primary cases. *Acta Orthopaedica* 84, 145–152. doi: 10.3109/17453674.2013.784660

Jagga, S., Sharma, A. R., Bhattacharya, M., Chakraborty, C., and Lee, S. S. (2019). Influence of single nucleotide polymorphisms (snps) in genetic susceptibility towards periprosthetic osteolysis. *Genes Genomics* 41, 1113–1125. doi: 10.1007/s13258-019-00845-3

Jamsen, E., Pajarinen, J., Kouri, V. P., Rahikkala, A., Goodman, S. B., Manninen, M., et al. (2020). Tumor necrosis factor primes and metal particles activate the nlrp3 inflammasome in human primary macrophages. *Acta Biomater.* doi: 10.1016/j.actbio.2020.03.017

Jiang, J., Jia, T., Gong, W., Ning, B., Wooley, P. H., and Yang, S. Y. (2016). Macrophage polarization in il-10 treatment of particle-induced inflammation and osteolysis. *Am. J. Pathol.* 186, 57–66. doi: 10.1016/j.ajpath.2015.09.006

Kandahari, A. M., Yang, X., Laroche, K. A., Dighe, A. S., Pan, D., and Cui, Q. (2016). A review of uhmwpe wear-induced osteolysis: the role for early detection of the immune response. *Bone Res.* 4:16014. doi: 10.1038/boneres.2016.14

Kang, B. J., Ha, Y. C., Ham, D. W., Hwang, S. C., Lee, Y. K., and Koo, K. H. (2015). Third-generation alumina-on-alumina total hip arthroplasty: 14 to 16-year follow-up study. *J. Arthroplasty* 30, 411–415. doi: 10.1016/j.arth.2014.09.020

Karin, M., Yamamoto, Y., and Wang, Q. M. (2004). The ikk nf-kappa b system: a treasure trove for drug development. *Nat. Rev. Drug. Discov.* 3, 17–26. doi: 10.1038/nrd1279

Katz, J. N. (2012). Total knee arthroplasty on the rise in younger patients: are we sure that past performance will guarantee future success? *Arthritis Rheum.* 64, 339–341. doi: 10.1002/art.33371

Kaufman, A. M., Alabre, C. I., Rubash, H. E., and Shanbhag, A. S. (2008). Human macrophage response to uhmwpe, tialv, cocr, and alumina particles: analysis of multiple cytokines using protein arrays. *J. Biomed. Mater. Res. A* 84, 464–474. doi: 10.1002/jbm.a.31467

Kubes, P. (2020). Damps, pamps, and lamps in immunity and sterile inflammation. *Annu. Rev. Pathol.* 15, 493–518. doi: 10.1146/annurev-pathmechdis-012419-032847

Kumar, H., Kawai, T., and Akira, S. (2011). Pathogen recognition by the innate immune system. *Int. Rev. Immunol.* 30, 16–34. doi: 10.3109/08830185.2010.529976

Kurtz, S. M., Lau, E., Ong, K., Zhao, K., Kelly, M., and Bozic, K. J. (2009). Future young patient demand for primary and revision joint replacement: national projections from 2010 to 2030. *Clin. Orthop. Relat. Res.* 467, 2606–2612. doi: 10.1007/s11999-009-0834-6

Kurtz, S., Ong, K., Lau, E., Mowat, F., and Halpern, M. (2007). Projections of primary and revision hip and knee arthroplasty in the united states from 2005 to 2030. *J. Bone Joint Surg. Am.* 89, 780–785. doi: 10.2106/JBJS.F.00222

Lahdeoja, T., Pajarinen, J., Kouri, V. P., Sillat, T., Salo, J., and Konttinen, Y. T. (2010). Toll-like receptors and aseptic loosening of hip endoprosthesis-a potential to respond against danger signals? *J. Orthop. Res.* 28, 184–190. doi: 10.1002/jor.20979

Landgraeber, S., Jager, M., Jacobs, J. J., and Hallab, N. J. (2014). The pathology of orthopedic implant failure is mediated by innate immune system cytokines. *Mediators Inflamm.* 2014:185150. doi: 10.1155/2014/185150

Learmonth, I. D., Young, C., and Rorabeck, C. (2007). The operation of the century: total hip replacement. *Lancet* 370, 1508–1519. doi: 10.1016/S0140-6736(07)60457-7

Li, Y., Yang, Y., Li, R., Tang, X., Guo, D., Qing, Y., et al. (2019). Enhanced antibacterial properties of orthopedic implants by titanium nanotube surface modification: a review of current techniques. *Int. J. Nanomed.* 14, 7217–7236. doi: 10.2147/IJN.S216175

Lin, T. H., Pajarinen, J., Sato, T., Loi, F., Fan, C., Cordova, L. A., et al. (2016). Nf-kappab decoy oligodeoxynucleotide mitigates wear particle-associated bone loss in the murine continuous infusion model. *Acta Biomater.* 41, 273–281. doi: 10.1016/j.actbio.2016.05.038

Lin, T. H., Tamaki, Y., Pajarinen, J., Waters, H. A., Woo, D. K., Yao, Z., et al. (2014). Chronic inflammation in biomaterial-induced periprosthetic osteolysis: Nf-kappab as a therapeutic target. *Acta Biomater.* 10, 1–10. doi: 10.1016/j.actbio.2013.09.034

Lucarelli, M., Gatti, A. M., Savarino, G., Quattroni, P., Martinelli, L., Monari, E., et al. (2004). Innate defence functions of macrophages can be biased by nano-sized ceramic and metallic particles. *Eur. Cytokine Netw.* 15, 339–346.

Lum, Z. C., Shieh, A. K., and Dorr, L. D. (2018). Why total knees fail-a modern perspective review. *World J. Orthop.* 9, 60–64. doi: 10.5312/wjo.v9.i4.60

Luo, G., Li, Z., Wang, Y., Wang, H., Zhang, Z., Chen, W., et al. (2016). Resveratrol protects against titanium particle-induced aseptic loosening through reduction of oxidative stress and inactivation of nf-kappab. *Inflammation* 39, 775–785. doi: 10.1007/s10753-016-0306-6

Maalouf, N. M. (2012). Safety of bisphosphonates. *Rheum. Dis. Clin. North Am.* 38, 681–705. doi: 10.1016/j.rdc.2012.09.001

MacInnes, S. J., Del Vescovo, E., Kiss-Toth, E., Ollier, W. E., Kay, P. R., Gordon, A., et al. (2015). Genetic variation in inflammatory and bone turnover pathways and risk of osteolytic responses to prosthetic materials. *J. Orthop. Res.* 33, 193–198. doi: 10.1002/jor.22755

Mahon, O. R., O'Hanlon, S., Cunningham, C. C., McCarthy, G. M., Hobbs, C., Nicolosi, V., et al. (2018). Orthopaedic implant materials drive m1 macrophage polarization in a spleen tyrosine kinase- and mitogen-activated protein kinase-dependent manner. *Acta Biomater.* 65, 426–435. doi: 10.1016/j.actbio.2017.10.041

Maitra, R., Clement, C. C., Scharf, B., Crisi, G. M., Chitta, S., Paget, D., et al. (2009). Endosomal damage and tlr2 mediated inflammasome activation by alkane particles in the generation of aseptic osteolysis. *Mol. Immunol.* 47, 175–184. doi: 10.1016/j.molimm.2009.09.023

Martinon, F., Burns, K., and Tschopp, J. (2002). The inflammasome: a molecular platform triggering activation of inflammatory caspases and processing of proil-beta. *Mol. Cell* 10, 417–426. doi: 10.1016/s1097-2765(02)00599-3

Matzinger, P. (1994). Tolerance, danger, and the extended family. *Annu. Rev. Immunol.* 12, 991–1045. doi: 10.1146/annurev.iy.12.040194.005015

Medzhitov, R. Janeway, and C. A. Jr. (1997). Innate immunity: the virtues of a nonclonal system of recognition. 91, 295-Ű298.doi: 10.1016/s0092-8674(00)80412-2

Moreau, M. F., Guillet, C., Massin, P., Chevalier, S., Gascan, H., Basle, M. F., et al. (2007). Comparative effects of five bisphosphonates on apoptosis of macrophage cells in vitro. *Biochem. Pharmacol.* 73, 718–723. doi: 10.1016/j.bcp.2006.09.031

Murray, P. J. (2017). Macrophage polarization. *Annu. Rev. Physiol.* 79, 541–566. doi: 10.1146/annurev-physiol-022516-034339

Naganuma, Y., Takakubo, Y., Hirayama, T., Tamaki, Y., Pajarinen, J., Sasaki, K., et al. (2016). Lipoteichoic acid modulates inflammatory response in macrophages after phagocytosis of titanium particles through toll-like receptor 2 cascade and inflammasomes. *J. Biomed. Mater. Res. A* 104, 435–444. doi: 10.1002/jbm.a.35581

Navarro, M., Michiardi, A., Castano, O., and Planell, J. A. (2008). Biomaterials in orthopaedics. *J. R. Soc. Interface* 5, 1137–1158. doi: 10.1098/rsif.2008.0151

Nich, C., Takakubo, Y., Pajarinen, J., Ainola, M., Salem, A., Sillat, T., et al. (2013). Macrophages-key cells in the response to wear debris from joint replacements. *J. Biomed. Mater. Res. A* 101, 3033–3045. doi: 10.1002/jbm.a.34599

Ning, C. Y., Zhou, L., and Tan, G. X. (2016). Fourth-generation biomedical materials. *Mater. Today* 19, 2–3. doi: 10.1016/j.mattod.2015.11.005

Oblak, A., Pohar, J., and Jerala, R. (2015). Md-2 determinants of nickel and cobalt-mediated activation of human tlr4. *PLoS One* 10:e0120583. doi: 10.1371/journal.pone.0120583

O'Neill, L. A., Golenbock, D., and Bowie, A. G. (2013). The history of toll-like receptors - redefining innate immunity. *Nat. Rev. Immunol.* 13, 453–460. doi: 10.1038/nri3446

Oonishi, H., Ueno, M., Kim, S. C., Oonishi, H., Iwamoto, M., and Kyomoto, M. (2009). Ceramic versus cobalt-chrome femoral components; wear of polyethylene insert in total knee prosthesis. *J. Arthroplasty* 24, 374–382. doi: 10.1016/j.arth.2007.10.021

Pajarinen, J., Cenni, E., Savarino, L., Gomez-Barrena, E., Tamaki, Y., Takagi, M., et al. (2010). Profile of toll-like receptor-positive cells in septic and aseptic loosening of total hip arthroplasty implants. *J. Biomed. Mater. Res. A* 94, 84–92. doi: 10.1002/jbm.a.32674

Pajarinen, J., Jamsen, E., Konttinen, Y. T., and Goodman, S. B. (2014). Innate immune reactions in septic and aseptic osteolysis around hip implants. *J. Long Term Eff. Med. Implants* 24, 283–296. doi: 10.1615/jlongtermeffmedimplants.2014010564

Pandey, R., Quinn, J. M., Sabokbar, A., and Athanasou, N. A. (1996). Bisphosphonate inhibition of bone resorption induced by particulate biomaterial-associated macrophages. *Acta Orthop. Scand.* 67, 221–228. doi: 10.3109/17453679608994677

Parvizi, J. (2015). Biological response to prosthetic debris. *World J. Orthop.* 6, 172–189. doi: 10.5312/wjo.v6.i2.172

Paulus, A. C., Frenzel, J., Ficklscherer, A., Rossbach, B. P., Melcher, C., Jansson, V., et al. (2014). Polyethylene wear particles induce tlr 2 upregulation in the synovial layer of mice. *J. Mater. Sci. Mater. Med.* 25, 507–513. doi: 10.1007/s10856-013-5095-y

Pearl, J. I., Ma, T., Irani, A. R., Huang, Z., Robinson, W. H., Smith, R. L., et al. (2011). Role of the toll-like receptor pathway in the recognition of orthopedic implant wear-debris particles. *Biomaterials* 32, 5535–5542. doi: 10.1016/j.biomaterials.2011.04.046

Petsatodis, G. E., Papadopoulos, P. P., Papavasiliou, K. A., Hatzokos, I. G., Agathangelidis, F. G., and Christodoulou, A. G. (2010). Primary cementless total hip arthroplasty with an alumina ceramic-on-ceramic bearing: results after a minimum of twenty years of follow-up. *J. Bone Joint Surg. Am.* 92, 639–644. doi: 10.2106/JBJS.H.01829

Prasad, K., Bazaka, O., Chua, M., Rochford, M., Fedrick, L., Spoor, J., et al. (2017). Metallic biomaterials: current challenges and opportunities. *Materials* 10:884. doi: 10.3390/ma10080884

Prieto-Alhambra, D., Lalmohamed, A., Abrahamsen, B., Arden, N. K., de Boer, A., Vestergaard, P., et al. (2014). Oral bisphosphonate use and total knee/hip

implant survival: validation of results in an external population-based cohort. *Arthritis Rheumatol.* 66, 3233–3240. doi: 10.1002/art.38789

Purdue, P. E., Koulouvaris, P., Potter, H. G., Nestor, B. J., and Sculco, T. P. (2007). The cellular and molecular biology of periprosthetic osteolysis. *Clin. Orthop. Relat. Res.* 454, 251–261. doi: 10.1097/01.blo.0000238813.95035.1b

Quinn, J., Joyner, C., Triffitt, J. T., and Athanasou, N. A. (1992). Polymethylmethacrylate-induced inflammatory macrophages resorb bone. *J. Bone Joint Surg. Br.* 74, 652–658. doi: 10.1302/0301-620x.74b5.1527108

Raghavan, B., Martin, S. F., Esser, P. R., Goebeler, M., and Schmidt, M. (2012). Metal allergens nickel and cobalt facilitate tlr4 homodimerization independently of md2. *EMBO Rep.* 13, 1109–1115. doi: 10.1038/embor.2012.155

Rao, A. J., Gibon, E., Ma, T., Yao, Z., Smith, R. L., and Goodman, S. B. (2012). Revision joint replacement, wear particles, and macrophage polarization. *Acta Biomater.* 8, 2815–2823. doi: 10.1016/j.actbio.2012.03.042

Rao, A. J., Nich, C., Dhulipala, L. S., Gibon, E., Valladares, R., Zwingenberger, S., et al. (2013). Local effect of il-4 delivery on polyethylene particle induced osteolysis in the murine calvarium. *J. Biomed. Mater. Res. A* 101, 1926–1934. doi: 10.1002/jbm.a.34486

Ravi, B., Jenkinson, R., O'Heireamhoin, S., Austin, P. C., Aktar, S., Leroux, T. S., et al. (2019). Surgical duration is associated with an increased risk of periprosthetic infection following total knee arthroplasty: a population-based retrospective cohort study. *EClinicalMedicine* 16, 74–80. doi: 10.1016/j.eclinm.2019.09.015

Ribeiro-da-Silva, M., Vasconcelos, D. M., Alencastre, I. S., Oliveira, M. J., Linhares, D., Neves, N., et al. (2018). Interplay between sympathetic nervous system and inflammation in aseptic loosening of hip joint replacement. *Sci. Rep.* 8:16044. doi: 10.1038/s41598-018-33360-8

Sabokbar, A., Pandey, R., Quinn, J. M., and Athanasou, N. A. (1998). Osteoclastic differentiation by mononuclear phagocytes containing biomaterial particles. *Arch. Orthop. Trauma Surg.* 117, 136–140. doi: 10.1007/s004020050213

Sakellariou, V. I., Sculco, P., Poultsides, L., Wright, T., and Sculco, T. P. (2013). Highly cross-linked polyethylene may not have an advantage in total knee arthroplasty. *HSS J.* 9, 264–269. doi: 10.1007/s11420-013-9352-x

Samelko, L., Caicedo, M. S., Lim, S. J., Della-Valle, C., Jacobs, J., and Hallab, N. J. (2013). Cobalt-alloy implant debris induce hif-1alpha hypoxia associated responses: a mechanism for metal-specific orthopedic implant failure. *PLoS One* 8:e67127. doi: 10.1371/journal.pone.0067127

Samelko, L., Landgraeber, S., McAllister, K., Jacobs, J., and Hallab, N. J. (2016). Cobalt alloy implant debris induces inflammation and bone loss primarily through danger signaling, not tlr4 activation: implications for damp-ening implant related inflammation. *PLoS One* 11:e0160141. doi: 10.1371/journal.pone.0160141

Sato, T., Pajarinen, J., Lin, T. H., Tamaki, Y., Loi, F., Egashira, K., et al. (2015). Nf-kappab decoy oligodeoxynucleotide inhibits wear particle-induced inflammation in a murine calvarial model. *J. Biomed. Mater. Res. A* 103, 3872–3878. doi: 10.1002/jbm.a.35532

Schalock, P. C. (2017). Metal hypersensitivity reactions to orthopedic implants. *Dermatol. Ther.* 7, 53–64. doi: 10.1007/s13555-016-0162-1

Schwarz, E. M. (2014). Are biologic treatments a potential approach to wear- and corrosion-related problems? *Clin. Orthop. Rel. Res.* 472, 3740–3746. doi: 10.1007/s11999-014-3765-9

Sharkey, P. F., Lichstein, P. M., Shen, C., Tokarski, A. T., and Parvizi, J. (2014). Why are total knee arthroplasties failing today–has anything changed after 10 years? *J. Arthroplasty* 29, 1774–1778. doi: 10.1016/j.arth.2013.07.024

Shi, J. Y., Zhu, W. C., Liang, S. H., Li, H. L., and Li, S. M. (2019). Cross-linked versus conventional polyethylene for long-term clinical outcomes after total hip arthroplasty: a systematic review and meta-analysis. *J. Invest. Surg.* 2, 1–11. doi: 10.1080/ 2019.1606370.

Shi, M., Chen, L., Wu, H., Wang, Y., Wang, W., Zhang, Y., et al. (2018). Effect of bisphosphonates on periprosthetic bone loss after total knee arthroplasty: a meta-analysis of randomized controlled trials. *BMC Musculoskelet Disord.* 19:177. doi: 10.1186/s12891-018-2101-z

Shi, M., Chen, L., Xin, Z., Wang, Y., Wang, W., and Yan, S. (2018b). Bisphosphonates for the preservation of periprosthetic bone mineral density after total joint arthroplasty: A meta-analysis of 25 randomized controlled trials. *Osteoporos Int.* 29,1525Ű1537. doi: 10.1007/s00198-018-4488-7

Shiratori, T., Kyumoto-Nakamura, Y., Kukita, A., Uehara, N., Zhang, J., Koda, K., et al. (2018). Il-1beta induces pathologically activated osteoclasts bearing extremely high levels of resorbing activity: a possible pathological subpopulation of osteoclasts, accompanied by suppressed expression of kindlin-3 and talin-1. *J. Immunol.* 200, 218–228. doi: 10.4049/jimmunol.1602035

Skytta, E. T., Jarkko, L., Antti, E., Huhtala, H., and Ville, R. (2011). Increasing incidence of hip arthroplasty for primary osteoarthritis in 30- to 59-year-old patients. *Acta Orthop.* 82, 1–5. doi: 10.3109/17453674.2010.548029

Solarino, G., Piconi, C., De Santis, V., Piazzolla, A., and Moretti, B. (2017). Ceramic total knee arthroplasty: ready to go? *Joints* 5, 224–228. doi: 10.1055/s-0037-1607428

Su, J., Wei, Y., Li, X. M., Diao, Y. P., Liu, H. G., and Zhang, L. (2018). Efficacy of risedronate in improving bone mineral density in patients undergoing total hip arthroplasty: a meta-analysis of randomized controlled trials. *Medicine* 97:e13346. doi: 10.1097/MD.0000000000013346

Sukur, E., Akman, Y. E., Ozturkmen, Y., and Kucukdurmaz, F. (2016). Particle disease: a current review of the biological mechanisms in periprosthetic osteolysis after hip arthroplasty. *Open Orthop. J.* 10, 241–251. doi: 10.2174/1874325001610010241

Swanson, T. V., Peterson, D. J., Seethala, R., Bliss, R. L., and Spellmon, C. A. (2010). Influence of prosthetic design on squeaking after ceramic-on-ceramic total hip arthroplasty. *J. Arthroplasty* 25(6 Suppl.), 36–42. doi: 10.1016/j.arth.2010.04.032

Takagi, M., Tamaki, Y., Hasegawa, H., Takakubo, Y., Konttinen, L., Tiainen, V. M., et al. (2007). Toll-like receptors in the interface membrane around loosening total hip replacement implants. *J. Biomed. Mater. Res. A.* 81, 1017–1026. doi: 10.1002/jbm.a.31235

Terkawi, M. A., Hamasaki, M., Takahashi, D., Ota, M., Kadoya, K., Yutani, T., et al. (2018). Transcriptional profile of human macrophages stimulated by ultra-high molecular weight polyethylene particulate debris of orthopedic implants uncovers a common gene expression signature of rheumatoid arthritis. *Acta Biomater.* 65, 417–425. doi: 10.1016/j.actbio.2017.11.001

Thiele, K., Perka, C., Matziolis, G., Mayr, H. O., Sostheim, M., and Hube, R. (2015). Current failure mechanisms after knee arthroplasty have changed: polyethylene wear is less common in revision surgery. *J. Bone Joint Surg. Am.* 97, 715–720. doi: 10.2106/JBJS.M.01534

Tian, Q., Zhao, Y., Mundra, J. J., Gonzalez-Gugel, E., Jian, J., Uddin, S. M., et al. (2014). Three tnfr-binding domains of pgrn act independently in inhibition of tnf-alpha binding and activity. *Front. Biosci.* 19:1176–1185. doi: 10.2741/4274

Trindade, M. C., Nakashima, Y., Lind, M., Sun, D. H., Goodman, S. B., Maloney, W. J., et al. (1999). Interleukin-4 inhibits granulocyte-macrophage colony-stimulating factor, interleukin-6, and tumor necrosis factor-alpha expression by human monocytes in response to polymethylmethacrylate particle challenge in vitro. *J. Orthop. Res.* 17, 797–802. doi: 10.1002/jor.1100170602

Tschopp, J. (2010). The inflammasomes. *Cell* 140, 821–832. doi: 10.1016/j.cell.2010.01.040

Tuan, W. H., Chen, R. Z., Wang, T. C., Cheng, C. H., and Kuo, P. S. (2002). Mechanical properties of al2o3/zro2 composites. *J. Eur. Ceram. Soc.* 22, 2827–2833. doi: 10.1016/S0955-2219(02)00043-2

Ulrich-Vinther, M., Carmody, E. E., Goater, J. J., Sb, K., O'Keefe, R. J., and Schwarz, E. M. (2002). Recombinant adeno-associated virus-mediated osteoprotegerin gene therapy inhibits wear debris-induced osteolysis. *J. Bone Joint Surg. Am.* 84, 1405–1412. doi: 10.2106/00004623-200208000-00016

Valladares, R. D., Nich, C., Zwingenberger, S., Li, C., Swank, K. R., Gibon, E., et al. (2014). Toll-like receptors-2 and 4 are overexpressed in an experimental model of particle-induced osteolysis. *J. Biomed. Mater. Res. A* 102, 3004–3011. doi: 10.1002/jbm.a.34972

Vanhegan, I. S., Malik, A. K., Jayakumar, P., Ul Islam, S., and Haddad, F. S. (2012). A financial analysis of revision hip arthroplasty: the economic burden in relation to the national tariff. *J. Bone Joint Surg. Br.* 94, 619–623. doi: 10.1302/0301-620X.94B5.27073

Venereau, E., Ceriotti, C., and Bianchi, M. E. (2015). Damps from cell death to new life. *Front. Immunol.* 6:422. doi: 10.3389/fimmu.2015.00422

Wada, T., Nakashima, T., Hiroshi, N., and Penninger, J. M. (2006). Rankl-rank signaling in osteoclastogenesis and bone disease. *Trends Mol. Med.* 12, 17–25. doi: 10.1016/j.molmed.2005.11.007

Weber, M., Renkawitz, T., Voellner, F., Craiovan, B., Greimel, F., Worlicek, M., et al. (2018). Revision surgery in total joint replacement is cost-intensive. *Biomed. Res. Int.* 2018:8987104. doi: 10.1155/2018/8987104

Yan, Z., Tian, X., Zhu, J., Lu, Z., Yu, L., Zhang, D., et al. (2018). Metformin suppresses uhmwpe particle-induced osteolysis in the mouse calvaria by promoting polarization of macrophages to an anti-inflammatory phenotype. *Mol. Med.* 24:20. doi: 10.1186/s10020-018-0013-x

Yang, C. L., Sun, Y. H., Yu, W. H., Yin, X. Z., Weng, J., and Feng, B. (2018). Modulation of macrophage phenotype through controlled release of interleukin-4 from gelatine coatings on titanium surfaces. *Eur. Cell Mater* 36, 15–29. doi: 10.22203/eCM.v036a02

Zhao, Y. P., Wei, J. L., Tian, Q. Y., Liu, A. T., Yi, Y. S., Einhorn, T. A., et al. (2016). Progranulin suppresses titanium particle induced inflammatory osteolysis by targeting tnfalpha signaling. *Sci. Rep.* 6:20909. doi: 10.1038/srep20909

**Conflict of Interest:** The authors declare that the research was conducted in the absence of any commercial or financial relationships that could be construed as a potential conflict of interest.

frontiers in Bioengineering and Biotechnology

ORIGINAL RESEARCH
published: 04 September 2020
doi: 10.3389/fbioe.2020.00773

# Investigation of Cancer Cell Migration and Proliferation on Synthetic Extracellular Matrix Peptide Hydrogels

*Zbigniev Balion[1], Emilija Sipailaite[1], Gabija Stasyte[1], Agne Vailionyte[2,3], Airina Mazetyte-Godiene[2,3], Ieva Seskeviciute[1], Rasa Bernotiene[4], Jaywant Phopase[5] and Aiste Jekabsone[1,4]**

[1] Institute of Pharmaceutical Technologies, Lithuanian University of Health Sciences, Kaunas, Lithuania, [2] Ferentis UAB, Vilnius, Lithuania, [3] Department of Nanoengineering, Center for Physical Sciences and Technology, Vilnius, Lithuania, [4] Laboratory of Molecular Neurobiology, Neuroscience Institute, Lithuanian University of Health Sciences, Kaunas, Lithuania, [5] Department of Physics, Chemistry and Biology, Linköping University, Linköping, Sweden

OPEN ACCESS

**Edited by:**
*Lia Rimondini, University of Eastern Piedmont, Italy*

**Reviewed by:**
*Nathaniel Huebsch, Washington University in St. Louis, United States*
*Cristina Carvalho Barrias, University of Porto, Portugal*

***Correspondence:**
*Aiste Jekabsone*
*aiste.jekabsone@lsmuni.lt*

**Specialty section:**
*This article was submitted to Biomaterials, a section of the journal Frontiers in Bioengineering and Biotechnology*

**Received:** *25 February 2020*
**Accepted:** *18 June 2020*
**Published:** *04 September 2020*

**Citation:**
*Balion Z, Sipailaite E, Stasyte G, Vailionyte A, Mazetyte-Godiene A, Seskeviciute I, Bernotiene R, Phopase J and Jekabsone A (2020) Investigation of Cancer Cell Migration and Proliferation on Synthetic Extracellular Matrix Peptide Hydrogels. Front. Bioeng. Biotechnol. 8:773. doi: 10.3389/fbioe.2020.00773*

Chemical and mechanical properties of a tumor microenvironment are essential players in cancer progression, and it is important to precisely control the extracellular conditions while designing cancer *in vitro* models. The study investigates synthetic hydrogel matrices from multi-arm polyethylene glycol (PEG) functionalized with collagen-like peptide (CLP) $CG(PKG)_4(POG)_4(DOG)_4$ alone and conjugated with either cell adhesion peptide RGD (mimicking fibronectin) or IKVAV (mimicking laminin). Human glioblastoma HROG36, rat C6 glioma cells, and A375 human melanoma cells were grown on the hydrogels and monitored for migration, proliferation, projected cell area, cell shape index, size and number, distribution of focal contacts in individual cells, and focal adhesion number. PEG-CLP-RGD induced migration of both glioma cell lines and also stimulated proliferation (assessed as metabolic activity) of HROG36 cells. Migration of C6 cells were also stimulated by PEG-CLP-IKVAV. These responses strongly correlated with the changes in adhesion and morphology parameters of individual cells – projected cell area, cell shape index, and focal contact number. Melanoma A375 cell proliferation was increased by PEG-CLP-RGD, and this was accompanied by a decrease in cell shape index. However, neither RGD nor IKVAV conjugated to PEG-CLP stimulated migratory capacity of A375 cells. Taken together, the study presents synthetic scaffolds with extracellular matrix (ECM)-mimicking peptides that allow for the exploration of the effect of ECM signaling to cancer cells.

**Keywords: collagen like peptide, cell adhesion peptides, glioblastoma, melanoma, migration, proliferation, focal adhesion**

## INTRODUCTION

The design of a realistic cell culture microenvironment is an important aspect in the development of cancer *in vitro* models. The way cancer cells sense and respond to both chemical and mechanical cues might strongly affect tumor cell invasiveness and modulate the disease progression (Papalazarou et al., 2018). Cancer cell ability to invade healthy tissue makes the difference between

not very dangerous locally growing tumors and life-threatening systemic disease (Friedl and Alexander, 2011). Besides soluble and extracellular vesicle-encapsulated factors, there are two key players instructing cancer cells to migrate and proliferate: cell–cell interaction and cell–extracellular matrix (ECM) interaction. For studies into the latter, it is necessary to develop a substrate that: (i) would mimic a natural cancer cell environment, (ii) would have precisely controlled composition of signaling elements, and (iii) would support a standardized and easy-to-monitor and analyze cell culture.

The most important and best studied structural proteins of ECM are collagens, fibronectins, and laminins (Paolillo and Schinelli, 2019). Collagens characterized by a supramolecular helix structure formed from three polypeptide α-chains are the most abundant proteins of ECM and make up about one third of the total human protein mass (Shoulders and Raines, 2009). Fibronectin dimers connect ECM elements by binding to collagens and other fibronectin molecules (Oxford et al., 2019). Heterotrimeric laminins form independent networks or bind to other ECM proteins (Colognato and Yurchenco, 2000). Collagens, laminins, and fibronectins provide binding sites for cellular integrin receptors to make focal adhesions (Mostafavi-Pour et al., 2003; Berrier and Yamada, 2007; Nissinen et al., 2012). Cell–matrix adhesions, or focal adhesions, are essential for the regulation of biological processes such as cell survival, proliferation, and tumorigenesis (Berrier and Yamada, 2007). Integrins act as receptors for ECM targets by transmitting outside-in and inside-out signaling that involves over 50 proteins (Zamir et al., 1999; Hynes, 2004). By means of focal adhesions, cells relocate and receive mechanical stimuli from the environment (Ingber, 2003; Berrier and Yamada, 2007; Parsons et al., 2010). Moreover, the cell migration directly depends on the focal adhesion size (Kim and Wirtz, 2013). These interactions between cells and ECM proteins control differentiation, shape, movement, cell phenotype, and viability (Colognato and Yurchenco, 2000; Smith et al., 2018). It is established that laminin produced by keratinocytes promotes both adhesion and migration of melanocytes and melanoma cells (Chung et al., 2011). On its turn, fibronectin increases the malignancy of glioma stem-like cells modulating the differentiation, proliferation, and chemoresistance via cell adhesion signaling (Yu et al., 2018). Thus, it is evident that the presence of these proteins in the environment of cancer cells makes a difference and it is important to have at least main ECM signals for designing realistic cancer *in vitro* models. However, here lies the challenge of controlled design, scaling, and standardization of such ECM mimetics, because the production of the proteins is expensive and contains the risk of relatively high batch-to-batch variations and biocontamination.

A promising strategy in ECM engineering was introduced by the discovery of so-called cell adhesion peptides, or short amino acid sequences, that contain the minimal information required to specifically bind to a cell receptor responsible for the cell adhesion (Huettner et al., 2018). The ability of RGD sequence to promote cell attachment in a way similar to fibronectin was demonstrated for the first time by Pierschbacher and Ruoslahti (1984), and soon after this, the peptide was applied for the designing of a cell-instructing hydrogel matrix (Hern and Hubbell, 1998; Rowley and Mooney, 2002; Nemir et al., 2010; Wall et al., 2010). Peptide motif IKVAV was first presented as a sequence responsible for neuritogenic bioactivity in laminin α-chain by Nomizu et al. (1995) and subsequently applied for the functionalization of hydrogels in neural tissue engineering (Adams et al., 2005). Efforts to design a synthetic collagen with self-assembling triple helical structure were successful in the studies of O'Leary et al. (2011), who managed to achieve the formation of homogeneous collagen mimetic nanofibers. Moreover, the peptides were able to form hydrogels with properties very similar to those of natural collagen. More recently, the collagen-mimicking triple helix peptides were stabilized by physical crosslinking to the polymeric scaffolds and exploited as all-synthetic ECM for tissue engineering (Luo and Kiick, 2013; Yuan et al., 2016).

Hydrogels are among the most attractive materials for tissue engineering due to their similarity to *in vivo* cellular microenvironments (Drury and Mooney, 2003). They are usually made by translating a hydrophilic polymer solution into a 3D network structure via physical or chemical crosslinking (Tibbitt and Anseth, 2009). Synthetic hydrogels comprising such ECM signal mimicking peptides are considered as a new promising tool in cancer model development because of their well-defined composition, structural integrity and robustness, controlled charge, stiffness, porosity, nanostructure, degradability, and adhesion properties (Worthington et al., 2015).

In this study, we examine ECM-mimicking hydrogels made of self-assembling collagen-like peptide attached to eight-armed polyethylene glycol (PEG-CLP; Islam et al., 2016) functionalized with fibronectin active site motif RGD (PEG-CLP-RGD) and laminin motif IKVAV (PEG-CLP-IKVAV) as matrices for cancer *in vitro* modeling. Previously, the hydrogels have promoted the attachment and self-assembly of primary neuronal-glial cells from developing rat cerebellum to functional organoids (Balion et al., 2020). In this study, the matrices were tested with two cancerous cell lines of astrocytic origin: rat glioma cells C6 and human glioblastoma HROG36. Also, a cancerous cell line of different origin human melanoma A375 was examined for comparison. All the three cell lines were investigated for migration, proliferation, and focal adhesion formation on PEG-CLP, PEG-CLP-RGD, and PEG-CLP-IKVAV hydrogel samples.

# MATERIALS AND METHODS

## Hydrogel Substrate Fabrication

Unless otherwise stated, all chemicals were purchased from Sigma-Aldrich.

The synthesis of CLPs, conjugation with multi-arm PEG, and CLPs-PEG hydrogels preparation were performed following previously described protocol (Islam et al., 2016). Peptides CLP (Cys-Gly-(Pro-Lys-Gly)$_4$(Pro-Hyp-Gly)$_4$(Asp-Hyp-Gly)$_4$), CLP-RGD (-Arg-Gly-Asp-Ser-Pro-Gly), and CLP-IKVAV (-Ile-Lys-Val-Ala-Val-Gly) were synthesized by UAB Ferentis (Vilnius, Lithuania). Functionalized PEG-CLP hydrogels containing additional motifs responsible for cell adhesion to the ECM

(RGD) or laminin (IKVAV) mimetic motifs were prepared in the same manner as PEG-CLP. Briefly, peptides were conjugated to 40 kDa 8-arm PEG-maleimide (JenKem, TX, United States). The composition of peptides and conjugation of CLP, CLP-RGD, and CLP-IKVAV with 8-arm PEG-maleimide were characterized using $^1$H NMR on a Bruker Ascend 400 MHz spectrometer at room temperature. Briefly, 2% solutions of CLP, CLP-RGD, CLP-IKVAV, PEG-CLP, PEG-CLP-RGD, and PEG-CLP-IKVAV were prepared in deuterium oxide ($D_2O$). The resonance of deuterated solvent ($D_2O$, $\delta = 4.79$) was used as the internal standard.

Further, 12% (w/w) PEG-peptide aqueous solution was crosslinked with 4-(4,6-dimethoxy-1,3,5-triazin-2-yl)-4-methylmorpholinium chloride (DMTMM) at RT (Haagdorens et al., 2019). Due to the hydrophobic nature of the CLP-IKVAV peptide, 10% (w/w) PEG-CLP-IKVAV solution was used. Amine molar ratio of PEG-peptide-$NH_2$ to DMTMM was 1:2. After thorough mixing, final solution containing 8.5 ± 0.2% (AVG ± STDEV, w/w) PEG-CLP, 8.5 ± 0.2% (w/w) PEG-CLP-RGD or 7.2 ± 0.2% (w/w) PEG-CLP-IKVAV was cast between two glass plates to form a flat 500 μm thickness sheet. The hydrogels were left to cure overnight in 100% humidity at RT. The molar concentration of peptides in the hydrogels were: 1.17 ± 0.10 mM of CLP in PEG-CLP, 1.17 ± 0.02 mM CLP-RGD in PEG-CLP-RGD, and 0.99 ± 0.02 mM of CLP-IKVAV in PEG-CLP-IKVAV. After crosslinking, 6 mm hydrogel disks were cut from the fabricated sheets using a threphine. Prior to use, hydrogels were kept refrigerated inside sterile vials filled with phosphate buffer solution containing 1% (v/v) chloroform to maintain sterility (Islam et al., 2018).

### 2D Cultures

HROG36 (RRID: CVCL_4U49), C6 (RRID:CVCL_0194), and A375 (RRID: CVCL_0132) cell lines were purchased from Cell Lines Service GmbH (Germany).

The cells were cultured in the specific medium (DMEM/Ham's F12 1:1 for HROG36, DMEM for C6 and RPMI for A375) and supplemented with 10% 0.22 μm pore filter-sterilized fetal bovine serum (FBS) and 1% penicillin-streptomycin at 37°C and 5% $CO_2$. Cells were grown in T75 flasks (15–20 mL of medium) until 75-95% confluency, then detached by 0.25% Trypsin-EDTA solution and used for spheroid formation and proliferation evaluation.

### Spheroid Formation

The "hanging drop" method was used to form spheroids of a similar shape and size.

For HROG36 and C6 cells, 5 μL (26,000 cells) drops of glioblastoma cell suspension were placed on the inside of the sterile tissue culture dish cover. Then the culture dish cover was turned around and placed on the respective cell dish containing 10 mL Phosphate-buffered saline (PBS). Spheroids were grown at 37°C temperature for about 24 h and after that were transferred into the 24 well plate, the bottom of which was covered with 1% agarose. Transferred spheroids were grown in the cell culture medium at 37°C temperature. Spheroids were fully formed after 5 days; the diameter of the spheroids for C6 cells was 113 ± 13 μm, and for HROG36 – 198 ± 59 μm.

For A375 spheroid formation, a slightly different procedure was applied due to different proliferation and spheroid formation capacities of the cells. Both glioma cell lines form connections faster and can join to integral spheroids at lower cell numbers compared to A375 melanoma cells. However, A375 cannot survive in hanging drops in larger amounts because of its very high proliferation rate and restricted amount of nutrients in small medium volume. Thus, seed-spheroids were initially formed by spotting 25 μL drops (500 cells) of the cell suspension onto the inner surface of the lid of a sterile non-adhesive cell culture dish. The lid was placed on the respective cell culture dish containing 10 mL PBS. After 10 days, the seed spheroids were gently transferred on agarose for further growth until the formation of integral shapes retaining spheroids of 473 ± 96 μm in diameter.

## Cell Migration Assessment

The formed spheroids were pipetted onto PEG-CLP, PEG-CLP-RGD, and PEG-CLP-IKVAV hydrogels, and incubated for 24 h. The brightfield phase contrast images of spheroids and cells migrated on hydrogels were taken by microscope Leica DMi1 and analyzed by Image J freeware. The migration was assessed by measuring the size of the area covered by cells around the spheroid (excluding the area covered by the spheroid itself), and by counting the number of cells in the area.

## Cell Proliferation Evaluation

Cell proliferation was assessed by evaluating the metabolic activity of the cells by means of PrestoBlue™ Cell Viability Reagent (Thermo Fisher Scientific). This is a resazurin-based, membrane permeable solution that upon reduction forms resorufin, a compound that is red and highly fluorescent. The rate of conversion corresponds to the rate of metabolic activity of the cells and can be applied for assessment of cell proliferation as described in Czekanska (2011). The procedure was performed according to the protocol provided by the manufacturer. For this, each cell type was seeded on hydrogel disks at a density of 3000 cells/well of a 96 well plate. Cell proliferation was assessed after 24 and 48 h. 10 μL of PrestoBlue™ reagent was added to each well of 96-well plate containing 90 μL of cell culture medium and incubated for 40 min at 37°C in a cell culture incubator, protected from direct light. After incubation, the fluorescence of resorufin was detected using a multimode plate reader Infinite M Plex (Tecan Austria, Salzburg, Austria) at excitation and emission wavelengths of 560 and 590 nm, respectively. The results were expressed as means ± standard deviation of relative fluorescent units.

## Immunocytochemistry

For the evaluation of focal adhesions, the cells were fixed with 4% paraformaldehyde in PBS for 5 min, permeabilized with 0.1% Triton X-100 for 5 min, and then incubated in 1% BSA in PBS for 30 min to block non-specific protein–protein interactions. The cells were then incubated with the primary vinculin-binding antibody (ab18058, RRID:AB_444215, diluted 1:200 making final concentration 3 μg/mL) for 2 h at room temperature. The secondary antibody ab150113 Alexa Fluor® 488 goat anti-mouse IgG (H + L, RRID:AB_2576208) used at a concentration of

2 μg/mL was applied for 45 min together with Texas Red™-X Phalloidin (Invitrogen, T7471, diluted 1:40 in 1% BSA, final concentration 5 units/mL, or 165 nM) for F-actin staining and 1.43 μM DAPI for nuclear visualization. The cell images were taken by fluorescent microscope Zeiss Axio Observer.Z1 (Carl Zeiss, Jena, Germany). Size distribution of individual focal contacts was plotted for three individual cells of each cell line on each hydrogel substrate. Gausian 4 parameter equation curves were fitted to the data by SigmaPlot software. Cell shape index was calculated as described in Cornhill et al. (1980), applying the equation:

$$\text{Shape index} = 4\pi A/P^2$$

where $A$ is the cell area and $P$ is the cell perimeter. Cell perimeter and cell area were calculated by means of ImageJ software. The number of focal adhesions were also evaluated by ImageJ as vinculin and actin colocalization points per cell.

## Statistical Analysis

The quantitative results are presented as mean ± standard deviation of 3–12 replicates. The statistical data analysis was performed by applying the ANOVA with LSD *post hoc* test. Differences were considered statistically significant when $p < 0.05$. The data were processed using Microsoft Office Excel 2010 (Microsoft) and SPSS 20 (IBM) software. Correlations were analyzed by means of Microsoft Office Excel 2010 (Microsoft) software using Correlation function.

# RESULTS

## PEG-Peptide Synthesis and Characterization

The peptide synthesis and peptide conjugation to PEG-maleimide was confirmed by $^1$H NMR spectroscopy. The $^1$H NMR spectra of CLP was similar to earlier published spectra (Islam et al., 2016). The CLP-RGD spectra had an additional arginine peak at δ 3.10 ppm and serine peak at δ 3.90 ppm (marked by blue arrows in **Figure 1**) from RGD motif (Balion et al., 2020). The CLP-IKVAV had an apparent valine peak at δ 0.75 ppm, isoleucine peak at δ 0.82 ppm, and alanine peak at δ 1.22 ppm (marked by green arrows in **Figure 1**) from additional IKVAV motif. The quantitative conjugation of CLP, CLP-RGD, and CLP-IKVAV peptides with 8-arm-PEG maleimide was confirmed by the disappearance of the maleimide peak at δ 6.5–7.0 ppm after conjugation of peptides to PEG template. The nominal surface concentration of the peptides estimated from molar concentration of each peptide was 1 pmol/cm$^2$, the values close to those previously reported by Hern and Hubbell, 1998.

## Cancer Cell Migration on PEG-CLP Hydrogels

To evaluate HROG36, C6, and A375 cell migration induced by different cell adhesion peptides, the spheroids were formed and placed on PEG-CLP, PEG-CLP-RGD, and PEG-CLP-IKVAV hydrogels. After 24 h, the area occupied by cells was measured and the number of cells around the spheroids was counted. The representative images of the spheroid-cultures on the hydrogels after 24 h are presented in **Figure 2**. The largest migration areas were found in human glioblastoma HROG36 samples, and the smallest areas in melanoma A375 samples (**Figures 2**, **3A**). The introduction of RGD signals to the

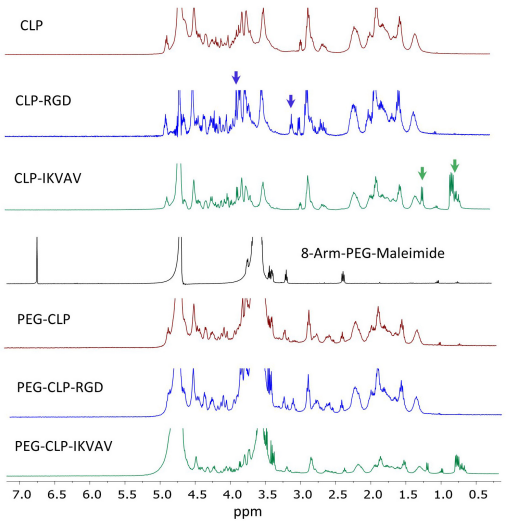


**FIGURE 1 |** NMR spectra of CLP, CLP-RGD, CLP-IKVAV, 8-arm-PEG (40kDa) and PEG-CLP derivatives. Blue arrows mark arginine at δ 3.10 ppm and serine peaks at δ 3.90 ppm of CLP-RGD peptide. Green arrows show valine at δ 0.75 ppm, isoleucine at δ 0.82 ppm, and alanine peaks at δ 1.22 ppm of CLP-IKVAV peptide. The maleimide peaks at δ 6.5–7.0 ppm disappeared after conjugation with CLPs peptides.

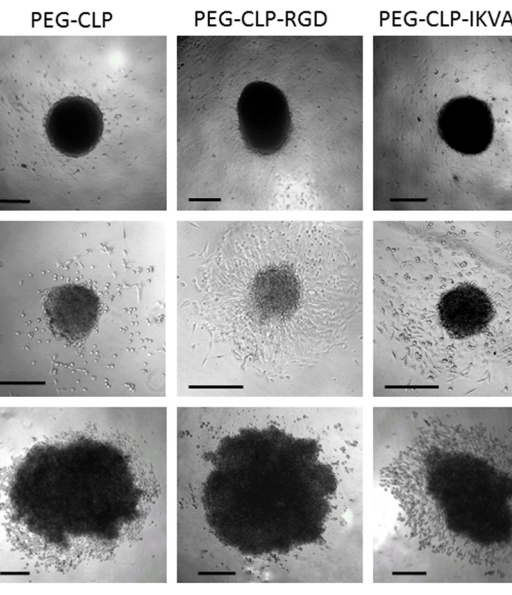


**FIGURE 2 |** Representative images of HROG36, C6, and A375 cell spheroid cultures on PEG-CLP, PEG-CLP-RGD, and PEG-CLP-IKVAV hydrogels after 24 h from spheroid positioning. Scale bar is 100 μm.

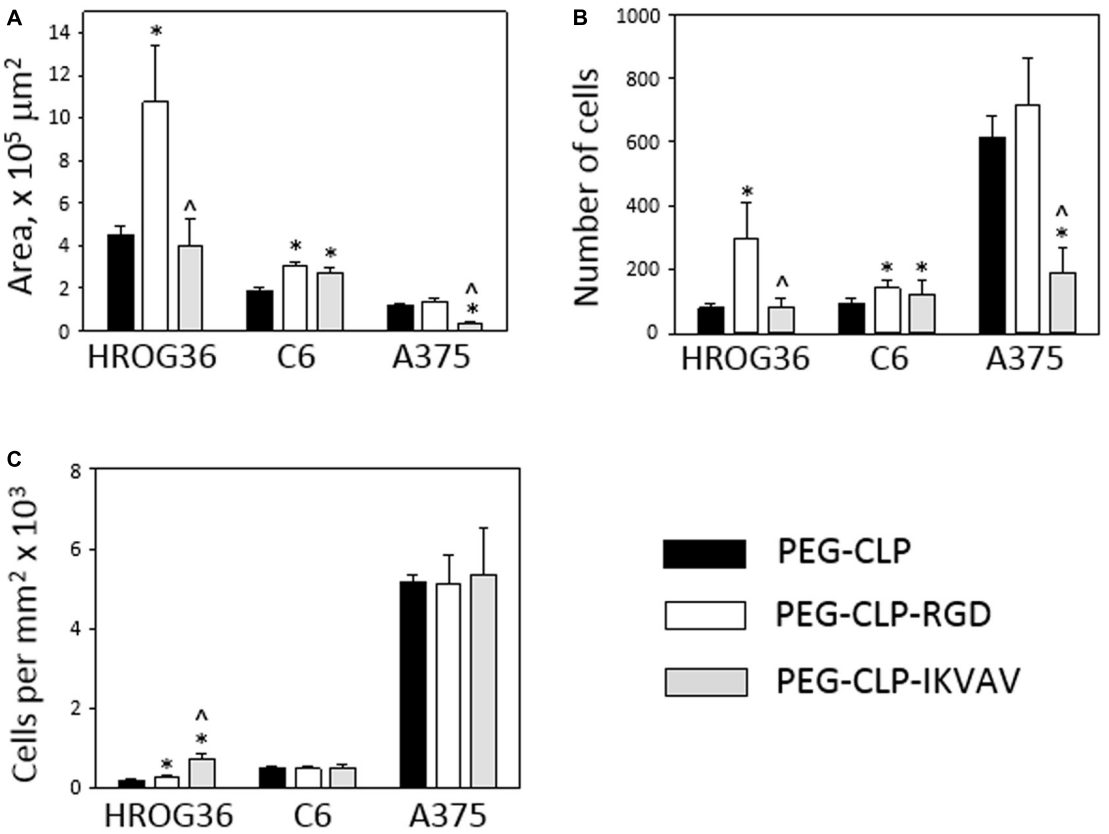


**FIGURE 3 |** Migration of HROG36, C6, and A375 cells on PEG-CLP, PEG-CLP-RGD, and PEG-CLP-IKVAV hydrogels. The cell migration was evaluated by measuring the area of cell spreading around the spheroid in 24 h **(A)**, by counting cells in the area **(B)**, and by indicating cell number per $mm^2$ **(C)**. The experiments were performed in three independent experimental sets, each of three replicates. *Indicates statistically significant difference compared with the samples of the same cell type grown on PEG-CLP hydrogels, ^ – with samples on PEG-CLP-RGD hydrogels, ANOVA with *post hoc* LSD test, $p < 0.05$.

PEG-CLP core dramatically increased the spreading area of HROG36 glioblastoma cells; the cell spreading area on PEG-CLP-RGD was 2.38 times bigger compared to that on PEG-CLP hydrogels (**Figure 3A**). On the contrary, laminin motif IKVAV did not significantly influence HROG36 cell migration and the spreading area on PEG-CLP-IKVAV remained similar to PEG-CLP. Migration of rat glioma C6 line cells was similarly stimulated both by fibronectin active sequence RGD and IKVAV from laminin. The average spreading area was by 1.68 times bigger on PEG-CLP-RGD and 1.45 times bigger on PEG-CLP-IKVAV compared to the area on PEG-CLP. Human melanoma cells A375 migrated similarly on both PEG-CLP and PEG-CLP-RGD. However, introduction of the IKVAV motif significantly blocked the melanoma cell migratory capacity. The cell spreading area on PEG-CLP-IKVAV was 79% smaller than on PEG-CLP (**Figure 3A**).

Counting cells in the area of spread around the spheroids after 24 h revealed the highest numbers in A375 melanoma samples, approximately 2–3 times lower in human glioblastoma HROG36 samples and about 2 times lower in rat glioma C6 samples. Similarly to the spreading area results, the number of glioblastoma HROG36 cells was 3.67 times bigger on PEG-CLP-RGD than on PEG-CLP, and IKVAV sequence did not significantly change cell number around the spheroid after 24 h (**Figure 3B**). The number of spread C6 cells was 1.56 times higher on PEG-CLP-RGD compared to the samples cultivated on PEG-CLP hydrogels. Laminin motif IKVAV significantly decreased cell number around the A375 spheroids; it was 69% smaller compared to that on PEG-CLP.

The calculation of cell number per unit area revealed more than 10 times higher values in A375 samples compared to both glioma cell lines HROG36 and C6 (**Figure 3C**). However, there was no significant difference in cell per unit area number between PEG-CLP, PEG-CLP-RGD, and PEG-CLP-IKVAV hydrogels in both A375 and C6 cell cultures. In contrast, the number of HROG36 cells per areal unit slightly yet significantly increased on PEG-CLP-RGD compared to PEG-CLP, and markedly increased on PEG-CLP-IKVAV compared to both PEG-CLP and PEG-CLP-RGD samples.

To summarize, human glioblastoma HROG36 cell cultures make the largest spreading area of all investigated cancer cell types, but the highest cell numbers around the spheroid and the highest cell per unit area values were found in human melanoma A375 samples. Both HROG36 and C6 cell migration was stimulated by RGD peptide, but C6 cells were similarly

stimulated by IKVAV. On the contrary, in A375 case, IKVAV peptide suppressed both spreading area and cell number. The difference in cell per unit area values between different hydrogels was found only in HROG36 cell cultures.

## Cancer Cell Proliferation on PEG-CLP Hydrogels

Changes in cell spreading area and especially in cell number around the spheroids might be induced by the adhesion peptide influence on cell proliferation. Therefore, next in the study, metabolic activity Presto Blue$^{TM}$ assay was applied to estimate cell proliferation. After 24 h, there were no significant proliferation differences between HROG36 samples on different hydrogel types (**Figure 4A**). It is not surprising, taking into account that the reported doubling time of the cells is 35–40 h (Mullins et al., 2013). When the evaluation time was prolonged to 48 h, the proliferation rate of HROG36 cells on PEG-CLP-RGD hydrogels was 2.25 times higher than on PEG-CLP (**Figure 4B**). For other cells evaluated in the study, the doubling time is shorter: 24 h for the C6 cells and 16 h for A375 cells, respectively (Benda et al., 1968; Benga, 2001). Indeed, in the samples of the latter cells with a shorter doubling time, the differences in proliferation rate on different hydrogels were already visible after 24 h. RGD significantly blocked the proliferation of C6 cells compared to PEG-CLP samples (**Figure 4A**). The average level of cell proliferation in C6 samples on PEG-CLP-RGD hydrogels were 33% lower than that on PEG-CLP hydrogels. In contrast, introduction of IKVAV peptide to the PEG-CLP core increased C6 proliferation rate by 1.3 times. RGD peptide increased the proliferation rate of A375 cells; on PEG-CLP-RGD hydrogels, it was 1.61 time higher compared to the PEG-CLP samples (**Figure 4A**). Evaluation of the proliferation after 48h confirmed the proliferation stimulating effects of RGD for C6 and A375 cells (**Figure 4B**). However, the extent of the effects was not so significant as after 24 h; the increase in the proliferation of the C6 cells compared to PEG-CLP hydrogel samples was 28%, and that of A375 cells was 33%.

Proliferation assessment results indicate that both human glioblastoma HROG63 and melanoma A375 cell proliferation is stimulated by RGD signaling, but the proliferation of C6 cells is stimulated by the IKVAV.

## Evaluation of Focal Adhesions on PEG-CLP Hydrogels

Both migration and proliferation of cancer cells can be controlled by focal adhesions to the ECM proteins (Provenzano and Keely, 2011; Nagano et al., 2012). To test if there are correlations between the effects of different hydrogels on cell migration, proliferation, and adhesion, we have evaluated the number of focal adhesions formed by cancer cells on PEG-CLP, PEG-CLP-RGD, and PEG-CLP-IKVAV hydrogels. The representative images of the cells after immunostaining for the cytoskeleton protein actin and focal adhesion forming protein vinculin is presented in **Figure 5**. There were many round- or oval-shaped cells on PEG-CLP hydrogels in HROG36 and C6 cell cultures with little actin fibers and small amoeboid lamellipodia. In A375 samples on PEG-CLP hydrogels, the cells were mostly rod-shaped and had parallel organization of actin filaments (**Figure 5C**). The presence of externally extended focal contacts with parallel and unparallel actin stress fibers were best visible on PEG-CLP-RGD hydrogels in all investigated cell types. This was also confirmed by the significantly lower cell shape index on this hydrogel substrate in all investigated cell cultures (**Figure 6B**, Cell shape index). Projected cell area on PEG-CLP-RGD hydrogels compared to PEG-CLP, however, was significantly higher only in both glioma cell cultures (**Figure 6B**, Projected cell area). Morphology of both types of glioma cells was also well defined on PEG-CLP-IKVAV (**Figures 5A,B**). The cells were elongated and had contact points at the ends. Projected cell area for both HROG36 and C6 was significantly higher, and cell shape index significantly lower on PEG-CLP-IKVAV hydrogel compared to PEG-CLP samples (**Figure 6B**). However, for HROG36 the average projected cell area on PEG-CLP-IKVAV was significantly lower compared to that on PEG-CLP-RGD. There was no significant difference in projected cell area between tested hydrogels revealed in A375 experimental group, however, the morphology of actin filaments was visibly less organized on PEG-CLP-IKVAV compared to PEG-CLP (**Figures 5C**, **6B**).

Examination of the size distribution of focal contacts in individual cells revealed the same tendency for HROG36 and C6 cells to make smaller amounts and larger area size contacts on PEG-CLP, increase in number and decrease in contact size on PEG-CLP-IKVAV, and further increase in number/decrease in size on PEG-CLP-RGD (**Figure 6A**). The distribution had completely different characteristics for A375 melanoma cells that made much larger contacts on PEG-CLP-RGD than on PEG-CLP or PEG-CLP-IKVAV.

In all investigated cell types, the number of focal adhesions was similar, ranging from about 10 to 25 in average (**Figure 6B**, Focal contacts per cell). The highest numbers (about 20–30) of focal adhesions were found in HROG36 glioblastoma cells on PEG-CLP-RGD hydrogels and in A375 melanoma cells on PEG-CLP hydrogels. The next slightly lower level of focal contacts (from 13 to 20) was induced to C6 cells by both PEG-CLP-RGD and PEG-CLP-IKVAV and to A375 cells by PEG-CLP-RGD. The lowest amount of focal contacts (from 5 to 15) was found in PEG-CLP-IKVAV cultures of HROG36 and A375 cells, and in PEG-CLP cultures of C6 cells. The differences in focal adhesions within the same cell cultures on different hydrogels were as follows. For HROG36 cell line, the amount of focal contacts per cell was 1.51 times bigger on PEG-CLP-RGD than on PEG-CLP, and 2.33 times bigger than on PEG-CLP-IKVAV. Moreover, the number of focal contacts per cell was 1.54 times bigger on PEG-CLP than on PEG-CLP-IKVAV. The amount of focal contacts per cell in C6 cultures was 1.9 times bigger on PEG-CLP-RGD than on PEG-CLP, and 1.82 times bigger on PEG-CLP-IKVAV than on PEG-CLP. The number of focal contacts per cell of A-375 cells was 1.32 times bigger on PEG-CLP than on PEG-CLP-RGD, and 2.28 times bigger than on PEG-CLP-IKVAV.

Correlations between cell behavior (migration/proliferation) and individual cell morphology/adhesion parameters are presented in **Table 1**. There were strong positive correlations found between the number of focal contacts per cell and the

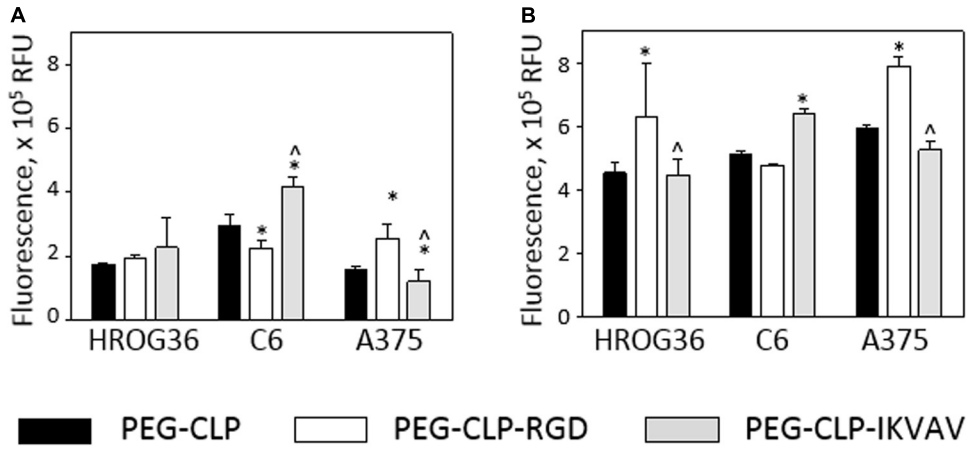


**FIGURE 4 |** Metabolic activity of HROG36, C6, and A375 cells on PEG-CLP, PEG-CLP-RGD, and PEG-CLP-IKVAV hydrogels after 24 h **(A)** and 48 h **(B)**. The metabolic activity of the cells corresponding to the proliferation intensity was assessed by Presto Blue™ assay in three independent experimental sets, each of three replicates. RFU, relative fluorescence units. *Indicates a statistically significant difference compared with the samples of the same cell type grown on CLP-only containing hydrogels, ^-with samples on PEG-CLP-RGD hydrogels, ANOVA with *post hoc* LSD test, $p < 0.05$.

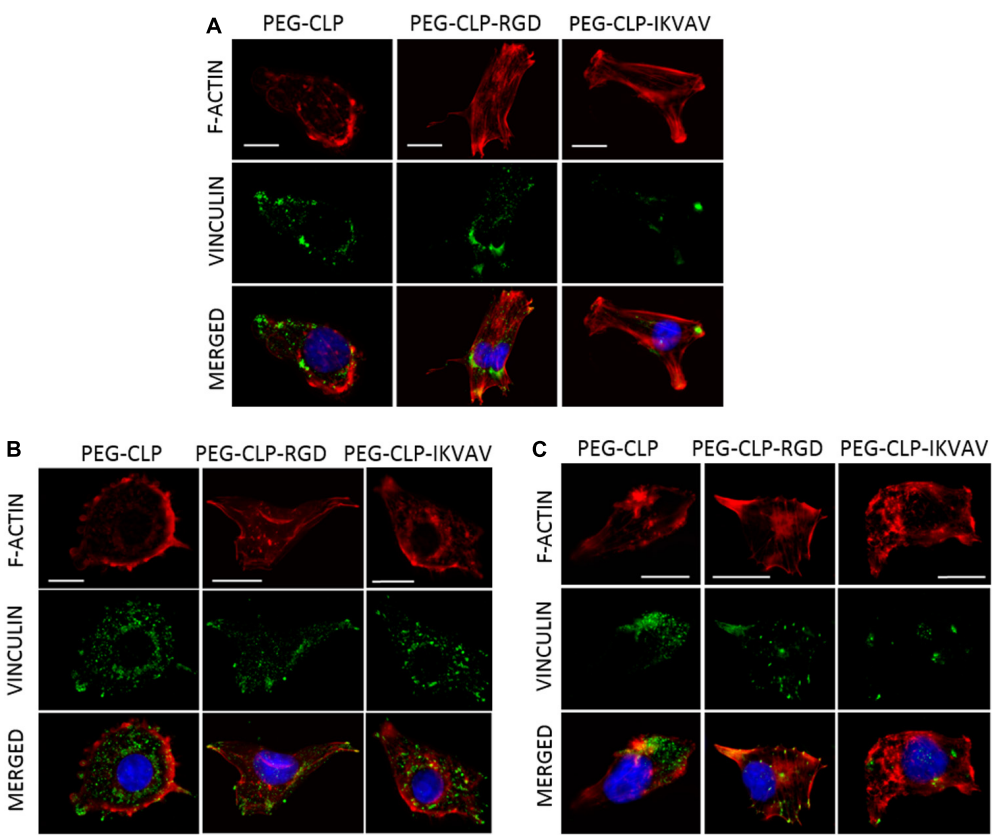


**FIGURE 5 |** Representative images of focal adhesions formed by HROG36 **(A)**, C6 **(B)**, and A375 **(C)** cells on CLP, CLP-RGD, and CLP-IKVAV hydrogels. The cells were immunostained for actin (red signal) and vinculin (green). Nuclei were visualized blue by DAPI. Scale bar is 10 μm.

area covered by cells from the spheroids ($r$ values between 0.81 and 0.98), and number of focal contacts and total cell number ($r$ between 0.91 and 1.00) in all investigated cell types. Both glioma cell lines also demonstrated strong positive correlations between projected individual cell area and area all cells covered due to migration ($r$ values 0.92 and 1.00 for HROG36 and C6 cells, respectively), and between projected cell area and cell number (0.95 and 1.00 for HROG36 and C6, respectively). Only

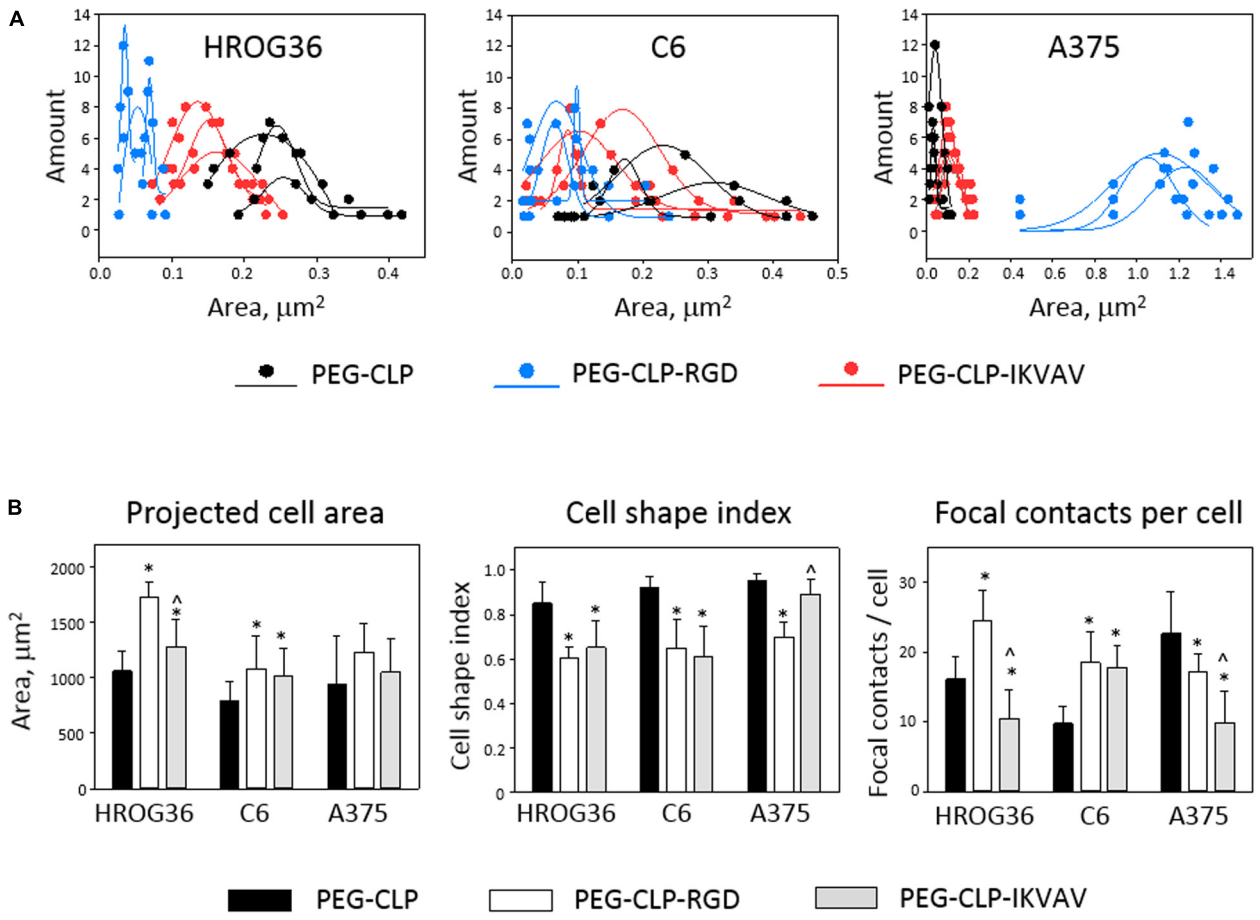


**FIGURE 6 |** Size distribution of individual focal contacts **(A)**, projected cell area, cell shape index, and number of focal contacts **(B)** of HROG36, C6, and A375 cells on PEG-CLP, PEG-CLP-RGD, and PEG-CLP-IKVAV hydrogels. The cells were immunostained for F-actin (red signal) and vinculin (green). Nuclei were visualized blue by DAPI. Size distribution of focal contacts of three cells on each hydrogel was plotted together with approximate distribution curve. Projected cell area and perimeter for cell shape index calculation were measured by ImageJ software. Focal adhesion number per cell was calculated according to the number of vinculin-actin colocalization points. The data are presented as AVG ± SDEV of 5–7 cells from three of each hydrogel sample. *Indicates statistically significant difference compared with the samples of the same cell type grown on PEG-CLP, ∧ – compared with samples on PEG-CLP-RGD. ANOVA with *post hoc* LSD test, $p < 0.05$.

**TABLE 1 |** Correlations between cell adhesion/morphology parameters and cell migration/proliferation.

| Cell type | Focal adhesion/morphology parameter (Figure 6B) | Area covered by cells (Figure 3A) | Cell number (Figure 3B) | Cell per unit area (Figure 3C) | Metabolic activity/ proliferation in 24 h (Figure 4A) | Metabolic activity/ proliferation in 48 h (Figure 4A) |
|---|---|---|---|---|---|---|
| HROG36 | Number of focal contacts per cell | 0.94** | 0.91** | −0.71* | −0.53 | 0.91** |
| | Cell shape index | −0.59* | −0.66* | −0.47 | −0.67* | −0.65* |
| | Projected cell area | 0.92** | 0.95** | −0.04 | 0.19 | 0.95** |
| C6 | Number of focal contacts per cell | 0.98** | 0.99** | −0.96** | −0.03 | 0.27 |
| | Cell shape index | −0.93** | −0.95** | 0.90** | −0.16 | −0.45 |
| | Projected cell area | 1.00** | 1.00** | −0.99** | −0.17 | 0.14 |
| A375 | Number of focal contacts per cell | 0.81** | 0.81** | −0.82** | 0.34 | 0.34 |
| | Cell shape index | −0.46 | −0.46 | 0.44 | −0.88** | −0.88** |
| | Projected cell area | 0.33 | 0.33 | −0.30 | 0.80** | 0.80** |

*The numbers in the table are correlation coefficient r for the two parameters indicated in the upper line and first left column of the table. Strong correlation are indicated by **, and mild correlation by **.*

HROG36 cells showed strong positive correlations between proliferation rate estimated by metabolic activity and number of focal contacts ($r = 0.91$). This correlation was observed only when metabolic activity was assessed after 48 h. Also, in both

human cancer cell line HROG36 and A375 cultures, there was strong positive correlation between projected cell area and metabolic activity/proliferation and projected cell area. For HROG36, this correlation was only when proliferation was monitored after 48 h ($r$ = 0.95), but for A375 the same $r$ = 0.80 correlation was established for both 24 and 48 h proliferation data sets. Both glioma cell lines showed negative correlations between cell shape index values and migration parameters. The correlation was strong for C6 cells (−0.93 and −0.95 for total cell spread area and cell number, respectively), and mild for HROG36 (−0.59 and −0.66). Also, strong negative correlations were found between the number of focal contacts and cell per unit area in C6 ($r$ = −0.96) and A375 ($r$ = −0.82) samples. In addition, a strong negative correlation was found between cell per unit area and projected cell area in C6 cell cultures ($r$ = −0.99). There were no correlations between metabolic activity/proliferation and focal adhesion/morphology parameters in C6 cell line experimental group.

To summarize, there were more similarities between responses of both glioma cell lines to different hydrogels than between any of the glioma lines and A375 melanoma cells. However, there were also several differences found between HROG36 and C6 cell behavior, such as response of proliferation assessed as increase in metabolic activity.

## DISCUSSION

In this study we have investigated the interaction between synthetic PEG-CLP hydrogels, alone and with conjugated cell adhesion peptides RGD or IKVAV, and three cancerous cell lines: human glioblastoma HROG36, rat glioma C6, and human melanoma A375. The background for this research were previous studies on PEG-CLP hydrogels as human corneal implants (Islam et al., 2016) and research performed on primary cerebellar cells grown on PEG-CLP and PEG-CLP-RGD (Balion et al., 2020). In the above-mentioned research, the material was characterized for mechanical properties, circular dichroism spectra, and surface topography (Islam et al., 2016; Balion et al., 2020). It was found that the values of storage modulus G' modulus of the materials were between 0.02 and 0.07 MPa, and the values of elastic (Young) E modulus were between 0.06 and 0.180 MPa, respectively. Both the shear storage and elastic moduli were lower for hydrogels with an additional peptide group attached to PEG-CLP, most likely because of the lower level of triple helical assemblies, as indicated by circular dichroism spectroscopy. The Young modulus values of the hydrogels are found to be the lowest in skin tissue; the latter vary from 0.0001 to 57 MPa, depending on the place on the body, age, and assessment conditions (Joodaki and Panzer, 2018). Regarding the mechanical properties of brain tissue, the Young modulus values reported for gray and white matter are 1.389 ± 0.289 kPa and 1.895 ± 0.592 kPa, respectively (Budday et al., 2015). Thus, the hydrogels of the current study have higher stiffness compared to the natural brain.

A nanometer-scale structure of hydrogel surfaces evaluated by atomic force microscopy (AFM) revealed relatively smooth and densely packed hydrogel surfaces with the surface roughness values measured as root mean square (RMS) between 2.7 ± 1.6 and 4.6 ± 2.8 nm. The data indicated the elastomechanical properties of the material is within the range of soft biological tissue (McKee et al., 2011), and it has the bioactive capacity to organize primary cerebellar cells to functional interconnecting organoids (Balion et al., 2020). Therefore, the idea of the study was to test whether PEG-CLP-based hydrogels might serve as an ECM mimetic to cancerous cell lines. Rat glioma C6 line was chosen as representative of brain astrocytic cancer originated from rats – the same species as cerebellar cells investigated in a previous study. HROG36 cells were selected as representative of highly invasive human glioblastoma, and human melanoma A375 cells were chosen as the other, non-glial human cancerous cell line. One of the reasons to investigate all three cell types under the same conditions was to find out if the cells respond to the peptide clues because such signals are similar to those that melanoma and glioblastoma cells might receive when growing *in vivo*. As the introduction of additional peptide motifs does not make substantial changes in hydrogel mechanical properties, the differences in cell responses between hydrogels should be attributed to the peptide signaling.

The findings of this study support the hypothesis of instructing cells with different ECM peptides. First of all, each cell line behaved in a different manner to hydrogels. In addition, hydrogels of different peptide composition induced distinct responses from the same cell type. Altogether, this suggests that PEG-CLP, PEG-CLP-RGD, and PEG-CLP-IKVAV as matrices provide a bioinstructing ECM-mimicking microenvironment for the cells. Of course, steps have to be taken to investigate the influence of the density of each peptide and their combination, to introduce other ECM molecules such as hyaluronic acid and proteoglycan signaling, and to elaborate their densities, to shape the matrix creating tissue-like structures like capillaries and nerves with the respective topography and biochemistry. Taking into account that PEG-CLP hydrogel is shape-retaining and can be precisely molded at a fine microscale level (Haagdorens et al., 2019), such organ-mimicking micro-shaping might be introduced for further microenvironmental tuning.

Regarding cellular responses on the hydrogels, the study revealed that both cell lines of astrocytic origin HROG36 and C6, as expected, had more same or similar correlations between hydrogel-induced changes of adhesion/morphology parameters and migration/proliferation capacity readouts compared to melanoma A375 cell line. Both C6 and HROG36 migrated better on PEG-CLP-RGD, and migration efficiency correlated to the number of focal contacts, projected cell area, and decrease in cell shape index. However, only human glioblastoma HROG36 cells demonstrated positive correlations between all three parameters and proliferations. Relatively rapidly proliferating rat C6 glioma cells are considered as a golden standard for complementary *in vitro* and *in vivo* glioblastoma modeling (Grobben et al., 2002). The cells share some common features with human glioblastoma, and for this reason are often used as a convenient model, allowing for the combination of *in vitro* and *in vivo* studies, because C6 gliomas can be implanted to laboratory rats and form tumors (Gunnersen et al., 2000; Gieryng et al., 2017). The current results

indicate that C6-based models might have biological responses that differ from the responses of human glioblastoma, thus, the responses obtained on C6-tumors should be tested on at least one human glioblastoma cell line.

Proliferation of both human cancer cell lines HROG36 and A375 was markedly stimulated by PEG-CLP-RGD. The fact it was not revealed in metabolic activity assessment after 24 h on hydrogels might be explained by the fact that average doubling time for HROG36 is from 35 to 40 h (Mullins et al., 2013), thus, 24 h of incubation could be not enough time to reveal the response. A375 cells demonstrated very similar levels of RGD-induced stimulation of proliferation after 24 and 48 h. The cells have the shortest average doubling time (16–20 h), Benga (2001) compared to other cells investigated in the study, thus, the effect of PEG-CLP-conjugated RGD peptide could be revealed both in 24 and 48 h time periods. On the contrary, proliferation of rat glioma C6 cells was not affected by any of the investigated hydrogel matrices, and the doubling rate of those cells (about 16 h), Benda et al. (1968) could not influence this result.

Different proliferation rates of the cells could also interfere with migration results. For HROG36, this would hardly be the case; as we have examined migration for 24 h, the time is far too short for proliferation of these cells to make a noticeable influence. However, this could happen in C6 and A375 experimental groups because the doubling time of those cells is shorter than 24 h. Assessment of proliferation by metabolic activity assay revealed there was no influence of the hydrogels to C6 proliferation. Thus, both C6 and HROG36 cells have spread from the spheroid mostly because of migration. Therefore, both area covered by cells, total cell number, and cells per $mm^2$ count for both glioma cells under these conditions might be assumed as parameters indicating cell migration intensity. Note that only HROG36 cells revealed differences in cells per $mm^2$ between the investigated hydrogel samples, and the highest impact on this factor was made by PEG-CLP-IKVAV. An increase in cells per unit area indicates that cells are prone to migrate onto the matrix and the subsequent attachment to it slows them down and forces them to accumulate. Migration of HROG36 cells was not significantly stimulated by PEG-CLP-IKVAV compared to PEG-CLP, however, two of the three adhesion and morphology parameters (projected cell area and cell shape index) of those cells on PEG-CLP-IKVAV were similar to those on CLP-PEG-RGD, the matrix promoting the highest level of migration. This indicates a different regulatory capacity between RGD and IKVAV promoted adhesion on HROG36 glioblastoma. Although most integrins can recognize several adhesion motifs, the signal they transmit from the contact to the cell might vary (Takada et al., 2007). Even after binding the same motif, the integrins provide distinct responses depending on the RGD-containing ECM protein (vitronectin, fibronectin, fibrinogen, or other) (Kapp et al., 2017). Also, cells, including cancer cells, might have different expressions of site-specific integrins (Frith et al., 2012; Nieberler et al., 2017) and thus, respond in a different manner to these stimuli.

In contrast to the glioma cells, A375 melanoma cells were not stimulated for migration by PEG-CLP-RGD. The migration was even inhibited by PEG-CLP-IKVAV compared to PEG-CLP samples. However, these cells responded to PEG-CLP-RGD by a significant increase in proliferation rate. These data also supports the hypothesis that different cells might have distinct intracellular signaling pathways activated in response to the same ECM stimuli.

Glioblastomas are characterized by their extreme aggressiveness (Hanif et al., 2017) which is in part attributed to binding and responding to the RGD signaling via integrin β8 (Tchaicha et al., 2011). Glioblastoma cells themselves express fibronectin, and this is responsible for their invasiveness (Serres et al., 2014). Fibronectin increases glioma stem-like cell differentiation, proliferation, and chemoresistance via cell adhesion signaling (Yu et al., 2018). Thus, the results of our study are in line with the data of other researchers and confirms PEG-CLP-RGD motif might affect glioblastoma cell behavior related to the invasiveness of this cancer. The size of response of C6 glioma cells was half of that of glioblastoma HROG36 cell line. However, C6 cells were equally responsive to both RGD and IKVAV motifs. IKVAV is shown to induce glioblastoma apoptosis by immobilizing β1-integrin at the cell membrane, activating integrin-linked kinase and inhibiting focal adhesion kinase (Srikanth et al., 2013.). On the other hand, micropatterned blood vessel wall mimicking laminin stimulated migration of both rat C6 glioma cells and human glioma–propagating cells (hGPCs) isolated from a patient via Arp 2/3 and formins (Monzo et al., 2016). Thus, the exact signaling role of laminin and its active sequence in the development of glioma cell invasiveness is yet to be discovered.

Human melanoma cells A375 demonstrated higher focal adhesion number on both PEG-CLP and PEG-CLP-RGD hydrogels compared to PEG-CLP-IKVAV, and higher proliferation on PEG-CLP-RGD. This is in accordance with the recent evidence that fibronectin promotes melanoma proliferation and metastasis by inhibiting apoptosis and regulating epithelial-mesenchymal transition (Li et al., 2019). Interestingly, the changes in focal adhesion size and number per cell in A375 samples was not reflected in the spread area of individual cells. This has to be considered together with the finding that migration of A375 was not so high compared to that of glioma cells. The more prominent response of A375 to different hydrogels was proliferation, thus, the changes in adhesion pattern were mostly related to redistribution of the cytoskeleton during mitosis. This could at least partially explain why the redistribution of the focal adhesions in the cells were not so visible on their projected area. However, adhesion changes correlated well with the changes in cell shape index, indicating that the cells did respond to the contact modulation. Introduction of IKVAV sequence significantly suppressed cell migration and focal adhesion formation, and had no effect on proliferation. This is in contrast to the results obtained by Chung et al., 2011, that extrinsic laminin-332 produced by keratinocytes promotes both adhesion and migration of melanocytes and A375 melanoma cells. Although the authors have tested that soluble factors produced by keratinocytes are not enough to stimulate such migration efficiency, there still might be a possibility of simultaneous action of factors other than laminin. In general, the data about the influence of laminins and their active sequences

to melanoma cell migration are contradictory and requires more detailed studies.

Phelps et al. (2012), have introduced 8- and 4-armed PEG-maleimide-hydrogels as a versatile tool for protein and cell delivery. PEG itself is a bioinert material that can form polymer chains with a defined chemical structure and have end groups that enable cross-linking. Conjugation of CLP to PEG imparts the close proximity between the CLP peptides facilitating the self-assembly, stability, and mechanical strength of the synthetized material (Islam et al., 2016). PEG-RGDS and PEG-PQ-PEG peptide hydrogel was successfully applied to model metastasis of lung adenocarcinoma (Gill et al., 2012). MMP-degradable (KGGGPQG↓IWGQERCG) crosslinking density regulating peptide and non-degradable (KGGGDQGIAGFERCG) PEG-peptide mixed together with incorporated RGD motif containing peptide (QEQVSPL-GRGDSPG) were used to encapsulate drug resistant ovarian cell lines V-MZ-6 and SKOV-3 (Loessner et al., 2010). CRGDS and a matrix metalloproteinase (MMP)-cleavable peptide were chemically incorporated and mixed with hyaluronic acid to make a brain ECM-mimicking environment to study the effects of environmental stiffness on human glioblastoma U87 cell behavior (C. Wang et al., 2014). Also, PEG-CRGDS peptides crosslinked by MMP-controlled peptide chains were designed to investigate the influence of biochemical and biophysical matrix properties on human fibrosarcoma HT-1080 cell migration. The findings of these studies support the importance of the development of hydrogel systems with defined ECM-mimicking cues as a tool for cancer biology research.

Hydrogel systems with encapsulated cells become more and more popular for *in vitro* studies because of their more realistic environmental cues. However, with the advantages come some challenges. For example, the experimental setup is more complicated and time consuming because of hydrogel preparation and the cell encapsulation procedure, the standardization and repeatability of the preparations makes it difficult to compare results provided by different research groups. There is a restriction to some evaluation assays adapted to optically transparent and monolayer cell cultures, and they are not suitable for hydrogel encapsulated cell cultures. In addition, most popular commercially available hydrogel matrices such as Matrigel®, Gelltrex™, and others are cell derived and have undefined and batch-to-batch variable composition. They provide similar to a real tissue environment, but can hardly serve as tools for the examination of what from the environment is signaling to the cells. Taking this into account, in this study, we have decided to apply a crosslinked PEG-CLP hydrogel system that shares some similarities with conventional 2D cell culture methods, such as a smooth horizontal plane and transparency (transmission 92.4 ± 0.95%, backscatter 0.90 ± 0.17%) (Islam et al., 2016), thus allowing for sample monitoring and analysis by all conventional optical assays. Although the hydrogels do not provide spatial distribution of cells in vertical axis, they have an ECM-mimicking surface structure and elastomechanical and chemical properties, making it a possible alternative for *in vitro* cell culture models.

In conclusion, PEG-CLP hydrogels with functional cell adhesion peptide motifs RGD and IKVAV promoted different cell adhesion and morphology behavior that correlated with changes in biological activity in three cancer cell lines. Such hydrogel systems can serve as convenient and informative research models to study the role of environmental factors in tumor invasiveness.

## DATA AVAILABILITY STATEMENT

The datasets generated for this study are available on request to the corresponding author.

## AUTHOR CONTRIBUTIONS

JP designed the peptides sequences and hydrogel synthesis protocol. AV performed the synthesis of peptides and hydrogels. AJ conceived and supervised the cell culture study. ES performed the experiments on HROG36 cells. GS performed the experiments on A375 cells. IS and RB performed the experiments on C6 cells. AM-G performed immunocytochemistry experiments. ZB carried out the confocal imaging and focal adhesion evaluation. All authors participated in the manuscript preparation.

## FUNDING

The study is a part of the EXOTARGET project funded by grant No. 01.2.2-LMT-K-718-01-0036 from the Research Council of Lithuania.

## ACKNOWLEDGMENTS

We acknowledge Ramūnas Valiokas and Vytautas Cėpla from Ferentis UAB for discussion and technical advice.

## REFERENCES

Adams, D. N., Kao, E. Y. C., Hypolite, C. L., Distefano, M. D., Hu, W. S., and Letourneau, P. C. (2005). Growth cones turn and migrate up an immobilized gradient of the laminin IKVAV peptide. *J. Neurobiol.* 62, 134–147. doi: 10.1002/neu.20075

Balion, Z., Cėpla, V., Svirskiene, N., Svirskis, G., Druceikaitė, K., Inokaitis, H., et al. (2020). Cerebellar cells self-assemble into functional organoids on synthetic, chemically crosslinked ECM-Mimicking peptide hydrogels. *Biomolecules* 10:754. doi: 10.3390/biom10050754

Benda, P., Lightbody, J., Sato, G., Levine, L., and Sweet, W. (1968). Differentiated rat glial cell strain in tissue culture. *Science* 161, 370–371. doi: 10.1126/science.161.3839.370

Benga, G. (2001). Basic studies on gene therapy of human malignant melanoma by use of the human interferon βgene entrapped in cationic multilamellar liposomes. 1. Morphology and growth rate of six melanoma cell lines used in

transfection experiments with the human interferon βgene. *J. Cell. Mol. Med.* 5, 402–408. doi: 10.1111/j.1582-4934.2001.tb00175.x

Berrier, A. L., and Yamada, K. M. (2007). Cell–matrix adhesion. *J. Cell. Physiol.* 213, 565–573. doi: 10.1002/jcp.21237

Budday, S., Nay, R., de Rooij, R., Steinmann, P., Wyrobek, T., Ovaert, T. C., et al. (2015). Mechanical properties of gray and white matter brain tissue by indentation. *J. Mech. Behav. Biomed. Mater.* 46, 318–330. doi: 10.1016/j.jmbbm.2015.02.024

Chung, H., Suh, E. K., Han, I. O., and Oh, E. S. (2011). Keratinocyte-derived laminin-332 promotes adhesion and migration in melanocytes and melanoma. *J. Biol. Chem.* 286, 13438–13447. doi: 10.1074/jbc.M110.166751

Colognato, H., and Yurchenco, P. D. (2000). Form and function: the laminin family of heterotrimers. *Dev. Dyn.* 218, 213–234. doi: 10.1002/(SICI)1097-0177(200006)218:2<213::AID-DVDY1<3.0.CO;2-R

Cornhill, J. F., Levesque, M. J., Herderick, E. E., Nerem, R. M., Kilman, J. W., and Vasko, J. S. (1980). Quantitative study of the rabbit aortic endothelium using vascular casts. *Atherosclerosis* 35, 321–337. doi: 10.1016/0021-9150(80)90130-6

Czekanska, E. M. (2011). Assessment of cell proliferation with resazurin-based fluorescent dye. *Methods Mol. Biol.* 740, 27–32. doi: 10.1007/978-1-61779-108-6_5

Drury, J. L., and Mooney, D. J. (2003). Hydrogels for tissue engineering: scaffold design variables and applications. *Biomaterials* 24, 4337–4351. doi: 10.1016/S0142-9612(03)00340-5

Friedl, P., and Alexander, S. (2011). Cancer invasion and the microenvironment: plasticity and reciprocity. *Cell* 147, 992–1009. doi: 10.1016/j.cell.2011.11.016

Frith, J. E., Mills, R. J., Hudson, J. E., and Cooper-White, J. J. (2012). Tailored integrin-extracellular matrix interactions to direct human mesenchymal stem cell differentiation. *Stem Cells Dev.* 21, 2442–2456. doi: 10.1089/scd.2011.0615

Gieryng, A., Pszczolkowska, D., Bocian, K., Dabrowski, M., Rajan, W. D., Kloss, M., et al. (2017). Immune microenvironment of experimental rat C6 gliomas resembles human glioblastomas. *Sci. Rep.* 7:17556. doi: 10.1038/s41598-017-17752-w

Gill, B. J., Gibbons, D. L., Roudsari, L. C., Saik, J. E., Rizvi, Z. H., Roybal, J. D., et al. (2012). A synthetic matrix with independently tunable biochemistry and mechanical properties to study epithelial morphogenesis and EMT in a lung adenocarcinoma model. *Cancer Res.* 72, 6013–6023. doi: 10.1158/0008-5472.CAN-12-0895

Grobben, B., De Deyn, P. P., and Slegers, H. (2002). Rat C6 glioma as experimental model system for the study of glioblastoma growth and invasion. *Cell Tissue Res.* 310, 257–270. doi: 10.1007/s00441-002-0651-7

Gunnersen, J. M., Spirkoska, V., Smith, P. E., Danks, R. A., and Tan, S. (2000). Growth and migration markers of rat C6 glioma cells identified by serial analysis of gene expression. *Glia* 32, 146–154. doi: 10.1002/1098-1136(200011)32:2<146::AID-GLIA40<3.0.CO;2-3

Haagdorens, M., Cėpla, V., Melsbach, E., Koivusalo, L., Skottman, H., Griffith, M., et al. (2019). In vitro cultivation of limbal epithelial stem cells on surface-modified crosslinked collagen scaffolds. *Eng. Cell Syst.* 2019, 1–17. doi: 10.1155/2019/7867613

Hanif, F., Muzaffar, K., Perveen, K., Malhi, S. M., and Simjee, S. U. (2017). Glioblastoma multiforme: a review of its epidemiology and pathogenesis through clinical presentation and treatment. *Asian Pacific J. Cancer Prev.* 18, 3–9. doi: 10.22034/APJCP.2017.18.1.3

Hern, D., and Hubbell, J. (1998). Incorporation of adhesion peptides into nonadhesive hydrogels useful for tissue resurfacing. *J. Biomed. Mater. Res* 39, 266–276. doi: 10.1002/(SICI)1097-4636(199802)39:2<266::AID-JBM14<3.0.CO;2-B

Huettner, N., Dargaville, T. R., and Forget, A. (2018). Discovering cell-adhesion peptides in tissue engineering: beyond RGD. *Trends Biotechnol.* 36, 372–383. doi: 10.1016/j.tibtech.2018.01.008

Hynes, R. O. (2004). The emergence of integrins: a personal and historical perspective. *Matrix Biol.* 23, 333–340. doi: 10.1016/j.matbio.2004.08.001

Ingber, D. E. (2003). Mechanosensation through integrins: cells act locally but think globally. *Proc. Natl. Acad. Sci. U.S.A.* 100, 1472–1474. doi: 10.1073/pnas.0530201100

Islam, M. M., Buznyk, O., Reddy, J. C., Pasyechnikova, N., Alarcon, E. I., Hayes, S., et al. (2018). Biomaterials-enabled cornea regeneration in patients at high risk for rejection of donor tissue transplantation. *npj Regen. Med.* 3:2. doi: 10.1038/s41536-017-0038-8

Islam, M. M., Ravichandran, R., Olsen, D., Ljunggren, M. K., Fagerholm, P., Lee, C. J., et al. (2016). Self-assembled collagen-like-peptide implants as alternatives to human donor corneal transplantation. *RSC Adv.* 6, 55745–55749. doi: 10.1039/c6ra08895c

Joodaki, H., and Panzer, M. B. (2018). Skin mechanical properties and modeling: a review. *Proc. Inst. Mech. Eng. H.* 232, 323–343. doi: 10.1177/0954411918759801

Kapp, T. G., Rechenmacher, F., Neubauer, S., Maltsev, O. V., Cavalcanti-Adam, E. A., Zarka, R., et al. (2017). A comprehensive evaluation of the activity and selectivity profile of ligands for RGD-binding integrins. *Sci. Rep.* 7, 1–13. doi: 10.1038/srep39805

Kim, D. H., and Wirtz, D. (2013). Focal adhesion size uniquely predicts cell migration. *FASEB J.* 27, 1351–1361. doi: 10.1096/fj.12-220160

Li, B., Shen, W., Peng, H., Li, Y., Chen, F., Zheng, L., et al. (2019). Fibronectin 1 promotes melanoma proliferation and metastasis by inhibiting apoptosis and regulating EMT. *Onco. Targets. Ther.* 12, 3207–3221. doi: 10.2147/ott.s195703

Loessner, D., Stok, K. S., Lutolf, M. P., Hutmacher, D. W., Clements, J. A., and Rizzi, S. C. (2010). Bioengineered 3D platform to explore cell-ECM interactions and drug resistance of epithelial ovarian cancer cells. *Biomaterials* 31, 8494–8506. doi: 10.1016/j.biomaterials.2010.07.064

Luo, T., and Kiick, K. L. (2013). Collagen-like peptides and peptide-polymer conjugates in the design of assembled materials. *Eur. Polym. J.* 49, 2998–3009. doi: 10.1016/j.eurpolymj.2013.05.013

McKee, C. T., Last, J. A., Russell, P., and Murphy, C. J. (2011). Indentation versus tensile measurements of young's modulus for soft biological tissues. *Tissue Eng. Part B Rev.* 17, 155–164. doi: 10.1089/ten.teb.2010.0520

Monzo, P., Chong, Y. K., Guetta-Terrier, C., Krishnasamy, A., Sathe, S. R., Yim, E. K. F., et al. (2016). Mechanical confinement triggers glioma linear migration dependent on formin FHOD3. *Mol. Biol. Cell* 27, 1246–1261. doi: 10.1091/mbc.E15-08-0565

Mostafavi-Pour, Z., Askari, J. A., Parkinson, S. J., Parker, P. J., Ng, T. T. C., and Humphries, M. J. (2003). Integrin-specific signaling pathways controlling focal adhesion formation and cell migration. *J. Cell Biol.* 161, 155–167. doi: 10.1083/jcb.200210176

Mullins, C. S., Schneider, B., Stockhammer, F., Krohn, M., Classen, C. F., and Linnebacher, M. (2013). Establishment and characterization of primary glioblastoma cell lines from fresh and frozen material: a detailed comparison. *PLoS One* 8:e0071070. doi: 10.1371/journal.pone.0071070

Nagano, M., Hoshino, D., Koshikawa, N., Akizawa, T., and Seiki, M. (2012). Turnover of focal adhesions and cancer cell migration. *Int. J. Cell Biol.* 2012:310616. doi: 10.1155/2012/310616

Nemir, S., Hayenga, H. N., and West, J. L. (2010). PEGDA hydrogels with patterned elasticity: novel tools for the study of cell response to substrate rigidity. *Biotechnol. Bioeng.* 105, 636–644. doi: 10.1002/bit.22574

Nieberler, M., Reuning, U., Reichart, F., Notni, J., Wester, H. J., Schwaiger, M., et al. (2017). Exploring the role of RGD-recognizing integrins in cancer. *Cancers* 9:116. doi: 10.3390/cancers9090116

Nissinen, L., Koivunen, J., Käpylä, J., Salmela, M., Nieminen, J., Jokinen, J., et al. (2012). Novel α2β1 integrin inhibitors reveal that integrin binding to collagen under shear stress conditions does not require receptor preactivation. *J. Biol. Chem.* 287, 44694–44702. doi: 10.1074/jbc.M111.309450

Nomizu, M., Weeks, B. S., Weston, C. A., Kim, W. H., Kleinman, H. K., and Yamada, Y. (1995). Structure-activity study of a laminin α1 chain active peptide segment Ile-Lys-Val-Ala-Val (IKVAV). *FEBS Lett.* 365, 227–231. doi: 10.1016/0014-5793(95)00475-O

O'Leary, L. E. R., Fallas, J. A., Bakota, E. L., Kang, M. K., and Hartgerink, J. D. (2011). Multi-hierarchical self-assembly of a collagen mimetic peptide from triple helix to nanofibre and hydrogel. *Nat. Chem.* 3, 821–828. doi: 10.1038/nchem.1123

Oxford, J. T., Reeck, J. C., and Hardy, M. J. (2019). Extracellular matrix in development and disease. *Int. J. Mol. Sci.* 20:205. doi: 10.3390/ijms20010205

Paolillo, M., and Schinelli, S. (2019). Extracellular matrix alterations in metastatic processes. *Int. J. Mol. Sci.* 20:4947. doi: 10.3390/ijms20194947

Papalazarou, V., Salmeron-Sanchez, M., and Machesky, L. M. (2018). Tissue engineering the cancer microenvironment—challenges and opportunities. *Biophys. Rev.* 10, 1695–1711. doi: 10.1007/s12551-018-0466-8

Parsons, J. T., Horwitz, A. R., and Schwartz, M. A. (2010). Cell adhesion: integrating cytoskeletal dynamics and cellular tension. *Nat. Rev. Mol. Cell Biol.* 11, 633–643. doi: 10.1038/nrm2957

Phelps, E. A., Enemchukwu, N. O., Fiore, V. F., Sy, J. C., Murthy, N., Sulchek, T. A., et al. (2012). Maleimide cross-linked bioactive PEG hydrogel exhibits improved reaction kinetics and cross-linking for cell encapsulation and in situ delivery. *Adv. Mater.* 24, 64–70. doi: 10.1002/adma.201103574

Pierschbacher, M. D., and Ruoslahti, E. (1984). Cell attachment activity of fibronectin can be duplicated by small synthetic fragments of the molecule. *Nature* 309, 30–33. doi: 10.1038/309030a0

Provenzano, P. P., and Keely, P. J. (2011). Mechanical signaling through the cytoskeleton regulates cell proliferation by coordinated focal adhesion and Rho GTPase signaling. *J. Cell Sci.* 124, 1195–1205. doi: 10.1242/jcs.067009

Rowley, J. A., and Mooney, D. J. (2002). Alginate type and RGD density control myoblast phenotype. *J. Biomed. Mater. Res.* 60, 217–223. doi: 10.1002/jbm.1287

Serres, E., Debarbieux, F., Stanchi, F., Maggiorella, L., Grall, D., Turchi, L., et al. (2014). Fibronectin expression in glioblastomas promotes cell cohesion, collective invasion of basement membrane in vitro and orthotopic tumor growth in mice. *Br. Dent. J.* 217, 3451–3462. doi: 10.1038/onc.2013.305

Shoulders, M. D., and Raines, R. T. (2009). Collagen Structure and Stability. *Annu. Rev. Biochem.* 78, 929–958. doi: 10.1146/annurev.biochem.77.032207.120833

Smith, L. R., Cho, S., and Discher, D. E. (2018). Stem cell differentiation is regulated by extracellular matrix mechanics. *Physiology* 33, 16–25. doi: 10.1152/physiol.00026.2017

Srikanth, M., Das, S., Berns, E. J., Kim, J. I., Stupp, S., and Kessler, J. A. (2013). Nanofiber-mediated inhibition of focal adhesion kinase sensitizes glioma stemlike cells to epidermal growth factor receptor inhibition. *Neuro Oncol.* 15, 319–329. doi: 10.1093/neuonc/nos316

Takada, Y., Ye, X., and Simon, S. (2007). The integrins. *Genome Biol.* 8:215. doi: 10.1186/gb-2007-8-5-215

Tchaicha, J. H., Reyes, S. B., Shin, J., Hossain, M. G., Lang, F. F., and McCarty, J. H. (2011). Glioblastoma angiogenesis and tumor cell invasiveness are differentially regulated by β8 integrin. *Cancer Res.* 71, 6371–6381. doi: 10.1158/0008-5472.CAN-11-0991

Tibbitt, M. W., and Anseth, K. S. (2009). Hydrogels as extracellular matrix mimics for 3D cell culture. *Biotechnol. Bioeng.* 103, 655–663. doi: 10.1002/bit.22361

Wall, S. T., Yeh, C. C., Tu, R. Y. K., Mann, M. J., and Healy, K. E. (2010). Biomimetic matrices for myocardial stabilization and stem cell transplantation. *J. Biomed. Mater. Res. Part A* 95, 1055–1066. doi: 10.1002/jbm.a.32904

Wang, C., Tong, X., and Yang, F. (2014). Bioengineered 3D brain tumor model to elucidate the effects of matrix stiffness on glioblastoma cell behavior using peg-based hydrogels. *Mol. Pharm.* 11, 2115–2125. doi: 10.1021/mp5000828

Worthington, P., Pochan, D. J., and Langhans, S. A. (2015). Peptide hydrogels - versatile matrices for 3D cell culture in cancer medicine. *Front. Oncol.* 5:92. doi: 10.3389/fonc.2015.00092

Yu, Q., Xue, Y., Liu, J., Xi, Z., Li, Z., and Liu, Y. (2018). Fibronectin promotes the malignancy of glioma stem-like cells via modulation of cell adhesion, differentiation, proliferation and chemoresistance. *Front. Mol. Neurosci.* 11:130. doi: 10.3389/fnmol.2018.00130

Yuan, Y., Jiang, Y. C., Sun, C. K., and Chen, Q. M. (2016). Role of the tumor microenvironment in tumor progression and the clinical applications (Review). *Oncol. Rep.* 35, 2499–2515. doi: 10.3892/or.2016.4660

Zamir, E., Katz, B. Z., Aota, S. I., Yamada, K. M., Geiger, B., and Kam, Z. (1999). Molecular diversity of cell-matrix adhesions. *J. Cell Sci.* 112, 1655–1669.

**Conflict of Interest:** The CLP hydrogel matrix technology described in this manuscript is disclosed in Ferentis UAB patent applications GB1506316.7, WO2016/165788. AM-G and AV were employed by the company Ferentis UAB.

The remaining authors declare that the research was conducted in the absence of any commercial or financial relationships that could be construed as a potential conflict of interest.

The handling editor declared a past co-authorship with one of the authors AJ.

frontiers in Bioengineering and Biotechnology

ORIGINAL RESEARCH
published: 23 October 2020
doi: 10.3389/fbioe.2020.554565

# Proliferation and Osteogenic Differentiation of hMSCs on Biomineralized Collagen

*Daniel de Melo Pereira, Maria Eischen-Loges, Zeinab Tahmasebi Birgani and Pamela Habibovic**

*Department of Instructive Biomaterials Engineering, MERLN Institute for Technology-Inspired Regenerative Medicine, Maastricht University, Maastricht, Netherlands*

Biomineralized collagen with intrafibrillar calcium phosphate mineral provides an excellent mimic of the composition and structure of the extracellular matrix of bone, from nano- to micro-scale. Scaffolds prepared from this material have the potential to become the next-generation of synthetic bone graft substitutes, as their unique properties make them closer to the native tissue than synthetic alternatives currently available to clinicians. To understand the interaction between biomineralized collagen and cells that are relevant in the context of bone regeneration, we studied the growth and osteogenic differentiation of bone marrow derived human mesenchymal stromal cells (hMSCs) cultured on biomineralized collagen membranes, and compared it to the cell behavior on collagen membranes without mineral. Cells proliferated normally on both biomimetic membranes, and were more triggered to differentiate toward the osteogenic lineage by the biomineralized collagen. This was shown by the elevated mRNA levels of RUNX2, SPP1, ENPP1, and OCN after 3 days of culture, and COL1A1 after 14 days of culture on mineralized collagen. The mRNA levels of the tested markers of osteogenesis were lower on collagen membranes without mineral, with the exception of OCN, which was more highly expressed on collagen than on biomineralized collagen membranes. Expression by hMSCs of OPG, a gene involved in inhibition of osteoclastogenesis, was higher on biomineralized collagen at day 3, while M-CSF, involved in osteoblast-osteoclast communication, was upregulated on both membranes at day 3 and 14 of culture. Alkaline phosphatase activity of hMSCs was high on both biomimetic membranes when compared with cells cultured on tissue culture plastic. Cell-induced mineralization was observed on collagen membranes, while the high mineral content of the biomineralized membranes prohibited a reliable analysis of cell-induced mineralization on these membranes. In conclusion, we have identified that both collagen and biomineralized collagen support proliferation, osteogenic differentiation and mineralization of hMSCs, with biomineralized membranes having a more pronounced positive effect. These findings support the existing evidence that biomineralized collagen is a promising material in the field of bone regeneration.

**Keywords: biomineralization, intrafibrillar, osteogenesis, hMSC, bone regeneration, graft substitute**

OPEN ACCESS

***Edited by:***
*Andrea Cochis,*
*University of Eastern Piedmont, Italy*

***Reviewed by:***
*Agata Przekora,*
*Medical University of Lublin, Poland*
*Michela Bosetti,*
*University of Eastern Piedmont, Italy*

****Correspondence:***
*Pamela Habibovic*
*p.habibovic@maastrichtuniversity.nl*

***Specialty section:***
*This article was submitted to Biomaterials, a section of the journal Frontiers in Bioengineering and Biotechnology*

***Received:*** *07 May 2020*
***Accepted:*** *05 October 2020*
***Published:*** *23 October 2020*

***Citation:***
*de Melo Pereira D, Eischen-Loges M, Birgani ZT and Habibovic P (2020) Proliferation and Osteogenic Differentiation of hMSCs on Biomineralized Collagen. Front. Bioeng. Biotechnol. 8:554565. doi: 10.3389/fbioe.2020.554565*

## INTRODUCTION

In the field of bone repair and regeneration, there is a growing need for alternatives to autologous bone transplant as the standard of care. A biomaterial that is able to promote bone growth and regeneration of the injury site, at least as efficiently as autologous bone, is highly desirable. The two main advantages would be increased availability offered by a synthetic biomaterial, and elimination of complications associated with harvesting of bone tissue for transplantation (Calori et al., 2014; Babbi et al., 2016).

A majority of commonly used synthetic bone graft substitutes in the clinic are calcium phosphate (CaP) ceramics, or composites of a CaP ceramic with an organic component, often collagen (Kurien et al., 2013; Tertuliano and Greer, 2016; Baldwin et al., 2019). Such composite biomaterials are similar in composition to the extracellular matrix (ECM) of bone, which consists of about 65 wt% inorganic matrix (hydroxyapatite – HA), 25 wt% organic matrix (mostly collagen type I) and 10% water (Olszta et al., 2007). However, they do not completely replicate the organized hierarchical structure of bone, which, in addition to the composite nature, is known to contribute to the unique mechanical properties of bone (Li and Aparicio, 2013; Reznikov et al., 2018). The structural organization of bone at different length scales comes as a natural source of inspiration for designing materials with potential to become next-generation synthetic bone graft substitutes.

Several attempts have been made to bridge the current gap between synthetic bone graft substitutes and native bone tissue, by replicating the organic-inorganic structure of bone from sub-micrometer to centimeter level (de Melo Pereira and Habibovic, 2018). The replication of the base unit of the bone ECM is of particular interest, as it potentially allows the bottom-up building of larger biomimetic constructs. The building block of bone ECM consists of collagen fibrils with high content ($\geq$65 wt%) of intrafibrillar mineral, specifically nano HA crystals with their c-axis aligned along the collagen fibril length (Olszta et al., 2007). Intrafibrillary mineralized collagen materials can be prepared *in vitro* (Li et al., 2011), via a mineralization method that typically involves one or more charged polymers. These polymers act *in vitro* as analogs of non-collagenous proteins present in the native ECM of bone. They effectively inhibit homogeneous crystallization, i.e., crystallization in solution, forming amorphous CaP-polymer complexes, and promoting mineralization primarily inside the ordered nanostructure of collagen type I fibers (Nudelman et al., 2010, 2012; Habraken et al., 2013).

The potential of biomineralized collagen as the basis for novel bone graft substitutes is evidenced by several studies that investigated this biomaterial in the context of induction of osteogenic differentiation *in vitro* and regeneration of bone defects *in vivo*. A few studies have looked at the extent of osteogenic differentiation of osteoblast-like cell lines (Liu et al., 2014; Wang et al., 2016), mouse (Jiao et al., 2015), or rat MSCs (Wang et al., 2018; Zhang et al., 2018), induced by biomaterials containing biomineralized collagen in their composition. With respect to the application of these materials in the context of bone regeneration, however, more relevant information can be obtained from studies with primary human cells which, though limited in number and using diverse experimental designs and cell types, all have the common denominator of having a scaffold composed of collagen with intrafibrillar mineral and studying the osteogenic differentiation of multipotent cells.

HMSCs were embedded in a collagen gel that was biomineralized with an adapted PILP method, using milk osteopontin as process-directing agent to obtain intrafibrillar as well as extrafibrillar apatite mineral. Gene expression analysis showed that cells within mineralized gels had similar or higher mRNA expression of runt-related transcription factor 2 (RUNX2), osteocalcin (OCN), podoplanin (PDPN) and dentin matrix protein 1 (DMP1), than cells encapsulated in a non-mineralized gel, and moreover that OCN, PDPN, and DMP1 were expressed at levels comparable to or higher than gel-encapsulated cells cultured with osteogenic induction medium. Protein quantification showed that the mineralized collagen gel induced cells to express a higher RANK-L to OPG ratio than either the un-mineralized gel or the osteogenic induction medium, showing the potential for this material to modulate the communication between osteoblast and osteoclast precursors (Thrivikraman et al., 2019).

In a study using periodontal ligament stem cells, increased expression of osteopontin, or secreted phosphoprotein 1 (SPP1), collagen type I (COL1A1), and bone morphogenetic protein 2 (BMP2) was shown after 7 and 14 days of culture on collagen with intrafibrillar mineral versus unmineralized collagen and collagen with extrafibrillar mineral controls. There was also an increased production of mineral nodules (Fu et al., 2016).

Umbilical cord-derived MSCs cultured on scaffolds made of biomineralized collagen showed alkaline phosphatase (ALP) activity similar to cells cultured in the established osteogenic differentiation medium on tissue culture plastic. The scaffolds were implanted in a rabbit femur defect model (Ø8 × 6 mm), showing almost complete healing after 12 weeks (Ye et al., 2016).

A scaffold composed of nano-HA, collagen and poly-L-lactic acid induced osteogenic differentiation of hMSCs, with upregulation of BMP2, COL1A1 and Cathepsin-K (CTSK), shown by microarray analysis (Xu et al., 2016). This biomaterial was also used to repair calcaneal fractures in human patients, where a comparison with autologous bone graft showed no difference in clinical outcome. Seven out of 24 patients had harvest-related complications after 12 months, which is avoidable with the use of synthetic a bone graft substitute (Lian et al., 2013). However, it is not entirely clear whether intrafibrillar mineral was present in this material (Liao et al., 2004). While these few studies show the potential for biomineralized collagen to induce osteogenic differentiation, as well as promising bone defect healing capacity, knowledge about if and how biomineralized collagen triggers osteogenic differentiation is by no means complete. More knowledge of differentiation processes triggered by this biomimetic material and how they relate to osteoinduction *in vivo* is

needed to ultimately develop more effective synthetic bone graft substitutes.

In this study, we applied a recognized method for producing biomineralized collagen membranes, and used this material to study the osteogenic differentiation of bone marrow-derived hMSCs. We looked into mRNA expression of early and late markers of osteogenesis and as well as markers involved in osteoblast-osteoclast communication. Furthermore, we characterized the cells regarding their ALP activity and capacity for mineralization.

# MATERIALS AND METHODS

## Materials

PureCol® collagen type I solution (col-I, 3 mg/mL, 97% bovine dermal type I atelo-collagen) was purchased from Advanced BioMatrix (California, United States, cat# 5005). Poly-L-aspartic acid sodium salt (pAsp, Mw = 27 kDa) was purchased from Alamanda Polymers (Alabama, United States, cat# 000-D200). 1-Ethyl-3-[3-dimethylaminopropyl] carbodiimide hydrochloride (EDC), *N*-hydroxysulfosuccinimide (sulfo-NHS), calcium chloride dihydrate, potassium phosphate dibasic, and all other chemicals were purchased from Sigma-Aldrich (Missouri, United States).

## Preparation of Collagen Membranes

Dense collagen films were prepared in a sterile environment according to the process described by Li et al. (2011), with some modifications. Briefly, the collagen solution, 10 × phosphate buffered saline (PBS) and 0.1 M NaOH were mixed in a volume fraction of, respectively, 0.706, 0.176, and 0.118, yielding a final collagen concentration of 2.1 mg/mL. Gels of 2 mL were formed in up-facing 5 mL syringes with the tip cut off (Sigma-Aldrich, cat# Z248010), at 37°C for 24 h. The syringes containing the gels were inverted on top of nylon meshes of 40 μm pore size (Fischer Scientific, Massachusetts, United States, cat# 11587522) and left at 37°C for 48 h to make the gels loose water under their own weight. After this compression step, syringes were removed, collagen membranes were washed with PBS and cross-linked with 50 mM EDC, 25 mM sulfo-NHS in 50 mM 4-Morpholineethanesulfonic acid (MES) buffer (pH = 7.0), overnight at room temperature. The following day, gels were washed with PBS and incubated with 0.1 M $Na_2HPO_4$ and 2 M NaCl for 2 h, to quench the remaining activated carboxylic acid residues. The membranes were washed three times with PBS for 2 h. Membranes were then mineralized or kept in PBS at 4°C for maximum 1 week.

## Mineralization of Collagen Membranes

Mineralization solution was prepared according to the polymer-induced liquid precursor (PILP) method (Li et al., 2011). Briefly, stock solutions of calcium (9 mM $CaCl_2$) and phosphate (4.2 mM $K_2HPO_4$) were prepared in a buffer with 50 mM TRIS base, 150 mM NaCl, with a pH of 7.8 at room temperature. Prior to incubation, pAsp was added to the calcium solution, mixed and let rest for 5 min, followed by addition of the same volume of phosphate precursor solution. The final concentration of pAsp was 100 μg/mL. After mixing the two precursor solutions, the col-I membranes were added (40 mL of solution was used per membrane) and incubated in a water bath at 37°C for 7 days. Before cell culture, membranes were punched with a 10 mm metal puncher for culture in 48-well plates. Collagen or biomineralized collagen membranes were washed with PBS and incubated in cell culture medium for 3–4 h, prior to cell culture. All steps were performed in a sterile environment.

## Cell Culture

Human mesenchymal stromal cells were isolated from bone marrow aspirates (Booth et al., 2007; Fernandes et al., 2010) obtained from one donor, who has given written informed consent. After isolation, the cells were seeded at a density of 1,500 cells/cm$^2$ in tissue culture T-flasks, and expanded in growth medium (GM), consisting of α-MEM without nucleotides and with Glutamax$^{TM}$ (Thermo Fisher Scientific, cat# 32561), supplemented with 10 v/v% fetal bovine serum (Sigma-Aldrich, cat# F7524, batch# BCBT6987), and 20 mM ascorbic acid (Sigma-Aldrich, cat# A8960). Osteogenic differentiation medium (OM) was prepared by supplementing GM with 100 nM dexamethasone (Sigma-Aldrich, cat# D8893). Mineralization medium (MM) was prepared by supplementing OM with 10 mM β-glycerophosphate (Sigma-Aldrich cat# 50020). Cells were cultured in standard conditions of 37°C in a humidified atmosphere with 5% $CO_2$, and medium was replaced every 2 or 3 days. Upon reaching 70–80% confluence, the cell layer was washed with warm PBS and detached using a 0.05% trypsin-EDTA solution (Thermo Fisher Scientific, cat# 253000) until detachment was visible under a light microscope, up to a maximum of 5 min. Trypsin was neutralized with addition of GM, the cell suspension was centrifuged at 300 rcf for 5 min and re-suspended in GM. Cells were counted with a haemocytometer and dilution of the cell suspension was made according to the seeding densities required.

For quantification of DNA and ALP activity, which were performed on the same set of samples, cells were seeded at a density of 10.000 cell/cm$^2$ in 48-well plates on collagen or biomineralized collagen, with tissue culture plastic (TCP) as a control. Cells on TCP were cultured in GM or OM, while on both types of membranes, the culture was performed in GM only. There were six replicates per condition. At each time point (3, 7, 14, and 21 days), medium was aspirated and samples washed with warm PBS. All PBS was removed and the plate was kept at −80°C until further analysis.

The same seeding and sample handling was performed for the quantitative real-time polymerase chain reaction (qRT-PCR) experiment, at 3, 7, and 14 days, also with 6 replicates per condition.

## DNA Quantification

Total content of nucleic acid, i.e., cell DNA, per sample was quantified with the Cyquant$^{TM}$ kit (Thermo Fisher Scientific, cat# C7026) following the manufacturer's instructions. Briefly, frozen plates were thawed and collagen and mineralized collagen membranes were transferred to new plates. Lysis buffer from

the kit was added to each well (300 μL) and two more freeze-thaw cycles were done. Subsequently, samples were placed on ice in a ultrasonic water bath for 30 min. Cell lysates were collected and transferred to micro centrifuge tubes, spun down for 10 s and 100 μL of the supernatant transferred to clear bottom black 96-well plates, with technical duplicates. The dye-containing buffer was added (2× concentrated, 100 μL) and plates were incubated at room temperature for 5 min in the dark. Fluorescence measurements were made with a CLARIOstar Plus microplate reader (BGM Labtech, Germany) with excitation and emission wavelength of 485 ± 10 and 530 ± 10 nm, respectively. A standard curve of known cell numbers vs. fluorescence intensity was prepared from the same cell suspension used in the experiment, i.e., 11, 22, 33, 44, and 110k cells in 48-well plate, frozen after 6 h in culture. Total cell number per condition was calculated by subtracting the blank fluorescence reading, i.e., dye-containing lysis buffer, from each measurement, and converting fluorescence to cell number with the standard curve. The results are presented as mean and standard deviation of the biological replicates.

## Quantitative Real-Time Polymerase Chain Reaction (qRT-PCR)

Samples were collected in TRIzol Reagent (Thermo Fisher Scientific). Extraction of RNA was performed using the phenol-chloroform method and purification was done using the RNeasy Minikit (QUIAGEN, Germany), in accordance with the manufacturer's recommendations. The extracted RNA of biological replicates were pooled in groups of 2, in order to increase the RNA quantity in each sample, resulting in 3 replicates per condition. RNA purity and quantity were determined using a BioDrop μLITE instrument (BioDrop, United Kingdom). For each sample, 250 ng of RNA were reverse transcribed into cDNA using iScript cDNA Synthesis Kit (Bio-Rad, CA, United States) following manufacturer's instructions. Amplification of cDNA (20 ng) by qRT-PCR was performed on a CFX96 Real-Time PCR Detection System (Bio-Rad) using the iQ SYBR Green Supermix for qPCR (Bio-Rad). Transcription levels of osteogenic biomarkers including runt-related transcription factor 2 (RUNX2), SPP1, ALP, COL1A1, osteocalcin (OCN), Ectonucleotide Pyrophosphatase/Phosphodiesterase 1 (ENPP1) as well as osteoclast modulatory biomarkers including receptor activator of nuclear factor kappa-B ligand (RANKL), osteoprotegerin (OPG) and macrophage colony-stimulating factor (MCSF), were determined. Primer sequences for each marker can be found in **Table 1**. Fold expression values were determined using ΔΔCt method after normalizing each target gene with respect to the housekeeping gene (GAPDH) and to the expression of the target gene in hMSCs at day 3 on culture plates in GM.

**TABLE 1 |** Primer sequences for qRT-PCT.

| Gene | Forward (5′–3′) | Reverse (5′–3′) |
|---|---|---|
| RUNX2 | CCGCCTCAGTGATTTAGGGC | GGGTCTGTAATCTGACTCTGTCC |
| SPP1 | GGTGATGTCCTCGTCTGTA | CCAAGTAAGTCCAACGAAAG |
| ALP | ACAAGCACTCCCACTTCATC | TTCAGCTCGTACTGCATGTC |
| COL1A1 | GAGGGCCAAGACGAAGACATC | CAGATCACGTCATCGCACAAC |
| OCN | TGAGAGCCCTCACACTCCTC | CGCCTGGGTCTCTTCACTAC |
| ENPP1 | CAAAGGTCGCTGTTTCGAGAG | TGCACGTCTCCTGGTAATCTAAA |
| RANKL | CAACATATCGTTGGATCACAGCA | GACAGACTCACTTTATGGGAACC |
| OPG | CACAAATTGCAGTGTCTTTGGTC | TCTGCGTTTACTTTGGTGCCA |
| MCSF | AGACCTCGTGCCAAATTACATT | AGGTGTCTCATAGAAAGTTCGGA |

## Quantification of ALP Activity

Alkaline phosphatase activity was quantified with the CDPStar® reagent (Sigma-Aldrich, cat# GERPN3682). 10 μl of cell lysate supernatant (as described for quantification of total cell number) were transferred, with technical duplicates, to a 96-well plate. 40 μL of CDPStar reagent was added to each well, followed by 30 min incubation at room temperature in dark. Luminescence intensity was read with a CLARIOstar Plus microplate reader. The results were normalized to the cell number, and are presented as mean and standard deviation of the biological replicates.

## Scanning Electron Microscopy (SEM) and Energy-Dispersive X-Ray Spectroscopy (EDS)

The morphology and chemical composition of the membranes were characterized using an SEM coupled with an EDS detector. Collagen and biomineralized collagen membranes were dehydrated using a sequence of, first, mixtures of PBS and ethanol (70:30, 60:40 and 50:50) for 15 min each; and second, mixtures of distilled water and ethanol (40:60, 30:70, 20:80, 10:90, and 100% ethanol) for 15 min each. This was followed with a 30 min incubation in a 50:50 mixture of ethanol and hexamethyldisiloxane (HMDS), followed by 30 min of incubation in HMDS. The last step consisted of removing the HMDS and leaving the membranes to dry overnight. Dried membranes were glued to aluminum stubs with carbon tape and silver paint. Samples were sputter coated with a 2 nm iridium layer for increased conductivity using a Q150TES sputter coater (Quorum, United Kingdom).

For observation of cell-induced mineralization, membranes with cells cultured on them were washed with warm PBS following cell culture medium aspiration, and fixed with warm 4% formaldehyde in PBS, at room temperature for 15 min. After washing with PBS, the samples were dehydrated and prepared for SEM as described above.

Samples were imaged with a TENEO electron microscope (FEI, OR, United States) operating in Optiplan mode at 2–5 kV and 2–10 mm working distance, using the T1 in-column, ETD or back-scatter detectors. For EDS analysis, samples were imaged with a VERSA electron microscope (FEI) equipped with an EDS detector (EDAX, NJ, United States), operating at 10 kV and 10 mm working distance.

## Statistical Analysis

Statistical testing of mean differences was performed in GraphPad Prism (version 8.3) using two-way analysis of variance

(ANOVA) of independent samples, looking at differences between conditions within each timepoint. A Bonferroni *post hoc* test was used to correct for multiple comparisons (one family for all comparisons). Mean differences were considered statistically significant for $p$-value $< 0.05$. Data in all figures is presented as mean and standard deviation, unless otherwise specified, and significance is denoted as (*) $p < 0.05$, (**) $p < 0.01$, (***) $p < 0.001$, (****) $p < 0.0001$.

# RESULTS

## Characterization of Collagen and Biomineralized Collagen Membranes

The morphology and elemental composition of both biomimetic membranes was analyzed by SEM-EDS, and the results are displayed in **Figure 1**. The membranes as used for cell culture are shown in **Figure 1A**.

The collagen membranes were compact films consisting of randomly oriented collagen fibers, with even surface morphology exemplified by the images in **Figures 1B,C**. Fibers of the collagen matrix had an average diameter of 60 ± 13 nm and displayed a banding pattern along their length (**Figure 1D**). The fibrous structure remained after the mineralization process, although the fibers were wider, 201 ± 56 nm (**Figure 1E**), and the banding pattern was no longer visible. Elemental analysis of both membranes showed that calcium and phosphorus was only present in biomineralized collagen membranes **(Figures 1D,E**).

## Effect of Collagen and Biomineralized Collagen on Proliferation of hMSCs

To explore the effect of collagen and mineralized collagen on the proliferation of hMSCs, using TCP as a control, DNA content of the cells on membranes was quantified and converted to cell number (**Figure 2**). Cells cultured on TCP in GM exhibited a steady increase in number until day 14. Beyond this time point, the cells were detached from the TCP due to overgrowth of the cell monolayer in the culture well, and hence, no measurement could be done for GM. hMSCs cultured in OM were proliferating at a lower rate than in GM at days 7 and 14, and no further growth in OM was observed between day 14 and 21. Cells cultured on collagen membranes showed a lower proliferation than on TCP in GM at days 3 and 7. A boost in proliferation was observed between day 7 and 14 on collagen membranes where cells reached the same cell number as on TCP in GM. No further increase in cell number was observed on collagen membranes at day 21. hMSCs cultured on mineralized collagen had a lower cell number than cells on TCP in GM at days 3, 7, and 14. No further growth was observed at day 21. On both collagen and mineralized collagen, cells followed a proliferation pattern similar to that on TCP in OM until day 7 of culture. At days 14 and 21, proliferation was increased on collagen membranes whereas cells on mineralized collagen maintained a proliferation similar to the cells cultured on TCP in OM. Taken together, both collagen and mineralized collagen supported proliferation of hMSCs, with, at the later time points of 14 and 21 days, a higher cell number on collagen than on mineralized collagen.

## Osteogenic Gene Expression of hMSCs on Biomimetic Membranes

Osteogenic differentiation of hMSCs was analyzed by quantifying the expression of osteogenic biomarkers at the mRNA level via qRT-qPCR (**Figure 3**). The selected markers were RUNX2, a transcription factor associated with activation of osteogenic genes (Ducy et al., 1997) and SPP1, a non-collagenous protein with roles in cell attachment and matrix mineralization (Komori, 2006). In addition, markers for two matrix proteins were assessed, COL1A1, the main constituent of the organic part of the matrix (Quarles et al., 1992) and OCN, which is involved in matrix mineralization by binding hydroxyapatite (Tsao et al., 2017), as well as two other markers involved in the regulation of inorganic phosphate, ALP and ENPP1 (Hessle et al., 2002; Johnson et al., 2003).

RUNX2, an early transcription factor (Ducy et al., 1997), was significantly upregulated at day 3 on collagen (1.6×) as well as on mineralized collagen (2.5×), compared with TCP. After 7 days of culture, a similar trend was observed, where a higher expression on both materials was detected as compared to the control, i.e., TCP, with the highest expression on biomineralized collagen. At day 14, when cells on both types of biomimetic membrane showed higher expression levels than the control, i.e., cells cultured on TCP, RUNX-2 expression on biomineralized collagen was significantly upregulated by 3.1×. When comparing collagen and mineralized collagen, a trend of a higher RUNX2 expression on mineralized collagen was observed at each time point.

A significant upregulation of SPP1 on biomimetic membranes as compared to TCP was detected at day 3, with a 4× increase on collagen and the highest increase of 18× on mineralized collagen, following a behavior similar to RUNX2. After 7 days, no differences in expression of SPP1 were observed between conditions and, after 14 days, a slight decrease in expression relative to the control was observed on collagen, without statistical significance, whereas cells on mineralized collagen showed similar expression levels as the control. A decrease in expression over time was observed on mineralized collagen, while expression for TCP slightly increased from days 3 to 7 and were maintained at day 14. The expression overtime on collagen was unchanged at 3 and 7 days and showed a slight decrease at 14 days.

Expression of ALP, which plays a role in matrix mineralization (Hessle et al., 2002; Johnson et al., 2003), was slightly downregulated early, at day 3, on collagen relative to the control, as well as on mineralized collagen with a 2× decrease. Comparable expression levels between all conditions were observed at day 7. After 14 days, the expression on collagen and mineralized collagen was increased as compared to TCP, with a 2.7× statistically

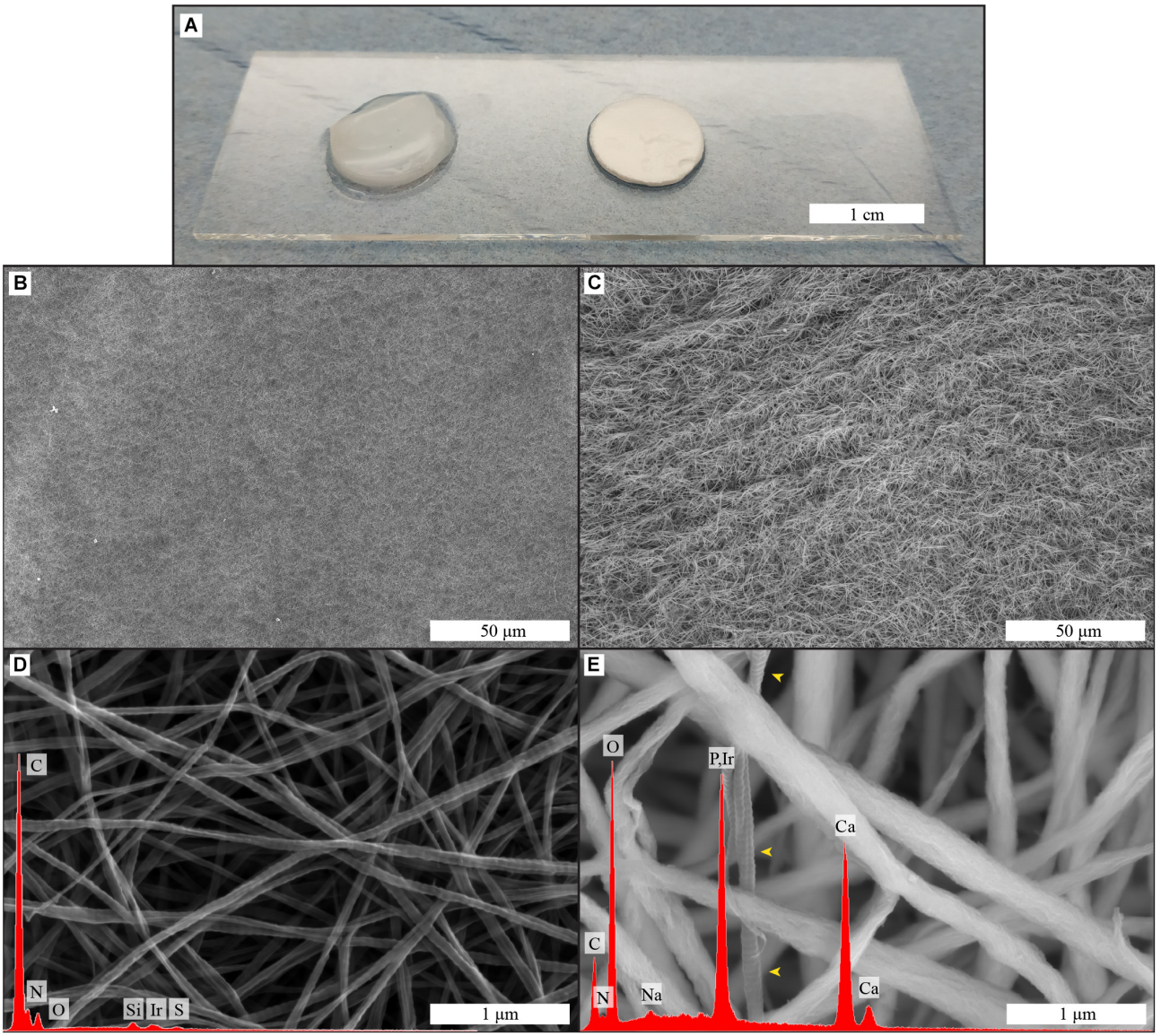


**FIGURE 1 |** Macroscopic image **(A)** of collagen and biomineralized collagen as used for cell culture experiments; surface structure and elemental composition of collagen **(B,D)** and biomineralized collagen **(C,E)** membranes, obtained by SEM-EDS. Low magnifications images of the surface of collagen **(B)** and biomineralized collagen **(C)**. High magnification image of collagen membrane with corresponding EDS spectrum **(D)**, collagen banding is visible and there is no calcium or phosphorus signal. High magnification image of biomineralized collagen and corresponding EDS spectrum **(E)**, where thicker fibers are visible, and no banding is discernible, expect in one fiber that is not mineralized (yellow arrowheads). Both types of membrane show fibrillar structure.

significant increase on mineralized collagen. ALP expression was downregulated in the TCP control overtime but collagen and mineralized collagen maintained the same level overtime.

Expression of ENPP1, an enzyme that regulates bone mineralization (Hessle et al., 2002; Johnson et al., 2003), was evaluated. Both ENPP1 and ALP are involved in maintaining bone mineralization in equilibrium. Bone mineralization relies on the availability of inorganic phosphate (Pi), which together with calcium crystallizes to form HA. ALP hydrolyses inorganic pyrophosphate (PPi) to generate Pi, which promotes mineralization, and ENPP1 generates PPi, which antagonizes mineralization. A statistically significant upregulation of ENPP1 was observed on both collagen (3×) and mineralized collagen (4.6×) relative to the control, at day 3. A significant increase of 1.6× was observed on mineralized collagen as compared to collagen. A pronounced decrease was observed at day 7 on collagen and mineralized collagen, as well as a smaller decrease on TCP. This trend was maintained after 14 days with a slight increase of expression on biomineralized collagen, without statistical significance.

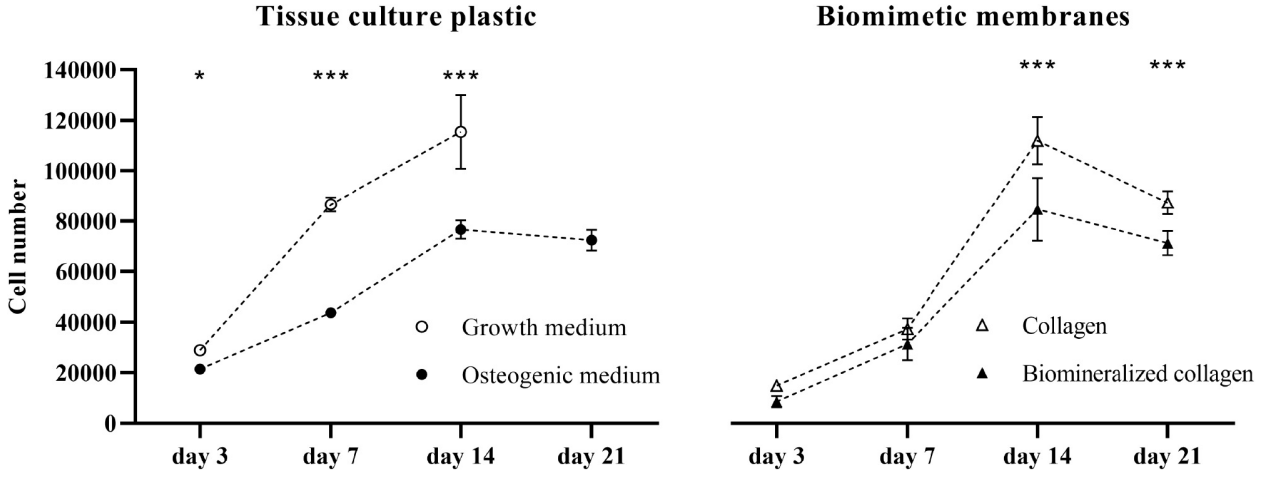


**FIGURE 2 |** Proliferation of hMSCs on tissue culture plastic in GM and OM as well as on the biomimetic collagen and biomineralized collagen membranes in GM. Cell proliferation is expressed as cell number at 3, 7, 14, and 21 days of culture. The data point for 21 days in the GM condition is missing, due to cells becoming over-confluent and eventually detaching from the tissue culture plate. Data are represented as mean ± SD ($n = 6$). Data is presented as mean and standard deviation and significance is denoted as $^{*}p < 0.05$, $^{***}p < 0.001$.

Osteocalcin expression was significantly upregulated on collagen, being 3× higher than on mineralized collagen and 8× higher as compared to TCP. The expression on mineralized was also significantly increased (2.4×) as compared to the control. This trend of highest expression on collagen, followed by mineralized collagen and the lowest being on TCP, was maintained at days 7 and 14, although the difference of expression between collagen and mineralized was not as pronounced as at the earliest time point. A decrease of OCN expression was observed over time for all substrates.

COL1A1, the main constituent of the organic matrix and therefore an indicator of ECM deposition (Quarles et al., 1992), was significantly downregulated on collagen at day 3, by half relative to the control, expression on mineralized collagen was similar as on TCP. No differences between conditions was observed at day 7. At day 14 on mineralized collagen, COL1A1 expression increased significantly by 5× relative to TCP and by 3.4× relative to collagen. A decreasing trend over time was observed on TCP.

## Expression of Osteoclast-Related Genes by hMSCs on Biomimetic Membranes

Potential modulation of osteoclast behavior by hMSCs cultured on collagen or biomineralized collagen was analyzed by assessing the expression of factors involved in osteoclastogenesis, including OPG, MCSF and RANKL (Lees and Heersche, 1999; Lee et al., 2010) at mRNA level (**Figure 4**). RANKL expression was below the detection limit of the qRT-PCR, indicating a very low expression level in all samples (**Supplementary Figure 1**). OPG expression in hMSCs on TCP was constant over time. An early upregulation at day 3 was observed on collagen, which was not statistically significant. An increase was also observed on mineralized collagen with a 3.5× increase relative to TCP and 2× increase relative to collagen, which were both statistically significant. At days 7 and 14, expression levels on collagen and mineralized collagen decreased to levels similar to those on TCP. MCSF expression at day 3 was significantly increased 4.5× on collagen and 5.5× on mineralized collagen relative to TCP. This trend, of a higher expression on both biomimetic membranes, was maintained at days 7 and 14. Overall, however, MCSF expression decreased over time, from day 3 until day 14, on all substrates.

## ALP Activity

In addition to assessing the mRNA expression levels of ALP, its activity was also analyzed as biochemical marker for osteoblast-like function in hMSCs undergoing osteogenic differentiation on different materials (**Figure 5**). ALP activity of hMSCs after 3 days was below the limit of detection for all conditions except the biomineralized collagen. On day 7, ALP activity was around two times higher on the biomineralized collagen than on the TCP control. Cells on mineralized collagen also showed a higher ALP activity than on collagen, although this difference was not statistically significant. There was a general increase from 7 to 14 days, and hMSCs cultured on both biomimetic membranes showed approximately twofold higher ALP activity than those cultured on TCP, while no significant effect of collagen mineralization was observed. Finally, on day 21, no measurement could be done on the TCP control, as cells grew over-confluent and samples had to be discarded. Collagen and biomineralized collagen showed comparable ALP activity on day 21, with a slight decrease compared to day 14.

## Cell-Induced Mineralization

Production of mineralized ECM by the hMSCs was evaluated by SEM and EDS analyses of membranes after 21 days of cell culture in MM. Mineral deposits produced by hMSCs were observed on collagen membranes (**Figure 6A**). The mineral deposits were found as a layer surrounding the collagen fibers of the membrane (inset **Figure 6A**), in close proximity to the

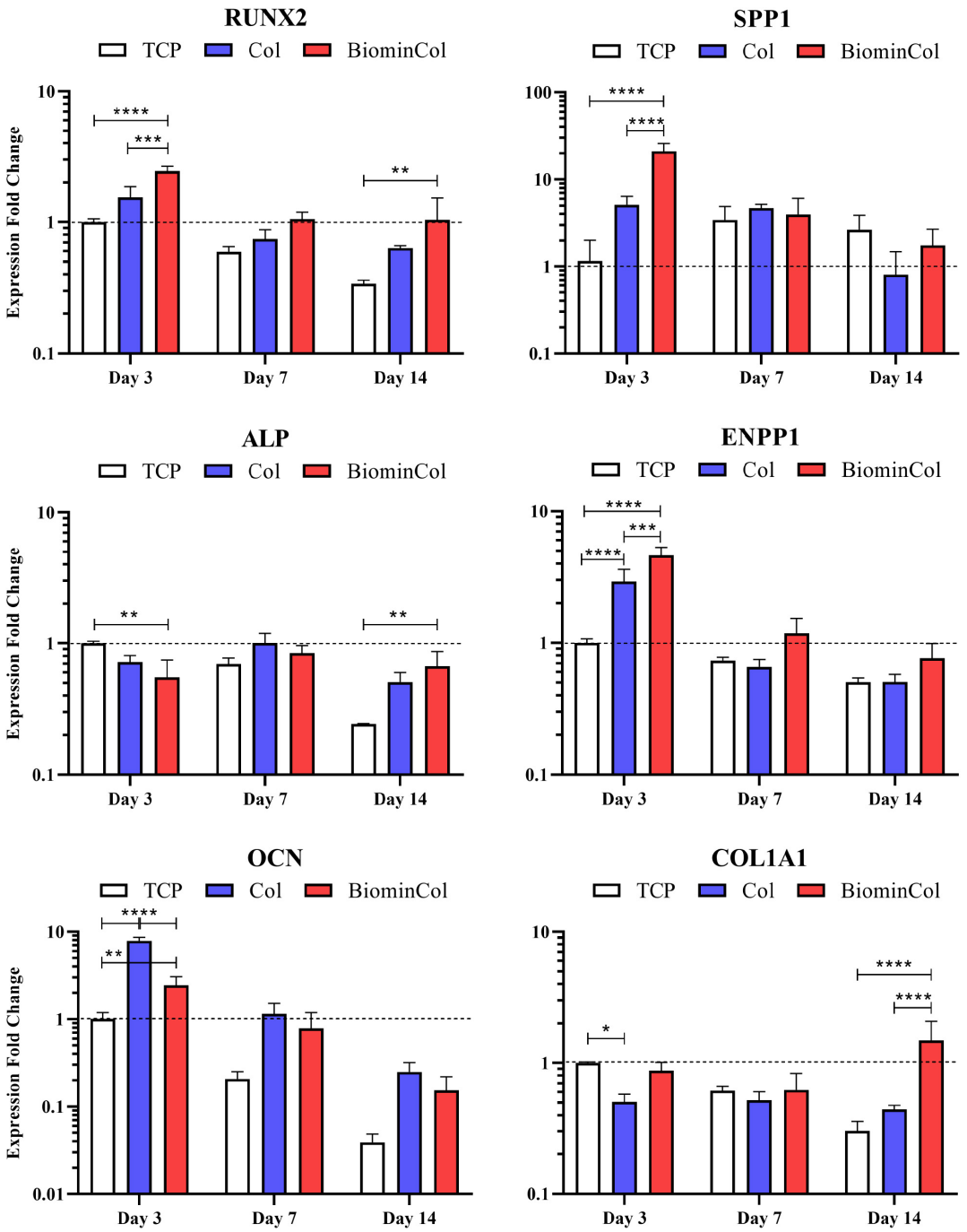


**FIGURE 3 |** Gene expression profiles for RUNX2, SPP1, ALP, ENPP1, OCN, and COL1A1 of hMSCs cultured on tissue culture plastic (TCP) control, collagen (Col), and biomineralized collagen (BiominCol) for 3, 7, and 14 days. Data are represented as mean ± SD ($n = 3$). Data is presented as mean and standard deviation and significance is denoted as $^{*}p < 0.05$, $^{**}p < 0.01$, $^{***}p < 0.001$, $^{****}p < 0.0001$.

cells on the membrane. These deposits were also found in the areas of the collagen membrane where no cells were observed. On mineralized collagen membranes, the only possible indication of cell-induced mineralization were spherical structures with the diameter of a few micrometers, which were observed in close association with cell filopodia (**Figure 6B**).

Elemental analysis by EDS showed presence of calcium and phosphorus on the collagen membranes after cell culture in MM (**Figure 7A**), and elemental mapping showed that the signal was originating from the mineral deposits (**Figures 7B–E**). No mineral deposits were observed by SEM and no calcium or phosphorus presence was detected by EDS when hMSCs

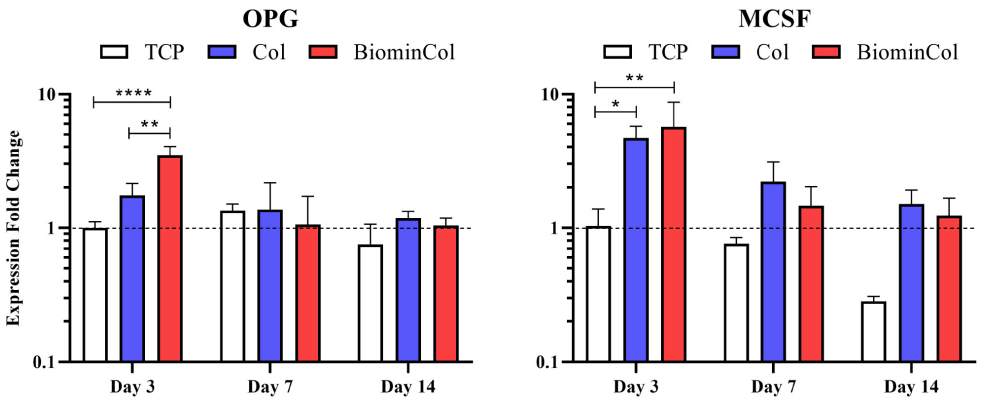


**FIGURE 4 |** Gene expression profiles for OPG and MCSF of hMSCs cultured on tissue culture plastic (TCP) control, collagen (Col), and biomineralized collagen (BiominCol) for 3, 7, and 14 days. Data are represented as mean ± SD ($n = 3$). Data is presented as mean and standard deviation and significance is denoted as $^{*}p < 0.05$, $^{**}p < 0.01$, $^{****}p < 0.0001$.

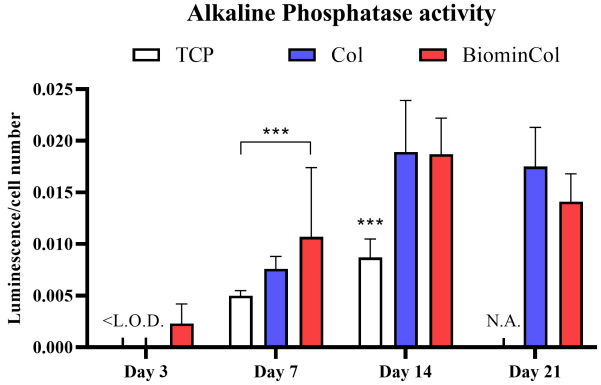


**FIGURE 5 |** Alkaline phosphatase (ALP) activity of hMSC, normalized to cell number. Cells were cultured on tissue culture plastic (TCP) control, collagen (Col), and biomineralized collagen (BiominCol) for 3, 7, 14, and 21 days. Data are represented as mean ± SD ($n = 6$). Data under the limit of detection are denominated as <L.O.D (growth medium and collagen at day 3), and missing data is labeled as N.A. (TCP control at day 21). Data is presented as mean and standard deviation and significance is denoted as $^{***}p < 0.001$.

were cultured on collagen membranes in GM for 21 days (**Supplementary Figure 2**). Similarly, no evidence for mineral deposits was found when collagen membranes were incubated in MM for 14 days in the absence of cells (**Supplementary Figure 3**).

## DISCUSSION

The intrinsic self-healing capacity of bone falls short in repairing critical-sized bone defects. To avoid drawbacks commonly associated with using bone grafts, such as limited availability as well as donor site morbidity (Calori et al., 2014; Babbi et al., 2016), synthetic bone graft substitutes are in demand as replacement for autologous bone (Kurien et al., 2013; Baldwin et al., 2019). Intrafibrillary biomineralized collagen is a promising biomaterial for bone regeneration applications, as it mimics not only the organic-inorganic composition, but also the structure of the ECM of bone tissue at the sub-micron scale. In this study, we aimed to complement the existing knowledge on the relevance of biomineralized collagen in bone regeneration, by evaluating the behavior of clinically-relevant hMSCs on intrafibrillarly mineralized collagen membranes in comparison with collagen membranes without mineral. The differentiation of undifferentiated stem cells into osteogenic progenitors, i.e., osteoinduction, is a key process in regeneration of bone defects (Bohner and Miron, 2019) and gaining further insight into this process is a valuable resource for designing novel and more functional bone graft substitutes. There are only a few *in vitro* studies exploring the effects of biomineralized collagen on osteogenic differentiation of human stem cells (Fu et al., 2016; Xu et al., 2016; Ye et al., 2016; Thrivikraman et al., 2019). The results with hMSCs described here contribute to the growing evidence that this biomaterial is a promising candidate for developing synthetic bone graft substitutes.

Biomineralized collagen membranes, consisting of collagen type I containing intrafibrillar CaP mineral, were prepared following the established PILP route (Li et al., 2011). Dense type I collagen membranes had a fibrillar structure with typical D-banding characteristic of native collagen, a requirement for intrafibrillar mineralization to occur (Olszta et al., 2007). Upon mineralization of the membranes, the fibrillar structure of the membrane was preserved. Typical crystal deposition from saturated $Ca^{2+}$ and $PO_4^{3-}$ solutions (Costa et al., 2012) was not observed on the surface of the material, while the elemental analysis showed that CaP was present in abundance. These observations indicate that CaP was present in the mineralized collagen membrane, but not on the surface of the fibers, and therefore must reside within the collagen fibers. Further evidence of this is the observed increase in fiber diameter after the biomineralization process, being roughly three times the size of the collagen membrane fibers. We therefore conclude that homogenous crystallization, i.e., crystallization in solution, did not occur, and mineral was instead deposited within the collagen fibrils, which is expected when a polyanion such as pAsp is added

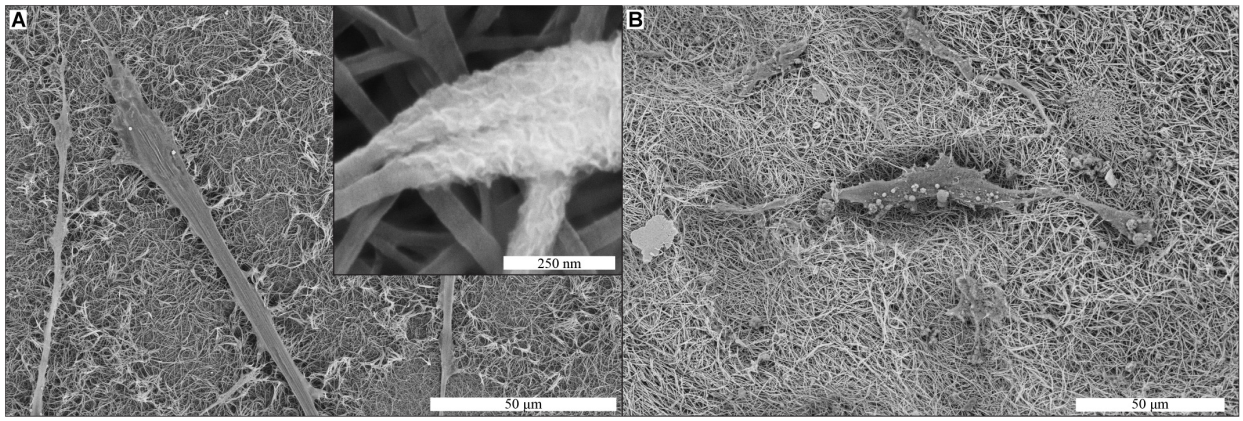


**FIGURE 6 |** Cell-induced mineralization on collagen **(A)** and biomineralized collagen **(B)** membranes, shown by SEM imaging. Cells were cultured on membranes for 21 days in MM. Mineral deposits are visible in the collagen membrane (inset A). These deposits were not observed on biomineralized collagen **(B)**.

to the mineralization process, and is in accordance with previous studies in which PILP was used for collagen biomineralization (Jee et al., 2010; Thula et al., 2011).

Mineralized collagen membranes were used to study proliferation and differentiation of hMSCs at the mRNA level, using collagen membranes without mineral as a control. Moreover, ALP activity and mineralization of the cells were analyzed.

Both biomimetic membranes with and without mineral supported the growth of hMSCs over a period of 21 days, with mineralized collagen showing a somewhat lower proliferation rate, in particular at the later time points of 14 and 21 days. Previous studies have also shown that collagen matrices with and without CaP mineral support cell proliferation. For example, in a study with MC3T3-E1 osteoblasts, a more pronounced proliferation on collagen without than on collagen containing mineral was observed, however, this analysis was only performed over a period of 7 days (Wang et al., 2016). Collagen with and without HA supported proliferation of rat MSCs over a period of 14 days without significant differences between the materials (Sun et al., 2018), whereas periodontal ligament stem cells were present in higher numbers on intrafibrillarly mineralized collagen than on the collagen control at 3, but not at 7 days of culture (Fu et al., 2016).

Regarding osteogenic differentiation, in general, hMSCs showed an upregulation of osteogenic differentiation markers when cultured on mineralized collagen as compared to collagen without mineral.

RUNX2, an essential transcription factor required for determination of the osteoblastic lineage in hMSC at an early stage (Ducy et al., 1997) as well as SPP1, another early marker of osteogenesis, that has been shown to be expressed in immature osteoblasts (Komori, 2006), were enhanced at an early time point on biomineralized collagen membranes. This effect on RUNX2 was maintained, however, at lower mRNA levels and decreased for SPP1 over time. We observed a similar trend in time on collagen, however, the expression of RUNX2 was always lower than on biomineralized collagen indicating a lower degree of osteogenic differentiation. An early upregulation of RUNX2, followed by a slow decrease, is a pattern found over the course of osteogenic differentiation of hMSCs *in vitro* (Shekaran et al., 2015). RUNX2 is regulated by several upstream pathways, which are involved in osteogenic differentiation, including BMP and WNT signaling pathways (Rutkovskiy et al., 2016). Its upregulation indicates an activation of these pathways and, hence, material-induced osteogenic differentiation. This also explains the upregulation of SPP1, which is a direct target of RUNX2 signaling (Ducy et al., 1997). SPP1 is an important factor of matrix mineralization, which also plays a role in many other functions such as cell survival, migration, regulation of inflammation and angiogenesis (Giachelli and Steitz, 2000).

ALP and ENPP1 are known to positively and negatively regulate matrix mineralization in native bone (Hessle et al., 2002; Johnson et al., 2003), respectively. The mRNA level of ALP was lower, while the ENPP1 mRNA was higher on biomineralized collagen compared to the control at day 3. The opposite trend in ALP levels overtime was observed, with cells cultured on TCP showing a significant decrease, while biomineralized collagen maintained the level comparable to that at day 3. A substantial decrease of overall ENPP1 expression was observed at later time points, plausibly indicating the onset of matrix mineralization. ALP and ENPP1 expression of cells cultured on the collagen membranes and biomineralized collagen were similar, with ENPP1 expression being slightly lower in the absence of mineral. ENPP1 expression has previously been shown to be upregulated on CaP ceramics with intrinsic osteoinductive potential (Othman et al., 2019). To our knowledge, this is, however, the first time that ENPP1 expression has been investigated on collagen and biomineralized collagen.

OCN, the most abundant non-collagenous protein in bone (Tsao et al., 2017), was surprisingly expressed at an early stage with an upregulation on biomineralized collagen compared to the control. This trend was maintained over time and a similar effect on OCN expression was observed on collagen membranes without mineral. OCN has been shown to play an

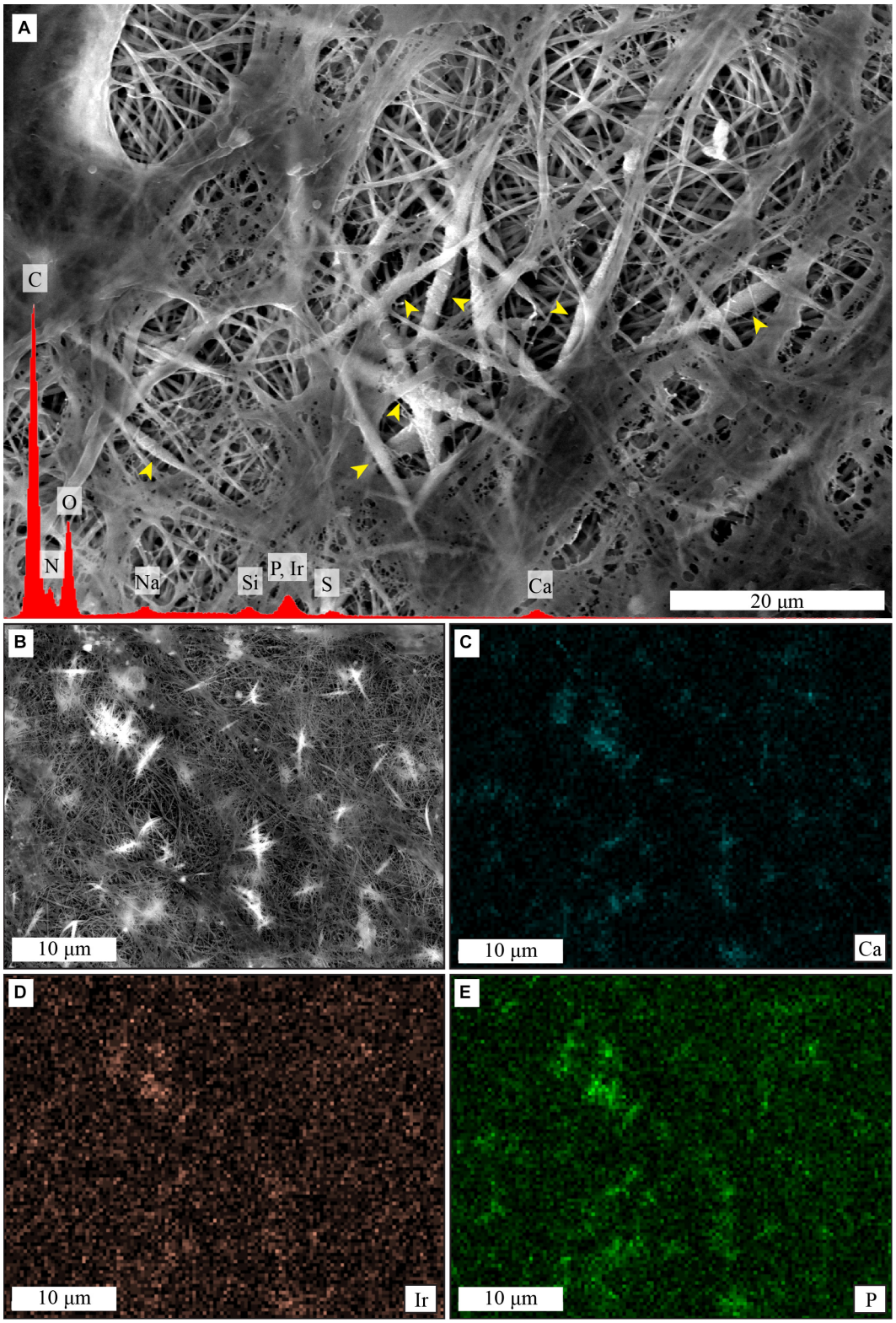


**FIGURE 7 |** Cell-induced mineralization on collagen membranes, shown by SEM imaging and EDS analysis. Mineral deposits are visible as thicker and whiter fibers in the center of the image **(A)**, yellow arrowheads. EDS spectra of **(A)**, in red, shows presence of calcium and phosphorus. ESD mapping **(B–E)** shows that signal from calcium **(C)** and phosphorus **(E)** comes predominantly from the thicker and whiter mineral deposits that surround the collagen fibers, as seen in the previous figures. In contrast, the signal from iridium **(D)** is more homogeneous.

important role in osteoblast maturation, inter alia, promoting matrix mineralization by binding to HA (Hauschka and Wians, 1989). A study by Tsao et al. (2017) showed that low OCN levels potentially lead to a delayed matrix mineralization. An early expression of OCN as observed here may indicate that biomimetic collagen membranes are able to accelerate osteogenic differentiation, however, further research is needed to provide conclusive evidence for this.

COL1A1, the main component of the organic matrix, was higher at day 14 on biomineralized collagen relative to TCP (3.4×) and collagen (4.9×), suggesting matrix deposition by cells of the osteoblastic lineage (Quarles et al., 1992). In contrast, collagen membranes without mineral were unable to stimulate COL1A1 expression, which was downregulated early on and kept at baseline until later time points. This effect of pure collagen scaffolds has previously been observed in different cell types (Fu et al., 2016; Sun et al., 2018).

In a study by Sun et al. (2018), osteogenic differentiation of rat MSCs on collagen versus a collagen/HA composite, without intrafibrillar mineral, was tested, showing the results consistent with those presented here. Cells cultured on collagen/HA scaffolds showed, overall, the highest osteogenic differentiation capacity, supported by a rapid activation of RUNX-2 and the high mRNA levels of ALP and especially COL1A1. The authors attributed these effects to the differences in microstructure and stiffness of the materials (Sun et al., 2018). An upregulation of RUNX2 was also observed on CaP ceramic controls without collagen and may therefore also be influenced by the presence of CaP and/or free calcium and inorganic phosphate ions.

mRNA expression of ALP in hMSCs cultured on collagen and mineralized collagen has been sparsely investigated. However, a study investigating osteogenic differentiation of hMSCs on nanoparticulate (mineralized) collagen glycosaminoglycan scaffolds showed a low ALP expression at day 3 and a slight increase at day 7 (Ren et al., 2016). Both scaffolds with and without mineral also showed an upregulation in matrix markers, such as OCN and COL1A1, as compared to the beginning of culture (day 0), which is in accordance with our results. In a study by Fu et al. (2016), osteogenic differentiation of human periodontal ligament stem cells was evaluated on collagen, intrafibrillarly mineralized collagen and extrafibrillarly mineralized collagen. Cells cultured on intrafibrillarly mineralized collagen showed an increased expression of osteogenic genes, such as SPP1, COL1A1, and BMP-2 as compared to collagen at days 7 and 14.

In the context of bone regeneration, not only the osteoblast function, as the bone-forming unit, but also the osteoclast function, the bone-resorbing unit, is of importance. In native bone, these two processes are in balance, maintaining a constant, homeostatically-controlled amount of bone ECM (Rodan, 1998). Therefore, in this study, we took first steps in analyzing how biomimetic membranes may influence osteoblast-osteoclast communication by assessing the mRNA levels of the biomarkers involved in this cellular crosstalk in hMSCs.

The RANKL/OPG ratio has an important role in osteoclast regulation. RANKL activates osteoclasts by binding to its membrane-bound receptor RANK, and OPG has an inhibitory effect by binding RANKL to prevent osteoclast activation (Lee et al., 2010). As reviewed by Kapasa et al. (2017), previous research indicated that changes in RANKL/OPG balance might reduce implant complications, which are caused by an increased osteoclastogenesis accompanied by chronic inflammation in which significantly elevated levels of RANKL are frequently observed. This results in poor osseointegration of the implant, prosthetic loosening and non-union of the defect. Here, low mRNA levels of RANKL in hMSCs were detected overtime. Osteoblasts can exhibit a pro-osteoclastic phenotype, expressing RANKL. This was previously observed in an immature subpopulation of osteoblasts and simulated *in vitro* by the stimulation with osteotropic factors vitamin D3, dexamethasone or their combination (Atkins et al., 2003). Here, however, low mRNA levels of RANKL were detected overtime. Ren et al. (2019) combined OPG adenoviral expression in hMSCs with nanoparticulate mineralized collagen glycosaminoglycan scaffolds or non-mineralized scaffolds and observed a decreased RANKL/OPG ratio. RANKL expression was detected not only in OPG transfected hMSCs but also in non-transfected hMSCs on mineralized and non-mineralized material. The major difference in Ren et al. (2019)' culture protocol compared to ours was the culture of hMSCs in osteogenic medium containing dexamethasone. We speculate that the lack of dexamethasone in our cultures, chosen to isolate the effect on the biomaterials from other stimulators of osteogenic differentiation, may be the reason for the low RANKL expression observed.

OPG mRNA expression, on the other hand, was upregulated in hMSCs cultured on biomineralized collagen indicating the potential of this biomaterials to modulate the osteoblast-osteoclast crosstalk.

Jiao et al. observed that mouse MSCs cultured on biphasic silica/apatite intrafibrillarly mineralized collagen scaffolds expressed higher mRNA levels of OPG (fivefold increase), and lower mRNA levels of RANKL relative to collagen scaffolds without mineral (Jiao et al., 2015). OPG expression on intrafibrillarly calcified collagen scaffolds without silica was only slightly increased and no difference in RANKL expression relative to collagen without mineral was observed. This indicated an inhibitory effect on RANKL-mediated osteoclastogenesis induced by biphasic silica/apatite intrafibrillarly mineralized collagen. This hypothesis was confirmed in a follow up experiment in which osteoclasts were exposed to conditioned medium from hMSCs cultured on these scaffolds, finally resulting in decreasing numbers of functional osteoclasts, i.e., tartrate-resistant acid phosphatase (TRAP)-positive cells.

In our study, we additionally observed an upregulation of MCSF mRNA expression, which has been suggested to activate osteoclastic bone resorption (Lees and Heersche, 1999), in hMSCs cultured on both collagen and biomineralized collagen membranes, with the effect remaining elevated compared to control, yet overall, decreasing overtime.

Taken together, our data suggests that collagen and biomineralized collagen can potentially modulate osteoclastogenesis and the osteoclast-osteoblast crosstalk during bone regeneration process. However, to gather a deeper understanding of these modulatory effects, further investigation

including direct osteoclast monoculture as well as hMSCs-osteoclast co-culture on these bioinspired biomaterials are required and suggested as next steps.

In addition to mRNA expression levels of osteogenic biomarkers, we also analyzed ALP activity, as an indicator of osteoblastic function in hMSCs cultured on collagen and biomineralized collagen membranes. ALP is an enzyme found in osteoblasts which increases matrix mineralization (Siffert, 1951; Hessle et al., 2002).

The analysis of the mRNA ALP levels showed that overtime, the ALP expression of hMSCs cultured on TCP control decreased, whereas on collagen and mineralized collagen, no decrease was observed, and the levels at 7 and 14 days were comparable between the two materials. In contrast, an increase in ALP activity was observed between day 3 and day 14, and remained at comparable level until day 21, for hMSCs cultured on both biomimetic membranes as well as the TCP control. This suggests that the peak in the ALP expression at the mRNA level was reached early during the cell culture, and that the effect at the enzyme level is observed at the later time points. Both biomimetic membranes showed a higher ALP activity than the TCP control, with the positive effect of biomineralized collagen being more pronounced at day 3 and day 7. This suggests an enhancing effect of the biomimetic matrices, and in particular the biomineralized one, on osteoblastic activity and, hence, evidence that hMSCs are differentiating into functional osteoblasts.

Previous studies have shown a higher ALP activity of cells cultured on intrafibrillarly mineralized collagen than on collagen without mineral (Jiao et al., 2015; Ye et al., 2016; Zhang et al., 2018) and even on collagen with extrafibrillar mineral (Wang et al., 2018). These findings are in line with ours, although we did not observe significant differences between the two biomimetic membranes. This may be due to differences in the materials used in different studies. Although all studies tested intrafibrillarly mineralized collagen, slight differences in method used for preparing biomineralized collagen could have an impact on important properties of the materials. For example, the extent of exposure of the intrafibrillar mineral from its collagen confinement may be different, affecting both the chemical composition, mechanical properties, and surface topography, which in turn may affect the cell behavior. This is not only the case for the ALP activity but also for expression of other markers of osteogenic differentiation, cell proliferation and ECM production. Therefore, comparisons of different studies that tested biomineralized collagen need to be made with caution.

The formation of cell-induced mineral deposits on collagen and biomineralized collagen membranes was investigated by SEM-EDS. Mineral formation was microscopically observed on the collagen membranes, and supported by the elemental analysis demonstrating the presence of calcium and phosphorus. Critically, calcium and phosphorus were not detected on two controls, i.e., hMSCs cultured on the collagen membranes in GM and collagen membranes incubated in MM medium for 14 days in the absence of cells. These observations strongly suggest that the mineral deposits were indeed produced by the hMSCs cultured in MM, which contains dexamethasone and β-glycerophosphate. Moreover, the morphology of these deposits is interesting, as the mineral appears to surround the collagen fibers. This type of mineralization has been previously described for hMSC undergoing osteogenic differentiation in collagen matrices, where toluidine blue staining allowed identification of mineralized fibers, which were always found in contact with cells (Neuss et al., 2008).

The high content of intrafibrillar CaP mineral in biomineralized membranes made detection of cell-deposited mineral difficult to analyze using SEM-EDS. On SEM images of biomineralized collagen membranes, we did not observe the same type of mineral deposits as seen on collagen membranes. Instead, round particles were observed surrounding the cells, the nature of which is unclear.

While it is reasonable to expect that hMSC cultured on biomineralized collagen in MM would produce mineralized matrix (Langenbach and Handschel, 2013), we did not find convincing evidence for this. One reason for the lack of cell-induced mineral deposits, similar to the ones observed on collagen membranes, may be that the pre-existing intrafibrillar CaP could significantly alter the way in which new mineral is formed, by, for example, prioritizing growth of pre-existing CaP crystals over the formation of new mineral clusters. As existing CaP crystals are inside the collagen fibers, crystal growth would not significantly alter the fibrous morphology of the membrane, consequently making it more difficult to identify "new" mineral using SEM. However, if sufficient new mineral forms, the increase in fiber diameter should be detectable.

While other studies have used Alizarin Red semi-quantification to identify cell-induced mineral deposits (Fu et al., 2016), due to the high content of CaP in our biomineralized collagen membranes, this approach was not successful here (data not shown). Another alternative method for detecting newly formed mineral would be to tag calcium ions in solution with a fluorescent label, which would then be incorporated in newly formed mineral, making detection of deposits possible by fluorescence microscopy (van Gaalen et al., 2010).

Cell-induced matrix mineralization is an important aspect of *de novo* bone formation, and the capacity for hMSCs to mineralize the collagen membrane under stimulation of MM was demonstrated. It is reasonable to expect that hMSCs would show the same behavior when cultured on biomineralized collagen membranes, though we were unable to provide conclusive evidence here.

Taken together, the results of this study that used bioinspired intrafibrillarly mineralized collagen and clinically-relevant hMSCs, have shown that this material supports cell growth and osteogenic differentiation, and also affects markers related to osteoblast-osteoclast crosstalk. Moreover, the ability of the material to support cell-induced mineralization is suggested. While these findings add to the existing knowledge, a few limitations of this study should be discussed. First, the experiments were performed using a single hMSC donor and therefore, donor variability is not taken into account. Second, the induction of osteogenic differentiation was predominantly analyzed at the mRNA level. A next step to support the claim on enhancement of osteogenic differentiation on biomineralized collagen, is to assess the differentiation at the protein level and

to further investigate the ECM deposition and mineralization. From a bone regeneration perspective, not only the formation of bone but also its resorption are relevant processes to be considered when developing a bone graft substitute. Our data on osteoblast-osteoclast interaction indicated a possible modulatory effect of both collagen and mineralized collagen on osteoclastic functions and on osteoblast-osteoclast communication, which would be interesting to further explore. Lastly, production of the (mineralized) ECM by hMSCs on biomineralized collagen should be studied further, to clarify the nature of the mineral deposited and how this process is influenced by the properties of the material.

## CONCLUSION

The results in this study demonstrate that biomineralized collagen membranes support the growth and osteogenic differentiation of hMSCs. The upregulation of the expression of osteogenesis-related genes such as RUNX2, SPP1, ENPP1, OCN, and COL1A1, as well as the enhancement of the ALP activity were observed. Furthermore, biomineralized collagen was shown to affect the expression of osteoclast-related genes OPG and M-CSF. hMSCs were able to deposit mineralized ECM on the collagen membranes and were suggested to have the ability to do the same on biomineralized collagen. We conclude that biomineralized collagen is a promising biomaterial for bone regeneration and merits further study.

## DATA AVAILABILITY STATEMENT

The original contributions generated for this study are publicly available. This data can be found here: https://hdl.handle.net/10411/BC3SR3.

## ETHICS STATEMENT

The studies involving human participants were reviewed and approved by the medical ethics committee of Medisch Spectrum Twente (K06-002). The patient provided written informed consent to participate in this study.

## AUTHOR CONTRIBUTIONS

DM designed the experiments, prepared biomaterials and performed cell culture, DNA and ALP quantification, and SEM-EDS experiments and analyses. ME-L performed qPCR experiments and analyses. DM and ME-L wrote the manuscript. ZB provided helpful insight during manuscript revision. PH supervised the project and reviewed the manuscript. All authors contributed to the article and approved the submitted version.

## FUNDING

This research has been made possible with the support of the Dutch Province of Limburg (LINK project) and the Interreg Vlaanderen-Nederland 'Biomat on Microfluidic Chip' collaboration. PH gratefully acknowledges the Gravitation Program 'Materials-Driven Regeneration,' funded by the Netherlands Organisation for Scientific Research (NWO).

## ACKNOWLEDGMENTS

The authors would like to thank Myraise van Stijn and Enabling Technologies/DSM for the assistance provided with SEM-EDS analyses.

## SUPPLEMENTARY MATERIAL

The Supplementary Material for this article can be found online at: https://www.frontiersin.org/articles/10.3389/fbioe.2020.554565/full#supplementary-material

**Supplementary Figure 1 |** Gene expression profile for RANKL. Osteoblasts in basic medium (BM) and osteoblasts stimulated with 20 nM vitamin D3 (VitD3) were used as controls (Ctrl) to validate the RANKL primers. hMSCs cultured on tissue culture plastic (TCP) control, collagen (Col), and biomineralized collagen (BiominCol) for days 3, 7 and 14 days. Data are represented as mean ± SD ($n$ = 2 for BM and VitD3 and $n$ = 3 on hMSCs).

**Supplementary Figure 2 |** SEM image of a collagen membrane with hMSCs cultured in GM for 21 days and EDS spectrum of the corresponding area. No calcium and phosphorus was detected.

**Supplementary Figure 3 |** SEM image of a collagen membrane incubated in MM for 14 days in the absence of cells (including media refreshment every 2–3 days) and EDS spectrum of the same area. No calcium and phosphorus signal was detected.

## REFERENCES

Atkins, G. J., Kostakis, P., Pan, B., Farrugia, A., Gronthos, S., Evdokiou, A., et al. (2003). RANKL expression is related to the differentiation state of human osteoblasts. *J. Bone Miner. Res.* 18, 1088–1098.

Babbi, L., Gasbarrini, A., and Boriani, S. (2016). Iliac crest bone graft: a 23-years hystory of infection at donor site in vertebral arthrodesis and a review of current bone substitutes. *Eur. Rev. Med. Pharmacol. Sci.* 20, 4670–4676.

Baldwin, P., Li, D. J., Auston, D. A., Mir, H. S., Yoon, R. S., and Koval, K. J. (2019). Autograft, allograft, and bone graft substitutes: clinical evidence and indications for use in the setting of orthopaedic trauma surgery. *J. Orthop. Trauma* 33, 203–213. doi: 10.1097/BOT.0000000000001420

Bohner, M., and Miron, R. J. (2019). A proposed mechanism for material-induced heterotopic ossification. *Mater. Today* 22, 132–141. doi: 10.1016/j.mattod.2018.10.036

Booth, S. K., Muijsenberg, A. J. C., van der Blitterswijk, C. A., Van Boer, J., and Bruijn, J. (2007). A rapid and efficient method for expansion of human mesenchymal stem cells. *Tissue Eng.* 13, 3–9. doi: 10.1089/ten.2005.0513

Calori, G. M., Colombo, M., Mazza, E. L., Mazzola, S., Malagoli, E., and Mineo, G. V. (2014). Incidence of donor site morbidity following harvesting from iliac crest or RIA graft. *Injury* 45, S116–S120. doi: 10.1016/j.injury.2014.10.034

Costa, D. O., Allo, B. A., Klassen, R., Hutter, J. L., Dixon, S. J., and Rizkalla, A. S. (2012). Control of surface topography in biomimetic calcium phosphate coatings. *Langmuir* 28, 3871–3880. doi: 10.1021/la203224a

de Melo Pereira, D., and Habibovic, P. (2018). Biomineralization-inspired material design for bone regeneration. *Adv. Healthc. Mater.* 7:e1800700. doi: 10.1002/adhm.201800700

Ducy, P., Zhang, R., Geoffroy, V., Ridall, A. L., and Karsenty, G. (1997). Osf2/Cbfa1: a transcriptional activator of osteoblast differentiation. *Cell* 89, 747–754. doi: 10.1016/S0092-8674(00)80257-3

Fernandes, H., Mentink, A., Bank, R., Stoop, R., Blitterswijk, C., and Van de Boer, J. (2010). Endogenous collagen influences differentiation of human multipotent Mesenchymal stromal CELLS. *Tissue Eng. Part A* 16, 1693–1702.

Fu, Y., Liu, S., Cui, S., Kou, X., Wang, X., Liu, X., et al. (2016). Surface chemistry of nanoscale mineralized collagen regulates periodontal ligament stem cell fate. *ACS Appl. Mater. Interf.* 8:15958. doi: 10.1021/acsami.6b04951

Giachelli, C. M., and Steitz, S. (2000). Osteopontin: a versatile regulator of inflammation and biomineralization. *Matrix Biol.* 19, 615–622. doi: 10.1016/S0945-053X(00)00108-6

Habraken, W. J. E. M., Tao, J., Brylka, L. J., Friedrich, H., Bertinetti, L., Schenk, A. S., et al. (2013). Ion-association complexes unite classical and non-classical theories for the biomimetic nucleation of calcium phosphate. *Nat. Commun.* 4, 1507–1512. doi: 10.1038/ncomms2490

Hauschka, P. V., and Wians, F. H. (1989). Osteocalcin-hydroxyapatite interaction in the extracellular organic matrix of bone. *Anat. Rec.* 224, 180–188. doi: 10.1002/ar.1092240208

Hessle, L., Johnson, K. A., Anderson, H. C., Narisawa, S., Sali, A., Goding, J. W., et al. (2002). Tissue-nonspecific alkaline phosphatase and plasma cell membrane glycoprotein-1 are central antagonistic regulators of bone mineralization. *Proc. Natl. Acad. Sci. U.S.A.* 99, 9445–9449. doi: 10.1073/pnas.142063399

Jee, S., Thula, T. T., and Gower, L. B. (2010). Development of bone-like composites via the polymer-induced liquid-precursor (PILP) process. Part 1: influence of polymer molecular weight. *Acta Biomater.* 6, 3676–3686. doi: 10.1016/j.actbio.2010.03.036

Jiao, K., Niu, L., Li, Q., Chen, F., Zhao, W., Li, J., et al. (2015). Biphasic silica / apatite co-mineralized collagen scaffolds stimulate osteogenesis and inhibit RANKL-mediated osteoclastogenesis. *Acta Biomater.* 19, 23–32. doi: 10.1016/j.actbio.2015.03.012

Johnson, K., Goding, J., Etten, D. V. A. N., Sali, A., Hu, S., Milla, L., et al. (2003). Linked deficiencies in extracellular PP. *J. Bone Miner. Res.* 18, 994–1004.

Kapasa, E., Giannoudis, P., Jia, X., Hatton, P., and Yang, X. (2017). The effect of RANKL/OPG balance on reducing implant complications. *J. Funct. Biomater.* 8:42. doi: 10.3390/jfb8040042

Komori, T. (2006). Regulation of osteoblast differentiation by transcription factors. *J. Cell. Biochem.* 99, 1233–1239. doi: 10.1002/jcb.20958

Kurien, T., Pearson, R. G., and Scammell, B. E. (2013). Bone graft substitutes currently available in orthopaedic practice: the evidence for their use. *Bone Jt. J.* 95, 583–597. doi: 10.1302/0301-620X.95B5.30286

Langenbach, F., and Handschel, J. (2013). Effects of dexamethasone, ascorbic acid and β-glycerophosphate on the osteogenic differentiation of stem cells in vitro. *Stem Cell Res. Ther.* 4:scrt328. doi: 10.1186/scrt328

Lee, J. C., Spiguel, L., Shenaq, D., Zhong, M., Wietholt, C., He, T.-C., et al. (2010). The role of RANK-RANKL-OPG axis in cranial suture homeostasis. *Plast. Reconstr. Surg.* 126:100. doi: 10.1097/01.prs.0000388825.27037.c3

Lees, R. L., and Heersche, J. N. M. (1999). Macrophage colony stimulating factor increases bone resorption in dispersed osteoclast cultures by increasing osteoclast size. *J. Bone Miner. Res.* 14, 937–945. doi: 10.1359/jbmr.1999.14.6.937

Li, Y., and Aparicio, C. (2013). Discerning the subfibrillar structure of mineralized collagen fibrils: a model for the ultrastructure of bone. *PLoS One* 8:e076782. doi: 10.1371/journal.pone.0076782

Li, Y., Thula, T. T., Jee, S., Perkins, S. L., Aparicio, C., Douglas, E. P., et al. (2011). Biomimetic mineralization of woven bone-like nanocomposites: role of collagen cross-links. *Biomacromolecules* 13, 49–59. doi: 10.1021/bm201070g

Lian, K., Lu, H., Guo, X., Cui, F., Qiu, Z., Xu, S., et al. (2013). The mineralized collagen for the reconstruction of intra-articular calcaneal fractures with trabecular defects. *Biomatter* 3:e27250. doi: 10.4161/biom.27250

Liao, S. S., Cui, F. Z., Zhang, W., and Feng, Q. L. (2004). Hierarchically biomimetic bone scaffold materials: nano-HA/Collagen/PLA composite. *J. Biomed. Mater. Res. Part B Appl. Biomater.* 69, 158–165. doi: 10.1002/jbm.b.20035

Liu, Y., Luo, D., Liu, S., Fu, Y., Kou, X., Wang, X., et al. (2014). Effect of nanostructure of mineralized collagen scaffolds on their physical properties and osteogenic potential. *J. Biomed. Nanotechnol.* 10, 1049–1060. doi: 10.1166/jbn.2014.1794

Neuss, S., Stainforth, R., Salber, J., Schenck, P., Bovi, M., Knüchel, R., et al. (2008). Long-term survival and bipotent terminal differentiation of human mesenchymal stem cells (hMSC) in combination with a commercially available three-dimensional collagen scaffold. *Cell Transplant.* 17, 977–986. doi: 10.3727/096368908786576462

Nudelman, F., Bomans, P. H. H., George, A., de With, G., and Sommerdijk, N. A. J. M. (2012). The role of the amorphous phase on the biomimetic mineralization of collagen. *Faraday Discuss.* 159:357. doi: 10.1039/c2fd20062g

Nudelman, F., Pieterse, K., George, A., Bomans, P. H. H., Friedrich, H., Brylka, L. J., et al. (2010). The role of collagen in bone apatite formation in the presence of hydroxyapatite nucleation inhibitors. *Nat. Mater.* 9, 1004–1009. doi: 10.1038/nmat2875

Olszta, M. J., Cheng, X., Jee, S. S., Kumar, R., Kim, Y. Y., Kaufman, M. J., et al. (2007). Bone structure and formation: a new perspective. *Mater. Sci. Eng. R Rep.* 58, 77–116. doi: 10.1016/j.mser.2007.05.001

Othman, Z., Fernandes, H., Groot, A. J., Luider, T. M., Alcinesio, A., Pereira, D., et al. (2019). The role of ENPP1/PC-1 in osteoinduction by calcium phosphate ceramics. *Biomaterials* 210, 12–24. doi: 10.1016/j.biomaterials.2019.04.021

Quarles, L. D., Yohay, D. A., Lever, L. W., Caton, R., and Wenstrup, R. J. (1992). Distinct proliferative and differentiated stages of murine MC3T3-E1 cells in culture: an in vitro model of osteoblast development. *J. Bone Miner. Res.* 7, 683–692. doi: 10.1002/jbmr.5650070613

Ren, X., Tu, V., Bischoff, D., Weisgerber, D. W., Lewis, M. S., Yamaguchi, D. T., et al. (2016). Nanoparticulate mineralized collagen scaffolds induce in vivo bone regeneration independent of progenitor cell loading or exogenous growth factor stimulation. *Biomaterials* 89, 67–78. doi: 10.1016/j.biomaterials.2016.02.020

Ren, X., Zhou, Q., Foulad, D., Tiffany, A. S., Dewey, M. J., Bischoff, D., et al. (2019). Osteoprotegerin reduces osteoclast resorption activity without affecting osteogenesis on nanoparticulate mineralized collagen scaffolds. *Sci. Adv.* 5, 1–12. doi: 10.1126/sciadv.aaw4991

Reznikov, N., Bilton, M., Lari, L., Stevens, M. M., and Kröger, R. (2018). Fractal-like hierarchical organization of bone begins at the nanoscale. *Science* 360:eaao2189. doi: 10.1126/science.aao2189

Rodan, G. A. (1998). Commentary bone homeostasis. *Commentary* 95, 13361–13362.

Rutkovskiy, A., Stensløkken, K.-O., and Vaage, I. J. (2016). Osteoblast differentiation at a glance. *Med. Sci. Monit. Basic Res.* 22, 95–106. doi: 10.12659/msmbr.901142

Shekaran, A., Sim, E., Tan, K. Y., Chan, J. K. Y., Choolani, M., Reuveny, S., et al. (2015). Enhanced in vitro osteogenic differentiation of human fetal MSCs attached to 3D microcarriers versus harvested from 2D monolayers. *BMC Biotechnol.* 15:218. doi: 10.1186/s12896-015-0219-218

Siffert, R. S. (1951). The role of alkaline phosphatase in osteogenesis. *J. Exp. Med.* 93, 415–426. doi: 10.1084/jem.93.5.415

Sun, X., Su, W., Ma, X., Zhang, H., Sun, Z., and Li, X. (2018). Comparison of the osteogenic capability of rat bone mesenchymal stem cells on collagen, collagen/hydroxyapatite, hydroxyapatite and biphasic calcium phosphate. *Regen. Biomater.* 5, 93–103. doi: 10.1093/rb/rbx018

Tertuliano, O. A., and Greer, J. R. (2016). The nanocomposite nature of bone drives its strength and damage resistance. *Nat. Mater.* 15, 1195–1202. doi: 10.1038/nmat4719

Thrivikraman, G., Athirasala, A., Gordon, R., Zhang, L., Bergan, R., Keene, D. R., et al. (2019). Rapid fabrication of vascularized and innervated cell-laden bone models with biomimetic intrafibrillar collagen mineralization. *Nat. Commun.* 10:3520. doi: 10.1038/s41467-019-11455-8

Thula, T. T., Svedlund, F., Rodriguez, D. E., Podschun, J., Pendi, L., and Gower, L. B. (2011). Mimicking the nanostructure of bone: composition of polymeric process-dorecting agents. *Polym. Basel* 3, 10–35. doi: 10.3390/polym3010010. Mimicking

Tsao, Y. T., Huang, Y. J., Wu, H. H., Liu, Y. A., Liu, Y. S., and Lee, O. K. (2017). Osteocalcin mediates biomineralization during osteogenic maturation in human mesenchymal stromal cells. *Int. J. Mol. Sci.* 18:159. doi: 10.3390/ijms18010159

van Gaalen, S. M., Kruyt, M. C., Geuze, R. E., de Bruijn, J. D., Alblas, J., and Dhert, W. J. A. (2010). Use of fluorochrome labels in in vivo bone tissue engineering research. *Tissue Eng. Part B. Rev.* 16, 209–217. doi: 10.1089/ten.teb.2009.0503

Wang, Y., Hua, Y., Zhang, Q., Yang, J., Li, H., Li, Y., et al. (2018). Using biomimetically mineralized collagen membranes with different surface stiffness to guide regeneration of bone defects. *J. Tissue Eng. Regen. Med.* 12, 1545–1555. doi: 10.1002/term.2670

Wang, Y., Van Manh, N., Wang, H., Zhong, X., Zhang, X., and Li, C. (2016). Synergistic intrafibrillar / extrafibrillar mineralization of collagen scaffolds based on a biomimetic strategy to promote the regeneration of bone defects. *Int. J. Nanomed.* 11, 2053–2067.

Xu, S., Qiu, Z., Wu, J., Kong, X., Weng, X., Cui, F., et al. (2016). Osteogenic differentiation gene expression profiling of hMSCs on hydroxyapatite and mineralized collagen. *Tissue Eng. Part A* 22, 170–182. doi: 10.1089/ten.tea.2015.0237

Ye, B., Luo, X., Li, Z., Zhuang, C., Li, L., Lu, L., et al. (2016). Rapid biomimetic mineralization of collagen fibrils and combining with human umbilical cord mesenchymal stem cells for bone defects healing. *Mater. Sci. Eng. C* 68, 43–51. doi: 10.1016/j.msec.2016.05.104

Zhang, Z., Li, Z., Zhang, C., Liu, J., Bai, Y., Li, S., et al. (2018). Biomimetic intrafibrillar mineralized collagen promotes bone regeneration via activation of the Wnt signaling pathway. *Int. J. Nanomed.* 13, 7503–7516.

**Conflict of Interest:** The authors declare that the research was conducted in the absence of any commercial or financial relationships that could be construed as a potential conflict of interest.

# Advantages of publishing in Frontiers

**OPEN ACCESS**
Articles are free to read for greatest visibility and readership

**FAST PUBLICATION**
Around 90 days from submission to decision

**HIGH QUALITY PEER-REVIEW**
Rigorous, collaborative, and constructive peer-review

**TRANSPARENT PEER-REVIEW**
Editors and reviewers acknowledged by name on published articles

**Frontiers**
Avenue du Tribunal-Fédéral 34
1005 Lausanne | Switzerland

**Visit us:** www.frontiersin.org
**Contact us:** frontiersin.org/about/contact

**REPRODUCIBILITY OF RESEARCH**
Support open data and methods to enhance research reproducibility

**DIGITAL PUBLISHING**
Articles designed for optimal readership across devices

**FOLLOW US**
@frontiersin

**IMPACT METRICS**
Advanced article metrics track visibility across digital media

**EXTENSIVE PROMOTION**
Marketing and promotion of impactful research

**LOOP RESEARCH NETWORK**
Our network increases your article's readership